Satyajit Patel
C. H. Solanki
Krishna R. Reddy
Sanjay Kumar Shukla   *Editors*

Proceedings of the Indian Geotechnical Conference 2019

IGC–2019 Volume I

Springer

Lecture Notes in Civil Engineering

Volume 133

Lecture Notes in Civil Engineering (LNCE) publishes the latest developments in Civil Engineering - quickly, informally and in top quality. Though original research reported in proceedings and post-proceedings represents the core of LNCE, edited volumes of exceptionally high quality and interest may also be considered for publication. Volumes published in LNCE embrace all aspects and subfields of, as well as new challenges in, Civil Engineering. Topics in the series include:

- Construction and Structural Mechanics
- Building Materials
- Concrete, Steel and Timber Structures
- Geotechnical Engineering
- Earthquake Engineering
- Coastal Engineering
- Ocean and Offshore Engineering; Ships and Floating Structures
- Hydraulics, Hydrology and Water Resources Engineering
- Environmental Engineering and Sustainability
- Structural Health and Monitoring
- Surveying and Geographical Information Systems
- Indoor Environments
- Transportation and Traffic
- Risk Analysis
- Safety and Security

To submit a proposal or request further information, please contact the appropriate Springer Editor:

– Pierpaolo Riva at pierpaolo.riva@springer.com (Europe and Americas);
– Swati Meherishi at swati.meherishi@springer.com (Asia - except China, and Australia, New Zealand);
– Wayne Hu at wayne.hu@springer.com (China).

All books in the series now indexed by Scopus and EI Compendex database!

More information about this series at http://www.springer.com/series/15087

Satyajit Patel · C. H. Solanki · Krishna R. Reddy ·
Sanjay Kumar Shukla
Editors

Proceedings of the Indian Geotechnical Conference 2019

IGC-2019 Volume I

Editors
Satyajit Patel
Department of Applied Mechanics
Sardar Vallabhbhai National Institute
of Technology
Surat, India

C. H. Solanki
Department of Applied Mechanics
Sardar Vallabhbhai National Institute
of Technology
Surat, India

Krishna R. Reddy
Department of Civil, Materials
and Environmental Engineering
University of Illinois
Chicago, IL, USA

Sanjay Kumar Shukla
Department of Civil Engineering
Edith Cowan University
Joondalup, WA, Australia

Preface

The Indian Geotechnical Society, Surat Chapter, and Sardar Vallabhbhai National Institute of Technology (SVNIT), Surat, India, organized the Indian Geotechnical Conference (IGC) in Surat during 19–21 December 2019. The main theme of the conference was "GeoINDUS: Geotechnics for INfrastructure Development and UrbaniSation". The sub-themes of the conference included:

1. Characterization of Geomaterials and Physical Modelling
2. Foundations and Deep Excavations
3. Soil Stabilization and Ground Improvement
4. Geoenvironmental Engineering and Waste Material Utilization
5. Soil Dynamics and Earthquake Geotechnical Engineering
6. Earth Retaining Structures, Dams and Embankments
7. Slope Stability and Landslides
8. Transportation Geotechnics
9. Geosynthetics Applications
10. Computational, Analytical and Numerical Modelling
11. Rock Engineering, Tunnelling and Underground Constructions
12. Forensic Geotechnical Engineering and Case Studies
13. Others Topics: Behaviour of Unsaturated Soils, Offshore and Marine Geotechnics, Remote Sensing and GIS, Field Investigations, Instrumentation and Monitoring, Retrofitting of Geotechnical Structures, Reliability in Geotechnical Engineering, Geotechnical Education, Codes and Standards and other relevant topics.

The proceedings of this conference consists of selected papers presented at the conference. The proceedings is divided into six volumes, including a special volume with all keynote/invited presentations.

We sincerely thank all the authors who have contributed their papers to the conference proceedings. We also thank all the reviewers who have been instrumental in giving their valuable inputs for improving the quality of the final papers. We greatly appreciate and thank the student volunteers, especially Vemula Anand Reddy, Mohit Mistry, Rahul Pai, Manali Patel, Rohan Deshmukh, Hrishikesh Shahane, Anand M. Hulagabali, Jiji Krishnan and Bhavita Dave, for their unwavering support that was instrumental in preparation of this proceedings. Finally, thanks to the Springer team for their support and full cooperation for publishing six volumes of this IGC-2019 proceedings.

<div align="right">

Editors

Satyajit Patel

C. H. Solanki

Krishna R. Reddy

Sanjay Kumar Shukla

</div>

Surat, India

Surat, India

Chicago, USA

Joondalup, Australia

Contents

About the Editors

Dr. Satyajit Patel is Associate Professor at the Civil Engineering Department, Sardar Vallabhbhai National Institute of Technology, Surat, India. His research area includes utilization of industrial solid wastes in civil engineering constructions, geoenvironmental issues, soil stabilization, ground improvement, and geosynthetics for road pavements. He has published 13 journal papers and presented 7 research papers internationally. He has guided more than 29 M.Tech. students and 9 students are currently pursuing their Ph.D. under his guidance. He is a life member of Indian Geotechnical Society, Institution of Engineers (India), and Indian Road Congress (IRC). He has received a research grant from the Department of Science and Technology, Government of India.

Dr. C. H. Solanki is Professor (Geotechnical Engineering) at the Civil Engineering Department, Sardar Vallabhbhai National Institute of Technology, Surat, India. He has guided 50 postgraduate dissertations and 16 Ph.D. thesis and he is currently supervising 11 Ph.D. research scholars. He has published 165 research papers in the reputed national, international journals and conferences. Dr. Solanki received the "Shri. M. S. Jain Biannual Award" for the Best Paper in IGC 2013, Prof. Dinesh Mohan Award in IGC 2017 and "Distinguished Faculty Award" form The Venus International Faculty Awards-2016. He has organized 20 national level events including STTP, FDP, conferences and seminars and he was the chairman for the Indian Geotechnical Conference (IGC 2019) held at Surat, Gujarat. Dr. Solanki has been elected as a member

of executive committee of IGS for the terms (2015–2022). His research interests include subsoil characteristics, predictions in geotechnical engineering, soil dynamics, ground improvement and geoenvironmental engineering. He has given 50 expert talks throughout India and abroad. He is a life member of Indian Geotechnical Society, Indian Society for Technical Education (ISTE), and Institution of Engineers (India).

Dr. Krishna R. Reddy is Professor of Civil and Environmental Engineering, Director of Sustainable Engineering Research Laboratory, and also Director of the Geotechnical and Geoenvironmental Engineering Laboratory at the University of Illinois at Chicago, USA. He received his Ph.D. in Civil Engineering from the Illinois Institute of Technology, Chicago, USA. Dr. Reddy has over 28 years of teaching, consulting, and research experience in the fields of civil engineering, geotechnical and geoenvironmental engineering, environmental engineering, and sustainable and resilient engineering. He is the author of 4 books, 246 journal papers, 21 edited books/conference proceedings, 22 book chapters, and 225 full conference papers. He has received several awards for excellence in research and teaching, including the ASCE Wesley W. Horner Award, ASTM Hogentogler Award, UIC Distinguished Researcher Award, the University of Illinois Scholar Award, and the University of Illinois Award for Excellence in Teaching.

Dr. Sanjay Kumar Shukla is the Founding Research Group Leader (Geotechnical and Geoenvironmental Engineering) at the Edith Cowan University, Perth, Australia. He is the Founding Editor-in-Chief of the International Journal of Geosynthetics and Ground Engineering. He holds the Distinguished Professorship in Civil Engineering at Delhi Technological University, Delhi, VIT University, Vellore, Amity University, Noida, Chitkara University, Himachal Pradesh and V. R. Siddhartha Engineering College, Vijayawada, India. He graduated in Civil Engineering from BIT Sindri, India, and earned his M.Tech. in Civil (Engineering Geology) Engineering and Ph.D. in Civil (Geotechnical) Engineering from the Indian Institute of Technology (IIT) Kanpur, India. His primary areas of research interest

include geosynthetics and fibres for sustainable developments, ground improvement techniques, utilization of wastes in construction, earth pressure and slope stability, environmental, mining and pavement geotechnics, and soil–structure interaction. He is an author/editor of 15 books, including 7 textbooks, and more than 260 research papers, including 160 refereed journal papers. He has been honoured with several awards, including IGS Award 2018 by the International Geosynthetics Society, USA, in recognition of outstanding contribution to the development and use of geosynthetics. He is a fellow of Engineers Australia, Institution of Engineers (India), and Indian Geotechnical Society, and a member of American Society of Civil Engineers, International Geosynthetics Society, and several other professional bodies.

Behaviour of Geosynthetics Clay Liner Under Direct Shear Test

Aditya Kumar Bhoi, Sunil Kumar Ahirwar, and Jnanendra Nath Mandal

Abstract Geosynthetics clay liner system is a key component of the engineered landfill. Both the internal and interface strengths of geosynthetics clay liner are very important for evaluating landfill stability. This paper presents a study on interface shear strength behaviour between geosynthetics clay liner and sand, and geosynthetics clay liner and Powai soil making use of a direct shear test. The experiments were carried out using dry state and submerged state of sand, and optimum moisture content and submerged condition of Powai soil. The interface shear strength of geosynthetics clay liner and sand, and geosynthetics clay liner and Powai soil found to be lower than the corresponding shear strength of sand and Powai soil. The apparent adhesion was increased, and interface friction angle was reduced during submerged condition.

Keywords Geosynthetics clay liner · Interface shear strength · Direct shear test

1 Introduction

Liner system is one of the most essential parts of the engineered landfill. The liner served as a hydraulic barrier to entrap the leachate within the landfill, with an aim to save groundwater from being polluted [1, 2]. Geosynthetics clay liners (GCLs) are one of the most prominent products in modern era to serve as liner, which is made

A. K. Bhoi (✉) · S. K. Ahirwar · J. N. Mandal
Department of Civil Engineering, IIT Bombay, Mumbai 400076, India
e-mail: bhoi.aditya@iitb.ac.in

S. K. Ahirwar
e-mail: sunilahirwar@civil.iitb.ac.in

A. K. Bhoi
Department of Civil Engineering, IGIT Sarang, Sarang, Odisha 759146, India

S. K. Ahirwar
Civil Engineering and Applied Mechanics Department, SGSITS, Indore, Madhya Pradesh 452003, India

up of bentonite, sandwiched between two geotextiles [3]. A landfill liner generally sandwiched between native/in situ soil and leachate collection system. In situ soil compacted to form subbase soil of landfill. Rounded stone and sand are commonly used as drainage materials in leachate collection system due to their high hydraulic conductivity [4]. Many landfills fail due to failure of liner system; hence, many research scholars have investigated the interface shear strength [5–12]. But there is limited literature available on effect of submergence on interface shear strength [13]. Therefore, it is necessary to refine the knowledge of interface strength between geosynthetics clay liner (GCL) and different types of soils [i.e. sand (*S*) and Powai soil (PS)] in submerged condition. This paper presents a study on effect of submergence on interface shear strength behaviour between geosynthetics clay liner (GCL) and sand (*S*) (i.e. GCL/*S*), and geosynthetics clay liner (GCL) and Powai soil (PS) (i.e. GCL/PS).

2 Testing Materials

2.1 Powai Soil

Locally available silty soil commonly known as Powai soil, obtained from IIT Bombay campus in Maharashtra, was used in this study. The specific gravity of Powai soil was 2.46 as per IS:2720 (Part III/Sec 1) 1980 [14]. The grain size distribution curve is depicted in Fig. 1. It contains 3% coarse sand size particles, 16% medium sand size particles, 26% fine sand size particles, 38% silt size particles and 17% clay size particles [15]. Its liquid limit, plastic limit and plasticity index were found out
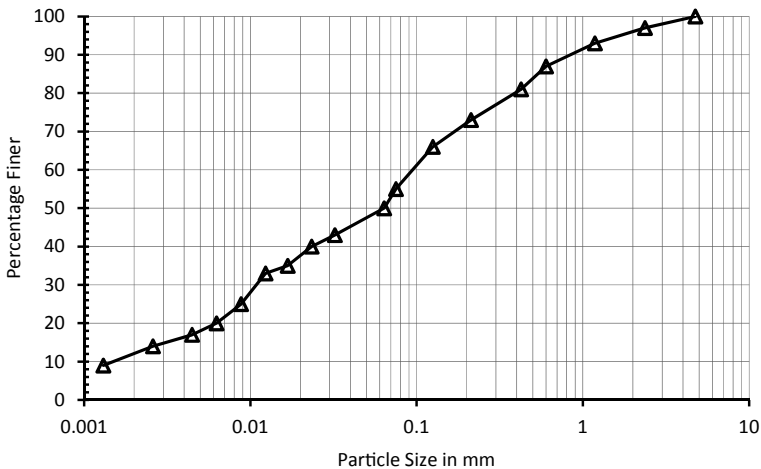
Fig. 1 Grain size distribution curve of Powai soil

to be 39%, 27% and 12%, respectively [16]. The mean particle size (D_{50}), effective particle size (D_{10}), particle size finer than 30% (D_{30}) and particle size finer than 60% (D_{60}) found out to be 0.065 mm, 0.0015 mm, 0.01 mm and 0.095 mm, respectively. The coefficient of curvature (C_c) was 70.17, and the coefficient of uniformity (C_u) was 63.33. The Powai soil was classified as inorganic silt (ML) [17]. The Proctor compaction characteristics were carried out as per IS:2720 (Part VII) 1980 [18]. The maximum dry density was 1.69 g/cm^3, with an optimum moisture content of 18%.

2.2 Sand

In the present study, commercially available sand from market was used. The specific gravity of the sand was 2.64 as per IS:2720 (Part III/Sec 2) 1980 [19]. The particle size distribution curve is depicted in Fig. 2. It contains about 98% medium sand size particles and 2% silt size particles [15]. The mean particle size (D_{50}), effective particle size (D_{10}), particle size finer than 30% (D_{30}) and particle size finer than 60% (D_{60}) found out to be 1.00 mm, 0.67 mm, 0.80 mm and 1.20 mm, respectively. The coefficient of curvature (C_c) was 0.99, and the coefficient of uniformity (C_u) was 1.79. The sand was classified as poorly graded sand (SP) [17]. The density index was carried out as per IS:2720 (Part 14) 1983 [20]. The maximum density, minimum density, maximum void ratio and minimum void ratio were found out to be 1.53 g/cm^3, 1.32 g/cm^3, 0.96 and 0.69, respectively.
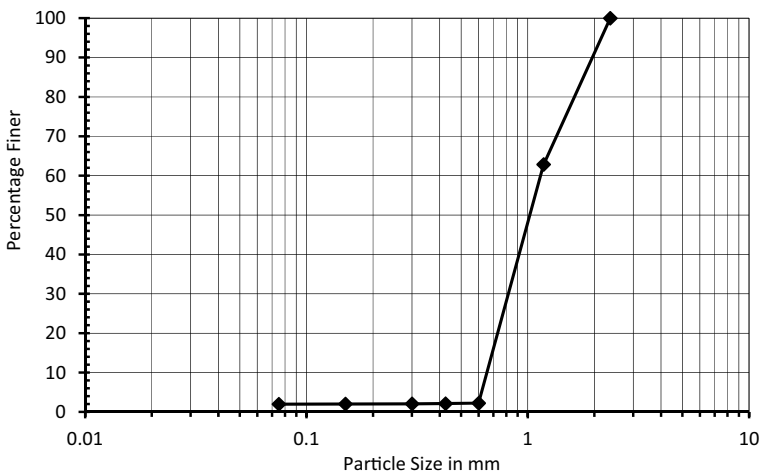
Fig. 2 Grain size distribution curve of sand

2.3   *Geosynthetics Clay Liners (GCLs)*

Geosynthetics clay liners (GCLs) with needle-punched non-woven geotextile filled with granular sodium bentonite were used in this study. The mass per unit area of GCL was 3800 g/m^2 as per ASTM D 5993-18 [21]. Its thickness was about 5.95 mm [22]. It contains granular sodium bentonite, and the free swell index of sodium bentonite was 24 ml/2 gm [23]. The tensile properties were carried out as per ASTM D 4595-17 [24]. The tensile strength in machine direction and cross-machine direction was found out to be 11.0 kN/m and 9.0 kN/m, respectively.

3   Testing Methods

A direct shear device of size 60 mm × 60 mm was used to measure the shear strength parameters of the soil to soil and geosynthetics clay liners to soil interface [25]. Figure 3 shows the cross-sectional schematic view of sand to sand (or Powai soil to Powai soil) and GCL/S (or GCL/PS) sample in direct shear box.

The samples were prepared in two batches. The aim of the first batch was to find the angle of internal friction of sand to sand and Powai soil to Powai soil. In case of angle of internal friction of sand to sand, both the lower half and upper half of the direct shear box were filled with sand with 56% relative density (1.43 g/cm^3) (see Fig. 3a). Similarly, for the case of angle of internal friction of Powai soil to Powai soil both the lower half and upper half of the direct shear box were filled with Powai soil with a dry density of 1.52 g/cm^3 and 15% moisture content (i.e. 90% of the maximum dry density) (see Fig. 3a). These (both sand to sand and Powai soil to Powai soil) samples were tested under two conditions, i.e. dry and submerged condition. In case of dry condition, the sample was sheared just after preparation of sample. But, in submerged condition, the soil sample was kept submerged for 24 h in water jacket before shearing. For every sand to sand (or Powai soil to Powai soil), three tests were conducted by applying normal stresses of 50 kPa, 100 kPa and 150 kPa. Tests were identified so that a sample tested in dry condition with a normal stress of 50 kPa was represented as 50(D) and the other sample tested in submerged condition was denoted as 50(W).
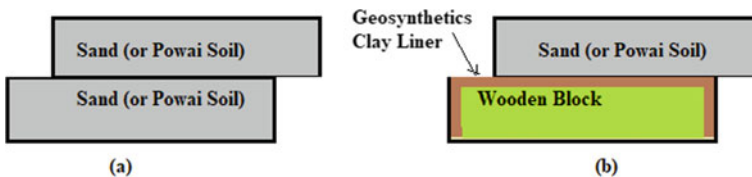
Fig. 3 Schematic diagrams for **a** sand to sand [or Powai soil to Powai soil] and **b** geosynthetics clay liner to sand [or geosynthetics clay liner to Powai soil] direct shear tests

The aim of the second batch was to find out the interface shear strength of GCL/Sand interface and GCL/Powai soil interface. In second batch of samples, a wooden box warped with GCL on its top was placed in the lower half of shear box (see Figs. 3b and 4a). And the top half was filled with sand with 56% relative density for GCL/S interface system (see Fig. 3b). Similarly, Powai soil was compacted in upper half of shear box to 90% of the maximum dry density for GCL/PS interface (see Figs. 3b, 4b, c). For both GCL/S and GCL/PS interfaces, three tests were conducted by applying normal stresses of 50 kPa, 100 kPa and 150 kPa. These (both GCL/S and GCL/PS) samples were tested under dry and submerged condition, similar to first batch (see Fig. 4d).

A gap of 1 mm was maintained between lower half and upper half of shear boxes for all tests in order to avoid friction between the lower half and upper half. The upper half containing sand or Powai soil remained constant, whereas the lower half

(a)   Placement of GCL in lower half

(b)   Placement of Powai soil in upper half

(c)   GCL/Powai soil after shearing

(d)   water jacket of GCL/Sand
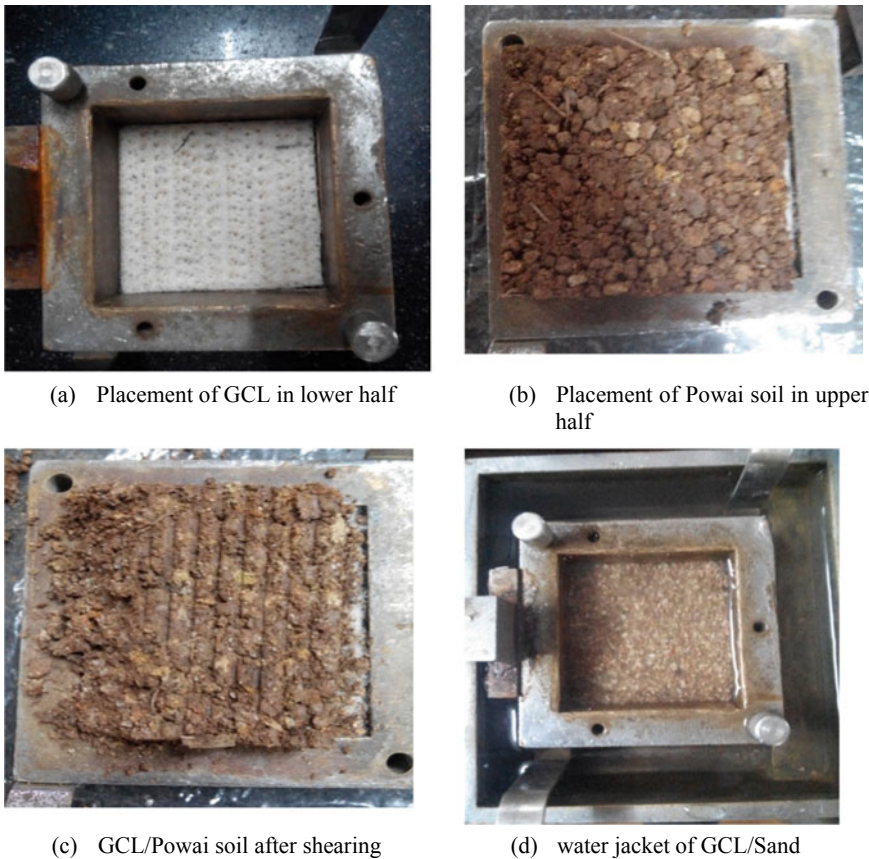
Fig. 4 Interface and internal shear test specimen arrangement in the shear box

of shear box was moved with a strain rate of 1 mm/min. The shear force and horizontal displacement were measured by a proving ring and dial gauge, respectively.

4 Results and Discussion

4.1 GCL/Sand Interface Shear Strength

The variation of shear stress of sand to sand with different horizontal strains, obtained from the direct shear test, is depicted in Fig. 5a. From Fig. 5a, it is clear that sand in dry condition attained peak shear stress (35.32 kPa) at 1.5% horizontal strain, when sheared under 50 kPa normal stress. Similarly, the magnitude of peak stress is 71 kPa and reached at 2% horizontal strain, when sheared under 100 kPa normal stress. It is also clear that the magnitude of peak stress is 105 kPa and reached at 2.5% horizontal strain, when sheared under 150 kPa normal stress. The stress–strain curves of submerged sand are similar to stress–strain curve of dry sand under identical normal stress. The variation of shear stress of sand with normal stress, obtained from the direct shear test, is presented in Fig. 5b. From Fig. 5b, it is clear that sand is a cohesionless material; hence, its shear strength is mainly by governed by angle of internal friction. The cohesion and angle of internal friction of sand at 56% relative density are found to be 0 kPa and 35.22°, respectively, under dry condition. But, when the sand sample was kept submerged for 24 h in water jacket before shearing, it develops a small apparent cohesion (1 kPa). The effect of submergence on sand is negligible.

Figure 6a, b represents the stress–strain curve and failure envelopes of GCL/sand interface. From Fig. 6a, it is observed that the peak value of shear stress is reached at 2.5% horizontal strain for the normal stress of 50 kPa, at 3% horizontal strain for the normal stress of 100 kPa and at 3.5% horizontal strain for the normal stress of 150 kPa for both dry and submerged conditions. The magnitude of interface peak

(a) Stress–strain curve   **(b)** Failure envelopes
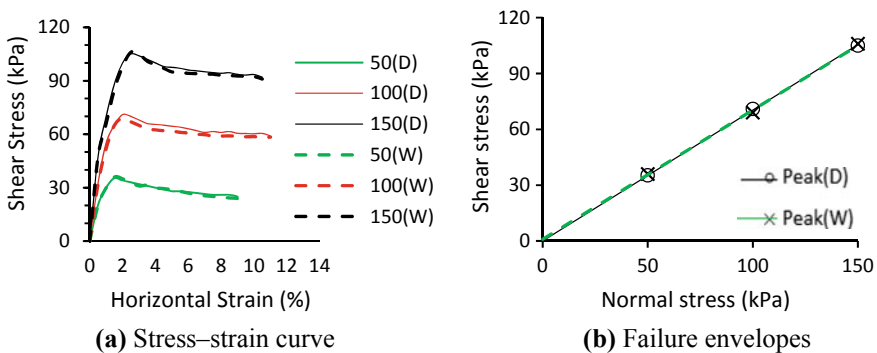
Fig. 5 Direct shear test of sand to sand

(a) Stress–strain curve

(b) Failure envelopes
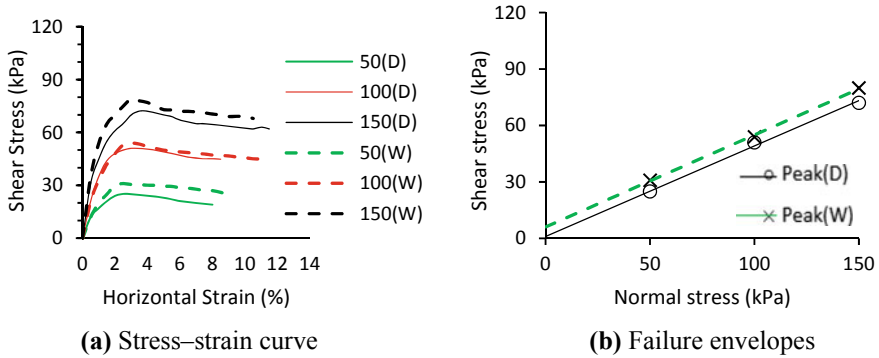
Fig. 6 Direct shear test of GCL/sand interface

shear stress of GCL/sand in dry condition is 25.01 kPa, when sheared under the normal stress of 50 kPa. And, the magnitude of interface peak shear stress turns out to be 51 kPa and 72.1 kPa, when sheared under 100 kPa and 150 kPa, respectively. But, the magnitude of peak shear stress of GCL/sand interface under 50 kPa, 100 kPa and 150 kPa normal stress turns out to be 31 kPa, 54 kPa and 80 kPa, respectively. This indicates that the shear stress of GCL/sand interface increases when it subjected to submerged condition.

It is observed that the interface friction angle remains nearly same for both dry and submerged conditions (i.e. 25.70° for dry condition and 26.10° for submerged condition), but the value of adhesion increased slightly for submerged condition. The increased value of adhesion may be due to hydration of the bentonite [26, 27]. The peak shear stress values in submerged condition are slightly higher than dry condition, because hydration of the bentonite in submerged condition gives extra adhesion to GCL/S interface.

4.2   GCL/Powai Soil Interface Shear Strength

The stress–strain curve of Powai soil to Powai soil, obtained from the direct shear test, is shown in Fig. 7a. From Fig. 7a, it is clear that Powai soil in dry state attained peak shear stress (42 kPa) at 4% horizontal strain, when sheared under 50 kPa normal stress. Similarly, the magnitude of peak stress is 72 kPa and reached at 5.5% strain, when sheared under 100 kPa normal stress. It is also clear that the magnitude of peak stress is 104 kPa and reached at 7.5% horizontal strain, when sheared under 150 kPa normal stress. The magnitude of peak shear stress under submerged condition turns out to be lower than the dry condition. From Fig. 7a, it can be observed that the magnitude of peak shear stress is 32 kPa and appeared at 5% horizontal strain, when sheared under 50 kPa normal stress. Similarly, when the Powai soil sample sheared under 100 kPa normal stress, peak value of shear stress turns out to be 61 kPa at

(a) Stress–strain curve   **(b)** Failure envelopes
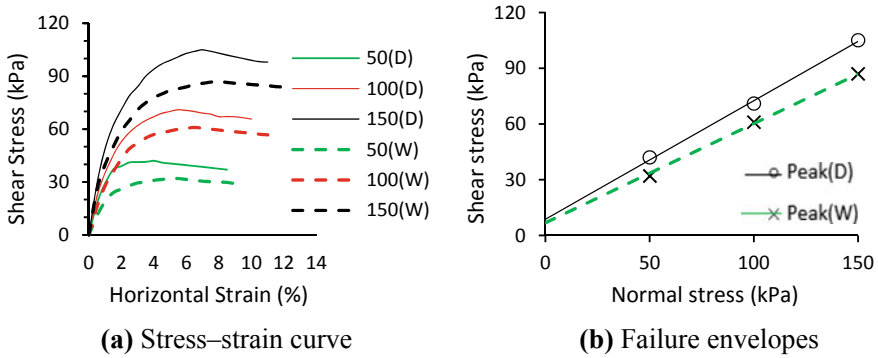
Fig. 7 Direct shear test of Powai soil to Powai soil

6.5% horizontal strain. It is also clear that the magnitude of peak stress is 87 kPa and reached at 8% horizontal strain, when sheared under 150 kPa normal stress. Failure envelopes of Powai soil to Powai soil in dry and submerged conditions are presented in Fig. 7b. The cohesion and angle of internal friction of Powai soil are 8.81 kPa and 32.33° when tested under dry condition. But, the cohesion and angle of internal friction of Powai soil decrease to 6.9 kPa and 28° when subjected to submerged condition.

The stress–strain curves and failure envelopes of GCL/Powai soil interface are shown in Fig. 8a, b, respectively. When the sample sheared under a normal stress of 50 kPa, its peak value of shear stress becomes 29 kPa, at 4% strain. Similarly, for normal stress of 100 kPa and 150 kPa the shear stress becomes 54 kPa and 74 kPa, respectively. But, in case of submerged condition the peak value of shear stress occurs at little bit higher strain than dry condition (i.e. 8%, 7% and 5% horizontal strain for the normal stress of 150 kPa, 100 kPa and 50 kPa, respectively).

(a) Stress–strain curve   **(b)** Failure envelopes
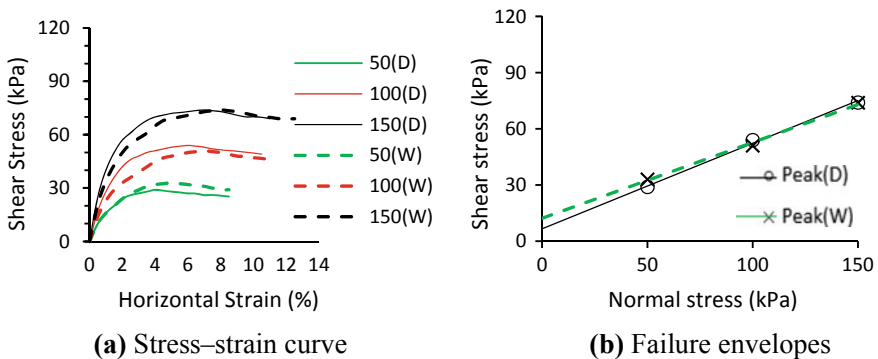
Fig. 8 Direct shear test of GCL/Powai soil interface

Table 1 Internal friction angle (Φ), interfacial friction angle (δ_{GCL}) and friction efficiency factors (E_Φ) values of GCL/sand interface and GCL/Powai soil interface

Soil type	Φ (°)	δ_{GCL} (°)	E_Φ
Sand (dry)	35.22	25.70	0.68
Sand (submerged)	34.90	26.10	0.70
Powai soil (dry)	32.33	24.57	0.72
Powai soil (submerged)	28.00	22.10	0.76

Trends depicted in Fig. 8b indicate that for Powai soil samples with GCL, the interface apparent adhesion increases, but the interfacial friction angle decreases, when it subjected to submerged condition. The results are similar to the results of the interface of GCL/clayey soil from the direct shear tests conducted by Chai and Saito [13].

4.3   Friction Efficiency Factors (E$_\Phi$)

The friction efficiency factors (E_Φ) were evaluated as per Mohr–Coulomb principle by using peak friction angle (Φ) of soil and interfacial friction angle (δ_{GCL}) of GCL/soil interface.

$$\text{Friction efficiency factors}(E_\Phi) = (\tan(\delta_{GCL}))/(\tan(\Phi)) \tag{1}$$

The peak friction angle (Φ) and interfacial friction angle (δ_{GCL}) evaluated for sand and Powai soil with GCL are presented in Table 1. It can be noted from the table that the friction efficiency factors (E_Φ) for submerged condition are higher than dry condition. These ranges of friction efficiency factors are consistent with the results obtained by Choudhary and Krishna [28], Lee and Manjunath [29], Evans and Fennick [30], Vaid and Rinnie [31], and Cazzuffi et al. [32].

5   Conclusion

This study presented the effect of submergence on the behaviour of GCL/S and GCL/PS interface through a series of laboratory tests. Considering the most important strength characteristics of the sand and Powai soil, and the GCL/S and GCL/PS interaction, the following conclusions can be made:

1.   The effect of submergence on sand to sand is minimal, and the angle of internal friction remains almost same for both dry and submerged conditions. But, in case of Powai soil to Powai soil the angle of internal friction reduced by 4°.

2. It has been found that the interface adhesion between GCL and soil (sand or Powai soil) increases significantly, due to hydration of bentonite. The interfacial friction angle (δ_{GCL}) found out to be lower than internal friction angle of soil (sand to sand or Powai soil to Powai soil).

References

1. Koerner, R.M.: Designing with Geosynthetics, 6th edn., Vol. 1. Xlibris Corporation, USA (2012)
2. Mandal, J.N.: Geosynthetics engineering. In: Theory and Practice. Research Publishing, Singapore (2018)
3. Bouazza, A.: Geosynthetic clay liners. Geotext. Geomembr. **20**(1), 3–17 (2002)
4. Townsend, T.G., et al.: Sustainable Practices for Landfill Design and Operation. Springer, Heidelberg (2015)
5. Eid, H.T.: Shear strength of geosynthetic composite systems for design of landfill liner and cover slopes. Geotext. Geomembr. **29**(3), 335–344 (2011)
6. Fox, P.J., Rowland, M.G., Scheithe, J.R.: Internal shear strength of three geosynthetic clay liners. J. Geotech. Geoenviron. Eng. **124**(10), 933–944 (1998)
7. Fox, P.J., Stark, T.D.: State-of-the-art report: GCL shear strength and its measurement. Geosynth. Int. **11**(3), 141–175 (2004)
8. Fox, P.J., Stark, T.D.: State-of-the-art report: GCL shear strength and its measurement – ten-year update. Geosynth. Int. **22**(1), 3–47 (2015)
9. Gilbert, R.B., Fernandez, F., Horsfield, D.W.: Shear strength of reinforced geosynthetic clay liner. J. Geotech. Eng. **122**(4), 259–265 (1996)
10. McCartney, J.S., Zornberg, J.G., Swan, J.R.H.: Analysis of a large database of GCL-geomembrane interface shear strength results. J. Geotech. Geoenviron. Eng. **135**(2), 209–223 (2009)
11. Triplett, E.J., Fox, P.J.: Shear strength of HDPE geomembrane/geosynthetic clay liner interfaces. J. Geotech. Geoenviron. Eng. **127**(6), 543–552 (2001)
12. Zornberg, J.G., McCartney, J.S., Swan, J.R.H.: Analysis of a large database of GCL internal shear strength results. J. Geotech. Geoenviron. Eng. **131**(3), 367–380 (2005)
13. Chai, J.C., Saito, A.: Interface shear strengths between geosynthetics and clayey soils. Int. J. Geosynth. Ground Eng. **2**(19), 1–9 (2016)
14. IS:2720 (Part III/Sec 1) 1980: Determination of specific gravity: Fine grained soils. Bureau of Indian Standards, New Delhi (2002)
15. IS:2720 (Part IV) 1985.: Grain size analysis. Bureau of Indian Standards, New Delhi (2006)
16. IS:2720 (Part V) 1985: Determination of liquid and plastic limit. Bureau of Indian Standards, New Delhi (2006)
17. IS:1498-1970: Classification and identification of soils for general engineering purposes. Bureau of Indian Standards, New Delhi (2007)
18. IS:2720 (Part VII) 1980: Determination of water content-dry density relation using light compaction. Bureau of Indian Standards, New Delhi (2011)
19. IS:2720 (Part III/Sec 2) 1980: Determination of specific gravity: Fine, medium and coarse-grained soils. Bureau of Indian Standards, New Delhi (2002)

20. IS:2720 (Part 14) 1983: Determination of density index (relative density) of cohesionless soils. Bureau of Indian Standards, New Delhi (2006)
21. ASTM D5993-18: Standard Test Method for Measuring Mass per Unit Area of Geosynthetic Clay Liners. ASTM International, West Conshohocken, USA (2018)
22. ASTM D1777-96: Standard Test Method for Thickness of Textile Materials. ASTM International, West Conshohocken, USA (2015)
23. ASTM D5890-19: Standard Test Method for Swell Index of Clay Mineral Component of Geosynthetic Clay Liners. ASTM International, West Conshohocken, USA (2019)
24. ASTM D4595-17: Standard Test Method for Tensile Properties of Geotextiles by the Wide-Width Strip Method. ASTM International, West Conshohocken, USA (2017)
25. IS:2720 (Part 13) 1986: Direct shear test. Bureau of Indian Standards, New Delhi (2002)
26. Vukelic, A., Szavits-Nossan, A., Kvasnicka, P.: The influence of bentonite extrusion on shear strength of GCL/geomembrane interface. Geotext. Geomembr. **26**(1), 82–90 (2008)
27. Chen, Y.-M., Lin, W.-A., Zhan, T.L.T.: Investigation of mechanisms of bentonite extrusion from GCL and related effects on the shear strength of GCL/GM interfaces. Geotext. Geomembr. **28**(1), 63–71 (2010)
28. Choudhary, A.K., Krishna, A.M.: Experimental investigation of interface behaviour of different types of granular soil/geosynthetics. Int. J. Geosynth. Ground Eng. **2**(4), 1–11 (2016)
29. Lee, K.M., Manjunath, V.R.: Soil–geotextile interface friction by direct shear tests. Can. Geotech. J. **37**(1), 238–252 (2000)
30. Evans, M.D., Fennick, T.J.: Geosynthetic/soil interface friction angles using a rotation shear device. Geotech. Test. J. **18**(2), 271–275 (1995)
31. Vaid, Y.P., Rinnie, N.: Geomembrane coefficients of interface friction. J. Geosynth. Int. **2**(1), 309–325 (1995)
32. Cazzuffi, D., Picarelli, L., Ricciuti, A., Rimoldi, P.: Laboratory investigations on the shear strength of geogrid reinforced soils. ASTM Spec. Tech. Publ. **1190**, 119–137 (1993)

Effect of Saturation and Cementation on the Stiffness of Gypsiferous Soils

Raghava A. Bhamidipati, **Michael E. Kalinski**, and **L. Sebastian Bryson**

Abstract Gypsiferous soils are found in several arid regions of the world and are known to cause structural hazards due to their collapsible nature. The collapsibility of gypsiferous soils is dependent on a number of soil parameters and gypsum content is one of the key factors. Gypsum acts as a weak cementing agent in the soils. In terms of macroscale procedures for site suitability investigations, the non-destructive testing methods, using shear-wave velocity measurements, are valuable to quickly characterize the stiffness properties of the sites and subsurface soil conditions. In this study, free-free resonant column testing was used to study the shear-wave velocity patterns of reconstituted specimens of sand and gypsum under different degrees of saturation. An overall increase in stiffness was observed with decrease in degree of saturation. The rise is stiffness was attributed to a combination of cementation and matric suction processes. Cementation was observed in specimens containing gypsum. For soils with less than 30% gypsum content, matric suction was a dominant factor in increasing the stiffness of the soil and cementation effect was not very strong. For soils with gypsum content of 30% or more, an appreciable amount of cementation was observed and matric suction showed little impact. The peaks in shear-wave velocity caused by matric suction were replaced by a plateauing feature. Using the soil water characteristic curve approach, regression relationships were developed to determine the contributions of matric suction and cementation toward the change in stiffness of the soils. The results from this study can be used to predict the stiffness behavior and gypsum content of gypsiferous soils in the field.

Keywords Gypsum · Matric suction · Cementation

R. A. Bhamidipati (✉)
IIT Gandhinagar, Palaj 382355, India
e-mail: jones.kgp@gmail.com

M. E. Kalinski · L. S. Bryson
University of Kentucky, Lexington, KY 40506, USA
e-mail: michael.kalinski@uky.edu

L. S. Bryson
e-mail: sebastian.bryson@uky.edu

1 Introduction

Gypsum-rich soils are often found in arid and semi-arid regions of the world along with calcite and dolomite in the form of evaporites. The mineral gypsum ($CaSO_4.2H_2O$) is soft, light, and moderately soluble in water. Soils in arid and semi-arid regions containing gypsum, calcium carbonate, and other such salts often exhibit an appreciable degree of cementation and suction. These properties have a considerable influence on the engineering behavior of these soils. Gypsum acts as a weak cementing agent and the introduction of water into gypsum soils leads to collapse settlement due to dissolution of gypsum and rearrangement of soil particles. Collapsibility is a major geotechnical concern for gypsum-rich soils and has been widely documented. Structures like irrigation canals and dams have been reported to show major deformations and failures. Many such instances have been reported in Iraq. The deformation of irrigation canals in Ebro Valley, Spain, constructed on gypsiferous loess soils is another prominent example [1]. Fourteen dam sites in the USA have been affected by dissolution of gypsum karst as of 1998 [2].

There is a need to develop non-destructive and non-intrusive tests for rapid assessment of sites with gypsum-rich soils. Geophysical testing methods such as seismic tests are attractive candidates for such tests. Parameters such as *P*-wave and *S*-wave velocities obtained from these tests can be correlated to a number of engineering parameters of the soils. On a laboratory scale, conventionally, fixed-free resonant column testing or the bender element testing methods have been in use for performing low-strain tests on soils. For this study, the free-free resonant column testing (FFRC) method was used, which is a simpler alternative to the conventional fixed-free resonant column test [3]. Tests were conducted on specimens of sand with varying amounts of gypsum and moisture contents. The changes in soil stiffness were measured in terms of their shear-wave velocity (v_s) and small-strain shear modulus (G_{max}). By studying the variations in stiffness profiles, judgments can be made about gypsum content and the physical state of the soil.

The engineering behavior of collapsible and partially cemented soils such as gypsiferous soils has been studied by numerous researchers. Fattah et al. [4] studied the effect of gypsum content on the collapse potential of gypsum soils in Iraq. They found that collapse potential of the soils increased with gypsum content. Al-Marsoumi et al. [5] studied the influence of gypsum content on the shear strength parameters of six different gypsiferous soil samples collected near Basrah, Iraq. They performed triaxial compression and unconfined compressive strength tests and found that the angle of internal friction and cohesion of the soil samples increased with gypsum content up to 20% and decreased thereafter. Haeri et al. [6] studied the effect of cementation on the stiffness of artificially cemented sands.

The impact of cementation and matric suction on the stiffness of sandy soils has been studied by several researchers. Khosravi et al. [7] studied the impact of effective stress on the dynamic shear modulus of unsaturated sand. They used a fixed-free resonant column device with a capacity to apply up to 10 kPa of matric suction to test the effect of normal stress and matric suction on the stiffness of

unsaturated sands. Qian et al. [8] used resonant column testing to study the effect of saturation, grain size, confining pressure, and void ratio on the dynamic properties of sand. Sawangasuriya et al. [9] investigated the nature of small-strain shear modulus of fine-grained compacted subgrade soils. They utilized bender element testing and developed relationships between shear modulus and the net effective confining stress and matric suction using the soil water characteristic curve (SWCC). Rinaldi and Santamarina [10] reported the cementation behavior of unsaturated soil deposits and its contribution toward the increase in small-strain stiffness.

2 Description of This Study

The term 'gypsiferous' is broadly used to describe soils containing at least 2% gypsum [1]. Gypsum is usually found in arid regions, where soils generally have substantial coarse-grained fractions. The natural gypsum content in these soils varies from around less than 10% in the surface layers to as high as 35–70% in the subsoil layers. Considering these aspects, mixtures of poorly graded fine sand and ground commercial gypsum (Allied Custom Gypsum) were reconstituted in the laboratory with different percentages of gypsum by weight. Figure 1 shows the gradation curves of the sand and gypsum used. Five specimens were tested with gypsum contents ranging from 0 to 40%. Cylindrical specimens were prepared by air pluviation method by tamping. The void ratio of the all specimens was kept close to 0.55.

The mixtures were constructed as cylindrical specimens with a 2:1 (length: diameter) aspect ratio using a latex membrane and two plastic end caps. A Ledex 500
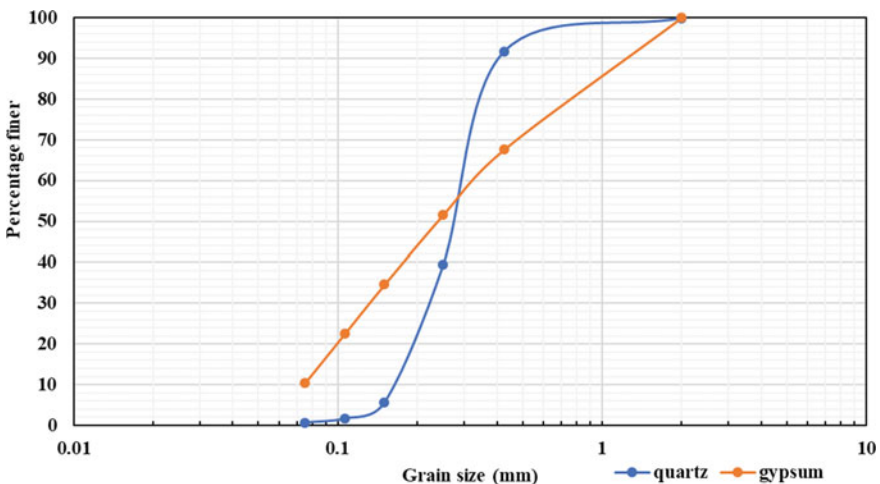
Fig. 1 Grain size distribution of the sand and gypsum used
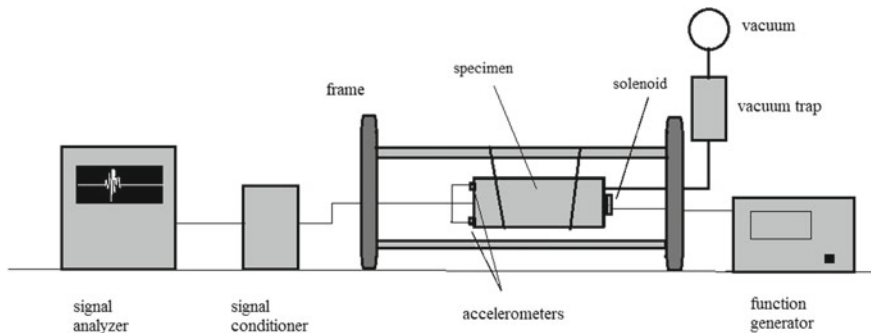
Fig. 2 Free-free resonant column testing arrangement

rotary solenoid was attached to one endcap, and a pair of PCB 353B16 accelerometers was attached to the other endcap across the diameter (Fig. 2). The solenoid, which is driven by a function generator, excites the specimen in the torsional mode by imparting a transient pulse. The time domain torsional excitation of the specimen measured by the accelerometers and the response was converted into the frequency domain. The resonant frequency of the specimen (f_n) was identified as the frequency which produces the maximum torsional acceleration [3]. For this test configuration, v_s is calculated using the relation:

$$v_s = 2 f_n l \tag{1}$$

where l is the length of the specimen in meters, and f_n is in Hz.

The small-strain shear modulus (G_{max}) for the specimens was calculated using the expression:

$$G_{max} = \rho v_s^2 \tag{2}$$

where ρ is the bulk density of the material (in kg/m^3).

Vacuum of 17″ Hg (58 kPa) was applied to one end of the specimen to provide confinement. The specimen was then mounted in a free-free configuration on an assembly of two end plates and supporting rods (Fig. 2). Shear-wave velocity measurements were initially taken on the dry specimen, and then the specimens were saturated by passing water through it, until no further increase in specimen weight was observed. A vacuum trap was attached to the assembly so that no water would escape into the vacuum source. The moisture in the specimens was continually reduced using a combination of vacuum and low pressure air. Low pressure air (5–10 kPa) was required at lower degrees of saturation to dry the specimen. Measurements of resonant frequency (f_n) were taken at varying degrees of saturation and the corresponding v_s and G_{max} values were calculated. Five soils were tested with gypsum contents ranging from 0 to 40%.

3 Results

The tests on the five specimens showed that v_s increased with decreasing degree of saturation ($S\%$). This trend continued up to the residual degree of saturation for the soils which was about 10–20%. Shear-wave velocity was lowest at moisture levels close to saturation. For all the specimens, stiffness increased sharply at saturations of around 10–20%. The increase was very pronounced for the 10% and 20% gypsum mixtures. With further increase in gypsum content, these peaks reduced and were gradually replaced by a plateauing feature. The plots of v_s versus S% for the five tested specimens are shown in Fig. 3. Using the bulk densities of the specimens, the small-strain shear modulus (G_{max}) was calculated. Figure 4 shows the plotos G_{max} versus S% for the specimens. The trends are in agreement with the findings of Qian et al. (1991), who observed an increase in G_{max} for sands with decreasing saturation, using resonant column testing. They found that, for different confining pressures, the maximum stiffness occurred around residual degrees of saturation which was close to 10%.

It was also observed that at low degrees of saturations, the 10% and 20% gypsum mixtures exhibited the highest v_s. Shear-wave velocities as high as 280 m/s were measured at these specific moisture and gypsum combinations. The corresponding G_{max} values for these specimens were as high as 140 MPa, which were around 1.75 times higher than the corresponding G_{max} value for 0% gypsum specimen.

Matric suction is the well established mechanism which contributes to the increase in stiffness of the soils at low moisture contents. Additionally, cementation between
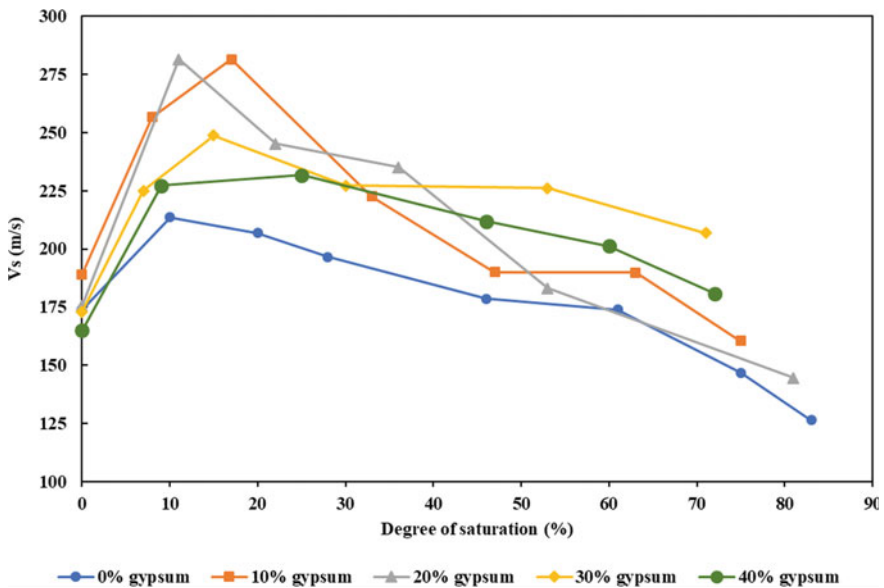
Fig. 3 Measured versus values from free-free resonant column testing
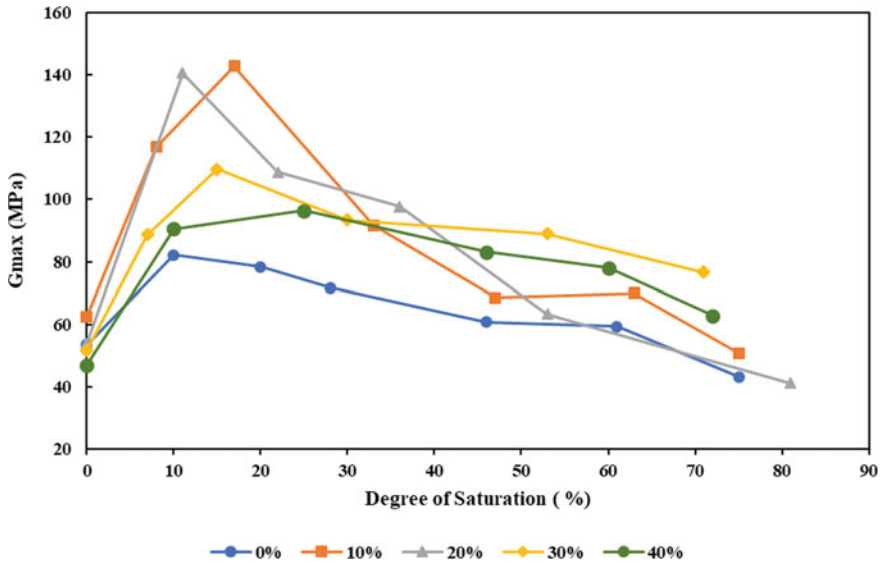
Fig. 4 Calculated G_{max} values from free-free resonant column testing

the gypsum and sand particles also enabled the increase in stiffness of the specimens. The contributions of both these factors vary for different gypsum percentages. Matric suction appeared to be the dominating factor at low gypsum contents as inferred by the distinct peaks in the curve. As the gypsum content was increased, cementation effect was more prominent and the specimens show a tendency to form crusts, causing the peaks to become smaller and less distinct. The cementing effect can also be seen from the fact that the 30 and 40% gypsum specimens possess relatively higher G_{max} values at higher S%.

4   Interpretation

It is necessary to evaluate the relative contributions of matric suction, and cementation toward increase in stiffness had to be estimated for different gypsum percentages. In order to accomplish this, the soil water characteristic curve (SWCC) had to be developed for the sand. The relationship between soil moisture content and the matric suction (ψ) is represented using the SWCC. For this study, an SWCC was constructed for the sand using the Fredlund and Ching model [11]. Using this model, the relationship between volumeric moisture content (θ) and matric suction (ψ) is defined as:

$$\theta = [1 - \ln(1 + \psi/\psi_r)/\ln(1 + 1{,}000{,}000/\psi_r)]$$
$$[\theta_s/\{\ln[\exp(1) + (\psi/a)^n])^m\}] \tag{3}$$

where a, m, and ψ_r are empirical parameters, dependent on the D_{60} of the soil and n = 7.5, for non-plastic soils [12].

The model parameters were chosen from the test data and gradation curve (Fig. 5). It has been shown by researchers that the small-strain shear modulus of soils increases with increase in matric suction [13]. Since matric suction increases with lowering in moisture content, it follows that stiffness also increases with decrease in moisture. The increase in stiffness is however limited till residual moisture content.

The gradation curve (Fig. 1) showed that the D_{60} value was almost the same for both sand and gypsum. As such, the SWCC constructed above was assumed to be valid for gypsum sands as well. The G_{max} values for soils with 0%, 10%, and 30% gypsum were plotted against matric suction and simple regression analyses were performed (Fig. 6) to model the stiffness increase. Since stiffness increase only took place between transition zone moisture and residual moisture, only those data points were chosen for the regression. In other words, ψ values corresponding a saturation range of 10 to 80% were considered for the model. Relationship between G_{max} and ψ were developed in the form of:

$$G_{max} = a \ln(\psi) + b \qquad (4)$$

where 'a' explained the weight of the matric suction term and 'b' represented the contribution of the cementation effect induced by gypsum content. It is seen from Fig. 6 that the parameter 'a' is the highest for the 10% gypsum soil. The parameter 'b' is the highest for the 30% gypsum soil. This quantifies the contribution of matric
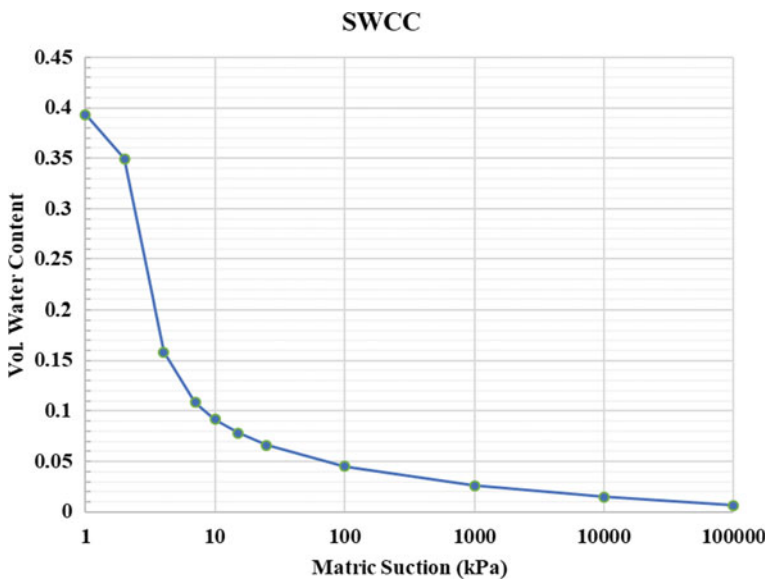
Fig. 5 Soil–water characteristic curve for the test sand
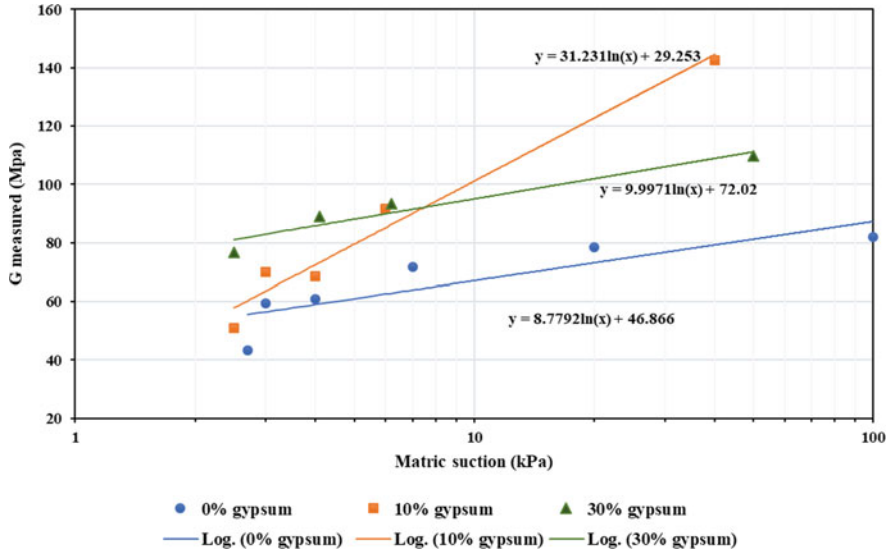
Fig. 6 Regression model for $G_{\max}$ versus matric suction for three gypsum percentages

suction and cementation features toward increase in stiffness at different gypsum concentrations.

At around 10–20% gypsum, the gypsum particles tend to fill the void spaces between the sand particles and the soil matrix becomes stiffer [14]. At greater than 30%, gypsum acts as a dispersing agent and also the cementing action becomes more predominant. With further increase in gypsum concentration, the bulk density of the soil matrix decreases. This is because of the lower specific gravity of gypsum (2.33) in comparison to sand (2.65). As the bulk density gets lowered, it follows from Eq. 2 that the stiffness also decreases with further increase in gypsum.

The matric suction has much pronounced influence on the $G_{\max}$ value at 10% gypsum soil in comparison to 30% gypsum soil as revealed by the steeper slope for the 10% gypsum relationship in Fig. 6. It is also clear that at low matric suction conditions the effect of cementation resulted in higher $G_{\max}$ value. The slope of the 30% curve is nearly same when compared to the 0% gypsum situation. This indicates that by 30% gypsum, the matric suction is just about as good as that for sand alone and whatever increase is obtained in the $G_{\max}$ is on account of cementation effect.

5   Conclusion

The stiffness of reconstituted gypsum sand mixtures was measured at varying degrees of saturation in terms of shear-wave velocity (v_s). The small-strain shear modulus was in turn calculated from the shear-wave velocities. The moisture content of the

sample and the presence of gypsum showed a marked effect on the stiffness of the sand. The following conclusions could be drawn from the study:

- Stiffness increased with decrease in moisture, up to the residual moisture (10–20%) content because of the effect of matric suction.
- The presence of gypsum and water brought about a cementing effect, also leading to a rise in stiffness of the soil.
- At lower gypsum concentrations, of 20% or less, the stiffness of the sand increased steeply with decrease in moisture due to matric suction effect.
- At higher gypsum concentrations (30% or more), the effect of cementation between sand and gypsum particles increases. This is countered by the dispersing action of gypsum and the decreasing unit weight of the soil, leading to a reduction in stiffness.
- The stiffness of gypsiferous sands was in general higher than that of sand without gypsum.

Results of this nature could be used as a basis for conducting non-destructive surface geophysical tests, such as multichannel analysis of surface waves (MASW), to measure the in situ v_s of soils in places where the engineering properties of gypsiferous soils are of concern. From the observed variations v_s trends, a judgement can be made about the gypsum content of the soil. The measurements can also be correlated with geotechnical parameters of soils such as SPT-N value, friction angle, unit weight, and shear strength at places where adequate data or measurements are not available.

References

1. Alphen., J.G.V., Rios Romero., F.D.L.: Gypsiferous soils: notes on their characteristics and management. International Institute for Land Reclamation and Improvement, Wageningen, The Netherlands (1971)
2. Cooper, A.H., Calow, R.C.: Avoiding Gypsum Geohazards: Guidance for Planning and Construction, British Geological Survey, Technical Report WC 98/5, Overseas Geology Series (1998)
3. Kalinski, M.E., Thummaluru, M.S.R.: A new free-free resonant column device for measurement of G_{max} and D_{min} at higher confining stresses. GTJ12187, Geotech. Testing J. **28**(2), 180–187 (2005)
4. Fattah, M.Y., Yousif, J., Huda, N.: Long-term deformation of some gypseous soils. Eng. Technol. J. Iraq, 1461–1483 (2008)
5. Al-Marsoumi, A.-M., H., Kadhum, M.J., Kadhum, S.K.: Some geotechnical properties of sandy gypsiferous soils in Rumaila-Khor Al-Zubair Area, Southern Iraq. Marina Mesopotamica **23**(2), 333–347 (2008)
6. Haeri, S.M., Hamidi, A., Tabatabaee, N.: The effect of gypsum cementation on the mechanical behavior of gravelly sands. Geotech. Testing J. (2005)
7. Khosravi, A., Ghayoomi, M., McCartney, J., Ko, H.: Impact of effective stress on the dynamic shear modulus of unsaturated sand. Geotech. Spec. Publ. 410–419 (2010). https://doi.org/10.1061/41095(365)38
8. Qian, X., Gray, D.H., Woods, R.D.: Resonant Column Tests on Partially Sands, American Society of Testing and Materials (1991)

9. Sawangsuriya, A., Edil, T.B., Bosscher, P.J.: Modulus-suction-moisture relationship for compacted soils in Postcompaction State. J. Geotech. Geoenviron. Eng. (2009). https://doi.org/10.1061/(asce)gt.1943-5606.0000108

10. Rinaldi, V., Santamarina, J.: Cemented soils: small strain stiffness. Deform. Charact. Geomater. **1**, 267–273 (2008)

11. Fredlund, D.G., Xing, A.: Equations for the soil-water characteristic curve. Can. Geotech. J. **31**, 521–532 (1994). https://doi.org/10.1139/t94-120

12. Zapata, C.: Uncertainty in soil-water-characteristic curve and impacts on unsaturated shear strength predictions (2019)

13. Lu, N., Likos, W.J.: Suction stress characteristic curve for unsaturated soil. J. Geotech. Geoenviron. Eng. 132 (2006). https://doi.org/10.1061/(asce)1090-0241(2006)132:2(131)

14. Bhamidipati, R.A., Kalinski, M.E., Bryson, L.S.: Estimating the collapse potential of gypsum rich soils using shear-wave velocity testing. In: Proceedings: 49th Ohio River Valley Soils Seminar, pp. 31–44, Lexington, KY, USA (2018)

Experimental Evaluation of Bearing Capacity of Single CFG Pile

N. B. Umravia and C. H. Solanki

Abstract Nowadays, geotechnical engineers are facing the problem of soft ground, which results into low bearing capacity and excessive settlement. On contrary, cement fly ash and gravel (CFG) pile is one of the emerging ground improvement techniques, which can be applied to enhance the load carrying capacity of the soft ground. It also reduces the possibility of settlement associated due to soft ground. This paper addresses the practical real-time results of laboratory model of single CFG pile. Moreover, the comparative evaluation between simulation results (i.e., numerical analysis) and laboratory model has been carried out considering variation in parameters such as diameter of the CFG pile, length-to-diameter ratio of CFG pile, and gravel particle size. The results obtained from this analysis clearly prove superiority of CFG pile over soft ground in terms of enhancing load carrying capacity.

Keywords Cement fly ash gravel (CFG) pile · Mix design · Load carrying capacity

1 Introduction

The bearing capacity of any piles depends on the types of pile, namely (i) bored cast in situ pile and (ii) precast embedded pile. Normally, CFG piles are bored piles. Its baring capacity depends on two components (i) negative skin friction and (ii) base resistance. Experimental full-scale modeling plays significant role for understanding geotechnical parameter. It is very difficult to develop a certain laboratory model of CFG pile for specific prototype condition. This laboratory model tests at abated scale would be able to identify basic information of stress, deformation, lateral resistance, and failure pattern of pile. In addition, the bearing capacity of the single pile has been also determined. However, a scale model of a static loading test of the pile has been considered more cost-effective and reasonable option than the corresponding on full-scale model.

N. B. Umravia (✉) · C. H. Solanki
Applied Mechanics Department, Sardar Vallabhbhai National Institute of Technology Surat, Surat, Gujarat, India
e-mail: nirav.umravia.gec@gmail.com

1.1 Literature Survey

In recent past, it has been observed that CFG pile composite foundation plays an important role for improvement in soft soil foundation strength, stability, and reduce the settlement [1]. Many researchers work on the railway embankment CFG pile which also plays a significant role in reducing subgrade settlement [2]. CFG pile is a kind of high bond strength pile, which is consisted with macadam, gravel, sand, fly ash, and mix up cement and water. It forms composite foundation with cushion and soil between piles [3]. The soil between CFG piles has been compacted. Subsequently, the strength has been improved and the liquefaction of loose foundation can be basically eliminated [4]. Based on the reported literature on rapid development of high-speed railways in China, it is inevitable that in order to meet challenges for high-speed railway embankments (HSRE), it is essential to utilize CFG pile composite foundation instead of soft clay [5–8]. Moreover, in order to limit the friction at top and bottom, the CFG pile composite foundation has been developed using both linear distribution of friction along pile. In spite of applying this technique in the field, it is required to carry out detailed study of it considering different parameters, which influence the performance of CFG pile reinforced in soft clay bed. It is to be noted that the size of gravel particle plays vital role on the performance of the CFG pile.

2 Laboratory Experimental Setup and Materials

2.1 Loading Frame and Displacement Sensors

In this paper, experimental investigations have been discussed using the small-scale laboratory model of single CFG pile with variable L/d ratio means slenderness and area replacement ratio. Mostly, this ratio focuses on the analysis of stress versus settlement behaviors of single CFG pile. Further, the entire test was conducted on circular steel tank having 300 mm diameter and 600 mm depth. In [9], the experimental setup consists of loading frame, load cell, rigid steel container, and other equipment is shown in Fig. 1. A capacity of 5 Ton self-weight steel framed structured fabricated and fixed a hydraulic jack at the center of main loading frame (attached with 130 mm plate). It had the power of 50 kN that was set on a horizontal beam of loading frame. In order to control the load rate during experimental work, hydraulic jack has been operated manually. A CFG piles are casted in center of the circular tank. The size of steel tanks does not cause any confinement against pile deformation. During the experimental, two different sensors have been used, which has been calibrated prior to testing. Further, one side of the high capacity, 100 kN, S-shape, load cell has been attached with connecting rod of the hydraulic jack and other end with loading plate. Moreover, two LVDT sensors with the capacity of 50 mm and accuracy 0.1 mm have been attached with loading frame. Tank size has been designed using unit cell approach. Here, the diameter and height of tank are taken 300 mm, and 600 mm,
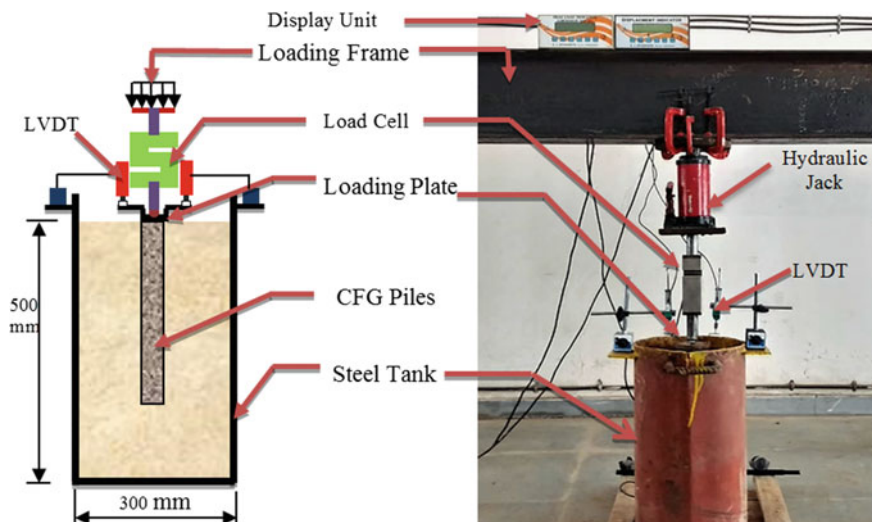
Fig. 1 Laboratory experimental setup

respectively. In order to make this presented work more qualitative, the permissible accepted settlement is taken as 50 mm for isolated footing.

2.2 CFG Pile Experimental Model and Model Consideration

In this presented work, total 15 numbers of experimental cases have been developed generated by changing the parameters such as different gravel size, length of pile, diameter of the pile (as shown in Table 1) for single CFG pile. However in field practices, this type of CFG pile has been considered as short column pile. The experimental results have been compared with the finite element method (FEM) results. It has been concluded from this comparison that the field results are almost mapped with the FEM results.

Many researchers have discussed the application of unit cell idealization method by assuming pile in a triangular pattern in column technology [2, 10–13]. The same have used for this experimental work. In this experimental set, length is represented using L/d ratio (i.e., 2.5, 3.0, 3.5, 4.0, and 4.5). It is to be noted that in this presented work, the shear strength of the soft soil has been maintained of the order of 13 kPa. In this study, all the boundary conditions are considered. Here, the area replacement ratio was defined as percentage area of virgin soil is replaced by the CFG pile. Further, during this study, the variation of CFG pile diameter is also represented as area replacement ratio. Here, the center to center distance and area replacement ratio (Ar) are taken as (i) 3.0 d and 12% considering 70 mm dia and (ii) 2.8 d and 10%

Table 1 List of single CFG pile Tests

Test	Diameter of pile (mm)	Garvel type	Length of pile		Types of pile	No. of test
			70 mm	100 mm		
Clay bed	–	–	–	–	Soft clay	02
CFG pile	70	G1	450	–	Floating pile	01
	70	G2	450	–	Floating pile	01
	70	G2		175, 210, 245, 280, 315	Floating pile	05
	100	G2		250, 300, 350, 400	Floating pile	04
	70	G1	500	–	End bearing	01
	100	G2	500	–	End bearing	01

G1 and G2 are variable gravel size used for present study

for 100 mm dia. CFG pile length-to-diameter ratio changes from 5-to-14, and soil replacement ratio varies from 0.08-to-4; it has been reported [6, 11, 14, 15].

2.3 Soil Properties

In this presented work, the soil was collected from rural area of Dahod City, Gujarat, India. It is yellow color, low plasticity soil, which is classified as CL (clay) based on IS: 1498: 2000. Figure 2 shows the particle size analysis of soil. Prior to use, the soil has been air-dried using oven. Thereafter, it is stored at room temperature before all experimental tests. The soil particle size is less than 75 μm. Subsequently, it easily passes from 200 no sieve. The physical properties of clay are presented in Table 2.
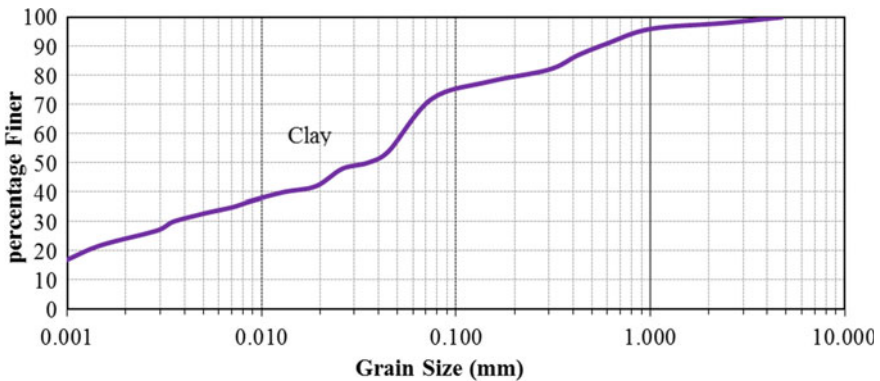
Fig. 2 Particle size distribution

Table 2 Properties of soil and gravel G1 and G2

Parameters	Unit	Clay	Gravel	
			G1	G2
Natural water content	(%)	14	–	–
Specific gravity	–	2.64	2.53	2.55
Maximum dry unit weight	kN/m^3	19.10	–	–
Bulk unit weight	kN/m^3	21.62	15.5	16.2
Liquid limit	(%)	29.5	–	–
Plastic limit	(%)	0	–	–
Plasticity index	(%)	29.5		
Uniformity coefficient (Cu)	–	–	2.19	2.86
Curvature coefficient (Cc)	–	–	1.40	0.38
Unified classification symbol	–	CL	GP	GP

2.4 Gravels

In CFG pile, gravel plays significant role to transfer the load. Further, the gravel enhances the strength of CFG pile. In this present study, two different sizes of particle sizes gravels have been used. These gravels are discussed as below. (i) G1: ranges from 6.3 mm-to-10 mm. (G1: Cu = 2.19, Cc = 1.40) and (ii) G2: 6.3 mm-to-4.75 mm. (G2: Cu = 2.86, Cc = 0.38). Further, the physical properties of gravels G1 and G2 are described in Table 2. In case of gravel G1, the maximum and minimum unit weight are 15.9 and 15.3 kN/m^3, respectively, whereas for G2 maximum and minimum unit weight 16.4 and 15.9 kN/m^3, respectively. The particle size distribution curve is shown in Fig. 3.
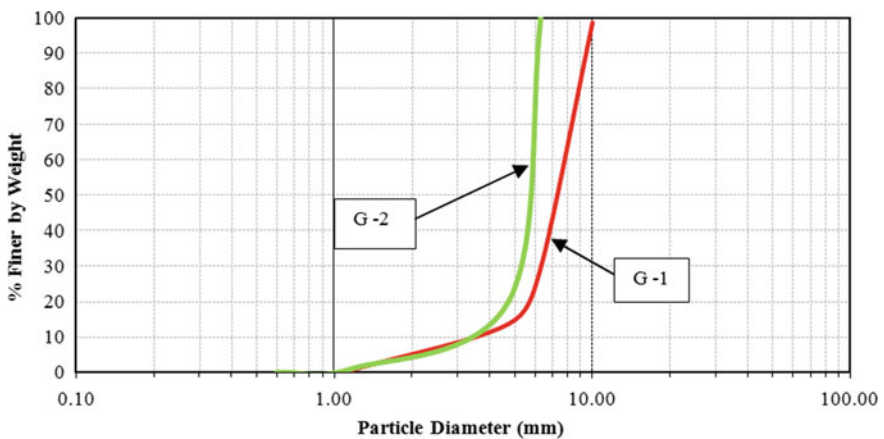
Fig. 3 Different particle distribution curved of gravel

Table 3 Basic properties of fly ash

Properties	Value
Classification	Garde-1
Color	Black
Specific gravity	1.55
Grain size distribution	–
(a) % Gravel	0
(b) % sand	25
(c) % Silt and clay	75
Maximum dry unit Wt. (kN/m^3)	13.21
Optimum moisture content (%)	21.5
Fineness, m^2/kg, Min (Blaine air permeability)	312
A particle retained on 45 μ IS sieve (Wet sieving)	22%

2.5   Cements and Sand

In this experimental work, the cement of 53 grade ordinary Portland cement has been used in all experimental work which was as per confining IS: 269-2015. The physical properties of cement, initial settlement time, and final setting time are mention in Table 3. Here, based on IS: 383-2016 the sand from a local query and river sand (i.e., natural disintegration of rock by alluvial sand) has been used in this study. Further, the size of particle is maintained from 1.0 mm-to-0.6 mm.

2.6   CFG Pile Concrete Mix

The CFG pile mix designs based on its compressive strength which is laying between C-5 and C-25 design. The mix design methods have been adopted from 'China Academy of Building Research' guideline. The making of concrete mixed was by the cement, sand, gravel, fly ash, water reducing agent, and water. It is required the compressive strength of cubic would be approximate 28 MPa after casting 28-day. Design of C-20 grade of concrete has been considering for mix design proportional as per You et al. [16] as the reference bench mark for study. The results of that concrete mixed have not been adopted worked in Indian fly ash and cement proportion. New concrete mixes for the present are mention in Table 4. It is adopted for all the experimental works.

Table 4 CFG pile mix design proportion

Material	Cement	Sand	Gravel	Fly ash	Water
Unit	kg/m^3	kg/m^3	kg/m^3	kg/m^3	kg/m^3
Mix design C-20	1	3.2	4.13	0.51	0.59
Unit Wt.	265	848	1094	135	160

Table 5 Results of unconfined compressive strength tests for clay

Water content (%)		23	22	21	20	19	18	17
Undrained shear strength (kPa)	7 Day	13.01	16.15	18.16	23.23	26.24	35.55	43.22

2.7 Soft Clay Bed Material Preparation

In order to prepare a soft soil clay bed for the all experimental work having shear strength of the order of 13 kPa, additional 23% water has been added in oven dry soil. The shear strength of the soft soil has been measures by performing unconfined compression strength (UCS) test at the laboratory. The results of these tests are shown in Table 5. Initially, 50 kg dry soil has been divided into five equal parts and stored in the plastic boxes. Thereafter, 23% water has been added. This mixture has been placed by covering plastic cover for 36 h. Afterward, this mixture has been poured in cylindrical tank at 50 mm height (as shown in Fig. 1). Further, each layered has been compacted using 9 kg temper rod. This rod is shown in Fig. 4. However, this compaction of soil has been achieved 18 kN/m^3 bulk density.

2.8 Construction of CFG Pile in Laboratory

The CFG pile has been constructed using below-mentioned stepwise procedure

1. A long hollow-stem pipe has been inserted gently to the standard depth into soft soil clay bed in the cylinder. In order to reduce the friction, lubricant has been applied on both the surface of the hollow pipe. Thereafter, the soil has been removed from the hollow pipe using auger.
2. After the removal of soft soil from the hollow pipe, concrete mixture has been filled in that space. During this filling, the hollow pipe has been lifted upwards at the rate of 10 mm/min.
3. After complete removal of hollow pipe, from top surface, the upper layer (approximately 50 mm of length) has been removed.
4. In order to provide sufficient time to gain the adequate strength of pile, this mixture is kept ideal for 07 days.

Fig. 4 Tamping rod

3   Numerical Modeling

In this presented analytical (simulation) study, Plaxis 3D software package has been used. Further, the software codding for CFG pile model has been carried out using finite element code. The dimensions of this CFG pile are taken same as experiment model. In this study, the boundary conditions of CFG pile are considered circular rather than rectangular (i.e., conventional). During this study, mesh size of 15 nodes with triangular element pattern has been used.

Based on the literature reported in this area, most of researchers used rectangle boundary surface with non-rigid confinement. On contrary, in this experimental setup, circular boundary surface has been used. Moreover, the rigid confinement is provided using steel plate.

The soft soil was modeled using the 'Undrained A' approach of Plaxis (undrained effective stress analysis with effective strength parameters). The CFG piled was modeled as a nonporous. The stiff soil providing end bearing was modeled as drained. Both stiff soil and soft soil were modeled by Mohr–Coulomb behavior; the parameter values and CFG piled were modeled by linear elastic material for analysis, and other
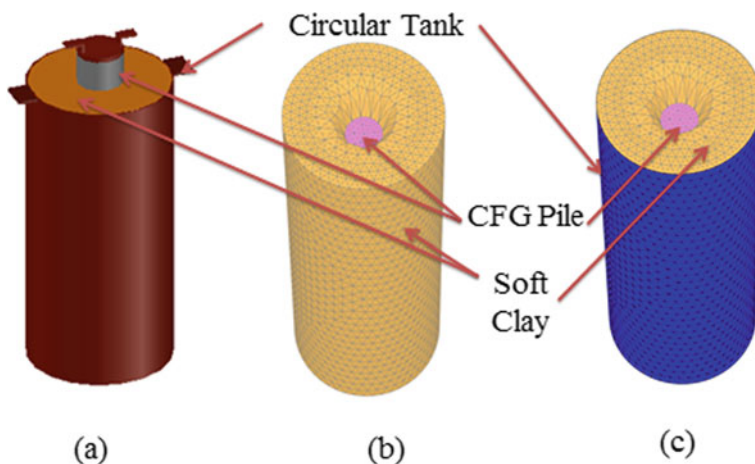
Fig. 5 Numerical model compared with experimental model. **a** Experimental model, **b** Plaxis 3D model without cylinder tank, and **c** Plaxis 3D model with cylindrical tank

details of numerical input data are listed in Table. While a small effective cohesion ($c = 1$ kPa) was adopted to avoid numerical problems, a bulk unit weight (γ) of 22 kN/m^3 has been adopted for the CFG pile. It has been reported in [17, 18] that Young's modulus of elasticity constant changes narrowly due to the effect of bearing earing capacity of CFG pile. Therefore, in this study, Young's modulus of elasticity constant has been selected of the order of $E = 21{,}000$ MPa instead of 25,000 MPa. Here, the angle of dilation (ψ') has been calculated according to the formula $\psi' = \varphi - 30$. Moreover, the poisson ratio of the order of 0.2 and 0.3 has been considered for CFG pile and soft soil, respectively. The experimental and Plaxis 3D models are described in Fig. 5.

4 Experimental Results with Numerical Analysis

In this section, the influences of some parameters on the load carrying capacity of CFG pile and the stress–settlement behavior of CFG pile for each section are presented. Here, the load on CFG pile has been increased up to maximum limit and subsequent load settlement curve is noted and plotted. The numerical analysis results of CFG pile for total vertical settlement against the given load are shown in Fig. 6. It has been observed from Fig. 6 that the linear displacement (bulging effect) changes narrowly clay bed.

The experiment results for the stress–settlement behavior of soft clay bed are shown in Fig. 7. It has been observed from Fig. 7 that the maximum stress of the order of 83 kPa has been obtained for corresponding 50 mm settlement. Further, the failure point has been easily identified.
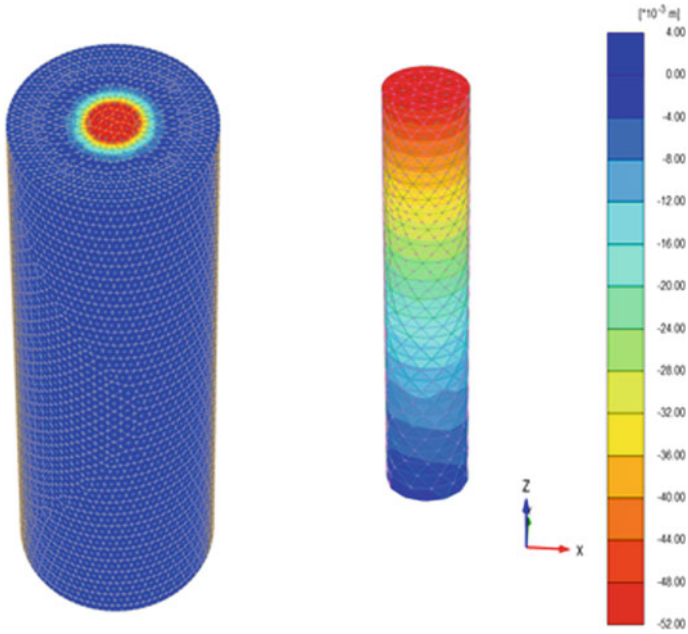
Fig. 6 Plaxis 3D image of total vertical displacement sheading
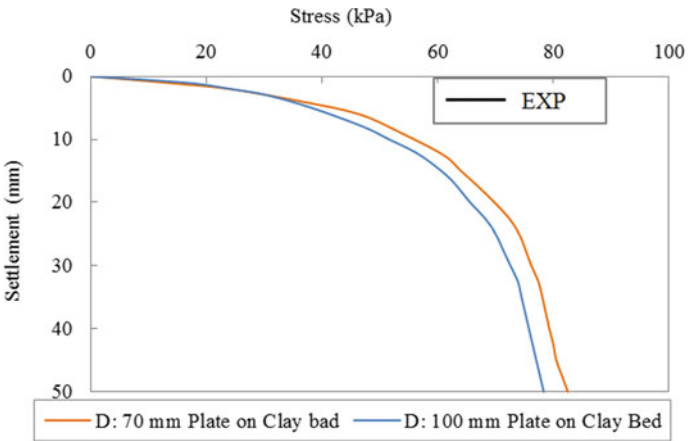
Fig. 7 Stress–settlement behaviors of clay bed under 70 mm and 100 mm foundation plate
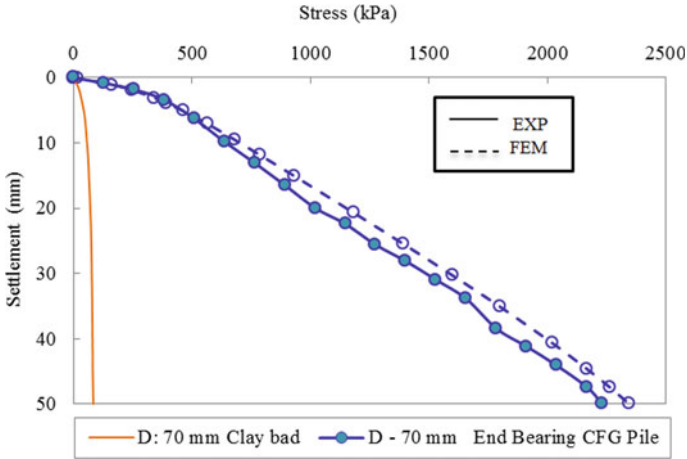
Fig. 8 Stress–settlement behaviors of experimental soft clay bed and 70 mm CFG pile

4.1 Influence of CFG Pile

In order to compare the performance of single CFG pile, load tests have been performed on soft clay bed and single CFG pile. Figure 8 shows the stress–settlement response obtained using laboratory tests and numerical analysis for both ends bearing CFG pile along with the untreated clay bed. These results were obtained by loading the CFG pile area only or an equivalent area in the case of the clay soil. It can be ascertained that after a very small vertical settlement, the mobilized vertical stress on top of the CFG pile is always greater than for the soft clay bed, and the difference increases with the additional settlement. It can be observed that clay bed fail at very nominal load, whereas there was not failure observed in the CFG pile. It is observed the experimental results of soft clay and 70 mm end bearing CFG pile stresses at 50 mm settlement were 83 kPa and 2230 kPa, respectively, which is approximate 27 times higher than the soft clay. This is due to the rigidity of the CFG pile which enhances increase in load carrying capacity. Figure 6 shows the shading of vertical settlement along with the depth of the CFG pile. It can be observed that vertical settlement is distributed throughout the length of the column. This is due to the rigidity of the CFG pile.

4.2 Influence of Column Diameter

Figure 9 shows the experimental performance of 70 mm and 100 mm diameter of end bearing CFG pile having 500 mm length. By analyzing the experimental results, it has been observed that the maximum stress for 70 mm and 100 mm diameter CFG pile is 2230 and 1811 kPa, respectively; i.e., the load carrying capacity of the 100 mm
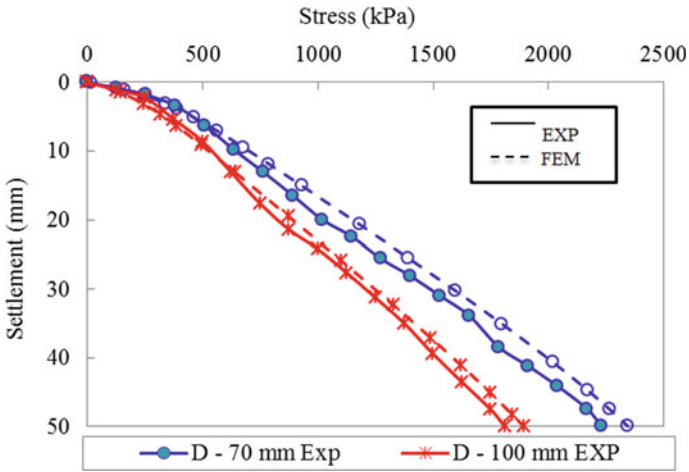
Fig. 9 Stress versus settlement response of 70 mm and 100 mm single CFG pile with end bearing

diameter CFG pile is about 1.23 times more than that of 70 mm diameter pile. On contrary, the stress concentrations have been reduced increasing the diameter of pile.

In order to investigate the ultimate stress of the CFG pile in floating condition at 50 mm settlement with 2.5, 3, 3.5, 4 L/D ratios are elaborate shown in Fig. 10. It may be noted that irrespective of CFG pile diameter, the stress carrying capacity of the soil decreasing by CFG pile.
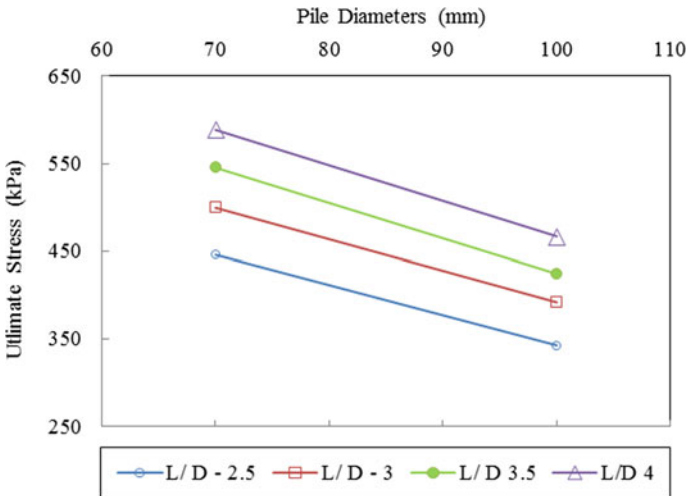
Fig. 10 Relationship between diameters versus ultimate stress with different L/D ratio
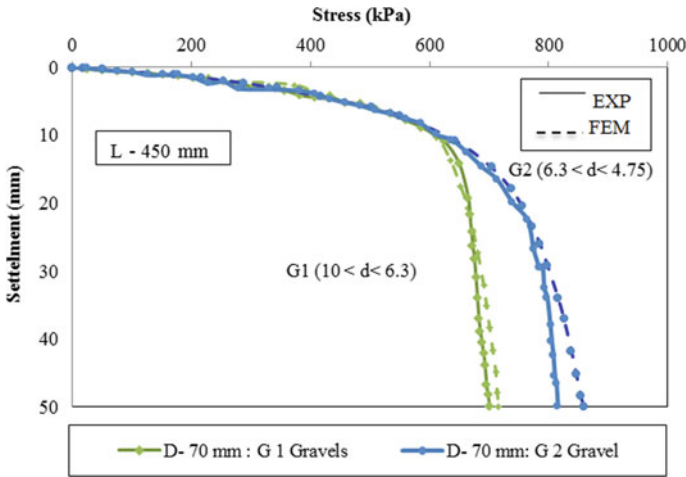
Fig. 11 Relationship between ultimate stresses with different L/D ratio (diameters)

4.3 Influence of Gravel Particle Size (d)

In order to investigate the effects of gravels particle size on the axial load carrying capacity of single CFG floating pile for soft clay, the tests (analytical study and experiments) have been performed. Here, soft clay bed and single CFG piles of 70 mm diameters with 450 mm length with using G1 size grave particle (10 mm < d < 6.3 mm) and G2 size grave particle (6.3 mm < d < 4.75) are used. Further, in this case, d represents the average gravels particle size. Figure 11 illustrates experimental and numerical results of stress–settlement behavior of the single CFG pile with G1 and G2 size gravel particle. It can be clearly seen from Fig. 11 that the load carrying capacity of smaller size grave particles CFG pile is greater than CFG piles having bigger size grave particles (roughly 20%). This is due to the densest packing forms by small size of gravel particle provides more strength than the bigger particles.

5 Conclusion

Both experimental and numerical investigations have been carried out to evaluate the stress–settlement behavior of CFG pile in soft soil. It is concluded that the CFG pile is considered as more suitable option compare to soft soil for ground improvement technique.

1. The experimental and numerical result of CFG pile has been compared with soft clay. It has been clearly observed that CFG pile improve the stress ratio approximate 28 time in comparison with soft soil.

2. The effect of different types of gravels G1 and G2 (shapes of particles and their distribution) on the load carrying capacity has been discussed. It has been concluded that as the size of gravel increases the stress concentration of the CFG pile decreases.
3. The results obtained from numerical analysis are almost mapped with the experimental results.
4. It is essential to study the behaviors of CFG pile scale effects of experimental model. This has been validated using small-scale test at laboratory model.
5. Behavior of the semi-stiffened rigid CFG pile on 10–18 mm settlement mobilize vertical load is discussed and finds improved results.
6. It can be concluded that by increase in diameters of CFG pile, the stress concentration in soil settlement decreases.

References

1. Zhao, L.C.: Construction method of current controlling length of cement mixing pile and CFG pile for soft soil subgrade. Appl. Mech. Mater. **443**, 123–128 (2013)
2. Zhang, J.S., Guo, C., Xiao, S.W.: Analysis of effect of CFG pile composite foundation pile spacing on embankment stability based on centrifugal model tests. Appl. Mech. Mater. **178–181**, 1641–1648 (2012)
3. Zhenxing, R., Xiao, H., Guo, X., Huang, L.: Analysis of the effect of groundwater exploitation on high-speed railway pile-slab structure subgrade. Open Mech. Eng. J. **9**(1), 455–459 (2015)
4. Zhang, M., Zhang, X.: A field experimental study of composite foundation with CFG pile + vibro-replacement stone column pile in liquefaction area, vol. 124, no. Isaeece, pp. 75–78 (2017)
5. Zheng, G., Jiang, Y., Han, J., Liu, Y.F.: Performance of cement-fly ash-gravel pile-supported high-speed railway embankments over soft marine clay. Mar. Georesour. Geotechnol. **29**(2), 145–161 (2011)
6. Jiang, D.P., Wang, B.L.: An analysis on failure pattern of CFG pile-net composite foundation of high-speed railway. Adv. Mater. Res. **594–597**, 1357–1362 (2012)
7. Li, W., Bian, X.: Dynamic performance of pile-supported bridge-embankment transition zones under high-speed train moving loads. Procedia Eng. **143**(Ictg), 1059–1067 (2016)
8. Feng, J., Wu, X.Y., Zhang, J.H.: Settlement formula of stabilized layer in CFG composite foundation of high-speed railway. Electron. J. Geotech. Eng. **19**(W), 6867–6878 (2014)
9. Hasan, M., Samadhiya, N.K.: Performance of geosynthetic-reinforced granular piles in soft clays: Model tests and numerical analysis. Comput. Geotech. **87**, 178–187 (2017)
10. Voottipruex, P., Suksawat, T., Bergado, D.T., Jamsawang, P.: Numerical simulations and parametric study of SDCM and DCM piles under full scale axial and lateral loads. Comput. Geotech. **38**(3), 318–329 (2011)
11. Cao, H.Y., Liu, Y.F.: Optimum design of CFG pile compound foundation based on numerical simulation method. Appl. Mech. Mater. **578–579**, 346–350 (2014)
12. Samanta, M., Bhowmik, R.: 3D numerical analysis of piled raft foundation in stone column improved soft soil. Int. J. Geotech. Eng. **6362**, 1–10 (2017)

13. Umravia, N.B., Parmar, M., Patil, S.V., Aman, M.: Recent study on the behaviour of CFG pile, DM (deep mixing) column and stone columns ground improvement technology, no. February, pp. 241–246 (2019)
14. Wu, L.: Performance of geosynthetic-reinforced and cement-fly ash-gravel pile-supported embankments over completely decomposed granite soil: a case study. Adv. Mater. Sci. Eng. **2018**, 1–11 (2018)
15. Pagar, V.V.: Review of existing design methods for CFG (cement-fly ash-gravel) pile supported composite foundation embankment, vol. 5, no. 3, pp. 799–806 (2018)
16. You, S., Cheng, X., Guo, H., Yao, Z.: Experimental study on structural response of CFG energy piles. Appl. Therm. Eng. (2016)
17. Abusharar, S.W., Zheng, J.J., Chen, B.G.: Finite element modeling of the consolidation behavior of multi-column supported road embankment. Comput. Geotech. **36**(4), 676–685 (2009)
18. Umravia, N.B., Solanki, C.H.: Evaluate the bearing capacity of CFG pile by numerical analysis method, vol. 6, no. 2, pp. 37–44 (2018)

Comparison Between Casagrande Method and Cone Penetrometer Method for Determination of Liquid Limit of Soil

Preksha Jain, Jennie Gandhi, Sudhir Trivedi, and Rajesh P. Shukla

Abstract The liquid limit is an essential property of soil due to its relationship with other properties and behaviour of soil directly or indirectly. The two methods for determining the liquid limit are widely used, viz. Casagrande method and cone penetrometer method. This paper presents a comparison of the liquid limit of soils determined by performing both experiments. The result demonstrates that the liquid limit value obtained from Casagrande method is a little higher than those obtained from cone penetrometer in high plastic soil. In low plastic soils, cone penetrometer gives the higher values of liquid limit. However, in medium plastic soil, it is difficult to make any conclusion.

Keywords Casagrande method · Cone penetrometer method · Cohesive soil · Liquid limit · Plasticity

1 Introduction

Liquid limit of soil is the minimum water content at which soil changes its state from plastic state to liquid state with least shearing strength. Determination of liquid limit is important as it is one of the essential properties of soil, which uses to classify the soil and assess the soil behaviour. The liquid limit not only used to calculate the activity of clays, plasticity index and toughness index of soil but also used to predict the allowable bearing capacity of soil and settlement of soil. There are two methods to determine the liquid limit of soil, namely Casagrande method and cone penetrometer method (IS 2720-V). As both the methods are used for determination of the same property of soil, there are chances of getting different results. The cone penetrometer method imposes the slow static shear deformation, while the Casagrande method imposes a sudden deformation of soil. A number of studies explored the relationship

P. Jain · J. Gandhi · S. Trivedi · R. P. Shukla (✉)
Adani Institute of Infrastructure Engineering, Ahmedabad, Gujarat, India
e-mail: rpshukla.2013@iitkalumni.org

between limit values determined using Casagrande and cone penetrometer methods [1]. However, in India, most of the studies use the Casagrande apparatus to determine the liquid limit of plastic soil.

The soft base Casagrande apparatus always gives higher liquid limits than those from the hard base of the Casagrande apparatus. The difference between soft and hard base Casagrande apparatus can be about 5% for soils with a liquid limit greater than 40%. In another study, Ozer [2] observed that Casagrande apparatus gives higher liquid limits than those determined from the cone penetration apparatus. The difference in values depends on the clay contents and types of mineral contents in the soil. Christaras [3] and Di Matteo [4] found the liquid limit value, determined by the Casagrande apparatus systematically 2–3% lower than the penetrometer values for soils with lower clay contents. The difference between the two methods is reduced with the decrease in the liquid limit, clay fraction and free swelling capacity of the bentonite present in the mixture. Similarly, the difference in the liquid limit values obtained by both these methods is reduced with an increase in salt concentration [5]. A correlation based on the results was also developed for standards clays and compared with other correlations from other studies. The similar correlation was developed by Spagnoli [6]. For a constant depth of penetration of 20 mm, it was observed by Hrubesovaa et al. [7] that standard cone penetrometer test (20 mm penetration) gives significantly lower value of liquid limit in comparison with Casagrande cup method for high plasticity soils. Another study carried out by El-Shinawi [8] shows that the liquid limit values determined by the Casagrande apparatus were generally lower than those obtained by the Russian cone apparatus. Based on the experimental results, Karakan et al. [9] concluded the liquid limit values obtained from the fall cone and Casagrande tests are consistent and close to each other. It was also observed that fall cone test is more useful and powerful tool for the practical soil classification test. The study of Letícia Garcia Crevelin et al. [10] reveals that the linear correlation exists between results of a relatively harder base Casagrande apparatus and cone penetrometer as compared to a softer base apparatus.

The number of studies has been explored the correlation between Casagrande apparatus and the cone penetrometer apparatus. Most of the studies are mostly carried out for soils found in other countries and found that the relationship between both the methods depends on soil properties. However, the studies on Indian soils are missing in the literature. Therefore, the experimental studies were carried out to find out the comparison between the liquid limit of different soils found in Gujarat, India.

2 The Material Used in the Study

The soil sample collected is from different regions in Gujarat as shown in Fig. 1. The locations of sample are Adalaj (Latitude 23.17, Longitude 72.14) (soil A), Bhavnagar (Latitude 21.76, Longitude 72.14) (soil B), Ahmedabad location 1 (Latitude 23.15, Longitude 72.54) (soil C), Ahmedabad location 2 (Latitude 23.16, Longitude 72.54) (soil D). The type of soil A is dry alluvial soil, soil B is black cotton soil, while soil
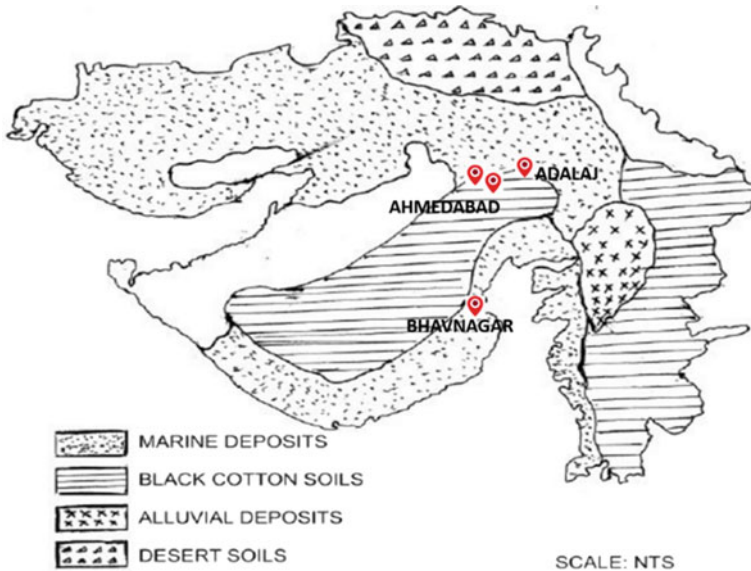
Fig. 1 Location of sites

C is low plastic sandy soil, and soil D is plastic dark brown soil. The collected soil samples are shown in Fig. 2.

3 Methodology and Apparatus Used in the Study

The liquid limit of soil is determined by the procedure described in the Indian standard method of test for soils, Part 5 Determination of liquid and plastic limit. The detailed procedure of both the methods is discussed separately in sections, namely "3.1 Casagrande method" and "3.2 Cone penetrometer method".

3.1 Casagrande Method

In this experiment, about 120 gm of air-dried soil passing from 425 microns I.S sieve is taken in mixing dish, and distilled water is mixed to form a uniform paste. A portion of the soil water paste is placed in the cup of Casagrande device and spread into portion with few strokes of a spatula. Then, groove is made with a grooving tool at the centre of cup as shown in Fig. 3. Lift and drop the cup by turning crank at the rate of two revolutions per second until the two halves of soil cake come in contact with each other for a length of about 1 cm by flow only. The number of blows shall
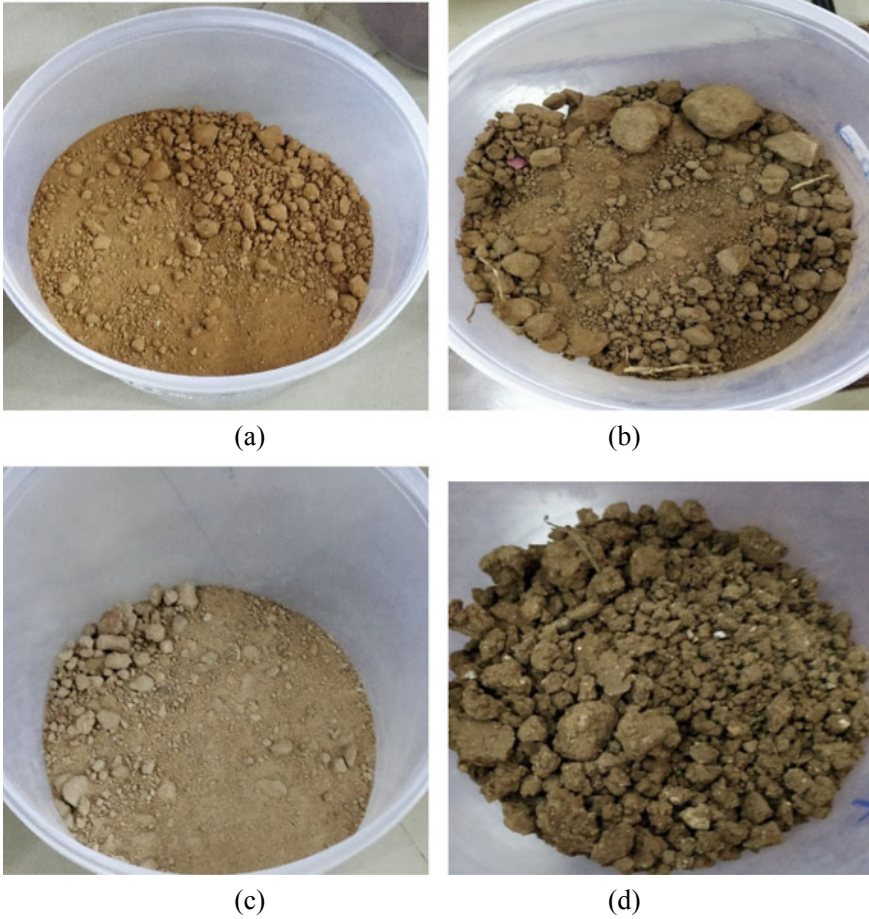
Fig. 2 Collected soil samples used in the testing: **a** Adalaj Soil (Soil A), **b** Bhavnagar Soil (Soil B), **c** Ahmedabad Location-1 (Soil C), **d** Ahmedabad Location-2 (Soil D)

be recorded, and this should be carried out with different moisture content for blows between 10 and 40.

3.2 Cone Penetrometer Method

In this experiment, about 150 gm. of air-dried soil passing from 425-micron Indian standard sieve is taken in mixing dish, and distilled water is mixed to form a uniform paste. Then, the wet soil paste is transferred to the cylindrical cup of cone penetrometer apparatus, with no air trapped and placed on the base of the cone penetrometer apparatus. The penetrometer is so adjusted that the cone point touches the surface
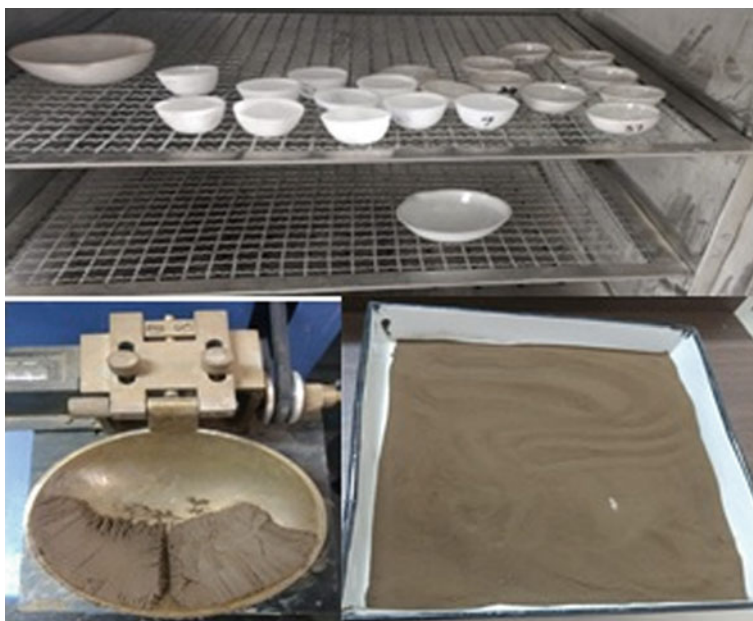
Fig. 3 Performing Casagrande test

of the soil paste in the cup, and the initial ready is to be taken. The vertical clamp is then released, allowing the cone to penetrate soil paste under its weight for 5 s, and reading is noted. The test is repeated with different water contents for values of penetration in the range of 15–25 mm. Cone penetrometer test apparatus used in the present is shown in Fig. 4.

4 Results and Discussion

All the five soils were tested for a number of times to ensure the repeatability of tests. A large number of experiments were carried out on soil samples. However, only some typical tests are presented here. In Casagrande method, the liquid limit is obtained at the value of water content to 25 blows from the graph, while in cone penetrometer, the liquid limit is obtained at the value of water content corresponding to 20 mm penetration from chart. The results are presented separately for low plastic soils and medium to highly plastic clays.

Fig. 4 Cone penetrometer apparatus used in testing

4.1 Low Plastic Soils

The results of liquid limit tests carried out in low plastic soil (liquid limit >35%) are shown in Fig. 5. The left and right parts in each figure represent the liquid limit test results obtained by Casagrande and the cone penetrometer apparatus. It shows that the liquid limit is minimum for soil A and increases higher for soils B and C in chronical order. Though soil B is black cotton soil, it is having alkaline nature. Therefore, liquid is found to be relatively small as compared to normal expansive soils. It is also observed that flow index (slope of flow line) increases with an increase in liquid limit of soil. For soils A, B and C, the liquid limit determined by Casagrande apparatus is found to be lower than those determined by cone penetrometer apparatus.

4.2 Medium to High Plastic Soils

The results of liquid limit tests carried out in soils (soils D and E) with medium to high plastic soils are shown in Fig. 6. Similar to Fig. 5, the left and right parts in each figure represent the liquid limit test results obtained by Casagrande and the cone penetrometer apparatus. The slope of curves in Casagrande apparatus is relatively higher than the slope of the curve in cone penetrometer test. It indicates that the effect of change in the water content is relatively more in case of Casagrande
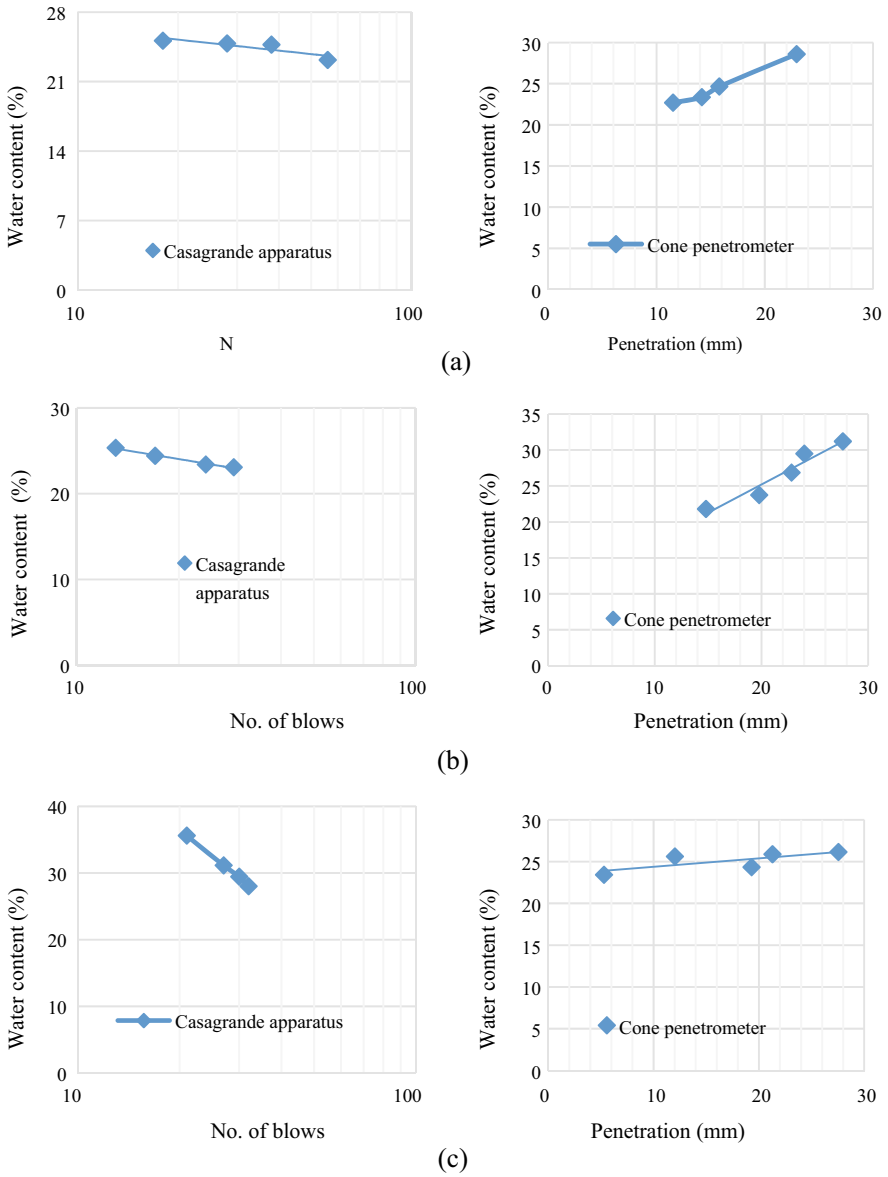
Fig. 5 Liquid limit determination for low plastic soils: **a** Soil A, **b** Soil B, **c** Soil C
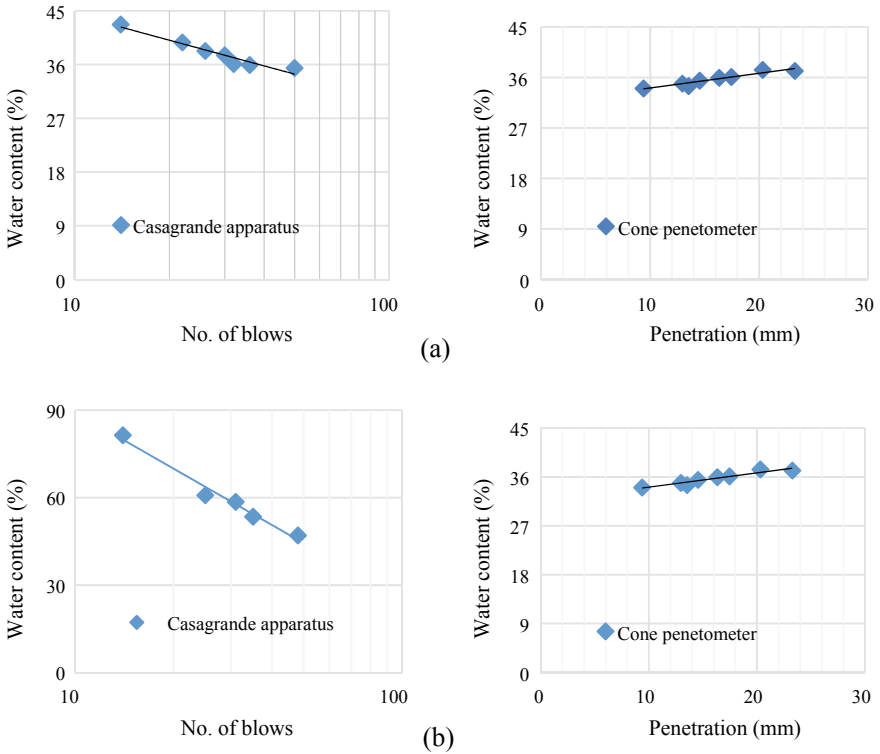
Fig. 6 Liquid limit determination for high plastic soils: **a** Soil D, **b** Soil E

apparatus compared to the cone penetrometer apparatus. The Casagrande method imposes sudden deformation of soil. Therefore, the Casagrande method might have been more sensitive to change in water content.

The comparison of the values of liquid limit obtained for a different type of soils is shown in Fig. 7. It shows that the difference in the liquid limit is varying with the types of soils. As per Indian standard, the soils are classified as low plastic soil if the liquid limit is below 35%. For soils with liquid limit less than 30%, the Casagrande apparatus estimates the lower value of the liquid limit.

The soils can be classified as medium plastic soils if the liquid limit is varying between 35 and 50%. However, no information is provided in the Indian standard about transition state, from low plastic to medium plastic state. It is difficult to come out with any correlation between Casagrande apparatuses, and the cone penetrometer results in soils with plasticity higher than 30% and less than 40%. This range is close to the boundary differentiating between low and medium plastic soil. A very small number of tests have been carried out for the soil with a liquid limit of 30–40%. Therefore, it is required to carry out a large number of tests on soils with liquid limit falling in this range. The liquid limit determined by Casagrande apparatus is found to be higher than those determined by the cone penetrometer apparatus for highly
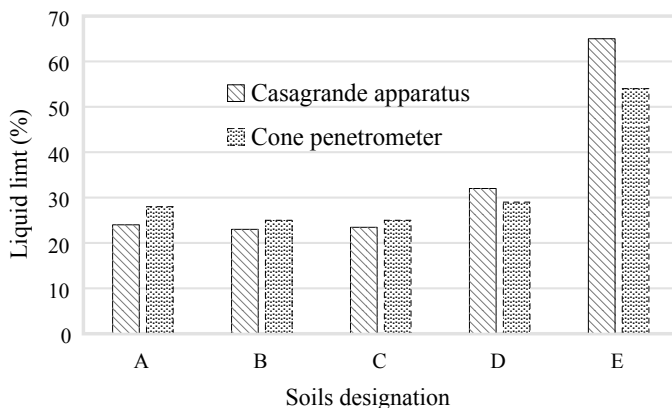
Fig. 7 Comparison of results of Casagrande and cone penetrometer test

plastic soil (soil E). The similar observation has been made in the earlier published studies for highly plastic soils [2–4].

5 Conclusions

The liquid limit was determined for low, medium and highly plastic soils found in Gujarat, India, using Casagrande method and the cone penetrometer method. The liquid limit of low plastic soil determined by cone penetrometer is higher than those obtained by Casagrande. For highly plastic soils, the opposite trends have been observed. The relationship between both the methods is clear for low plastic and high plastic soils. However, it is difficult to make any conclusion for soil with liquid limit ranging from 30%-40%. Therefore, it is required to carry out a large number of tests to make any conclusion regarding the soils close to the boundary of low to medium plastic.

References

1. Budhu, M.: The effect of clay content on liquid limit from fall cone and the British cup device. Geotech. Test. J. **8**(2), 91–95 (1985)
2. Özer, M.: Comparison of liquid limit values determined using the hard and soft base Casagrande apparatus and the cone penetrometer. Bull. Eng. Geol. Environ. **68**, 289–296 (2009)
3. Christaras, B.: A comparison of the casagrande and fall cone penetrometer methods for liquid limit determination in marls from Crete, Greece. Eng. Geol. **31**(2), 131–142 (1991)
4. Di Matteo, L.: Liquid limit of low- to medium-plasticity soils: comparison between Casagrande cup and cone penetrometer test. Bull. Eng. Geol. Environ. **71**, 79–85 (2012)

5. Mishra, A.K., Ohtsubo, M., Li, L.Y., Higashi, T.: Influence of various factors on the difference in the liquid limit values determined by Casagrande's and fall cone method. Environ. Earth Sci. **65**, 21–27 (2012)
6. Spagnoli, G.: Comparison between Casagrande and drop-cone methods to calculate liquid limit for pure clay. Can. J. Soil Sci. **92**, 859–864 (2012)
7. Hrubesova, E., Lunackova, B., Brodzki, O.: Comparison of liquid limit of soils resulted from casagrande test and modified cone penetrometer methodology. Procedia Eng. **142**, 364–370 (2016)
8. El-Shinawi, A.: A comparison of liquid limit values for fine soils: A case study at the north Cairo-Suez district, Egypt. J. Geol. Soc. India **89**(3), 339–343 (2017)
9. Karakan, E., Demir, S.: Liquid limit determination of various sand clay mixtures by Casagrande and fall cone test methods. J. BAUN Inst. Sci. Technol. **20**(2), 361–371 (2018)
10. Crevelin, L.G., Bicalho, K.V.: Comparison of the Casagrande and fall cone methods for liquid limit determinations in different clay soils. Rev. Bras. Cienc. Solo. **43**, e0180105 (2019)

Predictive Models for Estimating the Coefficient of Permeability for Sands

Indra P. Acharya, Anubhav, and Prabir K. Basudhar

Abstract Particularly, for granular soils, several correlations are available in the literature for predicting the coefficient of permeability of soils as a function of particle size, properties of pore fluid, void ratio, shape of particles, etc. In this paper, a comparative study of some of the existing predictive models is presented to examine how far these are applicable to natural sands. With the above in view, coefficients of permeability of two different types of sands (sub-angular Ganga sand and rounded Ennore sand) were found out with varying void ratios by constant head laboratory test. The laboratory test data is compared with various predictive models available in the literature. This study highlights the fact that there exists no unique relationship that would be the panacea for predicting the coefficient of permeability values for all types of soils. The expressions as given by Kozeny–Carman, Taylor and Chapuis are rational and scientific. These may be used for quick predictions of the coefficient of permeability, but the coefficients and parameters appearing in these equations need to be properly determined specific to the concerned soil.

Keywords Permeability · Sand · Void ratio · Particle size

1 Introduction

Permeability is one of the most important soil properties which indicates the relative ease with which fluid can flow through soils. Soil being a particulate system is inherently a multiphase and permits passage of water through their continuous but

I. P. Acharya
Institute of Engineering, Tribhuvan University, Kathmandu 395007, Nepal
e-mail: indrapd@ioe.edu.np

Anubhav (✉)
Solapur Super Thermal Power Project, NTPC Ltd., Solapur 413215, India
e-mail: anubhav@ntpc.co.in

P. K. Basudhar
Indian Institute of Technology Kanpur, Kanpur 208016, India
e-mail: pkbd@iitk.ac.in

disordered voids (or pores) whose size, cross-sectional shape and orientation are highly variable from point to point. Physical characterization of such a disordered system is very difficult. Size of the pore spaces and the nature of the soil particle play an important role on the flow of water through soils. The path of water through soils is generally tortuous. Therefore, the flow velocity would vary from point to point with variations in pore sizes, and its direction, which at times may even be in opposite direction of the macro-flow [10].

Flow of water through most soils mainly follows Darcy's law. The classic experiment conducted by Darcy in 1856 provided the physical basis for the analysis of flow through porous media; based on the experimental findings, he proposed a simple law for discharge velocity (v) of water:

$$v = ki \tag{1}$$

i = total head lost per unit length of macroscopic flow path, called hydraulic gradient, k = coefficient of permeability or simply the permeability.

k appearing in the above equation is one of the most important and widely used soil properties in estimating the quantity of water seepage either through the body or foundation of earth structures. For liquid flow at very high velocity, Darcy's law becomes invalid. The same is true also for clays with steady-state flow. Many experiments that have been performed to study the validity of Darcy's law have been summarized and discussed by Muskat [11] and Scheidegger [12]. Several empirical and semi-empirical relations for predicting the hydraulic conductivity or the permeability of granular soils are available in the literature. Two relations like that of Kozeny–Carman (proposed by Kozeny [9] latter modified by Carman [1, 2] and Taylor [13]) that have been developed for granular soils have a good theoretical basis. Recently, a renewed interest in reviewing various models for predicting the saturated hydraulic conductivity or the coefficient of permeability and checking the utility of the more theoretically sound predictive models to different local soils has been observed [3, 5]. By now, how the factors as stated above affect the permeability of clean sand and gravels are well understood. However, there is still a need to have more database on different local soils to assess how these changing factors affect the actual k values and either check the validity of the existing expressions or develop new expressions for estimating quickly the values of k. With the above in view, k is determined in the laboratory for two sands, namely Ganga sand (a clean river sand) and Ennore sand (a clean beach sand) pouring them at different void ratio. These data are then used to check the validity of a few empirical and semi-empirical relations that are available in the literature.

2 Models for Estimation of Coefficient of Permeability

Prior to the development of rational models on mathematical basis, few purely empirical correlations have been suggested. One of the earliest efforts based on grain size

distribution by Hazen [7] is for uniform sand ($C_U < 5$) having D_{10} between 0.1 and 3 mm in their loose condition, and Darcy's k equals,

$$k(\text{cm/sec}) = C D_{10}^2 \tag{2}$$

where D_{10} is in cm.; $C =$ Hazen's coefficient $= 80$–120 (a value of 100 is commonly used). The coefficient 100 is the average of many values; individual values ranged from 41 to 146, but most of the values were between 81 and 117 [7]. The pore shape and size are not considered in Eq. 2. Thus, this formula can be used only as an expression of average conditions for the range as mentioned and cannot reflect the changing variables as discussed.

Casagrande [4] proposed a simple relation for the coefficient of permeability for fine to medium clean sand in the following form:

$$k = 1.4e^2 k_{0.85} \text{ cm/sec} \tag{3}$$

where $k_{0.85}$ is the coefficient of permeability at a void ratio of 0.85.

The above correlation depends on the void ratio only and, as such, many of the limitations of Hazen's equation also apply herein also. The constant 1.4 appearing in the equation may also be not applicable for all types of sands.

The following Kozeny–Carman equation for the permeability of soils takes into account the specific surface area of the soil, tortuosity of the flow path apart from the other factors:

$$k = \frac{1}{k_0 S^2} \frac{\gamma}{\mu} \frac{e^3}{1+e} \text{ cm/sec; at } 20\,^\circ\text{C} \tag{4}$$

$k_0 =$ factor depending on pore shape and ratio of length of actual flow path to soil bed thickness; $S =$ specific surface area (1/cm); $\gamma/\mu =$ permeant unit weight/permeant viscosity (1/cm-sec); $e =$ void ratio.

Carrier III [3] suggested a procedure to estimate the specific surface area (S) form from the particle size distribution. For example, if a soil consists of uniform spheres of diameter D (cm),

$$S = \text{area/volume} = \left(\pi D^2\right)/\left[\left(\pi D^3/6\right)\right] = 6/D \tag{5}$$

If the soil consists of non-uniform spheres, then the effective diameter D_{eff} can be calculated from the particle size distribution

$$D_{\text{eff}} = 100\% / \left[\sum \left(f_i D_{av_i}\right)\right] \tag{6}$$

where $f_i =$ fraction of particles between two sieve sizes; larger [l] and smaller [s] (%); and $D_{ave_i} =$ average particle size between two sieve sizes (cm) $= D_{li}^{0.404} \times D_{si}^{0.595}$

Then,

$$S = 6/D_{\text{eff}} \, \text{cm}^{-1} \tag{7}$$

The smaller particles have the most influence on the calculated D_{eff} and therefore on S. Finally, to account for the angularity of the individual soil particles, a shape factor SF can be introduced

$$S = \text{SF}/D_{\text{eff}} \, \text{cm}^{-1} \tag{8}$$

Fair and Hatch [6] suggested the following values for the shape factor, SF: spherical—6.0; rounded—6.1; worn—6.4; sharp—7.4; and angular—7.7. Loudon (1952) suggested the following values: rounded—6.6; medium angularity—7.5; and angular—8.4.

Considering flow through soil similar to flow through a bundle of capillary tubes of extremely irregular shape, Taylor [13] developed the following equation using Poiseuille's law.

$$k = D_s^2 \frac{\gamma_w}{\mu} \frac{e^3}{1+e} C \, \text{cm/sec} \tag{9}$$

where k = the Darcy coefficient of permeability; D_s = some effective particle diameter; C = shape factor. As D_s is the diameter of particle having a specific surface of S, Taylor's equation can be considered simplification of Kozeny–Carman equation.

Chapuis [5] observed that the extended Hazen's equation and a specific Kozeny–Carman equation for sand and gravel give predictions that vary from good to questionable and then form the basic considerations developed a better semi-empirical predictive relationship for k in cm/sec;

$$k = 2.4622 \left[D_{10}^2 \frac{e^3}{1+e} \right]^{0.7825} \text{cm/sec} \tag{10}$$

Using the above correlations, it is possible to estimate the permeability values if the constants and the parameters appearing in the equations are known. Some of these aspects are looked into by conducting laboratory tests on local river and beach sands.

3 Experimental Studies

3.1 Materials Used

To meet the objective as enunciated, Ganga sand and Ennore sand were used in the present study. Ganga sand is river sand collected from the flood plains at Kanpur, situated in northern part of India. Ennore sand is Indian standard sand obtained

from Tamil Nadu, situated in southern part of India. The grains of Ganga sand are predominantly angular with minor amounts of flaky as well as rounded grains; however, the grains of Ennore sand are nearly spherical and highly rounded. Grain size distribution curves for Ganga and Ennore sands as obtained from sieve analysis are presented in Fig. 1.

The results of grain size analysis and other tests for both the sands are presented in Table 1. As per Unified Classification System, both the sands can be classified as poorly graded sand (Group Symbol—SP) but the Ganga sand has better particle size distribution than Ennore sand.
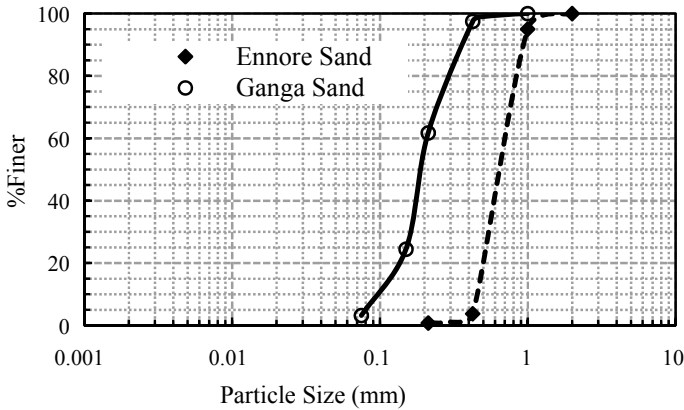
Fig. 1 Particle size distribution for Ganga and Ennore sands

Table 1 Physical properties of Ganga and Ennore sands

Margin	Ganga sand	Ennore sand
D_{10} (mm)	0.09	0.46
D_{30} (mm)	0.17	0.57
D_{60} (mm)	0.2	0.7
C_u	2.22	1.52
C_c	1.445	1.009
G_s	2.67	2.65
e_{max}	0.91	0.82
e_{min}	0.57	0.45

$D_{10}, D_{30}, D_{60}, C_u, C_c, G_s, e_{max}, e_{min}$ are standard notations

3.2 Test Procedure

Coefficient of permeability of Ganga and Ennore sands at different void ratios was determined by constant head permeability testing method as per [8]. Samples were prepared by dry pouring of sand into the mold in layers and subsequent tamping. A hydraulic constant gradient equal to 10 was set for all the tests. A downward water flow was applied, and steady flow was established for all the samples before taking the measurements. Coefficients of permeability obtained at room temperature were converted to the same at 20 °C.

4 Results and Discussions

Various theoretical expressions discussed above for predicting the coefficient of permeability and its variation with voids ratio were obtained for both Ganga and Ennore sands. The theoretical values were compared with the measured values.

Hazen's equation (Eq. 2) when applied to Ganga sand predicts higher permeability values; however, the permeability values are of the same order (Fig. 2). Predictions from Hazen's equation do not depend on the change in void ratio. But, in fact, the permeability values are dependent on the same, and it increases as the void ratio is increased.

In case of Ennore sand, the predictions were very high as compared to experimental results. The predicted permeability values were as high as 102 cm/sec (Fig. 3). Using Casagrande equation (Eq. 3) and measured k value for e value $k_{0.85}$ was found out for both Ganga and Ennore sands. Now using this $k_{0.85}$ value, the variation of
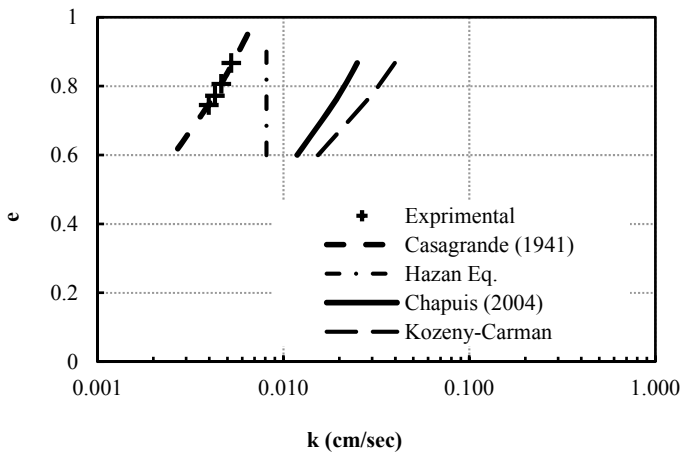
Fig. 2 Void ratio versus coefficient of permeability—Ganga sand
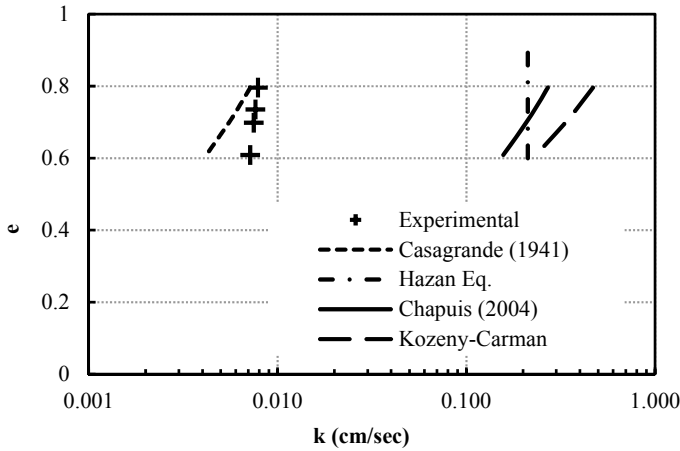
Fig. 3 Void ratio versus coefficient of permeability—Ennore sand

permeability with void ratio was calculated for Ganga sand and Ennore sand and plotted in Figs. 2 and 3.

From Kozeny–Carman equation (Eq. 4), the permeability values of both Ganga sand and Ennore sand were predicted with different void ratios and plotted in Figs. 2 and 3, respectively. The specific surface areas were predicted by the procedure described above [3]. It is observed that the predicted values are very high as compared to the experimental values.

The permeability equations (Eqs. 4 and 9) indicate that a plot between k and $e^3/(1 + e)$ can be represented by straight line. But it is also seen from experimental data [13] that other relationships between k and $e^3/(1 + e)$ or k and e^2 can be represented by linear equations as well. The variations of coefficient of permeability with e^2, $e^2/1 + e$ and $e^3/1 + e$ for Ganga sand and Ennore sand are shown in Figs. 4 and 5.

The test data on Ganga sand shows that the plot of k versus $e^3/1 + e$, $e^2/1 + e$ and e^2 can be approximated by straight line. Casagrande's equation (Eq. 3) shows that the permeability bears a linear relationship with the square of the void ratio. Similar behavior is observed when the data is plotted as a function of $e^2/1 + e$ as was first observed by Taylor [13]. But, straight lines passing through origin cannot be fitted through Ennore sand data. As the linear variation of k versus $e^3/1 + e$ is found suitable for Ganga sand, it can be concluded that Taylor's equation (Eq. 9) is applicable to Ganga sand. The expression given by Chapuis [5] could not predict the correct permeability values for Ganga sand and Ennore sand. Considering the trend of data, a power equation similar to Eq. 10 was fitted to the experimental data (Fig. 5), and the following equation can be used for sands considered in the present study:

$$k = A\left[D_{10}^2 \frac{e^3}{1+e}\right]^B \tag{11}$$
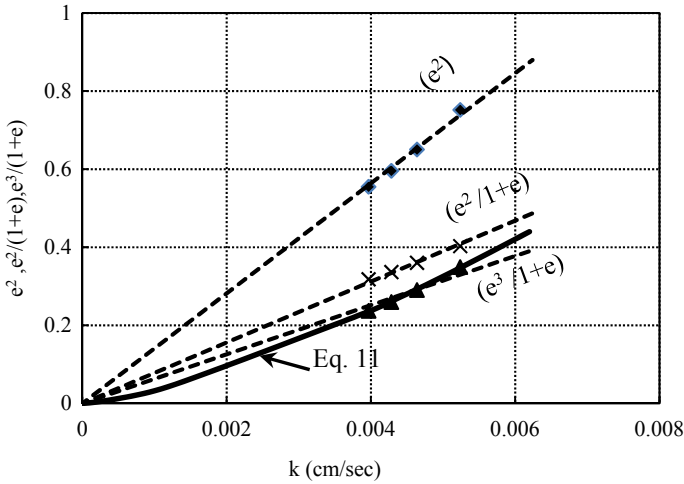
Fig. 4 k versus void ratio functions—Ganga sand
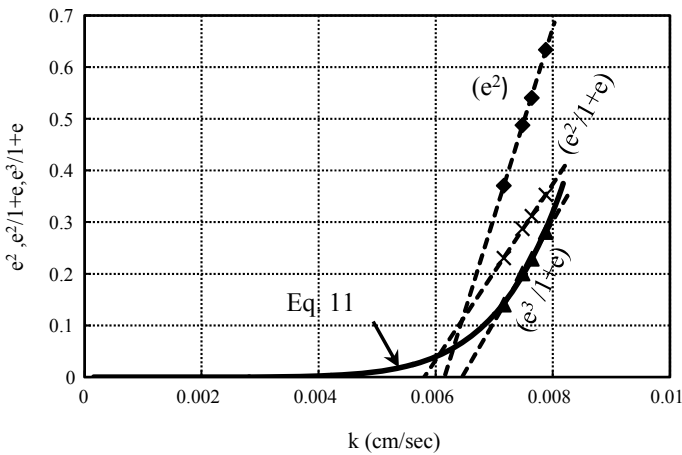
Fig. 5 k versus void ratio functions—Ennore sand

where for Ennore sand $A = 0.0116$ and $B = 0.1368$.

It is also observed (Fig. 4) that for Ganga sand, the variation of k with $e^3/(1 + e)$ can be better represented by Eq. 11 ($R^2 = 0.997$). Therefore, the constants 'A' and 'B' were also calculated for Ganga sand, and it was found that $A = 0.3406$ and $B = 0.7107$ can be used to predict the permeability values of Ganga sand.

5   Conclusions

Hazan equation gives correct order of permeability value for Ganga sand, but for Ennore sand, none of the permeability predictive models could provide the correct picture. Taylor's equation fitted the permeability data for Ganga sand better, and the empirical relation proposed by Casagrande [4] gives quite accurate variation of permeability with void ratio. Relations as suggested by Kozeny–Carman and Chapuis [5] could not predict the correct permeability coefficients for both Ganga sand and Ennore sand. For Ganga sand, predictions were one order higher, and for Ennore sand, predicted values were two orders higher than that of experimental values. For both Ganga sand and Ennore sand, equation as proposed by Chapuis [5] can be used for correct predictions of the permeability values provided the multiplication and power coefficients (*A* and *B*) are found from experiments conducted on the respective sands. The coefficients cannot be universally applied for all types of sand. The limited study shows that no single equations with well-defined parameters are adequate enough to predict the coefficient of permeability for all types of soils. This study also highlights the fact that there exists no unique relationship (whatever may be its rational and scientific basis) that would be the panacea for predicting the coefficient of permeability values for all types of soils.

References

1. Carman, P.C.: Fluid flow through granular beds. Trans. Inst. Chem. Eng. Lond. **15**, 150–166 (1937)
2. Carman, P.C.: Flow of Gases Through Porous Media. Butterworths, London (1956)
3. Carrier III, W.D.: Goodbye, Hazen; Hello, Kozeny-Carman. J. Geotech. Geoenviron. Eng. **129**(11), 1054–1056 (2003)
4. Casagrande, A.: Seepage through dams. In: Contributions to Soil Mechanics 1925–1940. Boston Society of Civil Engineering, Boston (1941)
5. Chapuis, R.P.: Predicting the saturated hydraulic conductivity of sand and gravel using effective diameter and void ratio. Can. Geotech. J. **41**, 787–795 (2004)
6. Fair, G.M., Hatch, L.P.: Fundamental factors governing the streamline flow of water through sand. J. Am. Water Works Assoc. **25**, 1531–1565 (1933)
7. Hazen, A.: Discussion: dams on sand foundations. Trans. ASCE **73**, 199 (1911)
8. IS: 2720 (Part 36): Method of test for soils—Laboratory determination of permeability of granular soil (Constant Head). Bureau of Indian Standards, New Delhi, India (1987)
9. Kozeny, J.: Ueber kapillare leitung des wassers im boden. Sitzungsberichte Wiener Akademie **136**(2a), 217–309 (1927)
10. Leonard, G.A.: Foundation Engineering. International Students Edition, McGraw Hill Book Company, New York and Kogakusha Company Limited, Tokyo (1962)
11. Muskat, M.: The Flow of Homogeneous Fluids Through Porous Media. McGraw Hill Book Company Inc., New York (1946)
12. Scheidegger, A.E.: The Physics of Flow Through Porous Media. MacMillan, New York (1957)
13. Taylor, W.D.: Fundamentals of Soil Mechanics. Wiley, New York (1948)

Geotechnical Characterization and Mineralogical Evaluation of Soils in Srinagar City, Jammu and Kashmir

Falak Zahoor [ID]**, K. Seshagiri Rao, Mohd Younis Hajam** [ID]**, Irfan Ahmad Kumar** [ID]**, and Hilal Ahmad Najar** [ID]

Abstract Srinagar city in the Kashmir valley of Jammu and Kashmir state has been studied to understand the types of soils present in the city. Disturbed and undisturbed samples were collected from 30 locations at a depth of 1 m in the main city. Index properties and engineering properties were evaluated from the geotechnical laboratory tests. X-ray diffraction technique was used to determine the mineralogical composition. Results indicate that soils at this depth in Srinagar city are predominantly fine grained. The proportion of clay size in the soils ranges from 7% to high values of about 42% in Batpora and Hawal. The soils have been classified as silty or clayey soils having intermediate to high plasticity according to the Indian Standard and Unified Soil Classification Systems. Low swelling potential and low activity were observed during laboratory tests. This behavior is supported by mineralogical analysis which revealed presence of Quartz and Illite minerals in the soils. Absence of high swelling minerals makes the soil less problematic. Shear strength parameters (c and φ) were found to be low to medium except in few areas like Hariparbat, Harwan, Cheshmashahi and a few areas in the central portion of the city. This suggests that bearing capacity of the soils is less and thus needs attention before starting any engineering work.

F. Zahoor · K. S. Rao (✉)
Indian Institute of Technology Delhi, Delhi, India
e-mail: raoks.iitd@gmail.com

F. Zahoor
e-mail: falaq.zahoor@gmail.com

F. Zahoor · M. Y. Hajam · I. A. Kumar · H. A. Najar
National Institute of Technology Srinagar, Srinagar, Jammu and Kashmir, India
e-mail: er.mohdyounis@gmail.com

I. A. Kumar
e-mail: irfaank4515@gmail.com

H. A. Najar
e-mail: er.ahmadhilal@gmail.com

1 Introduction

Soil is the most basic and easily available natural material and is encountered in
all civil engineering works. Civil engineering structures are constructed either of
the earth, on the earth or within the earth. Types of soils which are present in any
area depend on the mode of their origin through varied geological processes that the
region has undergone in the past. Characteristics and behavior of soils are further
influenced and continuously modified by climatic conditions and other environmental
factors which are prevalent in the region. The environmental factors govern the
nature and extent of weathering to which rocks and soils are subjected. This makes
their behavior highly unpredictable and therefore the safety and stability of any
engineering structure constructed of soil or on soil are entirely dependent on a proper
investigation of its geotechnical properties. It becomes an essential task to distinguish
amongst the various kinds of soils in order to reduce or avoid hazards while dealing
with soils [1].

The aim of this study is to characterize soils in Srinagar city and create a database
of information of the geotechnical properties. For this purpose, disturbed and undis-
turbed soil samples were collected at a depth of about 1 m from 30 locations within
the city. Laboratory tests were conducted on all soil samples to determine the index
properties and the engineering properties. Index properties including in situ water
content, in situ density, specific gravity, grain size distribution and Atterberg limits
and engineering properties including shear strength and compaction characteristics
have been determined directly from the tests. The database will help to understand
the general variation of soil properties in the study area and will serve as a source
of valuable information to determine the types of soils present in the region. The
engineering suitability of soils within Srinagar city may be further investigated by
utilizing this data.

1.1 Study Area

Srinagar is one of the most densely populated districts in Jammu and Kashmir. It is
the summer capital of the state and is situated in the Kashmir division. Kashmir is a
NW-SE-oriented oval-shaped valley within the Himalayan region. The North eastern
margin of the basin is delineated by Zanskar range and the South eastern margin by
Pir Panjal range. Himalayan region is highly active tectonically due to the presence
of a large number of faults which are mainly thrusts.

Kashmir valley basin has been filled by about 1300 m of sedimentary deposits
over a period of 4 million years, resulting from the uplifting of the Pir Panjal range

as a result of tectonic movements within the thrusts in the region [2]. Srinagar city lies in the center of the Kashmir valley and is, therefore, mostly plain. Figure 1 shows a map of Srinagar city superimposed by the topographic layer for the region and elevation contours at 100 m intervals. However, topography varies due to the presence of a few isolated hills like Hari Parbat and Shankaracharya hill within the city, and Zabarwan hills which form a part of the mountain range on the eastern end. The general elevation in the central portion of the city is 1585 m above mean sea level and varies gradually to about 1620 m in some of the peripheral areas. The hills stand up to an elevation of 200–300 m above the level of the city. Dal lake, Anchar lake, a few wetlands and the river Jhelum form a system of water bodies within the region, being originally depressions created during the formation of the valley filled with water in the past history. Jhelum flows through the middle of the study region in the NE-SW direction. Presence of lakes, rivers and hills within the city creates a depositional environment. The surficial soils in the study area are thus younger sediments deposited from the lakes, flooding of rivers and sediments brought down by gravity from hills and mountain ranges. There are hence, mostly soft, unconsolidated fluvial sediments around the water bodies.
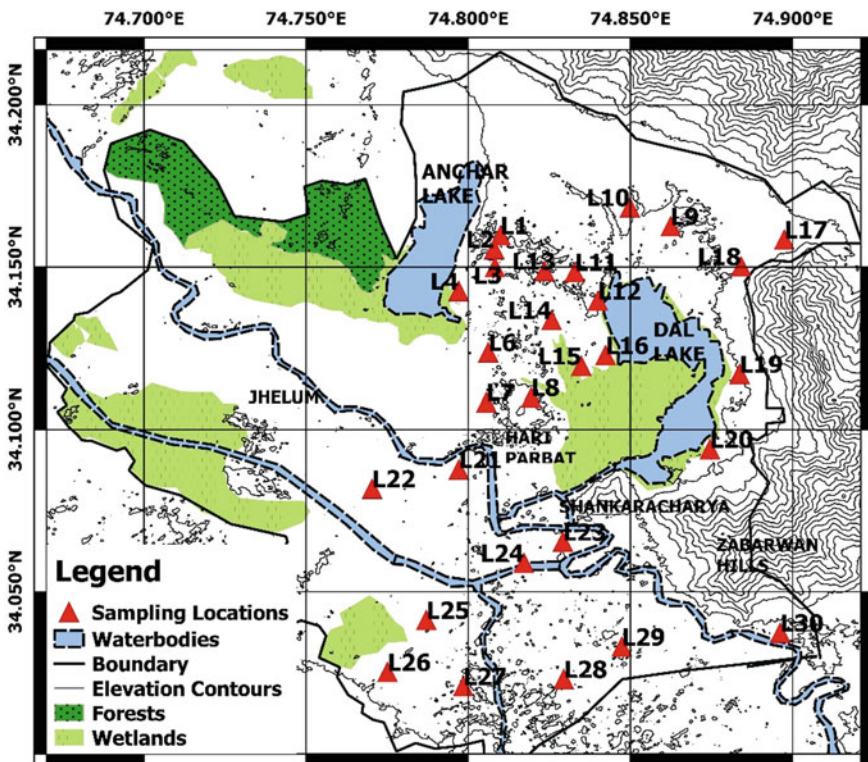
Fig. 1 Map of Srinagar city showing selected locations for sample collection

2   Testing and Methodology

2.1   Collection of Samples in the Field

Disturbed and undisturbed soil samples were collected from 30 locations within the Srinagar city (Fig. 1). Sample collection was done from April to May of the year 2019. Top layer was first removed and a trench then dug up to a depth of 1 m using basic digging tools. Undisturbed samples were collected using core cutters, sealed properly and taken to the laboratory in order to avoid change in structure and moisture content of the soil. Disturbed samples were also collected at the same depth from all locations.

2.2   Laboratory Soil Testing

The samples were taken to the geotechnical engineering laboratory in NIT Srinagar and all basic tests for characterization of soils were performed for each site. Indian Standards (IS): 2720 'Methods of Tests for Soils' outlines in separate parts the standardized procedures to be followed to conduct various geotechnical laboratory tests on soils. For this study, geotechnical laboratory tests have been performed in compliance with IS: 2720 (1973) and subsequent revised versions [3]. Index properties including in situ water content, in situ density, specific gravity, grain size distribution and Atterberg limits, and engineering properties including shear strength and compaction characteristics have been determined directly from the tests. Mineralogical analysis of the soils has been performed using X-Ray diffraction technique conducted in the XRD facility in the TEQIP section of NIT Srinagar. Using this data, the soils were classified based on Unified Soil Classification and Indian Soil Classification Systems. Important parameters and properties of the soils were derived from the results of the analyses. Compression index, which is required for the calculation of settlements of fine grained soils, has been calculated indirectly using an empirical equation given by Skempton involving liquid limit.

3   Results and Discussion

Detailed geotechnical information has been obtained for soils in Srinagar from the results of laboratory tests. Further, properties of soils obtained at discrete locations have been plotted in a GIS platform and then interpolated in order to get a spatial distribution of the respective parameters over the whole study region. This helps to visualize the general variation of any parameter over the city and to get a better

understanding of properties and behavior of soils in the region. However, it must be noted that in situ moisture content does not remian constant, and hence geotechnical properties may vary accordingly.

3.1 Index Properties

In situ Tests. The in situ water content of the samples varied between a minimum of 13.76% in Hariparbat and a maximum of 46.2% in Nowgam area. High values were obtained in the belt which extends through Rajbagh, Rawalpora, Nowgam and Sempora in the southern part of the region, which was also clearly observed during the sampling procedure. Dry density was found to be in the range 1.32–2.02 g/cc, with maximum values observed in the northern portion of the city.

Specific Gravity (G). G values of soils in the city lie between 2.409 and 2.688. Most of the sites have G greater than 2.6 except for a few areas like Ahmednagar, Malbagh, Habak, NIT and Cheshmashahi and low values (2.4) in the belt to the south of Jhelum which includes locations like Hyderpora, Peerbagh, Rawalpora, Nowgam and Sempora (L25–L30).

Grain Size Distribution. Sieve analysis revealed that the percentage of particles passing through the 75μ sieve is greater than 50% for soils at all the sites. Thus, they are classified as fine grained soils according to Indian Standard Soil Classification System. The fines content is more than 90% for most of the locations except Hawal, Hariparbat, Nishat, SKUAST (Shalimar) and Harwan, which have some proportion of gravel as well which is probably due to their proximity to hills and mountain ranges. Hydrometer test on the portion of soil passing 75μ sieve gives percentages of silt and clay sizes present in soils. Silt size is predominant in all the sites. Percentage of clay size ranges from very low (7–8%) in Bemina, Rajbagh and Jawaharnagar, to high (30–42.1%) in Soura, Hawal and Batpora (Fig. 2). The variation of percentage of silt size over the region follows a pattern opposite to that of clay size, as the soils are predominantly fine grained.

Atterberg Limits. Since the soils are fine grained, Atterberg limits are significant for further classification using Unified Soil Classification and Indian Soil Classification Systems. From Casagrande liquid limit test, it has been found that liquid limit (w_L) for soils in the region varies between 31.3% and 60.8%. The spatial distribution of liquid limit over the region is shown in Fig. 3. Liquid limit for the soils is mostly low for the whole region, reaching up to slightly higher values in areas like Peerbagh, Nowgam and Hawal. Plastic limit (w_P) was also determined and the results obtained indicated a range of 17.8–40.4%. Plasticity index (I_P) gives the degree of plasticity of a fine grained soil and is calculated from the Atterberg limits. The obtained values range from 8 to 27.9%, which means that the soils have intermediate to slightly high plasticity characteristics. Subsequently, points were plotted on the plasticity chart to classify the soils as silts and clays on the basis of their behavior (Fig. 4).
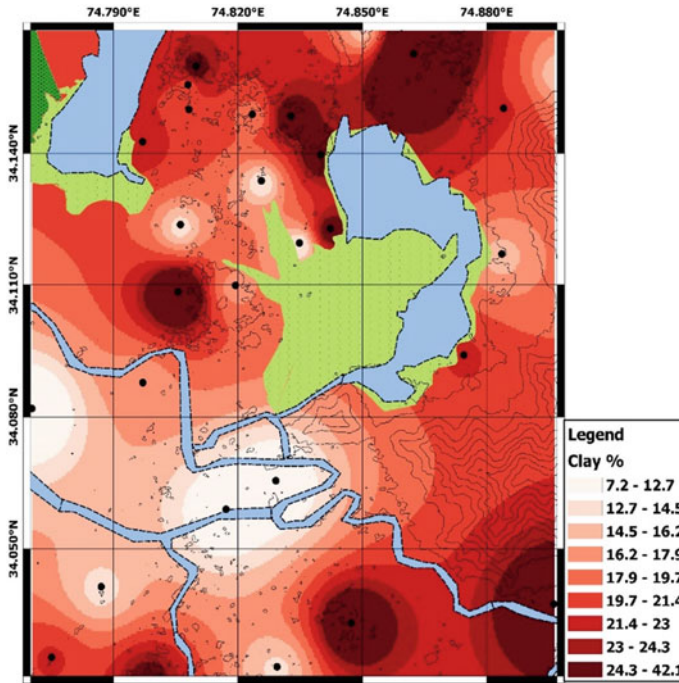
Fig. 2 Spatial distribution of percentage of clay size in soils in the Srinagar city

It was observed that soils around the Jhelum River behave as silts, whereas in areas in the northern part of the study region, the behavior is clayey. This might be due to the deposition of silt by the river during floods. As is indicated by the plasticity chart, soils of Hawal, Cheshmashahi, Rawalpora and Nowgam show high compressibility ($w_L > 50\%$) while others are categorized as low compressibility soils as per the USCS, and low and intermediate compressibility soils as per the ISSCS. Moreover, as the points are nearer to the A-line, it can be deduced that the clay mineral present in the soils is either Illite or Kaolinite, depending on whether the points lie above or below the A line, respectively. This suggests that the soils have low swelling and shrinkage potential. A number of parameters can be evaluated once the Atterberg limits are known.

Activity is another parameter derived from plasticity index I_P and percentage of clay fraction (F) in the soils defined by Skempton in 1953. Activity corresponds to plastic behavior over a large range of water content which means high shrinkage and swelling characteristics. The range of activity obtained for soils in Srinagar city was 0.43–1.5. It was observed that the soils are mostly Inactive (A less than 0.75) and Normal (A between 0.75 and 1.25), except for Bemina, Anchar, Lalbazar and Nigeen which are slightly active (A greater than 1.25). Low values indicate presence of Kaolinite and Illite as clay minerals. Values nearer to 1.5 may indicate presence of Montmorillonite which must be verified by mineralogical analysis through XRD.
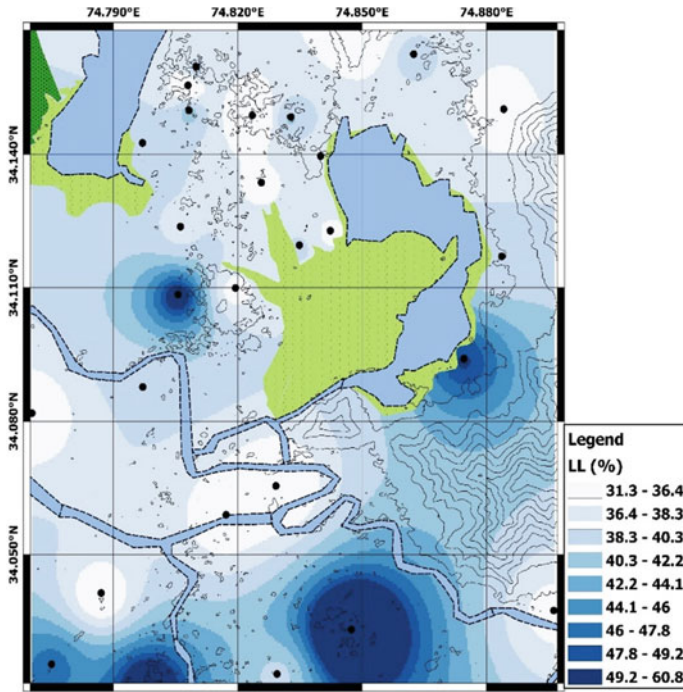
Fig. 3 Map showing variation of liquid limit of soils over the area in Srinagar city
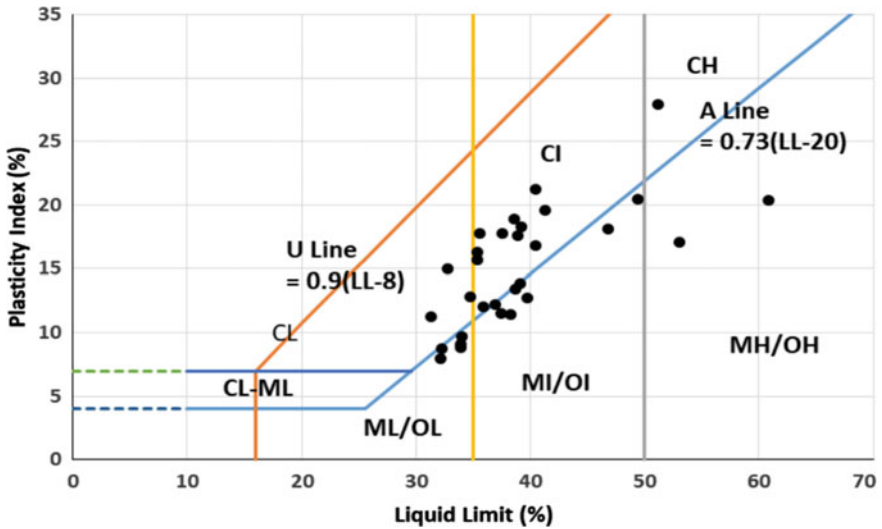
Fig. 4 Plasticity chart with points (represented as dots) plotted for the 30 selected locations

Flow index (I_F) signifies the rate of loss of shear strength of a soil with increase in water content. The values of flow index (I_F) for soils tested for the study region fall between 0.543 and 5.038. Higher values signify lower shear strength of soils. Toughness index (I_T) is a measure of shear strength of soils at plastic limit. The values obtained are greater than 1 for all locations which indicates good shear strength at plastic limit.

The in situ behavior of a soil deposit at its natural water content (w_n) is studied by using two indices: Liquidity index (I_L) and consistency index (I_C). Liquidity index gives nearness of the natural water content to the liquid limit of a soil, whereas consistency index gives nearness of the natural water content to the plastic limit of a soil.

From the results obtained from the analyses, most of the locations which lie in the northern portion of the city have low I_L (less than 0.5) and high I_C (greater than 0.5), suggesting that they are stiff and thus good as foundation materials in their natural state of water content. A few locations like Bemina, Rajbagh and Nowgam near river Jhelum have values nearer to 1, signifying that they have soft consistency, and thereby construction of foundation at the in situ water content may not be feasible. However, these indices are subject to change in natural water content which varies drastically with weather conditions.

3.2   Engineering Properties

Compression Index. Compression index is an important parameter with the help of which settlement can be calculated in a soil deposit under a loading. Compression index has been determined for the whole study area indirectly by using an empirical equation given by Skempton in 1944 [4]. The obtained values for the region range between 0.149 and 0.355. This equation signifies that compressibility is high in soils of high liquid limit. Thereby, a similar variation is observed for C_C for the region as w_L. Higher compression index means that a larger amount of settlement in the soils may be expected under loading, which thus needs to be taken care of in the design of engineering structures.

Compaction Characteristics. Proctor compaction test has been performed on all the samples to obtain the compaction characteristics for the region. The compaction curves were plotted for all soils and values of MDD and OMC were extracted. The range of MDD is 1.37–1.77 g/cc and that of OMC is 16.3–31.2% for the region. The results conform to the values generally anticipated for silty clays and clayey silts. MDD values are low for Nowgam, Rawalpora, Peerbagh, Hawal, Cheshmashahhi and Nowshera. It has been noticed that the variation in OMC and MDD is for most of the parts consistent with the distribution of clay, silt and sand content. The areas with higher content of clay size and/or lower proportion of sand have higher OMC and lower MDD values and vice versa.

Shear Strength Parameters. Direct shear tests have been conducted on samples compacted at corresponding MDD and OMC to find out the shear strength parameters (c and φ). Spatial distribution of friction parameter for the region is shown in Fig. 5. Higher shear strength parameters (c and φ) were obtained for soils of Cheshmashahi, Harwan and Hariparbat. It is worth mentioning that the high angle of internal friction in these locations might be due to the greater proportion of silt and/or sand contents as a consequence of their proximity to the hilly areas. These areas may thus be expected to possess higher bearing capacities. Areas in the northern part of the city have comparatively lower values of both c and φ which suggests that they may have low bearing capacities. Care must be taken in the geotechnical design of structures in these areas. Locations in the belt around Jhelum, except Sempora, have been found to have medium to high values of cohesion and low to medium values of angle of internal friction. There is an apparent similarity of properties in this belt perhaps due to the similar fluvial deposition from rivers. For the whole region, the angle of internal friction varies between 10.6° and 37.7° and cohesion parameter varies between 11.4 and 64.6 kN/m^2. These results fall in the general range generally obtained for clayey silts and silty clays. Unconfined compressions tests have been conducted on samples which revealed a good agreement with the results of DST.
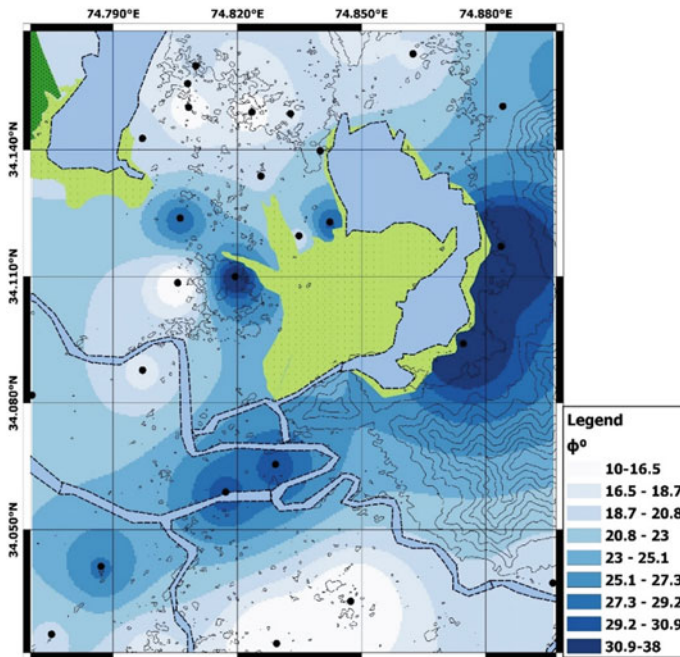
Fig. 5 Spatial variation of angle of internal friction for soils in Srinagar city
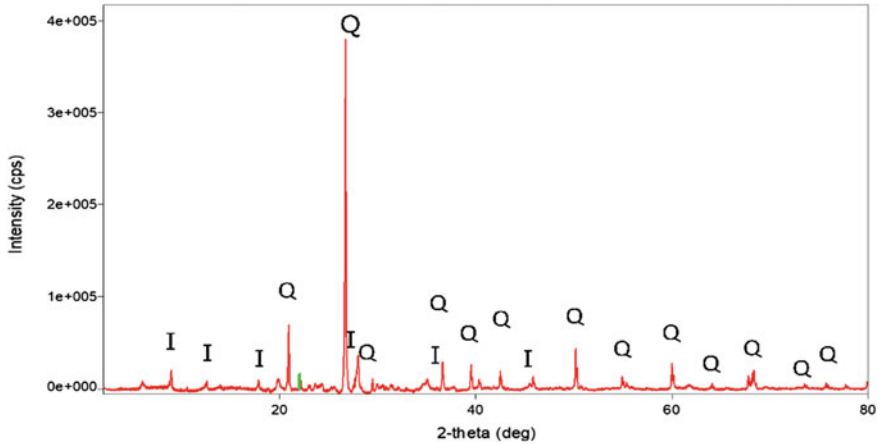
Fig. 6 X-Ray diffraction spectrum of <75μ of sample from location L9. *Q* quartz, *I* illite

3.3 Mineralogical Investigation

X-ray diffraction facility that was accessed in NIT Srinagar uses a C_U K_β filter. Analysis of the data revealed peaks at 2θ angles corresponding to d-spacing of Quartz and Illite minerals (Fig. 6). In the analysis of the data of soils at all the sites, presence of Quartz was established as the primary mineral and that of Illite as the clay mineral. Illite has low swelling potential, low activity and shows low liquid limit as compared to minerals like Montmorillonite and Smectite [5]. Therefore, swelling potential need not be considered during the design of structures in Srinagar. These soils do not pose any serious concern related to volume changes due to change in moisture content. Results of XRD verify the behavior of the soils captured through Atterberg limits.

4 Conclusion

Tables 1, 2, and 3 present the summary of various calculated and derived properties of soils from the results of laboratory tests collected at 1 m depth in Srinagar city.

An attempt has been made to extract maximum useful information about the behavior and nature of the soils from the results. This database may be used as a preliminary guide for planning and design of constructions in the city.

More tests need to be conducted at various depths and also borehole data might be collected to get an extensive and complete knowledge of the soils in Srinagar.

Table 1 Index properties of soils at all locations

Locations	Labels	w_n (%)	ρ_d (g/cc)	Silt (%)	Clay (%)	G
Ahmednagar	L1	21.15	2.006	72.40	26.04	2.531
Buchpora	L2	24.09	1.972	78.16	20.40	2.688
90 feet road	L3	32.05	1.697	76.43	20.53	2.590
Anchar	L4	20.45	1.937	85.05	14.33	2.659
Soura	L5	16.98	2.023	67.30	30.16	2.590
Nowshera	L6	24.20	1.688	78.30	13.53	2.570
Hawal	L7	20.77	1.977	54.43	32.27	2.617
Hariparbat	L8	13.76	1.770	71.44	17.05	2.653
Batapora	L9	18.99	1.898	57.34	42.10	2.655
Tailbal	L10	16.45	1.605	76.26	15.10	2.634
Zukura	L11	23.11	1.898	72.07	27.32	2.625
Habak	L12	25.12	1.721	68.24	26.66	2.532
Malbagh	L13	24.10	1.982	80.08	18.20	2.500
Lalbazar	L14	23.20	1.867	86.40	12.89	2.604
Nigeen	L15	25.85	1.687	85.40	12.56	2.657
NIT Hazratbal	L16	28.03	1.794	67.9	26.29	2.557
Harwan	L17	28.10	1.941	71.66	15.10	2.680
Skuast	L18	24.42	1.937	66.67	21.51	2.590
Nishat	L19	21.61	1.798	75.06	15.50	2.655
Cheshmashahi	L20	42.61	1.747	78.15	21.71	2.486
Karannagar	L21	28.71	1.944	77.26	16.47	2.673
Bemina	L22	31.22	1.318	85.70	07.20	2.640
Rajbagh	L23	32.77	1.765	89.50	07.74	2.688
Jawaharnagar	L24	26.73	1.809	92.00	08.00	2.663
Hyderpora	L25	26.57	1.702	78.76	13.71	2.544
Peerbagh	L26	34.47	1.799	78.76	21.68	2.457
Rawalpora	L27	36.01	1.772	71.45	25.52	2.450
CUK Nowgam	L28	36.88	1.819	78.76	14.06	2.463
Nowgam Railway	L29	46.20	1.658	69.94	28.65	2.409
Sempora	L30	20.33	1.756	71.56	28.03	2.525

Table 2 Results from soil classification tests

Labels	w_n (%)	w_L (%)	w_P (%)	I_P (%)	I_C (%)	I_L (%)	I_F	A	ISCS	USCS
L1	21.15	38.90	21.34	17.56	1.01	−0.01	3.17	0.6	CL	CI
L2	24.09	32.80	17.80	15.00	0.58	0.419	5.02	0.7	CL	CI
L3	32.05	41.33	21.70	19.63	0.47	0.527	8.41	0.9	CL	CI
L4	20.45	40.49	19.26	21.23	0.94	0.056	4.43	1.4	CL	CI
L5	16.98	38.66	25.31	13.35	1.62	−0.62	1.25	0.4	ML	MI
L6	24.20	37.40	25.9	11.50	1.14	−0.15	4.22	0.8	ML	MI
L7	20.77	51.25	23.34	27.91	1.09	−0.09	5.67	0.8	CH	CI
L8	13.76	35.44	19.70	15.74	1.37	−0.38	1.35	0.9	CL	CI
L9	18.99	39.20	34.79	04.41	4.58	−3.58	10.41	0.1	CL	CI
L10	16.45	32.25	24.28	07.97	1.82	−0.98	6.77	0.5	ML	ML
L11	28.03	40.46	23.73	16.73	1.03	0.257	4.73	0.6	CL	CI
L12	25.12	37.59	19.82	17.77	0.71	0.298	1.84	0.6	CL	CI
L13	24.10	31.33	20.01	11.32	0.63	0.361	4.44	0.6	CL	CL
L14	23.20	35.37	19.19	16.18	0.75	0.248	4.21	1.2	CL	CI
L15	25.85	38.64	19.67	18.97	0.67	0.326	4.06	1.1	CL	CI
L16	28.03	35.97	23.94	12.03	0.66	0.340	6.35	0.4	CL	CI
L17	28.10	36.95	24.70	12.25	0.72	0.278	6.93	0.8	ML	MI
L18	24.42	34.74	21.88	12.86	0.80	0.198	2.05	0.5	CL	CL
L19	21.61	39.19	25.24	13.95	1.26	−0.26	7.40	0.9	ML	MI
L20	42.61	49.43	28.91	20.52	0.33	0.668	8.28	0.9	ML	MI
L21	28.71	38.31	26.90	11.41	0.84	0.159	8.45	0.6	CL	CL
L22	31.22	33.86	24.80	9.06	0.29	0.709	10.79	1.2	ML	ML
L23	32.77	32.26	23.60	8.66	−0.06	1.059	2.96	1.1	ML	ML
L24	26.73	33.97	25.16	8.81	0.82	0.178	4.05	1.1	ML	MI
L25	26.57	34.00	24.30	9.70	0.77	0.234	6.15	0.7	ML	ML
L26	34.47	46.87	28.70	18.17	0.68	0.318	7.08	0.8	ML	MI
L27	36.01	53.01	35.91	17.01	0.99	0.006	5.58	0.6	MH	MH
L28	36.88	39.73	27.06	12.67	0.22	0.775	6.88	0.9	ML	MI
L29	46.20	60.8	40.40	20.40	0.71	0.284	11.6	0.7	MH	MH
L30	34.47	35.63	17.75	17.88	0.85	0.935	5.43	0.6	CL	CI

Table 3 Engineering properties of soils at each location

Locations	Compaction		DST		UCS	C_c
	MDD (g/cc)	OMC (%)	c (kPa)	Φ (°)	C_u (kPa)	
L1	1.643	19.76	26.98	19.92	40.37	0.20
L2	1.736	17.68	64.57	16.25	68.83	0.16
L3	1.648	18.23	37.12	14.00	31.19	0.22
L4	1.657	19.81	18.39	21.99	17.40	0.21
L5	1.667	20.30	11.74	17.56	20.77	0.20
L6	1.552	23.97	37.64	29.16	34.9	0.19
L7	1.560	24.00	35.21	12.78	39.58	0.29
L8	1.706	17.50	42.90	33.34	19.82	0.18
L9	1.671	20.20	19.65	18.42	14.98	0.20
L10	1.775	17.58	35.87	16.69	31.14	0.16
L11	1.687	18.62	13.68	18.42	18.00	0.21
L12	1.667	20.05	15.47	22.20	21.49	0.19
L13	1.716	18.40	33.25	14.03	41.98	0.15
L14	1.667	21.07	37.67	20.54	41.69	0.18
L15	1.648	20.50	40.44	19.92	42.07	0.20
L16	1.719	17.73	53.63	29.52	42.28	0.18
L17	1.712	19.44	50.96	26.17	30.93	0.19
L18	1.728	18.52	12.14	24.61	18.98	0.17
L19	1.557	20.00	13.49	37.76	15.78	0.20
L20	1.562	21.27	54.82	35.29	58.64	0.28
L21	1.643	21.00	27.96	18.00	35.6	0.19
L22	1.663	17.50	44.00	21.8	46.00	0.17
L23	1.716	17.74	30.84	30.24	34.6	0.16
L24	1.697	18.00	56.78	30.24	51.2	0.17
L25	1.736	16.30	34.05	27.69	31.5	0.17
L26	1.512	22.48	30.18	20.55	32.58	0.26
L27	1.491	25.64	49.32	17.56	29.32	0.30
L28	1.600	21.86	35.89	10.61	40.32	0.21
L29	1.370	31.20	39.35	12.44	33.16	0.36
L30	1.702	18.03	11.46	19.28	16.20	0.18

References

1. Terzaghi, K., Peck, R.B., Mesri, G.: Soil Mechanics in Engineering Practice, 3rd edn. Wiley, New York (1948)
2. Burbank, D.W., Johnson, G.D.: The Late Cenozoic, Chronologic and stratigraphic development of the Kashmir intermontane basin, north-western Himalaya. Paleogeogr. Paleoclimatol.

Paleoecol. **43**, 205–235 (1983)
3. BIS: IS: 2720 'Methods of Tests for Soils'. 2nd rev. Bureau of Indian Standards, India (1985, R2015)
4. Mitchell, J.K., Soga, K.: Fundamentals of Soil Behavior, 3rd edn. Wiley, Hoboken (2005)
5. Skempton, A.W.: Notes on the compressibility of clays. Q. J. Geol. Soc. Lond. **100**, 119–135 (1944)

Determination of Volumetric Shrinkage of Soils by Dish Method

Sanjay Kumar Verma, Sagar Shrivastava, Saleem Akhtar, and Rajesh Bhargava

Abstract Shrinkage characteristics of soils are very important parameters for consideration in the design of a safe and stable foundation. Volumetric shrinkage test gives a very effective idea about shrinkage behaviour of the soils. Bureau of Indian Standards (BIS) recommended the method of test for soils, for determination of shrinkage factors, as per Indian Standards IS: 2720 (Part 6)—1972 (Reaffirmed 1995). This method is commonly used to determine various shrinkage factors of soils. This laboratory method is very sophisticated, costly and time taking method. Generally, this test is not available easily in the middle class and small towns, and everyone cannot afford the expense of this test. Authors developed an alternative method named "Dish Method" to determine volumetric shrinkage of soils. The study suggests a very simple, quick, effective and economical procedure for the determination of volumetric shrinkage of soils by steel dish, plastic dish and paper dish methods. The proposed method provides a preliminary idea about the shrinkage characteristic of cohesive soil.

S. K. Verma (✉)
Takshshila Institute of Engineering and Technology, Jabalpur, India
e-mail: sanjayverma@takshshila.org

S. Shrivastava
Gyan Ganga Institute of Technology and Science, Jabalpur, India
e-mail: sagar.shrivastava@gmail.com

S. Akhtar · R. Bhargava
Rajiv Gandhi Proudyogiki Vishwavidhyalaya, Bhopal, India
e-mail: sargpv@gmail.com

R. Bhargava
e-mail: rajeshbhargava.bpl@gmail.com

1 Introduction

The study has been carried out in city Jabalpur and its surrounding. In central India, city Jabalpur (23° 10′ N, 79° 57′ E, MSL—402 M) is seismically sensitive because it is located in an earthquake-prone area. As per IS: 1893-1984, Jabalpur comes under earthquake zone III [2]. The study is particularly more applicable in cities like Jabalpur which are vulnerable to the occurrence of major earthquakes as one which took place earlier. An earthquake of M 6.0 on Richter scale rocked Jabalpur and the surrounding area in the early morning hours on 22 May 1997. The epicentre of the earthquake was located about 12 km SE to the city of Jabalpur [5]. The maximum intensity observed in the epicentre area due to this earthquake was VIII on MMI scale. Maximum losses were observed on non-engineered constructions. Its after-effects were the death of about 50 people and a great loss of property exceeding rupee 500 crores [7]. Looking to the seismic vulnerability of the city, a study has been done to bring out the engineering characteristics of soils in sensitive areas for safe and stable construction. In this case study, ten such sensitive locations have been selected. Field and laboratory tests, e.g. Trial Pits, Trial Bores, Soil Colour, Moisture Content, Specific Gravity, Grain Size Analysis, Liquid Limit, Plastic limit, Shrinkage Factors and Free Swelling Index, etc., have been carried out for determination of various parameters of the soil at selected locations [6]. All tests have been done as per Indian Standard methods recommended by Bureau of Indian Standard (BIS). During the case study in Jabalpur, a method named—dish method, has been originated and developed by the authors. This method may be used as an alternative method for the determination of volumetric shrinkage of soils. Dish method may be considered as a conventional method for assessment of volumetric shrinkage very easy, fast and economically. Selected locations on which study has been done are listed in Table 1 and also shown on the map of Jabalpur city in Fig. 1.

Table 1 List of selected locations

S. No.	Selected locations	Case study nos.	Longitude	Latitude
1	Deen Dayal Chowk Bus Stop	CS 1	23° 11′ 40″ N	79° 54′ 49″ E
2	Shatabdipuram	CS 2	23° 10′ 30″ N	79° 54′ 32″ E
3	Tilwara Ghat	CS 3	23° 06′ 15″ N	79° 52′ 40″ E
4	Rani Durgawati Park	CS 4	23° 09′ 40″ N	79° 56′ 13″ E
5	Gullawa Lake	CS 5	23° 09′ 44″ N	79° 54′ 20″ E
6	Kachhpura Bridge	CS 6	23° 10′ 10″ N	79° 54′ 13″ E
7	S.C. Bose Medical College	CS 7	23° 09′ 05″ N	79° 52′ 10″ E
8	Bhatoli Bridge	CS 8	23° 05′ 42″ N	79° 56′ 32″ E
9	Gokapur Lake J.E.C. Jabalpur	CS 9	23° 11′ 31″ N	79° 59′ 20″ E
10	Jawaharlal Nehru Agriculture University	CS 10	23° 12′ 13″ N	79° 57′ 15″ E
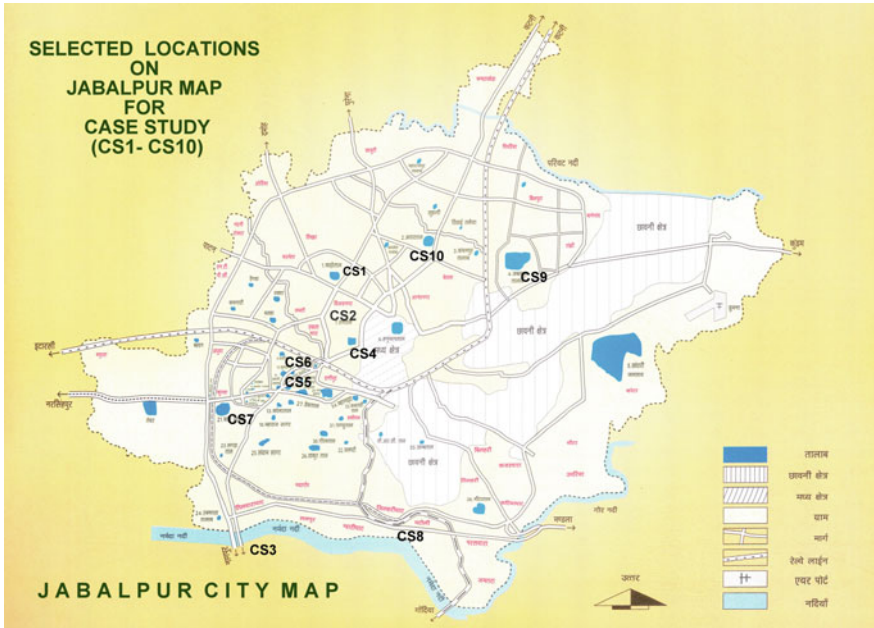
Fig. 1 Selected Locations on Map of Jabalpur. (Map Source: Jabalpur Ke Sarovar – Anmol Dharohar) [8]

2 Determination of Atterberg's Limits of Soil as Per IS: 2720 (Part 5) and Classification of Soil as Per IS: 1498–1970

Atterberg's limits, e.g. Liquid Limit, Plastic Limit and Plasticity Index of Soils as per IS: 2720 (Part 5), and classification of the soil as per IS: 1498–1970 for selected locations under study are compiled in Table 2.

3 Determination of Volumetric Shrinkage of Soil as Per IS: 2720 (Part 6)—1972

Shrinkage factors, e.g. shrinkage limit (%), shrinkage ratio, volumetric shrinkage (%) and degree of shrinkage (%) at all selected locations in Jabalpur (CS1–CS10) have been worked out as per the IS: 2720 (Part 6) [4]. Results of shrinkage factors are mentioned in Table 3.

Table 2 Atterberg's limits as per IS:2720 (Part 5) and soil classification as per IS: 1498-1970

S. No.	Case study nos.	Selected locations	Liquid limit (%)	Plastic limit (%)	Plasticity index (%)	Classification of soils as per IS: 1498–1970
1	CS 1	Deen Dayal Chowk Bus Stop	56	27	29	CH
2	CS 2	Shatbdipuram	56	26	30	CH
3	CS 3	Tilwara Ghat	33	28	5	SML
4	CS 4	Rani Durgavati Park	40	26	14	CI
5	CS 5	Gullawa Lake	51	26	25	CH
6	CS 6	Kachhpura Bridge	51	22	29	CH
7	CS 7	S.C. Bose Medical College	55	24	31	CH
8	CS 8	Bhatoli Bridge	36	22	14	SMI
9	CS 9	Gokalpur Lake J.E.C. Jabalpur	40	26	14	SMI
10	CS 10	Jawaharlal Nehru Agriculture University	52	27	25	CH

4 Determination of Volumetric Shrinkage of Soil by Dish Method

Dish method is developed by authors to determine volumetric shrinkage of soils. This method can be considered as a primary method to assess the shrinkage behaviour of soils. The proposed method suggests the test for determination of volumetric shrinkage of soil very easily and economically. This test can be performed by anyone dish out of three types of shrinkage dishes, e.g. steel dish, plastic dish or paper dish. As per this method; firstly determine inner diameter and depth of these dishes by steel scale up to a least count 0.5 mm (Vernier caliper scale can also be used for more accuracy). Determine the volume of each type of dish. (In this case study, steel dish has been used, and the diameter of the steel dish is 5 cm, and the depth of the dish is 2.5 cm). Take about 100 gm dry soil sample and mix with water in an amount sufficient to fill the soil voids fully and to make the soil pasty enough to be readily worked into the dish without entrapping air bubbles [3]. Fill the dish with the prepared soil sample in three equal layers properly pressed with a spoon. On filling each one-third layer, the dish should be gently struck on the firm surface until the paste is thoroughly compacted and all entrapped air has been brought to the surface. After filling the dish in three layers, strike off the excess soil by a flat

Table 3 Shrinkage Factors at Selected Locations as per IS:2720 (Part 6)

S. No.	Case study nos.	Selected locations	Shrinkage limit (%)	Shrinkage ratio	Volumetric shrinkage (%)	Degree of shrinkage (%)
1	CS 1	Deen Dayal Chowk Bus Stop	13.56	1.95	67.77	40.39
2	CS 2	Shatbdipuram	11.6	1.77	52.8	34.55
3	CS 3	Tilwara Ghat	18.24	1.74	28.03	21.87
4	CS 4	Rani Durgavati Park	14.46	1.84	23.93	19.31
5	CS 5	Gullawa Lake	14.36	1.92	65.3	39.5
6	CS 6	Kachhpura Bridge	16.34	1.87	42.05	29.6
7	CS 7	S.C. Bose Medical College	15.06	1.76	84.98	45.94
8	CS 8	Bhatoli Bridge	15.49	1.72	35.75	26.34
9	CS 9	Gokalpur Lake J.E.C. Jabalpur	13.31	1.91	35.46	26.05
10	CS 10	Jawaharlal Nehru Agriculture University	16.29	1.73	36.67	26.83

spoon. Put the dish for drying in the open air under sunlight for 24–48 h. On drying the sample, measure the dimensions of the dried soil pat with scale up to 0.5 mm. Finally, determine shrinkage in volume of the soil pat.

This method gives very appreciable results in comparison with laboratory test for determination of volumetric shrinkage as per Indian Standard IS: 2720 (Part 6). In this study, volumetric shrinkage of soils for selected locations has been carried out with steel dish. Calculations for the determination of volumetric shrinkage of soils by steel dish method are shown in Table 4, and pictures of the test procedure are shown in Fig. 2a, b.

5 Comparison of Volumetric Shrinkage of Soils

During this study, the volumetric shrinkage of the soils at selected locations has been determined by dish method (developed by the author) and as per Indian Standard method IS: 2720 (Part 6) [4]. The difference in results of volumetric shrinkage by both the above-mentioned methods has also been determined. Comparisons of the results of both the methods for all ten selected locations are shown in Table 5.

Table 4 Determination of volumetric shrinkage of soils by steel dish method

S. No.	Case study nos.	Steel dish			Wet volume of soil (V1)	Dry pat	Depth of dry pat	Volume of dry pat	Dry volume of pat (V2)	Volumetric shrinkage (%)
		Dia of steel dish	Depth of steel dish	Volume of steel dish		Dia of dry pat				
		CM	CM	CM³	CM³	CM	CM	CM³	CM³	{(V1 − V2) * 100}/V2 (%)
1	CS1	5	2.5	49.06	49.06	4.5	1.9	30.20	30.20	62.44
2	CS2	5	2.5	49.06	49.06	4.65	1.95	33.10	33.10	48.23
3	CS3	5	2.5	49.06	49.06	4.7	2.3	39.88	39.88	23.01
4	CS4	5	2.5	49.06	49.06	4.7	2.35	40.75	40.75	20.40
5	CS5	5	2.5	49.06	49.06	4.5	1.9	30.20	30.20	62.44
6	CS6	5	2.5	49.06	49.06	4.6	2.2	36.54	36.54	34.26
7	CS7	5	2.5	49.06	49.06	4.3	1.9	27.58	27.58	77.91
8	CS8	5	2.5	49.06	49.06	4.7	2.2	38.15	38.15	28.61
9	CS9	5	2.5	49.06	49.06	4.6	2.3	38.20	38.20	28.42
10	CS10	5	2.5	49.06	49.06	4.65	2.2	37.34	37.34	31.39
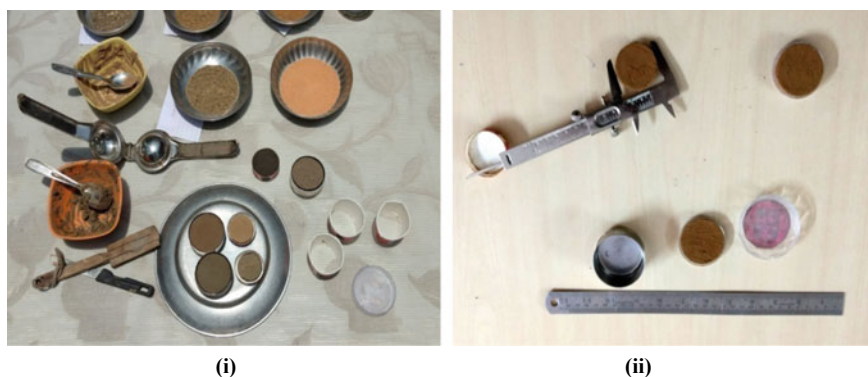
Fig. 2 a, **b** Dish method for determination of volumetric shrinkage (%) of soils

Table 5 Comparison of volumetric shrinkage (%) between IS: 2720 (Part 6) and dish method [1]

S. No.	Name of locations	Case study nos.	Volumetric shrinkage as per IS: 2720 (Part 6) (%)	Volumetric shrinkage by dish method (%)	Difference in volumetric shrinkage (%)
1	Deen Dayal Chowk Bus Stop	CS 1	67.77	62.44	5.33
2	Shatbdipuram	CS 2	52.8	48.23	4.57
3	Tilwara Ghat	CS 3	28.03	23.01	5.02
4	Rani Durgavati Park	CS 4	23.93	20.4	3.53
5	Gullawa Lake	CS 5	65.3	62.44	2.86
6	Kachhpura Bridge	CS 6	42.05	34.26	7.79
7	S.C. Bose Medical College	CS 7	84.98	77.91	7.07
8	Bhatoli Bridge	CS 8	35.75	28.01	7.74
9	Gokalpur Lake JEC Jabalpur	CS 9	35.46	28.42	7.04
10	Jawaharlal Nehru Agriculture University	CS 10	36.67	31.39	5.28
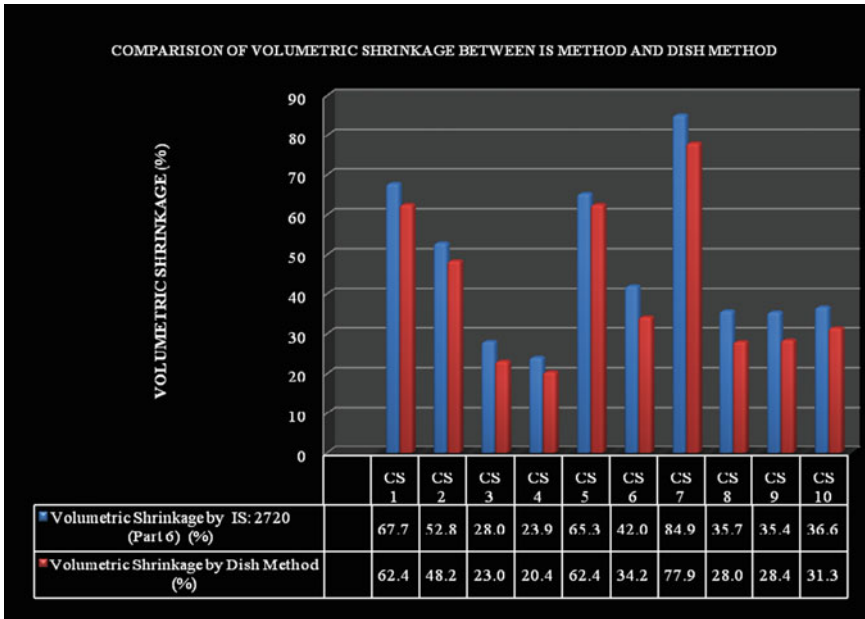
Fig. 3 Comparisons of volumetric shrinkage (%) by IS: 2720 (Part-6) method and dish method

6 Results and Discussion

Volumetric shrinkage of the soils at selected locations has been determined by Indian Standard method and by dish method. Volumetric shrinkage of the soils determined by dish method is on an average 3–8% less than that of the volumetric shrinkage determined by IS: 2720 (Part 6) [4]. Comparison of the result is shown graphically in Fig. 3.

7 Conclusions

Shrinkage on drying is indicative of the structure of the soil. The greater the shrinkage the more dispersed the structure. Volumetric shrinkage of soils at ten selected locations in Jabalpur city and its surrounding has been assessed. Based on the methodology employed and result obtained, it is quite appreciable that volumetric shrinkage of the cohesive soils determined by the dish method is very close to that of determined by laboratory method as per IS: 2720 (Part 6) 1972. Dish method is very easy and economical. This method is so simple and can be used by common persons to assess shrinkage behaviour of the cohesive soil in small towns and villages where soil test facilities are commonly not available. The proposed method can be further

extended to determine the degree of shrinkage of soil, and thus, soil can be easily classified as very poor, poor, medium or good soil.

References

1. IS:1498-1970, Classification and Identification of Soils for General Engineering Purposes, Reaffirmed 1987, BIS, New Delhi (1987)
2. IS:1893-1984, Criteria for Earthquake Resistant Design of Structures, Reaffirmed 2003, BIS, New Delhi (2003)
3. IS:2720-1983, Methods of Test for Soils: Part 1, Preparation of Dry Soil Samples for Various Tests, Second Revision, Reaffirmed 1990, BIS, New Delhi (1990)
4. IS:2720-1972, Methods of Test for Soils: Part 6, Determination of Shrinkage Factors, First Revision, Reaffirmed 1990, BIS, New Delhi (1990)
5. Kanwar, S.S.: Jabalpur Earthquake 22 May 1997, A Geoscientific Study, Geological Survey of India, Special Vol. No. 51, pp. 1-239 (2000)
6. Mittal, S., Shukla, J.P.: Soil Testing for Engineers, Khanna Publishers, New Delhi (1985)
7. Rai, D.C., Narayan, J.P., Pankaj, K.A.: Jabalpur Earthquake of May 22, 1997, Reconnaissance Report, Department of Earthquake Engineering, University of Roorkee, Sept. 1997, pp. 1–101 (1998)
8. Verma, S.: Jabalpur Ke Sarovar - Anmol Dharohar, First Edition, Jal Strot Sanrakshan Prakoshth, Jabalpur (2011)

Comparison Between the Soil Properties of the Coastal and Interior Regions of Gujarat

Param Shah and Manas Kumar Bhoi

Abstract Constructions in the coastal region have been a huge challenge in the civil engineering world for long years, and so, a solutions for the same have to be devised. To study this problem, this paper deals with the soil properties of some coastal belt places of Gujarat region and the soil properties of the non-coastal region of Gujarat. Gujarat's soil type has a wide range of classification, and so, the different properties like the N-value, type of sample, the depth at which the sample are obtained, type of soil in that region, depth of water table, moisture content, field dry density, the Atterberg limits are studied. After studying these properties from the soil reports obtained from various laboratories, a comparison is made between the soil at coastal belt region and non-coastal belt region of Gujarat and the variation is observed in the various properties. Considering, a school building at Hathab, which a coastal belt location, the N-value varies from 10 to 20 blows in a 6 m considered depth. While considering a building at Bhavnagar district, which is away from the coastal area, the N-value varies from 12 to 23 blows in a 6 m, considered depth. While considering the dry density at Hathab, it varies from 1.48 to 1.62 g/cm^3, and the dry density at Bhavnagar district varies from 1.47 to 1.49 g/cm^3, considering 6 m depth. These differences need to be studied, and it will helpful in designing suitable design solutions. Thus, this paper may contribute in future research studies to improve and strengthen soil properties of the coastal region.

Keywords Coastal region · Non-coastal soil · N-values · Dry density · Silica · Atterberg limits · Design solutions

1 Introduction

From the evolution of the construction industry, new challenges have always emerged and the solutions to it have always been tried out. One of the major problems in the construction industry is the construction of structures in coastal region by constantly

© Springer Nature Singapore Pte Ltd. 2021

83

Fig. 1 Places of which the soil reports have been analyzed
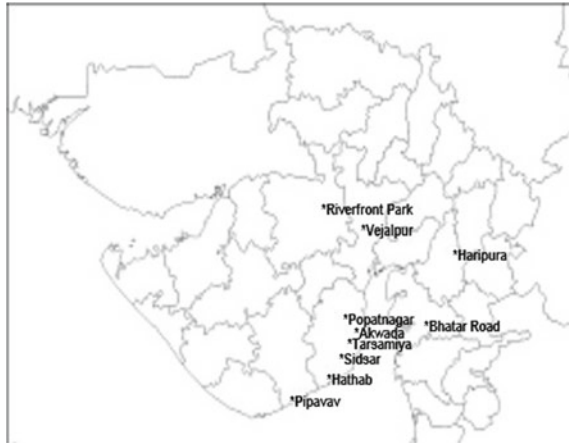
providing challenges to the industry due to complex and vexed behavior of soil in these regions [1]. Thus, to give a direction to design solution to the problems, this paper is written after analyzing the geotechnical properties of the soil like plasticity index, field dry density, cohesion factor, internal angle of friction, moisture content, bearing capacity and SPT value from the soil reports of different places in coastal region and some in the region away from coast, in the state of Gujarat from different laboratories of the state. The places in coastal region of whose the soil reports were analyzed are Tarsamiya, Sidsar, Akwada, Popatnagar and Hathab region of Bhavnagar, Pipavav region of Amreli district, Bhatar Road region of Surat district and riverfront in Surendranagar district. The places in non-coastal region whose soil reports were analyzed are Vejalpur region of Ahmedabad district and Haripura region of Vadodara district. Finally, the result and conclusions have been provided in the graphical form, from which we can interpret the variations that follows along the coastal and non-coastal belt of Gujarat (Fig. 1 and Table 1).

2   Geotechnical Properties

2.1   Plasticity Index (%)

Plasticity index gives an idea about the range in which the given soil shows plastic behavior. The range of water content basically indicates the plastic property of the soil [2].

    0: non-plastic
    0–7: slightly plastic
    7–17: medium plastic
    >17: highly plastic.

Table 1 List of symbols

Group symbol	Group name
GW	Well Graded Gravel
GP	Poorly Graded Gravel
GM	Silty Gravel
GC	Clayey Gravel
SW	Well Graded Sand
SP	Poorly Graded Sand
SM	Silty Sand
SC	Clayey Sand
ML	Silt
CL	Clay of Low Plasticity
OL	Organic Silt, Organic Clay
MH	Silt of High Plasticity
CH	Clay of High Plasticity
OH	Organic Clay, Organic Silt
Pt	Peat

Table 2 Plasticity index for coastal soil [4]

Location	Soil classification	Depth (m)	Plasticity index (%)
Hathab	CH	2.5	35
	CH	4	34
	CH	5.5	40
	CH	7	38
Pipavav	SC	1.5	9
	CH	2.5	37
	CH	4	36
	CH	5.5	38
	CH	7	35

The data is given in Table 2 for coastal and in Table 3 for non-coastal soil.

2.2 Field Dry Density (FDD in g/cc)

The maximum dry density possible is obtained by performing the laboratory standard proctor test on a given field soil, and then, the compaction ability of the layers of soil is determined from the field dry density of that particular soil. So, the compaction degree can be obtained by dividing the field dry density by the maximum dry density.

Table 3 Palsticity index for non-coastal soil [5]

Location	Soil classification	Depth (m)	Plasticity index (%)
Vejalpur Bh-1	CH	3	32
	SC	4.5	13
	SC	6	12
	SM	7.5	NP
	SM	9	4
Haripura	CL	2.5	16.8
	SC	4	11.3
	SC	5.5	16.5
	SC	7	17.2

So, more will be the field dry density more will be the compaction degree. This in turn will be fruitful for the construction purpose as it will be a much hard surface strata. The data is given in Table 4 for coastal and in Table 5 for non-coastal soil.

Table 4 FDD (g/cc) for coastal soil [4]

Location	Soil classification	Depth (m)	FDD (g/cc)
Hathab	CH	2.5	1.64
	CH	4	1.66
	CH	5.5	1.80
	CH	7	1.82
Pipavav	CH	2.5	1.12
	CH	4	1.18
	SC	5.5	1.22
	CH	7	1.27

Table 5 FDD (g/cc) for non-coastal soil [5]

Location	Soil classification	Depth (m)	FDD (g/cc)
Vejalpur Bh-1	CH	3	1.70
	SC	6	1.73
	SM	9	1.76
Haripura	CL	2.5	1.521
	SC	4	1.574
	SC	5.5	1.651
	SC	7	1.689

Table 6 Cohesion factor (C in kg/cm^2) for coastal soil [4]

Location	Soil Classification	Depth (m)	Cohesion Factor (C in kg/cm^2)
Hathab	CH	2.5	0.32
	CH	4	0.32
	CH	5.5	0.34
	CH	7	0.34
Pipavav	CH	2.5	0.4
	CH	4	0.45
	CH	5.5	0.6
	CH	7	0.5

Table 7 Cohesion factor (C in kg/cm^2) for non-coastal soil [5]

Location	Soil classification	Depth	Cohesion Factor (C in kg/cm^2)
Vejalpur Bh-1	CH	3	0.72
	SC	6	0.19
	SM	9	0.00
Haripura	CL	2.5	0.37
	SC	4	0.14

2.3 Cohesion Factor (C in kg/cm^2)

Cohesion factor is an engineering shear strength parameter. This represents the cohesion between the soil particles, and it is more prominent in the case of clay soil. Considering the soil consistency, the cohesion factor plays an important role. More cohesive the soil is, the more the shear strength of soil is, as it will hold the particles more firmly [3]. The data is given in Table 6 for coastal and in Table 7 for non-coastal soil.

2.4 Angle of Internal Friction (ϕ)

Internal friction angle or the angle of internal friction, a shear strength parameter, is the angle between the resultant shear stress and the applied normal effective stress. It is the angle at which shear failure occurs. This shear strength parameter is more prominent in case of granular cohesion less soil like sand and gravel. This can be obtained by both DIRECT SHEAR test and tri-axial shear test [2]. The data is given in Table 8 for coastal and in Table 9 for non-coastal soil.

Table 8 Angle of internal friction (ϕ in degree) for coastal soil [4]

Location	Soil Classification	Depth (m)	Angle of Internal Friction (ϕ in degree)
Hathab	CH	2.5	6
	CH	4	6
	CH	5.5	4
	CH	7	4
Pipavav	CH	2.5	0
	CH	4	0
	CH	5.5	0
	CH	7	0

Table 9 Angle of internal friction (ϕ in degree) for non-coastal soil [5]

Location	Soil classification	Depth (3)	Angle of internal friction (ϕ in degree)
VejalpurBh-1	CH	3	5
	SC	6	27
	SM	9	31
Haripura	CL	2.5	13
	SC	4	20

Table 10 Moisture content for coastal soil [4]

Location	Soil classification	Depth (m)	Moisture content (%)
Hathab	CH	2.5	11.3
	CH	4	12.3
	CH	5.5	12.24
	CH	7	12.90
Pipavav	CH	2.5	28.5
	CH	4	30.2
	CH	5.5	30.9
	CH	7	31.2

2.5 Moisture Content (%)

Moisture content is the percentage of water present in the soil by weight with respect to the dry weight of the soil. This water is present in the voids between the soil particles, and this does not include the water present in molecular double layer. It can be measured by doing the oven dry test in the laboratory at 105–110 °C. Moisture content is useful in finding the bearing capacity and settlement. It will also give you

Table 11 Moisture content for non-coastal soil [5]

Location	Soil classification	Depth (m)	Moisture content (%)
Vejalpur Bh-1	CH	3	7.34
	SC	6	13.59
	SM	9	15.31
Haripura	CL	2.5	21.8
	SC	4	23.4
	SC	5.5	22.7
	SC	7	24.3

an idea of the state of the soil. The data is given in Table 10 for coastal soil and in Table 11 for non-coastal soil.

2.6 Bearing Capacity (t/m²)

Bearing capacity is the ability of the soil to bear the loads coming from the foundation. It can be obtained by the equation

$$Q = C\,N_c S_c d_c + q\left(N_q - 1\right) S_q d_q + 0.5g\,B N_\gamma S_\gamma d_\gamma \tag{1}$$

where

C	Cohesion
q	Overburden Pressure,
γ	Density,
B	Width of the Footing,
N_c, N_q, N_γ	Bearing capacity Factor,
S_c, S_q, S_γ	Shape Factor,
d_c, d_q, d_γ	Depth factor,
Q_u	ultimate bearing capacity,
Q_{ns}	net safe bearing capacity.

The data is given in Table 12 for coastal soil and in Table 13 for non-coastal soil.

2.7 SPT Value (N)

It is the number of vertical blows applied on a standard split spoon sampler per a given standard penetration value, and it shows the resistance provided by the soil strata. This number (N) gives us an indication of the relative density of the soil, and

Table 12 Bearing capacity for coastal soil [6, 7]

Location	Depth of footing (m)	Q_{un} (t/m^2)	Q_{ns} (t/m^2)
Akwada	2	33.8	13.52
	2.5	37.875	15.15
	3	42.11	16.84
Bhatar Road	8	77.5	31
	8.5	80	32
	9	82.5	33

Table 13 Bearing capacity for non-coastal soil [5]

Location	Depth of footing (m)	Qun (t/m^2)	Qns (t/m^2)
Vejalpur	8.5	150	60
	9	182.5	73
	9.5	215	86
Haripura	1.5	35.2	14.08
	2	37.5	15
	2.5	39.88	15.94

various other correlations are used to obtain different geotechnical properties like shear strength, cohesion factor, bearing capacity, etc. The data is given in Table 14 for coastal and in Table 15 for non-coastal soil.

Table 14 SPT Value for coastal soil [4]

Location	Soil classification	Depth (m)	SPT value (N)
Hathab	CH	1.5	10
	CH	3	15
	CH	4.5	20
	CH	6	26
	CH	7.5	32
	CH	9	38
Pipavav	SC	1.5	3
	CH	3	8
	CH	4.5	10
	CH	6	11
	CH	7.5	12
	CH	9	15

Table 15 SPT value for non-coastal soil [5]

Location	Soil classification	Depth (m)	SPT value (N)
Vejalpur Bh-1	CH	1.5	19
	SC	4.5	38
	SM	7.5	56
Haripura	CL	2	14
	CL	3.5	24
	SC	5	27
	SC	6.5	31

3   Analysis of the Results Obtained from Soil Reports

The soil reports of six different coastal and non-coastal places of Gujarat were collected, the geotechnical properties were analyzed, and then the graphical results are plotted for the geotechnical property analyzed against the depths, depicting significant trends differing in coastal and non-coastal soil. There are some complexities observed from the graph due to the different soil types present and location of ground water table. The water table was encountered at the depth of 6 m at Vejalpur. The borehole depth for investigation was 20 m. The borehole depth was excavated for 9 m, and the water table was encountered at the depth of 1.5 m below ground level. These trends are shown for each property in the graphical form below.

3.1   Plasticity Index

The soil at Hathab ranges from 35 to 38%, and it increases as the depth increases. The same trend is also observed for the Pipavav. So, we can analyze that the higher plasticity in coastal soil may raise the instability nature of the soil. On comparing the soil at Vejalpur, the plasticity index is much lower than at the coastal soil region and at a depth of 7.5 m the soil becomes non-plastic. In Vejalpur, we can see that as we excavate deeper the plasticity index decreases. And at a depth of a 7.5 m, the soil becomes non-plastic. While neither at Hathab nor at Pipavav, the soil becomes non-plastic. This provides an insight to the problems in coastal area. At Vejalpur, the plasticity index above the ground water level decreases up to depth 6 m where the groundwater level is observed. Here, this decrease is drastic, but as you go deep below the water table, it increases up to depth of 15 m but then on it decreases but not as drastically as it did above the water table. For Haripura, it is observed that as excavating further below the ground water table, the plasticity index increases. From the two different soil strata, the CL and the SC, the SC posses more plasticity. In Hathab, the soil type found was CH for the entire excavated bore and the plasticity index with increase in depth increases. This trend was similar in the Pipavav region
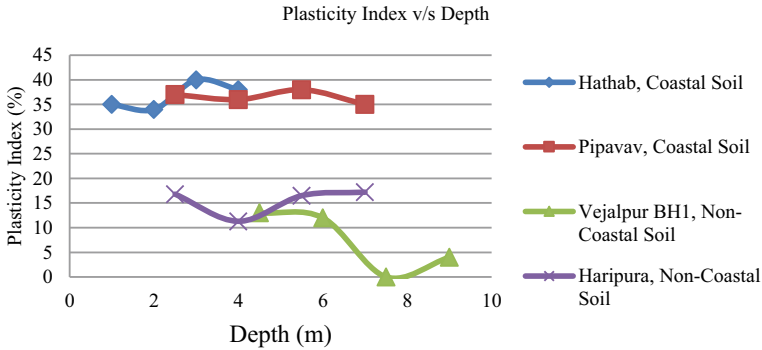
Fig. 2 Graph of plasticity versus depth for stated coastal and non-coastal soil

where the two soil types were found, SC at 1.5 m and CH from 2.5 m. Here, the SC had lower plasticity compared to CH, and in CH, same trend is observed as in Hathab. Thus, CH-type soil posses more plasticity for both coastal and no-coastal soil. At higher depths, the SM layer soil is found which posses lowest plasticity and also becomes non-plastic at depth of 9 m at Vejalpur (Fig. 2).

3.2 Field Dry Density

From the above graph, it can be observed that non-coastal soils at Vejalpur and at Haripura have high field dry density ranges from 1.7 to 1.76 g/cc for Vejalpur, and it ranges from 1.52 to 1.69 g/cc for Haripura. It can be seen that the field dry density at Hathab ranged 1.64–1.82 m/cc, which is higher than non-coastal soil at Haripura. This exception can be affirmed by difference in the water holding capacity of the soil, 12.9%, at Hathab which was CH at 7 m, while soil encountered was SM at 9 m. Considering at Vejalpur, the soil encountered was SM at 9 m. The field dry density both above and below the water table increases with depth from 1.70 to 1.83 g/cc at Vejalppur. For Haripura, the FDD for the SC strata is more than the CL strata and the SC has a higher degree of compaction. At the coastal areas, the FDD was found higher at a great depth of 7 m, while the FDD for non-coastal area was found higher a shallow depth of 3 m. But for FDD at coastal area of Pipavav, it was found much lower though having the same soil type, CH of that at Hathab. It was because the moisture content here was also enough more to that of Hathab and the moisture content at CH layer at depth 3 m at Vejalpur (Fig. 3).

Field Dry Density v/s Depth
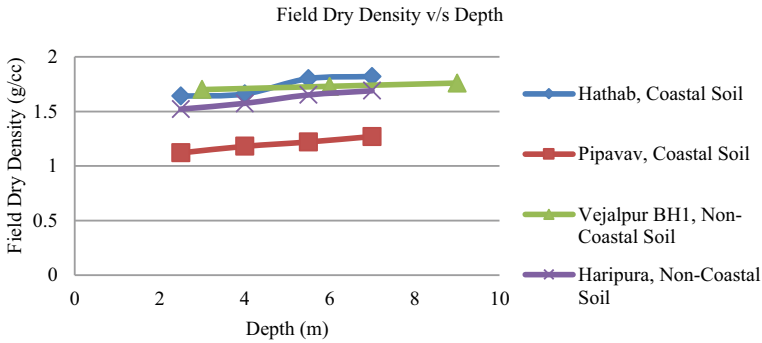
Fig. 3 Graph of field dry density versus depth for stated coastal and non-coastal soil

3.3 Cohesion Factor

From the above graph, it can be inferred that the cohesion for Vejalpur soil decreases with the depth from 0.19 kg/cm^2 at 6 m depth to 0 kg/cm^2 at a depth of 9 m. The cohesion factor for Haripura seems to follow the same trend. While in the coastal soil, the cohesion is much higher. In Hathab, it ranges from 0.32 to 0.34 kg/cm^2. At Pipavav, the same trend of increase in cohesion factor with depth follows. Also, as the cohesion increases, the shear strength increases. For Vejalpur, it was found that above the water table level the cohesion value decreases with depth up to the depth of water table. For Haripura, it decreases below the ground water level and is 0.14 kg/cm^2 at depth of 4 m. The soil also changes from CL to SC with increase in depth, which decreases the cohesive nature of soil as you go deeper. At both the coastal site, CH soil type was excavated and tested and the cohesion factor value varies between 0.32 and 0.5 kg/cm^2 at 4 m depth which compared to the CH at the non-coastal area is 0.72 kg/cm^2 for CH soil type at 3 m depth at Vejalpur. So the coastal area has less cohesive soil compared to the non-coastal area. The highest cohesion factor value is obtained for CH type of soil for both coastal and non-coastal soil, while the SC type has lower than CH type soil and the lowest is found for the SM type soil (Fig. 4).

3.4 Angle of Internal Friction

From the above graph, we can infer that the angle of internal friction for coastal soil is lower than that of non-costal soil. So, the shear strength at the non-coastal soil with higher internal angle of friction is higher, and it provides more stability to the soil. The angle of internal friction is highest at Vejalpur with 31° at a depth of around 9 m, and compared to that in the coastal soil of Pipavav region, the angle of internal friction is lowest with 0° at all the depths which were taken. Therefore,

Cohesion Factor v/s Depth
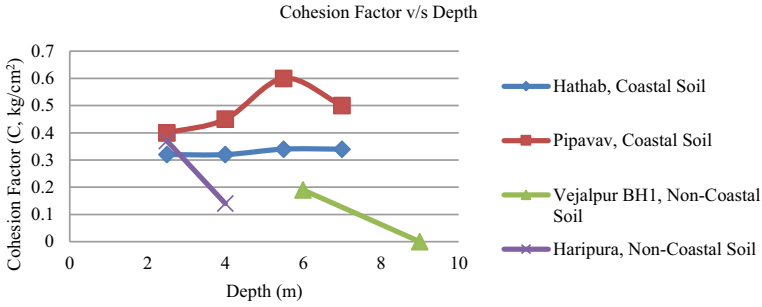
Fig. 4 Graph of cohesion versus depth for stated coastal and non-coastal soil

Angle of Internal Friction v/s Depth
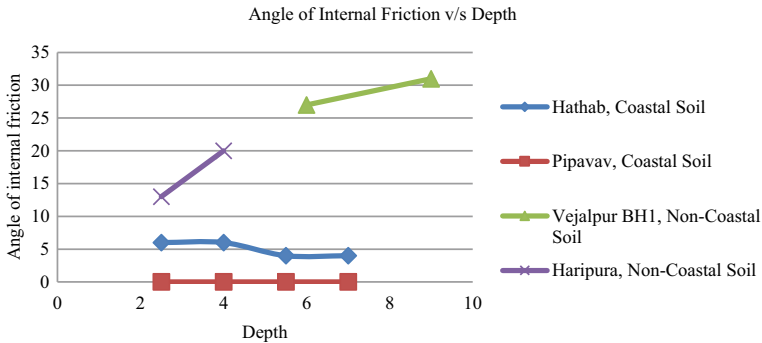
Fig. 5 Graph of angle of internal friction versus depth for stated coastal and non-coastal soil

the shear strength is lowest at this region, and the soil has very low stability in this region. The angle of internal friction increases and becomes maximum of 31° at the depth of 9 m at Vejalpur. For Haripura, the angle of internal friction for SC was more than the angle for the CL, which makes clear that the shear strength for the CL is more compared to the SC. In both the places, Hathab and Pipavav, coastal area in the soil type CH was found, and comparing this soil type with the CH type of soil at non-coastal area, the ϕ value does not increase beyond 6°. However in Pipavav, the ϕ value found is 0°. So for CH-type soil, the angle of internal friction was found maximum to be 6° at both coastal and non-coastal area While for other soil type, SC and SM, found at Vejalpur, it is 27° and 31°, respectively, at deeper depths (Fig. 5).

3.5 Moisture Content

For the coastal soil, the natural moisture content will be higher compared to the non-coastal soil, but the result plotted after the analysis shows some twists in the pattern. We can see that Hathab, has lower moisture content and Haripura has higher moisture
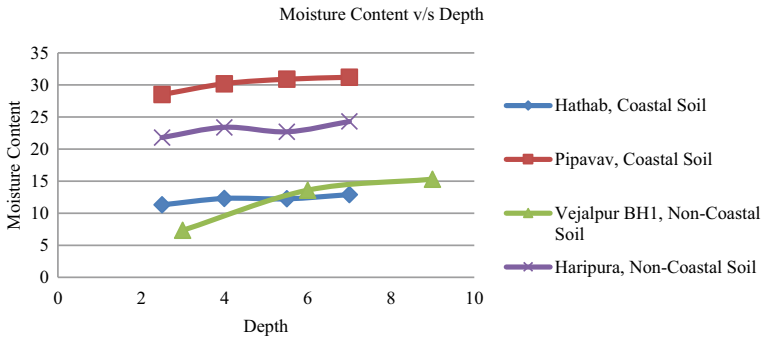
Fig. 6 Graph of moisture content versus depth for stated coastal and non-coastal soil

content compared to Hathab. This is because from the soil reports it was found that the water table level was encountered at an early depth of 1.5 m at Haripura. While at Pipavav, the normal trend of high moisture content was observed, and at Vejalpur, water table depth of 6 m was encountered and the moisture content was low. For existing, clayey soil (SC and CL) below the depth of water table, the moisture content increases at Vejalpur. For Haripura, the moisture content going deeper increases and the CL holds less moisture than the SC. Hathab and Pipavav, coastal area, both have CH type soil, and in both the soil types, the moisture content increases excavating deeper. Though for same type of soil CH, Vejalpur, the moisture content was found very less compared to coastal area, and this tells how even the same soil type differs in moisture content at coastal and non-coastal area on the basis of water table depth and soil type (Fig. 6).

3.6 Net Safe Bearing Capacity

The results found from the plot of net safe bearing capacity versus depth graph are not very conclusive. The net bearing capacity of the non-coastal soil is generally higher than the coastal soil, but here from four places analyzed, two places, Akwada ranges from 13.52 to 16.84 t/m^2 and Vejalpur from 60 to 86 t/m^2, increases with depth shows normal trend and is acceptable. While considering Haripura, the water table was encountered at a shallow depth of 1.5 m and the bearing capacity is lower and ranges from 14.08 to 15.94 t/m^2. Similar trend was obtained at Bhatar Road, a coastal soil, the safe bearing capacity ranged from 31 to 33 t/m^2; as the ground water table level was not encountered within 15 m of excavation, so it can carry more load compared to other places on coastal soil. The net safe bearing capacity observed for Vejalpur increases on going down from 8.5 m that is below the ground water table level. This can also be inferred from the N-value; the N-value in this region is more than 100. Thus, this region is good for foundation. The safe bearing capacity can be related with the N-value, and so, we can say that the SC has a higher safe bearing

Safe Bearing Capacity v/s Depth
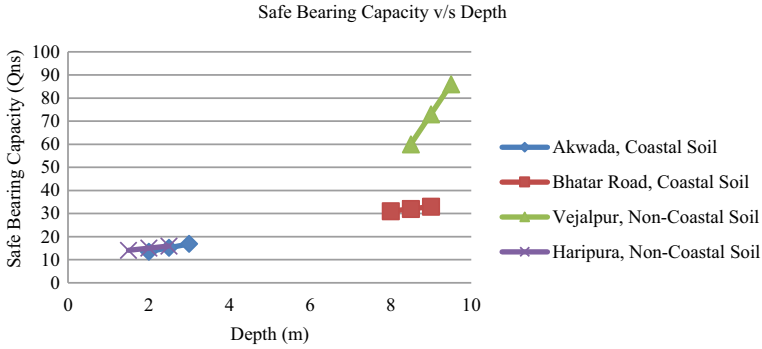
Fig. 7 Graph of net safe bearing capacity versus depth for stated coastal and non-coastal soil

capacity as the N-value obtained here is higher. For bearing capacity, we encountered the soil reports of other coastal places Akwada, Bhavnagar and Bhatar Road, Surat. Here, a different trend is observed; Haripura being a non-coastal area still has a similar trend like that of Akwada. This is due to as discussed at Haripura the water table was just observed at a depth of 1.5 m and bearing capacity was measured within 2.5 m depth. Also, the soil type found at both the places was similar, CL and SC. For Bhatar Road, the safe bearing capacity was relatively higher than other coastal area as the soil type here found was SM which generally has higher bearing capacity, which is also found at Vejalpur, having high bearing capacity up to 86 t/m^2 (Fig. 7).

3.7 SPT N-Value

The N-value seems to follow an obvious pattern. At coastal soil, it can easily penetrate and so the blows required is lower compared to the non-coastal soil. The blows required for the non-coastal soil, Vejalpur, reach more than 50, which will ensure good strata, and so, the overburden pressure check is not required. On the other non-coastal soil, Haripara, the blows do not reach up to 50 but the strata can be considered good. For the coastal soil due to the presence of ample moisture content, the penetration becomes easy and lesser blows are required. Considering Pipavav coastal soil, the N-value hardly reaches 15. While seeing other coastal region, Hathab, the blows increase after a depth of 6 m, which suggests that strata gradually start to harden below a depth of 6 m. Below the water table level, the N-value was 56 at 7.5 m and varies to 100 on going to further depth up to 20 m. The soil layer found beneath the water table is almost clay. And, so the plasticity index decreases. This shows that the ground surface is becoming much harder with increase in depth. For Haripura, with increase in depth, the N-value increases up to 33. The soil varies from CL to SC. It infers that the SC strata offer more resistance to the hammer blows than the CL strata. For the soil-type CH, the N-value limits up to 20 for a depth of 4.5 m,
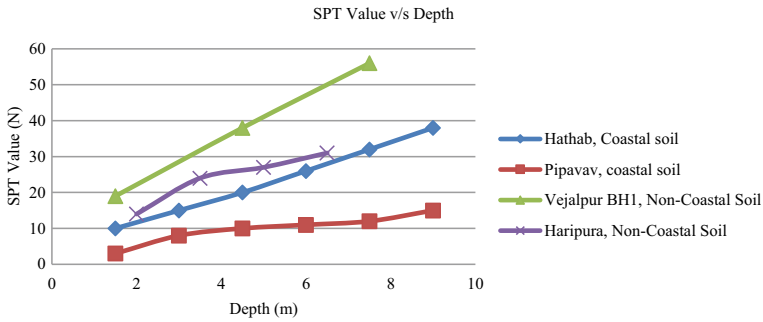
Fig. 8 Graph of SPT value versus depth for coastal and non-coastal soil

but going further, it even reached to N-value 38, for both coastal and non-coastal soil. For non-coastal soil where during excavation even other soil layer like SC was encountered, the N-value even exceeded 30, and for the SM-type soil at depth of 7.5 m, the N-value even crossed 50, and for CL, it was beyond 80 and even reaches more than 100, which gives a high resisting strata (Fig. 8).

4 Conclusions

The presence of different types of soil and the sourcing of the soil sample above the ground water table level or below the ground water table level affects the geotechnical properties of the soil, and it varies from their normal pattern or trend observed. The seasonal variation of the water table also affects the geotechnical soil properties. Considering the plasticity index for coastal soil, it ranges from 35 to 38% and increases with depth, while for non-coastal soil, it decreases from 32% and reaches to 0% (NP). For the field dry density for coastal soil should be low and non-coastal soil high, but at Hathab, it ranges to 1.82 g/cc as the boring work took place at 8.5 m and the water table level was at shallow depth. The cohesion for non-coastal soil was much lower, ranged from 0 to 0.37 kg/cm^2, and for coastal soil, it almost ranged twice to 0.6 kg/cm^2, where the water content played the role [8]. The angle of internal friction for non-coastal soil is higher and ranges up to 31° and provides good shear strength, and for the coastal soil due to the presence of high moisture content, the angle of internal friction ranges from 0 to 6° only, having lower shear strength. The complex trend can also be observed in the moisture content of Hathab which ranges from 11.3 to 12.90% though being a coastal soil as the water table encountered at a shallow depth, and for non-coastal soil at Haripura, the water content was found higher up to 24.3% as the water table was encountered at a depth 1.5 m where boring work took place apart from this the soil obtained here was SM, while at Hathab, the soil was observed to be SC. A mismatch trend was also seen in the bearing capacity. For coastal soil, the net safe bearing capacity of Bhatar Road ranging 31–33 t/m^2

was higher than that of non-coastal soil at Haripura ranging 14.08–15.94 t/m^2, as at Bhatar Road, the water table level was not observed up to 15 m of boring works, while at the Haripura, the water table was observed at 1.5 m. SPT value follows a simple and normal trend, and no complexions are observed. For coastal soil, the *N*-values are less compared to the non-coastal soil. Thus, this paper might be helpful for the further research in increasing the soil properties of coastal soil so that a healthy development in the infrastructure takes place at a sustainable level.

References

1. Al-Bared, M.A.M, Marto, A.: A review on geotechnical and engineering characteristics of marine clay and modern methods of improvement. Malays. J. Fundamental Appl. Sci. **13**(4), 825–831 (2017)
2. Arulrajah, A., Bo, M.W.: Characteristics of Singapore marine clay at Changi. J. Geotech. Geol. Eng. **26**(4), 431–441 (2008)
3. Yokoi, H.: Relationship between soil cohesion and shear strength. J. Soil Sci. Plant Nutr. **14**(3), 89–93 (1968)
4. Soil report of Hathab school building, Pipavav port building, by Shreeji Laboratory, Bhavnagar
5. Soil report of Proposed Site at Vejalpur, Ahmedabad and Vadodara industrial park at Haripura, Vadodara by KCT Consultancy Services, Ahmedabad
6. Soil report of Tarsamiya, Sidsar Pumping Station, Akwada Pumping Station, Popatnagar, by OM Geotech and Testing Services, Bhavnagar
7. Soil report of proposed site at Bhatar Road, Surat, by Bhumi Research Centre, Surat
8. Basack, S., Purkayastha, R.D.: Engineering properties of marine clay from the eastern cast of India. J. Eng. Technol. Res. **1**(6), 109–114 (2009)

Effect of Plastic Fines on Geotechnical Behavior of Ennore Sand

Sagarkumar Khunt and Ajanta Sachan

Abstract The soil is usually found in the combination of various size particles such as clayey silt, sandy silt and silty-sand. The geotechnical properties of soil such as index properties, permeability, compactability, shear strength and volumetric response rely on the gradation of the soil particles. In the present study, Ennore sand is used with varying kaolinite clay contents such as 0%, 5%, 10% and 15%. To determine the shear strength parameters of soil mixture, a series of large direct shear tests were conducted on Ennore sand–kaolinite clay mixtures. The specimens for direct shear tests were prepared at optimum moisture content and maximum dry density. The experimental results showed that shear strength increased with the increase in fines content up to 10%, and after that, it was observed to decrease. The cohesion of soil mixtures were found to be increased with the increase in kaolinite content due to its plastic nature.

Keywords Plastic fines · Shear strength parameter · Large direct shear test

1 Introduction

The shear strength of soil is a combination of friction, cohesion and interlocking between the soil grains. Coulomb [1] and Terzaghi (1925) investigated the shear behavior of pure sand and pure clay, respectively. However, the soils are found in combination, mixture of sand, silt and clay. The shear behavior of soil was influenced by the percentages of fines and coarse content. Carrro et al. [2] performed drain and undrained triaxial tests under static and monotonic conditions on the sand contained plastic and non-plastic fines to investigate the mechanical behavior of sand. They found that the both peak and critical-state friction angle of the soil increased with the

S. Khunt (✉) · A. Sachan (✉)
Civil Engineering, Indian Institute of Technology Gandhinagar, Gandhinagar, India
e-mail: sagarkumar.khunt@iitgn.ac.in

A. Sachan
e-mail: ajanta@iitgn.ac.in

Table 1 Basic geotechnical properties of Ennore sand

Properties	Values
Specific gravity	2.63
Coarse sand	0%
Medium sand	92.70%
Fine sand	7.30%
Minimum dry density	1.5 g/cc
Maximum dry density	1.7 g/cc
Visual appearance	Whitish Gray
Nature	Non-plastic

increase in non-plastic fines, whereas completely reverse behavior was observed in sand with plastic fines. Kolay et al. [6] investigated the shear strength characteristics of sand with varying content of fines in direct shear apparatus. The results of this study revealed that the internal friction angle was decreased, whereas cohesion value was observed to increase with the increase in fines content. In the current study, Ennore sand was mixed with kaolinite clay. The large direct shear was conducted on Ennore sand–kaolinite mixtures to investigate shear behavior. The kaolinite clay content was varied as 0%, 5%, 10% and 15% by weight. The Ennore sand–kaolinite clay specimens were prepared at OMC and MDD, which was obtained by standard Proctor tests. The relationship between shear stress and horizontal displacement and volumetric response and Mohr–Coulomb failure envelopes was derived to explore the shear behavior of soil.

2　Material Properties

Ennore sand is a standard soil and is found in the seashore area of Tamilnadu, India. Three types of Ennore sand are available commercially, based on their particle size, e.g., grade-1, grade-2 and grade-3. In the current study, grade-2 Ennore sand was used, which contained major soil particles varying from 0.5 mm to 1 mm. Kaolinite clay is a cohesive soil containing kaolinite clay mineral. The mixtures of Ennore sand and kaolinite clay were used in the present study. The basic geotechnical properties of Ennore sand are presented in Table 1.

3　Experimental Program

In the present study, a series of large direct shear tests were performed on Ennore sand–kaolinite clay mixture at normal pressure of 139 kPa, 188 kPa and 237 kPa.

The Ennore sand–kaolinite clay mixtures were prepared at varying kaolinite content such as 0%, 5%, 10% and 15%. The standard Proctor tests were performed on Ennore sand–kaolinite mixtures to obtain optimum moisture content and maximum dry density at each kaolinite clay content in Ennore sand. For direct shear test, soil specimens were prepared at their respective optimum moisture content and maximum dry density using moist temping method. The specimen was prepared in direct shear box itself in three equal layers of height. The specimen size was 30 cm * 30 cm in plane dimension and 15 cm in height. The large direct shear apparatus was deformation controlled device, and the deformation rate was kept 1 mm/min for all the tests.

4 Results and Discussions

4.1 Shear Stress-Horizontal Displacement Relationship

Figure 1 represents the shear stress and horizontal displacement relationship of Ennore sand–kaolinite clay mixtures at normal pressure of 139 kPa, 188 kPa and 237 kPa. The results from the direct shear tests revealed that well-defined peak was not observed in Ennore sand–kaolinite clay mixtures for all the three normal pressures. The shear strength characteristics of Ennore sand–kaolinite clay mixtures increased with an increase in normal pressure indicating pressure-dependent material response. The maximum shear stresses were mobilized within 6 mm of horizontal deformation. It further exhibited softening response for all the Ennore–kaolinite mixtures. The relationship between shear stress and horizontal displacement showed that the shear strength of Ennore sand notably increased by the addition of 5% kaolinite. For normal pressure 139 kPa, the shear strength of Ennore sand increased by 10.5%, 13.4% and 6.7% with the addition of 5%, 10% and 15% kaolinite content, respectively. A similar response was observed for the tests performed at normal pressures of 188 kPa and 237 kPa. For 188 kPa normal pressure, an increase of 6.9% and 10.4% in shear strength was observed for kaolinite clay content of 5% and 10%, respectively. There was an insignificant effect of 15% kaolinite clay on the shear resistance at normal load of 188 kPa. For the normal pressure of 237 kPa, an increase of 11.3%, 13.7%, 1.7% in shear strength was observed for kaolinite clay content of 5%, 10% and 15% respectively. The Ennore sand and kaolinite mixtures exhibited maximum shear strength response at 10% of kaolinite clay content for all the three normal loads.

4.2 Volumetric Behavior

Figure 2 illustrates the relationship of vertical and horizontal displacement for Ennore sand and kaolinite clay mixtures at normal pressures of 139 kPa, 188 kPa and 237 kPa.
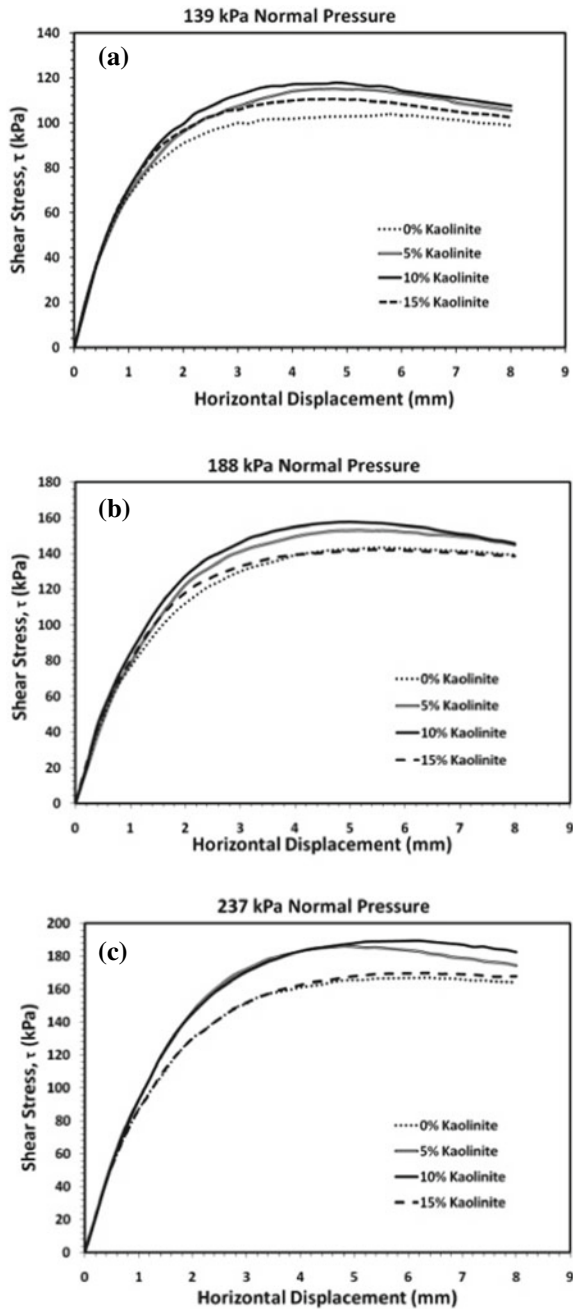
Fig. 1 Shear stress versus horizontal displacement relationship of Ennore sand–kaolinite mixtures at the normal pressures of **a** 139 kPa, **b** 188 kPa and **c** 237 kPa
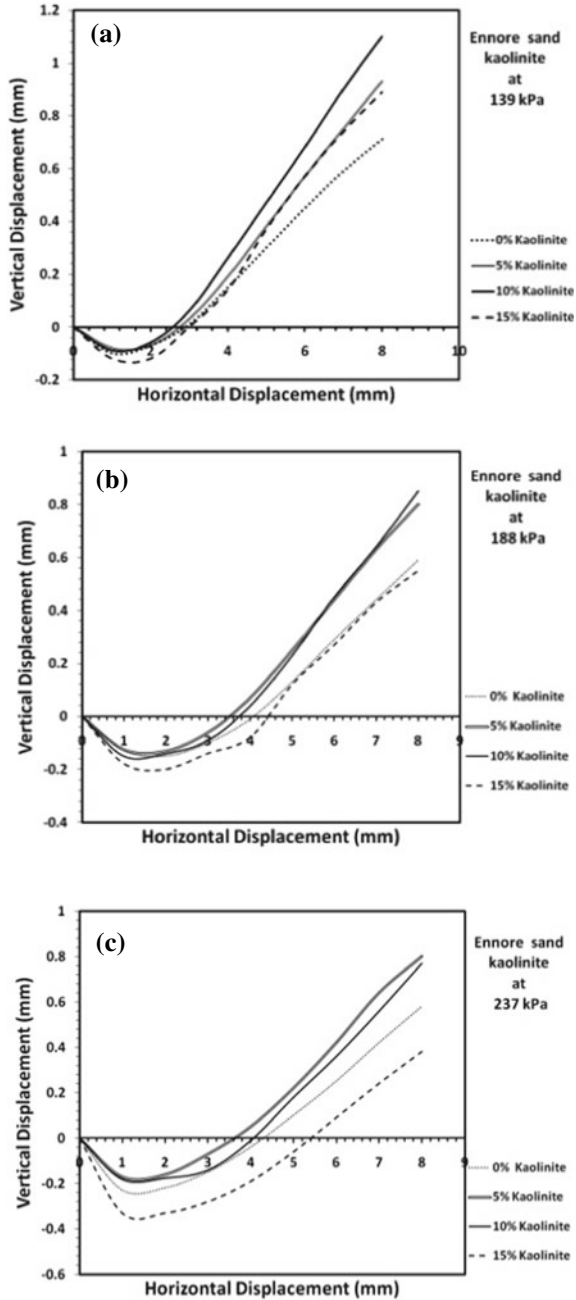
Fig. 2 Vertical versus horizontal displacement relationship of Ennore sand–Kaolinite mixtures at the normal pressures of **a** 139 kPa, **b** 188 kPa, and **c** 237 kPa

The Ennore sand–kaolinite clay mixtures showed initial settlement during shearing stage. The soil particles might be rearranged during shearing and achieved denser packing. After initial settlement, the soil behavior was observed to be dilative for all Ennore sand–kaolinite clay mixtures. The dilative response of Ennore sand–kaolinite clay mixtures indicated the rolling over and rearrangement of sand particles during shearing. Ennore sand with 15% kaolinite clay content exhibited maximum initial settlement for all three applied normal loads. At higher kaolinite clay content, the clay particles were facilitated with easy rearrangement of granular fraction and also contributed to the compressibility of the clay matrix present at few contacts of the large sand particles. This might be due to the lubrication effect of kaolinite clay that enabled the soil particles to rearrange easily during application of normal load.

4.3 Shear Strength Failure Envelopes

Mohr–Coulomb failure envelopes of Ennore sand with varying kaolinite clay contents (0%, 5%, 10%, and 15%) are shown in Fig. 3. It was evident from the failure envelope that the slope and intercept increased with the addition of 5%, 10% and 15% of kaolinite as compared to pure Ennore sand. The gain in shear strength parameters was found to be dependent on the kaolinite content. As the kaolinite content increased, the shear strength parameters were found to increase up to 10% of kaolinite clay content. At the 15% kaolinite content, the shear strength parameters reduced but always remained higher than that of the pure Ennore sand. A similar response was observed in shear stress and horizontal displacement relationship of Ennore sand with varying kaolinite clay contents.

The shear strength of Ennore sand–kaolinite clay mixtures increased with the increase in kaolinite clay content. The maximum value of shear strength was acquired at 10% of kaolinite clay. Significant reduction in shear strength was observed at

Fig. 3 Mohr–Coulomb Failure Envelopes of Ennore sand–kaolinite mixtures
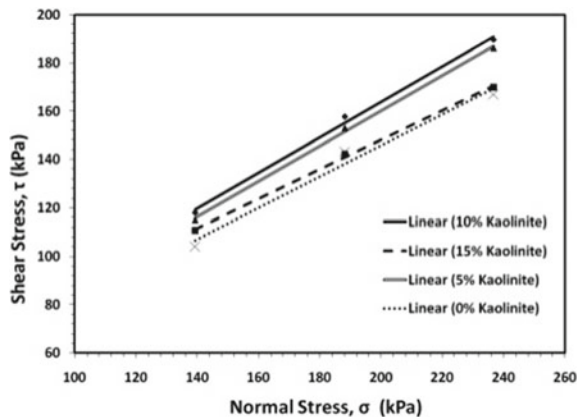
Table 2 Shear strength properties of Ennore sand–kaolinite mixtures

Kaolinite clay (%)	Cohesion, C (kPa)	Friction angle, ϕ (°)	shear strength at 139 kPa (kPa)
0	0	36.1	101
5	13	36.2	115
10	16	36.4	118
15	26	31.3	111

15% kaolinite clay content at normal pressures of 139 kPa, 188 kPa and 237 kPa. However, the shear strength of all the Ennore sand–kaolinite clay mixtures was observed to be higher than that of the pure Ennore sand. The observations revealed that the kaolinite clay content had a significant impact on shear strength parameters of Ennore sand–kaolinite clay mixtures. The shear strength parameters of Ennore sand–kaolinite clay mixtures are presented in Table 2. The results indicated that the friction angle increased slightly with the increase in kaolinite content and attained the maximum value of 36.4° at 10% kaolinite and after that the friction angle decreased to 31.3° at kaolinite content of 15%. As the kaolinite content increased, the voids between the sand particles were filled with kaolinite clay with the simultaneous decrease in sand-to-sand contacts. At low kaolinite content, voids of Ennore sand were occupied by kaolinite clay particles and the number of sand-to-sand contacts was comparable to that of pure Ennore sand. The low clay content exhibited negligible effect on the shear strength behavior as contact between sand particles remained nearly unchanged. By increasing kaolinite content to 15%, the kaolinite clay particles replaced with sand content, thereby decreasing the number of sand-to-sand contacts and consequently led to reduced shear strength as compared to 10% kaolinite content. However, the higher kaolinite content induced significant cohesion, which dominated the response and subsequently led to higher shear strength compared to pure Ennore sand. Due to the loss of contact between Ennore sand particles, the friction angle was decreased. Apart from the friction angle, kaolinite content had a significant impact on the cohesion of the Ennore sand–kaolinite mixture (Table 2). The cohesion value of the soil is mainly affected by the clay content. As samples were prepared at optimum moisture content, the added kaolinite induced the plasticity to the Ennore sand–kaolinite mixture and increased the compactness of the specimen. The plasticity of Ennore sand–kaolinite mixtures was observed to increase with increasing kaolinite content and was reflected in the cohesion values exhibited by the specimens with the simultaneous reduction in friction angle.

5 Conclusions

A series of large direct shear test were performed on Ennore sand–kaolinite mixtures at varying kaolinite clay contents. The results of the study are summarized as follows:

- The shear strength of Ennore sand–kaolinite clay mixture was observed to increase with the increase in kaolinite clay content and achieve maximum value at 10% kaolinite content. After that, the reduction in shear stress was observed at 15% kaolinite content.
- The volumetric response was exhibited initial settlement followed by dilation for all Ennore sand–kaolinite mixtures. The maximum initial settlement was observed in mixture with 15% kaolinite clay content.
- The internal friction angle increased slightly with the increase in kaolinite content and attained the maximum value of 36.4° at 10% kaolinite, and after that, the friction angle decreased to 31.3° at 15% kaolinite.
- The cohesion value of Ennore sand–kaolinite clay mixtures was observed to increase with increasing kaolinite content. That could be attributed to the plastic nature of kaolinite clay.

References

1. Coulomb, C.A.: Essai sur une application des regles de maximis et minimis a quelques problemes de statique relatifs a l'architecture (essay on maximums and minimums of rules to some static problems relating to architecture) (1973)
2. Carraro, J.A.H., Prezzi, M., Salgado, R.: Shear strength and stiffness of sands containing plastic or nonplastic fines. J. Geotech. Geoenviron. Eng. **135**(9), 1167–1178 (2009)
3. Thevanayagam, S.: Effect of fines and confining stress on undrained shear strength of silty sands. J. Geotech. Geoenviron. Eng. **124**(6), 479–491 (1998)
4. Shipton, B., Coop, M.R.: Transitional behaviour in sands with plastic and non-plastic fines. Soils Found. **55**(1), 1–16 (2015)
5. Kim, D., Sagong, M., Lee, Y.: Effects of fine aggregate content on the mechanical properties of the compacted decomposed granitic soils. Constr. Build. Mater. **19**(3), 189–196 (2005)
6. Kolay, P.K., Abedin, M.Z., Tiong, K.J.: Effect of fine content on shear strength characteristics of sandy soil
7. Ghahremani, M., Ghalandarzadeh, A., Moradi, M.: Effect of plastic fines on the undrained behavior of sands. Soil Rock Behav. Model., 48–54 (2006)
8. Phan, V.T.-A., Hsiao, D.-H., Nguyen, P.-T.L.: Effects of fines contents on engineering properties of sand-fines mixtures. Procedia Eng. **142**, 213–220 (2016)

Effect of Relative Density on Elastic Properties of Sand

Arpita V. Patel and Nitin H. Joshi

Abstract This investigation presents the variation in modulus of elasticity and modulus of subgrade reaction of dry sand with respect to change in relative density of sand. The sand was collected from Orsang River and Narmada River (Poicha). The effect of the relative density of sands on both elastic properties was carried out at 40%, 60% and 80% relative density. Modulus of subgrade reaction was obtained by performing model plate load test and modulus of elasticity using simple triaxial test. Correlations between modulus of elasticity and modulus of subgrade reaction developed by various investigators were found from the literature review, and it was observed that the pattern of changing of modulus of subgrade reaction with respect to change in the relative density of sand obtained in the present study was nearer to correlation developed by Vesic and Selvadurai. It was also observed that as relative density of sand increased the modulus of elasticity and modulus of subgrade reaction were also increased.

Keywords Modulus of elasticity · Modulus of subgrade reaction · Relative density · Gradation curve

1 Introduction

1.1 Elastic Properties of Soil

Modulus of elasticity (E_s), Poisson's ratio (μ_s) and modulus of subgrade reaction (k_s) are the main elastic properties of soil for flexible analysis of foundation. Modulus of elasticity of soil is defined as the slope of the initial tangent or secant tangent to

A. V. Patel (✉) · N. H. Joshi
Applied Mechanics Department, Faculty of Technology and Engineering, M S University of Baroda, Vadodara 390001, India
e-mail: arpsoham@gmail.com

N. H. Joshi
e-mail: nhjoshi-appmech@msubaroda.ac.in

Table 1 Typical range of values for the modulus of elasticity E_s for sandy soils

Soil	E_s (kPa)
Silty sand	5000–20,000
Loose sand	10,000– 25,000
Dense sand and gravel	50,000–81,000
Loose sand and gravel	50,000–150,000

Table 2 Typical range of values for Poisson's ratio of sandy soils

Type of soil	Poisson's ratio
Sandy clay	0.2–0.3
Silt	0.3–0.35
Sand, gravelly sand	0.1–1.0, commonly used 0.3–0.4

the deviator stress–strain curve of soil sample plotted from triaxial test. The initial tangent modulus is most often used for E_s. This is because the soil is elastic only near the origin, and there is less deviation between all plots in this portion. The ranges of modulus of elasticity are given in Table 1 [8]. Poisson's ratio of soil represents the ratio of Lateral strain to linear strain observed on cylindrical soil sample of triaxial test. As the direct determination of Poisson's ratio is extremely difficult, the commonly adopted value ranges are given in Table 2 [8] for different types of soils. Both E_s and μ_s are affected by the following.

1. Method of laboratory tests (confined, unconfined, drained, undrained).
2. Over-consolidation ratio.
3. Degree of confinement.
4. Density of soil.
5. Strain rate.
6. Sample disturbance.

Modulus of subgrade reaction of soil represents a ratio of load intensity (load per unit area (applied through a centrally loaded rigid body)) of horizontal surface of a mass of soil to corresponding settlement of the surface. It is determined as the slope of the secant drawn between the point corresponding to zero settlement and the point of 1.25 mm settlement, of a load–settlement curve obtained from a plate load test on a soil using a 75-cm diameter or smaller loading plate with corrections for size of plate used. Typical range of values for modulus of subgrade reaction k_s [8] is shown in Table 3.

Table 3 Typical range of values for modulus of subgrade reaction k_s

Soil	k_s (KN/m^2/m)
Loose sand	4800–16,000
Medium dense sand	9600–80,000
Dense sand	64,000–128,000
Clayey medium dense sand	32,000–80,000
Silty medium dense sand	24,000–48,000

1.2 Literature Review on Elastic Properties of Soil

Jamshid Sadrekarimi compared different correlations proposed for determination of the coefficient of subgrade reaction, k_s, by various authors as listed in Table 4. They had used advanced soil models in Safe and Plaxis software on Tabriz Marl soil. They discovered that for Tabriz Marl, soft soil model is the best governing model and Vesic relation among the methods of determination of k_s gives a negligible error in comparison with the soft soil model. Also, to achieve more accurate results from these methods, they proposed to use mean elasticity modulus which takes into account the effect of geometric and mechanical properties of sub-layers [1].

In Table 4, E_s = modulus of elasticity, μ_s = Poisson's ratio, B = width of footing, EI = flexural rigidity of footing, k_{s1} = the coefficient of subgrade reaction for a plate 1 ft wide, υ = non-dimensional soil mass per unit length, B' = least lateral dimension of footing, I_S and I_F = influence factors which depend on the shape of footing and parameter m takes 1, 2 and 4 for edges, sides and center of footing, respectively.

Table 4 Common relations suggested for k_s by various investigators [1]

No.	Investigator	Suggested expression
1	Biot	$k_s = 0.95 \frac{E_s}{B(1-\mu_s^2)} \left[\frac{B^4 E_s}{(1-\mu_s^2)EI} \right]^{0.108}$
2	Terzaghi	For sands $k_s = k_{s1}\left(\frac{B+1}{2B}\right)^2$ For clays $k_s = k_{s1}\left(\frac{1}{B}\right)$
3	Vlassov	$k_s = \frac{E_s(1-\mu_s)}{(1+\mu_s)(1-2\mu_s)}\left[\frac{\upsilon}{2B}\right]$
4	Vesic	$k_s = 0.65 \frac{E_s}{B(1-\mu_s^2)}\left[\frac{B^4 E_s}{EI}\right]^{(1/12)}$
5	Meyerhof and Baike	$k_s = \frac{E_s}{B(1-\mu_s^2)}$
6	Klopple and Glock	$k_s = \frac{2E_s}{B(1+\mu_s)}$
7	Selvadurai	$k_s = 0.65 \frac{E_s}{B(1-\mu_s^2)}$
8	Bowles	$k_s = \frac{E_s}{B'(1-\mu_s^2)mI_s I_F}$

Equations in sr. no. 1 and 4 of Table 4 are defined for infinite beams resting on an elastic soil continuum, but application of them in mat footings is observed widely in technical literatures [8]. Equation presented in sr. no. 2 of Table 4 can be used only when the quantity of the coefficient of subgrade reaction beneath a plate of 1 ft wide is defined. This equation is also relevant in analysis of plate load test results by substituting width of loading plate with 1ft, but some of the researchers instead of using these equations in plate load test suggest using of those modified by Arnold. Equation written in sr. no. 3 of Table 4 is introduced for beams and plates resting on elastic half space, but ambiguities of estimating μ make the problem more complex. Equations written in sr. no. 5, 6 and 7 of Table 4 are proposed for computing the coefficient of horizontal subgrade reaction in buried circular conduits and are employed for evaluation of k_s in few limited cases. Also, k_s can be determined using the theory of elasticity. By rewriting the relation of settlement of rectangular plates resting on elastic half space, k_s can be expressed as Equation written in sr. no. 8 of Table 4 [8].

R. Ziaie_Moayed and S.A. Naeini had obtained the correlation between SPT results $(N_1)_{60}$ and modulus of subgrade reaction (k_s) as below [2]

$$k_s = 3.143(N_1)_{60}^{0.489} \tag{1}$$

where:

$$(N_1)_{60} = N * C_N * C_S * C_R * C_B * C_E \tag{2}$$

N: Measured SPT below counts.
C_E: Energy effect coefficient.
C_B: Correction factor for borehole diameter.
C_R: Correction factor for rod length.
C_S: Correction factor for type of samplers.
C_N: Effective overburden pressure coefficient obtained from the following relation:
where: $C_N = \left(\frac{P_a}{\sigma'_{v0}}\right)$.
Pa: Atmospheric pressure.
σ'_{v0} = Effective vertical pressure at considered depth.

DaeSang Kim obtained the relationship between the subgrade reaction modulus and the strain modulus obtained using a plate loading test on railroad subgrade in Korea. They used unrepetitive plate loading test (UPLT) to obtain the subgrade reaction modulus (k_{30}) and repetitive plate loading test (RPLT) to obtain the strain modulus (E_v).

$$E_v = \alpha k_{30} \tag{3}$$

$$E_s = \frac{\Pi r \sigma_0}{2s} \left(1 - \mu^2\right) \tag{4}$$

$$E_v = \frac{1.5r}{a_1 + a_2 \sigma_{0\,max}} \tag{5}$$

where E_s = elastic modulus; σ_0 = average normal stress; r = radius of the plate; s = settlement of the plate associated with the pressure; and μ = Poisson's ratio. a_1 and a_2 represent the factors (mm/(MN/m^2), mm/(MN^2/m^4), respectively). Here, E_v = the strain modulus in MPa, K_{30} is the subgrade reaction modulus in MN/m^3, and α = the coefficient (ranges between 0.04 and 0.71 with a best fit of 0.36).

In spite of these shortcomings, use of E_s and μs is computational conveniences that generally work with the theory of elasticity equations. The field (in situ) tests such as standard penetration test and cone penetration test can also be used to obtain the modulus of elasticity of soil [3].

This paper represents the effect of relative density on elastic properties of sand. This study includes determination of index properties of sand, shear strength parameters, modulus of elasticity and modulus of subgrade reaction of sand at different relative densities. It also represents the comparison of the modulus of subgrade reaction obtained from model plate load test with the theoretical relationships developed by various researchers mentioned in Table 4.

2 Material and Test Setup

2.1 Material

Two types of sand were used in this study; one was procured from Orsang River and another from Narmada River. The particle size distribution curve of both types of soils was obtained by performing dry sieve analysis test as shown in Fig. 1, which
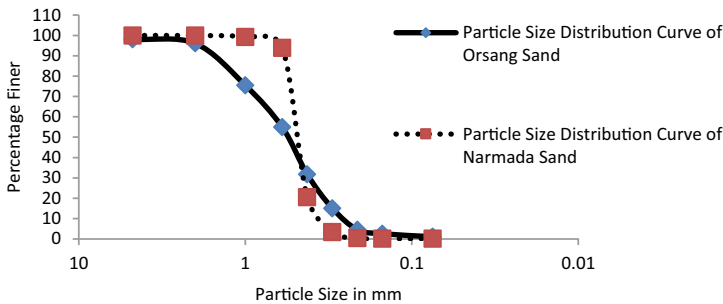
Fig. 1 Particle size distribution curve for Orsang sand and Narmada sand

Table 5 Index properties of both types of sands

S. No.	Property	Unit	Values for Orsang river sand	Values for Narmada river sand
1	Specific gravity	–	2.55	2.62
2	Coefficient of uniformity (Cu)	–	2.711	1.49
3	Coefficient of curvature (Cc)	–	0.94	1.108
4	Type of sand as per IS code method (sieve analysis)	–	SP—poorly graded sand	SP—uniformly graded sand
5	Maximum density	(gm/cm^3)	1.83	1.67
6	Minimum density	(gm/cm^3)	1.5	1.43
7	Density of sand at 40% relative density	(gm/cm^3)	1.62	1.52
8	Density of sand at 60% relative density	(gm/cm^3)	1.68	1.57
9	Density of sand at 80% relative density	(gm/cm^3)	1.75	1.62
10	Angle of internal friction at 40% I_D (from direct shear box test)	Degree	32	30
11	Angle of internal friction at 60% I_D (from direct shear box test)	Degree	35	32
12	Angle of internal friction at 80% I_D (from direct shear box test)	Degree	39	35

shows that Orsang sand (OS) has almost all particle size but less amount of fine sand (less than 0.2 mm) while Narmada sand (NS) has almost all particle sizes between 0.6 and 0.4 mm and few amounts of other sizes. The index properties of both types of sands are as listed in Table 5. The abbreviations used for Orsang sand at 40%, 60% and 80% relative density are OS-40, OS-60 and OS-80, respectively, and for Narmada sand NS-40, NS-60 and NS-80.

Mild steel plate having 220 mm × 220 mm × 25 mm dimensions was used to perform plate load test.

2.2 Test Setups

Triaxial Test Setup: To determine modulus of elasticity of sand, simple triaxial test was performed on both types of sand at 40%, 60% and 80% relative density. The

Table 6 Details of parameters used to achieve the desired density of sand using surface vibration technique

Type of sand	Density (gm/cm^3)	Relative density (%)	Thickness of layer (mm)	Duration of vibration (s)
Orsang	1.62	40	150	45
	1.68	60	100	85
	1.75	80	50	60
Narmada	1.52	40	100	30
	1.57	60	100	60
	1.62	80	50	90

dimension of cylindrical sand samples used in this test was 38-mm diameter and 81-mm height. It was performed as per IS: 2720-11[4]. The detailed procedure of the preparation of sand sample had been adopted as below.

A metal former, split mold of about 38.5-mm internal diameter, with vacuum pressure valve was used for preparing the soil sample. A porous stone was placed on the top of the pedestal of the triaxial base, and the pressure connection was attached to a vacuum pump. One end of a membrane was sealed to the pedestal by O-rings. The metal former was clamped to the base. The upper metal ring of the former was kept inside the top end of the rubber membrane and was held with the help of clamp before placing the funnel and the rubber bung in position.

The funnel and membrane were filled with oven-dried sand which was to be tested. Negative pressure of about 2 kN/ m^2 was applied on membrane while filling the sand in membrane. The funnel was then removed, and the sample was compacted if required. The surface of the sample was leveled, and a porous stone was placed on its top. The loading cap was placed gently on the top porous stone, and O-rings were fixed over the top of the rubber membrane [7].

Model Plate Load Test Setup: Modulus of subgrade reaction was obtained by performing model plate load test as per IS:9214-1979 [5].

Model plate load test was performed on both types of sand at 40%, 60% and 80% relative density. The size of plate used in plate load test was 220 mm × 220 mm × 25 mm, and size of tank was 1200 mm × 1200 mm × 1200 mm. To achieve the desired density, tank was filled layer by layer and each layer was vibrated for a particular duration by surface vibrator. Surface vibrator having surface area 32 cm × 31 cm, 16.9 kg weight and 1400 rpm frequency was used in this study. The detail of this procedure is given in Table 6.

3   Result and Discussion

Average modulus of elasticity of sand E_s and modulus of subgrade reaction k_s (kN/m^2/m) from triaxial test and model plate load test (MPLT) were obtained as

Table 7 Elastic properties of sands at different relative densities and comparison of modulus of subgrade reaction

Type of sand	Modulus of elasticity of sand E_s (KPa)	Modulus of subgrade reaction k_s (kN/m^2/m) from the present study and from theoretical relation developed by various investigators (Table 4)					
		Present study	Vesic	Biot	Meyerhof and Baike	Klopple and Glock	Selvadurai
OS-40	21,667	49,219	69,640	102,516	108,225	151,515	70,346
OS-60	33,889	87,500	109,744	162,822	164,310	246,465	106,801
OS-80	39,167	112,500	125,366	186,187	185,448	296,717	120,541
NS-40	13,879	26,250	42,985	62,587	69,327	97,058	45,063
NS-60	20,952	56,250	65,186	95,573	101,587	152,381	66,032
NS-80	25,229	65,625	77,847	114,366	119,454	191,127	77,645
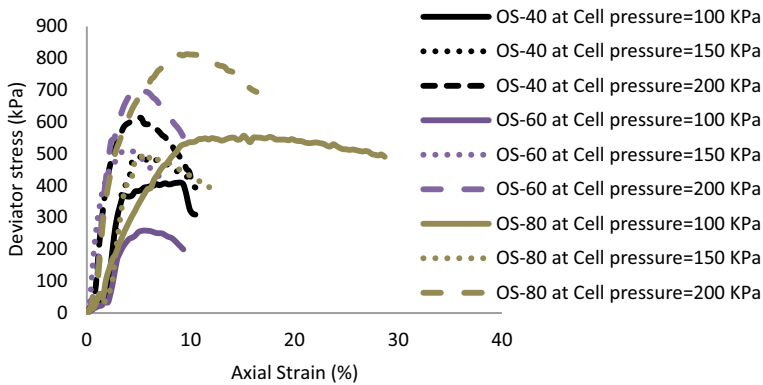
Fig. 2 Deviator stress–strain curve of Orsang sand at 40%, 60% and 80% relative density

shown in Table 7. Modulus of elasticity of sand Es was taken an average of three slopes of the initial tangent of deviator stress–strain curve at different cell pressures (Figs. 2 and 3). The values of Poisson's ratio were considered as 0.3, 0.25 and 0.2 for 40%, 60% and 80% relative density, respectively, in this study based on Table 11.2 of Arora book [7], which was used to calculate theoretical value of modulus of subgrade reaction k_s using correlations developed by various researchers, and it was compared with the value obtained by performing model plate load test.

3.1 Modulus of Elasticity of Sand E_s

As the relative density (I_D) of sand was increased, the modulus of elasticity of sand was also increased (Fig. 4).
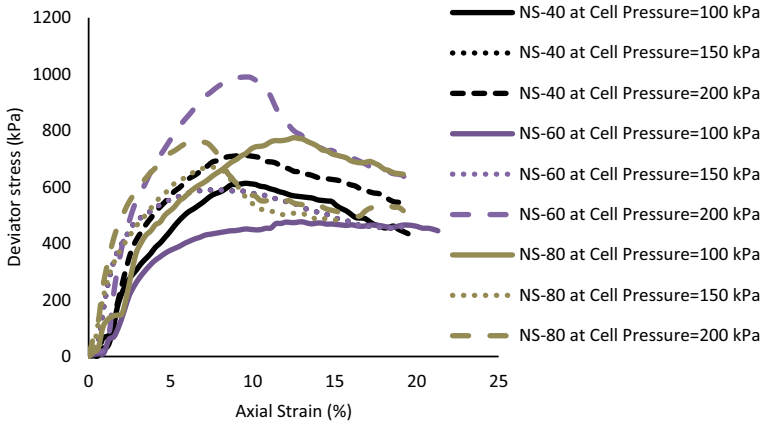
Fig. 3 Deviator stress–strain curve of Narmada sand at 40%, 60% and 80% relative density
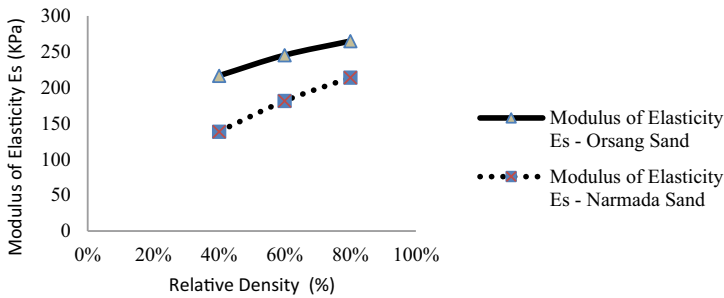
Fig. 4 Variation in modulus of elasticity E_s for relative density

3.2 Modulus of Subgrade Reaction (K_s)

Modulus of subgrade reaction was obtained from the model plate load test as per IS:9214-1979. Load–settlement curves for both types of sand at different relative densities were obtained as shown in Figs. 5 and 6.

Three types of corrections, namely corrections for load deflection curve, correction for bending of the plate and correction for size of plate, were applied for calculating corrected modulus of subgrade reaction in present study according to IS: 9214–1979 [5] Figs. 7 and 8 shows the comparison of various theoretical methods and present study for finding out modulus of subgrade reaction at different relative densities for orsang sand and narmada sand respectively.
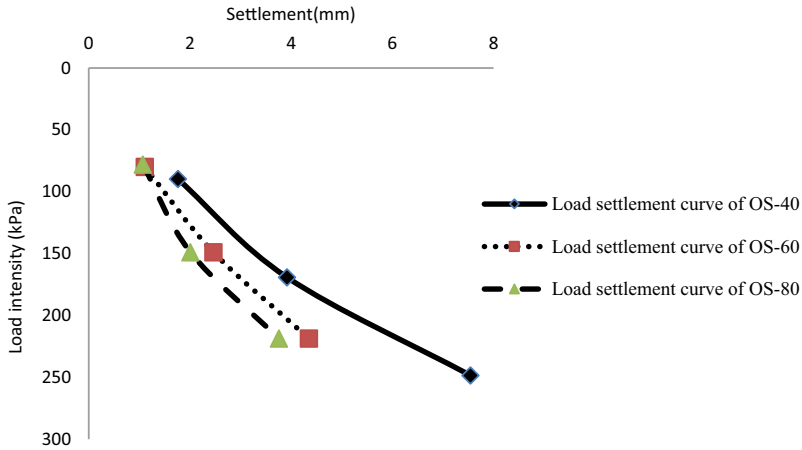
Fig. 5 Load–settlement curve for Orsang sand at 40%, 60% and 80% relative density
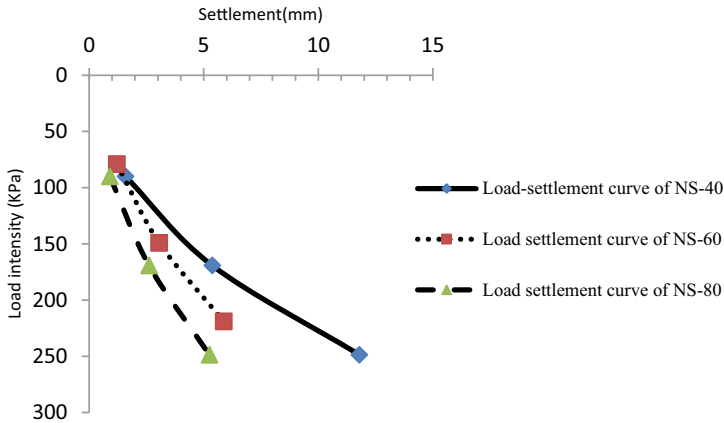
Fig. 6 Load–settlement curve for Narmada sand at 40%, 60% and 80% relative density

4   Conclusion

The following conclusions were obtained from this study:

1. As the relative density of sand increased, the modulus of elasticity and modulus of subgrade reaction of both types of sand were increased.
2. The value of subgrade reaction obtained by performing model plate load test (IS:9214,1979) was compared with the theoretical relation given by various researchers and found that the pattern of changing of modulus of subgrade reaction of both sands was nearly same as of Vesic and Selvadurai. From this experimental study, it can be concluded that in the absence of plate load test
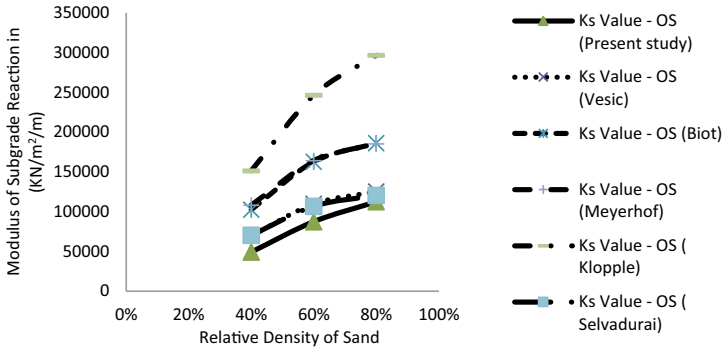
Fig. 7 Comparison of various theoretical methods and present study for finding out modulus of subgrade reaction of Orsang sand at different relative densities
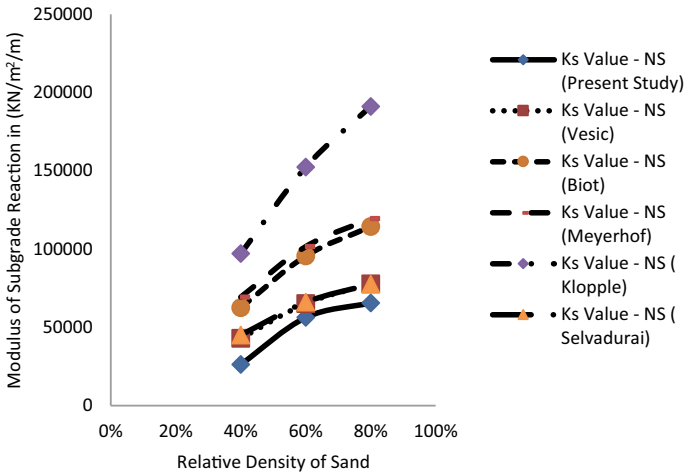
Fig. 8 Comparison of various theoretical methods and present study for finding out modulus of subgrade reaction of Narmada sand at different relative densities

    data of sand the theoretical relationship developed by Vesic and Selvadurai can be used to determine modulus of subgrade reaction by knowing modulus of elasticity of sand from triaxial test.

3. The value of modulus of subgrade reaction of Orsang sand at 60% and 80% relative density was increased by 78% and 128%, respectively, at 40% relative density, and for Narmada sand, it was increased by 114% and 150%, respectively.

4. As the relative density (I_D) of Orsang sand was increased to 60% (I_D) and 80% (I_D) from 40% (I_D), the modulus of elasticity of sand was found to be increased by 56% and 81%, respectively, as compared to E_s at 40% (I_D) and for Narmada sand it was 51% and 82%, respectively.

References

1. Jamshid, S.: Comparative study of methods of determination of coefficient of subgrade reaction. Electron. J. Geotech. Eng. **14**(E), 1–14 (2009)
2. Kim, D.S., Park, S.Y.: Relationship between the subgrade reaction modulus and the strain modulus obtained using a plate loading test. In: World Congress Railway Research 2011, vol. 9, pp. 1–11 (2011)
3. Ziaie Moayed, R., Naeini, S.A.: Evaluation of modulus of subgrade reaction (Ks) in gravely soils based on standard penetration test (SPT). In: Ng, Zhang & Wang (eds.), International Conference on Physical Modelling in Geotechnics 2006, vol. 6, pp. 801–805. Taylor & Francis Group, London (2006)
4. IS: 2720-Part-11-1993. Determination of the shear strength parameters of a specimen tested in unconsolidated undrained triaxial compression without the measurement of pore water pressure. Bureau of Indian Standards, Manak Bhavan, 9 Bahadur Shah Zafar Marg, New Delhi 110002, India (1993)
5. IS: 9214-1979. Method of determination of modulus of subgrade reaction (K-value) of soils in field. Bureau of Indian Standards, Manak Bhavan, 9 Bahadur Shah Zafar Marg, New Delhi 110002, India (1997)
6. IS: 2950 (Part I)-1981, Indian Standard Code of Practice for Design and Construction of Raft Foundations. Bureau of Indian Standards Manak Bhavan, 9 Bahadur Shah Zafar Marg New Delhi 110002 (2004)
7. Arora, K.R.: Soil Mechanics and Foundation Engineering, 3rd edn. Standard Publishers Distributors, Delhi (1992)
8. Bowles, J.E.: Foundation Analysis and Design, 6th edn. McGrow-Hill International press, New York (1998)

Characterization and Stabilization of Red Mud and Ash—Solid Industrial Waste from Aluminum Industry

A. Ghosh, Dalip Kumar, and Zamir Ahmaed

Abstract Ore processing and metal manufacturing industries generate huge quantity of residual wastes. Emphasis has been laid on the residual products of aluminum industries, e.g., red mud. The industry utilizes bauxite as raw material to extract aluminum out of it. Extraction of aluminum being power intensive, all the aluminum industries have captive power plants which generate huge quantity of ash as waste product in addition to red mud which comes out through the process of alumina (Al_2O_3) extraction. In the absence of any effective technology that can utilize red mud, industries have to incur heavy expenses in terms of land and space for storing red mud resulting in increased cost of aluminum production. Such a situation calls for an effective, economic and environment-friendly method to combat the challenges of disposal of the waste produced by such industries. One of the most common and feasible ways to utilize red mud in bulk is to utilize the wastes for civil construction, e.g., construction of embankments, roads, etc., utilizing the waste material. This paper aims at characterization of the waste material, i.e., red mud and ash through laboratory experiments. Analyzing the various aspects of their geotechnical parameter attempt has been made to characterize the mix of ash and red mud as well as cement and red mud. Result obtained through laboratory experiments has been discussed.

Keywords Red mud · Characterization · Industrial waste

1 Introduction

One of the major challenges before the processing and manufacturing industries is disposal of the residual waste products. Out of the various production industries, the ore dressing and mineral processing industries are the major contributors toward disposal of toxic waste products. Present emphasis has been laid on the residual products of aluminum industries (pond ash and red mud). The industry utilizes bauxite as raw material to extract aluminum out of it. Out of total aluminum production, India

A. Ghosh (✉) · D. Kumar · Z. Ahmaed
CSIR—Central Building Research Institute, Roorkee, Uttarakhand, India
e-mail: aghoshcbri@yahoo.com

contributes only about 5% of the total world's production. The major aluminum producers in India are HINDALCO, NALCO, BALCO and MALCO. In the absence of any technology that can utilize the industrial wastes like ash and red mud, the industries have to incur heavy expenses in terms of land and space. This calls for an effective, economic and environment-friendly method to combat the utilization and disposal problems of the waste produced by these industries. One of the most common and feasible ways to utilize the ash and red mud is to go for civil construction, e.g., construction of embankments, roads, etc., with the waste materials. This paper aims at characterization of the materials through laboratory experiments, analyzing the various aspects of their geotechnical behavior so that material can be used in bulk for civil construction like embankments, roads, etc.

For the study, samples are obtained from ash ponds and red mud ponds of HINDALCO (U.P), BALCO (Chhattisgarh) and NALCO (Orissa). However in this paper, results of only the red mud and ash collected from HINDALCO ponds are reported. Both the ash and red mud are collected from thick slurry disposal system. This system has the advantage over conventional thin slurry disposal system that the rate of consolidation of disposed materials in the ponds is quite faster. It takes maximum of 24 h to consolidate, and the deposit hardens to the extent that one is able to walk over the surface on account of lesser water content and certain chemical treatment undergone before the disposal.

2   Chemical Analysis

Chemical analysis reveals that red mud (RM) contains silica, aluminum, iron, calcium, titanium, as well as an array of minor constituents, namely Na, K, Cr, V, Ni, Ba, Cu, Mn, Pb, Zn, etc. The variation in chemical composition between different RMs worldwide is high. RM has a very high number of compounds present. The more frequently available compounds are:

Hematite (Fe_2O_3), goethite $Fe(1 − x)Al_xOOH$ ($X = 0$–0.33), gibbsite $Al(OH)_3$, boehmite $AlO(OH)$, diaspore $AlO(OH)$, calcite ($CaCO_3$), calcium aluminum hydrate ($x \cdot CaO \cdot yAl_2O_3 \cdot zH_2O$), quartz ($SiO_2$), rutile ($TiO_2$), anatase ($TiO_2$), $CaTiO_3$, Na_2TiO_3, kaolinite ($Al_2O_3 \cdot 2SiO_2 \cdot 2H_2O$), sodalites, aluminum silicates, cancrinite, hydroxycancrinite, chantalite, hydrogarnet. A wide variety of oxides is also present. Typical values are given in Table 1.

XRD was carried out with red mud sample. The XRD plot is shown in Fig. 1. Some of the important minerals identified on the plot are: rutile (TiO_2), boehmite ($AlHO_2$), quartz (SiO_2), hematite (Fe_2O_3), aragonite ($CaCO_3$), etc.

Table 1 Oxides present in bauxite ore

Oxides	Contents (%)
Fe_2O_3	33–35
Al_2O_3	10–20
SiO_2	6.5–8.0
Na_2O	5–6
CaO	4–5
TiO_2	18–20
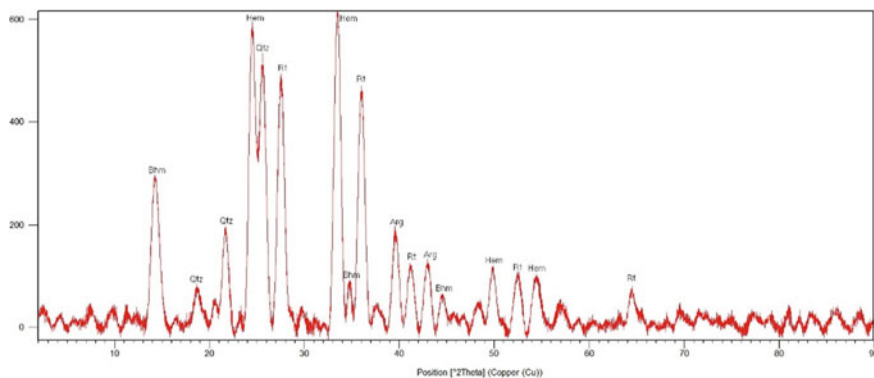
Fig. 1 XRD plot of red mud sample

3 State of the Art

The disposal of red mud is difficult, and the reports on this issue in the open literature seem scarce. However, information available in the open source has been collected about the disposal as well as common practice in the USA, India, China, Japan, France and Greece.

In a research by Hind et al. [1], it is reported that conventional disposal methods have revolved around the construction of clay-lined dams or dykes into which red mud slurry is pumped and allowed to dry naturally. The design and construction of such residue impoundments have varied considerably over the years, with disposal practices generally dependent upon the nature of the immediate environment [2]. However, the potential effect on groundwater and surrounding environment, and the difficulties associated with the surface rehabilitation forced significant changes in the disposal practices [3]. This leads to doubly sealed impoundment incorporating a polymeric membrane as well as clay lining.

In another report by Agrawal et al. [4], it is reported that out of the 84 alumina plants all over the world only seven are still practicing the sea disposal in a planned manner because of scarcity of land.

Ekrem Kalkan [5], in his investigation with red mud for its possible use as stabilization material for clay liners, used red mud and cement. This investigation showed that the addition of RM and cement improved the compressive strength, the hydraulic conductivity and the vertical swelling percentage values of compacted composite samples. Also, the results of this study proved that RM and cement are suitable for utilization in geotechnical applications and that RM can be used for the modification of clay liners. Consequently, it is concluded that red mud and cement materials can be successfully used for the stabilization of clay liners in geotechnical applications. Furthermore, the use of this waste material in clay stabilization could decrease the cost of stabilization and provide a beneficial end use for this by-product material.

Newson et al. [6] described a laboratory program to investigate the mechanical and physicochemical properties of red mud at a site in the UK. The red mud storage facility has been recently decommissioned and has been considered for future rehabilitation and construction activity. Based on a series of laboratory tests conducted on the red mud, it is concluded that the material has compression behavior similar to clayey soils, but frictional behavior closer to sandy soils. The red mud appears to be "structured" and has features consistent with sensitive, cemented clay soils. Exposure of the red mud to acidic conditions causes dissolution of the hydroxysodalite and a loss of particle cementation. The shape, size and electrically charged properties of the hydroxysodalite, goethite and hematite in the red mud appear to be causing mechanical behavior with features consistent with clay and sand, without the presence of either quartz or clay minerals.

Mohan et al. [7] illustrated a cost-effective method for reclaiming solid waste landfills by capping with clayey dredged material using a closure design developed for bauxite residue landfills in Texas. A research methodology comprised of laboratory cylinder tests, field revegetation tests and computer-based transport modeling was used to evaluate the effectiveness of the various capping alternatives and to select the final design parameters for the landfill. The design developed in this study can be applied to other similar solid waste sites with minor modifications depending upon the waste properties, site characteristics and closure requirements of the facility.

USA

Red mud and brown mud are precipitated from a caustic suspension of sodium aluminate in a slurry and routed to large on-site surface impoundments known as red and brown mud lakes. In these lakes, the red mud and brown mud settle to the bottom and the water is removed, treated, and either discharged or reused. The mud is not removed, but is accumulated and disposed in place. The mud dries to a solid with a very fine particle size (sometimes less than 1 μm). Red mud contains significant amounts of iron (20–50%), aluminum (20–30%), silicon (10–20%), calcium (10–30%) and sodium (10–20%). Red mud may also contain trace amounts of elements such as barium, boron, cadmium, chromium, cobalt, gallium, vanadium, scandium and lead, as well as radionuclides.

China

In China, things appear to be slightly different. In a research by Peng et al. [8], it is reported that most of the RM disposal is in landfill. However close to 10% of RM is being recycled for further metal extraction or as a raw material for brick production.

Japan

Hyuna et al. [9] report that in Japan, majority of RM is deposited into the ocean after neutralization. However, authors also reported that aluminum manufacturing companies in Japan have developed pretreatment techniques for bauxite before the Bayer process to reduce the amount of RM discharged.

France

Very limited information is available about the disposal practice. The practice used to be sea disposal, but it is speculated that this has changed in view of the new European legislation. Recently available satellite pictures show the presence of red mud pond referred as lagoons.

Greece

Situation concerning the disposal method is changing. Till 2006, red mud was discharged through a pipe line at the sea of Antikyra Bay. Currently, high pressure filtering and dry disposal and reuse of red mud are under implementation.

Fotini Kehagia [10] attempted to utilize red mud for embankment construction. 8.0-m-wide, 75.0-m-long and 3-m-high embankment was experimentally constructed to establish the feasibility of utilizing red mud for civil construction works. Encouraging results were obtained.

National (Indian) status

Hajela et al. [11] worked with red mud generated at Hindalco Industries Ltd, Renukut, to utilize the same for manufacture of building components. Fly ash was used as admixture to manufacture brick. High water absorption and cracks on the brick prohibited the material to be used for brick manufacturing.

4   Characterization of Red Mud and Ash

Red mud (RM) and ash have been collected from Hindalco, Red Mud Pond. Geotechnical characterization of RM and ash were carried out as per BIS code through the following laboratory tests:

- Grain size analysis
- Proctor density test
- Consolidation test
- Direct shear test.

Table 2 Physical and geotechnical properties of ash and red mud

Type of material	Grain size			Proctor density		Specific gravity
	Sand (%)	Silt (%)	Clay (%)	OMC (%)	Dry density (gm/cc)	
Ash	62	38	–	32	1.22	2.36
Red mud	22	60	18	29	2.04	3.15

Table 3 Direct shear, consolidation and permeability properties of ash and red mud

Material	Direct shear test				Consolidation test		Permeability (cm/s)
	Unsaturated		Saturated		C_v	C_v	
	C (kg/cm^2)	Φ (°)	C (kg/cm^2)	Φ (°)	(cm^2/s)		
Ash	0.07	40	0.05	38	1.29×10^{-3}	0.076	0.38×10^{-4}
Red mud	0.26	33	0.06	30	0.85×10^{-3}	0.23	0.43×10^{-5}

Tables 2 and 3 give the values of physical and geotechnical parameters of red mud and ash collected from Renukut Hindalco Red Mud Pond.

5 Stabilization of Red Mud

5.1 Red Mud Mixed with Ash

Red mud and ash were mixed homogeneously with different proportions, and samples were prepared for determination of engineering parameters. The following proportions of red mud and ash were evaluated:

- Red Mud + Ash—30% + 70%
- Red Mud + Ash—40% + 60%
- Red Mud + Ash—50% + 50%
- Red Mud + Ash—60% + 40%
- Red Mud + Ash—70% + 30%.

Tables 4 and 5 give the values of physical and geotechnical parameters of red mud mixed with ash in different proportions.

Table 4 Physical and geotechnical properties of mix composition

Mix composition (Mud + Ash)	Grain size			Proctor density		Specific gravity
	Sand (%)	Silt (%)	Clay (%)	OMC (%)	Dry density (gm/cc)	
50% + 50%	65	28	7	28	1.49	2.74
70% + 30%	50	40	10	28	1.56	2.91
30% + 70%	70	28	2	29	1.41	2.44
60% + 40%	58	35	7	27	1.54	2.64
40% + 60%	63	32	5	28	1.52	2.68

Table 5 Direct shear, consolidation and permeability properties of mix composition

Mix composition (Mud + Ash)	Direct shear test				Consolidation properties		Permeability (cm/s $\times 10^{-4}$)
	Unsaturated		Saturated		C_v	C_v	
	C (kg/c^2)	Φ (°)	C (kg/cm^2)	Φ (°)	(cm^2/s $\times 10^{-3}$)		
50% + 50%	0.18	36	0.04	33	1.05	0.059	0.14
70% + 30%	0.19	37	0.10	35	0.95	0.086	1.25
30% + 70%	0.12	39	0.05	38	1.14	0.082	0.42
60% + 40%	0.20	36	0.08	34	1.02	0.078	0.95
40% + 60%	0.17	37	0.06	36	1.08	0.075	0.87

5.2   Red Mud Stabilized with Cement

It was decided to stabilize RM with cement commercially available in the market. The decision to use cement as stabilizer was due to its easy availability, quick hardening properties as compared to other stabilizer, e.g., lime, most economical stabilizing material available in the market, etc. Mechanism of improvement in strength when cement is mixed with red mud is exactly same as gain in strength when sand is mixed with cement to prepare sand–cement mortar. Like in sand–cement mortar, cement acts as binding material and sand as filler; here too, cement binds the red mud particles. In both the cases, on hydration, cement gains strength with filler material present in the matrix. The water–cement reaction is well known and beyond the scope of the paper; hence, it is not described here.

After stabilization, experimental program was undertaken to study the effect of cement on RM with respect to the improvement in strength characteristics. The oven-dried RM was mixed with cement at liquid limit. The liquid limit of the red mud was found to be 32.5%. The cement content varied from 2 to 6% with increment of 2%, and the mix was transferred to a specially fabricated airtight perspex mold with inner diameter 38 mm and length 76 mm maintaining L/d ratio as 2. For every percentage of mix, minimum 3 samples were prepared.

After a rest period of 7, 21, 28 and 56 days, the samples were taken out from the mold and tested for unconfined compressive strength. Failure patterns are shown in Fig. 2. Compressive strength of cement stabilized red mud samples with variation of cement content is given in Table 6. Modulus and strain values at 28 days are given in Table 7.

Fig. 2 Failure pattern of cement stabilized sample by UCS test

Table 6 Unconfined compressive strength of cement stabilized red mud (kg/cm^2)

Rest period	Red mud + 2% cement	Red mud + 4% cement	Red mud + 6% cement
7 days	–	1.92	2.17
21 days	0.67	3.80	5.62
28 days	1.57	4.36	7.07
56 days	1.96	4.70	7.42

Table 7 Modulus and strain values at 28 days

RM + % of cement	Initial tangent modulus E_i (kg/ cm^2)	Strain at failure ϵ_f	50% failure strain ϵ_{50}	Secant modulus E_{50} (kg/ cm^2)
2%	38	0.044	0.018	42
4%	185	0.047	0.019	190
6%	200	0.049	0.021	200

Table 8 Coefficient of consolidation (C_v) of stabilized red mud (cm^2/s) $\times$ 10^{-3}

Rest period	RM + 2% cement	RM + 4% cement	RM + 6% cement
7 days	0.95	1.14	1.37
21 days	1.01	1.21	1.47
28 days	1.04	1.29	1.60
56 days	1.08	1.31	1.65

Table 9 Compression index (Cc) of stabilized red mud

Rest period	RM + 2% cement	RM + 4% cement	RM + 6% cement
7 days	0.202	0.106	0.056
21 days	0.191	0.087	0.053
28 days	0.118	0.079	0.051
56 days	0.109	0.071	0.048

Consolidation tests were carried out on cement stabilized RM samples in odeometers. The coefficient of consolidation (C_v) and compression index (C_c) were measured after the specified rest period of 7, 21, 28 and 56 days. Tables 8 and 9 give the values of C_v and C_c, respectively, with variation of cement content and time.

6 Discussion on the Test Results

6.1 Red Mud and Ash

Grain size analysis shows that the ash has mostly sand size particles (62%), whereas the red mud has only 22% of sand size particle. The total fines in the red mud are 78% as against 38% in ash. Ash does not have clay size particle, but in contrast red mud has 18% of clay size particle. The red mud is found to be heavier material as compared to ash because the specific gravity of red mud is nearly 33% more than the ash.

The shear properties of ash show that the friction angle is 40° under partially saturated condition and under saturation the value drops down to 38°. The similar trend is observed in case of red mud for friction angle, but the cohesion value of the red mud drops drastically from 0.26 kg/cm^2 under partially saturated condition to 0.06 kg/cm^2 under saturated condition. This shows that under saturated condition the red mud will loose its strength.

From the permeability values, it is observed that both ash and red mud are free draining material though red mud has large quantity of total fines (78%). However, uniformity could not be observed in the permeability value of the mixed material.

6.2 Red Mud Mixed with Ash

Under homogenous mix of different proportions, the properties get changed as per expectations. The density of the mixed material decreases as different proportions of ash are mixed. The range of specific gravity obtained is 2.44–2.91 for the mix composition Red Mud + Ash—(30% + 70%) and (70% + 30%), respectively. The specific gravity obtained for Red Mud + Ash (50% + 50%) is 2.74. Similarly, the shear test results also showed change in cohesion and friction value when red mud and ash were mixed in different proportions. While friction angle for the mixed material decreases marginally, the cohesion value increases as compared to ash.

6.3 Red Mud Stabilized with Cement

Red mud was mixed with ordinary Portland cement to form a homogenous mix. The quantity of cement varied from 2 to 6% with increment of 2%. The rest period was varied from 7 to 56 days. Two percentage of cement after 7 days failed to stabilize the red mud. The sample was unable to retain its shape. Hence, UCS could not be carried out. Unconfined compression tests were conducted to establish a general trend for gain in strength with different percentages of cement. However, after a rest period of 21 days the same sample got stabilized and marginal strength development took place. When the cement content increased to 4% after 7 days, the sample got stabilized, UCS value obtained was 1.92 kg/cm^2 and the same value was increased to 4.70 kg/cm^2 for the rest period of 56 days; i.e., 145% increase in UCS value could be recorded. The UCS value was increased from 2.17 kg/cm^2 to 7.42 kg/cm^2 when 6% cement was added as stabilizer and rest period was increased from 7 to 56 days; i.e., 240% increase in UCS value could be recorded in this case.

The value of initial tangent modulus E_i increased from 38 to 200 kg/cm^2 for 2% cement to 6% cement added as stabilizer. Thus, more than 425% increase in E_i value could be observed when 2% cement to 6% cement added as stabilizer. However, it is interesting to note that the value of the failure strain and the strain at 50% failure remains almost same.

The value of coefficient of consolidation C_v increased to 0.95×10^{-3} cm^2/s for a rest period of 7 days, and same value was increased to 1.08×10^{-3} cm^2/s for the rest period of 56 days with 2% cement added as stabilizer which show 14% increase between 7 and 56 days. The value of compression index C_c decreased to 0.202 for rest period of 7 days with 2% of cement, and further the same value decreased to 0.109

for a rest period of 56 days. This shows 46% decrease. As the value of compression index C_c decreased, settlement will also decrease.

References

1. Hind, A.R., Bhargava, S.K., Grocott, S.C.: The surface chemistry of Bayer process solids: a review. Colloids Surf. **146**, 359–374 (1999)
2. Salopek, B., Strazisar, J.: The influence of red mud impoundments on the environment. Light Metals, Warrendale, PA, United States 4–41 (1993)
3. Cooling, D.J., Glenister, D.J.: Practical aspects of dry residue disposal, Light Metals 25–31. In: Proceedings of the 121st TMS Annual Meeting, Published by Minerals, Metals & Materials Society, San Diego, CA, USA (1992)
4. Agrawal, A., Sahu, K.K., Pandey, B.D.: Solid waste management in non-ferrous industries in India. Resour. Conserv. Recycl. **42**, 99–120 (2004)
5. Kalkan, E.: Utilization of red mud as a stabilization material for the preparation of clay liners. Eng. Geol. **87**, 220–229 (2006)
6. Newson, T., Dyer, T., Adam, C., Sharp, S.: Effect of structure on the geotechnical properties of bauxite residue. J. Geotech. Geoenviron. Eng. Am. Soc. Civil Eng., 143–151 (2006)
7. Mohan, R.K., John, B., Herbich, B., Lloyd, R., Hossner, Fred S., Williams, D.,: Reclamation of solid waste landfills by capping with dredged material. J. Hazardous Mater. **53**, 141–164 (1997)
8. Peng, F., Liang, K., Shao, H., Hu, A.: Nano-crystal glass-ceramics obtained by crystallization of vitrified red mud. Chemosphere (2004)
9. Hyuna, J., Endoha, S., Masudaa, K., Shinb, H., Ohyaa, H.: Reduction of chlorine in bauxite residue by fine particle separation. Int. J. Miner. Proc. (2004)
10. Kehagia, F.: An innovative geotechnical application of bauxite residue. Electron. J. Geotech. Eng. **13**, 1–10 (2008)
11. Hajela, R.B., Gupta, R.G., Goel, R.K.: Disposal of solid wastes—Red mud and flyash in the production of heavy clay products. Int. J. Environ. Stud. **33**, 125–132 (1989)

A Study on Effect of Mica Content on Engineering Properties of Sands

Rajesh Deb and Indira Baruah Gogoi

Abstract It is often necessary to understand the interaction of mica mineral with the fine aggregates which is often used for construction purposes. Mica is one of the known deterious minerals which affects the engineering properties of sand and which ultimately affects the concrete. Different research work has already being conducted by different researchers. In the present study, an attempt has been made to study the effect of mica on different engineering properties. Here, the percentage of mica by weight adopted for different test procedures are 2%, 4%, 6% and 8%. Direct shear test, standard Proctor test, CBR test and compressive strength test were conducted by percentage replacement of locally available sand by mica. From the laboratory test results, it established that the presence of mica in fine aggregates causes reduction of compressive strength, and it increases the water demand. The dry density value, shear strength and the CBR value also reduce with the presence of mica content.

Keywords Direct shear test · Standard proctor test · CBR · Mica

1 Introduction

By volume, about 75% of the concrete ingredients are occupied by the aggregates. Aggregates play a vital role in civil engineering constructions. But aggregates with high mica content are mechanically weak due to its platy-shaped particles, and the fines content may increase significantly overtime due to the crushing under by the traffic loading and climatic weathering. Rock types with high mica content are often inhomogeneous.

R. Deb (✉)
Department of Civil Engineering, The Assam Royal Global University, Guwahati 781035, Assam, India
e-mail: rajeshdebk@gmail.com

I. B. Gogoi
Department of Civil Engineering, Assam Engineering College, Guwahati 781013, Assam, India
e-mail: indirabaruah33@gmail.com

Thus inclusion of platy particles in excess may affect the efficiency of the respective aggregates. There are several varieties of mica, but the two primary varieties are Muscovite, a hydrated silicate of aluminium and potassium, and Biotite, a ferromagnesium variety. Various researchers investigate the effect of presence of mica on the aggregates. Researchers like Harris et al. [1], Hobeda and Bunsow [2], Seethalakshmi and Ajanta Sachan [3], Frempong [4], Frempong [5], Mshali [6], etc., did some work in this domain. In this present study, percentage of mica by weight is increased, and the relative variation in the engineering properties is studied. The purpose of this study was to determine relationships between mica content and critical engineering parameters of sand.

2 Test Programme

2.1 Mica

Mica is widely distributed and occurs in igneous, metamorphic and sedimentary regimes. The mica content in fine aggregates is found to be in free form. But in case of coarse aggregates, mica is found to be in bonded forms with other minerals.

Scrap and flake mica is produced all over the world. Flake mica comes from several sources: the metamorphic rock called schist as a by-product of processing feldspar and kaolin resources, from placer deposits, and from pegmatite. Sheet mica is considerably less abundant than flake and scrap mica, and is occasionally recovered from mining scrap and flake mica. The most important sources of sheet mica are pegmatite deposits.

The mica group of sheet silicate minerals includes several closely related materials having close to perfect basal cleavage. All are monoclinic, with a tendency towards pseudo-hexagonal crystals, and are similar in chemical composition. The nearly perfect cleavage, which is the most prominent characteristic of mica, is explained by the hexagonal sheet-like arrangement of its atoms. Hobeda and Bunsow [2] have studied the packing properties of mica minerals and found that it deteriorates with the increase in mica content.

2.2 Material Characterization

The material used in the experimental programme are-

1. Sandy soil, for the purpose of preparing sub-grade
2. Mica mineral.

The sandy soil used to perform as sub-grade is collected from the bank of the river Khulsi near Kukurmara, Assam. Various laboratory tests, i.e., grain size distribution,

Table 1 Properties of sub-grade soil

S. No.	Property	Test value
1	Uniformity coefficient, C_u	2.67
2	Curvature coefficient, C_c	0.84
3	Effective size, D_{10} (mm)	0.6
4	D_{30} (mm)	0.9
5	D_{60} (mm)	1.7
6	Specific gravity, G	2.67
7	Optimum moisture content (%)	9.50
8	Maximum dry density (gm/cc)	1.97
9	Laboratory CBR value (unsoaked) (%)	16.18

specific gravity test, Proctor test and CBR test, are performed as per Indian standard codes to determine the properties of sub-grade soil which are given in Table 1.

Different percentage of mica is added to the Khulsi river sand, and its characteristics behaviour is analysed. Different types of mica are available in the market. The mica used in this study is silicate of aluminium and potassium. An image of mica mat is shown in Fig. 1.

Various properties of the mica sample used in this study is described in Table 2.

Fig. 1 View of mica

Table 2 Properties of mica

Mica properties	Description
Chemical composition	Silicate of aluminium or potassium
Crystal system	Monoclinic
Cleavage	Perfect
Streak	Colourless
Lustre	Pearly
Hardness	2–2.5
Specific gravity	2.7–3

2.3 Test Set-Up

2.3.1 Standard Proctor Test

This test is performed as per IS code 2720 (part 8)-(1980) [7]. Standard Proctor test is used to determine the dry density with change in moisture content. The water content corresponding to maximum dry density gives the OMC value.

2.3.2 Direct Shear Test

The maximum value of shear stress that can be mobilized within a sand mass is known as shear strength of sand. If the shear stress in any plane or surface at a point exceeds the value of shear strength, failure will occur in the sand. This test is performed as per IS 2720-13-(1986) [8].

2.3.3 CBR Test

The California bearing ratio test is a penetration test used to evaluate the sub-grade strength of roads and pavements. The results of these tests are used with the empirical curves to determine the thickness of pavement and its component layers. To keep the uniformity in different tests, the sub-grade was kept at its optimum moisture content 9.50% and within a field density range of 1.96–1.98 gm/cc. This test is performed as per IS 2720 (Part 16)-1987 [9].

2.3.4 Compressive Strength Test

Compressive strength of concrete is the maximum amount of compressive load that a material can bear before fracturing. The test is performed as per IS 516-(1959).

Different conditions for laboratory tests and its designation are listed in Table 3.

Table 3 Various conditions for lab tests and its designation

Designation	Test bed condition
A	Sandy soil
B	Sandy soil + 2% mica
C	Sandy soil + 4% mica
D	Sandy soil + 6% mica
E	Sandy soil + 8% mica
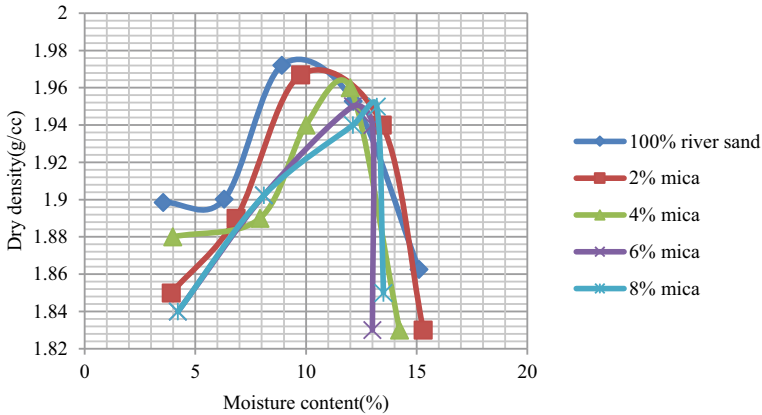
Fig. 2 Graph showing the variation of and OMC and dry density with increase in mica content

Table 4 Variation of dry density and moisture content with mica content

S. No.	Material	Dry density(g/cc)	Optimum moisture content (%)
1	A	1.975	9.5
2	B	1.970	10.5
3	C	1.965	11.5
4	D	1.955	12.0
5	E	1.950	13.0

3   Test Results

3.1   OMC

With the increase in mica content, OMC is increasing. It may be due to the reason that mica has a water retaining property, and it starts swelling with increase in mica content. There is also approximate linear decrease in dry density with increase in mica content.

Graphical representation of variation of dry density with moisture content is shown in Fig. 2. The variation of dry density and moisture content with mica content is given in Table 4, and it infers that with increase in mica content dry density value decreases.

3.2   *Determination of Shear Strength*

Shear strength parameter is determined from the cohesion value and the angle of internal friction value. For its calculation, direct shear test is done on the river sand

and with different mix of mica. The graphical representation of shear stress versus displacement for 0.5 kg/cm^2, 1 kg/cm^2 and 1.5 kg/cm^2 is shown in Fig. 3. The variation of shear stress with normal stress for material A is given in Table 5, and its graphical representation is shown in Figs. 4 and 5. And the variation of cohesion and angle of internal friction with mica content is given in Table 6 which reflects that the cohesion value for all the condition is same, but the angle of internal friction shows a decreasing trend.
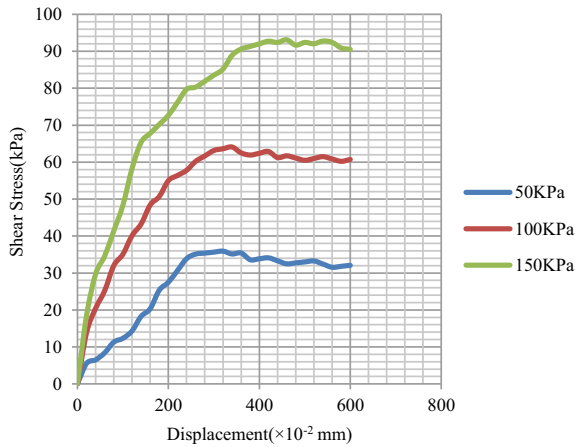
Fig. 3 Graph for shear displacement versus shear stress for river sand Khulsi

Table 5 Variation of shear stress with normal stress

Normal stress (kPa)	Proving ring reading	Load	Corrected area, A_c	Shear stress = Load/A_c (kPa)
50	35	1155	32.88	35.13
100	62	2046	32.40	63.15
150	87	2871	31.68	90.63
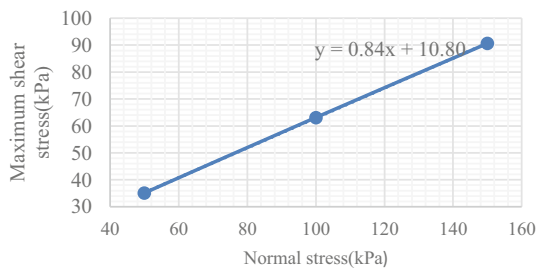
Fig. 4 Graph of normal stress versus shear stress for river sand
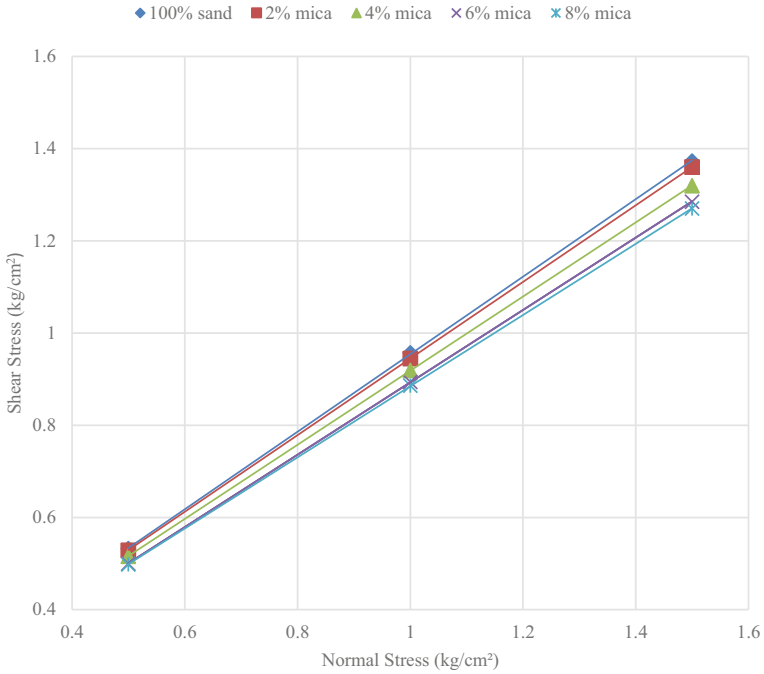
Fig. 5 Variation of angle of internal friction with mica content

Table 6 Variation of cohesion and angle of internal friction with mica content

S. No.	Material	Cohesion (kg/cm^2)	Angle of internal friction (φ)
1	A	0.11	40.03°
2	B	0.11	39.72°
3	C	0.11	38.79°
4	D	0.11	38.13°
5	E	0.11	37.82°

From the graph,

Angle of internal friction, $\varphi = 40.03$.
Cohesion, $c = 10.80$ kPa $= 0.113$ kg/cm^2.

3.3   CBR Test Results

The load versus penetration curve for sample A is shown in Fig. 6.

Test load at 2.5 mm penetration $= 204.93$ kg.
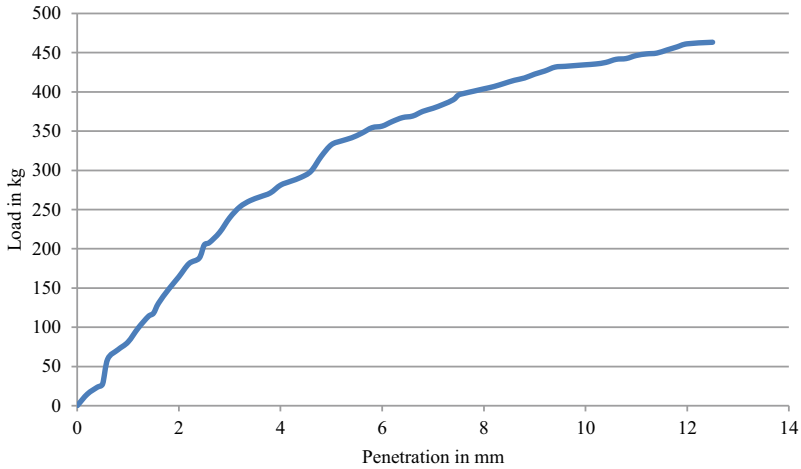
Fig. 6 Load vs. penetration curve for river sand (Khulsi)

Table 7 Variation of CBR values with mica content

S. No.	Material	CBR (%)
1	A	16.18
2	B	15.87
3	C	15.54
4	D	15.02
5	E	14.96

Standard load at 2.5 mm penetration = 1370 kg.
CBR at 2.5 mm penetration = $\frac{204.93}{1370} \times 100 = 14.95\%$
Test load at 5 mm penetration = 332.64 kg.
Standard load at 5 mm penetration = 2055 kg.
CBR at 5 mm penetration = $\frac{332.64}{2055} \times 100 = 16.18\%$
CBR value for sample (5 mm penetration) = 16.18%

The variation of CBR values with mica content for different materials is tabulated in Table 7, and it shows that the CBR value is least for material E with 8% mica content.

3.4 Compressive Strength

Cement used—Dalmia cement.
Water cement ratio—0.5
Concrete used—M20.

Table 8 Variation of compressive strength with mica content

Sample type	Compressive strength (N/mm²)					
	3 days strength (N/mm²)	Average (N/mm²)	7 days strength (N/mm²)	Average (N/mm²)	28 days strength (N/mm²)	Average (N/mm²)
A	16.35	17.95	23.11	22.75	34.84	32.70
	19.55		22.40		30.57	
B	15.46	16.26	22.04	22.75	31.28	31.81
	17.06		23.46		32.35	
C	17.80	18.30	22.10	22.57	33.73	32.96
	18.80		23.05		32.20	
D	16.30	17.25	22.05	22.50	33.13	32.60
	18.20		22.95		33.08	
E	18.70	18.39	23.25	22.67	32.23	31.68
	18.08		22.10		31.14	

Fineness Percentage—94.67%
Initial setting time—1 h 30 min.
Final setting time—3 h 30 min.

Table 8 shows the variation of compressive strength with increase in mica content. It indicates that with increase in mica content, there is an approximate decreasing trend in its 28 days compressive strength.

3.5 Petrographic Analysis

The petrographic test result for the sample A is tabulated in Table 9 which shows the approximate percentage of different mineral constituents with its shape, texture and colour. This test is performed as per Part VIII Petrographic Examination, IS: 2386 (part VIII) [10]. The microphotographs of sample A is shown in Fig. 7.

4 Discussion

From the values of dry density, shear strength and CBR values of various test samples (river sand and with percentage inclusion of mica); it was observed that the inclusion of mica reduces the strength.

Table 4 indicates that maximum dry density decreases with increase in mica content. This may be due to the inclusion of platy particles of mica with irregular boundaries.

Table 9 Petrographic analysis

Mineral constituents	Approximate amount (%)	Shape	Size	Surface texture	Colour
Quartz	86	Rounded to sub-rounded	Coarse grained	Even to uneven	White
(Rock fragments)	9	Elongated		Irregular and rough	Play of colours
Feldspar	2	Elongated		Irregular boundary	Grayish
Biotite	1	Flaky		Irregular boundary	Light brown
Muscovite	1	Flaky		Irregular boundary	Grayish
Others	1	–		–	–

(a)   (b)
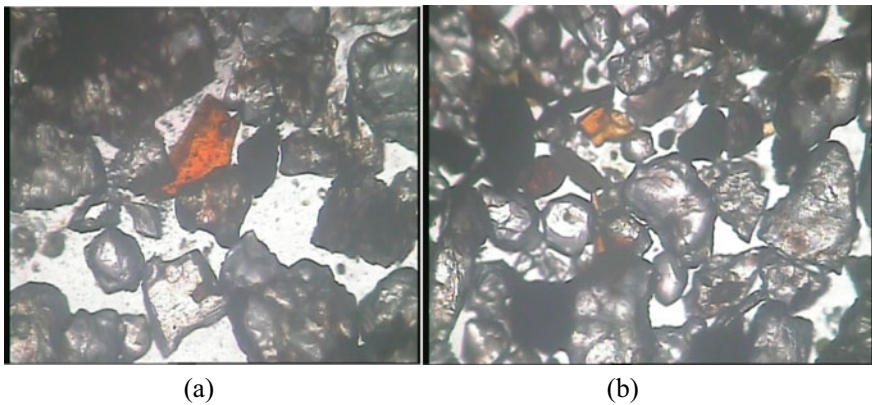
Fig. 7 Microphotographs showing different petrographic characteristics of Khulsi river sand (X25): **a** sample 1, **b** sample 2

Rogers [11] has examined the relation between mica content and permeability and found out that mica particles have the ability to retain water. This ability explains by the flats shape of the grains which provides the large specific surface per unit weight. Optimum moisture content shows an increasing trend with increase in mica content. It may be due to its water retaining power.

Shear strength and CBR values also show a decreasing pattern which increase in mica content. A very small value of cohesion is found from direct shear test. The influencing parameter is the angle of internal friction which reduces with inclusion of platy mica. The analysis is in accordance with the research work done by Harris et al. [1].

Compressive strength of concrete with increase in mica content does not show a proper trend.

Table 10 Percentage change in dry density values and OMC values with mica content

Material	% decrease in γ_d	% increase in OMC
B	0.25	10.52
C	0.50	21.05
D	1.01	26.31
E	1.26	36.84

Table 11 Percentage change in angle of internal friction values

Material	% decrease in angle of internal friction
B	0.77
C	3.09
D	4.74
E	5.50

Table 12 Percentage change in CBR values

Material	% decrease in angle of internal friction
B	1.91
C	3.95
D	7.16
E	7.54

Percentage variation of different engineering properties with increase in mica content (material B, C, D and E) is tabulated in Tables 10, 11 and 12.

5 Conclusions

Much research work has been reported on the effect of mica content on various engineering properties of crushed stone and river sand all over India. By studying on mica particles and its probable effects on engineering properties of fine aggregates, it has been tried to observe the variation of various engineering properties, which may be due to the presence of different proportion of mica content. The work is just an overview of probable effect of mica on fine aggregates. Indian standards are also not providing the permissible limit of mica and its various effect on engineering properties of aggregate, so lot of experimental work is still required on this field. Some writers like P.C Varghese in his book 'Building Materials' mentioned that 2–3% of mica are allowed in fine aggregates for mortar and concrete. Therefore, every text regarding aggregates should be checked individually to find out the actual effect of mica.

All the test results shows a decreasing trend in its values. So, it can be assumed that presence of mica in increasing amount can detoriate the engineering properties

of fine aggregates. However, this study can be further extended towards different test conditions considering other geotechnical parameters also.

References

1. Harris, W.G., Parker, J.C., Zelazny, L.W.: Effects of mica content on engineering properties of sand. Soil Sci. Soc. Am. J. **48**(3), 501–505 (1984)
2. Hobeda and Bunsow: Packing properties of mica minerals. ARPN J. Eng. Appl. Sci. **3**(8). ISSN 1819-6608
3. Seethalakshmi, P., Sachan, A.: Crushing effect of mica particles on mechanical behavior of micaceous sand at macro and micro level. In: International Geotechnical Engineering Conference, IGS Mumbai (2016)
4. Frempong, E.M.: Geotechnical properties of some residual micaceous soils in the Kumasi Metropolitan Area (Ghana). Bul. Int. Assoc. Eng. Geol. **49**(1), 47–54 (1994)
5. Frempong, E.M.: A comparative assessment of sand and lime stabilization of residual micaceous. Geol. Eng. **13**(4), 181–198 (1995)
6. Mshali, M.R., Visser, A.T.: Influence of mica on unconfined compressive strength of a cement-treated weathered granite gravel. J. South Afr. Inst. Civ. Eng. **54**(2), 71–77
7. Bureau of Indian Standards: Methods of test for soils, Part VII Determination of water content-dry density relation using light compaction, IS: 2720 (part VII). New Delhi, India (1980)
8. Bureau of Indian Standards: Methods of test for soils, Part 13 Direct shear test, IS: 2720 (part 13). New Delhi, India (1986)
9. Bureau of Indian Standards: Methods of test for soils, Part 16 Laboratory determination of CBR, IS: 2720 (part 16). New Delhi, India (1987)
10. Bureau of Indian Standards: Methods of test for aggregates for concrete, Part VIII Petrographic Examination, IS: 2386 (part VIII). New Delhi, India (1963)
11. Rogers, C.A., Szoke, S.I., Gorman, R.G.: Granular Base Failures in Low-Volume Roads in Ontario, Canada

Study of Thermal Conductivity of Soils for Varying Density and Water Content Profiles

Pooja Bhojani, L. S. Thakur, and D. L. Shah

Abstract In Analytical *Theory of Heat*, 1822 Joseph Fourier stated, "The problem of terrestrial temperatures presents one of the most beautiful applications of the theory of heat." The experimental schedule is planned so as to study a wide variety of artificially mixed soil using naturally available single component soils, i.e., sand, silt, and single mineral clay (kaolinite), to remove heterogeneity due to variation of various minerals in naturally occurring soils for the thermal conductivity as measured in laboratory setup, on the basis of physical properties of the soil. The objectives of this investigation of the thermal conductivity of soils are to employ the thermal probe method to obtain reliable thermal conductivity data for different local natural soils. For evaluating the radial flow of the heat, the soil is compacted in porcelain pipes. It has thermocouple controlled vertical heater rod placed at the center as source and 20 thermocouples placed radially in four directions perpendicular in plan for temperature profile readings. The second setup fabricated in house was aimed at studying the flow of thermal energy in longitudinal direction as well as with depth for which a rectangular steel tank was fabricated. The heat source was placed at one end of the tank, whereas the thermocouples were placed all along the length and a second row placed at different depths along the length. The influence of soil properties such as water content, dry density, and porosity on thermal conductivity is also observed.

Keywords Thermal conductivity · Thermocouple · Kaolinite

P. Bhojani (✉)
Department of Applied Mechanics, Faculty of Technology & Engineering, MSU, Vadodara 3900010, India
e-mail: pjbhojani-appmech@msubaroda.ac.in

L. S. Thakur
Department of Civil Engineering, BITS Edu Campus, Varnama, Vadodara 391240, India

D. L. Shah
Vadodara, India

1 Introduction

In 1822, Joseph Fourier stated that the theory of heat will always attract the attention of mathematicians, by the rigorous exactness of its elements and the analytical difficulties peculiar to it, and above all by the extent and usefulness of its applications; for all its consequences concern at the same time general physics, the operations of the arts, domestic uses, and civil economy. The migration of heat in porous media has attracted attention of the research fraternity, since almost a century. Studies conducted in the past reveal that heat migration in a medium primarily depends on its thermal resistivity (defined as the ability of the material to resist heat flow in it), its specific heat (defined as the ability of the material to store heat) and thermal diffusivity (which combines the transmission and storage properties of the material and is an indicative of the rate of change of temperature within the material). Soil thermal properties are of great importance in many engineering projects and other situations where heat transfer takes place in the soil. For example, they are of great importance in the design of roads, airfields, pipelines, or buildings in cold regions as well as underground power cables, hot water pipes, or cold gas pipelines in unfrozen ground. They are also important in such fields as agriculture, meteorology, and geology. Furthermore, soil–water interaction and soil microstructure are important to the renewed focus on the fundamentals of soil behavior.

1.1 *Literature Review*

Folaranmi et al. studied the effect of additives namely ashes and sawdust on the thermal conductivity of clay collected from a deposit with no moisture content. For average clay, the thermal conductivity is 0.25 W/m K for no moisture, about 1.0 W/m K for 10% clay moisture (% by volume), 1.25 W/m K at 14%, 1.67 W/m K at 30%, and about 2.0 W/m K at 50% [1]. Tien et al., Chu et al. (2005), Chuang et al. (2005), studied that in the thermal–hydraulic-mechanical environment, the thermal conductivity varies due to the change in clay density, the water content, and the volumetric fraction of sand or crushed granite. The result of thermal conductivity of pure bentonite with different dry density and different water content showed that the thermal conductivity rises while water content increases [2]. Abu-Hamdeh et al. and Reeder et al. (2000) carried out laboratory experiments using the single probe method to determine thermal conductivity. The soils used were classified as sand, sandy loam, loam, and clay loam along with two salts NaCl and $CaCl_2$. Thermal conductivity ranged from 0.58 to 1.94 for sand, from 0.19 to 1.12 for sandy loam, from 0.29 to 0.76 for loam, and from 0.36 to 0.69 W/m K for clay loam at densities from 1.23 to 1.59 g cm^{-3} and water contents from 1.4 to 21.2% [3]. Nusier et al., Abu-Hamdeh et al. (2003) found out the thermal conductivity of two soils investigated through laboratory studies. The soils used were classified as sand and loam. Thermal conductivity measured using single probe method ranged from 0.95 to 2.11 for sand

and from 0.49 to 0.76 W/m K for loam. Thermal conductivity measured using dual probe method ranged from 0.98 to 2.17 for sand and from 0.51 to 0.78 W/m K for loam [4]. Shah et al., Shroff et al. (1993), and Naik et al. (1993) studied the physical, engineering, and electrical properties of different soils that are discussed in this paper. A series of experimental for determination of resistivity, dielectric constants, and unconfined compressive strength of different types of soils (CH, CL, CI, and ML) at various densities and moisture content were performed in the laboratory. From the analysis of experimental results, it is observed that the resistivity value decreases with increases of dry density and moisture content. Resistivity value decreases with increases of unconfined compressive strength [5].

2   Material

The present study was carried out on artificially prepared/mixed soil using naturally available single component soils, i.e., sand, silt, and single mineral clay, to remove heterogeneity due to variation of various minerals in naturally occurring soils. Sand used for the study was collected from Bhadarpur, Gujarat, and washed to free it from any silt and clay content. This was then dried and used for the study further. Silt component for the study was collected from the college campus and sieved to pass through 75 micron sieve, and all organic matter removed. The soil was then put into suspension form to remove the clay content. The single mineral clay, kaolinite, was procured from the commercial market and used directly for the study. The various mix proportions studied are tabulated below in Table 1.

Basic physical and engineering properties for each of the mix were determined as per India Standard specifications. The properties found are: specific gravity, grain size distribution, liquid and plastic limit, maximum dry density (*MDD*), optimum moisture content (*OMC*), and shear strength parameters at 95% *MDD* on the wet side of *OMC* as tabulated in Table 2.

2.1   Thermocouple

Laboratory measurements typically employ a 150 mm long, 10 mm diameter stainless steel thermal heater and a 5 mm diameter, 160 mm long stainless steel thermocouple, which are both electrically isolated from the stainless steel (Shown in Figs. 1 and

Table 1   Mix proportions

Mix	Sand (%)	Silt (%)	Clay (%)
1	60	20	20
2	50	20	30
3	40	20	40

Table 2 Properties of soil

Mix		1	2	3
MDD (g/cc)		1.96	1.88	1.8
OMC (%)		9.4	12.4	15.8
Specific gravity, G_s		2.51	2.68	2.54
Liquid limit, $L.L.$ (%)		27.46	36.3	42.58
Plastic limit, $P.L.$ (%)		15.22	20.28	20.83
Plasticity index, PI (%)		12.24	16.02	21.75
Grain size	% Gravel	0.27	0.5	0.73
	% Sand	60	49.2	40
	% Silt & clay	39.73	49.5	59.27
IS soil classification		CL	CI	CI
Cohesion, C (g/cm^2)		0.1	0.13	0.15
Angle of internal friction		22	20	24

Fig. 1 Heater

2). Stainless steel thermal heater and steel thermocouple are combined to form a new modified thermocouple controlled heater rod as shown in Fig. 3. This new thermocouple is prepared, so that maximum surface area is obtained.

Fig. 2 Thermocouple

Fig. 3 Modified thermocouple controlled heater rod

Fig. 4 Experimental setup

2.2 Thermal Conductivity Measured Radially

The soil is compacted in porcelain pipes having an internal diameter of 20.32 cm (8 inch) with a height of 30 cm, with the soil being filled up to a height of 25 cm only. It is covered with acrylic sheet from bottom. It has thermocouple controlled vertical heater rod placed at the center as source and 20 thermocouples placed radially in four directions perpendicular in plan for temperature profile readings as shown in Fig. 4. The sample is placed in a porcelain pipe container and compacted at density 95% OMC on the wet side. The heat is supplied to the thermocouple till its temperature reaches 70 °C and left for 5 min. Then, the temperature distribution is noted from the 20 thermocouples for an hour.

2.3 Thermal Conductivity Measured Longitudinally

The soil sample is filled in a rectangular stainless steel tank having length 76.2 cm, height 30.48 cm, and width 17.78 cm. This tank is kept in another tank as shown in Fig. 5. Sawdust was spread at the bottom of the steel tank, and all sides are covered with cerra-wool for thermal insulation. The soil is compacted with the fabricated hammer till density 95% of OMC on the wet side achieved required depth (25 cm)

Fig. 5 Steel tank is kept within this tank for insulation

Fig. 6 Experimental setup

which is obtained. The heat source was placed at one end of the tank, whereas 15 thermocouples were placed all along the length and a second row of five thermocouples placed at different depths along the length as shown in Fig. 6. The heat is applied till the temperature of the thermocouple reaches 70 °C and left for 5 min.

3   Results

3.1   Radial Experiment

MIX-1

The graphs plotted below show the temperature variation with respect to time. The minimum temperature reached is 21.61 °C at 0 s, and the maximum temperature obtained is 74.24 °C at 480 s (Fig. 7).
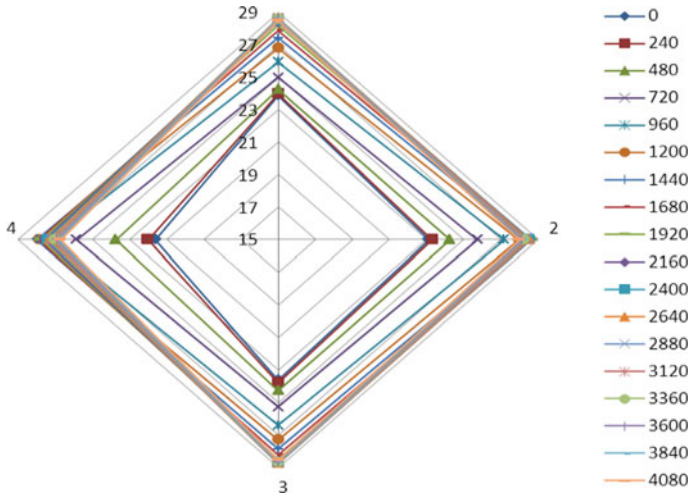
Fig. 7 Temperature versus time (Mix 1)

MIX-2

The graphs plotted below shows the temperature variation with respect to time. The minimum temperature reached is 21.98 °C at 0 s, and the maximum temperature obtained is 81.25 °C at 480 s (Fig. 8).
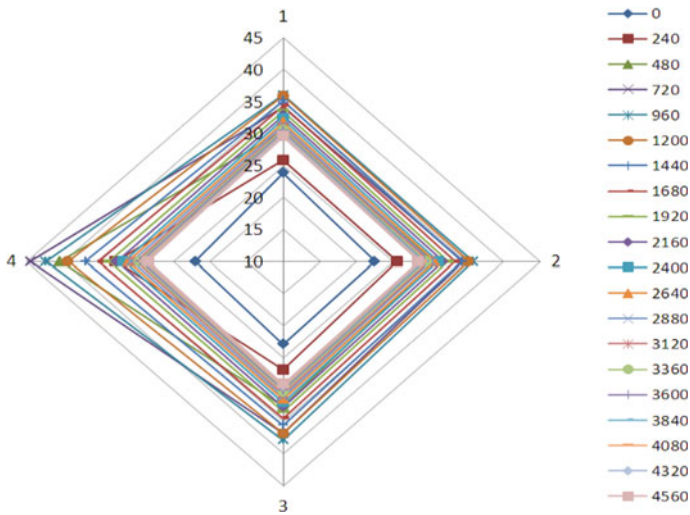
Fig. 8 Temperature versus time (Mix 2)
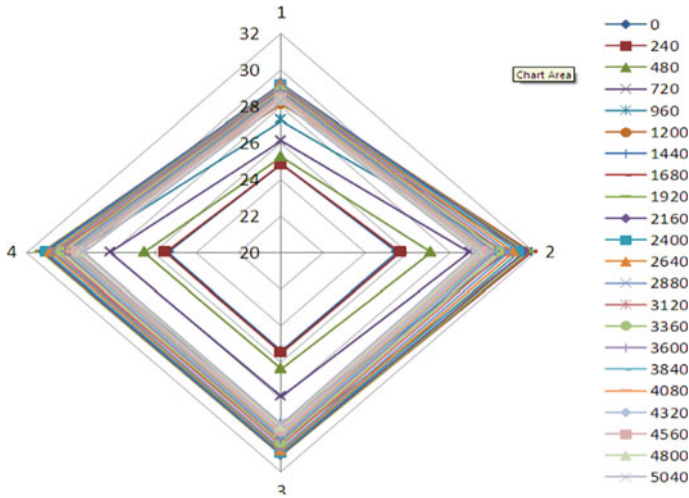
Fig. 9 Temperature versus time (Mix 3)

MIX-3

The graphs plotted below show the temperature variation with respect to time. The minimum temperature reached is 23.2 °C at 0 s, and the maximum temperature obtained is 45.73 °C at 1200 s (Fig. 9).

The coloring lines in the above graphs indicate the temperature variations from the 20 thermocouples placed radially in four directions perpendicular in plan (Fig. 4) with respect to time. From the above graph, it is observed that temperature distribution is almost same in all the directions. When the sand content increases, the thermal conductivity of such soil shall increase with increase in moisture content. The reason for this is that as air is replaced by water (which has thermal conductivity 22 times higher than air) the thermal conductivity of the soil increases as a whole. This same reason is responsible for soils with higher clay content showing higher conductivity with no apparent decrease in the value with time since the clay mineral can hold onto water better as compared to sand which in case the water content increase more than its holding capacity shall readily drain off the water. The results of thermal conductivity of radial arrangement was calculated using Johanson's model [6], as given in Table 3.

$$\rho_w = 1 \quad q = 0.4 \quad \lambda_0 = 2 \quad \lambda_w = 0.59 \quad \lambda_q = 7.7 \quad \lambda_s = 3.43 \tag{1}$$

$$\lambda = \left(\lambda_{\text{sat}} - \lambda_{\text{dry}}\right) K_e + \lambda_{\text{dry}} \quad \lambda_{\text{sat}} = \lambda_s^{1-n} \times \lambda_w^n \quad \lambda_s = \lambda_q^q \times \lambda_0^{1-q} \tag{2}$$

$$n = \frac{1 - \rho_d}{G \rho_w} \quad \lambda_{\text{dry}} = \frac{(0.135 \rho_b + 64.7)}{(2700 - 0.947 \rho_b)} \tag{3}$$

Table 3 Radial method calculation

Mix		1	2	3
ρ_d	g/cc	1.86	1.78	1.71
G		2.51	2.51	2.68
n		0.258	0.332	0.327
w	%	13.6	12.2	15.59
e		0.348	0.498	0.485
S_r	%	98.14	65.7	81.59
Soil	Kg	14.73	13.6	13.53
Water	Ml	2	1.66	2.11
Volume	cu m	0.0079	0.0076	0.0079
ρ_b	kg/cu m	2115.02	2007.37	1976.87
λ_{dry}	W/mK	0.5	0.42	0.4
λsat	W/mK	2.18	1.92	1.93
K_e	W/mK	0.00458	0.00367	0.00494
λ	W/mK	0.51	0.426	0.408

where ρ_d = dry density of soil, G = specific gravity, w = water content, e = void ratio, K_e = Kersten number, λ_{dry} and λ_{sat} = thermal conductivity of dry and saturated soils (Wm^{-1} K^{-1}), respectively, S_r = normalized soil water content ($S_r = \theta/\theta_s$), where θ_s is the saturated water content, λ_w = thermal conductivity of water (Wm^{-1} K^{-1}), n = soil porosity, λ_s = effective thermal conductivity of soil solids (Wm^{-1} K^{-1}), q = quartz content of the total solids content, λ_q = thermal conductivities of quartz (Wm^{-1} K^{-1}), λ_o = thermal conductivities of other minerals (Wm^{-1} K^{-1}), ρ_b = the bulk density of soil (kg m^{-3}), and λ = thermal conductivity of soil from radial test (Wm^{-1} K^{-1}).

3.2 Longitudinal Experiment

The temperature variation with respect to time is then noted for an hour along the length and depth (Figs. 10, 11, 12, 13, 14 and 15).

The variation of the temperature with the increase in the longitudinal distance is plotted. It is observed that at the distance near to the heat source, temperature is more. As the distance increases from the heat source, temperature decreases. Hence, the soil temperature is almost equal to the room temperature as distance increases from the source. Since the present setup could not be used to estimate the change in moisture content with respect to the applied thermal flux, neither the soil water flux measurements could be made. The temperature variation almost remains constant at greater depth. The results of thermal conductivity of longitudinal arrangement was then calculated using Johanson's model [6], as given in Table 4.
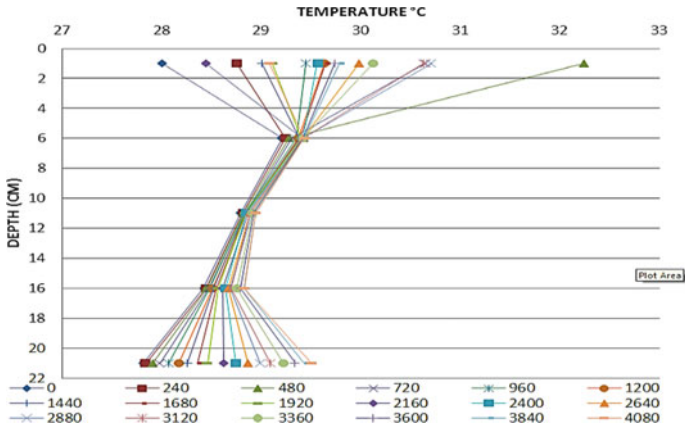
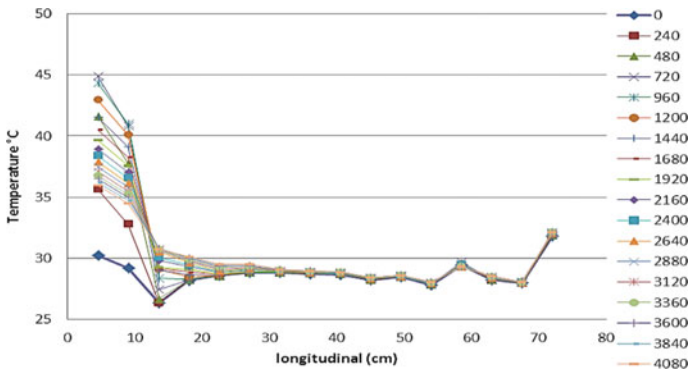**Fig. 10** Temperature versus depth (Mix 1)

Fig. 11 Temperature versus longitudinal distance from heat source (Mix 1)
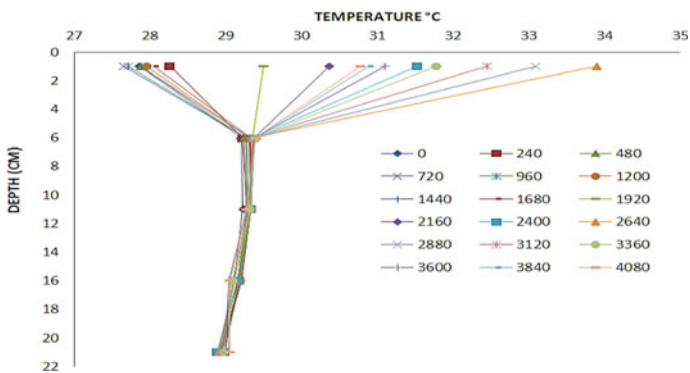
Fig. 12 Temperature versus depth (Mix 2)
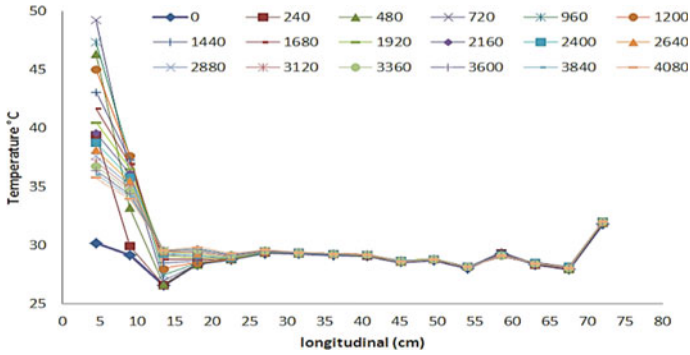
Fig. 13 Temperature versus longitudinal distance from heat source (Mix 2)
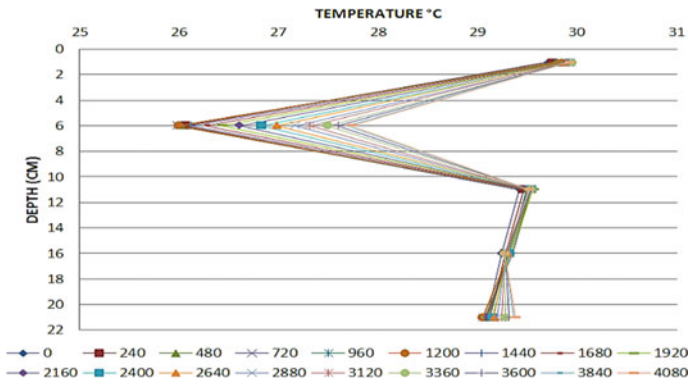
Fig. 14 Temperature versus depth (Mix 3)
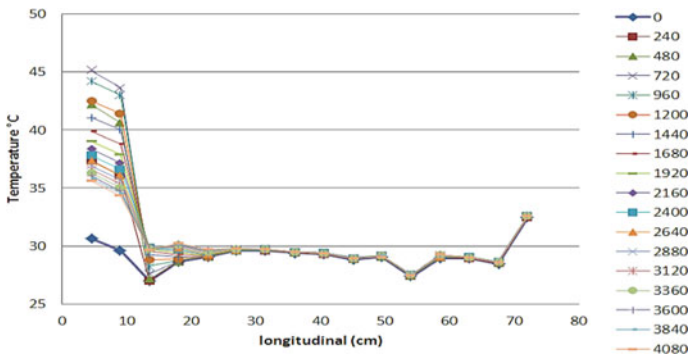
Fig. 15 Temperature versus longitudinal distance from heat source (Mix 3)

Table 4 Longitudinal method calculation

Mix		1	2	3
ρ_d	g/cc	1.86	1.78	1.71
G		2.51	2.68	2.54
λ_0	W/mK	13.6	12.2	15.57
w	%	35	51	49
e		0.26	0.34	0.33
S_r	%	98.17	64.32	80.29
Soil	kg	60.49	58	56
Water	kg	7.38	9.03	9.79
ρ_b	kg/cu m	2003.93	1979.19	1942.66
λ_{dry}	W/mK	0.42	0.4	0.38
λ_{sat}	W/mK	2.18	1.9	1.93
K_e	W/mK	0.00458	0.00367	0.00494
λ	W/mK	0.42	0.4	0.38

Where ρ_d = dry density of soil, G = specific gravity, w = water content, e = void ratio, K_e = Kersten number, λ_{dry} and λ_{sat} = thermal conductivity of dry and saturated soils ($Wm^{-1}\ K^{-1}$), respectively, S_r = normalized soil water content ($S_r = \theta/\theta_s$), where θ_s is the saturated water content, λ_w = thermal conductivity of water ($Wm^{-1}\ K^{-1}$), n = soil porosity, λ_s = effective thermal conductivity of soil solids ($Wm^{-1}\ K^{-1}$), q = quartz content of the total solids content, λ_q = thermal conductivities of quartz ($Wm^{-1}\ K^{-1}$), λ_o = thermal conductivities of other minerals ($Wm^{-1}\ K^{-1}$), ρ_b = the bulk density of soil ($kg\ m^{-3}$), and λ = thermal conductivity of soil from longitudinal test ($Wm^{-1}\ K^{-1}$)

$$\rho_w = 1 \quad q = 2 \quad n = 0.4 \quad \lambda_w = 0.59 \quad \lambda_q = 7.7 \quad \lambda_s = 3.43 \tag{4}$$

$$\text{Volume} = 0.03387 \text{ cu m} \tag{5}$$

$$\lambda = \left(\lambda_{sat} - \lambda_{dry}\right) K_e + \lambda_{dry} \quad \lambda_{sat} = \lambda_s^{1-n} \times \lambda_w^n \quad \lambda_s = \lambda_q^q \times \lambda_0^{1-q} \tag{6}$$

$$n = \frac{1 - \rho_d}{G\rho_w} \quad \lambda_{dry} = \frac{(0.135\rho_b + 64.7)}{(2700 - 0.947\rho_b)} \tag{7}$$
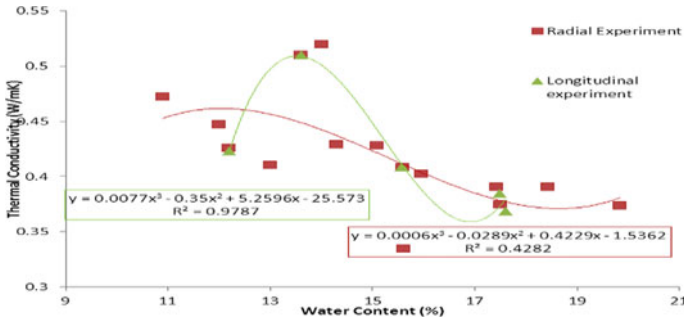
Fig. 16 Water content versus thermal conductivity
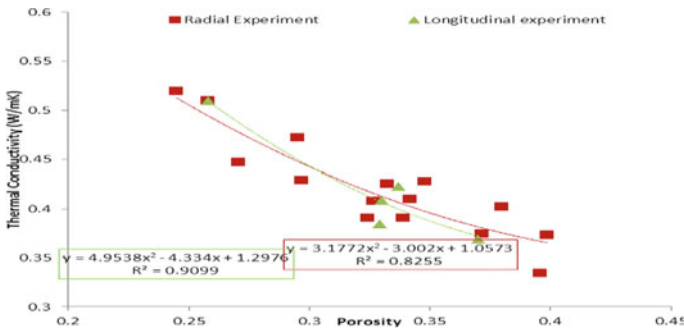
Fig. 17 Porosity versus thermal conductivity

3.3 *Effect of Soil Properties on Thermal Conductivity*

The influence of soil properties such as saturation, water content, density, porosity, and void ratio on thermal conductivity is plotted for radial and longitudinal experiments (Figs. 16, 17 and 18).

4 Conclusion

The plot for thermal conductivity with respect to water content concludes that the plot has three stages with respect to moisture content. The first stage can be stage from the point of zero moisture to the point when the moisture content is just below the critical moisture content, the second stage from this critical stage to the point when the thermal conductivity shows no change in the value with increase in the moisture content and thereafter the third stage which has the thermal conductivity approximately constant with increase in moisture content. During the stage two which is principally the stage under study for the present work, a continuous water layer
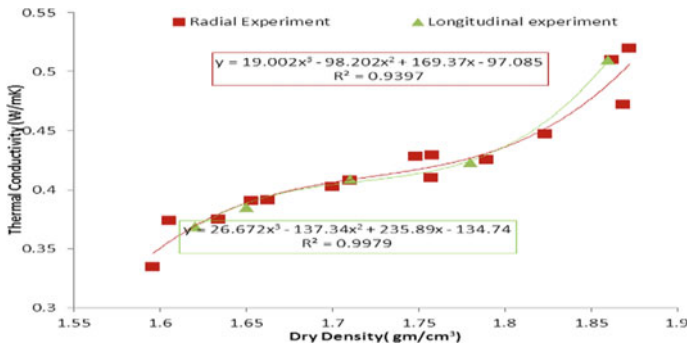
Fig. 18 Dry density versus thermal conductivity

is provided, and all the soil grains are coupled with water. It can be noted that as the percentage of fines in the soil increases, the critical moisture content shall also increase in the case. This can be attributed to increase in the total particle surface area as the amount of fines increase require more water to form a film around each of the particles. Same is the case with the radial experiments; the water starts to move toward the outer edge of the soil with increase in temperature as well as there is evaporation of the water from the surface which has not been taken into considerations. This in turn leads to cooling of the soil due to formation of vapor, since water is now free to move in both its liquid and vapor phase. The plot of dry density shows that as the density increases the thermal conductivity increases since increasing the density increase the number of particles per unit volume thereby increasing the point contact and decreasing the air volume resulting in better heat transfer. The trend followed in plot of porosity with thermal conductivity is a peculiar in nature and does not fall into any category for curve fitting as visible from the R2 values of the plot.

References

1. Folranmi, J.: Effect of Additives on the Thermal Conductivity of Clay (2009)
2. Tien, Y.M., Wu, P.L., Chuang, W.S., Wu, L.H.: Micromechanical Model for Compaction Characteristics of Bentonite-Sand Mixtures. Appl. Clay Sci. **26**, 489–498 (2004)
3. Abu-Hamdeh, N.H., Reeder, R.C.: Soil thermal conductivity: effects of density, moisture, salt concentration and organic matter. Soil Sci. Soc. Am. J. **64**(4), 1203–1548 (2000)
4. Nusier, O.K., Abu-Hamdeh, N.H.: Laboratory techniques to evaluate thermal conductivity for some soils. Heat Mass Transf. **39**(2), 119–123 (2003)
5. Shah D.L., Shroff A.V., Naik, D.N.: Correlation of physical properties of clayey soils and electrical resistivity (1993)
6. Johansen, O.: Thermal conductivity of soils. Ph.D. thesis, Trondheim, Norway, ADA 044002 (1975)

Electrical Resistivity Tomography in Geotechnical Engineering Applications

Deepak Sagar, S. B. Dwivedi, and Prabir K. Basudhar

Abstract Characterization of subsurface soil is essential for foundation design of important civil engineering structures. In conventional geotechnical investigation, the soil profiling and their characterization are done by collecting samples from the field either through open pit sampling or through boring and then performing laboratory test for their classification and determination of strength and compressibility characteristics. In-situ methods like standard penetration test (SPT), cone penetration test, e.g., static (SCPT) and dynamic (DCPT), pressure meter test (PMT), and dilatometer test (DMT) are also available. But these methods are time consuming and costly. If vast tracts are to be investigated for preliminary exploration, then geophysical methods can aid to collect information about the subsoil conditions. Geophysical methods allow to measure physical properties like electrical resistivity, seismic wave velocity, electrical permittivity, magnetic intensity, etc. These observations can be used for surveying large tracts or ancient structures composed of dissimilar materials. Apart from these, some problems that vex the civil engineers is significant increase in the permeability of desiccated soils due to cracks in these soils due to shrinkage. Such a situation may lead to the progressive failure in flood embankments. Geophysical methods have great potential to aid archeological investigation in identifying archeological features in unexcavated areas. Electrical resistivity tomography (ERT) is very commonly applied in such studies because of its adaptability in identifying walls, cavities, etc., at different depths. The paper pertains to the potential of application of ERT in geotechnical and archeological investigation providing an overview and its use in subsoil profiling and detection of foundation details of old structures. The power of the method in identifying the hidden features of buried objects and subsurface profiling has been demonstrated with examples.

D. Sagar (✉) · S. B. Dwivedi · P. K. Basudhar
Civil Engineering Department, IIT(BHU) Varanasi, Varanasi 221005, UP, India
e-mail: deepaksagar.civ17@itbhu.ac.in

S. B. Dwivedi
e-mail: sbd.civ@itbhu.ac.in

P. K. Basudhar
e-mail: pkbd.civ@itbhu.ac.in

1 Introduction

For successful design and construction of civil engineering infrastructures, it is essential to undertake geotechnical investigation to find out the nature, extent, and engineering properties of soils at the site. Such investigations are generally done by digging boreholes at different location at the site extending the same up to the desired depths for collection of soil sample from different depths. The various methods for extending such boreholes are use or trial pits, shafts and headings, percussion boring, mechanical augers, hand portable augers, wash borings, and rotary drilling. Position of the ground water table is also determined during the boring process. The collected soil samples can be divided into two main categories, undisturbed and disturbed. Undisturbed samples are required mainly for shear strength and compressibility characteristics, which are obtained by using techniques preserving the in-situ soil-structures and moisture content of the soil. On the other hand, disturbed sample are used for classification purpose only.

Alternatively in-situ tests for geotechnical investigation have also been devised. Commonly used techniques are as follow:

- Plate load test
- Standard penetration test
- Dynamic cone penetration test
- Static cone penetration test
- Pressure meter test
- Dilatometer test.

Each of the above tests has their merits and demerits. However, standard penetration test is most widely used all over the world. Specific correlations have been developed for each of these methods by several investigators to interpret and use the observed data for classifying in the soil strata and engineering properties. Conducting these test at the site needs lot of planning, time, and money. Some time, it become very large with respective to the total budget of the project.

In order to circumvent such difficulties, development of alternative methods is required.

'In 1912, Conrad Schlumberger conducted the first geo-electrical resistivity experiment in the fields of Normandy. Around 1915, a similar idea was developed by Frank Wenner in the United State of America [1]. The classical methods of geo-electrical resistivity surveys have undergone significant changes in the last four decades. Data acquisition was more or less carried out manually till the 1980s, which is labor intensive and slow, and the quality of the measured data might be of poor quality. Initially, multi-electrode systems with manual switching [2] were used before the emergence of computer-controlled multi-electrode systems with automatic measurements and

data quality control, which has tremendous impact on the quality of the data and the speed with which they are collected. When adequate computers became widely available, the inverse problem of ERT could be solved numerically, and the work of Loke and lane [3] at Birmingham University was among the first such solution, and their approach is still widely used.'

Recently geo-electrical resistivity survey in the area of archeology and geotechnical engineering has been reported, Abu-Zeid [7]**,** Ganiyu [4]. They have done investigation of soil moisture content over a cultivated farmland in Abeokuta Nigeria using electrical resistivity methods and soil analysis. Constantin et al. [5], Zhou et al. [6], Abu-Zeid et al. [7], Sudha et al. [9] used ERT in subsurface soil characterization. They correlated soil resistivity with standard penetration test resistance number. This study opens the avenue to estimate bearing capacity of foundations. Thus, determination of soil strength from ERT results can be very effective.

In India, application of these methods are in initial stage, and not much expertise is available; therefore, an initiative of undertaking research in the area is warranted. The main aim of this paper is to present a case study for characterization of the subsurface soil through application of ERT.

1.1 Brief Review of Available Geophysical Exploration Techniques

Different geophysical exploration methods like seismic reflection and refraction technique, electrical resistivity method, magneto telluric method, etc., are available of geophysical perspective; however, these methods are used in different fields cutting across in various disciplines in science and engineering.

Advantages of these methods are exploration which can be covered in wider area in lesser time and expense, and these techniques are non-invasive.

The imaging of the soil lying below the ground surface is based on the collection of data pertinent to the methodology used. The anomaly like presence of ground water, soil stratification, presence of rock, faults, joints and fissures, and their extent can be interpreted easily from their tomographic imaging. In this respect, geophysical exploration techniques score over the geotechnical techniques in site investigation procedures is described above. But it should be noted that these methods give approximate idea about the subsurface conditions. However, adoption of such procedures help the civil engineers in taking quick decision for site selection and planning the next stage of geotechnical investigation, saving plenty of money, time, and energy.

Seismic methods: These methods are based on the principles that elastic shock waves moves at different velocities in different materials. At the interface of the two different strata of different materials, the elastic stress waves are partly reflected and partly refracted. There are two types of body waves namely the compression waves (P-waves) and shear waves (S-waves). In the compression waves, the direction of the movements of the particles coincides with the direction of propagation. The shear

Table 1 Speed of velocity in different type of rock and soil

Types of rock/ soil	Granite	Sand stone	Shale	Hard clay	Loose gravel (wet)	Loose sand (wet)	Loose sand (dry)
Velocity (m/s)	4000-6000	1500–3000	1300–3000	600–1500	500–1000	500–1500	250–600

waves can be separated into two components: (1) SV-waves in which the motion of particles is in the plane of propagation and (2) SH-waves where in the motions of the particles is perpendicular to the plane of propagation. If a P-wave impinges on the boundary between two layers, there will be two reflected waves and two refracted waves. These waves follow certain laws. These are available in standard text books (Das and Ramana 2011; Kolsky 1963).

This method can be adopted by using a single geophone and producing a series of detonations or impacts at increasing distance from geophone. Then, arrival time is plotted against the distance between the source and the geophone. From this plot, the velocities of the direct wave and the refracted wave can be estimated. The general types of soil and rock can be determined from knowledge of these velocities. Typical values are as in Table 1.

Magneto telluric (MT) Method: It refers to a technique in which electrical resistivity is determined by making measurements of electric and magnetic fields related to naturally occurring currents ("telluric", caused mostly by lightning strikes) flowing in the ground. The MT theory, along with appropriate data inversion procedures, allows the determination of the resistivity distribution in the subsurface, on depth scale ranging from a few tens of meters to hundreds of kilometers. Magnetic data can also collect aerially using either a light helicopter or aeroplane by magnetometer mounted on it.

Gravimetric Method: It is a potential field technique which measures variations in the earth's gravitational field. These variations are caused by density contrasts in the near surface rock and sediment. Gravimetric surveys are carried out using extremely sensitive instruments capable of measuring tiny variations in the gravitational field. Instruments for measuring gravity are called gravity meters or gravimeters.

Electrical resistivity tomography (ERT): It is one of the most important geophysical tool for imaging the shallow subsurface soil and for characterization of soil for making the soil profile. Electrical resistivity method is also one of the methods mostly used in archeological geophysics, as well as in engineering geological investigations. Its other applications are characterizing subsurface hydrogeology, determining depth of bedrock/overburden thickness, determining depth of groundwater, mapping stratigraphy, mapping clay aquitards, mapping salt-water intrusion, mapping vertical extent of certain types of soil and groundwater contamination, and estimating landfill thickness. With the help of software (like RES2DINV and RES3DINV), we can create 1D, 2D, and 3D image of the anomaly. Among all the methods as described

above, electrical resistivity is simplest of all the method as described and easy to perform.

The method depends on differences in electrical resistance of different soils and rock types. The flow of current through soil is primarily due to electrolytic action and therefore depends on concentration of dissolved salts in pore water: The mineral particles of a soil are poor conductors of current. The resistivity of soil therefore decreases with increasing water content and concentration of salt. Dense sands above the water table would show high value of resistivity due to low degree of saturation and lack of the presence of dissolved salts. Saturated clay having high void ratio would exhibit low value of resistivity due to relative abundance of pore water and free ions in the pore water. For ERT, four electrodes are arranged in a manner in which direct current (DC) or low-frequency alternating current (AC) of known magnitude introduce in ground using a pair of current electrode at one point and measure the potential deference at potential electrode in terms of resistivity (ohm). After calculating the apparent resistivity (ohm-m) and comparing the apparent resistivity of soil with the standard resistivity of soil, we can characterize the soil. Different types of soil composition have different resistivity value, so that it is easy to characterize the soil at different location under the ground surface. Typical values of resistivity of different types of soils/rocks are as follows:

Apparent resistivity represents the weighted average of true resistivity in a large volume of soil, the close to the surface being more heavily weighted than the soil at depth. Presence of a stratum of oil of high resistivity lying below a stratum of low resistivity forces the current to flow closer to the surface, resulting in higher values of apparent resistivity. The opposite is true if a stratum of low resistivity lies below a stratum of high resistivity.

Electrical resistivity tomography (ERT) is one of the most commonly applied techniques of geophysical surveying. The purpose of electrical surveys is to determine the subsurface resistivity distribution by making measurements on the ground surface. From these measurements, the true resistivity of the subsurface can be estimated [8]. The aim of ERT is to scan the subsurface along the survey line using a selected array.

2 Soil Characterization

2.1 Experimental Procedure

For lateral and vertical profiling of soil using resistivity technique, resistance (ohm) is calculated in the field using any of the Wenner method, Fig. 5, and Schlumberger method, Fig. 6, using instrument SSR MP-1. In these methods, four electrodes are used in which inner electrodes are potential electrodes and outer electrodes are current electrodes. Direct current (DC) is applied at the current electrodes, and potential difference is measured at potential electrodes. Difference between Wenner
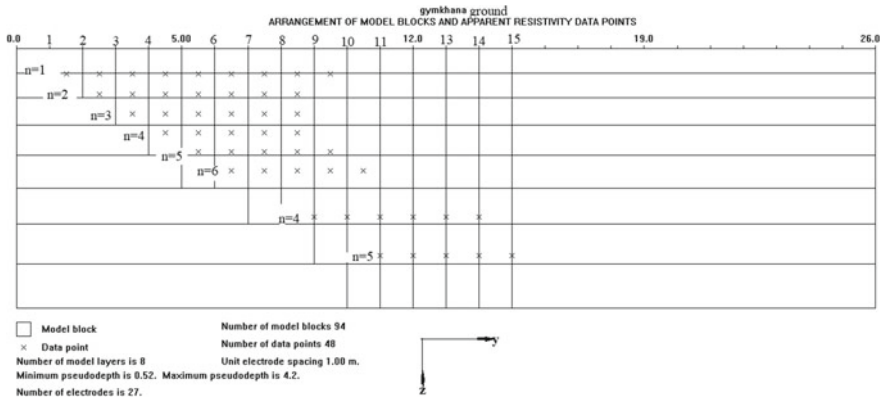
Fig. 1 Model block and apparent resistivity data point

and Schlumberger method is only about spacing between the electrodes. In Wenner method, the electrodes are equally spaced, but in Schlumberger method, spacing between the current electrodes is three times the spacing between the potential electrodes.

In Fig. 1, a schematic diagram of the arrangement of the model blocks and apparent resistivity data points is shown. The data points are designated as x, and its spatial locations in a two-dimensional Cartesian frame of reference (designated as x and y) are also shown in this figure. Layers are numbered as 0, 1, 2,…..as shown.

For measuring resistance for layer 1, the spacing is maintained as 1 m between all the electrodes taking '0' as the reference. It means that the current electrode is placed at 0 and 3 and putting the potential electrode at 1 and 2. After measuring the resistance at that location, all the four electrodes are moved by 1 m in the y-direction increasing the value of n by 1 unit up to the layer 6. For layer 7 and 8, the spacing between potential electrodes are kept as 2 m along with n value 4 and 5. Following the above procedure, resistance is measured at all the data points.

A location was chosen near the Gymkhana ground, IIT (BHU), and its coordinates were obtained with the help of a GPS. Remotely sensed photograph of the site with the marked point is shown in Fig. 2. Figure 3 shows the soil profile with the apparent resistivity inversion obtained using RES2DINV software. It extends up to 15 m in y-direction and 4.88 m in z-direction. From the diagram, it is seen that the measured resistivity of soil at the site lies in the range of 50–210 Ω-m, comparing the values with the standard resistivity of soil (Table 2), and the soil extending over the zone is identified as clayey sand. But for the soil lying between 3.96 and 4.88 m depth, they have high resistivity values ranging from 490–750 Ω-m, and comparing these values with standard values, it is inferred that soil type should be silty sand with the possibility of the presence of some gravel packet within the strata.

Fig. 2   Location of resistivity data point (coordinate: 25.259581, 82.988533)
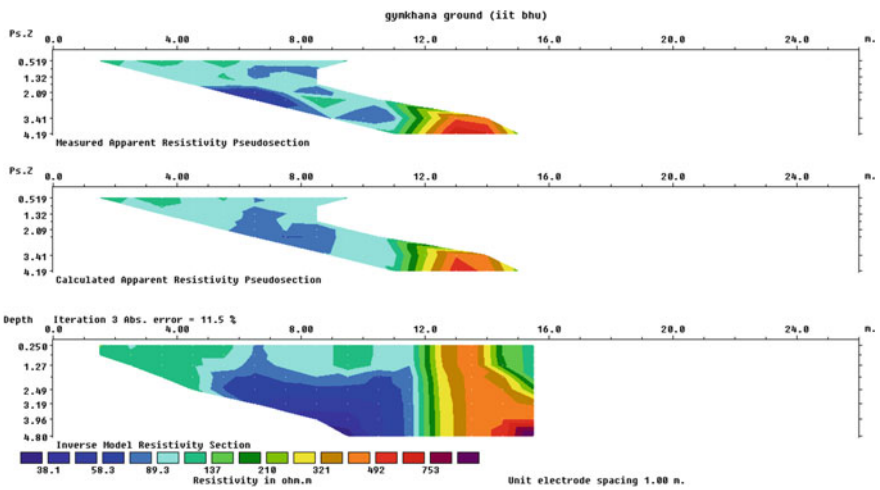
Fig. 3   Soil profile apparent resistivity inversion

Table 2   Resistivity of different type of soil and rock

Type of rock/soil	Sound rock	Weathered rock	Gravel	Sand	Clayey sand	Saturated clay and silt
Resistivity (ohm-m)	> 5000	1500–2500	1500–4500	500–1500	200–500	2–100

2.2 Observation Made and Interpretation of Data

To verify whether the inferred soil profile from the measured resistivity data is correct or not, grain size classification was made conducting sieve analysis following Indian Bureau of Standards in geotechnical engineering laboratory at IIT BHU, Varanasi.

Soil samples from an arbitrary depth 1 m were collected, and the test was conducted taking 1 kg of soil. The sieve test results are presented in Table 3.

Grain size classification of the collected soil sample as specified by Indian standard soil classification system (ISSCS) as presented in Table 4 has been made, and the type of soil as obtained from the test is included under the remark column of Table 3. Thus, the different constituents of the soil at the depth of 1 m are:

Sand: Coarse: 22.2%, Medium: 54.1%, Fine: 18.3%

Silt and clay: 4%

From the curve (Fig. 4), D10, D30, and D60 can be calculated; these values are:

D10 = 0.16954, D30 = 0.6411, D60 = 1.4457.

$C_u = \frac{D_{60}}{D_{10}}$, and the value is 8.5271.

$C_C = \frac{D_{30}^2}{D_{60*}D_{10}}$, and the value is 1.6768.

Table 3 Sieve test results

Sieve size	Wight retained (gram)	% weight retained	Remark
2 mm	222	22.2	Well graded sand
1 mm	311	31.1	
475 μ	230	23	
250 μ	89	8.9	
150 μ	44	4.4	
75 μ	50	5	
pan	40	4	Mixture of silt and clay

Table 4 Classification of soil as per Indian Standard (ISSCS)

Very coarse soil	Boulder size		>300 mm
	Cobble size		80–300 mm
Coarse soil	Gravel	Coarse	20–80 mm
		Fine	4.75–20 mm
	Sand	Coarse	2–4.75 mm
		Medium	0.425–2 mm
		Fine	0.075–0.425 mm
Fine soil	Silt		0.0002–0.075 mm
	Clay		<0.002 mm
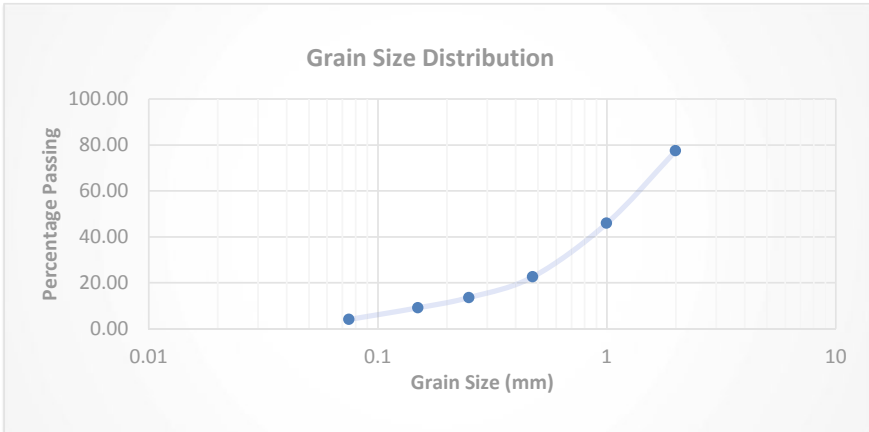
Fig. 4 Grain size distribution curve
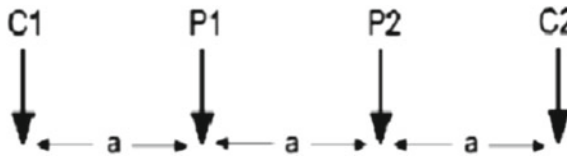
Fig. 5 Wenner array arrangement

Fig. 6 Schlumberger array arrangement

From the result analysis, it can be seen that the soil is SW (well graded sand) according to Indian standard soil classification system, and for SW, C_u should be greater than 6 and C_C should be between 1 and 6.

The soil as classified at that depth from electrical resistivity technique (ERT} is clayey sand. As per ISSCS classification, the soil passing through 75 μ sieve is fine grained and is classified either as silt and clay depending on its plasticity value, which is not possible from ERT test. Thus, the prediction as made by ERT is fairly close to the classification based on direct measurement.

Thus, it can be concluded that the predictions are close to the nature of soil at the ground. Similarly, soils from different depths are collected and categorized, and the predicted soil variation with depth is found to be fairly accurate.

Following the above procedure, the following cases were also taken up: determination of the extent of the foundation of a wall, foundation depth of the Rajputana

hostel (which is about 100 years old), extent of root zone of a tree, and finally, determination of the depth of the ground water table. All these are significance from civil engineering profession. As investigating foundations of ancient structures involves time, money, and elaborate procedure for getting permission to do so, even though it was the initial objective of the paper, instead of a very ancient structure investigation were carried out to explore the extent of a structure more than 100 years old with remarkable success. The method can be easily extended to ancient structure. However, these studies have not been reported here for reasons of space and brevity.

3 Conclusion

The characterization of the subsurface soil has been carried out in IIT BHU campus, India with application of electrical resistivity method. The resistivity value is correlated with the sieve analysis and grain size distribution result obtained in geotechnical laboratory, IIT BHU. The calculated value of $C_u = 8.5271$ and $C_c = 1.6768$ of the soil from the study area in the laboratory is similar to the field result through ERT. It is also concluded that the Schlumberger array arrangement gives good result for deep soil body as compared to the Wenner array arrangement. For getting the high accuracy in ERT, it is required to take minimum electrode spacing. In other problems like the extent of foundation of an wall and 100-year-old structure, determination of the extent of root zone of a tree having direct bearing on studying the foundations of ancient structure has also been applied successfully. For reasons of space and brevity, these are not presented here.

References

1. Kunetz, G.: Principles of Direct Current Resistivity Prospecting, p. 103. GebruderBorntraeger, Berlin (1966)
2. Barker, R.D.: The offset system of electrical resistivity sounding and its use with multicore cable. Geophys. Prosp. **29**, 128–143 (1981)
3. Loke, M.H., Lane, J.W.: Inversion of data from electrical imaging surveys in water-covered areas. In: ASEG, 17th Geophysical Conference and Exhibition, Sydney (2004)
4. Ganiyu, S.A., Olurin, O.T., ladunjoye, M.A., Badmus, B.S.: Investigation of soil moisture content over a cultivated farmland in Abeokuta Nigeria using Electrical Resistivity Methods and Soil Analysis (2006)
5. Constantin, P., Kurosch, T. Michaet, K., Reinhand, S.: Testing the effectiveness of an inverse Wenner-Schlumberger array for geoelectrical Karst void reconnaissance on the SwabianAlb high plain. New Line Wendlingen –Ulm, Southwestern Germany, Engineering Geology (2018)

6. Zhou, W., Beck, B.F., Adams, A.L.: Effective electrode array in mapping karst hazards in electrical resistivity tomography. Environ. Geol. **42**, 922–928 (2002)
7. Abu-Zeid, N., Botteon, D., Cocco, G., Santarato: Non-Invasive Characterization of Ancient Foundations in Venice Using the Electrical Resistivity Imaging Technique, NDT&E International 39, pp. 67–75 (2006)
8. Loke,M.H.: Tutorial: 2-D and 3-D electrical imaging surveys Copyright (1996–2004)
9. Sudha, K., Israil, M., Mittal, S., Rai, S.: Soil Characterization using electrical resistivity tomography and geotechnical investigation. J. Appl. Geophys., 76–79 (2009)

Analysis of Physical Modeling of Cast-In-Situ Concrete Piled Raft

J. M. Raut, S. R. Khadeshwar, and S. P. Bajad

Abstract Nowadays, there is competition for constructing high rise buildings, and the reason may be due to decreasing availability of land due rapid industrialization and urbanization. This has increased heavy load, complicated stress conditions, and having limitation of bearing capacity of soil. This results in settlement of high rise buildings. This leads to use of piled raft foundation. But the load-bearing capacity of piles is not considered, they are used as settlement reducers only, and load is carried by raft only. In another design method, axial capacity of the piles to carry the structural load and bearing capacity of raft is neglected. In both the design approach, piled raft foundation becomes uneconomical. Now research is going on for considering the load-bearing capacity of both pile and raft and developing detail analysis. In a pile raft foundation, pile-soil-raft interaction is complicated. Although several numerical studies have been carried out to analyze the behaviors of piled raft foundations, very few experimental studies are reported in the literature. The available laboratory studies mainly focus on piles made with steel or aluminum. The present study aims to study the behaviors of piled raft foundation, in the laboratory using physical model. The physical model is made up of cast-in-place reinforced concrete piles, and reinforced concrete raft are used for the tests. The test is conducted on single pile, pile group, un-piled raft, free-standing pile group, and piled raft foundation. We examine the effects of numbers of piles, the interaction between different components of foundation, and load-sharing ratio of pile and raft. The results indicate that the ultimate bearing capacity of the pile raft foundation is considerably higher than that of free-standing pile group with same number of piles.

Keywords Pile · Piled raft · Raft · Model

J. M. Raut (✉) · S. R. Khadeshwar
Department of Civil Engineering, Yeshwantrao Chavan College of Engineering, Wanadongari, Nagpur 441110, India
e-mail: jmrv100@gmail.com

S. P. Bajad
Dy. Secretary RBT, Pune, Maharashtra, India
e-mail: spbajad@gmail.com

1 Introduction

A piled raft foundation is not new approach and described by several authors including Zeevaert [1], Davis and Poulos [2], Hooper [3]. Piles as settlement reducers have been discussed in past [4] in raft foundation. The structures based on the piled raft structures are also reported in the literature [5]. The piled raft is a foundation which acts as a composite structure consisting of three load-bearing elements: piles, raft, and subsoil [6]. Piled raft foundations are treated as combined foundations on raft and pile groups. It is getting well known as one of the most economical foundations among engineers. But still very few structures are constructed over this foundation. The reason for this may be partly because design code for piled raft foundations has not been established. The use of pile raft foundation is an effective way of minimizing both total differential settlements, of improving the bearing capacity of a shallow foundation and of reducing in an economic way the internal stress levels and bearing moments within a raft. The concept of pile raft combines the load-bearing elements of piles, raft, and soil in a composite structure. The behavior of pied rafts is determined by complex soil structure interaction effects. There are no definite design strategies or standards available for reliable design and analysis of piled raft foundation. Although several numerical studies have been carried out to analyze the behaviors of piled raft foundations [6–10], very few experimental studies are reported in the literature. The available laboratory studies mainly focus on piles made with steel or aluminum. But in field, the piled raft is made up of concrete. So to stimulate the field situation, concrete is used for piled raft foundation. The present study aims to study the behaviors of piled raft foundation, in the laboratory using physical model. The physical model is made up of cast-in-place reinforced concrete piles, and reinforced concrete raft are used for the tests. Piled raft foundations utilize piled support for control of settlements with piles providing most of the stiffness at serviceability loads, and the raft element providing additional capacity at ultimate loading. Consequently, it is generally possible to reduce the required number of piles when the raft provides this additional capacity. In addition, the raft can provide redundancy to the piles, for example, if there are one or more defective or weaker piles, or if some of the piles encounter drastic conditions in the subsoil. Under such circumstances, the presence of the raft allows some measure of re-distribution of the load from the affected piles to those that are not affected and thus reduces the potential influence of pile "weakness" on the foundation performance. Another feature of piled rafts, and one that is rarely if ever allowed for, is that the pressure applied from the raft on to the soil can increase the lateral stress between the underlying piles and the soil, and thus can increase the ultimate load capacity of a pile as compared to free-standing piles.

Fig. 1 Actual test setup

2 Equipment and Test Set Up

2.1 Loading Frame

All tests were carried out in the specially fabricated loading frame of cubical size as shown in Fig. 1. The loading frame that consists of beam and column was fabricated by using box section of 60 mm × 60 mm. The loading frame is made up of steel box of size 60 mm × 60 mm and 1500 mm length. Bottom frame and top frame are made of four box sections of size 1500 mm. These top and bottom frame were connected by four boxes each at each corner of the frame at top and bottom. So, there was a formation of cubical shape frame.

2.2 Soil Tank

For placing soil, cubical specimen box of size 1500 mm × 1500 mm × 700 mm was made up and open in upper side. The box is made up of mild steel sheet of 2 mm thick at bottom of loading frame of depth 700 mm. Soil tank was sufficiently larger than the zone of influence to avoid edge effect.

2.3   *Loading Arrangement*

Loading was done with the help of mechanical screw jack of capacity 25 kN. Loading was measured with the help of S-type load cell of capacity 25 kN. The displacement was measured with the help of LVDT at corner of the foundation. The loading cell and the LVDT's are connected to the electronic display, so that we can take the reading comfortably. The setup was fabricated and kept at geotechnical laboratory. Mechanical screw jack is used for applying the loading to the model piled raft foundation. The mechanical screw jack is manually operated and easy to handle. The s-shaped load cell is attached below the mechanical screw jack for measuring the load applied.

2.4   *Model Piles*

In this laboratory model test cast, cast-in-place board concrete piles are used. All these testing are done under equal conditions in order to investigate the behaviors of pile raft foundation. The main important aspect is to find the load sharing ratio of raft. The model piles used in the tests are concrete piles with a reinforcement of 3 mm diameter mild steel, and the pile length was 50 cm. And the thickness of the concrete raft was 40 mm, so that the raft could behave as a rigid foundation. Generally, the contact pressure of the raft, stress, and settlement of the pile depends on the relative stiffness of the components. Concrete piles of uniform circular section of 25 mm diameter, and length of 400 mm, 500 mm, and 600 was used in the present investigation. To know the effect of change in material, piles are made by RCC of M35 grad and using reinforcement of 3 mm diameter. The arrangement is shown in Fig. 1.

2.5   *Model Raft (Pile Cap)*

The size of the raft is 400 mm × 400 mm which was used in model tests. The size and thickness of the raft are kept constant. The thickness of the raft was chosen 40 mm (rigid raft). The raft is made up of concrete material raft made by RCC of M35 grad and using reinforcement of 3 mm diameter as shown in Fig. 1.

2.6   *LVDT and Dial Gauge*

To measure settlement, two linear variable displacement transducers (LVDT) having 50 mm range with 0.01 mm sensitivity are used. They were placed at edges of the raft.

Table 1 Soil properties

S. No.	Soil properties	Results
1	Water content	16.51%
2	Specific gravity (G)	2.32
3	Particle size distribution	CH
4	Plastic limit	23%
5	Liquid limit	54%
6	Shrinkage limit	12.87%
7	Optimum moisture content	16.51
8	Permeability	8.11×10^{-4} cm/s

2.7 Electronic Display

Electronic display is required for the recording of the readings of load applied and the corresponding settlement. The digital electronic display is attached to the loading frame. One direct connection is done from load cell to the electronic display to read the load applied to the foundation. Another connection is done from LVDT to electronic display to record the settlement of the foundation.

2.8 Foundation Soil

The soil is collected from the site 40 km away from the geotechnical laboratory near village Kamptee site is shown in Fig. 1 of clay type. Tests mentioned in Table 1 are conducted to determine the properties of soil, and results are tabulated as in Table 1.

2.9 Soil Bed Preparation

The technique of artificial consolidation of soft clay plays an important role in the process of achieving reproducible shear strength. The reliability of results would depend upon the uniformity of the foundation medium. With this consideration, the soil was prepared in the laboratory to get similar shear strength and other properties of soil as follows.

Firstly, large lumps of oven-dried clay were broken, and water was added. Water and soil were thoroughly mixed till the water content of the soil was nearly 55% to ensure complete saturation and hand shaken to eliminate air voids. Then, the soil was placed in the mild steel bin (tank) in three layers, each being 150–200 mm in height and consolidated under the consolidation pressure. After placing the soil into the tank, a 50 mm layer uniformly graded sand was placed on the top of the soil layer to serve as a pervious base for reducing the consolidation time. Between the sand and

clay layer, a layer of jute was placed to prevent intermixing. Subsequently, covering the entire area of the test tank, a 5-mm-thick perforated plate was placed on top of the sand layer. In order to reach the specified consolidation pressure, a high stack of dead weights was required to be placed over the clay layer. Consolidation period for the first two layers was set as 48 h (2 days) for each layer, and for the third layer, it was set to 1 day. Un-drained shear strength of the consolidated clay as measured by vane shear/unconfined compression test was found to be $8\pm$ kPa. The optimum water content is maintained throughout test.

3   Load Settlement Behavior Test Procedure

Depending on the number of piles in a group and center-to-center spacing between piles, different pile configurations were identified. Consequently, following the consolidation of the clay bed, model piles of specified lengths were casted in the consolidated clay bed. Next, the model raft was placed over the piles. Finally, the horizontal alignment of the raft was checked using a sprit level. It was ensured that while performing tests on piled raft and individual raft, there was a full contact between the soil layer and the raft.

After the model setup is ready, the lever was placed over the piled raft for applying the load. To measure settlement, two linear variable displacement transducers (LVDTs) having a 50 mm range with 0.01 mm sensitivity were used. They were placed diagonally opposite on the model raft to get average settlement at the center of the raft. For determining the immediate settlement, loads were applied in gradual increment, and settlement was recorded till there was no appreciable change in settlement for a particular load increment. Then, the next load increment was applied. The tests were continued until the settlement was more than 10% of width of corresponding raft.

The working load were calculated by applying a factor of safety (F.S.) 2.5 and 1.5 to the ultimate load-carrying capacity of the corresponding un-piled raft. The ultimate load-carrying capacity was determined from the load settlement cure at an immediate settlement of 10% of B (width of raft) as suggested by Cooke [11]. These findings have been recently confirmed by centrifuge tests, as well as field tests [12]. This dependent settlement behavior for a period of 48 h, thereafter settlement ceases. During the experiment, soil deformation was monitored, and the settlement reading were taken at regular time intervals until the relationship between settlement and the logarithm of time become horizontal. Same procedure was adopted for centrally located piles by keeping uniform spacing. In all the cases, the test was repeated to check their reproducibility.

4   Experimental Result and Discussion

As we have already seen, a total of 40 number of load settlement tests and 45 time settlement tests were done, and the results are presented in graphical forms and discussed.

The length of pile kept 400 mm is kept constant, and the different combinations are tested to their ultimate capacity of raft and piles. Initially, only raft model 200 mm × 200 mm is tested without piles. On the other hand, only pile groups of 2 × 2, 3 × 3, and 4 × 4 are tested without raft. The raft is kept untouched to soil, so that all the loads were taken by piles only. After this, piled raft of above size and the different combinations of pile groups are tested and presented in Fig. 1. The sum of ultimate load-bearing capacity of single raft and the ultimate load-bearing capacity of 2 × 2 pile group must be nearly equal to the load-bearing capacity of combined piled raft of same identities. But the ultimate load-bearing capacity of combined piled raft is 2.75% more than the addition of individual capacities of pile and the raft. Also the ultimate load-bearing capacity of combined piled raft is 2.22% more than the sum of ultimate load-bearing capacity of single raft and the ultimate load-bearing capacity of 3 × 3 pile groups. And the ultimate load-bearing capacity of combined piled raft is 3.62% more than the sum of ultimate load-bearing capacity of single raft and the ultimate load-bearing capacity of 4 × 4 pile groups. As we increase the number of pile 4 to 9, there is increase in capacity by 33%, and when we increase the pile number from 9 to 16, then there is increase in capacities by 24%. Also in case of combined piled raft foundation when we increase the number of piles from 4 to 9, the ultimate load-bearing capacity of combined piled raft foundation increases by 17%, and for piles group 9 to 16, there is increase of 14%.

The size of the raft is changed to 300 mm × 300 mm, and different pile combinations are tested for the same pile length of 400 mm. As the size of the raft get increases, the ultimate load-bearing capacity of raft increases more than double. The same combination of piles groups of 2 × 2, 3 × 3, and 4 × 4 are tested combined with raft and then individual raft tested. There is no need to test pile groups individually as we have already tested and same values can be used here. The ultimate load-bearing capacity of combined piled raft is 1.50% more than the addition of individual capacities of pile and the raft. Also the ultimate load-bearing capacity of combined piled raft is 1.11% more than the sum of ultimate load-bearing capacity of single raft and the ultimate load-bearing capacity of 3 × 3 pile groups. And the ultimate load-bearing capacity of combined piled raft is 1.11% more than the sum of ultimate load-bearing capacity of single raft and the ultimate load-bearing capacity of 4 × 4 pile groups.

The size of the raft is changed to 400 mm × 400 mm, and different pile combinations are tested for the same pile length of 400 mm. As the size of the raft get increases, the ultimate load-bearing capacity of raft increases by 78%. The same combination of piles groups of 2 × 2, 3 × 3, and 4 × 4 are tested combined with raft and then individual raft tested. There is no need to test pile groups individually as we have already tested and same values can be used here. The ultimate load-bearing

capacity of combined piled raft is 1.3% more than the addition of individual capacities of pile and the raft. Also the ultimate load-bearing capacity of combined piled raft is 5.5% more than the sum of ultimate load-bearing capacity of single raft and the ultimate load-bearing capacity of 3 × 3 pile groups. And the ultimate load-bearing capacity of combined piled raft is 9.03% more than the sum of ultimate load-bearing capacity of single raft and the ultimate load-bearing capacity of 4 × 4 pile groups.

The above-described testing for the piled raft is repeated for the length of pile of 500 mm and 600 mm with different sizes of raft 200 mm × 200 mm, 300 mm × 300 mm, 400 mm × 400 mm with the different pile groups of 2 × 2, 3 × 3, and 4 × 4 pile groups. The load–settlement nature of these testing are shown in the graphs.
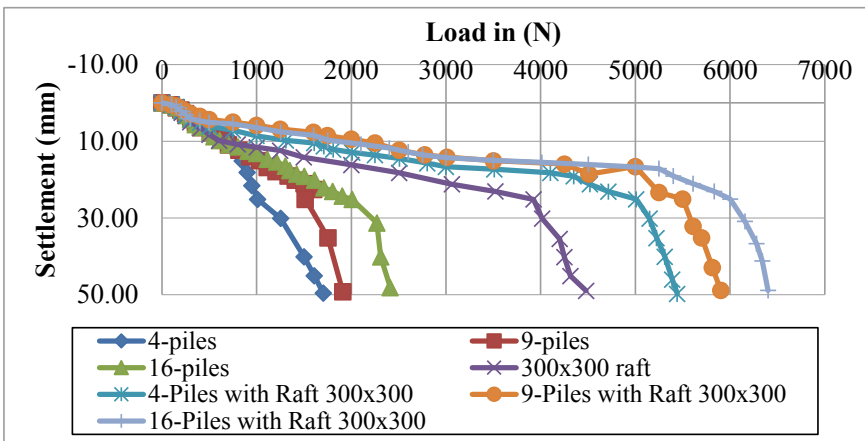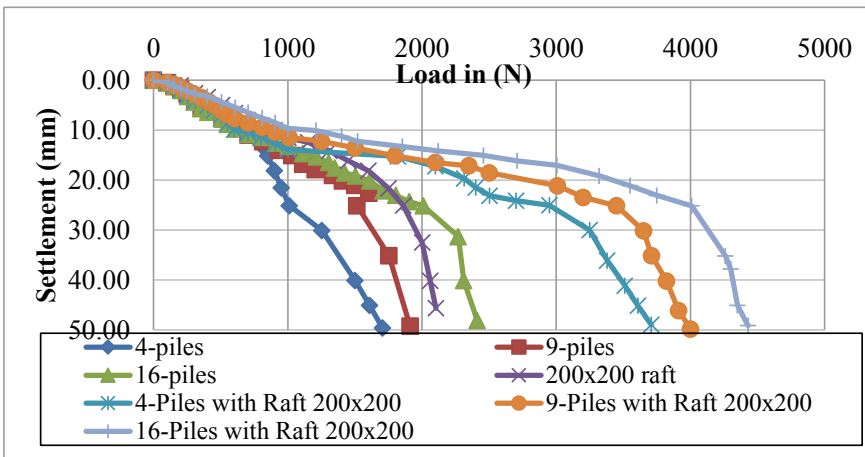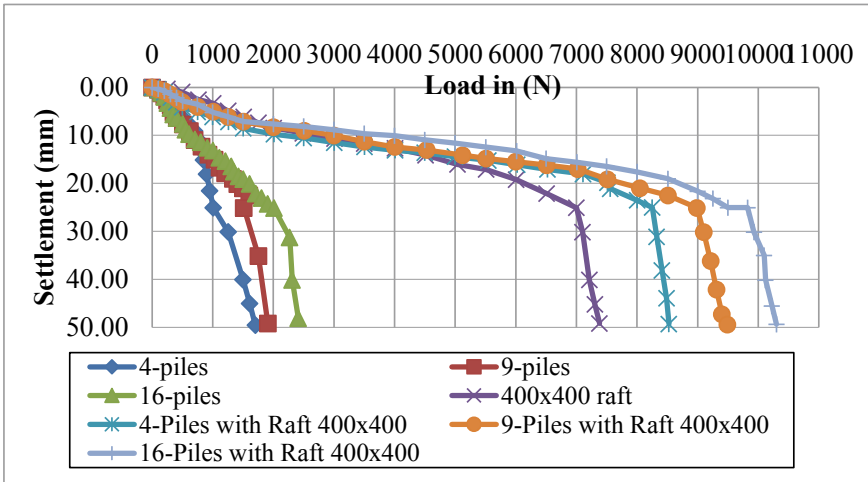
In this study, main objective was to calculate load-bearing ratio of piled raft foundation. Experimentally, we cannot determine the load taken by piles and load taken by raft separately in combined raft foundation. So we first determined the load taken by raft only up to failure and then load carried by piled raft foundation up to a failure point. This total load taken by combine piled raft foundation minus load taken by raft gives us the load carried by piles.

5 Conclusions

(1) The use of piled raft foundation plays very important role in reducing maximum as well as differential settlements. Also the use of piled raft foundation reduces the considerable number of piles or the length of pile as compared to the fully piled foundation. Due to this, piled raft foundation becomes economical and saves time as compared to piled foundation.

(2) Load-carrying capacity of piled raft foundation is always more than the addition of individual load-carrying capacity of pile and raft. The increase in the capacity is due to combined action of both pile and raft foundation, and the consolidation increases due to piles.

(3) The load distribution of the piled raft foundation depends on contact surface area with soil of raft as well as piles. The surface area ratio of 1.25–1.6 is more suitable for perfectly piled raft foundation. This ratio indicates that due to different load-resisting mechanism of raft and pile, i.e., pile resist load by skin friction and raft by bearing action.

(4) It is observed that load-sharing ratio of piled raft foundation depends on stiffness of pile and raft. While designing piled raft foundation depending upon

situations, we can adjust load sharing of piled and raft, by changing the stiffness (dimension) of the piles as well as raft. If we increase the thickness and dimension of raft, we can reduce the number of piles in piled raft foundation.

References

1. Zeevaert, L.: Compensated friction-pile foundation to reduce the settlement of building on the highly compressible volcanic clay of Mexico city. In: Proceedings of the 4th International Conference on Soil Mechanics Foundation Engineering, London, vol. 2, pp. 81–86 (1957)
2. Davis, E.H., Poulos, H.G.: The analysis of piled raft system. Austr. Geomech. J. **G2**(1), 21–27 (1972)
3. Hooper, J.A.: Observations on the behavior of pilled raft foundation on London Clay. In: Proceedings of the Institution of Civil Engineers, Part 2, vol. 55, pp. 855–877 (1972)
4. Burland, J.B., Broms, B.B., De Mello, V.F.B.: Behaviour of foundation and structure. In: State of Art, Rep. Proc, IX International Conf. of Soil Mechanics and foundation Engineering (ICSME), vol, 2 Tokyo, pp. 495–546, Balkema, Rotterdam, The Netherlands (1997)
5. Chow, H.S.W., Small, J.C.: Case histories for piled rafts. In: 2nd BGA International Conference on Foundations, Dundee, 24–27 June 2008, the conference is organized by British Geotechnical association (2008)
6. Raut, J.M., Khadeshwar, S.R., Bajad, S.P., Kadu, M.S.: Simplified design method for piled raft foundations. In: Advances in Soil Dynamics and Foundation Engineering, p. 462e71. American Society of Civil Engineers (2014)
7. Reul, O., Randolph, M.F.: Design strategies for piled rafts subjected to non-uniform vertical loading. J. Geotech. Geoenviron. Eng. **130**(1)
8. Comodromos, E.M., Papadopoulou, M.C., Laloui, L.: Contribution to the design methodologies of piled raft foundations under combined loadings. Can. Geotech. J. **53**(4):559–577 (2016)
9. Alnuaim, A.M., El Naggar, H., El Naggar, A.M.: Evaluation of piled raft performance using a verified 3D nonlinear numerical model. Geotech. Geol. Eng. **35**(4):1831–1845 (2017)
10. Huang, M., Jiu, Y., Jiang, J., Lie, B.: Nonlinear analysis of flexible piled raft foundations subjected to vertical loads in layered soils. Soils Found. **57**(4), 632–644 (2017)
11. Cooke, R.W.: Piled raft foundations on stiff clays. Contrib. Des. Philos. Geotech. **35**(2), 169–203 (1986)
12. Borel, S.: Comportement et dimensionnement des fondations mixtes. Ph.D. thesis de ENPC, Spécialité Géotechnique, Paris (2001)
13. Dung, N.T., Chung, S.G., Kim, S.R.: Settlement of piled foundations using equivalent raft approach. Proc. Instit. Civil Eng. Geotech. Eng. **163**(2), 65e81
14. Kim, K.N., Lee, S.-H., Kim, K.-S.: Optimal pile arrangement for minimizing differential settlements in piled raft foundations. Comput. Geotech. **28**(2001), 235–253 (2001)
15. Novak, L.J., Reese, L.C., Wang, S.-T.: Analysis of pile-raft foundations with 3D finite-element method. In: Structures Congress 2005 April 20–24, 2005 New York, New York, United States © 2005 American Society of Civil Engineers (2005)
16. de Sanctis, L., Mandolini, A.: Discussion on bearing capacity of piled rafts on soft clay soils. J. Geotech. Geoenviron. Eng. **132**(12), 1600–1610 (2006). https://doi.org/10.1061/ASCE1090-0241(2006)132:12(1600)
17. Vasquez, G., Wang, S.T., Isenhower, W.M.: Estimation of the capacity of pile-raft foundations by three-dimensional non-linear finite element analysis. In: Geo Congress 2006 Copyright @ ASCE 2006 (2006)
18. Fellenius, B.H.: Unified Design Of Piled Foundations With Emphasis On Settlement Analysis. Deep Foundations 2004 @ Copyright ASCE 2004

19. Hassen, G., De Buhan, P.: Fine element elastoplastic analysis of piled raft foundation based on use of multiphased model. In: VIII International conference on Computational Plasticity Complas VIII @Copyright CIMNE Barcelona (2005)
20. Katzenbach, R., Bachmann, G., Gutberlet, C.: Soil structure Interaction by high- rise buildings in Megacities. In: IGC 2006, 14–16 December 2006, Chennai, India (2006)
21. Fellenius, B.H.: Unified design of piled foundations with emphasis on settlement analysis. In: ASCE Geotechnical Special Publication (GSP 125) Honoring George G. Goble "Current Practice and Future Trends in Deep Foundations" Geo-Institute Geo-TRANS Conference, Los Angeles, 27–30 July 2004
22. Bakholdin, B.V.: Piled-raft foundations. Design and characteristics of construction procedures. Soil Mech. Found. Eng. **40**(5), 2003 (2003)

Assessment of 3D Consolidation Settlement of Soil by Considering the Effect of Surcharge Pressure

Arpan Laskar and **Sujit Kumar Pal**

Abstract The aim of the study is to assess 3D consolidation settlement of soil by considering the effect of surcharge pressure on surrounding soil. In this study, a 3D consolidation apparatus is developed and performed a series of 3D consolidation test under different surcharge pressures. Silty-clay soil and silty-sand with clay soil are used in this study. Consolidation tests are performed under different surcharge pressures like 0.0, 10.0, 15.0, and 20.0 kN/m^2. From this study, it is observed that with the increase of surcharge pressure, the compression indices and coefficient of consolidation values decrease for both the soils. The surcharge pressures have a significant effect on consolidation characteristics. With the increase of surcharge pressure on the surrounding soil, the void ratio of surrounding soil reduces, and it becomes denser, and as a result, the lateral strain of soil particles under consolidation as well as lateral extractions of pore water reduces, and corresponding compression index and the rate of consolidation also reduce. During the consolidation test as this apparatus allows vertical and lateral strain with vertical and lateral pore water dissipation under different surcharge pressures, it can be simulated to the in-situ field consolidation settlement.

Keywords Surcharge pressure · 3D consolidation · Compression index · Lateral strain · Pore water

A. Laskar
Techno College of Engineering Agartala, Agartala, India
e-mail: arpan2k8@yahoo.co.in

S. K. Pal (✉)
National Institute of Technology Agartala, Agartala, India
e-mail: skpal1963@gmail.com

1 Introduction

Deformation analysis of the soil is one of the most uncertain and indecisive tasks in geotechnical engineering. The work presented in this part of study is concerned with the deformation analysis of the soil under surcharge pressure. In the present days, the settlement of supporting soil has been calculated using one-dimensional consolidation of soil. Three-dimensional consolidation cases of soil have been considered as a modification to the one-dimensional consolidation. A natural porous medium like soil may have been created by sedimentation process, and this sedimentation makes horizontal stratification layers and hence the permeability of soil different in horizontal and vertical directions. Due to the anisotropic nature of the soil in horizontal and vertical directions, and different seepage characteristic through the different direction of soil, the coefficient of consolidation and coefficient of permeability in the horizontal direction is typically different from the coefficient of consolidation and coefficient of permeability in the vertical direction. There is also a large effect of surcharge pressure on the consolidation of soil. The effect of surcharge pressure is under-estimated in the process of consolidation. Hence, in this study, it is proposed to use the three-dimensional consolidation cases as the basic problem rather than a further extension of one-dimensional consolidation theory, where the effect of surcharge pressure on the three-dimensional consolidation process is also taken under consideration. In three-dimensional consolidation cases with the application of load and surcharge pressure, there is vertical as well as the lateral strain of soil along with vertical and radial drainage of water.

Significant efforts have been made in the development of concepts, theories, and formulations for evaluating consolidation characteristics of saturated soils during the last three decades. However, experimental confirmation has not kept pace with theoretical advance. The general theory of three-dimensional consolidation was first introduced by Biot [1], in which coupling between solid and fluid was considered. In the past few decades, many investigators had been developed different analytical solution based on Biot's consolidation theory. Skempton and Bjerrum [2] proposed a correction factor (μ) to modify one-dimensional consolidation settlements to bring out two- and three-dimensional effects. Ai and Cheng [3] reported numerical analysis for three-dimensional consolidation with the anisotropic permeability of a layered soil system, and the effect of anisotropy of permeability on the consolidation behavior had been discussed. Ai et al. [4], and Ai and Cheng [5] presented alternative approaches to solving the Biot's consolidation problem and obtained an organized solution to the consolidation problems. Several attempts by different researchers also had been taken to evolve an analytical procedure to solve the Biot's consolidation equations using directly Laplace transform [6] and [7]. The effects of soil particles on consolidation characteristics had been evaluated, and it was found that the fine fraction had a more significant influence on the consolidation characteristics [8]. In all the past investigations, evaluation technique of three-dimensional consolidation was analytical or numerical based, and assumptions were not as replicating to the field condition. The previous investigators do not considered the effects of surcharge pressure on the

consolidation of soil. Hence, it is important to develop an experimental solution for three-dimensional consolidation problems by considering the effects of surcharge pressure.

2 Aim and Scope of the Study

The study aims to predict consolidation characteristics of soil based on three-dimensional consolidation of soil under different surcharge pressures. In this study, a three-dimensional consolidation apparatus is developed and performed a series of three-dimensional consolidation test under different surcharge pressures. During the three-dimensional consolidation test, vertical and lateral strains of the soil, and vertical and lateral movements of pore water are allowed. In this study, two different types of soil are used to perform the three-dimensional consolidation tests under different surcharge pressures. It is observed that the three-dimensional consolidation settlement of the same soil changed with the changes of surcharge pressure. With the increase of surcharge pressure, the lateral strain of soil reduces during the consolidation process; and due to this, compression index and coefficient of consolidation also reduced. Using developed apparatus, three-dimensional consolidation characteristics of soil can be evaluated under different surcharge pressures. As this apparatus allows vertical and lateral strain with vertical and lateral pore water movement under different surcharge pressures, it is possible to correlate with in-situ field conditions during the consolidation process.

3 Development of Apparatus to Apply Surcharge Pressure During Three-Dimensional Consolidation Test

Figure 1 shows the developed three-dimensional consolidation apparatus, where three-dimensional consolidation can perform under different consolidative pressures. In the mentioned three-dimensional consolidation apparatus surcharge pressure is introduced as shown in Fig. 2 to measure the effect of surcharge pressure on three-dimensional consolidation of soil. In this test, soil sample is bounded by the porous cast iron consolidation cell which is open at top and bottom sides. The internal and external dimension of this porous cast iron consolidation cell is 300 mm × 300 mm × 450 mm (height) and 310 mm × 310 mm × 450 mm (height), respectively. This porous box is surrounded by porous stone plates of 12 mm thick. A concrete tank of internal dimension 334 mm × 334 mm × 450 mm (height) is fabricated to hold that porous consolidation cell along with porous stone plates. Surcharge pressures are applied on top of the soil sample using cast iron plates of cross-sectional area 299 mm × 299 mm, with 61 mm diameter center hole and under this surcharge loading plate, a porous stone plate is placed of the same cross-sectional area and center hole as
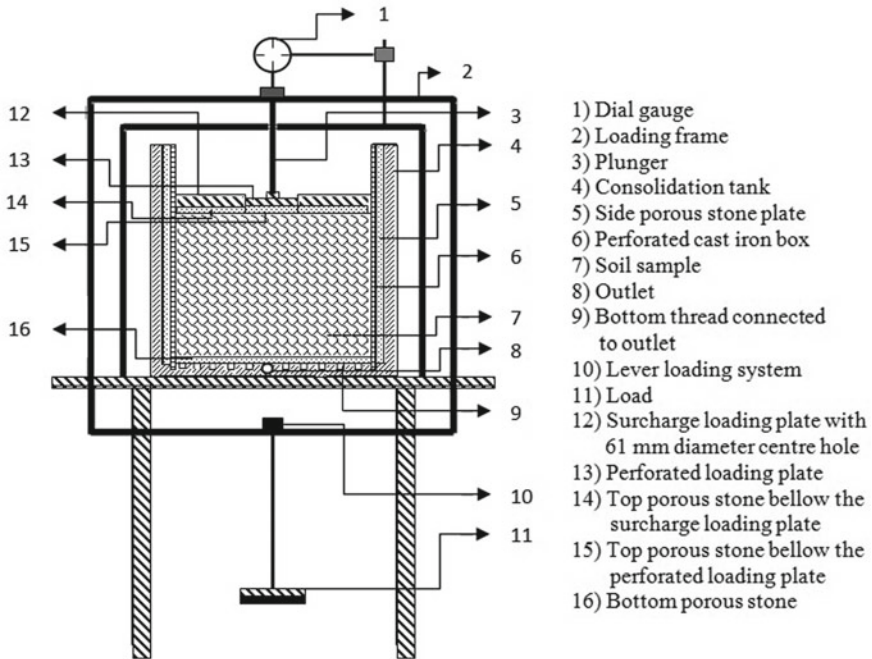
Fig. 1 Schematic diagram of developed three-dimensional consolidation apparatus to apply surcharge pressure during three-dimensional consolidation test
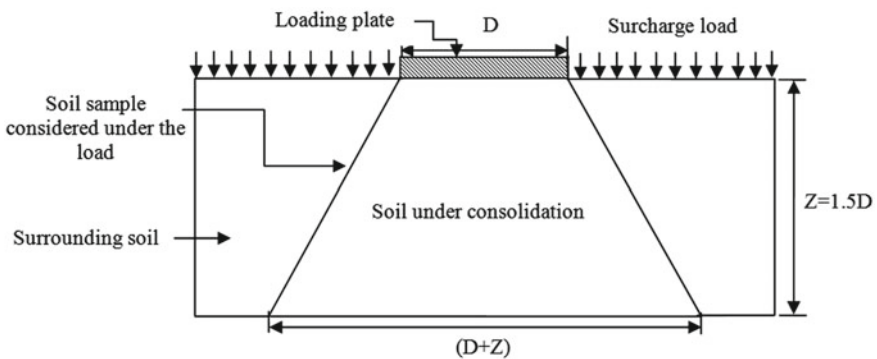
Fig. 2 Schematic diagram of soil under consolidation and surcharge pressure on surrounding soil

surcharge loading plate. A filter paper, a porous stone, and a perforated loading plate of 60 mm diameter are consecutively inserted through 61 mm diameter hole of surcharge loading plate. Below the porous stone plate of 60 mm diameter, a filter paper is used having the same diameter. To apply the load on that loading plate, a lever loading frame is fabricated as shown in Fig. 1. A dial gauge (0.0–25 mm) of

sensitivity 0.01 mm is installed in the loading frame to measure the vertical settlement of loading plate.

4 Theoretical Considerations for Consolidation

Assumptions of present three-dimensional consolidation test are as follows:

1. The soil layers are homogeneous, and the soil properties are isotropic;
2. The soil layers are two-faced saturated;
3. Vertical and horizontal movements of soil particles are allowed during the process of consolidation;
4. The compression of the soil layer is due to the change in volume only, which in turn is due to the squeezing out of water from the void space in vertical as well as in horizontal directions;
5. Darcy's law is valid;
6. In case of plastic settlement, if all the soil particles are inter-connected, then vertical movement of soil particles occurs due to horizontal movements of underneath soil particles; and
7. The lower boundary of stress remains constant throughout the consolidation process.

5 Testing Materials and Program

Silty-clay soil and silty-sand with clay soil are used in this investigation. A series of standard classification tests are carried out to categorize these test materials. The physical properties along with maximum dry density (MDD) and optimum moisture content (OMC) using standard Proctor compaction energy of two types of soils are listed in Table 1.

   Using silty-clay soil and silty-sand with clay soil, eight numbers of three-dimensional consolidation tests are performed under different surcharge pressures.

6 Specimen Preparation and Experimental Procedures

Soil samples are remolded at a maximum dry density (MDD) obtained from standard Proctor compaction in porous cast iron box in three consecutive layers, and these soil samples are considered as an ideal two-faced soil system during the test. The inner sides of the cast iron consolidation cell are covered by filter paper before molding the soil sample. After molding the sample, four consecutive sides of the cast iron consolidation cell are covered by porous stone plates (side porous stone plate) as shown in Fig. 1. Over the soil sample filter paper, porous stone and cast iron plate

Table 1 Basic properties of soils

Soil properties	Silty-clay soil	Silty-sand with clay soil
Specific gravity (G)	2.60	2.58
Liquid limit, LL (%)	53.35	25.30
Plastic limit, PL (%)	29.32	19.03
Plasticity index, PI (%)	24.03	4.27
Sand (<4.75 mm and >0.075 mm), (%) Silt (<0.075 mm and >0.002 mm), (%) Clay (< 0.002 mm), (%)	4.86 41.46 53.68	61.60 21.68 16.72
Soil classification as per USCS	CH	SM
Optimum moisture content, OMC (%)	25.75	13.10
Maximum dry density, MDD (kN/m^3)	15.60	18.80

of the cross-sectional area of 299 mm × 299 mm with the center hole of 61 mm diameter are placed one above the other. The cast iron plates of size 299 mm × 299 mm with the center hole of 61 mm diameter are placed over the soil specimen to apply initial seating pressure of 5.0 kN/m^2, and surcharge pressures of 10.0, 15.0, and 20.0 kN/m^2. A filter paper, a porous stone, and a perforated loading plate of 60 mm diameter have been placed consecutively through the 61 mm diameter center hole. The load is applied by lever-loading frame system to the top perforated loading plate of 60 mm diameter through a plunger connecting the loading frame and perforated loading plate. Initially, 5.0 kN/m^2 stress is applied as a seating pressure and kept it for 48 h to saturate the soil sample. After 48 h, 100, 200, 400, and 800 kN/m^2 stresses are consecutively applied to the soil sample, and each stress is applied for 24 h. With the application of stresses on soil, vertical settlements corresponding to different time interval are measured by a strain gauge.

7 Test Results and Analysis

In this study, three-dimensional consolidation tests are performed under different surcharge pressure using developed three-dimensional consolidation apparatus as shown in Fig. 1. Consolidation tests are performed under different surcharge pressures like 0.0, 10.0, 15.0, and 20.0 kN/m^2. Figure 2 shows the schematic diagram of the soil under consolidation and surcharge pressure on surrounding soil. Figures 3 and 4 show the compression indices of silty-clay soil and silty-sand with clay soil, and Figs. 5 and 6 show the coefficient of consolidation values of silty-clay soil and silty-sand with clay soil under different consolidative vertical stresses and surcharge pressures. From Figs. 3, 4, 5 and 6, it is observed that with the increases of surcharge pressure, for the same soil and under the same consolidation pressure, the consolidation settlement of soil reduces.
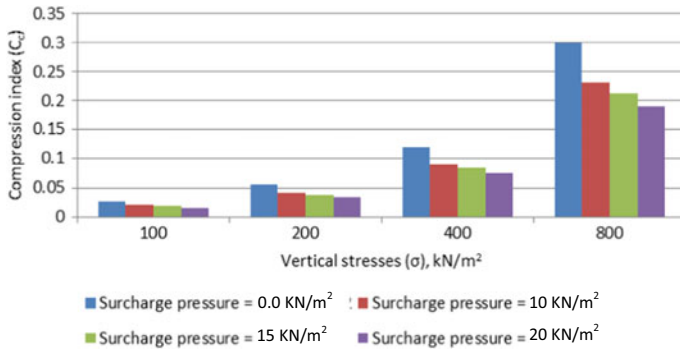
Fig. 3 Compression indices of silty-clay soil under different vertical stresses and surcharge pressures
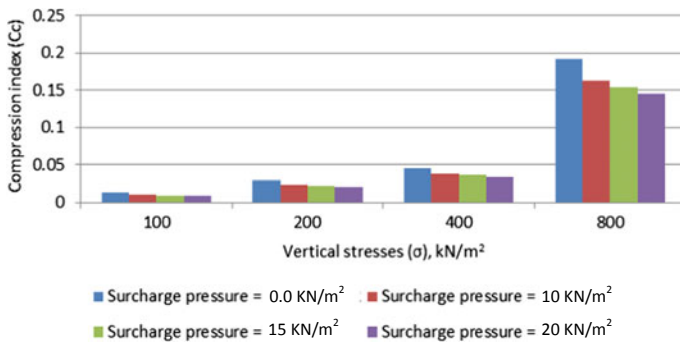

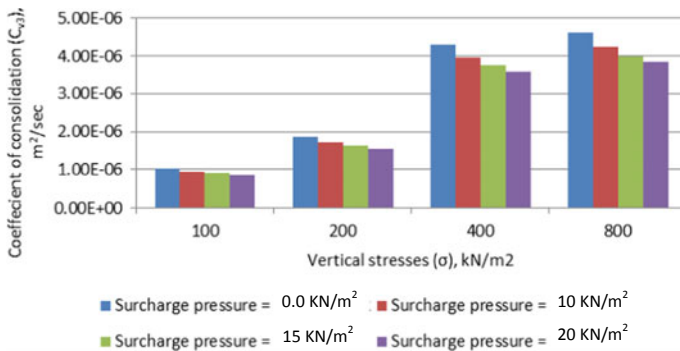**Fig. 4** Compression indices of silty-sand with clay soil under different vertical stresses and surcharge pressures

Fig. 5 Coefficient of consolidation values of silty-clay soil under different vertical stresses and surcharge pressures
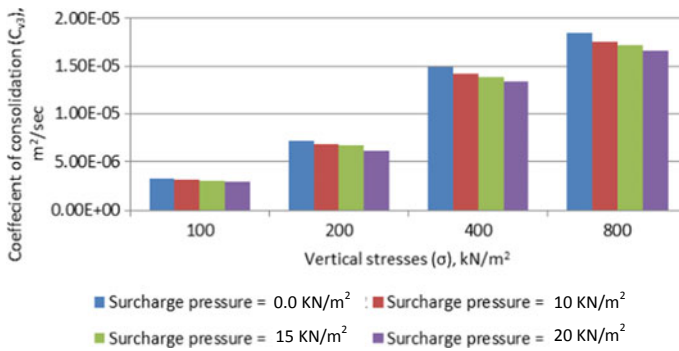
Fig. 6 Coefficient of consolidation values of silty-sand with clay soil under different vertical stresses and surcharge pressures

8 Discussions

In this study, three-dimensional consolidation tests are performed on silty-clay soil and silty-sand with clay soil under different surcharge pressures using developed three-dimensional consolidation apparatus as shown in Fig. 1. In the three-dimensional consolidation of soil, lateral and vertical movements of soil particles, and lateral and vertical movements of pore water are taken into consideration. The soil under consolidation may have surrounding soil as shown in Fig. 2, which affects the lateral movements of soil particles under consolidation, and it also affects the lateral movement of pore water. If surcharge pressure increases on the surrounding soil particles, these surrounding soils become denser, and as a result, lateral movements of soil under consolidation get resisted, and at the same time, horizontal pore water movements will also reduce. The compression indices and coefficient of consolidation values of silty-clay soil and silty-sand with clay soil under different vertical stresses and surcharge pressures are shown in Figs. 3, 4, 5 and 6, and Table 2. From these figures and table, it is observed that with the increase of surcharge pressure, the compression indices and coefficient of consolidation values decrease for both the soils. The surcharge pressures have a significant effect on consolidation characteristics. The rate of consolidation of soil is proportional to the rate of extraction of pore water from the soil. With the extraction of pore water from soil mass, the arrangement of the skeleton of soil changes and due to which settlement occurs. At the time of rearrangement of soil particles with the extraction of water, it may move in horizontal as well as in vertical directions. With the increase of surcharge pressure on the surrounding soil, the void ratio of the surrounding soil reduces, and it becomes denser, and as a result, the lateral movement of soil particles under consolidation as well as lateral extractions of pore water reduces. Due to this reason corresponding compression index and the rate of consolidation also reduce.

Table 2 Three-dimensional consolidation of soils under different surcharge pressures

Types of soil	Surcharge pressure (kN/m^2)	Consolidative vertical stress σ (kN/m^2)	Compression index C_c	Coefficient of consolidation c_{v3} (m^2/s)
Silty-sand with clay soil	0.0	100	0.013	3.26E−06
		200	0.029	7.13E−06
		400	0.0461	1.49E−05
		800	0.192	1.85E−05
	10.0	100	0.0106	3.08E−06
		200	0.0243	6.78E−06
		400	0.0387	1.42E−05
		800	0.1632	1.76E−05
	15.0	100	0.0099	3.04E−06
		200	0.0228	6.65E−06
		400	0.0365	1.39E−05
		800	0.1542	1.72E−05
	20.0	100	0.0093	2.94E−06
		200	0.0215	6.15E−06
		400	0.0345	1.34E−05
		800	0.1458	1.66E−05
Silty-clay soil	0.0	100	0.0261	1.03E−06
		200	0.056	1.87E−06
		400	0.119	4.30E−06
		800	0.2993	4.61E−06
	10.0	100	0.0202	9.40E−07
		200	0.042	1.72E−06
		400	0.0904	3.95E−06
		800	0.2304	4.24E−06
	15.0	100	0.0181	9.00E−07
		200	0.0382	1.62E−06
		400	0.0831	3.77E−06
		800	0.2119	4.00E−06
	20.0	100	0.0157	8.60E−07
		200	0.0334	1.53E−06
		400	0.0739	3.60E−06
		800	0.1907	3.85E−06

9   Conclusion

This study concentrates on the development of a three-dimensional consolidation apparatus through which three-dimensional consolidation tests are performed under different surcharge pressures. The entire tests are performed on silty-clay soil and silty-sand with clay soil of Agartala, Tripura, India. From this study, it is observed that the consolidation characteristics are largely affected by the surcharge pressures during the three-dimensional consolidation of soil. With the increase of surcharge pressure on the surrounding soil, the surrounding soils become denser, and it reduces the lateral movements of consolidating soil particles, and at the same time, it also reduces the lateral pore water movement. From this study, it is also observed that the compressibility and the rate of consolidation of the soil under three-dimensional consolidation reduced due to an increase of surcharge pressure on the surrounding soil.

References

1. Biot, M.A.: General theory of three-dimensional consolidation. J. Appl. Phys. Am. Inst. Phys. **12**(2), 155–164 (1941)
2. Skempton, A.W., Bjerrum, L.: A contribution to the settlement analysis of foundations on clay. Geotechnique, ICE **7**(4), 168–178 (1957)
3. Ai, Z., Cheng, Y.: 3-D consolidation analysis of layered soil with anisotropic permeability using analytical layer-element method. Acta Mech. Solida Sin. **26**(1), 63–70 (2013)
4. Ai, Z.Y., Wang, Q.S., Han, J.: Transfer matrix solutions to axisymmetric and non-axisymmetric consolidation of multilayered soils. Acta Mech. **211**(1), 155–172 (2010)
5. Ai, Z.Y., Cheng, Z.Y.: Transfer matrix solutions to plane-strain and three-dimensional Biot's consolidation of multi-layered soils. Mech. Mater. **41**(3), 244–251 (2009)
6. Ai, Z.Y., Wang, Q.S.: A new analytical solution to axisymmetric Biot's consolidation of a finite soil layer. Appl. Math. Mech. (English Edition), Shanghai University and Springer **29**(12), 117–1624 (2008)
7. Ai, Z.Y., Wang, Q.S., Wu, C.: A new method for solving Biot's consolidation of a finite soil layer in the cylindrical coordinate system. Acta Mech. Sin. **24**(6), 691–697 (2008)
8. Bogireddy, C., Solanki, C.H., Vasanwala, S.A.: Influence of fine fraction on shear parameters and consolidation behavior of tropical residual soil. Indian J. Sci. Technol. **9**(41) (2016)

Compaction Characteristics of Red Earth and Quarry Dust Combinations

Neba C. Tony , **G. Devdas, Sandra G. Raj, and Renjitha Mary Varghese**

Abstract Quarry dust is a waste material obtained during the quarrying process. It exhibits high shear strength and good permeability. An efficient method to dispose it off is by using it in combination with red earth to strengthen the soil. This paper presents effects of addition of quarry dust on properties of red earth and the relationship between water content and dry density of quarry dust–red earth mixes. Preliminary studies concluded that the optimum proportion of quarry dust–red earth mixes was found as 40% and 60%, respectively. The optimum values of the mixes are defined with respect to the dry density of quarry dust alone. It is observed that there was an increase of 11.61% in the dry density when 40% of the red earth is replaced with quarry dust. The optimum value of quarry dust to be mixed with red earth so as to have maximum shear strength is also determined. The shear strength of the mix was found from direct shear tests, and it was observed that there is a reduction in the shear properties when quarry dust was mixed with red earth. However, quarry dust can be a sustainable solution to sub-base stabilization especially in case of highways.

Keywords Compaction characteristics · Quarry dust–red earth mix · Shear parameters

N. C. Tony (✉)
Indian Institute of Technology, Delhi, India
e-mail: nebactony@gmail.com

G. Devdas
College of Engineering, Thiruvananthapuram, India

S. G. Raj
Rajiv Gandhi Institute of Technology, Kottayam, India

R. M. Varghese
National Institute of Technology, Calicut, India

1   Introduction

Laterite, also known as red earth, is a non-expansive soil having kaolinite as the major constituent. It is found abundantly in and around south India. It is a mixture of clayey iron and aluminum oxides and hydroxides formed as a result of the weathering of basalt under humid, tropical conditions. Incidence of laterite is reported in Indian states of Karnataka, Maharashtra, Gujarat, and Kerala. The intense southwest monsoon rainfall in Kerala coupled with the high temperature and lush vegetation has accentuated the chemical process over the base rocks, which has resulted in the formation of laterites. Thick deposits of red earth are found in Alappuzha, Kollam, Thiruvananthapuram, Kottayam, Thrissur, Palakkad, and Kannur districts of Kerala. Kerala is a coastal region and have soft soils throughout the boundary line along the coast, and hence, due to the desirable properties of red earth, it is needed in bulk quantities to construct subways by filling the site with red earth. However, scarcity of lateritic soil had led to the adoption of technically viable and economically feasible solution to address this problem.

Aggregate crusher units produce large quantities of quarry dust, during crushing of gravel and rock such that about 20–25% of the byproducts of the crushing rock operation is quarry dust. It amounts to nearly 250 million tons of the total output of quarrying operations. Disposal of these large quantities of quarry dust produces serious problems in the environment and health hazards. There is much requirement to utilize these waste materials in an effective manner.

Studies have revealed that quarry dust can be used to improve the properties of lateritic soil in case of sub-base construction works. This can potentially reduce the usage of red earth. This paper aims at the judicious usage of red earth and effectiveness of quarry dust which is a waste material with in the field of civil engineering.

2   Literature Review

Road construction is an area where the industrial wastes can be utilized in bulk with advantage. Quarry dust is a waste material which can be effectively utilized to minimize the usage of red earth. As the gradation of the material does not satisfy the specification requirements for concrete works due to large specific surface, they can be effectively mixed with soils to enhance its properties. Owing to high shear strength and permeability, variation in water content does not seriously affect its desirable properties. The test results revealed the dry density–water content relationship is comparatively flat at peak values, and the effect of variation in water content from optimum moisture content on dry density is marginal [1]. A study involving the use of laterite stabilized with cement using quarry dust as additive for use as base course material showed that liquid limit, plastic limit, plasticity index, and maximum dry density (MDD) decrease with increased quarry dust content, in all the cement proportions used [2]. A study on the variation of Atterberg limits on mixing the

admixtures with red earth yielded that the addition of the chemical admixture can improve the engineering properties of soil. The soil liquid limit is found to decrease with an increase in cement and fly ash content while the soil void ratio was found to decrease with increase in admixtures [3].

A study on the use of industrial byproduct mixtures as construction materials concluded that when fly ash is mixed with fine grained soils, it resulted in an improvement in the properties of both fly ash and fine grained soils. Results from laboratory tests indicate the improved material properties of combined fly ash aggregate waste which proved that a composition of fly ash and aggregate can be used as highway materials in flexible pavements [4].

Studies suggest that lime has a significant effect on the engineering properties of red earth treated with mine tailings. There is significant increase in strength due to long-term pozzolanic reaction of the calcium oxide present in mine tailings with red earth resulting in the flocculation of particles. This encourages the effective utilization of mine tailings for geotechnical applications [5]. From the immediate compaction and unconfined compressive strength test up to 30 days of curing, black cotton soil with 3% CaCl2 (by weight of soil) combination has higher factor of safety with higher curing periods for an embankment slope of 1:2.5 [6]. Lateritic soil–cement mixture combinations revealed that as the amount of the added chemical calcium silicate hydrate (CSH) increased, the unconfined compressive strength (UCS) of the sample also exhibited corresponding increase. Hence, improved lateritic soil can be used instead of crushed rock, as the base course material for highway pavement construction [7].

The use and application of direct shear tests to determine the cohesion and angle of internal friction for angular soils yielded that adding clay contributed in increasing the dry density of the mixture and rendered the increase as well [8].

3 Materials and Methods

Two types of soils were used in the present study, and the preliminary material characterizations of these two soils were done. The preliminary studies on this soil such as grain size distribution, liquid limit, plastic limit, shrinkage limit, direct shear, and standard proctor test were conducted. The physical properties of red earth and quarry dust samples taken for study is given in Tables 1 and 2, respectively.

3.1 Light Compaction Test

The light compaction test was conducted on various proportions of red earth (laterite soil) and quarry dust as per IS 2720(Part 7):1980 [9]. For each compaction test, about 3 kg of soil was used. Required amount of water was added to the soil and mixed thoroughly. The test code is tabulated in Table 3. In case of $Q_{100}R_0$, the test mix

Table 1 Properties of red earth

Property	Value
Specific gravity	2.57
Grain size distribution	
Sand size (0.075–4.75 mm) (%)	62.1
Silt and clay size (<0.075) (%)	37.9
IS specification	SW
D_{10} (mm)	0.165
D_{50} (mm)	1.25
C_u	9.41
C_c	1.46
Consistency limits	
Liquid limit (%)	45
Plastic limit (%)	23.76
Shrinkage limit (%)	29.16
Plasticity index (%)	21.24

Table 2 Properties of quarry dust

Property	Value
Specific gravity	2.62
Grain size distribution	
Sand size (0.075–4.75 mm) (%)	60.12
Silt and clay size (<0.075) (%)	39.88
D_{50} (mm)	0.086
Relative density	
ρ_{max} (g/cc)	1.512
ρ_{min} (g/cc)	1.175
Bulking	
Maximum bulking (%)	62.96
Water content for maximum bulking (%)	6

Table 3 Test code

Test code	Quarry dust (%)	Red earth (%)
$Q_{100}R_0$	100	0
$Q_{80}R_{20}$	80	20
$Q_{60}R_{40}$	60	40
$Q_{40}R_{60}$	40	60
$Q_{20}R_{80}$	20	80
Q_0R_{100}	0	100

Fig. 1 Quarry dust–red earth mixes

Table 4 Dry density and optimum moisture content for quarry dust–red earth mixes

Quarry dust–red soil mixes	Maximum dry density (g/cc)	Optimum moisture content (%)
Q_0R_{100}	1.76	18
$Q_{100}R_0$	1.584	21

contains only quarry dust and no traces of red earth. However, the test code $Q_{80}R_{20}$ has quarry dust and red earth mixed in 4:1 ratio. The same is shown in Fig. 1. Standard Proctor test for light loads was conducted on these proportions, and the dry density and optimum moisture content for red earth and quarry dust are given in Table 4.

3.2 Direct Shear Test

The direct shear test was conducted as per IS 2720(Part 13):1986 [10]. The sample was oven dried and used for the test. The soil sample was prepared by mixing it with distilled water at various water contents. The Coulomb envelope was plotted between normal stress and shear stress at failure to get the value of c as well as Φ. The direct shear test was conducted to investigate the influence of red earth–quarry dust mixtures on shear strength properties of the soil and to find out the optimum value of quarry dust to be mixed with red earth so as to obtain maximum shear strength. The tests were conducted on red earth and quarry dust to get the c and Φ values at optimum moisture contents. The results are given in Table 5.

On conducting direct shear test, it was seen that this mix yielded no cohesion but had a lower value of angle of shearing friction. The shear strength of this soil proportion at a depth of 1 m was found to be 0.899 kg/cm2. This shows poor shear strength. Hence, quarry dust alone cannot be used for the purpose of soil stabilization.

Table 5 Shear stress values for quarry dust and red earth mixes

Quarry dust–red soil mixes	Cohesion(c) (kg/cm^2)	Angle of shearing friction (°)	Normal stress (kg/cm^2) $\sigma = \Upsilon \times 1\ m$	Shear stress (kg/cm^2) $S = c + \sigma\ t\ an\ \phi$
$Q_{100}R_0$	0	29.59	1.584	0.899
Q_0R_{100}	0.4804	39.76	1.76	1.464

4 Results and Discussions

4.1 Influence of Percentage of Red Earth on the Compaction and Shear Characteristics of Quarry Dust

The standard Proctor test and direct shear tests were conducted on these proportions, and the normal stress and shear stress for red earth and quarry dust are shown in Table 6.

Compaction tests were conducted in different proportions of soil and are shown in Fig. 2. From the graph, it was seen that all mixes had maximum dry density greater than quarry dust ($Q_{100}R_0$). The maximum dry density for red earth was 27% more compared to the density obtained for quarry dust alone. When quarry dust was mixed with red soil, a reduction in the optimum moisture content was observed with increase in dry density. Three mixes namely $Q_{100}R_0$, $Q_{80}R_{20}$, and Q_0R_{100} had flatter peaks, whereas remaining mixes, $Q_{60}R_{40}$, $Q_{40}R_{60}$, $Q_{20}R_{80}$, had well-defined peaks for the dry density. When the graphs of $Q_{20}R_{80}$ and $Q_{60}R_{40}$ are considered, it was seen that there was not much of a difference in their dry densities. Maximum dry density was obtained for the mix $Q_{40}R_{60}$.

The dry density and optimum moisture content for quarry dust–red earth mixes are given in Table 7.

Based on the above analysis, the dry density versus percentage red earth graph was plotted. It was found that the dry density of $Q_{40}R_{60}$, (viz, 1.769) was greater than the dry density of quarry dust when compacted alone, (viz, 1.76) as depicted in Fig. 3.

Table 6 Normal stress and shear stress for quarry dust–red earth mixes

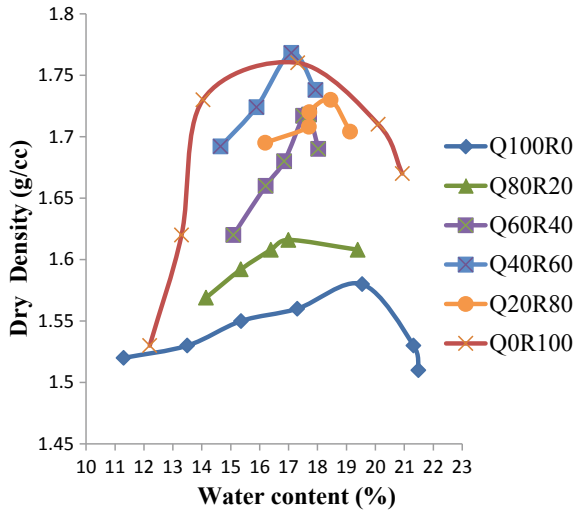| Test code	Cohesion (c) (kg/cm^2)	Angle of shearing friction (°)	Normal stress (kg/cm^2) $\sigma = \Upsilon \times 1\ m$	Shear stress (kg/cm^2) $S = c + \sigma t\ tan\ \phi$
$Q_{100}R_0$	0	29.59	5.28	0.899
$Q_{80}R_{20}$	0.0495	21.06	5.19	0.675
$Q_{60}R_{40}$	0.329	35.13	5.304	1.537
$Q_{40}R_{60}$	0.1529	24.09	5.154	0.943
$Q_{20}R_{80}$	0.4347	38.81	4.875	1.825
Q_0R_{100}	0.4804	39.76	4.644	1.944

Fig. 2 Compaction curves for various proportions of red earth and quarry dust

Table 7 Dry density and optimum moisture content for quarry dust–red earth mixes

Test code	Maximum dry density (g/cc)	Optimum moisture content (%)
$Q_{100}R_0$	1.584	21
$Q_{80}R_{20}$	1.625	20
$Q_{60}R_{40}$	1.718	19
$Q_{40}R_{60}$	1.768	18
$Q_{20}R_{80}$	1.73	18
Q_0R_{100}	1.76	18

There was an increase of nearly 11.62% in the dry density. Also this dry density can be obtained by compacting the soil mix in its optimum moisture content. This is evident from Fig. 3. There was a gradual increase of dry density with the decrease in the percentage of quarry dust. However, when the proportion of mix contained 20% quarry dust and 80% red earth ($Q_{20}R_{80}$), a decrease was found in the dry density. This was due to the change in the grain size. The soil was well graded until this proportion but later due to the change from well-graded soil to poorly graded soil, the dry density decreased. The reason for the increase of optimum moisture content for this mixes also accounts to the same fact as seen in Fig. 4.

Based on the above results, the dry density versus C and Φ values were plotted, and the optimum proportion of quarry dust and red earth as obtained from the compaction results was $Q_{40}R_{60}$. This value had a fairly better cohesion index and angle of internal friction. Further to obtain the trend followed by cohesion, angle of internal friction, and percentage of red earth, c/c_{max} and Φ/Φ_{max} curves were also drawn. The values
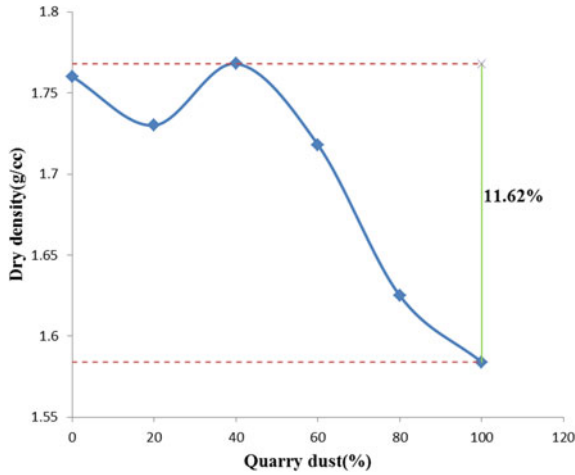
Fig. 3 Dry density versus percentage quarry dust for various mix proportions
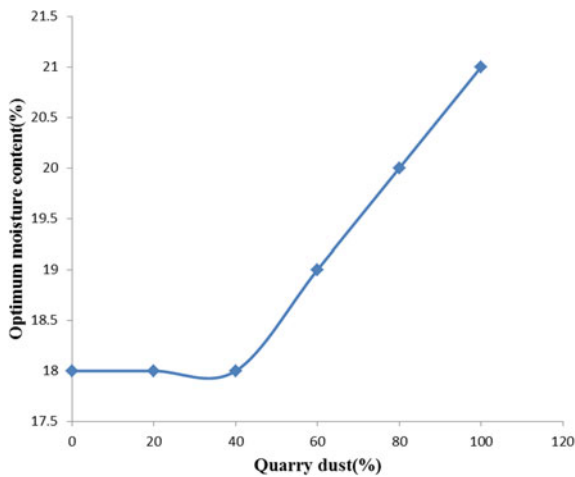

Fig. 4 Optimum moisture content versus percentage quarry dust for various mix proportions

obtained at optimum moisture content was utilized for this purpose. This is shown in Figs. 5 and 6. The c/c_{max} versus percentage quarry dust graph showed a gradual drop with increase in quarry dust content. This was due to the fact that cohesion decreased with increase in moisture content. The Φ/Φ_{max} versus percentage quarry dust graph did not show a definite trend with increase in moisture content due to the difference in mineralogical characteristics for different quarry dust–red earth mixes [8].
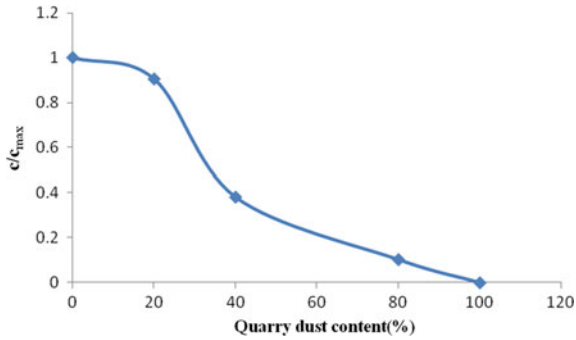
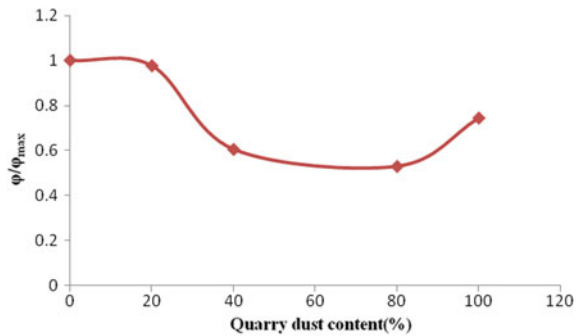**Fig. 5** c/c_{max} versus percentage quarry dust for various mix proportions.

Fig. 6 Φ/Φ_{max} versus percentage quarry dust for various mix proportions

5 Conclusions

From the studies conducted, the following conclusions were derived.

- The dry density is higher for a mixture containing 60% red earth and 40% quarry dust
- The optimum moisture content of this mix is 18%.
- The cohesion of soil decreases with increase in quarry dust content.
- The angle of internal friction increases with increase in quarry dust content

Quarry dust, a waste material from rubble crusher units, consists of mainly sand size particles. Studies on quarry dust–red earth samples indicate that the dry density is higher for a mixture containing 60% red earth and 40% quarry dust when compared with the dry density of quarry dust alone. Furthermore, this proportion had a fairly better cohesion index and angle of internal friction. Due to this reason, this mix could be used to enhance partial replacement of red earth. When maximum dry density is obtained, the strength of soil gets increased thereby increasing its safe bearing capacity. As a result, heavy foundation is not required. Thus, there is overall

economy. There is also reduction in the amount of red soil to be used. Hence, there is economy. It also contributes toward an environmental cause by preventing the excavation of hills for obtaining red earth.

Hence, quarry dust can be disposed of efficiently by using it in combination with red earth to strengthen the soil. This proportion can be utilized for sub-base stabilization especially in case of highways.

The project can be further extended to find the number of blows which can yield the exact maximum dry density in a mini compaction apparatus. The scope also lies in usage of coir fiber to improve the shear strength characteristics of the quarry dust–red earth mixes.

References

1. Soosan, T., Sridhan, A., Jose, B., Abraham, B.: Utilization of quarry dust to improve the geotechnical properties of soil in highway construction. Geotech. Test. J. **28**(4), 391–400 (2005)
2. Agbo, D., Eze-Uzomaka, O.J.: Suitability of quarry dust as improvement to cement stabilized-laterite for road bases. EJGE. **15**, 1053–1063 (2010)
3. Sai Darshan, T.R., Mayanaik, N.: Effect of chemical admixtures on the engineering properties of red earth treated with cement. IOSR J. Mech. Civ. Eng. **11**(1), 43–45 (2014)
4. Seung, W.L., Fishman, K.L.: Waste products as highway materials in flexible pavement system. J. Transp. Eng. **119**(3), 433–449 (1993)
5. Ramesh, H.N., Krishnaiah, A.J., Supriya, M.D.: Effect of lime on the compaction and strength behaviour of red earth treated with mine tailings. IOSR J. Mech. Civ. Eng. **2**(4), 01–06 (2012)
6. Manoj Krishna, K.V., Ramesh, H.N.: Strength and FOS performance of black cotton soil treated with calcium chloride. IOSR J. Mech. Civ. Eng. **2**(6), 21–25 (2012)
7. Jaritngam, S., Yandell, W.O., Taneerananon, P.: Development of strength model of lateritic soil-cement. Eng. J. **17**(1), 69–78 (2013)
8. Dafalla, M.A.: Effects of clay and moisture content on direct shear tests for clay-sand mixtures. Adv. Mater. Sci. Eng. 308–328 (2005)
9. IS 2720-7: Methods of test for soils, Part 7: determination of water content- dry density relation using light compaction (CED 43: Soil and Foundation Engineering) (1980)
10. IS 2720-7: Methods of test for soils, Part 13: Direct Shear test limit (CED 43: Soil and Foundation Engineering) (1980)
11. Adebisi N.O., Adeyemi, G.O., Oluwafemi, O.S., Songca, S.P.: Important properties of clay content of lateritic soils for engineering project. J. Geogr. Geol. (2) (2013)
12. Arun Kumar, U., Biradar, K.B.: Soft subgrade stabilization with quarry dust-an industrial waste. IJRET **3**(8), 383–389 (2014)
13. Chinkulkijniwat, A., Man-Koksung, E., Uchaipichat, A., Horpibulsuk, S.: Compaction characteristics of non-gravel and gravelly soils using a small compaction apparatus. J. ASTM Int. **7**, 678–693 (2010)
14. Blotz, L.R., Benson, C., Boutwell, G.P.: Estimating optimum water content and maximum dry unit weight for compacted clays. J. Geotech. Engg. **124**, 907–912 (1998)
15. Boutwell, G.: Effects of variation of fill construction on the material properties and the subsequent fill performance. J. Geotech. Engg. 907–912 (1998)
16. Donaghe, R.T., Torrey, V.H.: A compaction test method for soil-rock mixtures in which equipment size effect are minimized, Geotech. Test. J. **17**, 363–370 (1994)
17. Lotze, E.G., Datta, N.P., Tomar, K.P., Motsara, M.R.: Mineralogical composition of some red and black soils of India, Indian agricultural research institute **40B**(2), 216–226

18. Arora, K.R.: Soil mechanics and foundation engineering (Geotechnical Engineering), (First edition 1987, Standard publishers)
19. IS 2720-5: Methods of test for soils, Part 5: determination of liquid and plastic limit (CED 43: Soil and Foundation Engineering) (1985)
20. Mohan, S.D.V., Ramesh H.N.: Volume change behaviour of alkalis treated expansive and Non-expansive soils contaminated with acids. In: Proceedings of Indian Geotechnical Conference, December 22–24 (2013)

Effect of Placement Moisture Content on Swelling–Shrinkage Behaviour of Expansive Soil

Arshad K. Siddiqui and Trudeep N. Dave

Abstract Rapidly increasing infrastructural activities across the world demand suitable land for founding the substructure. The coming era shall face trouble both with the scarcity of suitable land as well as challenges to deal with the existence of problematic soils at the site. Volumetric changes in the form of swelling and shrinkage with moisture variation are most commonly observed in expansive soils. Large damage/distress to the infrastructure founded on this type soils has been observed. Understanding of swelling and shrinkage of expansive soils with moisture variation is of primary importance. This paper presents an experimental study on determination of swelling–shrinkage and its variation with time and placement moisture content. An experimental setup has been designed and developed to accommodate three soil samples of 100 mm diameter and 100 mm height and swelling pressure measurement through constant volume method. Soils were procured from Delhi–Mumbai Expressway site near Ankleshwar, Gujarat, which was later aired dried and pulverized. Soil samples were prepared at three different preparation moisture content (i) at optimum moisture content, (ii) 5% on the dry side of optimum and (iii) 5% on the wet side of optimum. Experimental findings revealed maximum swelling pressure generation within first 24 h after commencement of the experiment. Swelling pressures of 41.8 kPa, 59.44 kPa and 23.22 kPa were observed for specimen prepared at optimum moisture content, at 5% dry side of optimum and 5% wet side of optimum, respectively. While swelling pressure found to increase till seven days, though at a lower rate, observed swelling pressure values were 55.73 kPa, 83.6 kPa and 37.25 kPa for specimen prepared at optimum moisture content, at 5% dry side of optimum and 5% wet side of optimum, respectively. The % shrinkage area were found as 22%, 33.8% and 15.2% for the samples prepared at OMC, WSO (OMC + 5%) and DSO (OMC-5%), respectively.

Keywords Expansive soil · Swelling pressure · Moisture content · Experimental study

A. K. Siddiqui · T. N. Dave (✉)
Civil Engineering Department, Institute of Infrastructure Technology Research and Management, Ahmedabad 380026, India
e-mail: trudeepdave@iitram.ac.in

1 Introduction

Expansive soil undergoes significant volume change in the form of swelling or shrinkage. The change in moisture content and temperature causes volumetric deformation in the soil with time [1]. Expansive soils are mainly found in arid and semi-arid region of world. The amount of damages caused by such type of soil is alarming such as damages to road, underground utilities, and building. The factors affecting the swelling/shrinkage behaviour of expansive soil include moisture content, clay mineralogy, dry density, index properties, pore fluid, and time. The negative electric charges on the surface of clay minerals, strength of interlayer bonding, and cation exchange capacity all contribute to the swelling potential of expansive soil. According to previous studies, the highest value of liquid limit and shrinkage limit belongs to montmorillonite (clay mineral), while this group possess the lowest shrinkage limit in the soil [2]. In a swelling type of soil, two different processes take place when a swelling soil dries or get saturated. During drying, soil decreases its volume by shrinkage, and desiccation cracks appear because of internal stresses in the shrunken and dried soil mass [3]. As a result of shrinkage, soil decreases its height by subsidence. On the other hand, during wetting, the soil increases its volume by swelling, the cracks are closed, and soil level rises [4–6].

2 Problem Description

Literature review highlighted the fact that very limited studies were performed to understand swelling and shrinkage behaviour of expansive soil and their variation with change in temperature and moisture content. Further, the variation in swelling and shrinkage characteristics of soil with time was not clear. Though a number of studies related to shrinkage behaviour of expansive soil were conducted, most of them were performed on the soil prepared at wet side of optimum and study related to soil sample prepared at dry side of optimum and optimum moisture content is sparse. Hence, this study is aimed at evaluating effect of placement moisture content and time on both swelling and shrinkage behaviour of expansive soils.

3 Laboratory Scale Modelling

The soil used in this study was procured from Delhi–Mumbai Expressway site near Ankleshwar city. The properties of soil are given in Table 1.

As per Unified Soil Classification System, the soil was classified as CH type. Experimental investigation was carried out to observe swelling phenomenon in expansive soil through laboratory scale model setup. The schematic diagram is shown in Fig. 1. The soil sample was compacted in a mould of size 18 cm × 10 cm having

Table 1 Summary of soil properties used in experimental study

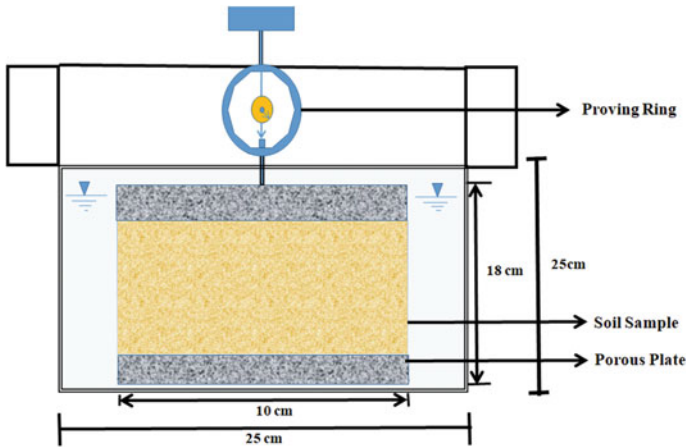| Property	Value
Specific gravity	2.51
Liquid limit	76.12%
Plastic limit	37.26%
Shrinkage limit	12.93%
Optimum moisture content	25.81%
Maximum dry density	1.5 g/cm^3

Fig. 1 Swelling apparatus model

porous medium at both top and bottom side, and then, the mould containing soil sample was placed in a 25 cm high cylindrical container of 25 cm diameter containing water to full height. Above the top porous plate, loading pad was placed, and a proving ring was attached with it to monitor swelling pressure variation with time. Swelling pressure was monitored up to 7 days after placing the mould assembly in to the cylindrical container.

Tests were performed by preparing soil samples at (i) optimum moisture content (OMC), (ii) moisture content 5% dry side of OMC and (iii) moisture content 5% wet side of OMC. Experimental findings revealed maximum swelling pressure generation within first 24 h after commencement of the experiment. Swelling pressures of 41.8 kPa, 59.44 kPa and 23.22 kPa were observed for specimen prepared at optimum moisture content, at 5% dry side of optimum and 5% wet side of optimum, respectively. While swelling pressure found to increase till seven days, though at a lower rate, observed swelling pressure values were 55.73 kPa, 83.6 kPa and 37.25 kPa for specimen prepared at optimum moisture content, at 5% dry side of optimum and 5% wet side of optimum, respectively (Figs. 2 and 3).

Fig. 2 Swelling test on soil using apparatus

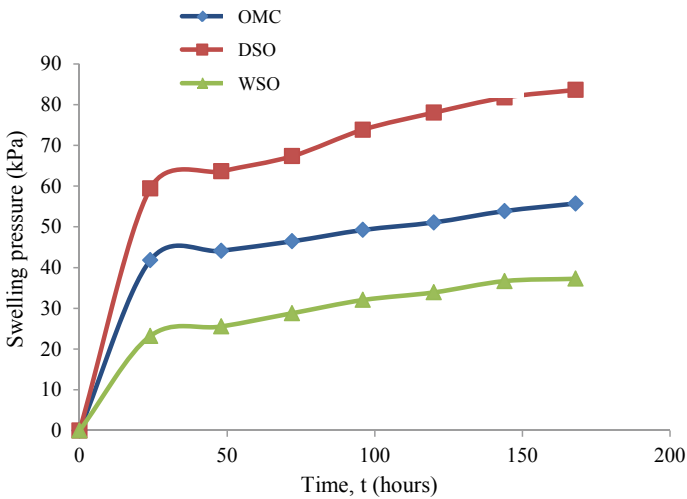**Fig. 3** Variation of swelling pressure with time

4 Image Analysis Techniques

The process of conversion of raw image into an improved image to obtain the meaningful data is known as image processing. Digital camera was used to capture images of soil sample at different time interval and further image processing. Image processing involves converting the initially captured RGB image into grey-scale

image, and then, binary image is obtained by thresholding the grey-scale image (Fig. 4).

The steps involved during image processing are mentioned below:

(a) Preparation of raw image:

During preparation of raw image, image enhancement is done by increasing contrast, sharpness and adjusting brightness, saturation and colour. It can further be changed into binary images for edge separation.

(b) Grey-scale processing:

The picture taken by camera is an RGB (red–green–blue) image. In ImageJ software, "circular crop" option can be used to crop any circular area depending upon shape and size of mould. Preparation of image consists of selecting the inner circular area of mould and cropping the outer area to get a centred RGB image with white/black background. This image is then converted to 8-bit grey-scale image by selecting option "Image-type-8 bit".
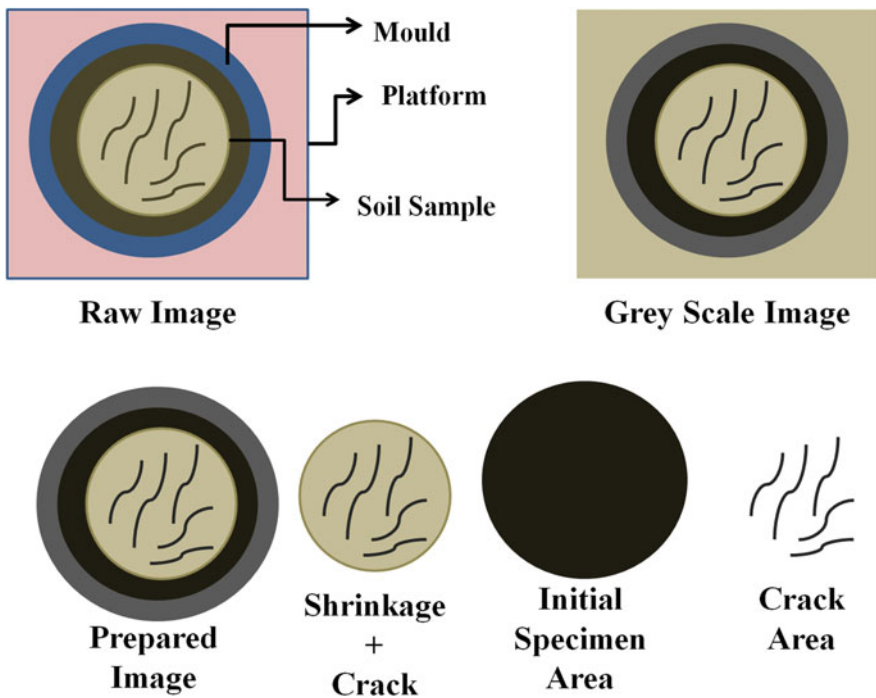

Fig. 4 Various steps involved during image processing

(c) Image segmentation:

Image segmentation is done to separate the crack and shrinkage area from intact soil. It is done by thresholding the grey-scale image with a fixed threshold value. In ImageJ, it can be done by going to the option Image-Adjust-Threshold.

(d) Determination of shrinkage area:

The shrinkage area (%) can be determined by the equation given below:

$$\% \text{ SA} = \left(\frac{S_a}{I_{sa}} \right) \times 100$$

(1)

SA (%) = Shrinkage area (square pixel);
I_{sa} = Initial specimen area.

For the preparation of soil specimens, the soil samples were mixed at different moisture content, i.e., DSO (OMC − 5%), OMC, WSO (OMC + 5%), and these mixes were kept in air-tight polythene bags for 48 h to homogenize the moisture content without any loss of water due to evaporation. Specimens were prepared in the properly greased cylindrical mould of dia. 10 cm and thickness 1.5 cm. Before placing them in mould, they were suitably compacted to the maximum density by means of compactor and collar. After compaction, collar was removed and specimen surface was levelled by using knife. All specimens were kept at two different temperature of 27 and 40 °C for drying at least for 72 h. Specimens were brought to the setup where camera was placed on a platform. Bubble tube was used to ensure that the camera was placed perfectly. Raw images obtained were then processed and analysed by using image analysis technique. For this purpose, a high resolution digital camera 'Canon Coolpix B700' was used, and images were captured from a fixed height of 15 cm.

Figure 5 presents various steps of image processing. In order to determine the shrinkage area, soil samples were prepared at different moisture contents, i.e., DSO (OMC-5%), OMC, and WSO (OMC + 5%), and image processing was performed using ImageJ software. The samples were kept under the influence of two different temperatures, i.e., 27 and 40 °C. The shrinkage area of the soil samples were quantified at various time interval. The results are shown in Figs. 6, 7 and 8 for samples at dry side of optimum, optimum moisture content and wet side of optimum, respectively.

Figure 6 represents the variation in shrinkage area with time and temperature variations while maintaining sample preparation moisture content, i.e., DSO (OMC − 5%). As presented, the sample placed at 40 °C shows higher shrinkage area compared to the sample placed at 27 °C. During first three hours, % shrinkage area for the samples placed at room temperature (27 °C) was found to be 3.5%, while for the sample placed at 40 °C was observed to be 4.57%. After 72 h, the percentage shrinkage area was found as 12.6% and 15.2%, for samples maintained at 27 °C and 40 °C, respectively.
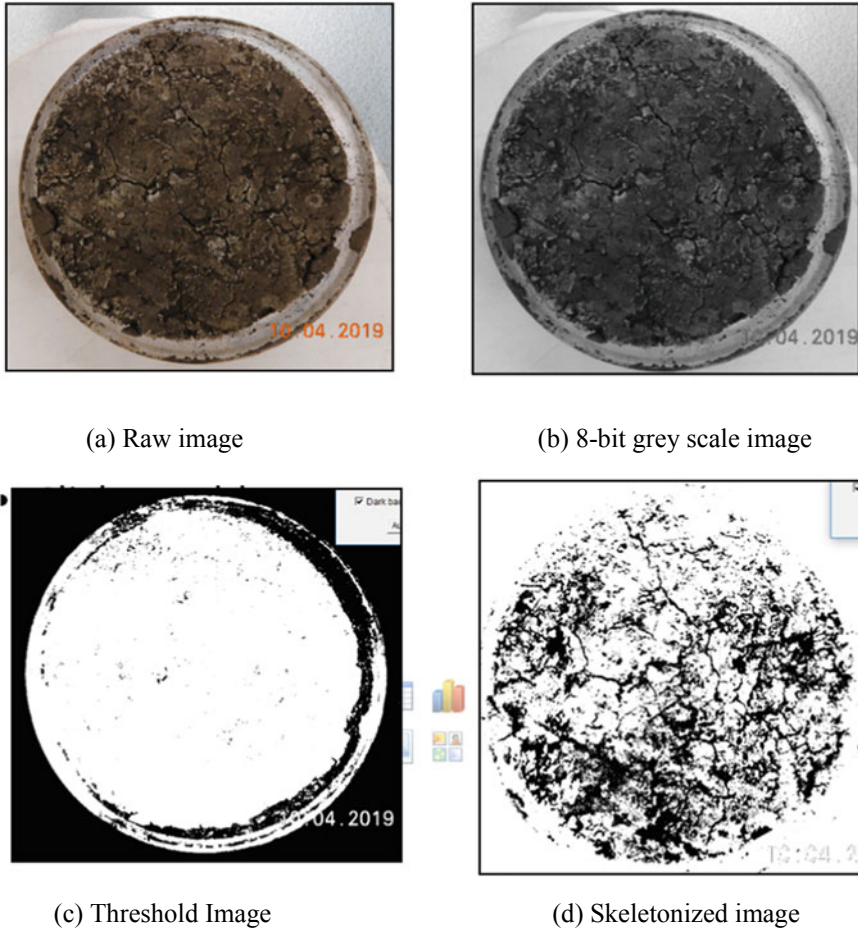
(a) Raw image

(b) 8-bit grey scale image

(c) Threshold Image

(d) Skeletonized image

Fig. 5 Outcomes of image analysis techniques

Figure 7 presents the variation in shrinkage area with time and temperature variations while maintaining sample preparation moisture content, i.e., at OMC. As presented, the sample placed at 40 °C shows higher shrinkage area compared to the sample placed at 27 °C. During first three hours, % shrinkage area for the samples placed at room temperature (27 °C) was found to be 5%, while for the sample placed at 40 °C was observed to be 6.5%. After 72 h, the percentage shrinkage area was found as 15% and 20.9%, for samples maintained at 27 °C and 40 °C, respectively.

As presented in Figs. 6 and 7, drop in the shrinkage area was observed during 40–50 h. This phenomenon was not expected to associate with variation in placement moisture content or drying temperature, and further studies are required to reconfirm the observed behaviour.
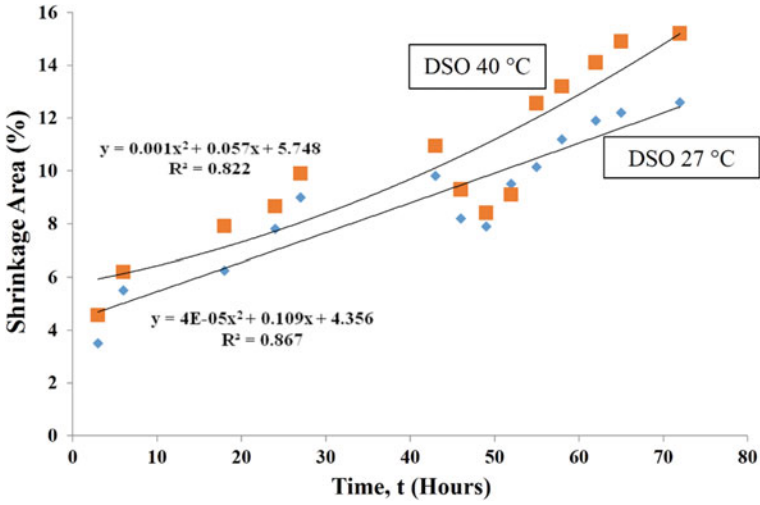
Fig. 6 Variation of shrinkage area with time at different temperature for DSO samples
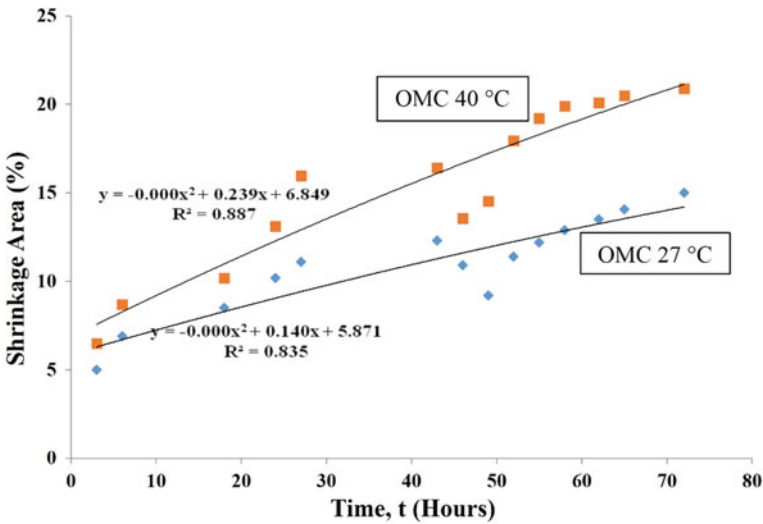
Fig. 7 Variation of shrinkage area with time at different temperature for OMC sample

Figure 8 presents the variation of shrinkage area with time and temperature variation while maintaining sample preparation moisture content, i.e., WSO (OMC + 5%). As presented, the sample placed at 40 °C shows higher shrinkage area compared to the sample placed at 27 °C. During first three hours, % shrinkage area for the samples kept at room temperature (27 °C) was found to be 6%, while for the sample placed at

Fig. 8 Variation of shrinkage area with time at different temperature for WSO sample

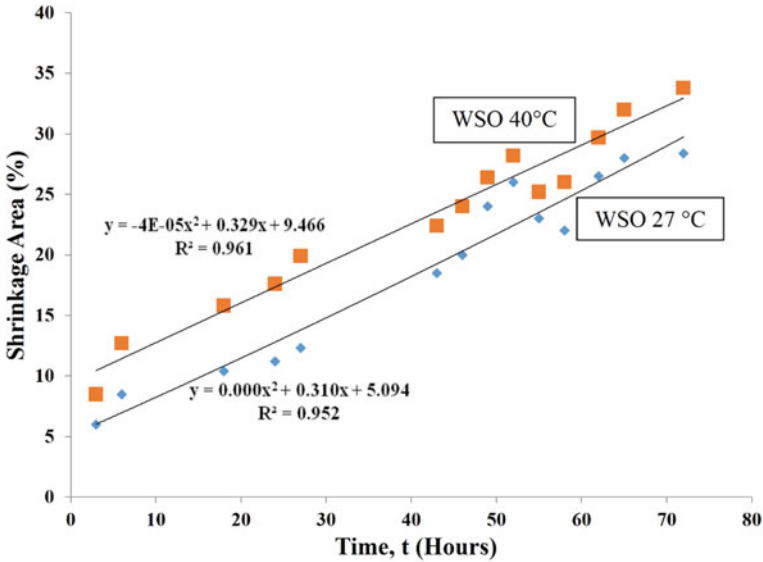40 °C was observed to be 8.5%. After 72 h, the percentage shrinkage area was found as 28.4% and 33.8%, for samples maintained at 27 °C and 40 °C, respectively.

5 Conclusions

Based on experimental investigation, following conclusions were made:

- Among the samples tested, the swelling pressure was maximum in case of soil sample prepared at DSO (OMC − 5%), and minimum in soil sample prepared at WSO (OMC + 5%).
- Experimental findings revealed that maximum swelling pressure generation was within first 24 h after commencement of the experiment. Swelling pressures of 41.8 kPa, 59.44 kPa and 23.22 kPa were observed for specimen prepared at optimum moisture content, at 5% dry side of optimum and 5% wet side of optimum, respectively. While swelling pressure found to increase till seven days, though at a lower rate, observed swelling pressure values were 55.73 kPa, 83.6 kPa and 37.25 kPa for specimen prepared at optimum moisture content, at 5% dry side of optimum and 5% wet side of optimum, respectively.
- Among the samples tested, the shrinkage area is maximum in case of soil sample prepared at wet side of optimum and minimum in case of soil sample prepared at dry side of optimum. The sample kept at greater temperature shows greater area of shrinkage irrespective of initial moisture content.

- The % shrinkage area was found as 22%, 33.8% and 15.2% for the samples prepared at OMC, WSO (OMC + 5%) and DSO (OMC-5%), respectively.

References

1. Chen, F.H.: Foundations on Expansive Soils. Elseveir Scientific Publishing Co., Amsterdam (1975)
2. White, W.A.: Atterberg plastic limits of clay minerals. Am. Mineral. **34**, 508–512 (1949)
3. Taboada, J.: A fuzzy expert system application to the evaluation of ceramic- and paper quality kaolin 287–297 (2006)
4. Low, F.P., Margheim F.J.: The swelling of clay: I-basic concepts and empirical equations 1. Soc. Sci. Soc. Am. J. (1979)
5. William M.S., Singer M.J.: A new method of measuring shrink-swell potential using soil pastes **1** (1976)
6. Parker, J.C., Amos, D.F., Zelazny, L.W.: Water adsorption and swelling of clay minerals in soil systems. Soil Sci. Soc. Am. J. **46**, 450–456 (1982)

Foundation Bearing Capacity Estimation on Rock-Mass Using Hoek–Brown Failure Criterion and Equivalent Mohr–Coulomb Parameters

Shikhar Prakash , **Dhiraj Raj** , **and Yogendra Singh**

Abstract In general practice, the shallow foundations serve as economic and reliable solution to support high-rise buildings, bridges, and other heavy structures constructed on rock-mass. The aim of the present study is to simulate fractured homogenous rock-mass in finite element framework and to obtain bearing capacity of a strip footing. For this purpose, both displacement-based finite element (FE) analysis and finite element limit analysis (FELA) are carried out and results are compared. Finite element models of the flat rock-mass with supported foundations are developed in finite element package ABAQUS. The foundation is modeled using two-node cubic beam (B23) and rock-mass using plane-strain quadratic (CPE8R) element with reduced integration, having "Equivalent Mohr–Coulomb parameters." Models with the same rock and foundation properties are modeled in OptumG2 based on FELA to obtain the upper-bound (UB) and lower-bound (LB) solutions with a constitutive model based on the Hoek–Brown failure criterion. The comparative study illustrates the critical issues that arise while implementing the failure criterion using the equivalent Mohr–Coulomb parameters, particularly in bearing capacity estimation, where the overburden pressure is low.

Keywords Foundation · Bearing capacity · Finite element method · Finite element limit analysis · Hoek–brown failure criterion · Equivalent mohr–coulomb parameters

S. Prakash · D. Raj (✉) · Y. Singh
Indian Institute of Technology, Roorkee 247667, India
e-mail: dhirajraj.iitr@gmail.com

S. Prakash
e-mail: sprakash@eq.iitr.ac.in

Y. Singh
e-mail: yogenfeq@iitr.ac.in

1 Introduction

Bearing capacity estimation is an important design consideration in the construction of foundations to support high-rise buildings, bridges, and other heavy structures. The type of geo-material supporting the foundation uniquely characterizes its bearing capacity. Various methods have been developed in past for the accurate estimation of bearing capacity of soil, the most widely used foundation material in case of shallow foundations. However, it has been observed that in specific cases foundations are also placed on rocks and majority of rocks have been proven to be an excellent foundation material. The engineering characteristics of rock have been found to be different from the soil. Thus, it is necessary to exclusively establish techniques for the bearing capacity estimation of rocks. However, unlike soil, simple closed form solutions or rigorous charts for bearing capacity estimation for rock-mass are limited owing to its more complex natural state as compared to soil.

In the past, efforts have been made to estimate the bearing capacity of rock-mass. The non-homogenous, discontinuous rock-matrix with the presence of naturally existing faults, bedding planes, and fractures makes it difficult to derive a simple expression for the bearing capacity estimation using the limit equilibrium method [1]. Largely, the bearing capacity estimation has been carried out using the nonlinear Hoek–Brown failure criterion [2] and its subsequent modifications, as the linear Mohr–Coulomb was found inconsistent in capturing the pressure dependent failure envelope exhibited by the rock-mass. Serrano et al. [3] have obtained the bearing capacity using the modified Hoek–Brown criterion [4] for a strip footing placed on a weightless rock medium using the method of stress characteristics. Further, MSC was employed by Keshavarz, Kumar [5] to obtain bearing capacity for strip and circular footings and by Keshavarz et al. [6] for seismic bearing capacity. Yang and Yin [7] employed the limit analysis theorems [8] to find the upper-bound solutions for ultimate bearing capacity using the modified HB criterion. Further, limit analysis theorem was employed by Merifield et al. [9] to obtain both the upper- and lower-bound estimates of the bearing capacity using the generalized HB criterion [10] and by Saada et al. [11] for its upper bound estimates. Numerical analysis also offers a good tool for the estimation of bearing capacity of rock-mass. However, it is difficult to explicitly model fractures and discontinuities that occur in rock mass using the displacement finite element method. So mostly bearing capacity estimation is carried out using the HB criterion in the elastoplastic domain of the conventional displacement-based finite element method. It is also observed that "Equivalent Mohr–Coulomb Parameters" as suggested by Hoek et al. [10] are used in the FE framework for the bearing capacity estimation. Clausen [12] implemented the modified HB criterion in the FE framework without any corner or apex approximations to obtain the bearing capacity of circular footings on rock-mass using the axis-symmetric FE model. However, such a comprehensive implementation of the HB criteria in the FE framework is limited and the use of "Equivalent Mohr–Coulomb Parameters" is quite prevalent.

The primary aim of this work is to carry out a comparative study of the two methods of implementing the HB criteria in the FE framework to understand and illustrate the fine intricacies involved in the implementation of the HB criterion.

2 Generalized Hoek–Brown Failure Criterion

It is evident from a substantial amount of experimental evidence that unlike soil, the failure envelope of almost all rock masses is nonlinear in the $\sigma_1 - \sigma_3$ stress space. This nonlinearity has a significant effect on the bearing capacity estimation. Various researchers have given semi-empirical nonlinear failure criteria to capture the observed nonlinearity in the experiments. However, the Hoek–Brown failure criterion [2] given in 1980 and its subsequent updates in the year 1983, 1988, 1992, 1995, 1997, 2001, 2002, 2007, and 2018 has been the most widely accepted failure criterion. A detailed history of the development of the criteria over the years can be understood from [13].

In the present study, the generalized Hoek–Brown failure criterion [10] is used which is written in terms of principal stress as given in Eq. (1).

$$\sigma_1^{'} = \sigma_3^{'} + \sigma_{ci}\left(m_b \frac{\sigma_3^{'}}{\sigma_{ci}} + s\right)^{\alpha} \tag{1}$$

where σ_{ci} represents the uniaxial compressive strength of intact rock mass obtained through experiment, σ_1 and σ_3 represent the major and minor principal stresses, respectively, and α, m_b and s represent the dimensionless material parameters which are defined in Eqs. (2–4).

$$\alpha = \tfrac{1}{2} + \tfrac{1}{6}(e^{\frac{-\text{GSI}}{15}} - e^{\frac{-20}{3}}) \tag{2}$$

$$m_b = m_i \exp(\tfrac{\text{GSI}-100}{28-14D}) \tag{3}$$

$$s = \exp(\tfrac{\text{GSI}-100}{9-3D}) \tag{4}$$

where geological strength index (GSI) signifies the state of fracture in the natural state of the rock, varying between 10 to 100 with 10 and 100 representing highly fractured and unfractured state, respectively. *D,* Disturbance factor signifies the degree of disturbance in the rock matrix due to blasting, varying between 0 and 1 with 0 and 1 representing the undisturbed and highly disturbed state, respectively. Both of the parameters are non-dimensional in situ parameters obtained from the observation from the site. m_i is a dimensionless parameter that represents the type of rock, varying from 4 for very fine weak rock like claystone to 33 for coarse igneous rock like granite.

It is obtained experimentally however if the test data is not available then Hoek [14] has provided approximate values for five types of rocks.

Further, the unconfined strength of the rock-mass can be obtained from Eq. (1) by substituting $\sigma_3 = 0$ and given as in Eq. (5).

$$\sigma_c = \sigma_{ci} s^\alpha \tag{5}$$

Here, it can be observed that the parameters s and α, which factor the fracture state of the rock, limit the value of the unconfined compressive strength of the fractured rock-mass to be less than the intact rock mass.

Also, the tensile strength of the rock-mass is given by Eq. (6).

$$\sigma_t = -\frac{s\sigma_{ci}}{m_b} \tag{6}$$

Here, it can be observed that parameter s limits the tensile strength to be less than the unconfined compressive strength of the intact rock. Also, it can be seen that m_b reduces the tensile strength of the rock-mass as the rock type improves from soft carbonate rocks to hard igneous rocks owing to their brittle nature.

2.1 Equivalent Mohr–Coulomb Parameters

Mohr–Coulomb failure criteria are a well-established failure criterion for soil and it is widely used in the predefined constitutive models of the prevalent finite element tools. Owing to this fact, the developers of the HB failure criteria have given an "Equivalent Mohr–Coulomb Parameters" using the regression analysis in Hoek et al. [10]. An equivalent c' and ϕ' values were obtained by fitting an average linear Mohr–Coulomb relationship to the curve generated by solving Eq. 1 for a range of minor principal stress values defined by $\sigma_t < \sigma_3 < \sigma'_{3max}$. As a result of this regression analyses the values of c' and ϕ' were given by Eqs. (7–8).

$$c' = \frac{\sigma_{ci}\left[(1+2\alpha)s + (1-\alpha)m_b\sigma'_{3n}\right]\left(s + m_b\sigma'_{3n}\right)^{\alpha-1}}{2(1+\alpha)(2+\alpha)\sqrt{1+(6\alpha m_b(s + m_b\sigma'_{3n})^{\alpha-1})}} \tag{7}$$

$$\phi' = \sin^{-1}\left[\frac{6\alpha m_b\left(s + m_b\sigma'_{3n}\right)^{\alpha-1}}{2(1+\alpha)(2+\alpha) + 6\alpha m_b(s + m_b\sigma'_{3n})^{\alpha-1}}\right] \tag{8}$$

where $\sigma_{3n} = \sigma'_{3max}/\sigma_{ci}$. Rest other parameters are same as defined in Eq. (1–4). A major concern above is the selection of the maximum minor principal stress, σ'_{3max} up to which the regression analysis gives satisfactory results. Hoek et al. [10] have provided a comprehensive guidelines for selecting the value of σ'_{3max} for slopes as

well as shallow and deep tunnels. However, in case of bearing capacity of foundation placed on rock, no such recommendation is provided. Only an approximate value of $\sigma'_{3max} = 0.25 \, \sigma_{ci}$ is suggested by Hoek, Brown [15] with a guideline to always verify the validity of the recommendation with respect to the stress range encountered in a specific problem.

Calibration with Hoek–Brown criterion. In the present study, the equivalent Mohr–Coulomb parameters have been obtained with the maximum minor principal stress, σ'_{3max} considered to be equal to 0.25 times the unconfined compressive strength of the rock-mass, σ_{ci}. The c' and ϕ' values obtained from Eqs. 7–8 have been used to define the Mohr–Coulomb criteria given by Eq. (9) for different input parameters of the Hoek–Brown failure criterion.

$$\tau = c + \sigma \tan \phi \tag{9}$$

Further, the Mohr–Coulomb failure criterion has been expressed in terms of principal stresses, σ_1 and σ_3 using the Eq. (10) and plotted on the principal stress plane with the Hoek–Brown failure criterion so that the efficacy of this technique for different rock properties can be studied. Illustrative graphs were shown in Figs. 1 and 2.

$$\sigma'_1 = \frac{2c' \cos \phi'}{1 - \sin \phi'} + \frac{1 + \sin \phi'}{1 - \sin \phi'} \sigma'_3 \tag{10}$$

It has been observed from Fig. 1 that as the m_i value of the rock-mass increases, the curvature of Hoek–Brown failure criterion increases. The increase in curvature can be attributed to the improvement in the quality of rock, from being soft at lower
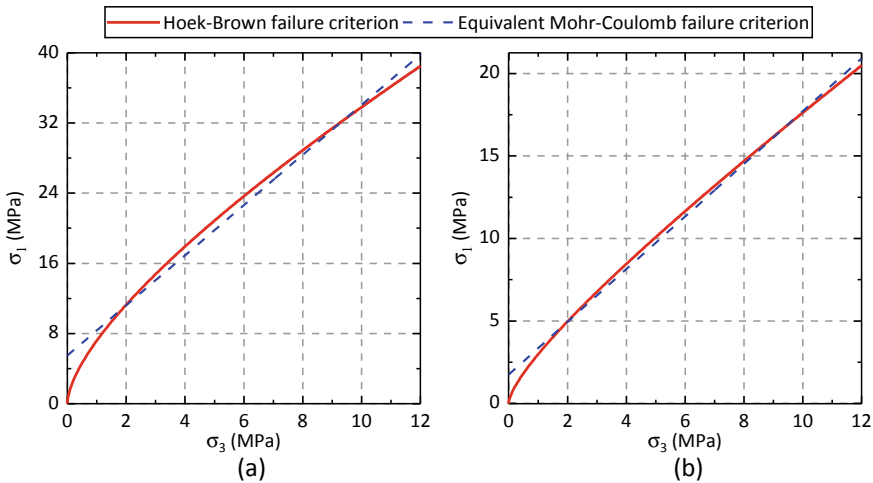

Fig. 1 Failure criteria in principal stress plane for $GSI = 10$, **a** $m_i = 35$ and **b** $m_i = 5$
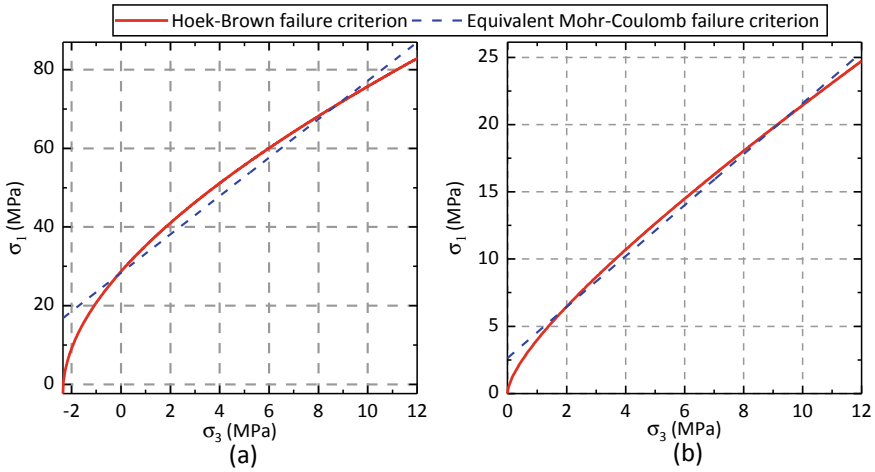
Fig. 2 Failure criteria in principle stress plane for $m_i = 10$, **a** GSI $= 90$ and **b** GSI $= 10$

m_i and hard at higher values. With the increase in curvature, the two criteria lose agreement with each other.

Further, it has been observed from Fig. 2 that as the GSI value of rock increases the curvature of the Hoek–Brown failure criterion increases. The increase in curvature can be attributed to the improvement in the fracture state of rock, from being highly fractured at lower values to intact at higher values. With the increase in curvature, the agreement between the two graphs reduces.

It was also observed that as the fracture sate of rock improves with the increasing *GSI* the tensile strength of the rock also increases. The rock-mass gains its tensile strength from the intact.

From Figs. 1 and 2, it has been noted that for lower ranges of principal stresses, the equivalent Mohr–Coulomb failure criteria will overestimate the strength by a significant amount. This is a concerning issue particularly in the case of problems involving low over-burden pressure such as bearing capacity problem.

Further, it has been suggested that, since the Hoek–Brown failure criterion limits the tensile strength of the rock-mass by Eq. 6, it would be advantageous to estimate the bearing capacity factor using the modified Mohr–Coulomb criteria with a tension-cutoff corresponding to tensile strength of the rock-mass so that a more comprehensive comparative analysis could be done.

3 Comparative Study

In the present study, in order to understand and illustrate the cogency of the calibration technique involving "Equivalent Mohr–Coulomb Parameters," a comparative study

has been carried out by displacement-based finite element (DBFE) method using ABAQUS [16] and finite element limit analysis (FELA) method using OptumG2 [17].

3.1 DBFE with "Equivalent Mohr–Coulomb Parameters"

A DBFE analysis has been carried out to estimate the bearing capacity of the rock-mass whose strength was characterized using the "Equivalent Mohr–Coulomb parameters" in the Mohr–Coulomb and the modified Mohr–Coulomb material model with a tension cutoff. A 2D plane-strain FE model of a footing resting on the rock-mass has been developed. A DBFE analysis has been carried out to obtain the collapse load Q using the load–displacement curve and bearing capacity factor N_σ given by Eq. (11) as suggested by [9].

Finite element (FE) model. A 2D plane-strain FE model of a rigid strip footing resting on the rock mass has been developed as shown in Fig. 3. The dimensional domain and the mesh density, as shown in Fig. 3, has been ascertained after carrying out the sensitivity and convergence study. The base and the lateral boundaries of the model have been set as fixed in x & y directions and x-direction (as per the coordinate system shown in Fig. 3), respectively. The rigid foundation has been modeled as deformable elastic beam using two-node cubic beam (B23) and rock-mass having "Equivalent Mohr–Coulomb parameters" using the plane-strain quadratic (CPE8R) element with reduced integration. Both the Mohr–Coulomb and Modified Mohr–Coulomb failure criteria with a tension cutoff have been used to characterize the strength of rock-mass. An associated flow rule ($\psi = \phi$, where ψ is the dilation angle) has been assumed to obtain the plastic strain.

Load displacement curve. In order to obtain the load–displacement curve, a conventional displacement-based finite element method was employed in the elastoplastic
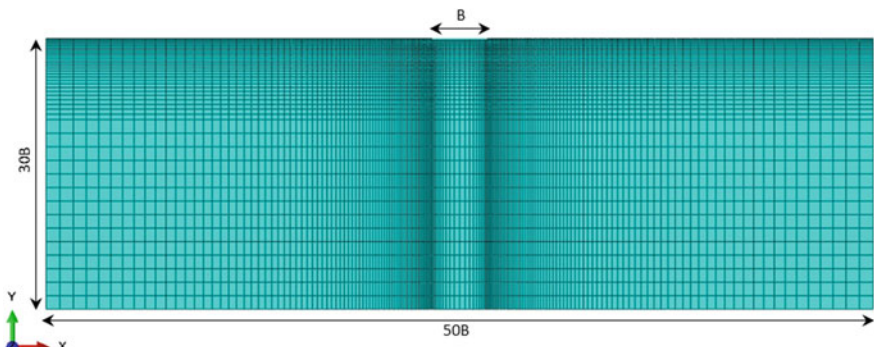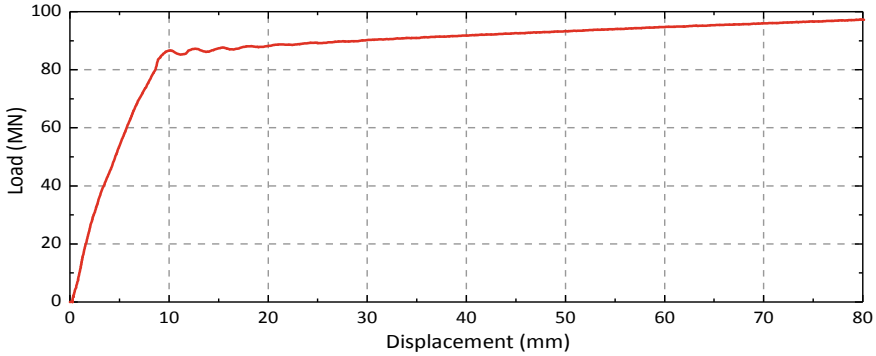

Fig. 3 FE model

Fig. 4 Load–displacement curve

framework. The strength criteria of the rock-mass defined the yield criteria in this framework. Forced displacement has been applied to the footing nodes corresponding to the footing displacement and the sum of the reactions at the footing node has been considered as the load carried by the rock-mass. The displacement and the load at each time step have been plotted to obtain the load displacement curve. The load carrying capacity of the rock-mass, Q, is considered corresponding to the yield as shown in Fig. 4

Estimation of N_σ: A non-dimensional bearing capacity factor, as proposed by Merifield et al. [9], is given by Eq. (11).

$$N_\sigma = \frac{q_u}{\sigma_{ci}} \tag{11}$$

where σ_{ci} is the unconfined compressive strength of the rock-mass and q_u is the bearing capacity of the rock-mass obtained by dividing the load carrying capacity, and Q is obtained from the load–displacement by the area of the footing.

3.2 FELA with Hoek–Brown Failure Criterion

A FELA has been carried out to estimate the bearing capacity of the rock-mass with the same properties as used in the DBFE analysis. However, the strength of the rock-mass was characterized using the Hoek–Brown failure criterion instead of the equivalent MC parameters. A 2D plane-strain FELA model of a footing resting on the rock-mass has been developed. A FE limit analysis has been carried out to obtain the collapse load Q using the limit analyses theorem as given by Chen [8] in the finite element FE framework provided in the OptumG2 software. N_σ has been similarly calculated using Eq. (11).
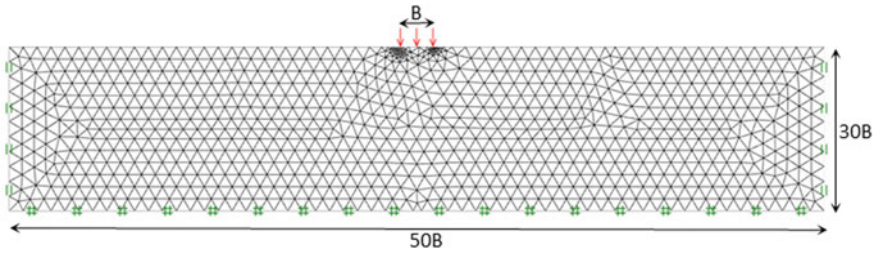
Fig. 5 FELA model

Finite element (FE) model. A 2D plane-strain FE model of a rigid footing resting on the rock-mass has been developed as shown in Fig. 5. The dimensional domain as shown in Fig. 5 has been ascertained after carrying out the sensitivity study. Adaptive meshing based on shear dissipation has been employed.

As shown in Fig. 5, at the base of the FE model, the displacement in both the directions (i.e., both x and y displacements) is restrained, while for the lateral boundaries, only vertical displacement is allowed (i.e., x displacement is zero). The strip foundation has been modeled using "plate" element. The interface material between the foundation and the surrounding rock-mass has been considered to be same as the rock-mass. An elastoplastic constitutive model based on Hoek–Brown failure criterion and following associated flow rule ($\psi = \phi$, where ψ is the dilation angle) has been used for modeling of rock-mass using triangular elements with LB and UB formulations.

Estimation of N_σ: In the FELA framework, the load carrying capacity of the rock-mass, the upper-bound (UB) and lower-bound (LB) estimates of Q have been obtained using the limit analysis theorem. The average of UB and LB estimates has been further used to estimate the non-dimensional factor, N_σ in a similar manner as described in the above section.

3.3 Comparison and Discussion

The comparative study in this work has been done to primarily examine the efficacy of the "Equivalent Mohr–Coulomb parameters." For this purpose, N_σ factors have been ascertained using the equivalent MC parameters with and without tension cutoff for the specified stress range ($\sigma_t < \sigma_3 < \sigma'_{3max} = 0.25\sigma_{ci}$) in the DBFE and using the HB criterion parameters in the FELA framework, respectively. The results are illustrated, compared, and validated with [9] in Table 1 and Fig. 6.

It has been observed that the bearing capacity factor, N_σ has a good aggrement with [9] when the nonlinear Hoek–Brown failure criteria is used in the bearing capacity estimation.

Table 1 N_σ values obtained using different analyses

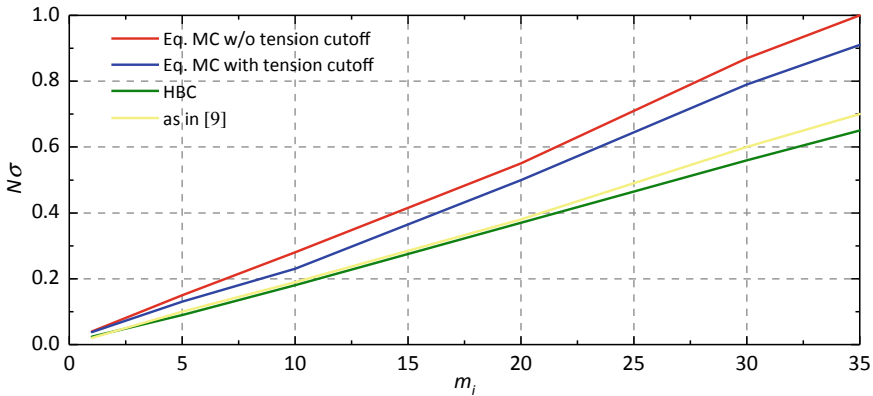| m_i (rock type)	N_σ using MC criteria w/o tension cut-off	N_σ using MC criteria with tension cutoff	N_σ using HBC criteria	N_σ from [9]
1	0.040	0.038	0.024	0.020
5	0.150	0.130	0.090	0.100
10	0.280	0.228	0.180	0.190
20	0.550	0.500	0.370	0.380
30	0.870	0.780	0.560	0.600
35	1.000	0.910	0.650	0.700

Fig. 6 N_σ values corresponding to different analyses

However, N_σ varies by a significant amount when estimated using the equivalent Mohr–Coulomb parameters. The variation varies from 40% at $m_i = 1$ (i.e., for very soft rock) upto 54% at $m_i = 35$ (i.e., for very hard rock). The difference in the values increases as the rock type improves from soft to hard rocks. This disagreement in values can be attributed to the disagreement in the failure criteria of the two techniques. N_σ values with the equivalent MC parameters are over-estimated because in the stress range usually encountered in the bearing capacity problem, the equivalent linear criterion over-estimates the strength in comparison to the nonlinear HB criterion.

Although the use of modified MC criteria with a tension cutoff reduces the N_σ value but the reduction is not significant. The tension cutoff although limits the MC criteria upto the tensile strength of the rock-mass as given in Eq. (6), but the limit to the strength is not leading upto significant reduction in the N_σ values as can be seen from Fig. 6.

This leads to the assertion that the over-estimation in the N_σ is primarily due to the strength over-estimation by the linear MC failure criterion in the low stress range

and marginally due to the incompetence of the linear MC criterion to incorporate the limiting tensile strength of the rock-mass.

4 Conclusions

In the present study, it is concluded that in case of bearing capacity estimation of footings placed on the highly fractured homogenous rock-mass, characterized by the nonlinear Hoek–Brown failure criterion, the usage of equivalent Mohr–Coulomb parameters as suggested by Hoek et al. [10] over-estimates the N_σ values by a significant amount.

This linearization technique has been found to be very sensitive to the stress range encountered in the problem, and thus should be implemented cautiously in the FE framework, with due consideration of the stress range ecountered in a specific problem.

As most of the available commercial software are provided with a graphical user interface (GUI)-based material model based on linear MC criteria, the use of equivalent MC criterion is quite prevalent. It is strongly recommended that in case of bearing capacity problems, the equivalent MC criteria should be implemented, cautiously.

References

1. Meyerhof, G.: The ultimate bearing capacity of foudations. Geotechnique **2**(4), 301–332 (1951)
2. Hoek, E., Brown, E.T.: Empirical strength criterion for rock masses. J. Geotechn. Geoenviron. Eng. **106**(ASCE 15715), 1013–1035 (1980)
3. Serrano, A., Olalla, C., Gonzalez, J.: Ultimate bearing capacity of rock masses based on the modified Hoek-Brown criterion. Int. J. Rock Mech. Mining Sci. **6**(37), 1013–1018 (2000)
4. Hoek, E., Wood, D., Shah, S.: A modified Hoek–Brown failure criterion for jointed rock masses. In: Rock Characterization: ISRM Symposium, Eurock'92, Chester, UK, 14–17 September 1992 1992, pp. 209–214. Thomas Telford Publishing
5. Keshavarz, A., Kumar, J.: Bearing capacity of foundations on rock mass using the method of characteristics. Int. J. Numer. Analyt. Methods Geomech. **42**(3), 542–557 (2018). https://doi.org/10.1002/nag.2754
6. Keshavarz, A., Fazeli, A., Sadeghi, S.: Seismic bearing capacity of strip footings on rock masses using the Hoek-Brown failure criterion. J. Rock Mech. Geotech. Eng. **8**(2), 170–177 (2016). https://doi.org/10.1016/j.jrmge.2015.10.003
7. Yang, X.-L., Yin, J.-H.: Upper bound solution for ultimate bearing capacity with a modified Hoek-Brown failure criterion. Int. J. Rock Mech. **42**(4), 550–560 (2005). https://doi.org/10.1016/j.ijrmms.2005.03.002
8. Chen, W.-F.: Limit Analysis and Soil Plasticity. Elsevier (2013)
9. Merifield, R.S., Lyamin, A.V., Sloan, S.W.: Limit analysis solutions for the bearing capacity of rock masses using the generalised Hoek-Brown criterion. Int. J. Rock Mech. Mining Sci. **43**(6), 920–937 (2006). https://doi.org/10.1016/j.jrmms.2006.02.001
10. Hoek, E., Carranza-Torres, C., Corkum, B.J.P.O.N.-T.: Hoek-Brown failure criterion-2002 edition. **1**(1), 267–273 (2002)

11. Saada, Z., Maghous, S., Garnier, D.: Bearing capacity of shallow foundations on rocks obeying a modified Hoek-Brown failure criterion. Comput. Geotech. **35**(2), 144–154 (2008). https://doi.org/10.1016/j.compgeo.2007.06.003
12. Clausen, J.: Bearing capacity of circular footings on a Hoek–Brown material. Int. J. Rock Mech. Mining Sci **57**, 34–41 (2013) https://doi.org/10.1016/j.ijrmms.2012.08.004
13. Hoek, E.: A brief history of the development of the Hoek-Brown failure criterion (2002)
14. Hoek, E.: Estimating Mohr-Coulomb friction and cohesion values from the Hoek-Brown failure criterion. Int. J. Rock Mech. & Min. Sci. & Geomech. Abstracts **3**, 227–229 (1990)
15. Hoek, E., Brown, E.T.: Practical estimates of rock mass strength. Int. J. Rock Mech. Mining Sci. **34**(8), 1165–1186 (1997). https://doi.org/10.1016/S1365-1609(97)80069-X
16. Abaqus: ABAQUS Documentation Dassault Systèmes, vol. 76. pp. 68–77. Providence, RI, U.S.A. (2016)
17. OptumG2: v2.2018.02.09, Optum Computational Engineering, vol. 76. pp. 68–77. Copenhagen NV, Denmark (2018)

Carrying Capacity of Model Steel Pile Foundation with Different Cross-Sectional Shapes in Sand

Khushal Paliwal, Nitin H. Joshi, and Pooja Bhojani

Abstract In present time, the steel piles are widely used for foundation of various structures constructed onshore and offshore. They are getting popularity because of easy availability, handling and splicing, and also durable. In the present investigation, the load-carrying capacity was compared of model steel piles having different cross-sectional shapes under vertical load in sand by keeping the equal cross-sectional area and equal length of pile. For this purpose, model steel piles of different shapes, i.e., solid circular, hollow circular, L-shaped, and H-shaped pile having equal cross-sectional area ($A = 1.767$ cm^2) and equal embedded length 30 cm and total length of 33 cm were used. For this work, the effect of shape of single model pile and model pile group of 2×2 with spacing 3d, 4d, 5d on load-carrying capacity was studied in sand of two different relative densities under vertical load. For experimental work, circular tank of diameter 90 cm and height 60 cm was used and natural Bahadarpur sand near Sankheda, Vadodara district of Gujarat having angle of internal friction (φ) = 34$^\bullet$ and density (ρ) = 1.687 g/cm^3 (60% relative density) and angle of internal friction (φ) = 40$^\bullet$ and density (ρ) = 1.747 g/cm^3 (80% relative density) was used. The load was applied at the center of pile cap through jacking mechanism and pile cap was kept 3 cm above the soil layer to neglect the effect of cap in the capacity of pile. From investigation of results, it has been observed that the load-carrying capacity of H-shaped single pile is more as compared to all other cross-sectional shapes in 60% as well as 80% relative density. In pile group, all shapes of pile show an increase in load-carrying capacity with an increase in spacing from 3d to 4d and 5d but capacity trend is different in H-shaped pile as here the load capacity decreases with increasing spacing in both 60% and 80% relative density. Consequently in pile

K. Paliwal (✉) · N. H. Joshi · P. Bhojani
Applied Mechanics Department, MSU, Vadodara, Gujarat 390002, India
e-mail: khushalpaliwal29@gmail.com

N. H. Joshi
e-mail: nhjoshi-appmech@msubaroda.ac.in

P. Bhojani
e-mail: pjbhojani-appmech@msubaroda.ac.in

225

group the hollow circular pile shows maximum capacity with increasing spacing and relative density.

Keywords Carrying capacity · Model steel pile · Cross-sectional shapes · relative density

1 Introduction

The pile foundation is used to transmit the load of a superstructure to the strong soil strata lying at greater depth. The cross-sectional shapes of pile, relative density of soil (sand), pile spacing, pile installation process are important factors that influence the load-carrying capacity of pile and pile group. Model pile load test performed in large test tank plays a significant role to understand the load–settlement behavior of pile model tests that are better than real field tests irrespective of good control on soil condition and also better to understand the soil–structure interaction process during installation process; however, small laboratory model tests do not perfectly reflect the real test data due to some scale and boundary effect of chamber and piles model. These are manufactured in various shapes, lengths, and dimensions providing for both vertical and lateral load capacity. These piles have advantages over the other piles as they are easy to handle, splice, and drive into the ground. Loukidis and Salgado [1], performed tests on H-pile and solid circular pile under vertical load in sand and concluded the results as in solid circular pile the load capacity is mainly due to frictional resistance and end-bearing resistance. However, the frictional resistance has more effect on load-carrying capacity as compared to end-bearing resistance because of less area of soil which comes in contact with base. Behavior of hollow circular pile is different from solid circular pile. Szechy [2] test results show that blow count necessary for hollow circular pile is less than the solid circular for driving a pile under same condition of sand. However, results of Smith [3], Brucy [4] have showed that the mode of pile driving is important factor to predict the driving resistance of pile. If pile is driven under fully plugged mode, the plugged soil already attached to the surface of pile will resist the further entering of soil. According to test results of Fattah et al. [5] performed test on hollow and solid circular pile under vertical load in sand and concluded that hollow circular pile will behave as a solid circular pile if soil inside the hollow circular pile is in partially or fully plugged mode. Also, the settlement of hollow circular pile is more than the solid circular pile. H-pile is generally considered as a partial displacement pile because while inserting this pile into soil the displacement means volume change of pile is small. It works between fully displacement pile and non-displacement pile. Loukidis and Salgado [1] performed the test on H-shaped pile and solid circular in multilayered soil under vertical load and concluded that the shaft capacity of H-pile is 20% less than the solid circular pile and this may be due to plugging behavior of the H-pile driven in sand on the other sand base capacity of H-pile which is almost twice as large as that of solid circular pile because of the difference in base area contact with the soil and thus the

different influences zone below the base of pile. The information about load-carrying capacity of L-shaped pile is still missing and no detailed research has been found about this pile. Generally the information about load-carrying capacity of different cross-sectional shapes (solid circular, hollow circular, L-shape, H-shape) of pile by keeping the cross section equal and equal length has not been found in researches. So in the present investigation the load-carrying capacity of different cross-sectional shapes, i.e., solid circular, hollow circular, L-shape, H-shape of pile model under the equal cross-sectional area and length has been investigated under vertical load in sand by considering two different relative density of 60 and 80%.

2 Materials Properties

2.1 Model Piles

Pile model of different shapes was constructed using mild steel and following important properties have been listed here in Table 1.

Pile Testing Program

For initial increment of loading and for finding the single pile and group of pile, ultimate load capacity was calculated on a single and group of pile using IS-2911 (part-I) and for load application IS-2911 (part-IV) followed (Fig. 1).

Table 1 Cross section properties of Solid circular, Hollow circular, L-shape, H-shape

S. No	Properties or specifications	Solid circular	Hollow circular	L-shape	H-shape
1	Area (mm^2)	1.767×10^2	1.767×10^2	1.767×10^2	1.767×10^2
	Dimensions-				
	I. Pile cap thickness (mm)	20	20	20	20
	II Flange width (mm)	–	–	–	24.45
	III. Web height (mm)	–	–	–	10
	IV. Flange and web thickness (mm)	–	–	–	3.0
	V. Two leg length equal in (mm)	–	–	30.95	–
	VI. Thickness of both leg (mm)	–	–	3.0	–

Fig. 1 Final setup of pile
load testing program

3 Results and Discussion

The tests were performed on a single pile and group of piles of solid circular, hollow
circular, L-shaped, and H-shaped pile under vertical load in sand of 60 and 80%
relative density by placing the pile through pre-installation and driving process.
Following results were obtained for ultimate load of all tests for both densities,
which are listed here below in Table 2.

Table 2 Values obtained from present investigation of ultimate load

Description of shapes of pile	Pile-single/group (Spacing)	Driving process	Ultimate load (N) (60% R.D.)	Ultimate load (N) (80% R.D.)
Solid circular	Single	Pre-installation	60	75
	Group-3d	Pre-installation	300	335
	Group-4d	Pre-installation	470	490
	Group-5d	Pre-installation	1640	1878
Hollow circular	Single	Pre-installation	52	128
	Group-3d	Pre-installation	727	1230
	Group-4d	Pre-installation	3520	4080
	Group-5d	Pre-installation	4340	4363
L-shape	Single	Driven	300	363
	Group-3d	Driven	1055	1260
	Group-4d	Driven	1407	1550
	Group-5d	Driven	1583	1609
H-shape	Single	Driven	400	430
	Group-3d	Driven	2420	2520
	Group-4d	Driven	2100	2120
	Group-5d	Driven	1750	2100

3.1 Load Versus Settlement Analysis

For pile of all shapes, the tests were performed on single and group of piles (2 × 2) of 3d, 4d, 5d for 60% and 80% and following tests results have been found.

From Fig. 2a, the load-carrying capacity of single pile is more in H-shaped pile as compared to other cross-sectional shapes. It is seen the capacity of H-pile is about 7.6 times more from hollow circular pile and about 6.6 time more than solid circular pile and around 1.3 times of L-shaped pile. Similarly the L-shaped pile capacity is about 5.7 times more from hollow and about 5 times more than solid circular pile. Load-carrying capacity of hollow circular and solid circular pile is not so much different. Also, from Fig. 3a the load-carrying capacity of all single pile is more for 80% relative density as compared to 60% relative density of sand. The load trend is same as in 60% relative density, except the hollow circular showing increase in capacity as compared to solid circular pile. Again seen that the H-pile capacity is about 5.6 times more from solid circular and 3.3 times more from hollow circular pile and from L-shape it is not so much different. Similarly the capacity of L-pile is 4.4 times more from solid circular and 2.6 times from hollow circular pile. The capacity of hollow circular pile is observed 1.7 times the solid circular in this case. Now the comparison was also done between all four shapes of pile for center to
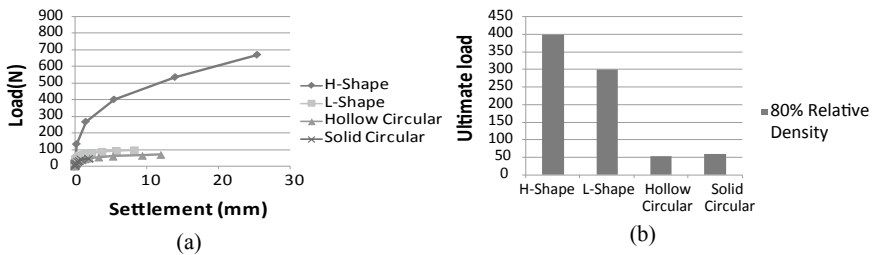

Fig. 2 **a** Characteristic load versus settlement curve and **b** bar chart for ultimate load of all single pile corresponding to 60% relative density of sand
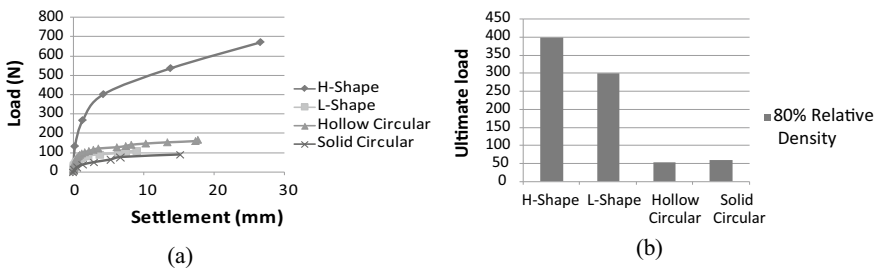

Fig. 3 **a** Characteristic load versus settlement curve and **b** bar chart for ultimate load of all single pile corresponding 80% relative density of sand

centre spacing of 3d, 4d, and 5d. The following graph has been plotted for various spacing for 60 and 80% relative density of sand.

It is seen from curves of Figs. 4, 5 and 6 that in pile group ultimate load will increase as compared to single pile means group pile has load-carrying capacity more as compared to single pile. The loading trend is same as in single pile and the capacity of H-pile is about 8 times more from solid circular, 3.3 times from hollow circular pile, and 2.2 times from L-pile. Similarly capacity of L-pile is 3.5 times more as compared to solid circular and 1.4 times more from hollow circular and the hollow circular pile's capacity is 2.4 times more from solid circular pile in 60%
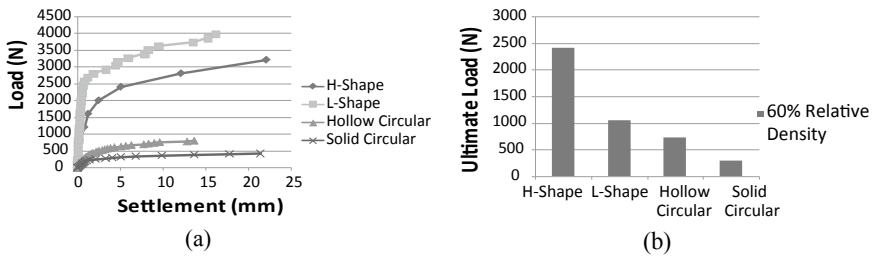

Fig. 4 **a** Characteristic load versus settlement curve and **b** bar chart for ultimate load of pile group (2 × 2) of c/c spacing of 3d (where $d = 1.5$ cm) for 60% relative density of sand

Fig. 5 **a** Characteristic load versus settlement curve and **b** bar chart for ultimate load of pile group (2 × 2) of c/c spacing of 4d (where $d = 1.5$ cm) for 60% relative density of sand
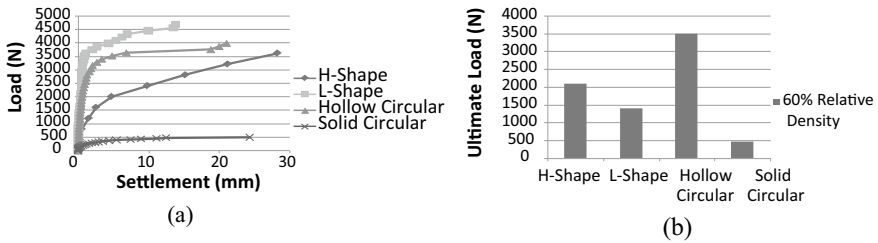

Fig. 6 **a** Characteristic load versus settlement curve and **b** bar chart for ultimate load of pile group (2 × 2) of c/c spacing of 5d (where $d = 1.5$ cm) for 60% relative density of sand
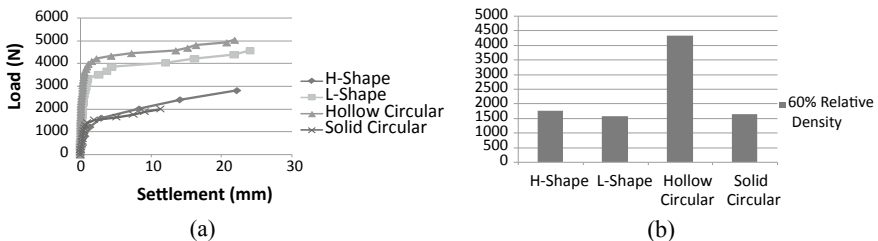
relative density. Similarly from Fig. 5a it is seen that pile group of 4d spacing ultimate increases in all shapes except H-shape compared to 3d spacing. It means maximum increase in capacity is observed in hollow circular pile as compared to other piles. In hollow circular pile the capacity is about 1.6 times more from H-pile, 2.5 times from L-pile, and 7.6 times from solid circular pile. Similarly H-pile capacity is about 4.4 times more from solid circular pile and 1.4 times from L-pile. In L-pile the capacity is 2.9 times more as compared to solid circular in 60% relative density case. Now from Fig. 6a,the capacity of solid circular pile is slightly more as compared to L-shaped pile. The hollow pile capacity is around 2.5 times from all other shapes pile. Same way if the load-carrying capacity for 80% relative density is compared the following graph is obtained for 3d, 4d, 5d spacing as shown below.

Form Fig. 7a the capacity is more in H-pile as compared to all other pile. Capacity of H-pile is around 2 times more from L-pile and hollow circular pile and 7.5 times from solid circular pile. Similarly capacity of L-pile and hollow circular pile is approximate same and around 3.7 times more from solid circular pile. Similarly from Fig. 8a the load-carrying capacity is observed maximum in hollow circular pile as compared to all other piles. In hollow circular pile capacity is approximately 8.3 times, 2.6 times, and 1.9 times more from solid circular, L-pile, and H-pile, respectively. Similarly capacity of H-pile and L-pile is about 4.3 times and 3.2 times of solid circular pile. Figure 9a shows the curves for load-carrying capacity of pile
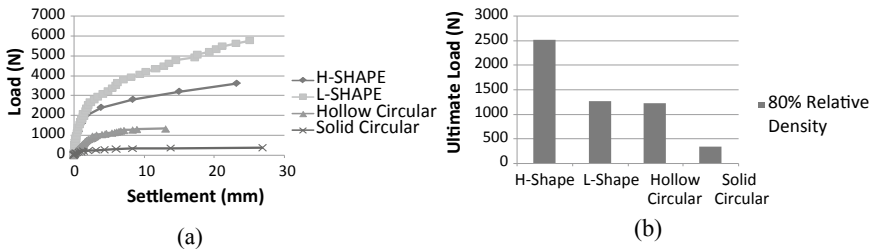

Fig. 7 **a** Characteristic load versus settlement curve and **b** bar chart for ultimate load of pile group (2×2) of c/c spacing of 3d (where $d = 1.5$ cm) 80% relative density of sand

Fig. 8 **a** Characteristic load versus settlement curve and **b** bar chart for ultimate load of pile group (2×2) of c/c spacing of 4d (where $d = 1.5$ cm) for 80% relative density of sand
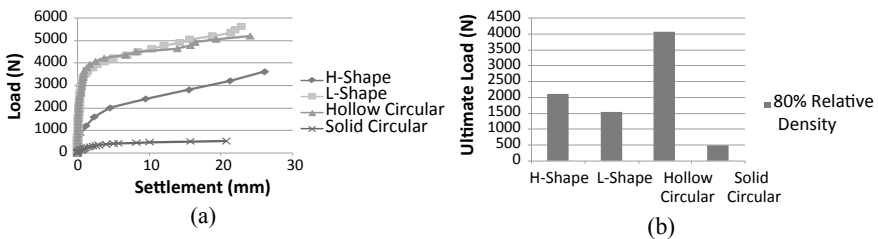
Fig. 9 **a** Characteristic load versus settlement curve and **b** bar chart for ultimate load of pile group (2 × 2) of c/c spacing of 5d (where $d = 1.5$ cm for 80% relative density of sand
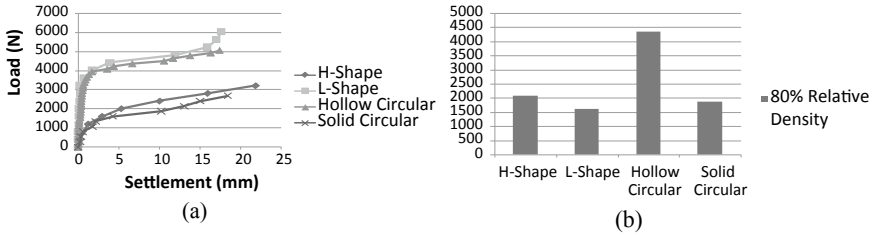
group of c/c spacing of 5d, in which the capacity of hollow circular pile is approximate 2 times of all other piles (Figs. 10, 11, 12 and 13).

Also in this analysis the settlement was calculated at particular value of loads and compared within all shapes for single and pile group and for all c/c spacing of 3d, 4d, 5d with 60% and 80% relative density of sand. The value of settlement has been shown in tabular form below.

In settlement analysis from Table 3 it has been observed that for 60% relative density in single pile for 20 N load the maximum settlement was observed in solid circular pile, i.e., of 0.15 mm and minimum of nil settlement was observed in H-pile as compared to other shapes of pile. Similarly for 80% relative density the

Fig. 10 Characteristics load versus settlement curves for solid circular pile for 3d, 4d, 5d spacing in **a** 60% relative density of sand **b** 80% relative density of sand
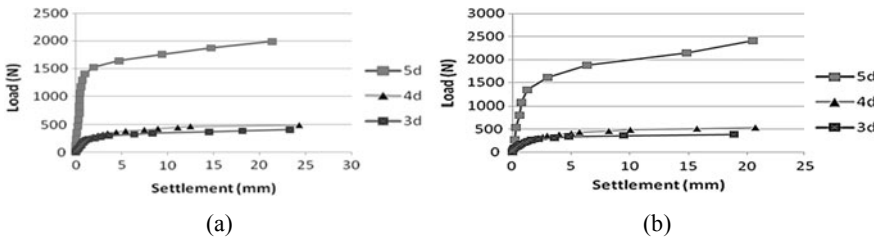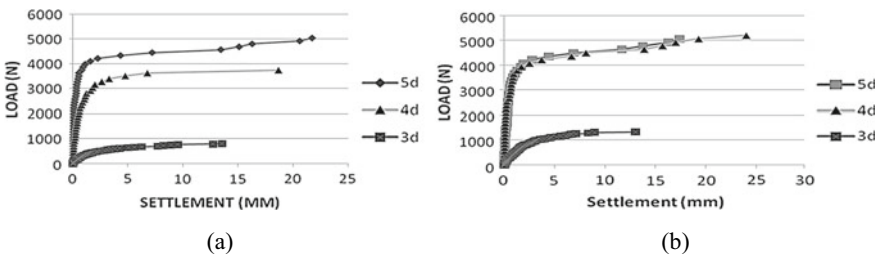

Fig. 11 Characteristics load versus settlement curves for hollow circular pile for 3d, 4d, 5d spacing in **a** 60% relative density of sand **b** 80% relative density of sand

(a)   (b)

Fig. 12 Characteristics load versus settlement curves for L-shaped pile for 3d, 4d, 5d spacing in **a** 60% relative density of sand **b** 80% relative density of sand

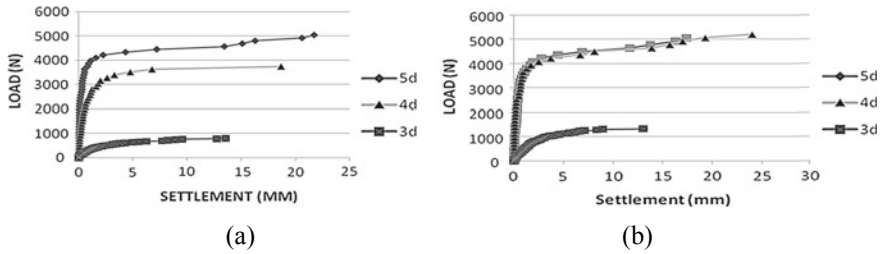(a)   (b)

Fig. 13 Characteristics load versus settlement curves for H-shaped pile for 3d, 4d, 5d spacing in **a** 60% relative density of sand **b** 80% relative density of sand
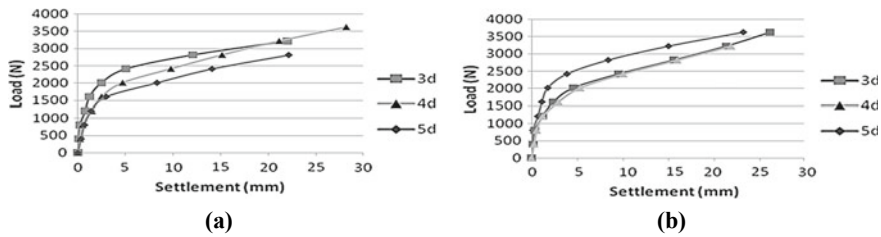
Table 3 Settlement values for single pile

Load (N)	Relative density (%)	Settlement (mm)			
		Closed ended	Hollow	L-shape	H-shape
20	60	0.15	0.10	0.045	Nil
	80	0.15	0.09	0.035	Nil
40	60	1.915	0.065	0.16	0.1
	80	1.345	0.155	0.085	0–1

same trend was observed as in 60%. For 40 N load in 60% relative density the maximum settlement, i.e., 1.91 mm was observed in solid circular pile and minimum was observed in hollow circular pile of 0.065 mm. Similarly for same load in 80% relative density maximum settlement of 1.345 mm was observed in solid circular pile and minimum settlement of 0.1 mm was observed in H-pile. It is seen from Table 4 for pile group in c/c spacing of 3d and for 50, 100, 150, and 200 N the maximum settlement of 0.22, 0.45, 0.65, and 1.05 mm was observed in solid circular pile and minimum settlement of nil, 0.02, 0.04, and 0.06 was in H-shaped pile for 60% relative density. Similarly for 80% relative density and for same order of load as in 60% relative density the maximum settlement and minimum settlement pattern was same as in 60% as shown in same table. For pile group in c/c spacing of 4d and for 50, 100, 150, and 200 N the maximum settlement of 0.01, 0.08, 0.35, and

Table 4 Settlement values for pile group (c/c-3d spacing)

Load(N)	Relative density (%)	Settlement (mm)			
		Close ended	Hollow	L-shape	H-shape
50	60	0.22	0.06	Nil	Nil
100		0.45	0.17	0.15	0.02
150		0.65	0.34	0.16	0.04
200		1.05	0.50	0.20	0.06
50	80	0.52	0.07	Nil	Nil
100		0.26	0.15	0.02	0.02
150		0.56	0.21	0.07	0.02
200		1.04	0.28	0.10	0.05

Table 5 Settlement values for pile group (c/c-4d spacing)

Load(N)	Relative density (%)	Settlement (mm)			
		Close ended	Hollow	L-shape	H-shape
50	60	0.01	Nil	Nil	0.01
100		0.08	Nil	0.01	0.05
150		0.35	0.01	0.04	0.075
200		0.90	0.02	0.06	0.11
50	80	0.06	Nil	Nil	0.02
100		0.24	Nil	0.01	0.05
150		0.66	Nil	0.02	0.075
200		0.96	0.5	0.05	0.11

0.90 mm was observed in solid circular pile and minimum settlement of nil, nil, 0.01, and 0.02 was in hollow circular pile for 60% relative density. Similarly for 80% relative density the trend was same as was in 60% as shown in Table 5. Same here for c/c 5d spacing and 60% relative density maximum settlement was observed in H-shaped pile and in other shapes approximate equal settlement was observed for all range of load and for 80% relative density maximum settlement was observed in H-shape and minimum was observed in hollow circular pile and for other shapes shown in Table 6.

3.2 Ultimate Load Versus Spacing of Pile Group Analysis

In this analysis, the effect of spacing, i.e., 3d, 4d, and 5d, on the ultimate load of pile has been done.

Table 6 Settlement values for pile group (c/c-5d spacing)

Load (N)	Relative density (%)	Settlement(mm)			
		Close ended	Hollow	L-shape	H-shape
50	60	Nil	Nil	Nil	0.035
100		0.01	Nil	Nil	0.07
150		0.03	0.01	0.02	0.10
200		0.02	0.01	0.03	0.15
50	80	Nil	Nil	Nil	0.03
100		0.11	Nil	0.05	0.07
150		0.12	Nil	0.09	0.10
200		0.18	0.01	0.10	0.15

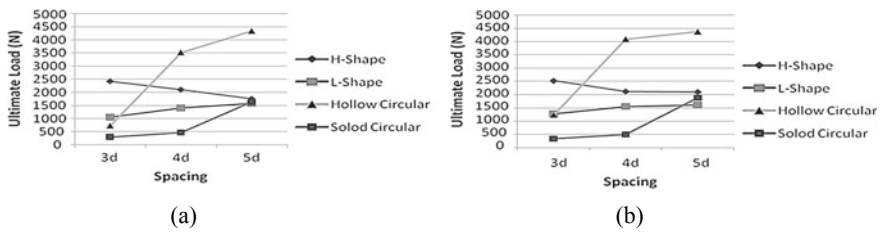(a)   (b)

Fig. 14 Line chart of variation of ultimate load with spacing (3d, 4d, 5d) for cross-sectional shapes of pile (solid circular, hollow circular, L-shape, H-shape) for **a** 60% relative density **b** 80% relative density

From Fig. 14a, b the line chart variation shows the load-carrying capacity of solid circular pile increases as increase c/c spacing of pile group from 3 to 4d and 5d spacing for 60 and 80% relative density of sand, respectively, means in solid circular pile effect of spacing and relative density of sand have significance effect on load-carrying capacity of pile group. Similarly the load-carrying capacity of hollow circular pile increases as increase in c/c spacing of pile group from 3 to 4d and 5d spacing for 60 and 80% relative density of sand, respectively, means in hollow circular pile the effect of spacing on load-carrying capacity of pile has significant effect but the relative density of sand has not so much effect in 4d and 5d spacing. Also the load-carrying capacity of L-shaped pile increases as increase in c/c spacing of pile group from 3 to 4d and 5d spacing for 60 and 80% relative density of sand, respectively, also the load-carrying capacity of H-pile decreases as increase in c/c spacing of pile group from 3 to 4d and 5d spacing for 60 and 80% relative density of sand, respectively, means in H-shape the trend is completely different as compared to other shapes where the load-carrying capacity decreases instead of increase.

4   Conclusion

In present investigation, the load-carrying capacity has been analyzed of different cross-sectional shapes of pile, i.e., solid circular, hollow circular, L-shaped pile, H-shaped pile by keeping equal cross-sectional area and length. From results of test graph it has been concluded that in single pile the load carrying of H-shaped pile was more as compared to other shapes in both relative densities. With increasing density all shapes show increase in load-carrying capacity but it was not true for spacing because in all shapes generally the with increasing spacing load carrying was increasing but it was different in H-shaped pile as in this pile the capacity was observed decreased with increase in spacing. Also, the effect of relative density was not so much effect on the pile group in all shapes of pile as compared to single pile. The maximum effect of load-carrying capacity was observed in hollow circular pile, and with increasing spacing, it showed maximum increment in load-carrying capacity in single as well as group and also in both relative density. Means with increasing density and c/c spacing of pile group the hollow piles carry maximum load as compared to all other pile group on equal cross-sectional area. Also, on the basis of equal cross-sectional area, it has been found that with increasing relative density from 60 to 80%, the load-carrying capacity always increases in any shape of single and group of pile under the same loading condition. Also, the load-carrying capacity of group of pile is more as compare to single pile. Load-carrying capacity of model test pile in group action also increases with increase in spacing from 3 to 4d and 5d in all shapes of pile except H-shaped pile. Also, the efficiency of all shapes of single pile increased in both relative density but in pile group all shapes except H-shaped pile showed increase in efficiency as in this decrease in efficiency was observed with increasing spacing of pile groups. Maximum efficiency was observed in hollow circular pile.

References

1. Loukidis, D., Salgado, R.: Analysis of the shaft resistance of nondisplacement piles in sand. Geotechnique **58**(4), 283–296 (2008)
2. Szechy, C.: The effect of vibration and driving upon the voids in granular soil surrounding a pile. Proceedings of the 5th international conference on Soil Mechanics and Foundation Engineering, vol. 2, pp.161–164 (1961)
3. Smith, I.M., To, P., Willson, S.M.: Plugging of pipe piles. In: Proceedings of the 3rd international conference numerical methods in offshore piling, pp. 53–73 (1986)
4. Brucy, F., Meunier, J., Nauroy, J.F.: Behavior of pile plug in sandy soils during and after driving. Proceedings of the 23rd Annual Offshore Technology Conference. Houston **6514**, 145–154 (1991)
5. Fattah, M.Y., Al-Soudani, W.H., Omar, M.: Estimation of bearing capacity of open-ended model piles in sand. Arab. J. Geosci. **9**(3), 1–14 (2016)

An Experimental Study of the Piled Raft Foundation Subjected to Combined Vertical and Lateral Load

Uttam Kumar and Sandeep A. Vasanwala

Abstract 1-g experimental tests have been carried out to investigate the behavior of piled raft foundation subjected to combined vertical and lateral load. The vertical load was applied till a constant settlement of test models and it was followed by the horizontal incremental load. The piled raft models including a single pile, unpiled raft, and pile group models had been tested on cohesionless soil. The pile configurations of 2 × 2 and 3 × 3 with a constant spacing of 3.5 times diameter of a pile and constant pile length of 25 times diameter of a pile were adopted for the piled raft models in this study. The raft-soil contact was an important factor to reduce the horizontal displacement of the piled raft. There was a significant reduction found in the horizontal displacement of the piled raft foundation due to the presence of the vertical load. At an assumed horizontal load of 100 N, there was about 3.75–5.33 times reduction in the horizontal displacement of adopted piled raft models in the presence of vertical load till 10 mm settlement.

Keywords Piled raft foundation · Horizontal incremental load · Horizontal displacement · Weight-pulley mechanism

1   Introduction

Piled raft foundation is a progressive foundation concept to support high-rise superstructures. It consists of three bearing elements, which are piles, raft, and subsoil. A new design philosophy of piled raft has been proposed to improve the loading capacity of conventional pile groups [1, 2]. The detailed study of average settlement and differential settlement of piled raft foundation and its implementation for the support of heavily loaded structures has been compiled by different authors [3, 4].

A number of experiments have been carried out to study the piled raft foundation system by applying vertical load [5, 6]. The load–settlement relations of the piles, raft, and the piled raft were analyzed and the improvement in the load–settlement

U. Kumar (✉) · S. A. Vasanwala
Applied Mechanics Department, SVNIT, Surat, India
e-mail: uttam.form@gmail.com

curve due to the combined action of piles and raft was studied by authors [6, 7]. These experimental studies mostly describe the reduction in the settlement of piled raft and load sharing percentage of raft and piles.

The behavior of piled raft foundation subjected to static lateral load has been studied with 1-g experimental tests on piled raft models by different authors [8–10]. The confining stress of isolated pile and piles beneath the raft was different and so the lateral stiffness of piled raft was different from the piles. It was concluded that at a lower horizontal load, the horizontal load–displacement relation proposed linear relation. The experimental tests on piled raft models subjected to horizontal load and moment load have been performed too [11]. As the height of the horizontal load point increased, the horizontal displacement and inclination of piled raft models also increased for a given horizontal load. It was also reported that the initial lateral stiffness of piled raft decreased with an increase in the height of the horizontal load point. To study the lateral load behavior of piled raft foundation, the centrifuge modeling tests have been carried out [12, 13]. The effect of pile head connections has been also analyzed by the authors and a significant decrease was concluded at the moment at pile head of hinged connected piled rafts during lateral load analysis [14, 15]. It was reported by the lateral load tests on the piled raft that most of the lateral force was carried by the friction of raft and soil because of the high contact pressure beneath the raft [16].

Since the horizontal displacement of the piled raft during lateral loading is essentially analyzed in the design practices, but without a vertical load of the superstructure on the foundation, the lateral load analysis can lead to the overestimation of the design. A very few experiments have been reported on the combined effect of vertical and lateral load on the piled raft foundation system [17]. It was reported that the lateral displacement of the vertically loaded piled raft was reduced drastically.

A design concept based on the lateral load alone may not be able to reveal the exact behavior of the foundation system. The settlement of structure should be within permissible limit under vertical load and the lateral load analysis would be performed for vertically loaded foundation. In the present study, 1-g experimental tests have been carried out to study the response of the displacement behavior of vertically loaded piled raft foundation system, where the vertical load was applied to the corresponding settlement of 10 mm and it was followed by a constant increase in horizontal load. A constant value of 10 mm settlement of each model has been considered which is less than 10% of the raft width.

2 Test Methodologies

In the first step, the test models in the experiment were subjected to a constant horizontal increment load. In the second step, these experimental models have been tested by applying vertical concentrated load till the settlement of 10 mm and followed by applying constant increment of the horizontal load to investigate the behavior of piled raft foundation system under the combined action of vertical and lateral load.
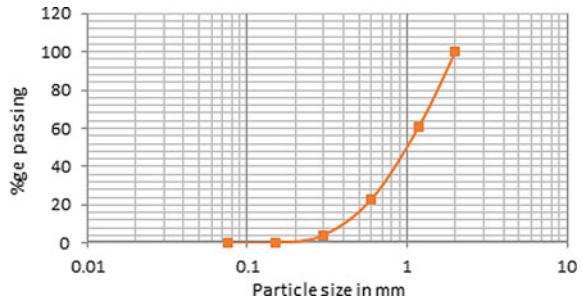
Fig. 1 Particle size distribution curve

Table 1 Physical properties of soil

S. No.	Physical properties	Values and description
01	Specific gravity	2.63
02	Maximum dry density	16.20 kN/m^3
03	Minimum dry density	14.40 kN/m3
04	Uniformity constant, Cu	2.60
05	Coefficient of curvature, Cc	0.90
06	Soil classification	SP
07	Secant modulus of soil at the density of 15.15 kN/m^3, E$_{50}$	3200 kN/m^2
08	Angle of internal friction by direct shear test, Φ	32.4°

3 Test Materials

3.1 Sand

The river bed sand was taken to perform the experimental tests. It was free from organic materials and sieved with 2 mm sieve. The particle size distribution curve of the sand has been plotted and shown in Fig. 1, and the physical properties of the sand have been presented in Table 1.

3.2 Raft and Pile Models

The raft of dimension 120 mm × 120 mm × 10 mm was adopted throughout the experiment. The geometrical and material properties are represented in Table 2.

The material properties of piles and raft models were similar. The pile of 10 mm diameter and 250 mm length was adopted throughout all the tests. The pile groups of configurations 2 × 2 and 3 × 3 were adopted for pile groups and piled raft system with a constant spacing of 3.5 times diameter of a pile. The layout of piled raft models

Table 2 Geometrical and material properties of the raft and piles

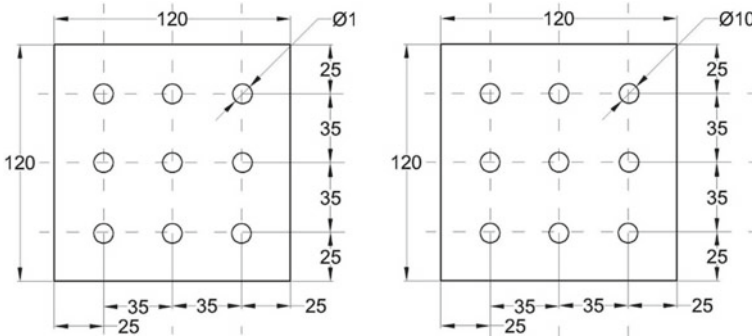| S. No.	Description	Raft details	Pile details
01	Shape	Square	Solid circular
02	Dimension	120 mm × 120 mm × 10 mm	250 mm in length and 10 mm in diameter
03	Material	Mild steel	Mild steel
04	Modulus of elasticity	180×10^6 (kN/m^2)	180×10^6 (kN/m^2)

Fig. 2 Piled raft models layout of 2 × 2 and 3 × 3 configurations (All the dimensions are in mm)

has been shown in Fig. 2. Those piles were welded with each other in a group with thin plates to act monolithically during the load tests.

The length to diameter ratio of the pile, L/D = 25, was referred to in the study, which lies between short to the long pile, as per IS 2911-Part-I (Section II).

4 Test Procedures

4.1 Test Setup

The steel tank of dimension 850 mm × 850 mm × 600 mm was placed on the loading frame, which was fabricated for both vertical load and lateral load, shown in Fig. 3a with its descriptions.

The lateral load was applied with the help of hanging dead weight, which moves down with the help of non-extensible wire moving on the pulley mechanism to ease the constant increase in the horizontal load. This loading test facility has been shown in Fig. 3b. The vertical load was applied with a constant strain rate of 1 mm/min. The lateral load was similar to the dead weight, which increased with the constant addition of dead weight.
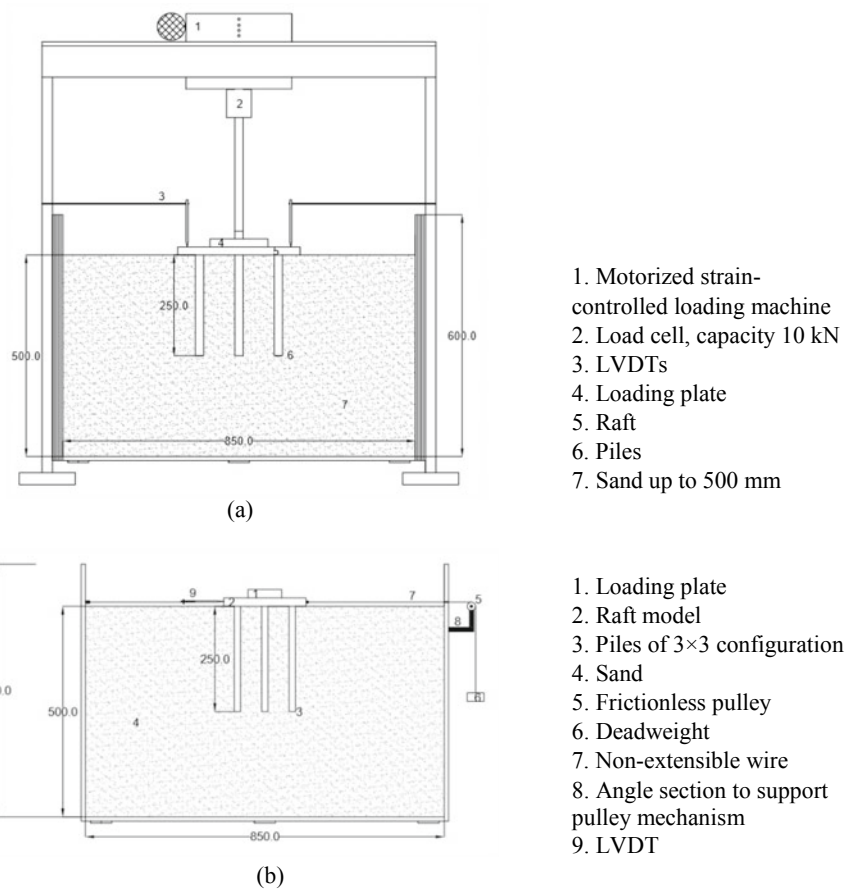
1. Motorized strain-controlled loading machine
2. Load cell, capacity 10 kN
3. LVDTs
4. Loading plate
5. Raft
6. Piles
7. Sand up to 500 mm

(a)

1. Loading plate
2. Raft model
3. Piles of 3×3 configuration
4. Sand
5. Frictionless pulley
6. Deadweight
7. Non-extensible wire
8. Angle section to support pulley mechanism
9. LVDT

(b)

Fig. 3 Experimental set-up with descriptions: **a** vertical load facility and **b** lateral load facility (all dimensions are in mm)

4.2 Installation of Piles

The pile models were installed one-fifth length, i.e., 50 mm first on the sand bed and then the soil was filled with the desired density up to the full length of pile, i.e., 250 mm length, without disturbing the pile. In the case of 3 × 3 configurations, the sequence of pile installation started with the inner pile, following by corner piles and edge piles at last. To assure the rigid pile head connection with the raft, 6 mm bolts were tightened to the threads of piles. On the account of the vertical load test, the free-standing single pile and pile groups were installed about 10 mm above the sand surface.

4.3 Soil Distribution

The sand bed was prepared with each layer of 50 mm up to 500 mm with a relative density of 47%. To achieve a density of 15.15 kN/m^3 corresponding to 47% relative density, the rainfall technique was used from a height of fall of sand 300 mm. The precalculated volume of each layer was maintained and leveled with its desired density to the full test height of the tank during the entire experiment.

4.4 Loading Test Procedure

1. The sand bed was prepared with the desired density of each 50 mm layer.
2. In the first phase of the experiment, the purely lateral load was applied to the piled raft models along with a raft and piles. The horizontal load was increased with a constant load of 10 N placing the dead weight on the weight assembly, which was moving freely over the frictionless pulley with non-extensible steel wire. The displacement of these models was measured with the help of a linear variable differential transducer (LVDT), which was installed horizontally to the foundation system. It was waited till a constant value of settlement by LVDTs before placing another load on the weight assembly. In the second phase of the experiment, the vertical concentrated load was applied to each test model with a constant strain rate of 1 mm/min till the constant settlement of 10 mm, which was followed by the lateral load with the help of wire-pulley mechanism.
3. The calibrated load cell was used to perform the vertical load test, and LVDTs were placed vertically in the middle of sides of a raft to measure the corresponding settlement. The channel box was able to display the load and corresponding displacement.
4. The soil was replaced for each test in the loading tank.

A number of model tests in the experimental program were carried out to investigate the behavior of piled raft foundation in the present study and presented in Table 3.

Table 3 Experimental program

Models	Purely lateral load test	Combined load test (vertical load applied till 10 mm settlement and followed by lateral load)
Unpiled raft	Yes	Yes
Single pile	Yes	Only vertical load was applied
Pile group and piled raft (2 × 2 and 3 × 3)	Yes	Yes

5 Results and Discussions

The results of the lateral load test and combined vertical and lateral load tests have been discussed with horizontal load versus horizontal displacement of the test models. The vertical load tests were also discussed with the vertical load versus average settlement.

5.1 Horizontal Load Test Results

The horizontal load–displacement behavior of a single pile and pile groups has been shown in Fig. 4a. The horizontal stiffness of 2×2 and 3×3 configurations of pile groups were found higher than the single pile. It justified that with an increase in
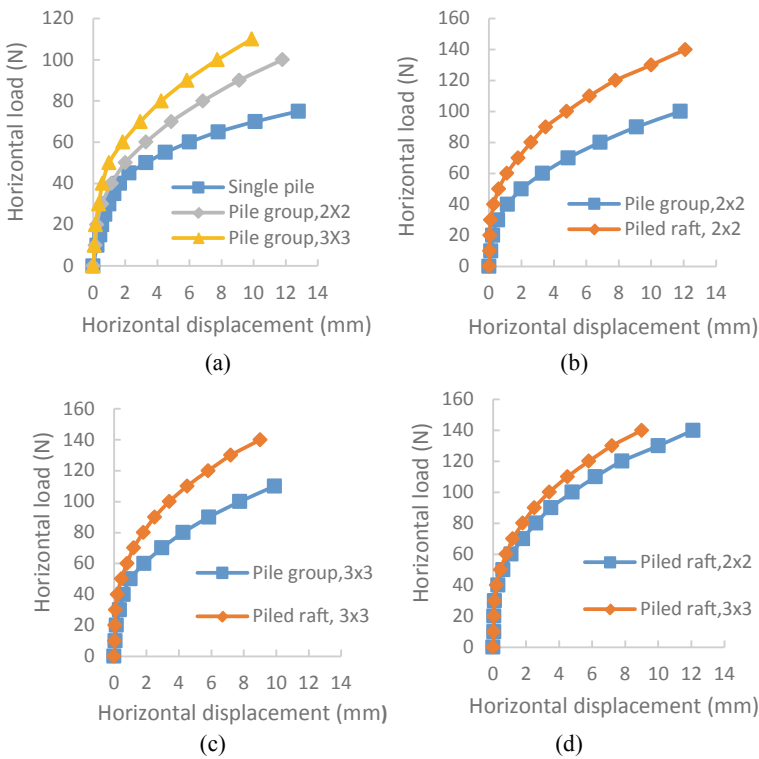

Fig. 4 Horizontal load–displacement graphs: **a** single pile and pile groups **b** pile group and piled raft of configuration 2×2 **c** pile group and piled raft of configuration 3×3 **d** piled rafts of configuration 2×2 and 3×3

the number of piles in a group, there was an increase in the lateral stiffness of pile groups.

It was seen in Fig. 4b, c, the lateral loading capacity of piled raft foundation was higher than pile groups at a given displacement because the horizontal load of the piled raft was carried by both the piles and raft-soil friction. The combined stiffness of raft and piles increased the horizontal load capability of piled raft foundation, where the raft–soil contact was an important factor to increase the horizontal stiffness of piled raft. Before yielding up to the elastic stage, the lateral stiffness of both the configurations of the piled raft was almost the same as shown in Fig. 4d. The lateral stiffness of configuration 3×3 of piled raft foundation was found about 1.2 times to the configuration 2×2 of piled raft foundation at a given displacement of 0.1D, where D is the diameter of a pile.

5.2   Vertical Load Test Results

Figure 5a shows the load–settlement behavior of single pile and pile groups of 2×2 and 3×3 configurations. The single pile was yielded earlier than pile groups. The stiffness of pile groups was increased with an increase in the number of piles in a group and the average settlement was also reduced.

The load–settlement curve of the unpiled raft and piled rafts are shown in Fig. 5b. The average settlement of the piled raft foundation was found remarkably less than the unpiled raft. There was a considerable improvement in load–settlement behavior of piled raft foundation over free-standing pile groups, as shown in Fig. 5c, d.

The vertical loading capacity of piled raft foundation of configurations 2×2 and 3×3 was found increased 1.32 times and 1.20 times to a pile group of 2×2 and 3×3 configurations, respectively, at a considered settlement of 10 mm due to combined stiffness of both raft and piles.

For both the vertical and horizontal load tests, the linear trend on the graphs presents that during the first stage both the pile–soil and raft–soil system of piled raft foundation behaves elastic and then after yielding it shows the elastic–plastic behavior and the similar response of piled raft experimental models have been reported by the author [1].

5.3   Combined Vertical and Horizontal Load Test Results

The constant increase in horizontal load and corresponding displacement of test models with influence of the vertical load and without vertical load is presented in Fig. 6. The horizontal displacement reduced rapidly with the influence of the applied vertical load. The greatest influence of vertical load on horizontal displacement was recorded by piled raft foundation models. The horizontal load capacity of the unpiled raft was increased 1.2 times by applying a vertical load of 488 N, corresponding to
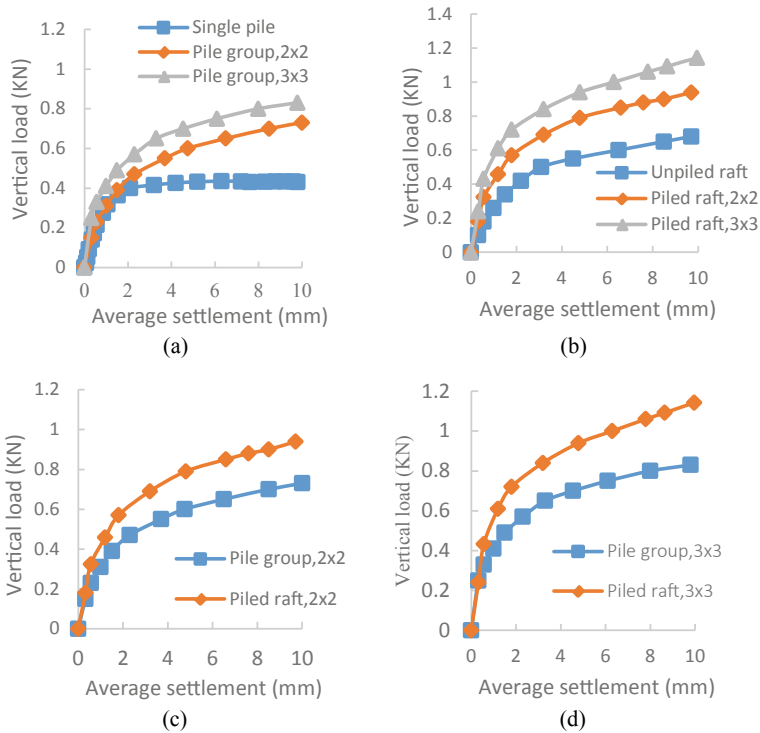
Fig. 5 Vertical load–displacement curve of **a** single pile and pile groups **b** unpiled raft and piled rafts **c** pile group and piled raft of 2 × 2 configuration **d** pile group and piled raft of configuration 3 × 3

a 10 mm settlement at a given displacement of 10% of the diameter of a pile as shown in Fig. 6a. The horizontal loading capacity of pile groups of 2 × 2 and 3 × 3 configurations was increased by about 1.2 and 1.4 times respectively with applying vertical load till 10 mm of corresponding settlement presented in Fig. 6b, c. At a given settlement of 0.1 D, the horizontal loading capacity increased to 1.67 and 2.4 times of configurations 2 × 2 and 3 × 3 of piled raft foundations, respectively, as shown in Fig. 6d and e.

At a horizontal load of 100 N, there were about 3.75 times and 5.33 times reduction in the displacement of a piled raft of configurations 2 × 2 and 3 × 3, respectively, in presence of vertical load corresponding to 10 mm settlement.

There was a significant effect on horizontal displacement of unpiled raft, piles, and piled raft foundation on applying vertical load on medium dense sand. The strongest influence was recorded for the piled raft foundation. On applying the vertical load, the horizontal loading behavior of the piled raft foundation shows a similar behavior published by the author [17].
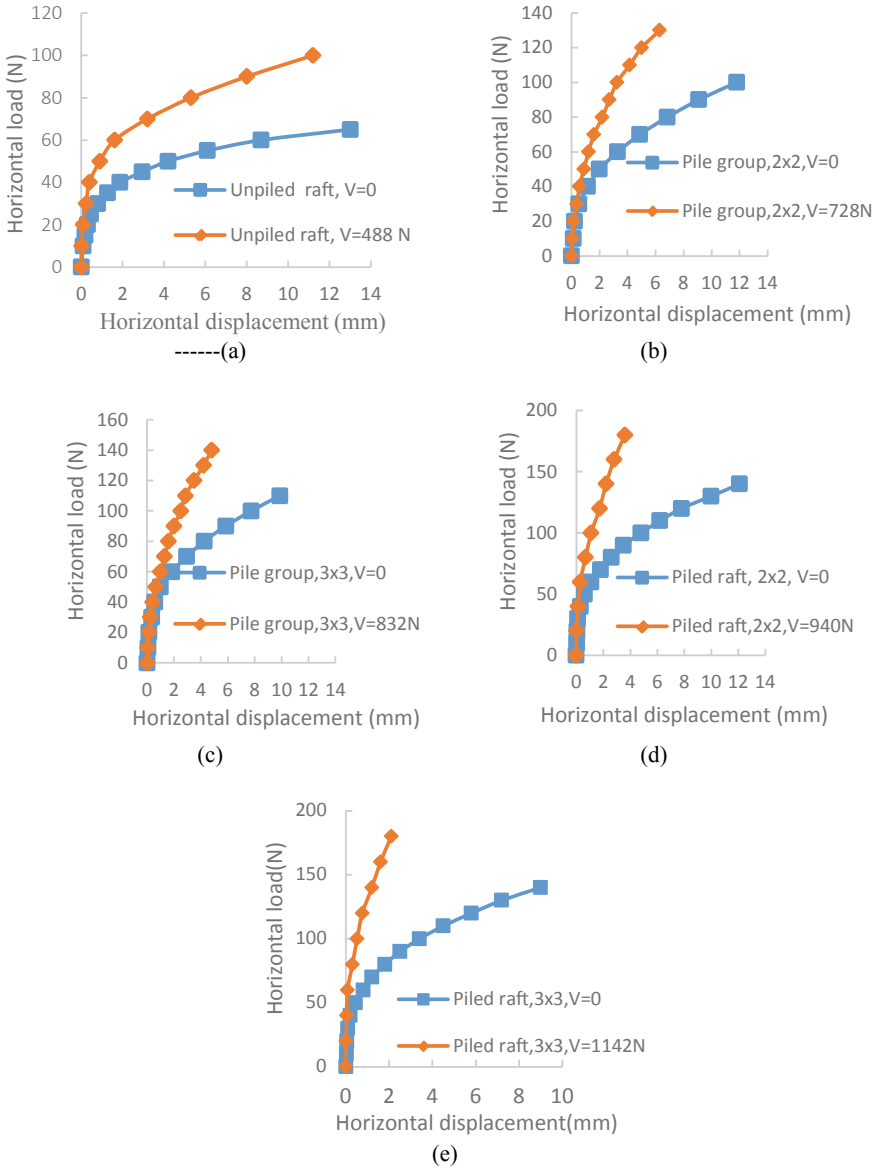
Fig. 6 Horizontal load–displacement behavior of **a** unpiled raft **b** pile group of 2×2 configuration **c** pile group of 3×3 configuration **d** piled raft of 2×2 configuration **e** piled raft of 3×3 configuration in presence of vertical load

6 Conclusion

The 1-g experimental tests on piles, raft, and piled raft have been carried out to investigate the behavior of piled raft foundation system subjected to combined vertical and lateral load. These experimental model tests were conducted on a dry sand bed of density 15.15 kN/m^3. As per the material and geometrical properties of 1-g model test conditions in the study, the following conclusions were drawn:

1. The raft contact with soil was found very effective to reduce the horizontal displacement and the vertical settlement of the piled raft foundation system.
2. The initial horizontal stiffness of the piled raft was higher than the piles and unpiled raft. At a lower lateral load level, the horizontal stiffness contributes a linear relation between the horizontal load and displacement, but with an increase in horizontal load, there was a nonlinear trend observed.
3. The horizontal load–displacement behavior of piles, raft, and the piled raft was found dependent on vertical load. In the presence of vertical load, there was a significant reduction of horizontal displacement during the lateral load test. The horizontal displacement was reduced by about 3.7–5.33 times of the vertically loaded piled raft of adopted configurations and geometrical properties in the study at a considered horizontal force of about 100 N. The maximum reduction in horizontal displacement is recorded in piled raft foundation among piles, unpiled raft, and piled raft foundations in the presence of vertical load.

It was very clear that neglecting the vertical load on a piled raft, the horizontal displacement of piles is very high during the lateral load test and it may lead to overestimation in design.

References

1. Poulos, H.G.: Piled raft foundations: design and applications. Geotechnique **51**(2), 95–113 (2001)
2. Randolph, M.F.: Design methods for pile groups and piled rafts. Proc. 13th ICSMFE, 61–82 (1994)
3. Hemsley, J.A.: Design Applications of Raft Foundations. Thomas Telford, England, London (2000)
4. Poulos, H.G.: Method of analysis of piled raft foundations, ISSMGE TC-18, Report (2001)
5. Balakumar, V., Kalaiarasi, V., Ilamparuthi, K.: Experimental and analytical study on the behavior of circular piled raft on sand. In: Proceeding 16th International Conference on Soil Mechanics and Geotechnical Engineering, Osaka, Japan, pp. 1943–1947 (2005)
6. Patil, J., Vasanwala, S., Solanki, C.H.: An experimental study on behavior of piled raft foundation. Ind. Geotechn. J. **46**(1), 16–24 (2016)
7. Kumar, V., Kumar, A.: An experimental study to analyze the behavior of piled-raft foundation model under the application of vertical load. Innovative Infrastruct. solutions (2018)
8. Hashizume, Y., Matsumoto, T.: Lateral load tests on model pile groups and piled raft foundations in sand. In: International Conference on Physical Modelling in Geotechnics, St. John's, Canada, pp. 709–714 (2002)

9. Horikoshi, K., Matsumoto, T., Hashizume, Y., Watanabe, T., Fukuyama, H.: Performance of piled raft foundations subjected to static horizontal loads. IJPMG – Int. J. Phys. Modell. Geotech. **2**, 37–50 (2003a)
10. Pastsakorn, K., Hashizume, Y., Matsumoto, T.: Lateral load tests on model pile groups and piled raft foundations in sand. In: International Conference on Physical Modelling in Geotechnics, St. John's, Canada, 709–714 (2002)
11. Matsumoto, T., Fukumura, K., Kitiyodom, P., Horikoshi, K., Oki, A.: Experimental and analytical study on behaviour of model piled rafts in sand subjected to horizontal and moment loading. Int. J. Phys. Model. Geotechn. **4**(3), 1–19 (2004)
12. Horikoshi, K., Matsumoto, T., Hashizume, Y., Watanabe, T., Fukuyama, H.: Performance of piled raft foundations subjected to dynamic loading. Int. J. phys. Model. Geotech. **2**, 51–62 (2003b)
13. Matsumoto, T., Fukumura, K., Horikoshi, K., Oki, A.: Shaking Table tests on model piled rafts in sand considering the influence of superstructures. Int. J. Phys. Model. Geotech. **4**(3), 21–38 (2004)
14. Kumar, A, Chaudhary, D., Katzenbach, R.: Behaviour of the combined piled-raft foundation under static and Pseudo-static conditions using Pla × is 3D. In: 6th International Conference on Earthquake Geotechnical Engineering. Christchurch, New Zealand (2015)
15. Matsumoto, T., Nemoto, H., Mikami, H., Yaegashi, K., Arai, T., Kitiyodom, P.: Load tests of piled raft models with different pile head connection conditions and their analyses. Soils Found. **50**(50), 63–81 (2010)
16. Hamada, J., Tsuchiya, T., Tanikawa, T., Yamashita, K.: Lateral Loading Tests on Piled Rafts and Simplified Method to Evaluate Sectional Forces of Piles. Geotech. Eng. J. SEAGS & AGSSEA, **46**(2) (2015)
17. Katzenbach, R., Turek, J.: Combined pile-raft foundation subjected to lateral loads. In: Proceeding of the 16th International Conference on Soil Mechanics and Geotechnical Engineering (2006)

Bell-Shaped Anchor with Geotextile Ties Embedded in Clay—A Numerical Study

Arya Das and Ashis Kumar Bera

Abstract A parametric numerical simulation has been carried out to study the behavior of bell-shaped anchor with and without geotextile ties within clayey soil. The study has been done with help of FEM software ABAQUS. Three types of soil and one typical model of belled anchor with diameter 0.125 m have been considered for the numerical analysis. Properties of geotextile sheets and soil mass have been studied and reported in the present work. Variation of uplift capacity with different parameters such as embedment ratios (H/D) of anchor, and cohesion of soil have also been studied. In the numerical study, weight of the soil as well as gravity has been taken into account. A sensitivity analysis and a mesh convergence study also have been performed to determine the model dimension and meshing criteria. Breakaway condition has been adopted here as no resistance is acting below the anchor against the soil mass. Both the anchor and the geotextile sheet as linear material and clay mass as elasto-plastic material have been considered in the analysis. With introduction of geotextile tie to the anchor, the uplift capacity of anchor with tie increases. Optimum value of L_g/D (Lg-diameter of geotextile sheet) is found to be 3 from the current investigation. Optimum numbers of geotextile tie layers are found to be 3 for a specific type of soil. Stress profile also has been plotted to identify the maximum stress in geotextile.

Keywords Bell-shaped anchor · Geotextile · Uplift capacity · Elasto-plastic material

A. Das (✉) · A. K. Bera
Civil Engineering Department, IIEST, Shibpur 700118, India
e-mail: aryanbesu@gmail.com

A. K. Bera
e-mail: ashis@civil.iiests.ac.in

1 Introduction

Anchor foundation is one of the most important structures for resisting the uplift forces, overturning moments. In case of many off-shore platforms, chimneys, transmission towers where, there is an issue of tensile pullout forces, anchor can be used to counter those forces. There have been different types of anchors in the field of geotechnical engineering. Bell-shaped anchor is one of the concerning matter in this field, where an enlarged base (bell) is attached below the cylindrical shaft. Many authors have worked on anchor foundation with different parameter of foundation material, shape of the anchor, etc. Sowa [1] investigated the resisting capacity of cylindrical piles of reinforced concrete cast in situ in bored holes constructed in cohesive soils. Based on an empirical relationship between soil adhesion and the undrained shear strength, he evaluated the pulling capacity of the uplift piles. He observed that the active lateral pressure as well as the active skin friction of the soil mass can be improved by rapidly placing the concrete mass and vibrating the same methodically. He also found that the estimation of short time pullout capacity of cast in situ piles within cohesive soil can be accounted based on undrained shear strength and the long-term pile pullout capacity by the creep and effective shear strength parameters. Das [2] performed model tests for determining the uplift capacity of square and rectangular foundations in clay mass. He determined the net uplifting loads experimentally with varying the length-to-width ratio of the anchor plates from one to five. He presented the non-dimensional breakout factors F_c and F_q. He also observed that the value of F_c increases with increase in embedment depth up to a critical depth and after that F_c reached an approximately constant value. Das [3] performed a rigorous study on uplifting capacity of plate anchor with various parametric conditions such as embedded depth in clayey soil and in sloping ground and gave a general methodology to determine the uplift capacity of plate anchors in clayey soil. He had also considered the suction force, creep in soil, etc. factors in the study. He also found that the value of breakout factor F_c increased with embedment ratio up to a certain limit and got constant afterward. Degenkamp and Dutta [4] developed a technique to estimate the tensile force acting at the anchor point of the chain conformation in the soil mass for an soil-chain-anchor system where a pile is embedded in soil mass with combined anchor pile and the mooring chain. With the help of incremental-integration technique, they have developed the equilibrium equations for the embedded chain. Soil resistance against the chain was modeled as same way used for strip footing in clayey soil. Rao et al. [5] investigated the behavior of single as well as group of granular pile anchors (GPA) of varying diameter and length embedded in expansive clayey beds. They found that higher surface area of GPA increased the pullout capacity. The increment was about in the range of 33–55%. It was also found from their experiment that the required load for pullout also increased with diameter because of increased surface area. They also found that with increasing length and decreasing length-to-diameter (L/D) ratio the pullout capacity increased. They also found that in case of group of GPA anchor the uplift capacity increased compared to single pile cause of group action and the increment was about

22%. Merifield and Smith [6] have investigated on multi-plate anchors embedded in clayey soil. They have adopted plane strain numerical model with ABAQUS and executed a numerical limit analysis procedure. They found that ultimate uplift resistance of multi-plate anchor increased up to a limiting value indicating the shift in shallow to deep anchor mechanism. O'kelly et al. [7] investigated the pullout resistance of granular anchors (GA) in undrained over consolidated clay. They found that the mode of failure of GAs depended upon the length-to-diameter (L/D) ratios. For short granular anchors, the pullout resistance is offered by shaft and for long GA the same is offered by end-bulging of the granular column. With the help of PLAXIS 2D considering the soil mass as Mohr–Coulomb material they have performed a numerical investigation and found the range of the bulging zone of about 8 times diameter of pile. Tho et al. [8] investigated the uncertainty of different approaches for determining the uplift capacity of the plate anchors by forming the capacity factors for square plate anchors within a soil of linearly increasing strength using three-dimensional large deformation finite element approach. Liu et al. [9] analyzed the Ultimate Pullout Capacity (UPC) of the anchor and suggested for using the large deformation finite element analysis. Adopting the coupled Eulerian–Lagrangian (CEL) technique with the help of the ABAQUS they performed the behavioral study and then carried out experimental studies on different types of plate anchors in different types of the soil. Considering the soil mass as elastic-perfectly plastic material with Tresca yield criterion they carried out the analysis. They found that for square anchor in uniform clay the value of bearing capacity factor (N_c) increases rapidly with H/B of 4, whereas for square plate anchors in linear-type clay the pullout resistance increased linearly up to maximum capacity and reduced to zero at mud line. Banerjee and Mahadevuni [10] investigated the effects of different parameters and uplift capacity of square plate anchors reinforced with geosynthetics buried in cohesive soil with the help of ABAQUS. They incorporated the material nonlinearity by considering hypo-elastic model for soil mass and investigated the effect of embedment depth, size, and depth of geotextile sheet. They found that the uplift capacity of the plate anchor increased proportionally with embedment depth up to a critical value, which also indicates the transition stage of shallow behavior to deep anchor criteria. With the application of reinforcement, the improvement in uplift capacity was about 52–72%. From their study, they found that the ultimate capacity as well as breakout factor of the anchor increased with embedment ratio up to 4 but with size of plate had an insignificant effect on breakout factors. From the previous research works, it has been found that analysis and experimental works have been done with different types of anchors such as plate anchor, granular pile anchors in clayey soil mass but detail study about bell-shaped anchors with attached tie embedded in soil mass (clayey soil) is still very limited. In the present investigation, an attempt has been taken to numerically analyze the bell-shaped anchor with tie embedded in clayey soil mass and also to study its behavior, stress characteristic, etc.
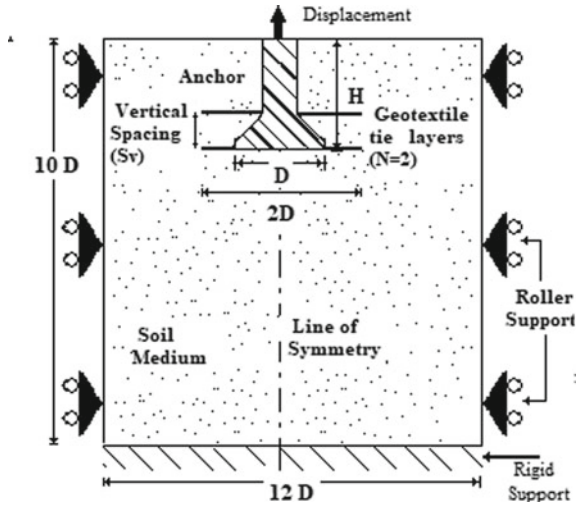
Fig. 1 Schematic diagram of soil-tie-anchor system used for analysis

2 Statement of the Problem

A 2D axisymmetric bell-shaped anchor embedded in clayey soil mass with geotextile ties is analyzed with the help of FEM software (ABAQUS). The numerical analysis has been performed by varying different parameters of soil, geotextile ties, and anchor. One typical anchor with attached geotextile ties has been used for the analysis. Figure 1 presents the illustrative diagram of the numerical model.

3 Materials Used for the Analysis

One typical model bell-shaped anchor, diameter (D) of 0.125 m, has been chosen for the present analysis. Three types of soils (Type I, Type II, and Type III) have been collected for the present work. Type I soil is Kaolinite, which has been procured from local market Kolkata, West Bengal, India. Type II and Type III soils are also locally collected soils from different places around Howrah District, West Bengal. The engineering properties of the above three soils have been presented in Table 1. In accordance with ASTM 2487 [11], the Soil Type I, Soil Type II, and Soil Type III may be classified as CH, CL, and CL, respectively. Woven geotextile made of polypropylene ties has been used for analysis purposes. Tensile strength for the geotextile has been found as 41 N/m and 37 kN/m in machine direction and cross-machine direction, respectively.

Table 1 Properties of soil mass

Soil designation	Type I	Type II	Type III
Dry density (DD) kN/m^3	17.85	14.32	16.28
Optimum moisture content (OMC) %	12.1	26.56	21.63
LL	51.40	35.00	33.54
PL	29.84	21.60	17.34
Type of soil	CH	CL	CL
ϕ, Angle of friction (°)	4.4	3.5	3.0
c, Cohesion (kN/m^2)	21.15	15.50	12.00
Specific gravity	2.597	2.685	2.587

4 Analysis Procedure

In the present numerical simulation, the anchor, soil mass, and the ties have been modeled as elastic material, elasto-plastic and homogeneous element, respectively. The properties of the anchor have been taken as follows: density of the anchor as 2.5 kg/m^3, modulus of elasticity 25 MPa, and Poisson's ratio 0.15. As for geotextile ties, material has been chosen as woven polypropylene, whose mass per unit area, modulus of elasticity, and Poisson's ratio have been taken as 0.250 kg/m^2, 193 MPa, and 0.25, respectively, for numerical study purpose. Detailed properties of the geotextile sheet have been described elsewhere [12]. Breakaway condition has been considered after the failure occurs. From symmetric consideration, half model has been accounted for numerical analysis and performing sensitivity study the boundary of the soil mass has been assigned as 6D as width and 10D as height. Detail procedure of analysis has been discussed in, Das and Bera [13]. In the current study, cohesive interaction has been chosen between soil and anchor. In the numerical simulation, the model of anchor, tie, and soil has been modeled as solid homogeneous plane-strain element. Friction as well as cohesion has been applied between geotextile and soil mass due to direct non-applicability of adhesion.

5 Plan for the Numerical Analysis

In the present numerical simulation, analysis has been done in four different series (Series F1, Series F2, Series F3, and Series F4). In Series F1, H/D ratio (H—depth of embedment and D—diameter of the anchor) of the anchor has been varied from 0.5 to 3.0 for three types of soil without any ties. F2 represents the variation of H/D ratio for $L_g/D = 2$ (L_g = length of geotextile) for three types of soil. F3 represents the variation of L_g/D ratios for H/D = 3 in all three types of soil and F4 represents the variation of number of layers (1–4) for H/D = 3 in three types of soils. Series F1 has been performed to know the effect of H/D ratio with varying types of soil

Table 2 Plan of analysis

Series	Anchor	H/D	Soil type	Ties
F1	1	0.5–3	Soil Type I, Soil Type II, Soil Type III	–
F2		0.5–3		L_g/D-2
F3		3		L_g/D-2,3,4,5
F4		3		N-1,2,3,4

on uplift capacity of anchor without tie, whereas Series F2, F3, and F4 have been performed to study the effect of application of geotextile ties on uplift capacity of the tie attached anchor. In the present paper, one particular anchor (diameter 0.125 m) has been chosen for the entire analysis. The detail of the plan for analysis has been presented in Table 2.

6 Convergence Study

For improving the accuracy of the numerical analysis, a convergence study has been performed. A model anchor of diameter 0.125, $L_g/D = 2$, $N = 1$, and H/D $= 3$ has been selected for the analysis purpose. The results of the convergence study have been presented in Fig. 2. From the figure, it has been found that 2170 no. of CAX4R of 2D elements are sufficient to analyze the model accurately.
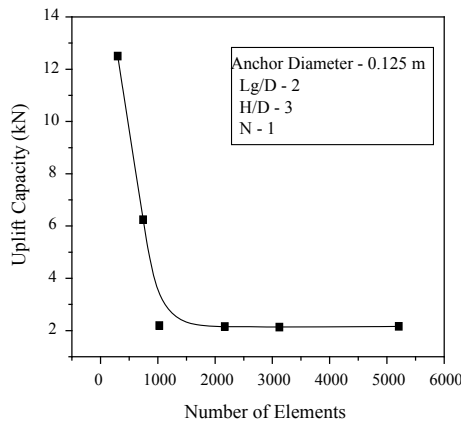
Fig. 2 Convergence study for the analysis

7 Validation of the Numerical Study

For the purpose of validating of the present work, a series of model tests with the model anchor (diameter 0.125 m) with geotextile tie have been carried out in the laboratory for Soil Type I with varying H/D ratio, L_g/D ratio. The model tests have been carried out in Type I soil at MDD and OMC. Typical uplift capacity versus displacement curve for H/D = 1.0, L_g/D = 3 (within soil Type 1) is shown in Fig. 3. Figure 4 shows the comparison between the result obtained from experiment and numerical investigation. From the curve, it is observed that the experimental results are very close to results obtained from ABAQUS analysis. From the curve, it is also found that the maximum deviation is around 9% only.
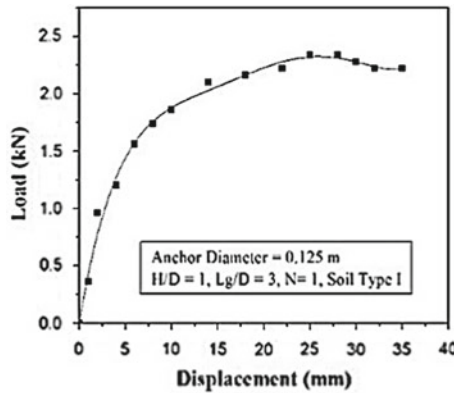
Fig. 3 Uplift displacement versus uplift capacity in Type I soil
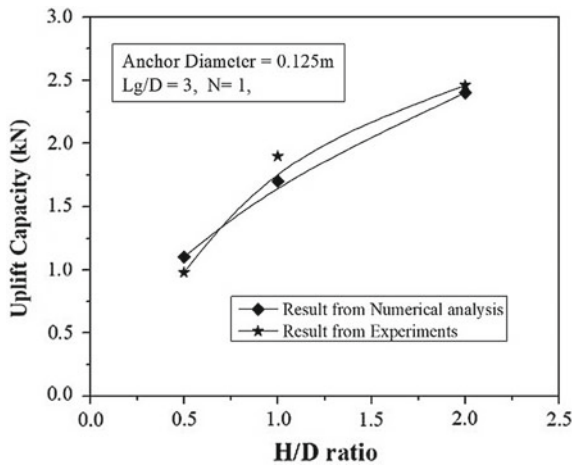
Fig. 4 Comparison between experimental and numerical result

8 Results and Discussion

The data obtained from the ABAQUS analysis have been presented in the graphical form. Figure 5 displays the displacement contours of the anchor-tie-soil system after application of the load. Figure 6 presents the typical load versus displacement curve for anchor without and with geotextile ties of L_g/D-2 (Soil Type II, H/D = 3). Figure 7 presents the variation of ultimate uplift capacity with H/D for a particular L_g/D (=2)
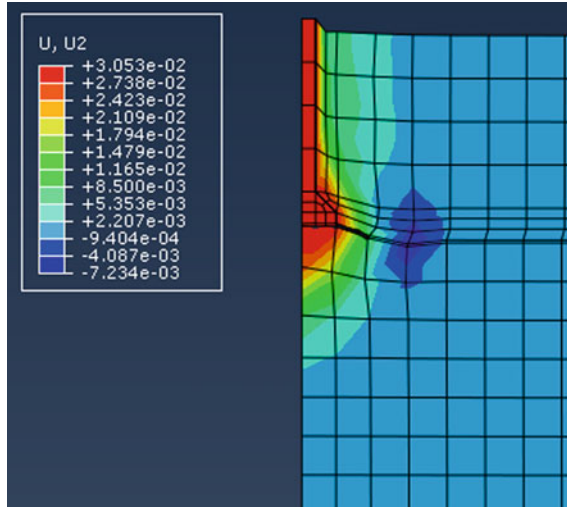

Fig. 5 Displacement contour obtained from numerical simulation
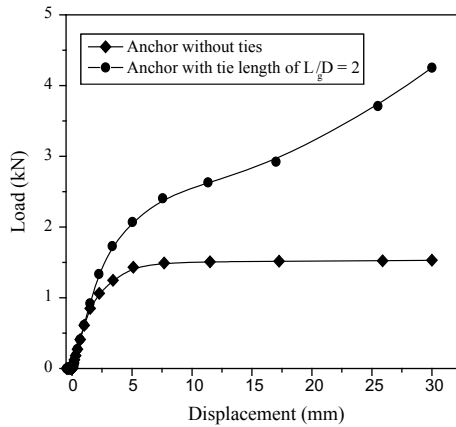
Fig. 6 Typical uplift load versus displacement curve for anchor without and with ties (H/D = 3, Soil Type II)
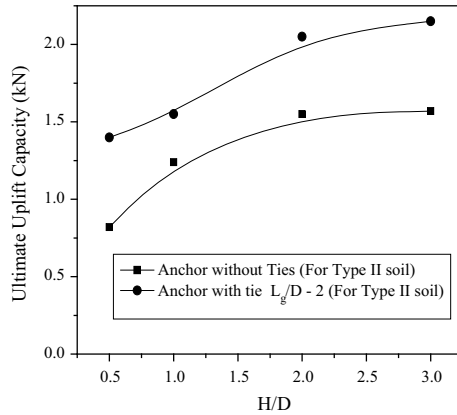
Fig. 7 Uplift capacity versus H/D for $L_g/D = 2$ for Soil Type II

for Soil Type II. Figure 9 displays the variation of uplift capacity versus L_g/D for single layer ties in Soil Type II. Figure 10 represents the variation of the ultimate uplift capacity with number of layers for $L_g/D = 2$ in Soil Type II. The improvement in ultimate uplift capacity for a typical H/D (=3) with increasing the L_g/D for all three types of soil has been shown in Fig. 8. Figure 11 represents the variation of maximum tensile stresses in geotextile with increasing the L_g/D for Soil Type II. Based on the results acquired in the present analysis, discussions are made as follows.
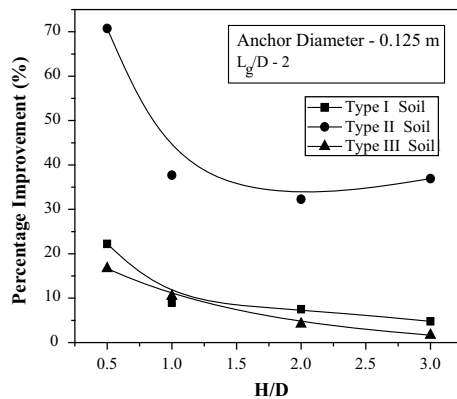

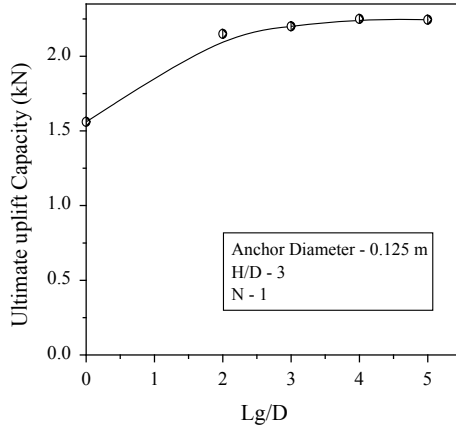**Fig. 8** Improvement for uplift capacity with H/D for $L_g/D = 2$

Fig. 9 Uplift capacity versus L_g/D for $N = 1$ for Soil Type II
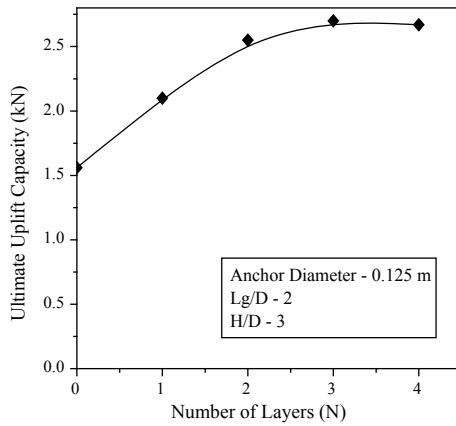

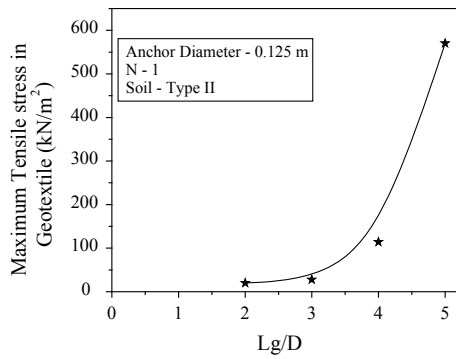**Fig. 10** Uplift capacity versus N for $L_g/D = 2$, $H/D = 3$ for Soil Type II

Fig. 11 Maximum tensile stress variation with L_g/D for N-1 Soil Type II

8.1 Effect of Tie on Uplift Capacity of Anchor

The uplift loads versus displacement curve with and without ties are shown in Fig. 6. From the curve it is observed that the inclusion of geotextile ties increases the ultimate uplift capacity. From the curves (Fig. 6), it is also found that the improvement of uplift capacity starts after the measurable displacement (1.15 mm). Figure 7 displays the ultimate uplift capacity versus H/D ratio curve for anchor with ties and without ties. From the curve, it is found that with increase in H/D ratio the values of ultimate uplift capacity of both the anchor (anchor with ties and anchor without ties) increases. Also from Fig. 7 it can be found that with respect to H/D the inclusion of geotextile ties to the anchor definitely improves the uplift capacity. Figure 8 shows the improvement for uplift capacity of anchor with tie versus H/D ratio curve. From the curve, it is found that the maximum improvement achieved at $L_g/D = 0.5$ after that it is decreases with increase in H/D ratio for all three types of soil (Soil Type I, Soil Type II, and Soil Type III). Reason behind this can be stated that with increment of the embedment ratio (H/D) as more shaft-soil adhesion force comes into play the effect of geotextile tie reduces. From the present analysis, it is found that the respective percentage improvement for inclusion of geotextile ties ($L_g/D = 2$) for $H/D = 0.5$ is 70% and for $H/D = 3$ is about 37% for Type II soil. Also, for $H/D = 0.5$, the percentage improvement in uplift capacity is about 22% and 17% for Type I and Type 3 soil respectively whereas for $H/D = 3$ the percentage improvement is about 5 and 2%.

8.2 Effect of L_g/D on Ultimate Uplift Capacity

L_g/D is one of the important factors for evaluating the ultimate uplift capacity of anchor with ties. Figure 9 explains that the increment of L_g/D increases the ultimate uplift capacity up to a critical value. For this particular case in Soil Type II the critical value of L_g/D is found to be 3.

8.3 Effect of Number of Layers of Ties on Uplift Capacity of Anchor

Figure 10 represents that increment of the number of layers of the geotextile ties increases the ultimate uplift capacity of the anchor and after a certain number of layer it achieves a constant value. In the present investigation for this particular case in Soil Type II, the critical value of number of ties is found to be 3. The percentage increments in uplift capacity for inclusion three layers of geotextile ties are about 73% compared to the anchor without ties for Soil Type II whereas for Soil Types I

and III the maximum percentage increment is about 11% and 44% for three layers of geotextile with H/D = 3.

8.4 Tensile Stress in Geotextile Ties

From the present study, it can be found that increasing the number of geotextile ties layers improves the ultimate uplift capacity of the bell-shaped anchor and simultaneously tensile stresses have been generated in the geotextile ties. Figure 11 represents the tensile stress variation with increasing the L_g/D ratio curve for Soil Type II, $N = 1$. The maximum tensile stress is found to be generated at the junction point of anchor and geotextile ties. Also, for the particular case in Soil Type II for $L_g/D = 5$, the maximum tensile stress is found to be 570 kN/m^2. For a typical case of $L_g/D = 5$, $H/D = 3$, it has been found that tensile stress takes place at displacement of 1.15 mm, we can say after 1.15 mm of displacement, the geotextile ties start to take tensile stresses.

9 Conclusion

From the numerical simulations performed in the present work, the following conclusions can be drawn.

1. Inclusion of geotextile ties increases the uplift capacity of the bell-shaped anchor. The improvement of uplift capacity starts to take place after a measurable displacement.
2. Increasing the length of geotextile ties increases the ultimate uplift capacity up to a certain limit. From the current study, the optimum value for L_g/D is found to be 3 for Type II soil.
3. Increasing the number of geotextile ties layer also increases the ultimate uplift capacity of the anchor up to a certain value. The optimum number of layers of the geotextile ties is found to be 3 for Type II soil.
4. Maximum tensile stress is observed to be generated at the junction of geotextile ties and anchor. Tensile stresses increase with increment of length of geotextile ties.

References

1. Sowa, V.A.: Pulling capacity of concrete cast in situ bored piles. Canad. Geotech. J. **7**, 482 (1970)
2. Das, B.M.: Model tests for Uplift capacity of foundations in clay. Soils Foundations **18**(2) (1978)
3. Das, B.M.: Uplift Capacity of plate anchors in Clay. In: Proceedings of the Fourth International Offshore and Polar Engineering Conference (1994), Osaka, Japan, April-15 (1994)
4. Degenkamp, G., Dutta, A.: Soil resistances to embedded anchor chain in Soft Clay. J. Geotechn. Eng. **115**(10) (1989)
5. Rao A.S., Phanikumar, B.R., Babu, R.D., Suresh, K.: Pullout behavior of granular pile-anchors in expansive clay beds in situ. J. Geotech. Geoenviron. Eng. **133**(5), 531–538 (2007)
6. Merifield, R.S., Smith, C.C.: The ultimate uplift capacity of multi-plate strip anchors in undrained clay. Comput. Geotech. **37**, 504–514 (2010)
7. O'Kelly, B.C., Brinkgreve, R.B.J., Sivakumar, V.: Pullout resistance of granular anchors in clay for undrained condition. Soils Found. **54**(6), 1145–1158 (2014)
8. Tho, K.K., Chen, Z., Leung, C.F., Chow, Y.K.: Pullout behaviour of plate anchor in clay with linearly increasing strength. Can. Geotech. J. **51**(2014), 92–102 (2014)
9. Liu, H., Su, F., Li, Z.: The criterion for determining the ultimate pullout capacity of plate anchors in clay by numerical analysis. Am. J. Eng. Appl. Sci. **7**(4), 374–386 (2014)
10. Banerjee, S., Mahadevuni, N.: Pull-out behaviour of square anchor plates in reinforced soft clay. Int. J. Geosynth. Ground Eng. **3** (2017)
11. ASTM D2487 – 17: Standard Practice for Classification of Soils for Engineering Purposes (Unified Soil Classification System)
12. Das, A., Bera. A.K.: Study on effect of tie length on uplift capacity of anchor with geotextile tie using finite element software "ABAQUS". Indian Geotechnical Conference, IGC-2018, Bangalore, India (2019)
13. Das, A., Bera. A.K.: Ultimate uplift capacity of bell-shaped anchor in river sand using finite element software "ABAQUS". Geotechn. Geolog. Eng. (2019)

Studies on Tilt of Closely Spaced Strip Footings on Unreinforced and Reinforced Sands

S. Anaswara and R. Shivashankar

Abstract Two or more strip footings are quite often built close to each other, due to which there will be overlapping of stresses in zones or at points between the footings. There is a non-uniform pressure distribution in the foundation soil beneath the footings, in the space between the footings and beyond. There is also an increase in confining pressure of the soils between the footings. All these result in the tilt of the footings. This numerical study looks into the tilt of the already existing strip footings due to the construction of an adjacent new strip footing on the surface of cohesionless soils. A parametric study is conducted including the effect of geogrid reinforcement/s beneath the new footing. One of the footings representing an already existing foundation is loaded with half of the estimated failure load of a single-strip footing, and adjacent new strip footing is loaded up to failure. The property boundary line is assumed to be midway between the two footings. Geogrid reinforcement layers beneath the new footing are considered to be extending equally beyond the footing on either side, up to the property line. Both unreinforced and reinforced sands are considered beneath the new footing for analyses. Tilts are observed to increase with the width of footing. At closer spacings, tilt was found to be more in case of loose sand. Results of this study indicate that there is a considerable increase in the tilt of the old footing in the presence of reinforcements beneath the new footing.

Keywords Interference · Tilt · Strip footings · Reinforced new foundation · Existing foundation

S. Anaswara · R. Shivashankar (✉)
Department of Civil Engineering, National Institute of Technology Karnataka, Surathkal, Mangalore 575025, India
e-mail: shivashankar.surathkal@gmail.com

1   Introduction

The primary function of the foundation of a structure is to safely transfer the loads from the superstructure to the soil beneath without occurrence of shear failure and excessive settlements. Due to rapid urbanisation, very often structures and their foundations are built close to each other. The closer spacing between the footings leads to interference effect, which may alter the bearing capacity, settlement, rotational characteristics and failure mechanisms of footings. Due to large stresses at points between the footings (due to the overlapping of stresses), there is a non-uniform pressure distribution beneath the footings in the gap between the footings and beyond. There is also an increase in the confining pressures of the soils between the footings. All these cause a tilt in the footings. This numerical study looks into the tilt of two adjacent strip footings on the surface of cohesionless soils. The presented numerical analyses are based on finite element software PLAXIS 2D.

Interference effects of strip footings were first studied by Stuart [1]. Kumar and Saran [2] conducted laboratory-scale model tests to study interference effects, including tilts, of the closely spaced square and strip footings resting on geogrid-reinforced sand. Lavasan and Ghazavi [3] and Lavasan et al. [4], who performed laboratory tests, found interference to have a significant effect on the ultimate bearing capacities, settlements, tilts and the failure mechanisms of the footings. Experimental studies were made by Salampatoor et al. [5] on unequally loaded and sequentially constructed footings to study interference effect. Their study shows that settlement and tilting of old footing increase due to a new footing. It was reported that there would be an inward tilt of the two footings. Gupta and Sitharam [6] studied interference effects from the point of view of increased bearing capacities. They attributed interference to increase in confining pressure due to the interaction between the failure zones of interfering footings.

2   Problem Definition

Two identical rough strip footings 0.75 m thick, spaced at clear spacing S, are assumed to be placed on the surface of the sand (Fig. 1). One of the footings representing the existing/old foundation is loaded with half of the estimated failure load (factor of safety 2) of isolated footing and adjacent footing loaded up to failure. The footings are loaded unequally and sequentially to simulate the mechanism of the new and old footing with different construction orders. The property boundary line is assumed to be midway between the two footings. Geogrid reinforcement layers beneath the new footing are also considered to be extending equally beyond the footing on either side, only up to the property line. Analyses are performed on reinforced soil with reinforcement placed in one layer and two layers. The reinforcements are placed at 0.3 B depth from the top of the soil bed in case of one layer, and at 0.3 B and 0.5 B depths in case of two layers. Both unreinforced and reinforced sands are considered
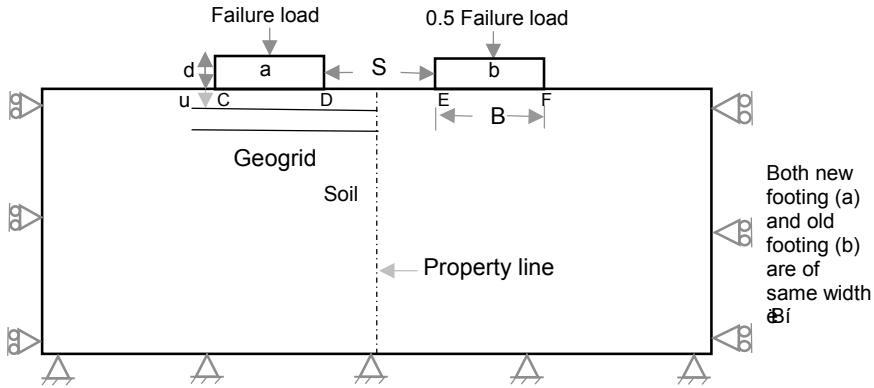
Fig. 1 Problem definition

beneath the new footing for analyses. The study is carried out by varying the spacing between the footings. The study is done for spacing ratio, S/B of 1.0, 1.5, 2.0, 2.5 and 3.0, where S is the clear spacing between the footings and B is the width of the footing. The footing width is varied as 1, 2 and 3 m. The main objective is to study the tilt behaviour of old and new footings when the spacing between the footings is varied from 1.0 to 3.0 B.

Plane strain condition and 15-noded triangular elements are used for the analyses. Both vertical displacement and horizontal displacements are restricted for the bottom horizontal boundary, whereas only horizontal displacements are restricted for the vertical boundaries. The Mohr–Coulomb failure criterion, which is an elastic, perfectly plastic model, is considered. The footing is simulated by using plate elements. Modulus of elasticity, E, of concrete is taken as 25×10^6 kN/m², and Poisson's ratio, v, is considered as 0.15. Geogrid is provided as reinforcement. The property assigned is flexural rigidity (*EA*), which is taken as 500 kN/m. The soil parameters used for finite element analyses are shown in Table 1 [7].

Table 1 Properties of soils [7]

Parameter	Cohesionless soils	
	Medium dense sand	Loose sand
Unsaturated unit weight, γ (kN/m³)	18.2	17.4
Saturated unit weight, γ_{sat} (kN/m³)	21	20.9
Young's modulus, E (kN/m²)	30,000	15,000
Poisson's ratio, v	0.28	0.25
Cohesion, C (kN/m²)	0	0
Angle of internal friction, Φ (°)	35	30

3   Results and Discussion

Construction of a new footing adjacent to the old footing will alter the bearing capacity, settlement, rotational characteristics and failure mechanism of latter. In the present study, one of the footings representing an already existing foundation is loaded to half of the estimated failure load of a single-strip footing and adjacent new strip footing is loaded up to failure.

3.1   Bearing Capacity of New Footings in the Presence of Existing Footing

Figure 2 presents the bearing pressure–settlement curves of new footing in the presence of existing footing placed at the different spacing ratios, S/B. The figure also shows bearing pressure–settlement curve of a single-strip footing. It is seen that bearing capacity is increased due to the presence of the other footing, which can be attributed to the interference effect.

To quantify the effect of old footing on the ultimate bearing capacity of new footing, the interference factor for new footing is determined. Interference factor for new footing IF $_{(new)}$ is defined in Eq. 1.

$$F_{(new)} = \frac{\text{Ultimate load carrying capacity of the new footing in the presence of old footing}}{\text{Ultimate load carrying capacity of single independent strip footing}} \quad (1)$$

The IF$_{(new)}$ versus spacing ratio S/B is plotted in Fig. 3 for both medium dense sand and loose sands. IF $_{(new)}$ is more when the spacing between the footings is less.
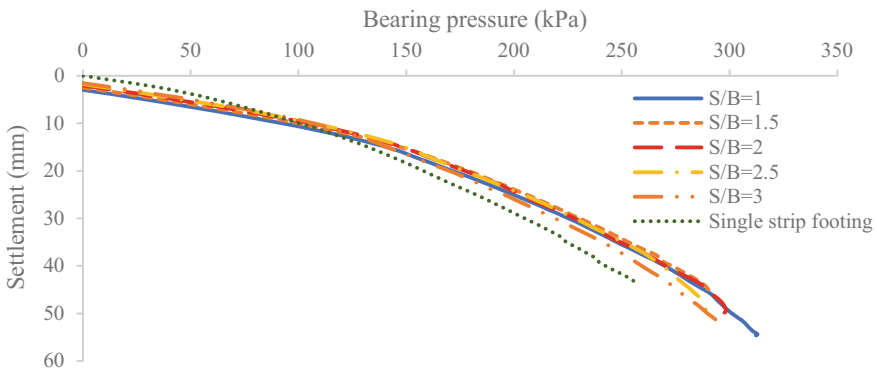

Fig. 2   Bearing pressure versus settlement for new footing, when independent and in the presence of old footing of width 1 m on medium dense sand on unreinforced soil condition
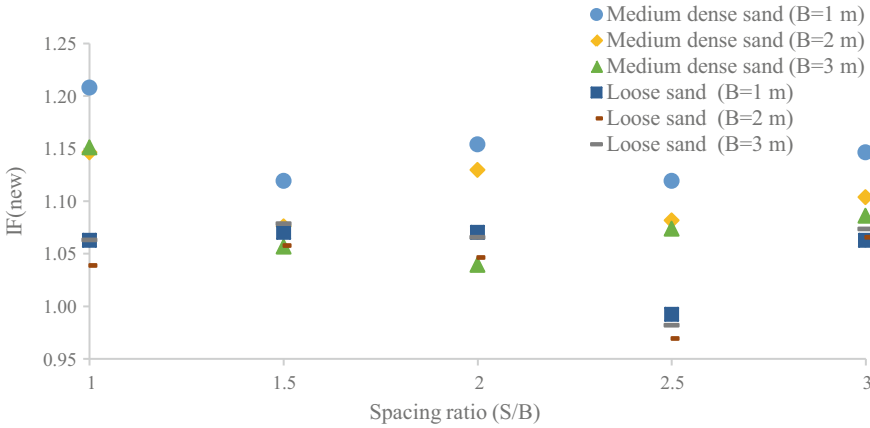
Fig. 3 Interference factor of new footing adjacent to the existing footing versus spacing ratio, S/B, for different footing widths on unreinforced soil

3.2 Tilt of Existing Footing Due to the New Footing

3.2.1 Tilt of Existing Footing Due to the New Footing on Unreinforced Soil

The tilt of existing footing due to the new footing is being studied. Tilt is expressed in terms of percentage. To study the effect of footing widths, tilt is plotted against spacing ratio for medium dense sand and loose sand for different widths ($B = 1$ m to $B = 3$ m) (Fig. 4). Tilt is observed to increase with footing width and is found to be less for medium dense sand as compared to loose sand. Maximum differential
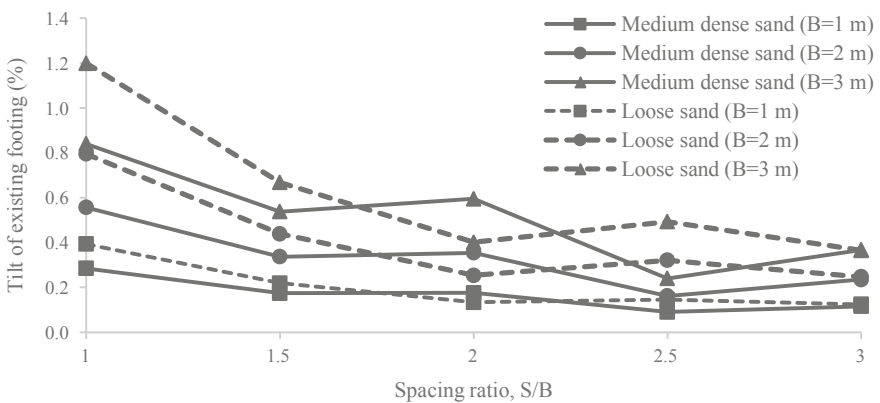

Fig. 4 Tilt of old footing due to new footing versus spacing ratio, S/B, for medium dense sand and loose sand on unreinforced soil conditions
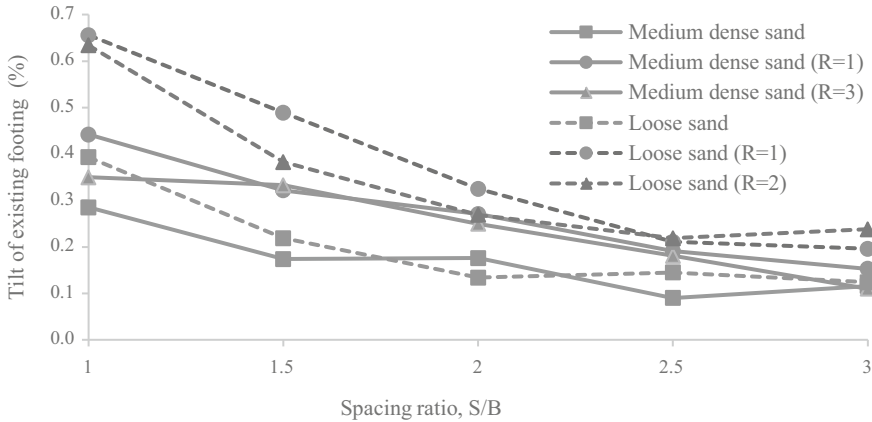
Fig. 5 Tilt of old footing due to new footing versus spacing ratio, S/B, for medium dense sand and loose sand on unreinforced and reinforced soil conditions (footing width 1 m, R in bracket denotes the number of reinforcement layers beneath new footing)

settlement for a 3-m-wide strip footing on medium dense sand works out to be about 25 mm (for about 0.8% tilt), whereas in case of loose sand the differential settlement works out to be about 38 mm (for about 1.2% tilt). Discussion on the direction of tilt of both the existing and new footings on unreinforced soil is done in Sect. 3.2.3.

3.2.2 Tilt of Existing Footing Due to the New Footing on Reinforced Soil

To study the effect of reinforcement provided beneath new footing adjacent to the existing footing, on the tilt of existing footing, tilt is plotted against spacing ratio for both unreinforced and reinforced conditions for footing width $B = 1$ m (Fig. 5). In Fig. 6, tilt is plotted against spacing ratio for both unreinforced and reinforced conditions for footing width $B = 3$ m. In both cases, the tilt of existing/old footing due to the construction of the new adjacent footing is found to be more when there is reinforcement beneath the new footing. Discussion on tilts of existing and newly built strip footings, with the newly built trip footing supported on reinforced soil, is done in the next Sect. 3.2.3.

3.2.3 Direction of Tilts of Both Existing and New Footings

The direction of tilt is shown in Fig. 7 (which is a computer output). CD represents new strip footing, and EF represents the old/already existing strip footing. In the present study, loading is done sequentially; i.e. the new footing is loaded after old footing is already in place. Also, differential loading is considered, old footing loaded to only 50% and new footing loaded to 100% of failure load of strip footings on sands.
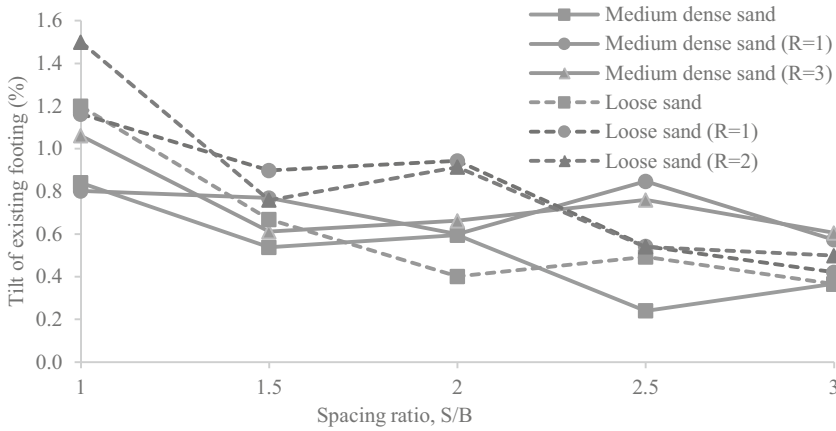
Fig. 6 Tilt of old footing due to new footing versus spacing ratio, S/B, for medium dense sand and loose sand on unreinforced and reinforced soil conditions (footing width 3 m, R in bracket denotes the number of reinforcement layers beneath new footing)

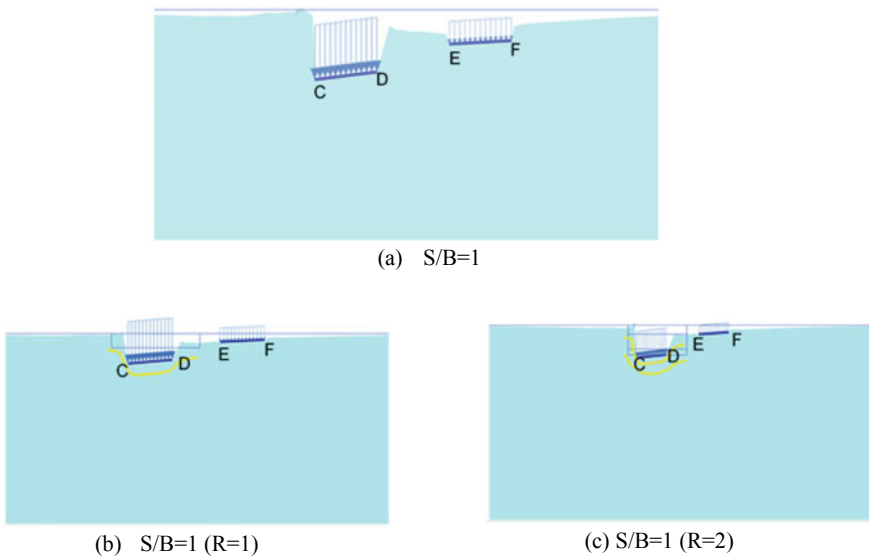(a) S/B=1

(b) S/B=1 (R=1)

(c) S/B=1 (R=2)

Fig. 7 Computer output showing directions of tilt of old and new footings for spacing ratio, S/B = 1, for medium dense sand for **a** unreinforced case and **b** and **c** reinforced cases with one and two layers of reinforcements beneath the new footing

Both footings are tilting in the same anticlockwise direction as shown in Fig. 7. It can be explained in the following way. For the old/existing footing, in the initial stages, increased stresses in the soil between the footings must have caused it to rotate anticlockwise or inwards. But in case of the new footing, as it is gradually loaded, the soil between the footings gets more and more confined, and makes it hard for the inner edge (D) of the new footing to compress, whereas the outer edge which is having lesser confinement effect undergoes larger settlements, thus resulting in anticlockwise rotation or tilt. Thus, although there is an increase in stress in soil between the footings due to stress overlap, the confinement effect seems to dominate and dictate the direction of tilt.

In the case of reinforcement beneath new strip footing, larger load and stiffer foundation soil must have made it undergo larger and uniform settlements (compared to already existing footing). This will cause larger rotation of the old strip footing when the new strip footing is on reinforced soil.

3.3 Failure Zones of Interfering Footings

The elastic zones, as envisaged in Terzaghi's or Meyerhof's analyses, beneath old/already existing footings at all spacings on sands, are not very clear. It must be recollected here that only the new footing is loaded up to failure and the already existing old footing is considered to be loaded to 50% capacity. Therefore, it is to be expected that the failure surfaces are fully or better developed in the case of new footings but certainly influenced by the presence of the already existing and loaded (up to 50%) old footings. The variation of failure surface and incremental displacement pattern beneath the strip footings are shown in Fig. 8. Maximum bearing capacity and tilt values are noted at spacing ratio 1. Therefore, the failure mechanisms at a spacing ratio of one are being studied. At unreinforced soil conditions, failure surface from beneath the new footing is developed fully (Fig. 8a). When the new footing is provided with a single layer of reinforcement, failure surface is seen to get wider and deeper (Fig. 8b, c).

4 Conclusions

The following conclusions are drawn from this study.

- In this study, the two strip footings (old and new on unreinforced and reinforced sands) are loaded sequentially and unequally. More load is considered on new strip footing. Both footings are tilting in the same direction.
- Large tilts are observed at a spacing ratio of one in both medium dense sand and loose sand. As expected, tilts were less for medium dense sand when compared to loose sand.
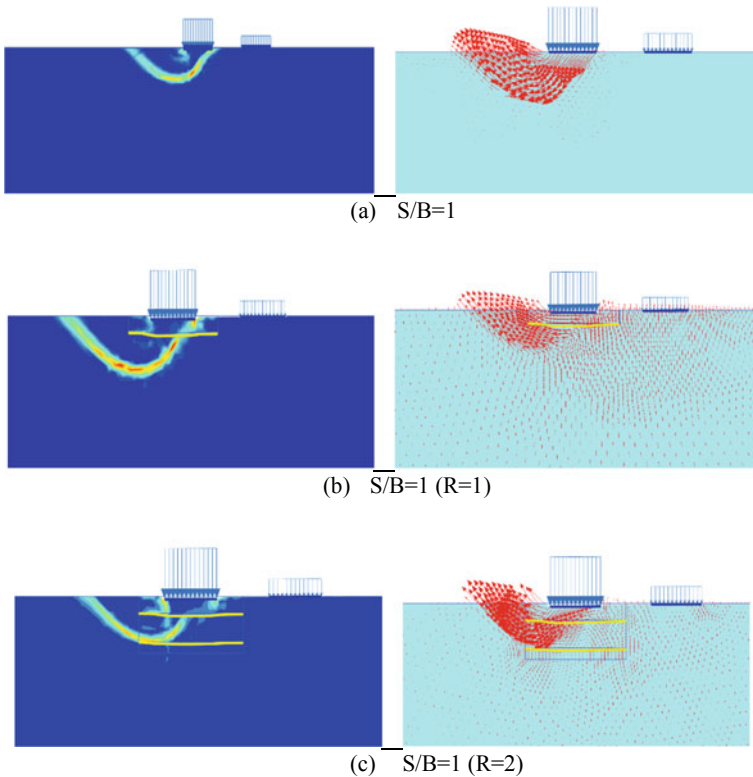
(a) S/B=1

(b) S/B=1 (R=1)

(c) S/B=1 (R=2)

Fig. 8 Shear strain contours and incremental displacement in case of footings on medium dense sand for footing width $B = 1$ m and ($S/B = 1$) (R in bracket denotes the number of reinforcement layers)

- Tilt increases with increase in footing width for sands.
- Providing reinforcement beneath the new footing and loading it to maximum cause a somewhat larger tilt of already existing strip footings supporting lightly loaded structures.

References

1. Stuart, J.G.: Interference between foundations, with special reference to surface footings in sand. Geotechnique **12**(1), 15–22 (1962). https://doi.org/10.1680/geot.1962.12.1.15
2. Kumar, A., Saran, S.: Closely spaced footings on geogrid-reinforced sand. J. Geotech. Geoenviron. Eng. **129**(7), 660–664 (2003). https://doi.org/10.1061/(ASCE)1090-0241(2003)129:7(660)

3. Lavasan, A.A., Ghazavi, M.: Behavior of closely spaced square and circular footings on reinforced sand. Soils Found. **52**(1), 160–167 (2012). https://doi.org/10.1016/j.sandf.2012.01.006

4. Lavasan, A.A., Ghazavi, M., Schanz, T.: Analysis of interfering circular footings on reinforced soil by physical and numerical approaches considering strain-dependent stiffness. Int. J. Geomech. **17**(11), 04017096 (2017). https://doi.org/10.1061/(ASCE)GM.1943-5622.0000992

5. Salamatpoor, S., Jafarian, Y., Hajiannia, A.: Bearing capacity and uneven settlement of consecutively constructed adjacent footings rested on saturated sand using model tests. Int. J. Civ. Eng. **17**(6), 1–13 (2018). https://doi.org/10.1007/s40999-018-0295-y.

6. Gupta, A., Sitharam, T.G.: Experimental and numerical investigations on interference of closely spaced square footings on sand. Int. J. Geotech. Eng. 1–9 (2018). https://doi.org/10.1080/19386362.2018.1454386

7. Bowles L.E.: Foundation Analysis and Design. McGraw-hill (1996)

Experimental Evaluation of Failure Zone in Sand Beneath the Ring Footing and Cutting Edge of Open Caisson Using Image Analysis

Jitesh T. Chavda and **G. R. Dodagoudar**

Abstract The analytical evaluation of the bearing capacity of the ring footing and cutting edge of the open caisson requires a definition of the size of failure zone in the soil, whereas the failure zone in soil depends on the type of soil and the configuration of the ring footing and cutting edge of the open caisson. In the study, the 1 *g* model tests are carried out to evaluate the failure zone in the sand beneath the ring footing and cutting edge of the circular open caisson. The radii ratio of the ring footing and cutting edge of the open caisson models are varied as $r_i/r_o = 0.615, 0.737$, and 0.783, and the tapered angle of cutting edge models is varied as $\beta = 30°$ and $45°$. The radius ratio is the ratio of internal radius to the external radius of the ring footing and cutting edge of the open caisson. The ring footing and caisson models are fabricated using Teflon tubes, and Indian standard sand is used as soil medium. The image-based deformation measurement technique is used to evaluate the failure zone in sand. The image analysis results are validated from the rigid displacement test.

Keywords Ring footing · Open caisson · 1 g model test · Cutting edge · Image analysis · Failure zone

1 Introduction

Open caissons are provided with a cutting edge at the bottom to allow the failure of the soil within the caisson and subsequent sinking. The cutting edge has a sloping angle with respect to the vertical face of the cutting edge. This sloping angle is called as tapered angle (β). The tapered angle of the cutting edge can vary from $\beta = 30$ to $90°$. It is noted that the cutting edge with flat base (i.e., $\beta = 90°$) represents the ring footing. Ring footings are used as foundations to support the structures with

J. T. Chavda (✉)
Department of Civil Engineering, SVNIT Surat, Surat 395007, India
e-mail: jiteshchavda03@yahoo.in

G. R. Dodagoudar
Department of Civil Engineering, IIT Madras, Chennai 600036, India
e-mail: goudar@iitm.ac.in

symmetrical geometries such as silos, storage tanks, chimneys, cooling towers, and bridge piers. The use of ring footing decreases the amount of material usage; hence, they are economical apart from providing a beneficial effect of arching.

The bearing capacity of the cutting edge of open caisson and ring footing depends on the size of the failure zone, i.e., influence zone, whereas the size of influence zone depends on the type of soil, configuration of the cutting edge, width and radii ratio of the ring footing and caisson. The bearing capacity factors of the cutting edge of the open caisson for a predefined influence zone are evaluated by limit equilibrium method [5, 26, 33]. However, the different configuration of the cutting edge, i.e., variation in the tapered angles of the cutting edge is not explicitly accounted in their study. It is noted that only one study reports the experimental evaluation of the influence zone in sand for varying tapered angles of the cutting edge considering plane strain idealization [22]. The bearing capacity of ring footing is evaluated by experimental investigations [6, 10, 12, 20, 23, 24], the limit equilibrium method, the upper- and lower-bound plastic limit analyses [16], the method of characteristics [11, 15], the finite difference method [3, 4, 13, 21, 35], and the finite element method [7, 9, 17, 18, 30]. In the above-mentioned studies, the bearing capacity of the footing depends on the size of failure zone used in the study. However, the literature on the experimental evaluation of the influence zone in soil beneath the cutting edge and ring footing is limited.

In many projects, the large diameter caissons ($D_o > 10$ m) are used (e.g., [2, 19, 22, 25, 34]). In such projects, the sequential excavation is adopted for the uniform and control sinking of the caisson. A rough estimation of the extent of the influence zone in the soil based on the configuration of the cutting edge and the soil type helps in proper planning of sequential excavation strategies [19]. In the present study, the formation of soil displacements field (i.e., influence zone) is evaluated when the caisson ($\beta = 30$ and $45°$) and ring footing ($\beta = 90°$) models are penetrated in the sand. The image-based deformation measurement technique is used in the study. The experimentally evaluated influence zone in sand beneath the cutting edge and ring footing is normalized by dividing the radial extent of the influence zone with the width of the cutting edge and ring footing. These normalized influence zones can be used in the analytical evaluation of the bearing capacity of the cutting edge and ring footing.

2 Experimental Program

2.1 Apparatus

In order to fully assess the soil displacement field, i.e., influence zone, the progressive monitoring of the soil movement is of crucial importance until the required depth of penetration of the caisson and ring footing models is achieved. In order to assess the zone of influence, the image-based deformation measurement technique is used

to track the particle movement around the half-cut caisson models. The images are captured through a viewing window of the tank. The caisson model is fixed such that its cut planar face is parallel and in contact with the viewing window of the tank. This particular arrangement of the test is shown in Fig. 1. The cutting edge of the caissons is embedded in the sand to represents the field conditions. The relative displacement between the camera and the tank is fully arrested during the test, i.e., the tank and the camera are moving upward with the same strain rate whereas the half-open caisson model is stationary. Indirectly the captured photographs show the penetration of the half-open caisson in the sand medium.
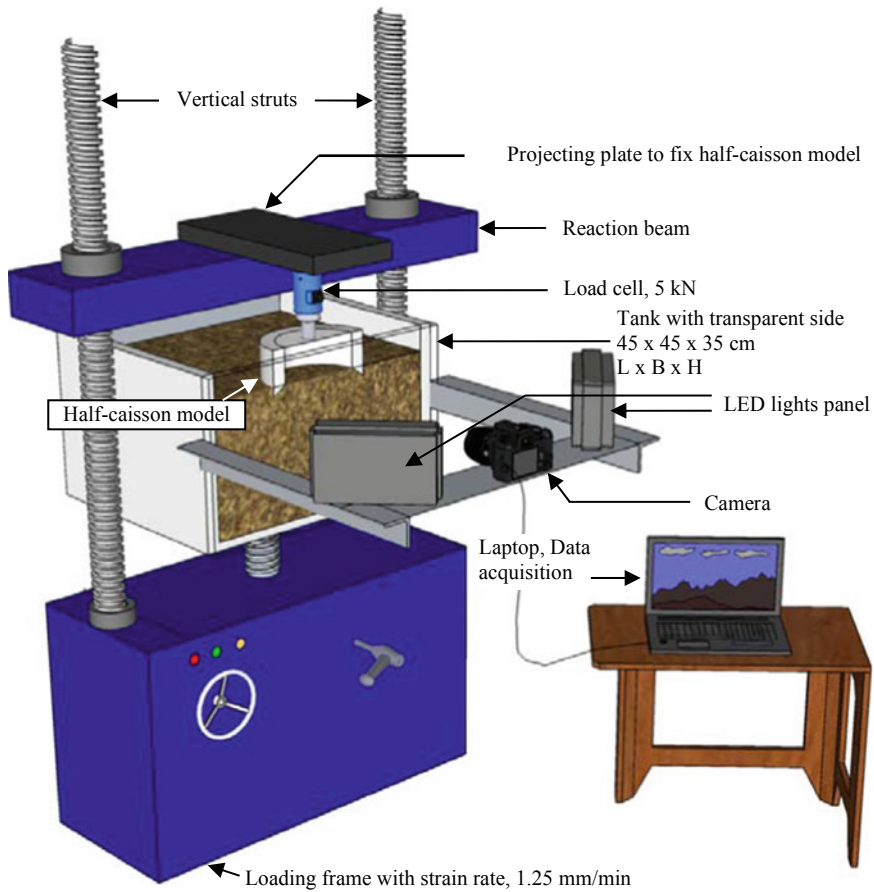

Fig. 1 Experimental setup of caisson model test [8]

Table 1 Index properties of Indian standard sand, Grade II

Parameter	Unit	Value
Specific gravity	–	2.64
Max. unit weight	kN/m^3	16.81
Min. unit weight	kN/m^3	14.50
Relative density	%	50
Unit weight of sand	kN/m^3	15.57
Unified soil classification	–	SP[a]

[a]SP—Poorly graded sand

2.2 Sand Sample, Caisson, and Ring Footing Models

Grade II, Indian standard (IS) sand has been used for all the model tests [14]. The properties of the sand are given in Table 1. During the entire experimental investigations, the relative density of the sand is maintained as $D_r = 50\%$ in order to limit the scope of the study to one density. For the image-based deformation measurement analysis, the sand texture has been optimized to maximize the precision in the measurement of the soil displacements [28, 29, 31, 32]. The procedure reported in Chavda et al. [8] is used for the preparation of the dyed sand and the methodology to achieve the optimum texture. The texture is generated by mixing the IS sand with 65% of dyed sand by weight. The sand used in all the experiments comprises of 35% of the IS sand and 65% of the dyed sand. The dyed sand is prepared by mixing the black color ink with IS sand such that the geotechnical properties of the dyed sand are not altered.

For the image analysis, the caisson models are half-cut to represent an axisymmetric problem. The transparent side of the tank is made of Perspex acrylic sheet. For maximum repetitive use of the transparent acrylic sheet, the caisson and ring footing models are fabricated with Teflon tubes for the investigation of the soil displacement field. The models has unit weight = 11 kN/m^3, Young's modulus = 500 MPa, and Poisson's ratio = 0.46. The Young's modulus of the caisson models is almost 80 times higher than the sand ($E = 5.768$ MPa), and hence, the models are relatively rigid and hence they experience negligible deformations.

2.3 Data Processing

The soil displacement field around the cutting edge of the open caisson and ring footing is examined by performing the image-based deformation measurement analysis using the open-source MATLAB program, GeoPIV-RG [27, 28, 31]. The GeoPIV-RG follows the principle of particle image velocimetry (PIV), originally developed in the field of experimental fluid mechanics [1]. Certain modifications to the PIV technique have been proposed by White et al. [31] and Stanier et al. [27] to

enhance its applicability in geotechnical engineering. The images obtained from the tests consist of series of images from the initial to the final penetration depth, i.e., up to the penetration depth same as the half-width of the cutting edge and ring footing. The resistance load of the caisson is reached to the ultimate value (i.e., the failure load) corresponding to the penetration depth lesser than half-width of the cutting edge having $\beta = 30$ to $90°$ [8]. In the study, the influence zone in the soil is obtained corresponding to the penetration depth of half-width of the cutting edge and ring footing.

2.4 Test Procedure

In the present study, a Nikon D5300 digital single-lens reflex camera is used for image analysis. An external lighting is provided by the two 16 W LED light panels as shown in Fig. 1. The test is performed by moving the tank in the upward direction with a constant strain rate of 1.25 mm/min and the photographs are captured at an interval of 3 s (0.33 Hz). This frequency of image acquisition is decided based on the strain rate and displacement of the soil medium between the two successive images. The tests are stopped when the penetration of the models reach the penetration same as the half-width of the cutting edge and the ring footing.

The test results are validated by performing rigid displacement test. In the test, the tank is moved in the upward direction at the same strain rate of 1.25 mm/min and the rigid displacement of the tank is measured from the dial gauge positioned over the pedestal. At the same time, the displacement of the tank is also captured by the camera. The vertical displacement is calculated from the GeoPIV-RG program and the same is also noted from the dial gauge. From this test, it is found that the displacements obtained from the GeoPIV-RG program are predicted within the error range of $\pm 3\%$ of the dial gauge readings.

2.5 Evaluation of Size of Failure Zone

The vectorial displacement plots and horizontal displacement plots corresponding to the penetration depth of 0.5 B are obtained from GeoPIV_RG. In the horizontal displacement plot, only the radial inward horizontal displacement vectors are plotted in order to get the clear picture of the failure zone. The typical plot of the vectorial displacement, horizontal displacement contours, and the radial inward displacement contours are shown in Fig. 2 corresponding to the cutting edge having radius ratio of 0.783 and the tapered angle of $60°$. The failure zone is evaluated from these three plots corresponding to the penetration results of cutting edge and ring footing. The influence zone is normalized by diving the radial and vertical extent of the failure zone by the width of the cutting edge and ring footing. Thus, the failure zone obtained is called normalized influence zone.
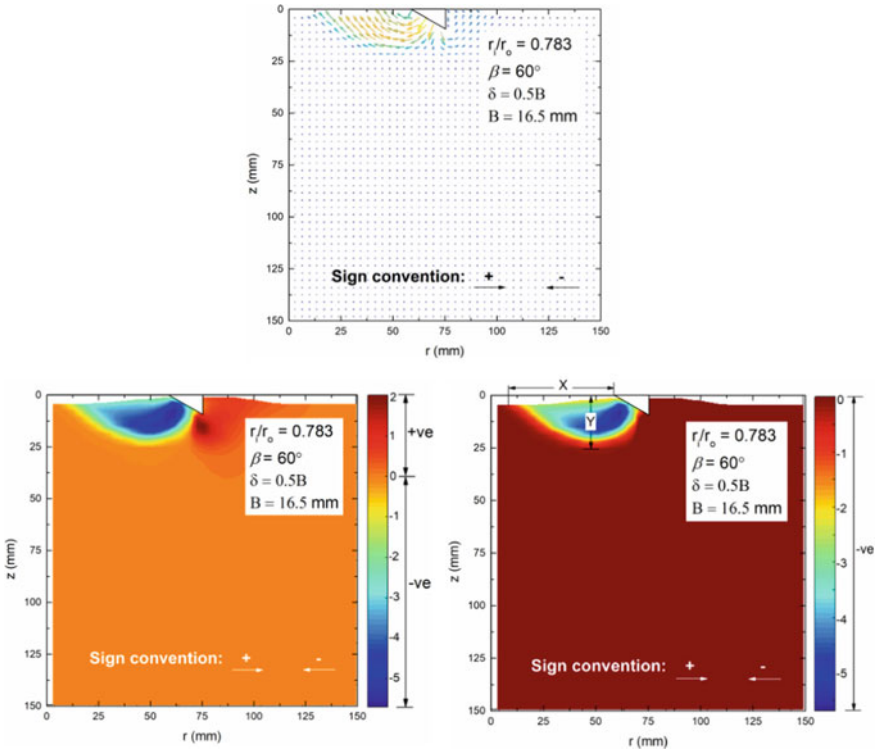
Fig. 2 Typical vectorial displacement, horizontal displacement contour, and the radial inward displacement contour plots

3 Results and Discussion

In the study, the shear strain (τ) of 10% and 20% is also evaluated. The region of soil between the shear strain value of $\tau = 10\%$ and 20% represents the soil whose shear strain is mobilized up to 20%. In the present study, the normalized failure zone and the shear strain = 20% is presented for varying radii ratio ($r_i/r_o = 0.615, 0.737$, and 0.783) and different tapered angles ($\beta = 30, 45$, and 90°) of the cutting edge. The tapered angle $\beta = 90°$ represents the ring footing.

3.1 Failure Zone: Ring Footings

The failure zones in the sand beneath the ring footings obtained from the image analysis for varying radii ratio are shown in Fig. 3. It is seen from the figure that with increase in the radii ratio, the failure zone tends to move away from the centroidal axis of the ring footing. It is also noted that the failure zone tends to move asymmetric
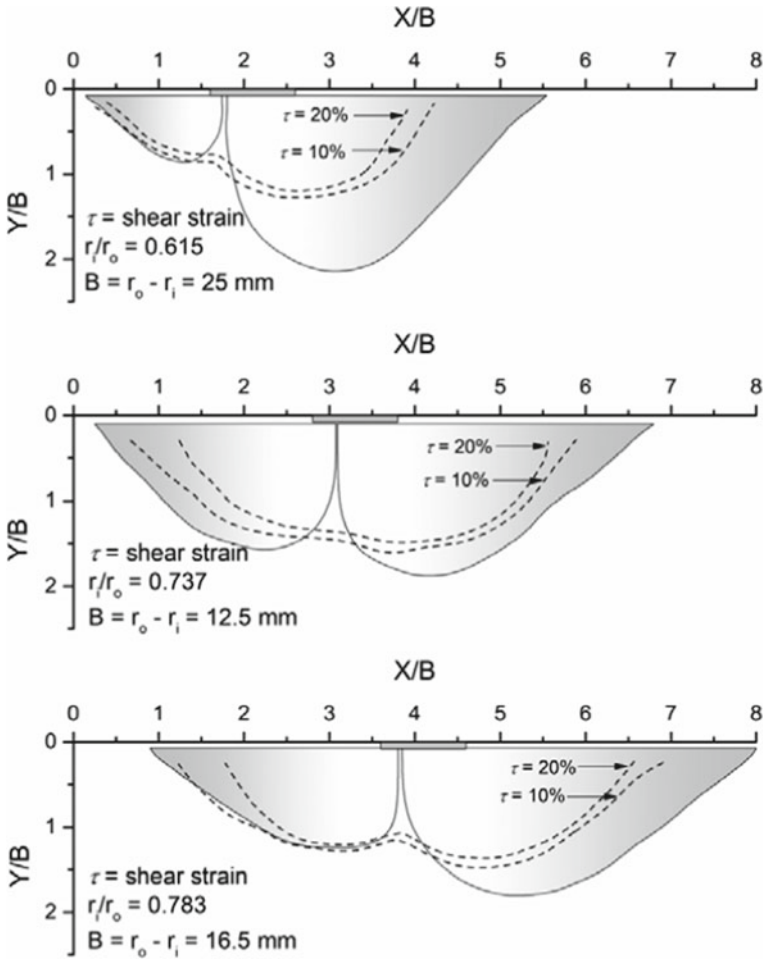
Fig. 3 Failure zone in sand beneath ring footing

failure zone to symmetric failure zone with increase in the radii ratio of the ring footing. Hence, it is opined that with increase in the radii ratio of ring footing nearly to 1, the failure zone will be similar to the strip footing having width same as the width of the ring footing. The size of failure zone is less within the ring footing and it increases with increase in the radii ratio, whereas the size of failure zone outside the ring footing increases with increase in the radii ratio. At lower value of radius ratio ($r_i/r_{\text{-o}} = 0.615$), the size of failure zone within footing is lesser than the size of failure zone outside the footing. This is possibly due to the arching action, i.e., more volume of soil, present outside the footing, contributes the capacity of the footing.

3.2   Failure Zone: Cutting Edge of Open Caisson

The failure zones in the sand beneath the cutting edge of circular open caisson obtained from the image analysis for varying radii ratio and different tapered angles are shown in Fig. 4. It is seen from the figure that with increase in the radii ratio, the size of the failure zone increases for both the tapered angles of cutting edge. However, the size of failure zone is higher for $\beta = 30°$ compared to the cutting edge with $\beta = 45°$. The region of soil whose shear strain is mobilized up to 20% tends to move outside the cutting edge for $\beta = 45°$ compared to the cutting edge with $\beta = 30°$. The failure zone is attributed within the caisson only when steeper cutting edges are used (i.e., $\beta = 30°$).

4   Conclusions

In the study, the 1 g model tests are carried out and the failure zone in the sand beneath the ring footing and cutting edge of circular open caisson is evaluated. The caisson and ring footing models are fabricated with varying radii ratio ($r_i/r_o = 0.615, 0.737,$ and 0.783) and caisson has cutting edge with two different tapered angles ($\beta = 30$ and 45°). The present study results can be used in the analytical studies in determination of the bearing capacity of the cutting edge and ring footing. The following conclusions are drawn from the experimental investigations.

- The failure zones in sand beneath the ring footing and cutting edge of circular open caisson are evaluated using image processing technique.
- At lower value of radius ratio = 0.615, the size of failure zone in sand is less within the ring footing compared to the size of failure zone in sand outside the ring footing. The size of failure zone in sand within ring footing increases with increase in the radii ratio of the footing. The failure zone tends to move asymmetric failure zone to symmetric failure zone with increase in the radii ratio of the ring footing.
- The size of the failure zone in the sand beneath the cutting edge of caisson increases with increase in the radii ratio for both the tapered angles of the cutting edge. The size of the failure zone decreases with increase in the tapered angles of the cutting edge. The steeper cutting edge has higher capacity than the flatter cutting edge. The steeper cutting edges restrict the failure of soil within the caisson only.

The mean stress level can influence the failure process of the granular material. For the usage of results in practice, the failure zone obtained in the study is normalized by the width of the cutting edge. However, it is opined that the further consideration of scaling effects can be made by a comprehensive numerical approach to calibrate the model with the experimental results and extrapolated later to the real-field situations.
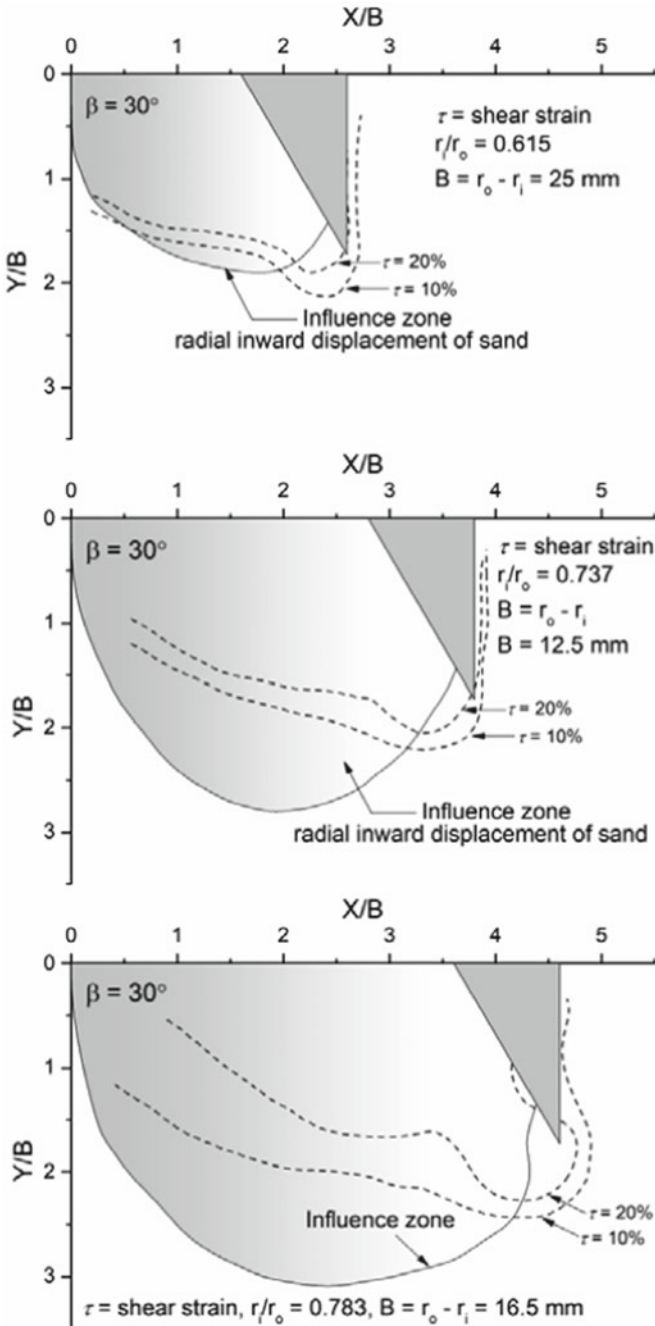
Fig. 4 Failure zone in sand beneath cutting edge of open caisson

References

1. Adrian, R.J.: Particle imaging techniques for experimental fluid mechanics. Annu. Rev. Fluid Mech. **23**, 261–304 (1991)
2. Allenby, D., Waley, G., Kilburn, D.: Examples of open caisson sinking in Scotland. Proc. ICE Geotechn. Eng. **162**(1), 59–70 (2009)
3. Benmebarek, S., Saifi, I., Benmebarek, N.: Undrained vertical bearing capacity factors for ring shallow footings. Geotech. Geol. Eng. **35**(1), 355–364 (2017)
4. Benmebarek, S., Remadna, M.S., Benmebarek, N., Belounar, L.: Numerical evaluation of bearing capacity factor Ng' of ring footings. Comput. Geotech. **44**, 132–138 (2012)
5. Berezantsev: Axisymmetric problem of the theory of limiting equilibrium of granular media. Gosstroiizdat, Moscow [in Russian] (1952)
6. Boushehrian, J.H., Hataf, N.: Experimental and numerical investigation of the bearing capacity of model circular and ring footings on reinforced sand. Geotext. Geomembr. **21**(4), 241–256 (2003)
7. Chavda, J.T., Dodagoudar, G.R.: Finite element evaluation of vertical bearing capacity factors N'c, N'q and N'γ for ring footings. Geotech. Geol. Eng. **37**(2), 741–754 (2019)
8. Chavda, J.T., Mishra, S.R., Dodagoudar, G.R.: Experimental evaluation of ultimate bearing capacity of the cutting edge of open caisson. Int. J. Phys. Model. Geotech. (2019). https://doi.org/10.1680/jphmg.18.00052
9. Choobbasti, A.J., Hesami, S., Najafi, A., Pirzadeh, S., Farrokhzad, F., Zahmatkesh, A.: Numerical evaluation of bearing capacity and settlement of ring footing; case study of Kazeroon cooling towers. Int. J. Res. Rev. Appl. Sci. **4**(3), 263–271 (2010)
10. Clark, J.I.: The settlement and bearing capacity of very large foundations on strong soils: 1996 RM Hardy keynote address. Can. Geotech. J. **35**(1), 131–145 (1998)
11. Gholami, H., Seyedi Hosseininia, E.: Bearing capacity factors of ring footings by using the method of characteristics. Geotech. Geol. Eng. **35**(5), 2137–2146 (2017)
12. Hataf, N., Razavi, M.R.: Behavior of ring footing on sand. Iran J Sci Technol Trans B: Eng **27**, 47–56 (2003)
13. Hosseininia, E. S.: Bearing capacity factors of ring footings. Iran. J. Sci. Technol. Trans. Civ. Eng. **40**(2), 121–132 (2016)
14. IS: 650: Standard sand for testing cement—Specification. Bureau of Indian Standards, New Delhi (1991)
15. Kumar, J., Ghosh, P.: Bearing capacity factor Nγ for ring footings using the method of characteristics. Can. Geotech. J. **40**(3), 1474–1484 (2005)
16. Kumar, J., Chakraborty, M.: Bearing capacity factors for ring foundations. J. Geotech. Geoenviron. Eng. **141**(10), 06015007–1-7 (2015)
17. Lee, J.K., Jeong, S., Lee, S.: Undrained bearing capacity factors for ring footings in heterogeneous soil. Comput. Geotech. **75**, 103–111 (2016)
18. Lee, J.K., Jeong, S., Shang, J.Q.: Undrained bearing capacity of ring foundations on two-layered clays. Ocean Eng. **119**, 47–57 (2016)
19. Nonveiller, E.: Open caissons for deep foundations. J. Geotech. Eng. ASCE **113**(5), 424–439 (1987)
20. Ohri, M.L., Purhit, D.G.M., Dubey, M.L.: Behavior of ring footings on dune sand overlaying dense sand. In: Proceedings of International Conference of Civil Engineering, pp. 4–6. Tehran, Iran (1997)
21. Remadna, M.S., Benmebarek, S., Benmebarek, N.: Numerical evaluation of the bearing capacity factor Nc' of circular and ring footings. Geomech. Geoeng. **12**(1), 1–13 (2016)
22. Royston, R., Phillips, B.M., Sheil, B.B., Byrne, B.W.: Bearing capacity beneath tapered edges of open dug caissons in sand. In: Proceedings of Civil Engineering Research in Ireland. Galway, Ireland (2016)
23. Saha, M.C.: Ultimate bearing capacity of ring footings on sand. Masters in Engineering Thesis, University of Roorkee, Roorkee (1978)

24. Saran, S., Bhandari, N.M., Al Smadi, M.M.A.: Analysis of eccentrically obliquely loaded ring footings on sand. Ind. Geotech. J. **33**(4), 422–446 (2003)
25. Sheil, B., Royston, R., Byrne, B.: Real-time monitoring of large-diameter caissons. In: Proceedings of China-Europe Conference on Geotechnical Engineering, pp. 725–729 (2018). https://doi.org/10.1007/978-3-319-97112-4_162
26. Solov'ev, N.B.: Use of limiting-equilibrium theory to determine the bearing capacity of soil beneath the edges of caissons. Soil Mech. Found. Eng. **45**(2), 39–45 (2008)
27. Stanier, S.A., Blaber, J., Take, W.A., White, D.J.: Improved image-based deformation measurement for geotechnical applications. Can. Geotech. J. **53**(5), 727–739 (2016)
28. Stanier, S.A., White, D.J.: Improved image-based deformation measurement for the centrifuge environment. Geotech. Test. J. **36**(6), 915–927 (2013)
29. Take, W.: The influence of seasonal moisture cycles on clay slopes, Ph.D. Thesis, University of Cambridge, Cambridge, U.K (2003)
30. Tang, C., Phoon, K.K.: Prediction of bearing capacity of ring foundation on dense sand with regard to stress level effect. Int. J. Geomech. ASCE **18**(11), 04018154 (2018)
31. White, D.J., Take, W.A., Bolton, M.D.: Soil deformation measurement using particle image velocimetry (PIV) and photogrammetry. Géotechnique **53**(7), 619–631 (2003)
32. White, D.J., Take, W.A.: Discussion on: application of particle image velocimetry (PIV) in centrifuge testing of uniform clay by Zhang, Y.D., Tan, T.S., Leung, C.F. Int. J. Phys. Modell. Geotech. **5**(4), 27–31 (2005)
33. Yan, F.Y., Guo, Y.C., Liu, S.Q.: The bearing capacity analyses of soil beneath the edge of circular caisson. Adv. Mater. Res. **250**, 1794–1797 (2011)
34. Yao, Q., Yang, X., Li, H.: Construction technology of open caisson for oversize surge shaft in drift gravel stratum. Electron. J. Geotech. Eng. **19**, 5725–5738 (2014)
35. Zhao, L., Wang, J.H.: Vertical bearing capacity for ring footings. Comput. Geotech. **35**(2), 292–304 (2008)

Influence of Soil Variability in SPT Data for Predicting the Bearing Capacity of Piles

Kotra Saikumar and Kaustav Chatterjee

Abstract Standard penetration test (SPT) is one of the most commonly adopted methodologies to determine the soil profile at any particular site for calculating the bearing capacity of the pile foundations. Soil variability is inevitable. In this regard, the present study focusses on the statistical process of characterising the same based on the SPT data. This data was obtained from 20 boreholes at a site in Kolkata, which is proposed to adopt pile foundation for its upcoming structures. The vertical variability is characterised by a probability density function. The statistics of vertical variability comprising of mean and standard deviation are calculated, and the scale of fluctuation using the random field theory is obtained. The range of scale of fluctuation is found to be in good agreement with the globally accepted literature. This variability has been incorporated in predicting the bearing capacity of the piles for the proposed site using different correlations given by Meyerhof (1956), Aoki and De'Alencar (1975) and Decourt (1995).

Keywords SPT · Bearing capacity · Soil variability · Probability density function · Scale of fluctuation

1 Introduction

Foundations are the substructures which distribute the load from the superstructures to the underlying soil or to the bedrock as per the design. Foundations are generally classified as shallow and deep. Pile foundations, categorised under deep foundations, are commonly used for the massive structures, opted when the underlying soil is weak and prone to excessive settlement. Standard penetration test is one of the widely followed methodologies for the soil investigations as well as in determining the bearing capacity of the pile foundations. Many researchers, after the experimental evaluations, developed specific empirical correlations for calculating the ultimate bearing capacity for different kinds of piles. Among them, Meyerhof (1956), Aoki

K. Saikumar (✉) · K. Chatterjee
Indian Institute of Technology Roorkee, Roorkee 247667, India
e-mail: ksaikumar@ce.iitr.ac.in

and De'Alencar (1975) and Decourt (1995) have been utilised in this study. In general, the methodologies restrict the parameters as deterministic entities. However, various researchers such as Vanmarcke [1], Phoon [2], Haldar [3] indicated that the response variability of the foundations considering soil variability is appropriate.

1.1 Uncertainty Application

Uncertainties prevail in any natural process, which is undesirable. Soil is no more an inferior material in this regard. Soil, being a geological material, is packed with the uncertainties in its parameters, which is inevitable. Uncertainties are of three kinds; inherent uncertainty, arises by the natural conditions and cannot be left out; measurement uncertainty arises with the usage of equipment for the investigations; model uncertainty arises due the mathematical models and equations involved in the analysis. In the present study, a stochastic model has been deployed to quantify the inherent uncertainty lying with the primary parameter engaged with the bearing capacity calculation, i.e. SPT N value.

1.2 Stochastic Modelling

The stochastic modelling has been deployed with the help of one-dimensional random field characterised by probability density function, comprising mean, standard deviation and the scale of fluctuation which denotes the measure of the soil property in a statistical manner using the in situ data. The present study focuses only on the vertical variability of the SPT N considered in the study, and the data is analysed using the random field theory. Vanmarcke [1] suggested that the fit of the theoretical correlation model could determine the statistical measure in the vertical variation of the property, i.e. the scale of fluctuation to the sample autocorrelation function [4]. Few autocorrelation models, such as exponential, squared exponential, second-order Markovian and cosine exponential functions, are available in the literature and utilised in this study (Table 1).

1.3 Monte Carlo Simulation

The Monte Carlo simulation technique is the process of allowing all the uncertainties with the input parameters to the considered mechanism or the system of analysis. Regarding the stochastic uncertainty analysis, Monte Carlo simulation, which is a very diversely applied technique in the engineering applications, has been implemented here. With the help of this simulation, the uncertainty involved with the SPT N is considered in determining the bearing capacity of piles.

Table 1 Fit of one-dimensional correlation models

Autocorrelation model	Correlation function	Correlation constants	Correlation Length, dv (m)	R^2
Exponential	$y = e^{-kx}$	$k = 1.639$	$2/k = 1.2203$	0.7639
Squared exponential	$y = e^{\left(-\left(\frac{x}{k}\right)^2\right)}$	$k = 1.473$	$k\sqrt{\pi} = 2.6108$	0.7871
Second-order Markovian	$y = e^{-kx}(1 + kx)$	$k = 1.874$	$4/k = 2.1345$	0.7782
Cosine exponential	$y = e^{-lx}\cos(kx)$	$k = 2.023;$ $l = 0.3961$	$\frac{2k^2}{k^2+l^2} = 1.9262$	0.9282

This study presents the methodology on incorporating the vertical soil variability in SPT N for determining the bearing capacity of the pile foundation in the sandy soil.

2 Case Study

The SPT data was collected from a site located at Kolkata. It was planned to have a kind of high rise structure in that site. So, pile foundation has opted. SPT was performed for the soil investigations at that site, and twenty borehole data are considered for the analysis. The profiles are displayed in Fig. 1. In most of the boreholes,
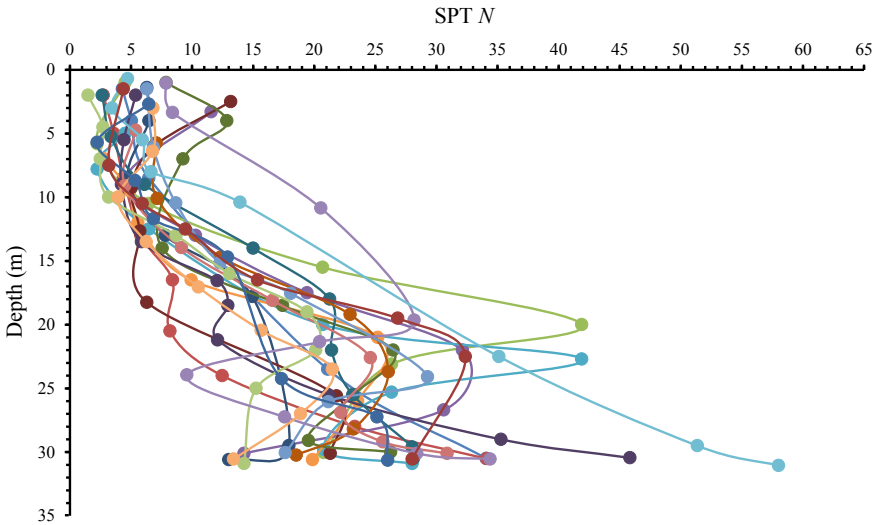

Fig. 1 SPT profiles for twenty borehole data

it was observed that the soil in the top 5 m approximately of depth is almost a kind of fill up material; after that, the soil is classified as silty sand.

As suggested by Vanmarcke [1], for the application of random field theory, the data needs to be stationary. To determine the scale of fluctuation or the deviation, the following steps need to be carried out for each SPT profile.

- Using the ordinary least squares method, trend function needs to be evaluated and deducted from the measured to obtain the stationarity.
- The residuals need to be considered for the random field application, and the autocorrelation samples are generated.
- Since the study is concerned with only vertical variability, one-dimensional correlation models are required to make to fit with the samples.
- The scale of fluctuation is calculated for the best-fitted model, i.e. when the coefficient of determination will become closer to unity.

To illustrate the above methodology as well for the bearing capacity calculations, a typical SPT profile of borehole-5 has been considered for the study, and it has been explained in the following sections.

3 Example Illustration

The illustration is done in two parts. First one relates to the measurement of the scale of fluctuation, and the other relates to the uncertainty analysis in bearing capacity calculation using different correlations.

3.1 Determination of Scale of Fluctuation

The SPT data was collected for borehole-5 which was shown in Fig. 2. Along with the profile, the polynomial trend of second degree has been displayed. To obtain the stationarity, the trend has been deducted from the measured data. The de-trended profile was shown in Fig. 3.

The residuals obtained after the de-trending have been considered for the random field application. Random field theory was applied by the use of shifts in the data mathematically, and the autocorrelation samples have been found. As the information is limited, and so, the present study is concerned only with the direction of availability of the data, i.e. vertical direction. The obtained samples were fitted with the available one-dimensional autocorrelation models to find the scale of fluctuation. The statistical fits are displayed in Table 1. Various correlation models such as exponential, square exponential, second-order Markovian and cosine exponential models have been considered for the study. Fits are displayed in Fig. 4. It is found that the samples are best-fitted with the cosine exponential correlation model with a coefficient of determination as 0.9282, which is close to 1.0. The correlation length
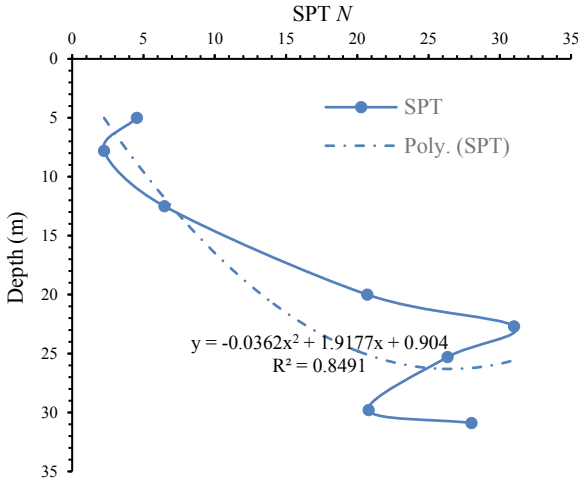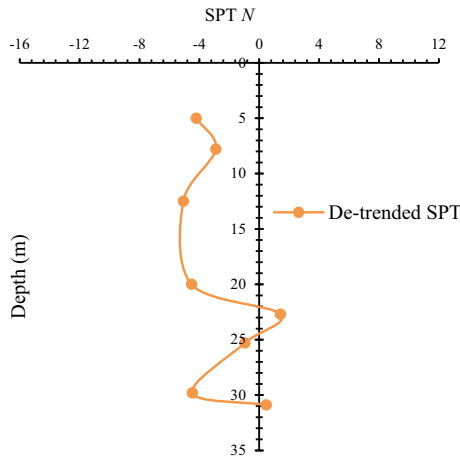
Fig. 2 SPT profile for the borehole-5

Fig. 3 De-trended SPT profile for the borehole-5

is calculated as 1.9262 m. According to Phoon [2], the vertical scale of fluctuation is 0.6–5 m. So, it can be said that the obtained scale of fluctuation for borehole-5 is within the prescribed range by Phoon [2].

The scale of fluctuation will be different for all the boreholes. So, the above-mentioned procedure needs to be followed for all the boreholes to obtain a specific scale of fluctuations. The variation in the SPT N values of all the 20 boreholes is displayed in Fig. 5. By using the above stochastic modelling, considering cosine exponential correlation fit, the coefficient of determination, i.e. the statistical measure
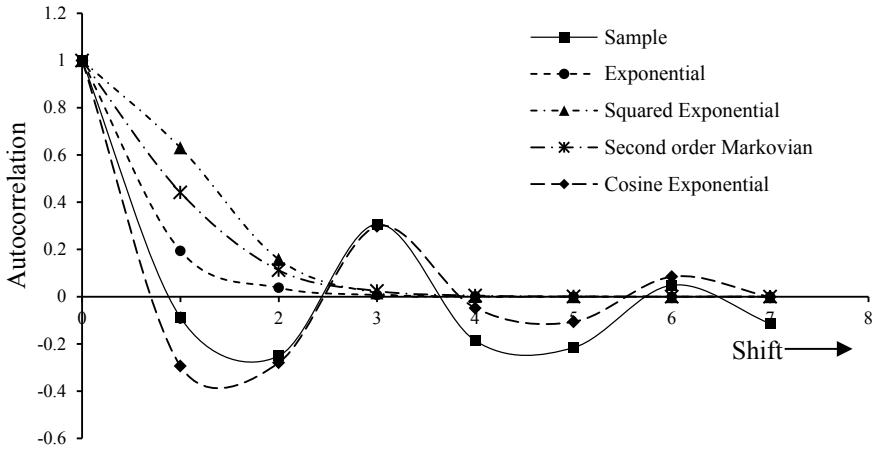
Fig. 4 Fitting for autocorrelation models
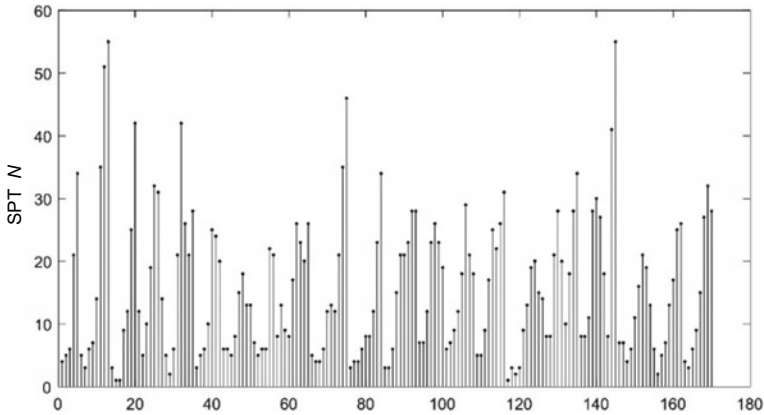
Fig. 5 SPT values of all the boreholes

of the error and the scale of fluctuation for all the boreholes was calculated and detailed in Table 2.

3.2 Determination of Bearing Capacity of Piles

To determine the bearing capacity, assumed pile parameters and the coefficient of variation for the example problem are given in Table 3. Three different correlations generated by Meyerhof (1956), also mentioned in IS 2911 [5], Aoki and De'Alencar (1975) and Decourt (1995) are used in the study [6–8]. They are shown in Table 4.

Table 2 Scale of fluctuation obtained with cosine exponential model for 20 SPTs

Bore hole	R^2	Scale of fluctuation
1	0.9935	1.8226
2	0.9890	1.7907
3	0.9802	1.7724
4	0.9978	1.8918
5	0.9282	1.9262
6	0.9979	1.8653
7	0.9932	1.8116
8	0.9658	1.6745
9	0.9844	1.8026
10	0.9402	1.6915
11	0.9935	0.9155
12	0.9939	1.8779
13	0.9966	1.8350
14	0.9933	1.8313
15	0.9959	1.8819
16	0.9296	1.6453
17	0.8945	1.8861
18	0.9957	1.8090
19	0.9989	1.8608
20	0.9993	1.8764

Table 3 Pile and Statistical parameters considered in the study

Parameter	Range
Diameter of Pile (m)	0.6, 0.8, 1.0
Length of Pile, Lp (m)	21–25
Coefficient of variation of N (%)	25, 35, 50

Table 4 Correlations utilised for bearing capacity calculation

Method	Ultimate Capacity (MPa) ($Q_u = Q_b + Q_s$)		Remarks
	Base resistance (Q_b)	Shaft resistance (Q_s)	
Meyerhof [6]	$4N_b A_b$	$N_s A_s/50$	–
Aoki and De'Alencar [7]	$\left(\frac{k}{1.75}\right)N_b$	$\left(\frac{ak}{3.5}\right)N_s$	$a = 14, k = 1$
Decourt [8]	$k_b N_b$	$\alpha(2.8N_s + 10)$	$k_b = 0.325$ $\alpha = 0.5 - 0.6$

N_b = N value at the pile base
N_s = Average N of the embedded depth
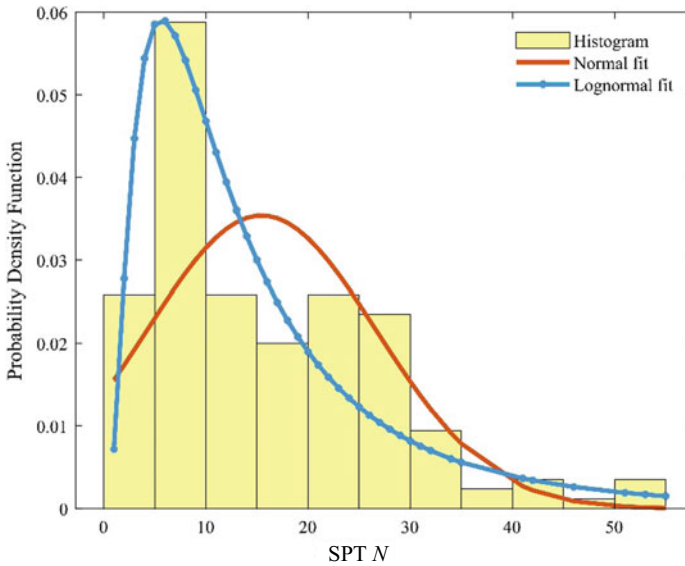A_b = Area of the pile base
A_s = Surface area of the pile

Fig. 6 Histogram and probabilistic distributional fit of SPT *N* values

As mentioned earlier, SPT *N* is considered as the random variable in the present study. The term "coefficient of variation" which is defined as the ratio of the standard deviation to mean of the samples is one of the important factors in the stochastic uncertainty analysis. According to Phoon [2], coefficient of variation for *N* is 25–50%. In general, it can be determined by making the probability distribution fit. Based on the available literature, normal and lognormal distributions are considered in the study. The plots of histogram and probability distributions are shown in Fig. 6. The SPT *N* values from all the boreholes are found to be best-fitted in the lognormal distribution with the mean of 2.4258 and the standard deviation as 0.8416, and the resulting coefficient of variation of *N* is 0.3469 and can be rounded up to 0.35. The errors in the lognormal fit are 0.4% in the mean and 0% in the standard deviation, which shows that their magnitudes are acceptable. As mentioned in the previous sections, Monte Carlo simulation has been implemented for the stochastic uncertainty analysis. The analysis was done as per the parameters are shown in Table 3.

4   Results and Discussion

Based on the literature, the plots are generated with the parameter dv/Lp as the abscissa and ultimate bearing capacity as the ordinate. Three different correlations, as mentioned in the previous sections, are considered in the generation of plots.

As Meyerhof's relationship is the function of the diameter of the pile and the SPT *N*, three different plots (Figs. 7, 8 and 9) are generated. Aoki and De'Alencar
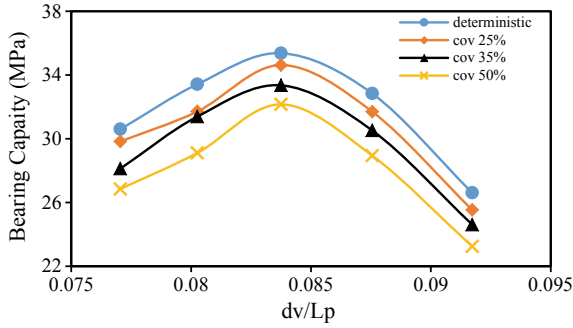
Fig. 7 Bearing capacity variation for pile diameter of 0.6 m using Meyerhof (1956) [6]
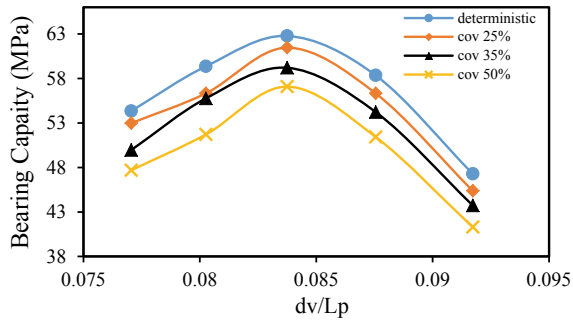
Fig. 8 Bearing capacity variation for pile diameter of 0.8 m using Meyerhof (1956) [6]

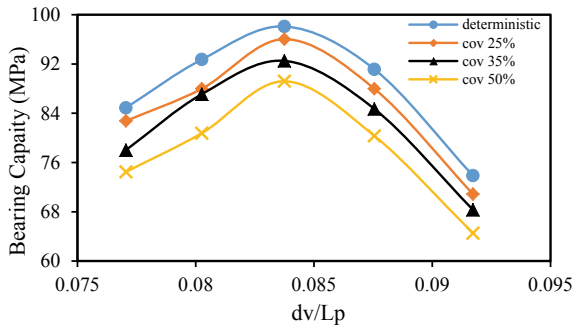**Fig. 9** Bearing capacity variation for pile diameter of 1.0 m using Meyerhof (1956) [6]

(1975) and Decourt (1995) are the functions of SPT N only and so, only one for each has been generated (Figs. 10 and 11).

The lowest magnitude of bearing capacity has been observed when the coefficient of variation reaches higher to the maximum, i.e. 50%. Considerable variation in
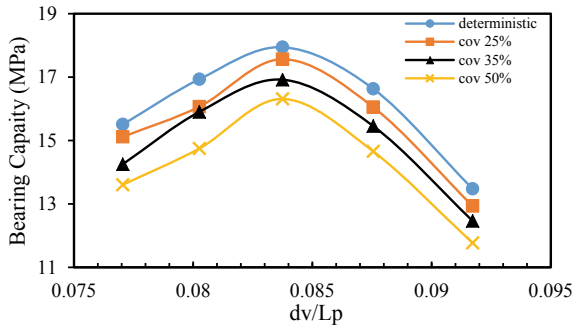
Fig. 10 Bearing capacity variation using Aoki and De'Alencar 1975 [7]
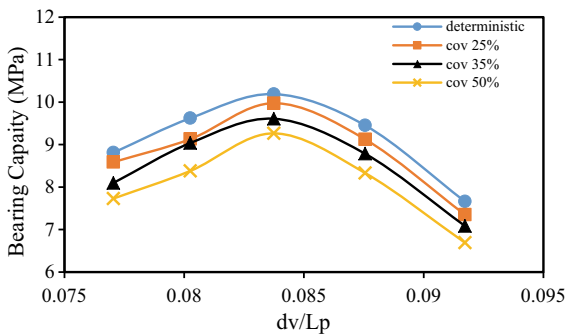
Fig. 11 Bearing capacity variation using Decourt 1995 [8]

the capacity can be seen with the consideration of coefficient of variation of 35% relatable to the problem of concern. The same has been observed in all the plots. So, with the inclusion of variability in SPT N, it can be seen that the capacity of the piles decreases.

5 Summary and Concluding Remarks

SPT data for twenty boreholes has been collected for a site which is planned to adopt pile foundation for the upcoming structure. Due to the complexity constraint, the analysis has been briefly explained for the borehole-5 only. As the present study focusses on the measurement of the scale of fluctuation, random field theory has been implemented for a given site and a given borehole. The above procedure has been performed for all the boreholes, and the individual scale of fluctuations is calculated. The measurements are in the range from 0.91 to 1.89 m, which is in good agreement as prescribed in the well-recognized literature. The bearing capacity

has been calculated using different correlations. Meyerhof's correlation resulted in higher capacity when compared to others. For the coefficient of variation of 35%, pile capacities are significantly varying. For the other two coefficients of variations, pile capacities have been observed to be in decreasing trend. Using the stochastic modelling presented in this study, the pile capacity variations can be investigated for other boreholes too. The present study shows the necessity of consideration of uncertainties in the analysis for more safer design.

References

1. Vanmarcke, E.H.: Random Fields: Analysis and Synthesis. MIT Press, Cambridge, MA (1983)
2. Phoon, K.K., Kulhawy, F.H.: Characterization of geotechnical variability. Can. Geotehcnical J. **36**(4), 612–624 (1999)
3. Haldar, S., Babu, G.L.S.: Reliability measures for pile foundations based on cone penetration test data. Can. Geotech. J. **45**, 1699–1714 (2008)
4. Bouayad, D.: Assessment of soil variability based on CPT data. In: 1st International Conference on the Material Point Method, MPM 2017, pp. 310–315. Elsevier, Netherlands (2017)
5. IS 2911-1-2: Design and construction of pile foundations, Part 1: Concrete Piles, Bureau of Indian Standards.
6. Meyerhof, G.G.: Penetration tests and bearing capacity of cohesionless soils. J. Soil Mech. Found. Div. **82**(1), 1–19 (1956)
7. Aoki, N., De'Alencar. D.: An approximate method of estimate the bearing capacity of piles. In: Proceeding of the fifth Pan-American conference on soil mechanics and foundation engineering, pp. 367–376. Buenos Aires, Argentina (1975)
8. Decourt, L.: Prediction of load-settlement relationships for foundations on the basis of SPT-T, Ciclo de conferencias Internationale, Leanordo Zeevaert, pp. 85–104. Mexico (1995)

Nonlinear Analysis of Laterally Loaded Pile Group in Layered Soil–Ash Deposit

Amit Kumar Ram and Supriya Mohanty

Abstract The current scenario for the geotechnical engineering is not only to take care of vertical load of superstructure impending to the soil but also the lateral load subjected to the structure must be taken into consideration for the safe design of foundation. For designing pile foundation, knowledge of load–deflection behavior of pile under moderate to heavy load is necessary. In the present study, numerical analysis of pile group in a layered soil–ash system has been performed using Soil-Works software. The analysis is based on *P-Y* curve method which is a realistic and practical method for the load deflection analysis of pile under lateral loads. The pile arranged in grid form in 3×3 and 4×4 pattern. The influence of pile diameter effects along with various pile spacing on the behavior of the pile–soil system has also been studied. The stability of pile was checked under horizontal and vertical condition. The pile group has been analyzed with vertical load, lateral load, and moment at the top end of the pile. The response of the pile includes horizontal displacement, shear force, moment, and ground reaction along the pile length.

Keywords *P-Y* curve · Lateral load · Pile group · Layered soil–ash system

1 Introduction

Pile foundations are the muse consisting of range of piles connected with a pile cap to transmit structural load from low bearing capacity layer to onerous strata. It is not solely made to take care of axial load however conjointly the lateral loads. Lateral loads are quite common to the structures like tall building, transmission towers, offshore platforms, wharfs and jetties, bridge abutment wall, and it is because of the result of wind action, wave action, traffic load, earthquake, lateral pressure, ground movement and impact load from ships. Therefore, a proper understanding of response of pile under lateral loading includes a nice importance in analysis and design of

A. K. Ram (✉) · S. Mohanty

Department of Civil Engineering, Indian Institute of Technology (BHU), Varanasi, Uttar Pradesh 221005, India

e-mail: amitkumarram.rs.civ18@itbhu.ac.in

piles. There are many approaches/methods are available for the analysis of behavior of laterally loaded piles. Based on theory of elasticity, an elastic solution of single pile subjected with lateral load was given by Poulos [1] and it assumed the soil is homogenous, isotropic, elastic which is not the practical situation. This theory gives more accurate results for the soil which is linearly elastic in nature but soil is nonlinear in nature. According to theory of subgrade reaction, a method was presented by Broms [2] for computing moment and lateral deflection of pile under drained situation in the case of cohesive soil. The advantage of this method is that it can be applicable for pile with free-headed or perfectly fixed, whereas it is applicable only in working load range. The past methods assume the subgrade modulus is linearly varying with depth [3]. The concept of 'p-y' curve was first introduced by McClelland and Focht [4], and it was used to find the subgrade modulus along the depth. The p-y method is simple and quite realistic because of it assumptions and semi-analytical approach. Different researchers used the p-y curve with separate assumptions considering the different types of soils, like medium stiff clay, submerged soft clay, submerged stiff clay, sand, unified clay [5–8]. Based on the results of past study, the p-y curve majorly contains nonlinear steep incremental parts and flat linear part when it reaches a certain level of pressure. After p-y method, Brown [9] developed a method called p-multiplier method, and in this method, the p-y curve of single pile is multiplied by a constant for the lateral response of pile.

The laterally loaded pile was investigated using finite element techniques by several researchers [10–12]. The FEM softwares used for the study include ABAQUS, OASYS Alp 19.2, FLPIER, etc. To perform the analysis, the pile was considered as linear elastic beam with different models like Mohr–Coulomb, Drucker–Prager, and modified Drucker–Prager model.

The findings of the present study focus mainly on the capacity of laterally loaded pile with stratified soil deposits. The analysis of stratified soil system is done using SoilWorks software using the concept of *P-Y* analysis. Here, the influence of length, diameter, arrangement, and pile cap dimension has been considered for lateral behavior of piles. The results of the pile response are presented in the form of horizontal displacement, ground reaction, shear force, and bending moment along the pile length.

2   Overview of SoilWorks

SoilWorks is a finite element software which has major application in geotechnical as well as structural engineering field. It is made especially for the analysis and design for tunnel, slopes, foundation, seepage, excavation cases under normal and seismic conditions. Using SoilWorks, the modeling of any types of structure can be done easily, and also, it can import AutoCAD files directly. SoilWorks also has one specific module dedicated to analysis of foundation. Here, the analysis of laterally loaded pile group in layered soil–ash deposit has been performed based on *P-Y* analysis. The horizontal stability of foundation is checked by *P-Y* analysis, and it
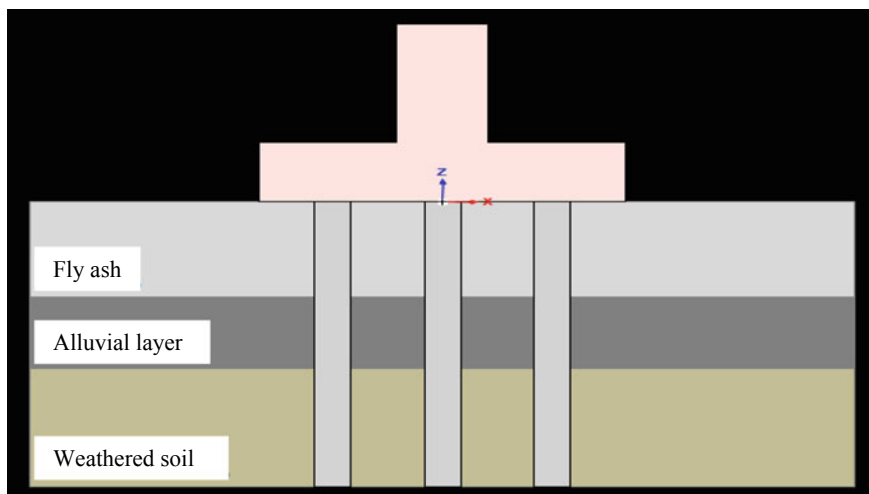
Fig. 1 Typical representation of piles with layered soil system

considered the allowable displacement limited to 1% of pile diameter. The soil was represented by means of a series of nonlinear *P-Y* curves that changes in magnitude with depth and soil type. The layered soil system consists of three layers, namely fly ash, alluvial layer, and weathered soil. In the present study, the pile of length— 12 m and 14 m and diameter—1.0 m and 0.5 m has been considered for the analysis. Figure 1 represents the schematic figure of soil–pile interaction model with stratified soil system.

3 Materials Used

The material used in the present study is made up of concrete having modulus of elasticity 2.5×10^7 kN/m^2 and Poisson's ratio of 0.18. The layering of soil was done by placing fly ash as top layer followed by alluvial layer and then weathered soil with depth of 4 m, 7 m, and 12 m, respectively. The lateral load applied at the top level of pile taken from the load–deformation plot by fixing the load corresponding to 10 mm deformation. In this case, pile capacity is calculated considering both the skin friction and end bearing. Table 1 depicts the material properties of soil which was used in analysis of laterally loaded pile.

Table 1 Properties of layered soils used for the present study

Name	Fly ash	Alluvial layer	Weathered soil
Model type	Silty	Sand	Sand
Unit weight (kN/m^3)	15.89	16	17
Saturated unit weight (kN/m^3)	16.866	18	19
Cohesion (kN/m^2)	45.45	–	–
Angle of internal friction (°)	31	25	26
Material type	Silt	Sandy soil (API)	Sandy soil
Horizontal reaction (kN/m^3)	30,000	–	16,000
Unit ultimate skin friction (kN/m^2)	31.82	20	30
Unit ultimate bearing capacity (kN/m^2)	440	600	4000

4   Load–Deflection Response

The representation of pile response when subjected to lateral load with deflection of pile head has been plotted considering variation in pile geometry. The load–deflection response of laterally loaded pile is nonlinear in nature most of the time. Because of this nonlinearity, there is no well-defined peak point to determine ultimate load. Therefore, the lateral load corresponding to 10 mm of deflection can be taken as ultimate lateral load for each case. Figure 2 shows the load–deflection plot for different *L/D* ratio. Similarly, lateral load determined at 10 mm of deflection has shown in Table 2.
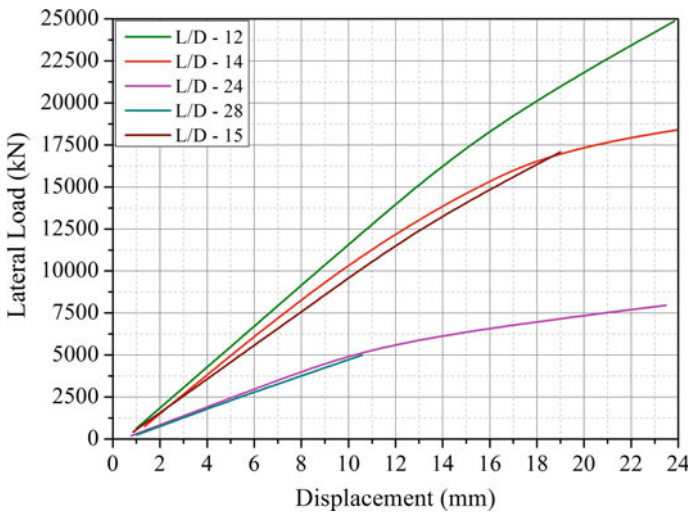

Fig. 2   Load–deflection curves for different *L/D* ratio

Table 2 Lateral load capacity corresponding to 10 mm deflection

S. No.	Case	Pile parameters (m)	Lateral load (kN)
1	Case-1	$L = 12$ and $D = 1.0$	11,650
2	Case-2	$L = 12$ and $D = 0.5$	5000
3	Case-3	$L = 14$ and $D = 1.0$	10,400
4	Case-4	$L = 14$ and $D = 0.5$	4750
5	Case-5	$L = 12$ and $D = 0.8$	9500

5 *P-Y* Analysis

The *P-Y* investigation helps in correlating soil resistance with deflection, and soil is configured as nonlinear springs. In this analysis, '*P*' represents the soil pressure per unit length of the pile and '*Y*' is the pile deflection. The lateral deflection of pile decreases the carrying capacity of pile and surrounding soil. At small deflection, the soil behaves as stiffer material; similarly, the stiffness of pile decreases with increase in applied moment. Since numerical analysis is involved, therefore it can be used to analyses soil with varying depth and variation in pile configuration. The *P-Y* analysis gives results in good agreement with field loading test and also with several available approaches like characteristics load method (CML) [13]. Figure 3 represents the typical plots of *P-Y* curve of single pile at different depths. The slope of *P-Y* curve represents the tangent soil stiffness at any deflection. From Fig. 3, it can be seen that for lower depth the *P-Y* curve is linear in nature and peaks can be identified easily whereas for higher depth the *P-Y* curve changes from linear to nonlinear. And also the soil resistance is increasing with increase in depth of soil. The soil resistance depends on stiffness of the spring in *P-Y* analysis.

6 Response of Pile Subjected to Lateral Load

For the determination of pile response, first of all the ultimate load that the pile can take was determined using the IS 2911-P-3 (2010) method. The load consists of both skin friction and end bearing under different length and diameter of pile. After determination of load, the load–deflection curve was plotted so that the lateral load can be found out. The lateral load was the load corresponding to the deflection of 10 mm. Also, the variation in pile response according to the change in arrangement [4 × 3, 5 × 3, 6 × 3, and 7 × 3 in which *L*: 13 m, 16 m, 19 m, 22 m, and *B*: 10 m, respectively] has been studied. The results of pile response have been discussed in the following sections.
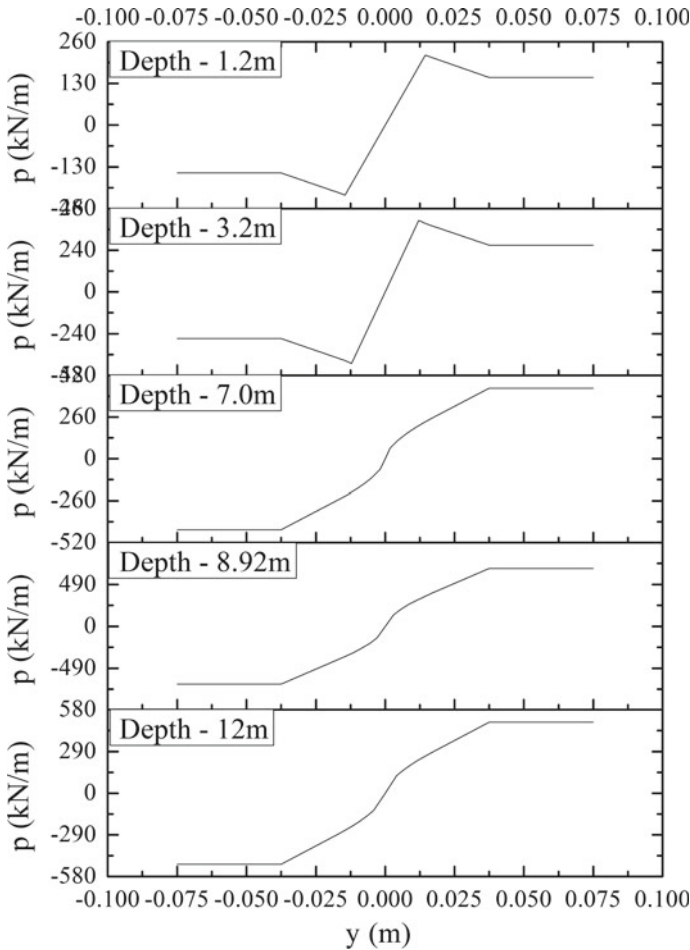
Fig. 3 *P-Y* curves for single pile (*L*-12 m and *D*-1.0 m)

6.1 Horizontal Displacement

In the present study, the horizontal displacement is the lateral displacement caused due to lateral load of 11,650 kN, vertical load of 31,088.16 kN, and moment of 7772.04 kN-m. The displacement response of pile has been represented in terms of variation in length and diameter and arrangements of piles. The contribution of change in length of pile for displacement was very less as compared to change in diameter. This may be because of the variation of length influences the surface resistance only whereas diameter influences both surface and base resistance of pile. The plots of different *L/D*, diameter, and arrangements are presented in Figs. 4, 5, and 6, respectively. From Fig. 4, the horizontal displacement is found to be maximum at

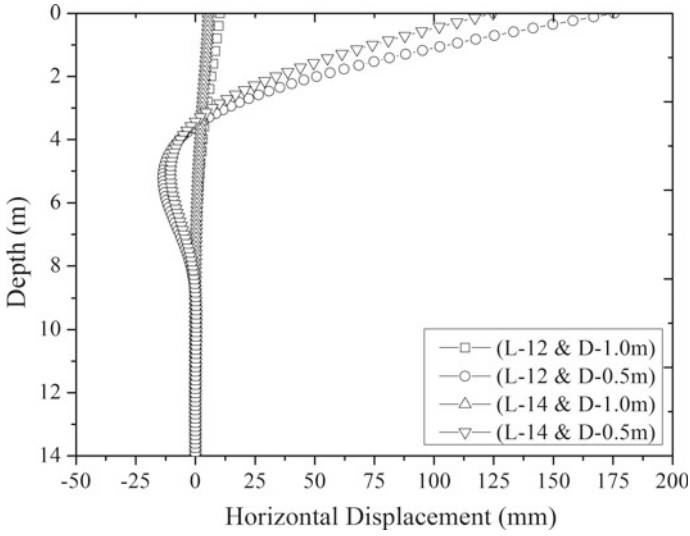**Fig. 4** Typical plot of horizontal displacement with depth for different *L/D* ratio (Arrangement—7 × 3)
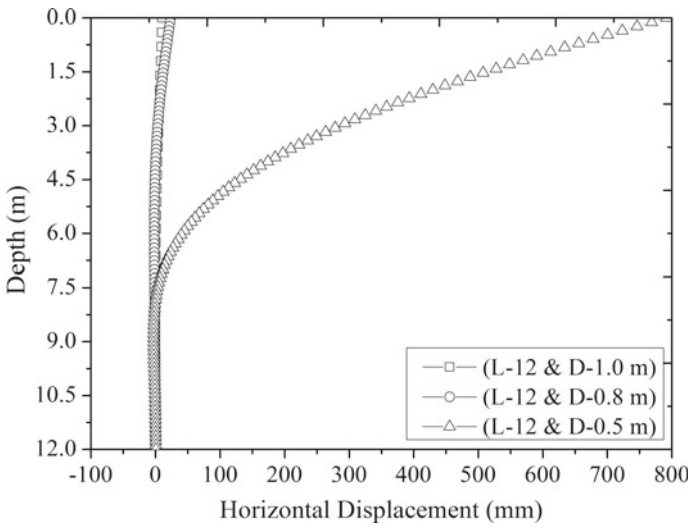

Fig. 5 Typical plot of horizontal displacement with depth for different diameter (Arrangement—4 × 3)
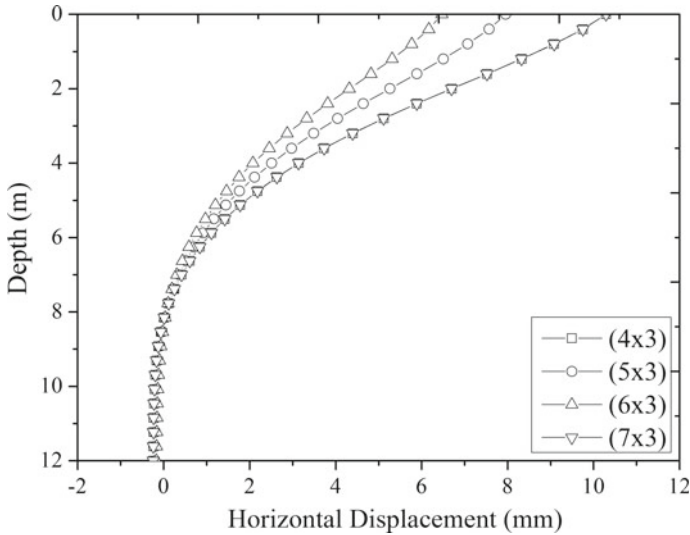
Fig. 6 Typical plot of horizontal displacement with depth for different arrangements (*L*-12 m and *D*-1.0 m)

the top of the pile and decreases as the depth increases, because the soil resistance increases with depth. In the same way, horizontal displacement is increasing with decrease in pile diameter, and this occurs due to the decrease in surface area of pile which is represented in Fig. 5. In Fig. 6, it is clearly shown that when the pile cap size is increasing the horizontal displacement decreasing and also shadowing and edge effect is more in higher pile number arrangement.

6.2   Ground Reaction

Ground reaction is also known as soil resistance, which is developed when pile subjected to lateral load/movement. In this case also, the pile was subjected to lateral load, vertical load, and moment of magnitude 11,650 kN, 31,088.16 kN, and 7772.04 kN-m, respectively. The ground reaction was plotted by taking into consideration of *L/D* effect and change in arrangement of piles. It is increasing with increase in *L/D*, and also, it shows sharp increase in reaction when the density of soil changes. With increase in number of piles, ground reaction increases upto certain limit and then decreases. The plot of different *L/D* and arrangements is shown in Figs. 7 and 8, respectively. Figure 7 shows much variation in ground reaction for smaller diameter of pile than that of larger diameter, and there is a sharp change in ground reaction as the density changes. Figure 8 shows that the ground reaction is maximum below the ground surface, and it can be identified upto certain depth after that the all arrangements merge one over the other.

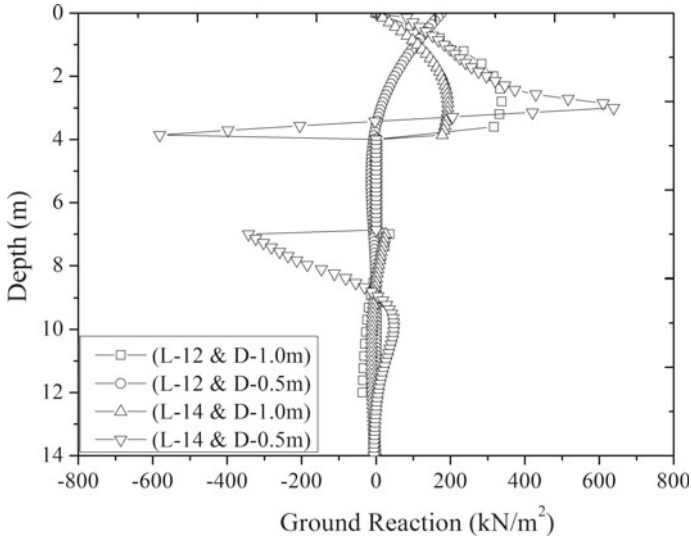**Fig. 7** Typical plot of ground reaction with depth for different *L/D* ratio (Arrangement—7 × 3)
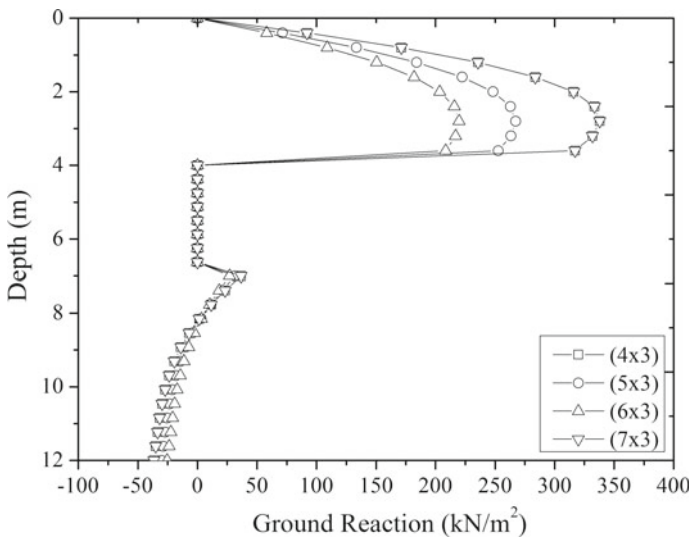

Fig. 8 Typical plot of ground reaction with depth for different arrangements (*L*-12 m and *D*-1.0 m)

6.3 Shear Force

Shear force is the summation of all vertical forces either left or right side of the section considered. For this case also, the load subjected to pile is same as discussed above.
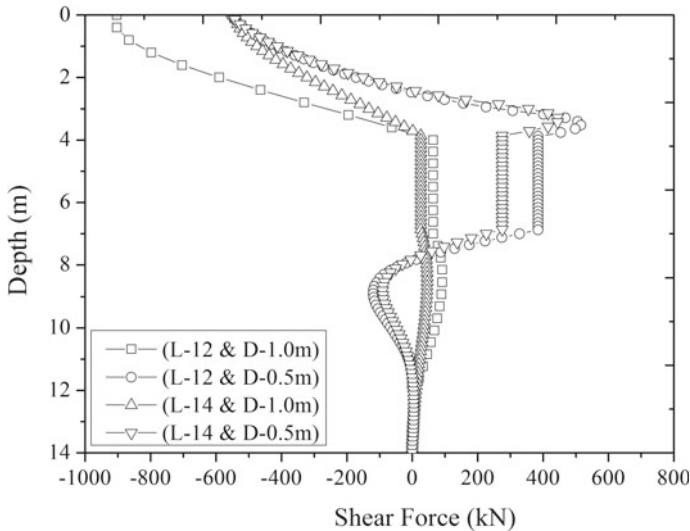
Fig. 9 Typical plot of shear force with depth for different *L/D* ratio (Arrangement—7 × 3)

The shear force also plotted to observe the effect of *L/D* and change in arrangement effect of piles. When diameter is decreasing as a result of which positive shear force is increasing and similarly with increase in number of pile, the shear force is decreasing. The reason behind increase in shear force is due to decrease in stiffness of pile member. The plot of different *L/D* and arrangements is shown in Figs. 9 and 10, respectively. Figure 9 shows that, the shear force is maximum at the pile top for larger diameter of pile, and also, it remains almost constant after the first layer of soil (i.e., fly ash) but for smaller diameter, the nonlinearity is significant. Figure 10 shows that, the change in maximum shear force is at the top of ground level only and becomes same after the thickness of first layer. Shear force is more dependent on location of pile in group and less on their group size.

6.4 Bending Moment

Bending moment is the moment induced into the member when external force/moment is applied to the member causing the member to bend. The load applied at the top of pile is same for all cases. The variation of bending moment with different *L/D* ratio and change in arrangement of piles are plotted to see their effects. The bending moment increases upto its peak at the top layer of soil because the effect of lateral load decreases with increase in depth of pile. And also for larger diameter the position of point of contraflexure is at lesser depth, whereas point of contraflexure position increases with decrease in diameter. The plot of different *L/D* and arrangements is shown in Figs. 11 and 12, respectively. From Fig. 11, it can be
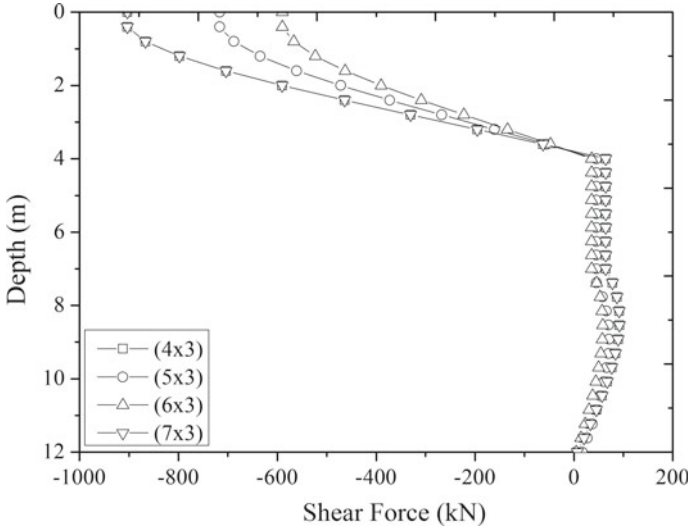
Fig. 10 Typical plot of shear force with depth for different arrangement (*L*-12 m and *D*-1.0 m)
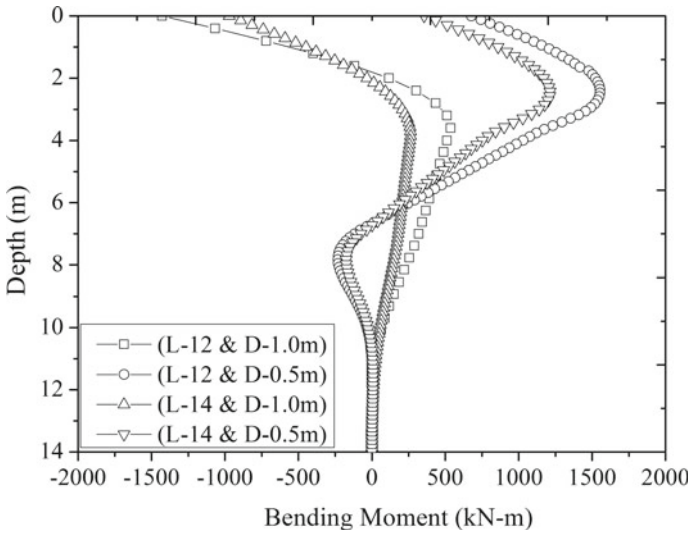
Fig. 11 Typical plot of bending moment with depth for different *L*/*D* ratio (Arrangement—7 × 3)

seen that bending moment is increasing with decrease in pile diameter and length; this may be due to the reduction in pile resistance by decreasing the surface area of pile. Similarly, in Fig. 12, there is not much difference between the bending moment profile with depth for different pile group (i.e., 4 × 3 to 7 × 3), this occurs because
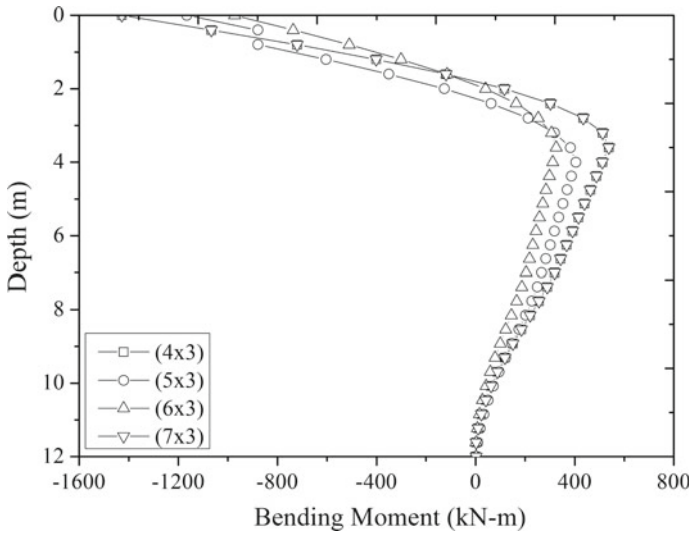
Fig. 12 Typical plot of bending moment with depth for different arrangements (L-12 m and D-1.0 m)

the bending moment is independent of group size but it is function of position of pile within the group.

7 Conclusions

The *P-Y* analysis was performed to study the behavior of laterally loaded pile in stratified soil–ash system. The behavior of pile covers horizontal displacement, ground reaction, shear force, and bending moment along the pile length. The effect of various parameters such as pile length and diameter or L/D ratio and change in arrangements of pile were considered. From the results of pile response, the following conclusion can be drawn:

1. The *P-Y* curves are not truly nonlinear at lower depth but it becomes nonlinear as the depth increases.
2. The load–deflection plots increases nonlinearly with increase in L/D ratio and pile diameters.
3. The change in horizontal deflection is very small for small change in diameter of pile but it changes significantly with large change in diameter.
4. When length and diameter of pile is fixed, then with increase in number of pile leads to the decrease in shear force and bending moment.
5. With increase in number of pile based on arrangement, the ground reaction increases reaches to maximum and then decreases.

References

1. Poulos, H.G.: Behavior of laterally loaded piles: I-single piles. J. Soil Mech. Found. Div. ASCE **97**(5), 711–731 (1971)
2. Broms, B.B.: Lateral resistance of piles in cohesive soils. J. Soil Mech. Found. Div. ASCE **90**(2), 27–64 (1964)
3. Broms, B.B.: Lateral resistance of piles in cohesionless soils. J. Soil Mech. Found. Div. ASCE **90**(3), 123–158 (1964)
4. McClelland, B., Focht, J.: Soil modulus for laterally loaded piles. J. Soil Mech. Found. Div. ASCE **82**(4), 1–22 (1956)
5. Wu, D., Broms, B.B., Choa, V.: Design of laterally loaded piles in cohesive soils using p-y curves. J. Soils Found. **38**(2), 17–26 (1998)
6. Matlock, H.: Correlations for Design of Laterally Loaded Piles in Soft Clay. ASCE (2006)
7. Reese, L.C., Cox, W.R., Koop, F.D.: Analysis of Laterally Loaded Piles in Sand. ASCE (2006)
8. Sullivan, F.: Geometrical properties determined by the higher duals of a Banach space. Ill. J. Math. Univ. Ill. Urbana-Champaign **21**(2), 315–331 (1977)
9. Brown, D.A., Morrison, C., Reese, L.C.: Lateral load behavior of pile group in sand. J. Geotech. Eng. **114**(11), 1261–1276 (1988)
10. Fan, C.C., Long, J.H.: Assessment of existing methods for predicting soil response of laterally loaded piles in sand. Comput. Geotech. **32**(4), 274–289 (2005)
11. Nur Eldayem, F.E.E., Mohamedzein, Y.E.A.: Finite Element Analysis of Laterally Loaded Piles in Clays. Geotechnical Special Publication, 259 GSP, pp. 175–182 (2016)
12. Zhang, L., McVay, M.C., Lai, P.: Numerical analysis of laterally loaded 3×3 to 7×3 pile groups in sands. J. Geotech. Geoenviron. Eng. **125**(11), 936–946 (1999)
13. Duncan, J.M., Evans, L.T., Ooi, P.S.K.: Lateral load analysis of single piles and drilled shafts. J. Geotech. Eng. **120**(6), 1018–1033 (1994)

Rationalization of LRFD Method for Safe Bearing Capacity of Shallow Footings to Incorporate the Type of Shear Failure

Ronak Kotadia, K. N. Sheth, and Avani Malaviya

Abstract The geotechnical design philosophy is in the transformation stage to implement load and resistance factor design (LRFD). IS 6403 uses working stress method to calculate safe bearing capacity for shallow foundations, while Euro Code 7 and AASHTO use the LRFD method and provide guidelines for proportioning shallow foundations using partial safety factors. Hence, in order to adopt the LRFD design method, it has to be rationalized to have the convincing bearing capacity with respect to IS Code results to incorporate the shear failure criteria. In present work, safe bearing capacity for shallow footing is calculated as per IS Code, Euro Code 7 and AASHTO by taking the variations in shear failure criteria, i.e., with and without consideration of shear failure criteria (only for Euro Code design), soil parameters (cohesion, C and angle of internal friction, ϕ), size and depth of footing. Problems are then identified by checking the consistency of results obtained by Euro Code 7 and AASHTO with respect to IS Code results. Further, as a part of rationalization, the recommendation is given that in Euro Code 7 design, the partial safety factors must be applied to bearing capacity factors, instead of applying to soil properties (C, ϕ). Also, net safe load (kN) obtained from AASHTO is on lower side as compared to IS results because it considers higher average FOS than IS Code.

Keywords LRFD · Shallow footings · Codes · Rationalization · Shear failure criteria

R. Kotadia (✉) · A. Malaviya
Geotechnical Engineering, Dharmsinh Desai University, Nadiad 387001, India
e-mail: ronakkotadia93@gmail.com

A. Malaviya
e-mail: avanimalaviya09@gmail.com

K. N. Sheth
Civil Engineering Department, Dharmsinh Desai University, Nadiad 387001, India
e-mail: hod.cl@ddu.ac.in

1 Introduction

Structural design philosophy and implementation to codes of practice has transformed from conventional working stress method to limit state method—load and resistance factor design (ACI) or partial safety factor approach (IS Code). Geotechnical design philosophy is in the transformation stage to implement load and resistance factor design (LRFD). IS 6403 provides guideline to calculate ultimate bearing capacity for shallow foundations. It gives bearing capacity factors and other factors, viz. inclination factors, depth factors, shape factors, etc., and accounts for the effect of water table [3]. To calculate allowable bearing pressure, a Factor of Safety 2.50 is recommended separately by IS 1080. Euro Code 7 uses LRFD method and provides guideline for proportioning shallow foundations using partial safety factors for action, material parameters, and resistance [2]. The action includes dead loads as well as imposed loads. Material parameters include shear parameters 'c' and 'φ' in drained and/or undrained state. The resistance factors are assigned based on the design methods used. For shallow foundations, three design approaches are considered, for which partial safety factors are given. In Euro Code 7, shear failure criteria is not considered for design as in case of IS Code. As per the AASHTO LRFD, resistance side of the equation is multiplied by the statistically based resistance factor, φ, whose value is usually less than one. As applied to the geotechnical design of substructures, φ accounts for factors such as weaker foundation soils than expected, poor construction of the foundations, and foundation materials such as concrete, steel or wood that may not completely satisfy the requirements in the specifications [1]. Also, the partial factors for different load cases and load combination have been provided to get the design action. When properly developed and applied, the LRFD approach provides a consistent level of safety for the design of all structure components.

Euro Code 7 uses three partial safety factors, i.e., for load action, material parameter, and resistance, while AASHTO uses two partial safety factors, i.e., for load action and resistance. Unlike IS Code and AASHTO, Euro Code 7 does not consider any kind of shear failure criteria for SBC calculation. Thus, the design philosophies adopted by Euro Code 7 and AASHTO differ from that of IS Code, safe bearing capacity for shallow footing calculated as per these codes widely differs from each other. Hence, in order to adopt Euro Code 7 LRFD design method for the calculation of SBC of shallow footing, it has to be rationalized in order to have the consistent results with respect to IS Code results to incorporate the shear failure criteria given by IS.

2 Method

The safe bearing capacity of shallow foundation as per IS Code, EC 7, and AASHTO is calculated for various ranges of soil parameter (C and ϕ) for a strip and square footing with variation in size and depth of foundation on a soil with bulk density 18 kN/m^3 and FOS of 2.5 for IS design as follows (Table 1).

Since Euro Code 7 is silent about shear failure criteria, for the pure cohesionless and cohesive soil, two cases in Euro Code design are considered as follows:

EC7 (I): Considering type of shear failure based on factored values of angle of friction.

EC7 (II): Without considering type of shear failure based on angle of friction and using general parameters for all values.

The results are obtained for all the problems in terms of net safe load (kN). Also, the graphs of net safe load ratio, i.e., EC7 (I)/IS and AASHTO/IS versus soil properties (C, ϕ), are plotted for varying D_f/B. Let this be considered as Case I: Partial safety factors applied to soil properties (C, ϕ) as prescribed by Euro Code provision.

2.1 Theoretical Formulation

2.1.1 Formulation as per IS 6403:1981 [3]

For General Shear Failure Criteria

$$q_{na} = \frac{1}{\text{FOS}} * CN_c d_c s_c i_c + q(N_q - 1)d_q s_q i_q + 0.5 B\gamma N_\gamma d_\gamma s_\gamma i_\gamma W'$$

Table 1 Parametric study

Parameter	Variations
Cohesionless soil with ϕ	24° to 44°
Cohesive soil with C (kN/m^2) (at interval of 15)	Upto 200 kN/m^2
Size of strip footing, m^2	1 × 5 m^2 2 × 10 m^2 3 × 15 m^2 4 × 20 m^2
Size of square footing, m^2	1 × 1 m^2 2 × 2 m^2 3 × 3 m^2 4 × 4 m^2
Depth of footing D_f, m	0–3 m

For Local Shear Failure Criteria

$$q_{na} = \frac{1}{\text{FOS}} * \frac{2}{3} C N'_c d_c s_c i_c + q(N'_q - 1)d_q s_q i_q + 0.5 B \gamma N'_\gamma d_\gamma s_\gamma i_\gamma W'$$

where

q_{na}	Net allowable bearing pressure, kN/m^2.
N_c, N_q, N_γ	Bearing capacity factors based on ϕ for general shear failure.
N'_c, N'_q, N'_γ	Bearing capacity factors based on ϕ for local shear failure.
	where $\phi = \tan^{-1}(0.67 \tan \phi)$.
B	Width of footing.
D	Depth of footing.
γ	Unit weight of footing.
W'	Effect of water table.
d_c, d_q, d_γ	Depth factors.
s_c, s_q, s_γ	Shape factors.
i_c, i_q, i_γ	Inclination factors = 1 for vertical loads (Tables 2, 3 and 4).

For Mixed Shear Failure

Table 2 Shape factors

S. No	Shape of base	s_c	s_q	s_γ
1	Continuous strip	1	1	1
2	Rectangle	1 + 0.2 B/L	1 + 0.2 B/L	1 − 0.4 B/L
3	Square	1.3	1.2	0.8
4	Circle	1.3	1.2	0.6

Source: IS 6403:1981 (Reaffirmed 2002). Indian Standard Code of Practice for Determination of Breaking Capacity of Shallow Foundations, (First Revision). Bureau of Indian Standards, New Delhi

Table 3 Depth factors

S. No.	Depth factor	
1	d_c	$1 + 0.2 (D/B)\sqrt{N_\phi}$
2	$d_q = d_\gamma$	1 for $\phi < 10$
3	$d_q = d_\gamma$	$1 + 0.1 (D/B) \sqrt{N_\phi}$ for $\phi > 10$

Source: As in Table 2

Table 4 Effect of water table

W'	1 if $D_w > (D + B)$
	0.5 if $D_w < D$ and for GWT at and above footing level

Source: As in Table 2

$$q_{na} = \frac{1}{\text{FOS}} * C N_c'' d_c s_c i_c + q(N_q'' - 1)d_q s_q i_q + 0.5\, B\gamma\, N_\gamma'' d_\gamma s_\gamma i_\gamma\, W'$$

where

$N_c'' = N_c' + \left(\frac{N_c - N_c'}{8}\right) * \text{difference}$

$N_q'' = N_q' + \left(\frac{N_q - N_q'}{8}\right) * \text{difference}$

$N_\gamma'' = N_\gamma' + \left(\frac{N_\gamma - N_\gamma'}{8}\right) * \text{difference}$

Difference $= \phi_m - 28°,\ \phi_m = 29°$ to $35°$.

2.1.2 Formulation as per Euro Code 7 [2]

ULS verifications are carried out with the three possible Design Approaches:

DA1—Combination 1: A1 + M1 + R1.
DA1—Combination 2: A2 + M2 + R1.
DA2: A1 + M1 + R2.
DA3: (A1/A2)* + M2 + R3.

*A1 is for Structural actions and A2 is for Geotechnical actions (Table 5).
For Drained Conditions:
The design bearing resistance is calculated as:

$$R/A' = C' N_c b_c s_c i_c + q' N_q b_q s_q i_q + 0.5\, B' \gamma' N_\gamma b_\gamma s_\gamma i_\gamma$$

where

$N_q = e^{\pi \tan \phi'} \tan^2\left(45 + \frac{\phi'}{2}\right)$

$N_c = \left(N_q - 1\right)\cot \phi'$

$N_\gamma = 2\left(N_q - 1\right)\tan \phi'$

are dimensionless factors for bearing resistance and

b_c, b_q, b_γ Inclination factors of the foundation base.

Table 5 L-M-R combination for shallow foundation

Partial safety factor					
Design approach	Action		Material		Resistance
	Permanent load γ_G	Variable load γ_Q	Drained γ_ϕ, γ_C	Undrained γ_{Cu}	Bearing γ_{Rv}
DA1-C1	1.35	1.50	1.00	1.00	1.00
DA1-C2	1.00	1.30	1.25	1.40	1.00
DA2	1.35	1.50	1.00	1.00	1.40
DA3	1.00	1.30	1.25	1.40	1.00

Table 6 Shape factor for drained condition

Shape factor	Value	Shape of footing
s_c	$(s_q N_q - 1)(N_q - 1)$	Rectangular, square or circular
s_q	$1 + (B'/L')\sin\phi'$	Rectangular
	$1 + \sin\phi$	Square or circular
s_γ	0.7	Square or circular
	$1 - 0.3(B'/L')$	Rectangular

s_c, s_q, s_γ Shape factors of foundation.
i_c, i_q, i_γ Inclination factors of load.
$A' = B'L'$ Effective foundation area (Table 6).

2.1.3   Formulation as per AASHTO [1]

The AASHTO LRFD specifications prescribe the procedures used to compute loads and detail how to factor and combine the loads for comparing to the factored resistance.

For the present work, the partial safety factor for permanent and live load are considered as 1.25 and 1.75, respectively.

Bearing Resistance of soil:

The factored resistance, q_R, at the strength limit state shall be taken as:

$$q_R = \phi_b * q_n$$

where

ϕ_b Resistance factor (taken as 0.45 as per AASHTO specifications for all soil).
q_n Nominal bearing resistance (ksf).

The nominal bearing resistance of a soil layer, in ksf, should be taken as:

$$q_n = cN_{cm} + qN_{qm}C_{wq} + 0.5B\gamma N_{\gamma m}C_{wy}$$

in which,

$N_{cm} = N_c s_c i_c.$
$N_{qm} = N_q d_q s_q i_q.$
$N_{\gamma m} = N_\gamma s_\gamma i_\gamma.$

where

N_c, N_q, N_γ Bearing capacity factors.
     $N_c = (N_q - 1)\cot\phi$, (from Prandtl, 1921).

Table 7 Shape correction factor

Factor	Friction angle	Cohesion term (s_c)	Unit weight term (s_γ)	Surcharge term (s_q)
Shape factor s_c, s_q, s_γ	$\phi = 0$	$1 + \left(\frac{B}{5L}\right)$	1	1
	$\phi > 0$	$1 + \left(\frac{B}{5L}\right)\left(\frac{N_q}{N_c}\right)$	$1 - 0.4\left(\frac{B}{L}\right)$	$1 + \left(\frac{B}{L}\tan\phi\right)$

Table 8 Correction for groundwater depth

D_w (ground water depth)	C_{wq}	C_{wy}
0	0.5	0.5
D_f	1	0.5
$>1.5B + D_f$	1	1

$$N_q = e^{\pi \tan\phi} * \tan^2\left(45 + \frac{\phi}{2}\right), \text{ (from Reissner, 1924)}.$$
$$N_\gamma = 2(N_q + 1)\tan\phi, \text{ (from Vesic, 1975)}.$$

C	Cohesion, (ksf).
Φ	Friction angle.
B	Width of footing (ft).
D	Depth of footing (ft).
γ	Unit weight of footing (kcf).
C_{wq}, C_{wy}	Correction factor for GWT.
d_q	Depth correction factor.
s_c, s_q, s_γ	Shape correction factors.
i_c, i_q, i_γ	Inclination factors $= 1$ for vertical loads (Tables 7 and 8).

If local or punching shear failure is possible, the nominal bearing resistance shall be estimated using reduced shear strength parameters C^* and Φ^* in nominal bearing resistance equation. The reduced shear parameters may be taken as

$$C^* = 0.67C.$$

$$\Phi^* = \tan^{-1}(0.67\tan\phi).$$

3 Results and Discussion

3.1 Results and Observation Obtained from Parametric Study

Some representative results obtained from parametric study are shown below (Figs. 1, 2, 3 and 4).
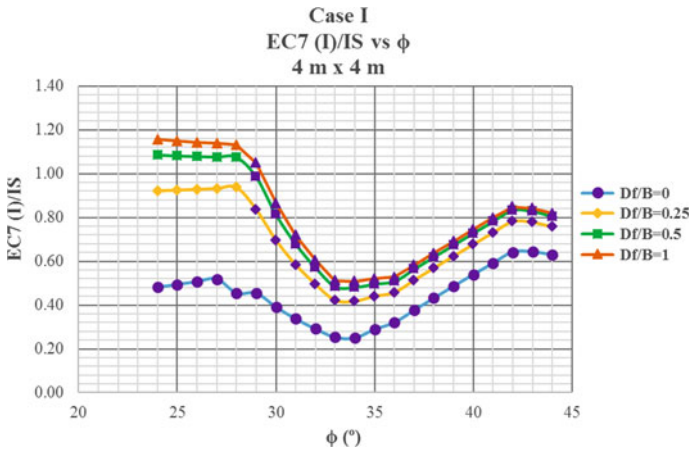
Fig. 1 Net safe load ratio versus ϕ for EC7 (I) Case I (4 m × 4 m)
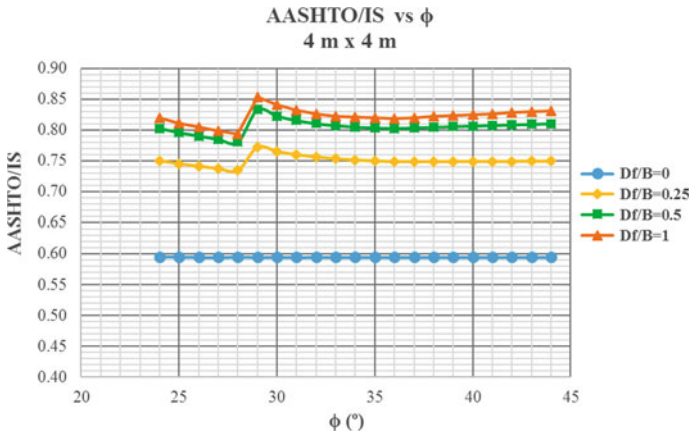
Fig. 2 Net safe load ratio versus ϕ for AASHTO (4 m × 4 m)

Note: In representation of graph for Euro Code, the below-mentioned markers indicate design approach governed by DA1-C2, while other markers indicate DA2.

Observation for ϕ soil:

- For square footing, net safe load obtained by EC7 (I) ranges from 0.25 to 1.19 times IS results with drop in value as 0.25 to 0.5 times IS values for $\phi = 29$–35.
- Net safe load obtained by EC7 (II) are 2–3 times higher than IS results for both square and strip footing.
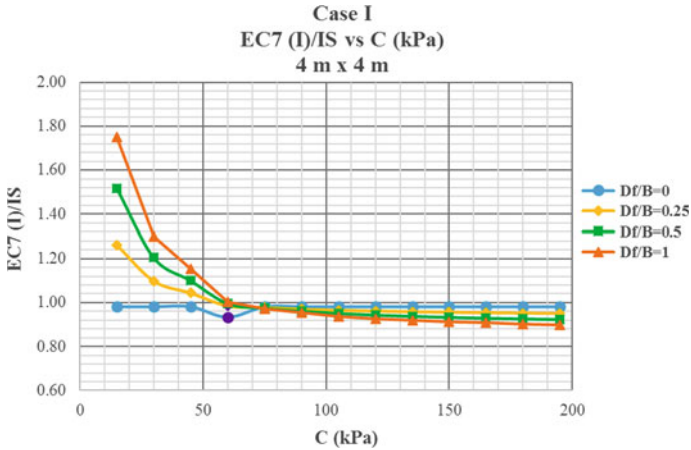
Fig. 3 Net safe load ratio versus C (kPa) for EC7 (I) Case I (4 m × 4 m)
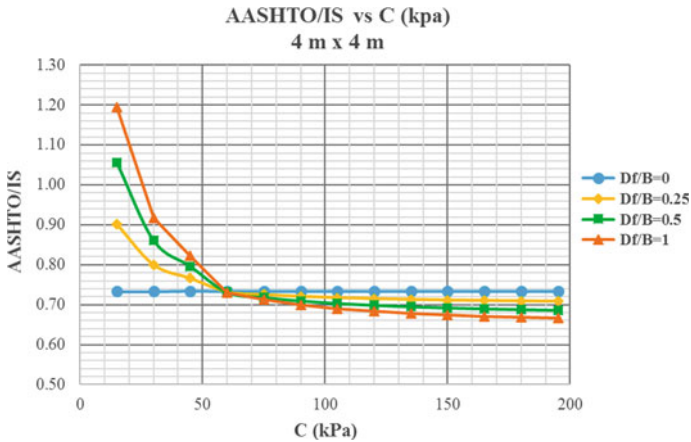
Fig. 4 Net safe load ratio versus C (kPa) for AASHTO (4 m × 4 m)

- For square footing, AASHTO gives consistent values as 0.6 times IS results for surface footing while it ranges from 0.75 to 0.83 times IS results for other depth of foundation.
- Similar trends were observed for strip footing.

Observation for C soil:

- For square footing, EC7 (I) gives consistent values of net safe load as 0.98 times IS results for surface footing while it ranges from 0.84 to 1.75 times IS results for other depth of foundation.

- For both square and strip footing, EC7 (I) shows drop in value of net safe load for $C = 60$ kPa as governing design approach changes from DA-2 to DA1-C2.
- Net safe load obtained by EC7 (II) is 2–2.5 times higher than IS results for both square and strip footing.
- For square footing, AASHTO gives consistent values as 0.73 times IS results for surface footing while it ranges from 0.63 to 1.20 times IS results for other depth of foundation.

3.2 Recommendation and Results Obtained from Revised Parametric Study

On the basis of the above observation and as a part of rationalization, another case for Euro Code 7 is considered where partial safety factors are applied to bearing capacity factors (N_C, N_q, N_γ) instead of material properties (C, ϕ) in order to incorporate the shear failure criteria in Euro Code design and to bring the results in considerable range with respect to IS Code design. Considering the above recommended case, the parametric study is repeated for all variations mentioned in Table 1 to get the revised net safe load (kN). Let this be considered as Case II: Partial safety factors applied to bearing capacity factors (N_C, N_q, N_γ), recommended as a part of rationalization to incorporate shear failure criteria in Euro Code design. Some of the results obtained from this revised parametric study is shown below in order to compare with the results obtained from Case I shown above (Figs. 5 and 6).
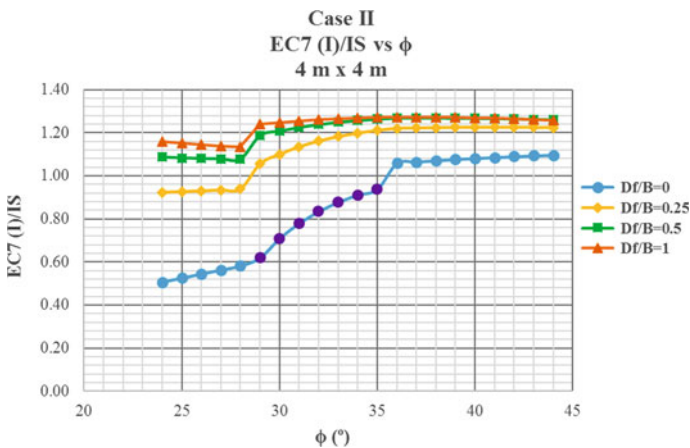

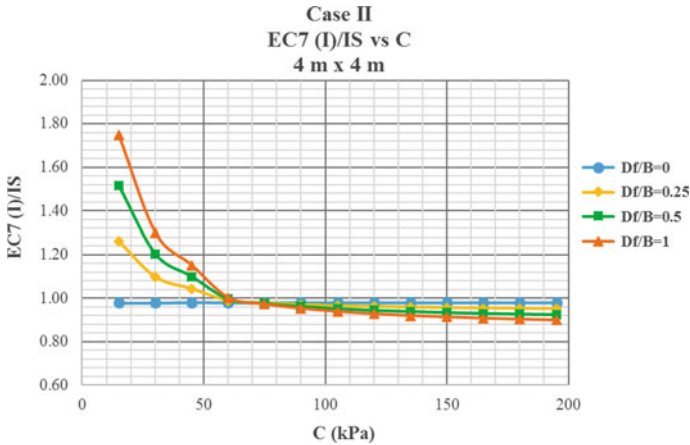**Fig. 5** Revised net safe load ratio versus ϕ for EC7 (I) Case II (4 m $\times$ 4 m)

Fig. 6 Revised net safe load ratio versus C (kPa) for EC7 (I) Case II (4 m $\times$ 4 m)

4 Observations Obtained From Revised Parametric Study

For ϕ soil:

- For square footing, Case I gives net safe load by EC7 (I) ranging from 0.25 to 1.19 times IS results, while Case II gives this range as 0.98–1.25, thereby showing reasonable results of Euro Code with respect to IS Code.
- The drop observed in net safe load ratio EC7 (I)/IS obtained for $\phi = 29$–35 for Case I is removed by considering Case II.
- For surface footing, net safe load ratio EC7 (I)/IS for Case II varies from 0.51 to 0.62 for local shear failure, thereby showing the need of change in depth correction factor.
- The net safe load obtained from EC7 (II) is quite on higher side with respect to IS results for both Case I and Case II, and hence, it is not advisable to consider EC7 (II) for design of shallow footing.
- AASHTO gives consistent values as 0.6 times IS results for surface footing while it ranges from 0.75 to 0.83 times IS results for other depth of foundation. The differences in results are due to the fact that the average factor of safety adopted by AASHTO is 3.15, whereas that of IS Code is 2.5.
- Similar trends were observed for strip footing as well with slight variation in net safe load ratio.

For C soil:

- There is no difference in results obtained by Case I and Case II for both square and strip footing.
- For both square and strip footing, EC7 (I) shows drop in value of net safe load for $C = 60$ kPa for Case I as governing design approach changes from DA-2 to

DA1-C2, while for Case II, no such drop in value is observed as the governing design approach for Case II is DA2.

- Net safe load obtained by EC7 (II) is 2–2.5 times higher than IS results for both square and strip footing designed by both Case I and Case II, which is not considerable.
- For square footing, AASHTO gives consistent values as 0.73 times IS results for surface footing while it ranges from 0.63 to 1.20 times IS results for other depth of foundation. For strip footing, AASHTO gives consistent values as 0.79 times IS results for surface footing while it ranges from 0.68 to 1.39 times IS results for other depth of foundation. The differences in results are due to the fact that the average factor of safety adopted by AASHTO is 3.15, whereas that of IS Code is 2.5.

Thus, from above all observations, it can be recommended that for Euro Code design, material partial safety factors must be applied to bearing capacity factors (N_C, N_q, N_γ) instead of applying to material properties in order to incorporate the shear failure criteria for Euro design.

References

1. AASHTO LRFD Bridge Design Specifications (2012). American Association of State Highway and Transportation Officials, Washington, DC
2. Bond, A.J., Harris, A.J.: Decoding Eurocode 7, p. 618. Taylor & Francis, London (2008)
3. Bowles, L.E.: Foundation Analysis and Design. The McGraw-Hill Companies, Inc., New York (1997)

Case Study on Underpinning of Foundation for an Industrial Building Renovation

A. Karthikeyan

Abstract Underpinning involves strengthening of foundation for existing structures using various methods. One of the suitable methods is adapted according to the subsoil and site conditions. One such method is extending the dimensions of existing foundation to rest under supportive soil strata. This method is effective in renovation of existing buildings where more space is available for working condition and requires skilled manpower. This paper deals with a case study on underpinning for an industrial building at Virudhunagar, Tamil Nadu, India. Since there is a need for a conversion of an existing spinning mill to an industrial plant, the necessity for strengthening the existing structures was proposed. The suggested method of underpinning by extending the breadth and depth of existing foundation was carried out and the outcome proved to be successful.

Keywords Existing building · Foundation · Underpinning · Industrial building · Renovation · Case study

1 Introduction

Underpinning is a process of strengthening the existing foundation of a structure. This may be required in case of ground subsidence, excessive settlement of the structure, construction of a new basement beneath a building, change in the usage of structure, increasing the height of the existing structure and enable a building to be with stand the additional loads [1].

A team of researchers in Nigeria [2] investigated the cause and the suitable remedial measures for the foundation failure. It has been found that differential settlement was the major reason and providing new continuous strip foundation was the widely accepted remedial measure.

A potash refinery industry near Regina, Saskatchewan, has investigated [3] to double the production capacity. The existing sub-structure has pile foundation with

A. Karthikeyan (✉)
Structural and Geotechnical, Karthikeyan Associates, Chennai 600106, India
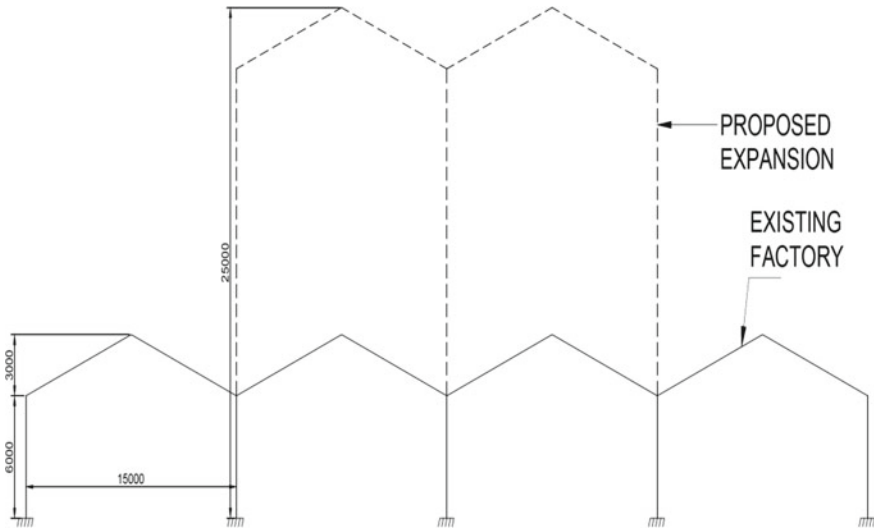e-mail: karthikeyanassociates@gmail.com

323

Fig. 1 Typical line diagram showing cross section of existing and proposed structure

pile cap. After the careful study of sub-soil and analyzing for the additional capacity, additional pile with extended pile cap suggested.

In this case study, an existing spinning mill industry of height 6 m at eaves level and 9 m at ridge level is proposed to be modified to suit for the polymer film manufacturing industry. The span of the existing and proposed truss was maintained same as 15 m. The new polymer film industry has a requirement of 22 m clear height at eaves level and 25 m at ridge level to enable new machinery to be installed for the production. The typical cross section of existing and proposed modification of structure is shown in Fig. 1.

The factory authorities entrusted M/s. Karthikeyan associates, Chennai, India, as consultants to renovate the industrial building to fit for their best use. This operation would not only include renovation or remodeling but also requires rigorous rehabilitation from the foundation level. This paper deals with the entire underpinning of the existing foundation as well as structural rehabilitation.

2 Existing Soil and Foundation

To analyze the existing foundation, it is very important to study the characteristics of soil substrata. An field exploration was carried out upto a depth of 10.5 m from the existing level. To collect the undisturbed soil samples, four numbers of bore hole done with in the site boundary. This soil exploration carried out by Sceba Consultancy Services, Madurai, Tamil Nadu.

2.1 Sub-soil Data

Tables 1, 2, and 3 give the index properties of soil, geotechnical design, and type of soil in critical borehole data out of four acquired from the soil investigation. The bearing capacity of soil [4] at 3.00 m from finished floor level was calculated to be 157.5 kN/m^2. However considered as 150 kN/m^2 for design calculations.

2.2 Existing Foundation

The existing foundation was physically examined and measured which was an isolated footing with a circular column of dia 0.6 m placed in the center. The size of the footing was 2.4 m in both length and breadth with raft thickness of 0.45 m.

3 Methodology

3.1 Analysis of Proposed Structure

We have analyzed the proposed structure in Staad pro software (see Fig. 2) and found that the existing foundation would not be sufficient to withstand the proposed extension and alteration of the structure. So, we have decided to strengthen the existing foundation, as well as the columns. The reaction from the structural analysis given for critical column is shown in Table 4. The suitable underpinning method according to the site conditions adaptable was increasing the dimensions of the foundation to rest under supportive soil strata. In this, we excavated till the bottom of foundation with sufficient space to work and drill near to the existing reinforcement of the isolated footing and fixed new reinforcement grouted with an approved chemical. The rebar grouting is done along the foundation and existing column. The operation increases both the dimensions of the footing and the thickness of footing. The existing column was 600 mm circular, but the structural requirement was 1400 × 1400 mm^2 column using M20 grade concrete and Fe500 steel reinforcement. For this condition, the foundation structure also requires a higher thickness of 1000 mm.

Below load combinations as per IS 456:2000 [5] and IS 800:2007 [6] are considered

1. 1.5 D.L + 1.5 L.L
2. 1.5 D.L + 1.5 W.L
3. 1.0 D.L + 1.0 L.L
4. 1.0 D.L + 1.0 W.L
5. 0.9 D.L + 1.5 W.L
6. 1.0 D.L + 0.8 W.L
7. 1.2 D.L + 1.2 L.L + 1.2 W.L.

Table 1 Index properties of soil sample from bore hole no. 4

S. No.	Depth (m)	'N' value corr	Type of soil	Density (gm/cc)	Liquid limit (%)	Plastic limit (%)	Plasticity index (%)	Shrinkage limit (%)	Degree of free swelling (%)
1	0.0–1.80 m	6 @ 1.5 m	Type A	NA	65	30	35	6	80
2	1.80–3.0	18 @ 3.0 m	Type B	1.75	39	18	21	12	50
3	3.0–4.50 m	35 @ 4.50 m	Type C	>2.0	Not Significant	Not Significant	Not Significant	Not Significant	20
4	4.5–6.0 m	45 @ 6.0 m	Type D	>2.0	Not Significant	Not Significant	Not Significant	Not Significant	20
5	6.0–7.5 m	Refusal @ 7.5 m	Type E	>2.0	Nil	Nil	Nil	Nil	Nil
6	7.5–9.0 m	Refusal @ 9.0 m	Type F	>2.0	Nil	Nil	Nil	Nil	Nil
7	9.0–10.5 m	Refusal @ 10.5	Type F	>2.0	Nil	Nil	Nil	Nil	Nil

Table 2 Soil geotechnical design of bore hole no. 4

S. No.	Depth (m)	'N' value corr	Type of soil	Natural density (kN/m³)	Bearing capacity Parameter			'Φ' value in degree	C' (kN/m²)	SBC based on kN/m²	
					N_c	N_r	N_q			"C"	Settlement for 40 mm
1	0.0–1.80 m	6 @ 1.5 m	Type A	NA	NA	NA	NA	NA	NA	NA	Highly reactive
2	1.80–3.0	18 @ 3.0 m	Type B	17.5	35.49	23.18	30.21	32°	NA	NA	157.5 @ 3.0 m
3	3.0–4.50 m	35 @ 4.50 m	Type C	>20	55.63	42.92	66.19	37°	NA	NA	336 @ 4.5 m
4	4.5–6.0 m	45 @ 6.0 m	Type D	>20	67.87	55.96	92.25	39°	NA	NA	440
5	6.0–7.5 m	Refusal @ 7.5 m	Type E	>20	50.59	37.75	56.31	36°	NA	NA	>450
6	7.5–9.0 m	Refusal @ 9.0 m	Type F	>20	75.31	64.20	109.4	40°	NA	NA	>450
7	9.0–10.5 m	Refusal @ 10.5 m	Type F	>20	75.31	64.20	109.4	40°	NA	NA	>450

Table 3 Detailed description of soil type for bore hole no. 4

S. No.	Type	Description of Soil
1	Type A	(Made up soil sand with clay observed for 50 cm) Clay soil black in color
2	Type B	Coarse to medium lime stones with blackish clay
3	Type C	Coarse lime stone gravel with cobbles and traces of weathered sand stone
4	Type D	Fragmented calcareous stone with sand stones and white fines
5	Type E	Combined fragmented calcareous stones and sand stones
6	Type F	Hard strata
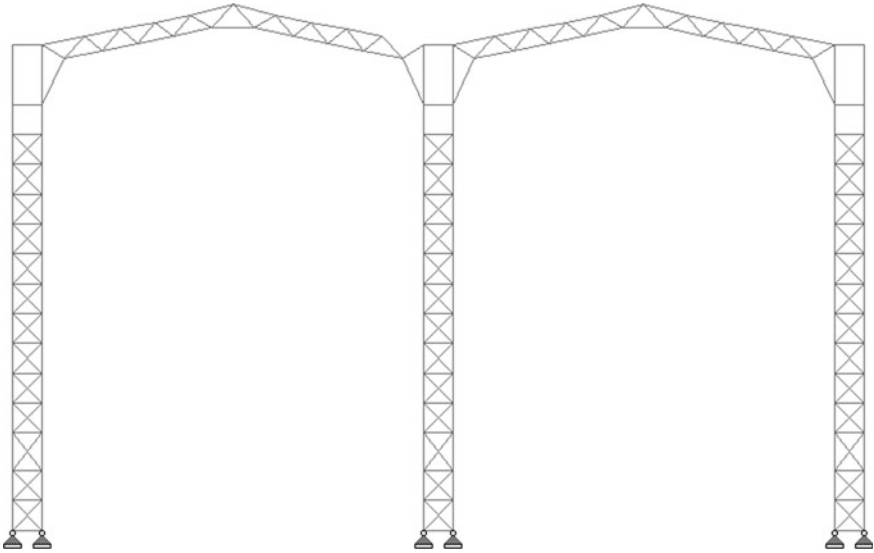
Fig. 2 Typical cross section showing steel truss

Table 4 Reactions (kN) from built-up steel column to RCC column

Node No.	Fx	Fy	Fz
4755	1.663	190.618	2.491
	−29.806	−437.552	−2.807
4756	2.163	167.405	0.331
	−0.195	−359.807	−0.104
4757	2.346	290.714	0.397
	−0.201	−147.346	−0.183
4758	1.741	373.343	3.544
	−22.954	−188.378	−6.369

where

D.L   Dead Load.
L.L.   Live load or Imposed Load.
W.L   Wind Load.

The foundation was designed based on Eq. (1), where P is working load on the column, A is the area of the foundation, M is the lateral moment, due to horizontal wind force and Z is section modulus of the foundation. SBC is safe bearing capacity of soil.

$$\frac{P}{A} + \frac{M}{Z} \leq \text{SBC} \tag{1}$$

3.2 Methods of Underpinning

There are following methods of under pinning available

1. Underpinning by chemical injections
2. Underpinning by continuous strip foundations
3. Underpinning using micropiles
4. Underpinning using additional piles with extended pile cap
5. Underpinning by widening the size of foundation.

3.3 Decision-Making Process

Some of the underpinning widely used shown above, in which chemical injections method can be used to increase the soil bearing capacity but it requires more construction time and evaluation of SBC requires further investigations. It may also be noted that the foundation is subjected to uplifting forces due to the wind action; hence, it requires larges base with mass concrete for good stability, and hence, it has been decided to widen the size of the existing footing from 2.4 × 2.4 m to 5.0 × 5.0 m.

3.4 Construction Carried Out

The existing steel roof truss dismantled over the proposed modification area, and it was kept safe for using again at elevated height with some strengthening. Then the excavation work carried out to a depth of 2.4 m from the existing ground level and the size of the excavation maintained 5 m × 5 m at 2.4 m level (see Fig. 3).
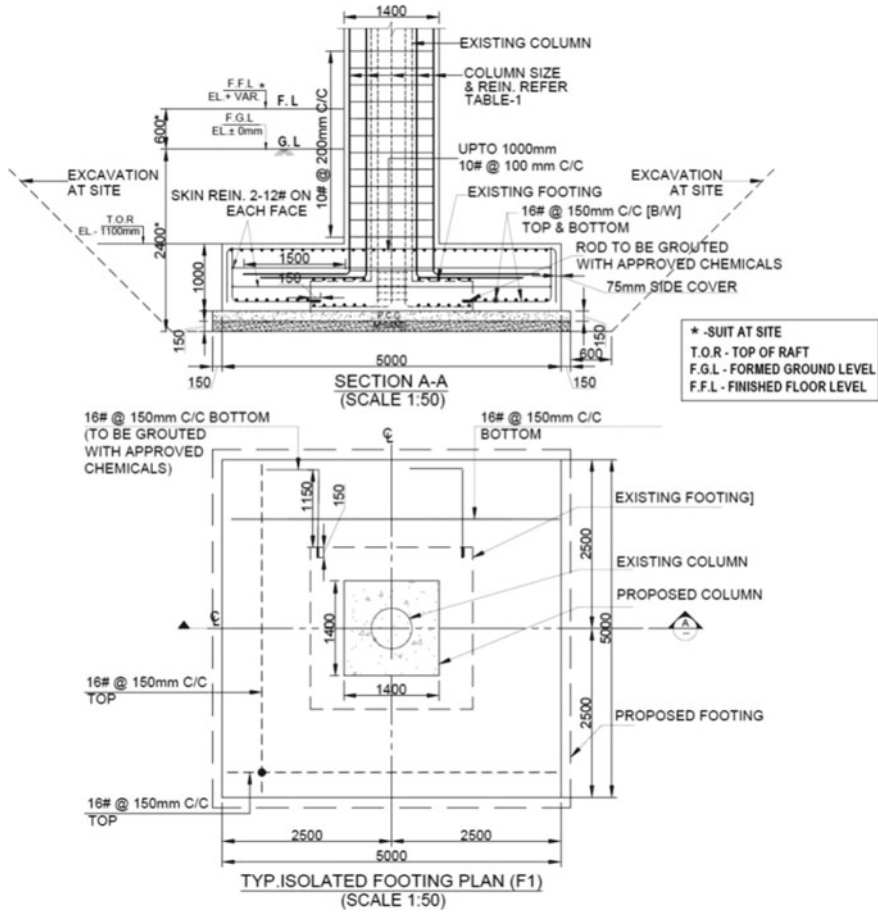
Fig. 3 Underpinning of existing footing and column details

One of the foundation after the excavation is shown in Fig. 4. After the excavation, the existing footing concrete cleaned and chipped off and bonding agent applied to create the good interaction between existing and new concrete. In addition to that, the reinforcement dowel 16 mm dia rods grouted to the existing foundation at 150 mm c/c has shown in Fig. 5 with the additional reinforcement before concreting and the same foundation shown in Fig. 6 after concreting.

The proposed 1400 × 1400 mm RC column constructed over the renovated footing up to a height of 6 m. Above the RCC column, the steel column erected upto new eaves level at 22 m height from the ground level. After the successful erection of all columns with the bracing, the roof truss erected over the steel column. The erected truss partially covered with the roof sheet shown in Fig. 7. After successful completion of this rehabilitation and renovation job, the structure was handed over to the mechanical engineering department to fabricate their machinery.

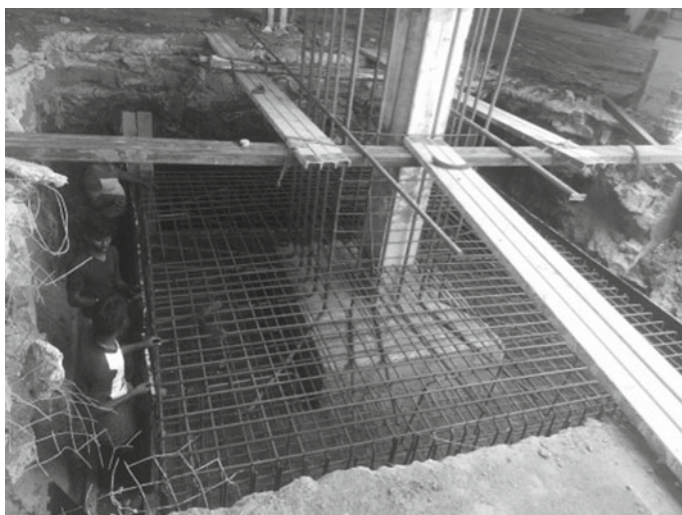**Fig. 4** Site photographs showing existing footing and underpinning before concreting

Fig. 5 Site photographs showing underpinning before concreting

.

Fig. 6 Site photographs showing footing after concreting

4 Conclusion

Underpinning is a state of the art for geotechnical and structural engineers with sound technical background. Structural engineers must have sound knowledge about the existing foundation and sub-soil condition, plan for renovation and rehabilitation of the existing structure. Before rehabilitation process non-destructive testing (NDT) on existing structure is emphasized. After underpinning, periodical study of the renovated structure is also important.

In this renovated structure, no specific monitoring device fixed for structural health monitoring due to cost constraints and cumbersome to fix and monitor regularly. The industrial structure has been serving for more than 4 years experienced all climatic conditions without any sign of distress being observed during our periodic site visit. This project gets success not only because of structural strengthening but also due to strong underpinning.

Fig. 7 Site photographs showing the erected steel structure on renovated RC column over the Underpinned foundation

References

1. Tomlinson, M.J.: Foundation Design and Construction, 6th edn.
2. Dahiru, D., Salau, S., Usman, J.: A study of underpinning methods used in the construction industry in Nigeria. Int. J. Eng. Sci. **3**(2), 05–13 (2014)
3. Hesham, M.: Underpinning of existing industrial plant foundation. Can. J. Civ. Eng. **15**, 176–181 (1988)
4. IS 1904: 1986, Indian Standard Code of Practice for Design and Construction of Foundations in Soils: General Requirements. Bureau of Indian Standard, New Delhi
5. IS 456: 2000, Indian Standard Plain and Reinforced Concrete—Code of Practice. Bureau of Indian Standard, New Delhi
6. IS 800: 2007, Indian Standard General Construction in Steel—Code of Practice. Bureau of Indian Standard, New Delhi

Evaluation of WSM, LRFD and FE Methods for Pile Capacity Calculation with Pile Load Test for IGM

Pratik V. Shah and Kandarp K. Thaker

Abstract As many infrastructures, projects are going on in Ahmedabad like metro rails and bridges which are being constructed, for that behaviour of pile foundation capacity is must, and in that too the behaviour of pile in overconsolidated soil. Sometimes the overconsolidated soil is considered as intermediate geomaterials (IGM); i.e. behaviour comes in between the continuum of soil and rock. There are many analytical methods for evaluating pile capacity in any type of soil. But for overconsolidated soil, it may be exhibited the wide range of properties. Using an analytical method, 17 problems were analysed and there results were calculated from LRFD method (O'Neill and Reese) and IS code (IS 2911 P1/S2, 2010) were compared, and the FEM modelling of this soil was done using software PLAXIS 2D. The load settlement curve from FEM software and actual load test data were super-imposed, and the result was quiet matching. Skin friction was found to be over predicted by 37.26%, 212.37%, and 32.46% when determined from static formula (IS 2911 P1/S2, 2010), Cole and Stroud method (IS 2911 and IRC 78, 2014) and LRFD method (O'Neill and Reese), respectively. End bearing was found to be over predicted by 754.31%, 864.89%, and 55.04% when determined from static formula (IS 2911 P1/S2, 2010), Cole and Stroud method (IS 2911 and IRC 78, 2014) and LRFD method (O'Neill and Reese), respectively.

Keywords Intermediate geomaterial (IGM) · Overconsolidated soil · LRFD method · IS code method

P. V. Shah (✉)
Department of Civil Engineering, RNGPIT, Surat, India
e-mail: pvs.fetr@gmail.com

K. K. Thaker
K. C. T. Consultancy Services, Ahmedabad, India
e-mail: kctconser@yahoo.com

1 Introduction

When the soil is having a low bearing capacity and hard strata is available at larger depth, piles are used to transfer the load to deeper and strong medium. The first pile was used by the romans; Vitruvius (59 A.D.) records the use of such foundations. Evidence was found out that a pile driving device was used in building artificial islands at Oakbank in Scotland as early as 5000 years ago. It is believed that the first pile was used in 1848 in Chicago. Pile foundation is used to carry the load coming over it along the lateral loads without the failure and excessive settlement.

In present research work, the work is done on the soil named IGM, i.e. intermediate geomaterials. IGM's is a soil material which is harder and denser than the ordinary soils but which are not cemented to an extent which are found in rock. It comes between the continuum of soil and rock mass. The study shows whether the static method (IS 2911, P1/S2, 2010) or Cole and Stroud method (IS 2911 and IRC 78, 2014) is applicable to the pile carrying capacity of IGM material, which is further compared with the LRFD method for IGM and pile load test data were calibrated with the PLAXIS 2D. For soil properties required in PLAXIS 2D, N-values were used to calculate using correlations.

2 Pile Carrying Capacity

The capacity of pile foundation is determined with combination of skin friction and end bearing. The skin friction is related to the shear strength parameters of the soils as well as the friction between the soil and concrete. The end bearing is related to function of a pile displacement, and the peak value differs with the displacements. The concept of separate calculation of skin friction and end bearing resistance forms the base of all static calculation of pile carrying capacity.

2.1 IS Code Method

Piles in Granular Soil: IS 2911 (Part 1/Sec. 2): 2010

$$Q_u = (A_p * 0.5 * D * \gamma * N_\gamma + P_D * N_q) + (\Sigma(K_i * P_{Di} * \tan \delta_i * A_{si})) \quad (1)$$

where

A_p = cross-sectional area of pile tip, in m^2, D = diameter of pile shaft, in m, γ = effective unit weight of the soil at pile tip, in kN/m^3, N_γ and N_q = bearing capacity factors depending upon the angle of internal friction, ϕ at pile tip, P_D = effective overburden pressure at pile tip, in kN/m^2, K_i = coefficient of earth pressure applicable for the ith layer, P_{Di} = effective overburden pressure for the ith layer,

in kN/m², δ_i = angle of wall friction between pile and soil for the ith layer, A_{si} = surface area of pile shaft in the ith layer, in m².

Piles in Cohesive Soils: IS 2911 (Part 1/Sec. 2): 2010

$$Q_u = (A_p * N_c * C_p) + (\Sigma(\alpha_i * c_i * A_{si})) \tag{2}$$

where

A_p = cross-sectional area of pile tip, in m², N_c = bearing capacity factor, may be taken as 9, C_p = average cohesion at pile tip, in kN/m², α_i = adhesion factor for the ith layer, c_i = average cohesion for the ith layer, in kN/m², A_{si} = surface area of pile shaft in the ith layer, in m² (Figs. 1 and 2; Table 1).

Piles in Weather/Soft Rock: IRC-78-2014

$$Q_u = \left(A_p * \{C_{u1} * N_c/Fs\}\right) + [\Sigma(\{\alpha * C_{u2}/Fs\} * A_{si})] \tag{3}$$

where

A_p = cross-sectional area of pile tip, in m², A_{si} = surface area of pile shaft in the ith layer, in m², C_{u1} = average shear strength of rock in the socketed length of pile in kN/m², C_{u2} = average shear strength of rock in the socketed length of pile,
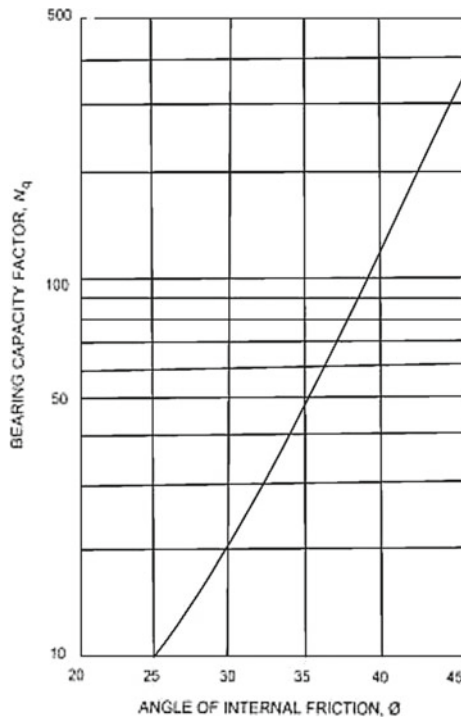

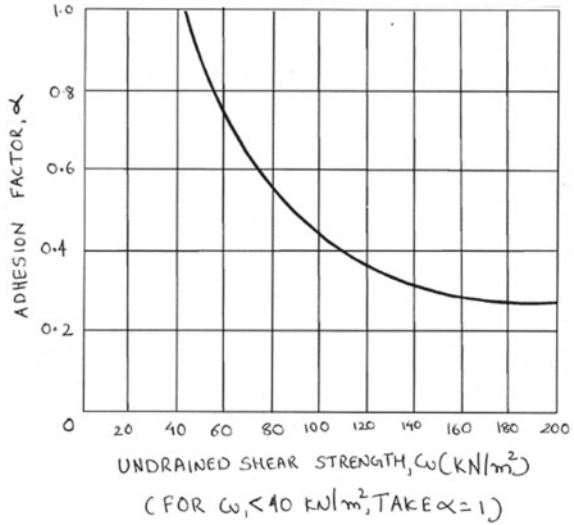**Fig. 1** Bearing capacity factor N_q [1]

Fig. 2 Variation of α with C_u [1]

Table 1 General shear failure factors for N_γ [2]

ϕ	0	5	10	15	20	25	30	35	40	45	50
N_γ	0	0.45	1.22	2.65	5.39	10.88	22.4	48.03	109.41	271.76	762.89

in kN/m^2, N_c = bearing capacity factor taken as 9, α = 0.9, Fs = factor of safety usually taken as 3 for end bearing and 6 for skin friction.

2.2 Piles in IGMs: FHWA-IF-99-025

Cohesionless IGMs:

$$q_{pbk} = 0.59 * \left(\left(N_{60} * \left(P_a/\sigma_v' \right) \right)^{0.8} \right) * \sigma_v' \qquad (4)$$

$$q_{psik} = k_{oi} * \tan \varphi_i' * \sigma_{vi}' \qquad (5)$$

where

q_{pbk} = is the characteristic value of the resistance per unit area of the base, q_{psik} = is the characteristic value of the resistance per unit of the shaft in layer i, A_p = cross-sectional area of pile tip, in m^2, A_{si} = surface area of pile shaft in the ith layer, in m^2, N_{60} = hammer efficiency, P_a = atmospheric pressure, in kN/m^2, σ_v' = effective overburden pressure at pile tip, in kN/m^2, σ_{vi}' = effective overburden pressure for the ith layer, in kN/m^2, k_{oi} = design value of earth pressure at rest for ith layer

$$k_{oi} = \left(1 - \sin \varnothing_i'\right) * \left(\frac{0.2 * P_a * N_{60i}}{\sigma_{vi}'}\right)^{\sin \varnothing_i'} \tag{6}$$

$\varphi_i' =$ design value of internal friction for ith layer.

$$\varphi_i' = \tan^{-1} * \left[\left\{\frac{N_{60}}{12.3 + 20.3\frac{\sigma_{vi}'}{P_a}}\right\}^{0.34}\right] \tag{7}$$

Cohesive IGMs:

$$Q_u = (A_p * q_{max}) + (\Sigma(a_i * q_{ui} * A_{si})) \tag{8}$$

where $A_p =$ cross-sectional area of pile tip, in m^2, $A_{si} =$ surface area of pile shaft in the ith layer, in m^2, $q_{max} = [s^{0.5} + (m * s^{0.5} + s)^{0.5}] * q_u$, $a_i =$ adhesion factor, $q_{ui} =$ unconfined compressive strength at ith layer, $q_u =$ unconfined compressive strength at pile tip.

3 Collection of Data and Data Analysis

Borelog data with the actual pile load test of Ahmedabad City and Surat is collected from various consultancy agencies. The borelog data will be used to find out the parameters for constitute model and other soil properties like frictional angle, undrained shear strength, etc.

3.1 Correction for the N-values ($(N)_{60}$)

The N-values have many correlations with relative density (R_d), undrained shear strength (S_u), angle of internal friction (ϕ), and other parameters.

$$(N)_{60} = ((N * C_N) * C_d) * C_E * C_B * C_R * C_S \tag{9}$$

where
$N =$ measured standard penetration resistance (raw data of N at the site), $C_N =$ depth or overburden correction factor, $C_d =$ dilatancy correction factor, $C_E =$ hammer energy ratio correction factor, $C_B =$ borehole diameter correction factor, $C_R =$ rod length correction factor, $C_S =$ correction factor for samplers with or without liners.

3.2   Angle of Internal Friction (ϕ)

The ability of a unit of a soil or rock is to withstand a shear stress.

$$\phi = 0.28 * N_{\text{corr}} + 27°$$
$$\phi = \sqrt{12 * N_{\text{corr}}} + 15 \tag{10}$$

3.3   Saturated Density of Soil (γ_{sat})

It is the ratio of the weight per unit of volume.

$$\gamma_{\text{sat}} = \frac{N_{\text{corr}}^2}{390} - \frac{N_{\text{corr}}}{11.5} + 19.15 \tag{11}$$

3.4   Undrained Shear Strength (S_u)

For finding out the value of S_{u} for weather rock a Fig. 3 given Cole and Stroud will be used. And for other method, S_{u} will be equal to $5.985 * N_{\text{corr}}$ and $4.5 * N_{\text{corr}}$.

3.5   Stress–Strain Modulus (E_s)

It is the ratio of stress along an axis over the strain along that axis in the range of elastic soil behaviour. The E_{s} will be found out from Figs. 4 and 5.

3.6   Dilatancy Correction (ψ)

$$\psi = \phi - 30 \tag{12}$$

3.7   Poisson's Ratio (μ)

See Table 2.

Value of N	Shear Strength (kg/cm²)	Strength	Grade	Breakability	Penetration	Scratch
	400	Strong	A	Difficult to break against solid object with hammer		Cannot be scratched with knife
600	200	Moderately Strong	B	Broken against solid object by hammer		Can just be scratched with knife
	100					
	80					Can be just scratched by thumb nail
	60		C	Broken in hand by hitting with hammer		Can be scratched by thumb nail
400	40		D	Broken by leaning on sample with hammer	No penetration with knife	
	20	Moderately weak				
200	10	Weak	E	Broken by hand	2 mm with knife	
	8					
100 80	6		F	Easily broken by hand	5 mm with knife	
60	4	Hard or very weak				

(N less than 60 are considered as soil)

Fig. 3 Consistency and shear strength of weather rock [3]

Soil

		Use the undrained shear strength s_u in units of s_u
Clay and silt	$I_P > 30$ or *organic*	$E_s = (100 \text{ to } 500)s_u$
Silty or sandy clay	$I_P < 30$ or *stiff*	$E_s = (500 \text{ to } 1500)s_u$
		Again, $E_{s,OCR} \approx E_{s\,nc}\sqrt{OCR}$
		Use smaller s_u-coefficient for highly plastic clay.

Of general application in clays is

$$E_s = Ks_u \qquad \text{(units of } s_u\text{)} \qquad (a)$$

where K is defined as

$$K = 4200 - 142.54I_P + 1.73I_P^2 - 0.007\,1I_P^3 \qquad (b)$$

and I_P = plasticity index in **percent**. Use $20\% \leq I_P \leq 100\%$ and round K to the nearest multiple of 10.

Another equation of general application is

$$E_s = 9400 - 8900I_P + 11\,600I_c - 8800S \qquad \text{(kPa)} \qquad (c)$$

I_P, I_c, S = previously defined above and/or in Chap. 2

Fig. 4 Equations for E_s [4]

Soil	SPT	CPT
Sand (normally consolidated)	$E_s = 500(N + 15)$ $= 7000\sqrt{N}$ $= 6000N$ — — — $E_s = (15\,000 \text{ to } 22\,000) \cdot \ln N$	$E_s = (2 \text{ to } 4)q_u$ $= 8000\sqrt{q_c}$ — — — $E_s = 1.2(3D_r^2 + 2)q_c$ $E_s = (1 + D_r^2)q_c$
Sand (saturated)	$E_s = 250(N + 15)$	$E_s = Fq_c$ $e = 1.0 \qquad F = 3.5$ $e = 0.6 \qquad F = 7.0$
Sands, all (norm. consol.)	$E_s = (2600 \text{ to } 2900)N$	
Sand (overconsolidated)	$E_s = 40\,000 + 1050N$ $E_{s(OCR)} \approx E_{s,nc}\sqrt{OCR}$	$E_s = (6 \text{ to } 30)q_c$
Gravelly sand	$E_s = 1200(N + 6)$ $= 600(N + 6) \qquad N \leq 15$ $= 600(N + 6) + 2000 \qquad N > 15$	
Clayey sand	$E_s = 320(N + 15)$	$E_s = (3 \text{ to } 6)q_c$
Silts, sandy silt, or clayey silt	$E_s = 300(N + 6)$ If $q_c < 2500$ kPa use $\qquad E_s' = 2.5q_c$ $2500 < q_c < 5000$ use $\qquad E_s' = 4q_c + 5000$ where $E_s' = $ constrained modulus $= \dfrac{E_s(1 - \mu)}{(1 + \mu)(1 - 2\mu)} = \dfrac{1}{m_v}$	$E_s = (1 \text{ to } 2)q_c$
Soft clay or clayey silt		$E_s = (3 \text{ to } 8)q_c$

Fig. 5 Equations for E_s [4]

Table 2 Value of μ [6]

Soil condition	Type of consolidation	Value of μ
Sand	NC OC	0.35 0.30
Clay unsaturated	NC OC	0.35 0.30
Clay fully saturated	NC OC HOC	0.50 0.40 0.30
IGM		0.25

4 Numerical Modelling

Finite element model is a method of solving continuous problems governed by differential equations by dividing the continuum into a finite number of elements, which are specified by a finite number of parameters. A problem is solved by dividing the larger geometry into small elements, which are interconnected with nodes. Each element is assigned an element property. In solid mechanics, the properties include stiffness characteristics for each element.

4.1 Hardening Soil (HS) Model

The HS model is a hyperbolic elasto–plastic model and which models the dependence of stiffness moduli on stress level but does not take the viscous effects such as creep and stress relaxation. The HS model is based on the Mohr–Coulomb failure criterion, and its yield surface may expand due to plastic strains. In the HS model, the volumetric hardening has been complemented by deviatoric (shear) hardening to overcome this; it is an extension of the hyperbolic model developed by Duncan and Chang.

Advantages:

- More accurately stiffness is defined than the MC model
- It takes into consideration soil dilatancy

Disadvantages:

- The higher computational costs
- It does not include viscous effects

    It does not include softening.

4.2 PLAXIS 2D Analysis [8]

In order to perform a numerical analysis with PLAXIS 2D, some general assumptions with regard to material behaviour, stress state, geometry, and parameters selection is to be made,

1. Assumption of axisymmetry.
2. The elements used in the model are 15 nodded triangular element.
3. The geometry in X-direction is fixed to 20.1 m and in Y-direction is approximately 1.25 times of the depth of pile.
4. The gravitational constant is 9.8 m/s^2.
5. The density of water is taken as 10 kN/m^3.
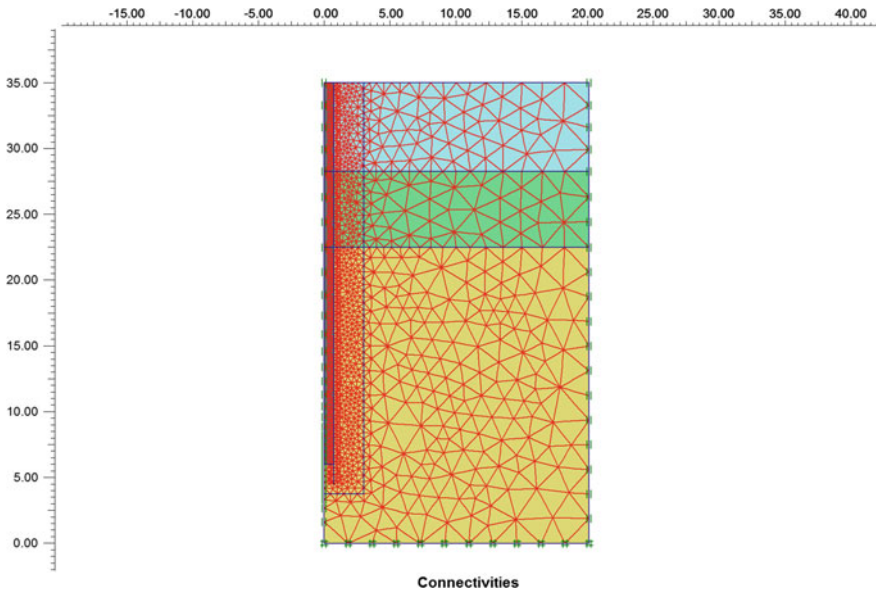
Connectivities

Fig. 6 Geometry of model

6. The clay material is undrained type of soil material, and granular soils are drained type soil material.
7. The meshes are made two times more refined in the region of three times from the pile for more accurate result.
8. For modelling in HS model, the value of m is fixed to 0.6 for HOC and 0.5 for cohesionless soil.
9. The value of R-inter is fixed to 0.9 for all soil models and 1.0 for pile materials (Fig. 6).

5 Result

The study was not limited to Ahmedabad region only, and the data for Surat region were also taken into consideration for the thesis. The results obtain from the PLAXIS 2D show similar behaviour to the actual pile load test data. And the assumption for different values was found to be accurate (Figs. 7 and 8; Table 3).

6 Conclusion

Consistent with usual practice, the static formula is used for determination of the safe load on piles in soils. It was observed in many actual load tests that the safe load
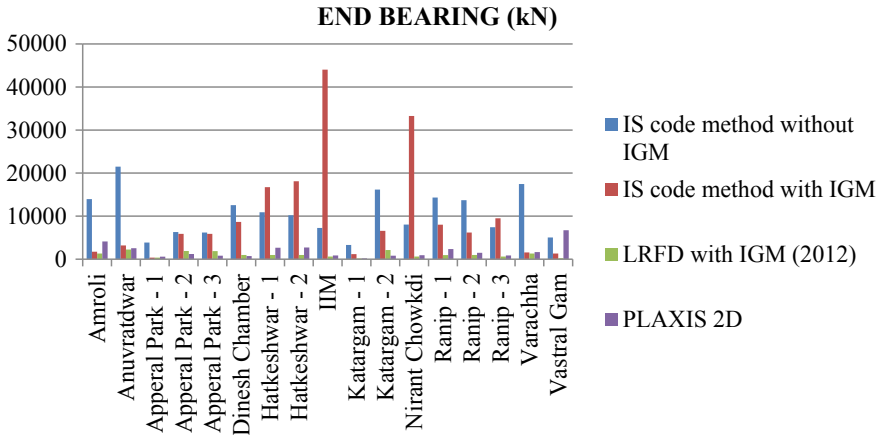
END BEARING (kN)

Fig. 7 Comparison of end bearing capacity
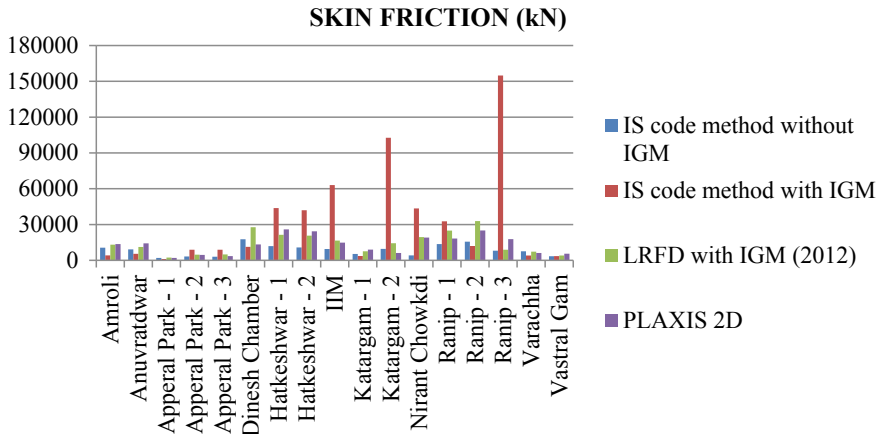
SKIN FRICTION (kN)

Fig. 8 Comparison of skin friction

obtained is reasonably on higher side compared to theoretically determine safe load. This warrants a study to find the most suitable approach to narrow such difference and optimising pile design.

Data from various regions were collected for studying the behaviour. Analyses were performed using the borelog, laboratory, and filed test results and actual load test data. The study was conducted on both the Ahmedabad and Surat soils, and following conclusion was drawn based on that.

1. A reasonable match was found between the result of full-scale pile load test and that obtain in FE analyses using axisymmetry model in PLAXIS 2D. Though limited data set was analysed, available findings provide a good insights.

Table 3 Value of safe load

Location	IS 2911 Part-1/Sec. 2 2010	IRC 78-2014	LRFD method
	Total ultimate load (kN)	Total ultimate load (kN)	Total ultimate load (kN)
Amroli	9826.78	2366.31	8575.61
Anuvratdwar	12,277.81	3459.84	7931.31
Apperal Park-1	2350.68	614.92	1613.54
Apperal Park-2	3827.18	5911.57	3909.64
Apperal Park-3	3685.84	5911.57	3986.48
Dinesh Chamber	12,086.87	7983.18	17,207.31
Hatkeshwar-1	9114.82	24,192.59	13,401.36
Hatkeshwar-2	8410.94	24,024.83	12,974.39
IIM	6679.29	42,832.74	10,276.78
Katargam-1	3458.76	1925.57	4669.46
Katargam-2	10,290.65	43,713.84	9790.83
Nirant Chowkdi	4857.71	30,694.66	12,031.84
Ranip-1	11,176.97	16,270.30	15,509.47
Ranip-2	11,729.68	7287.64	20,294.59
Ranip-3	6198.76	65,731.61	5688.15
Varachha	10,017.91	2246.95	5117.53
Vastral Gam	3406.25	1951.00	2551.79

2. In over and heavily over consolidated soils in study area, the static formula gives lower value of safe load compared to that from the approaches used in the IGM. Safe load on pile is under estimated when static formula is used.
3. By idealising the over and heavily over-consolidated soils as IGM and by using the O'Neill and Reese method, more reliable estimate of safe load can be obtained. It is also confirmed that the LRFD method by O'Neill and Reese gives more realistic safe load compare to the method of Cole and Stroud as recommended by IRC-78-2014 for IGM for the piles in the study area.
4. It can be concluded from study that above conclusions hold good even for geographically different locations within study area having over consolidated soils.
5. The skin friction evaluated using PLAXIS 2D modelling matches fairly with the end bearing derived using the approach of O'Neill and Reese (LRFD method for IGM). Skin friction was found to be over predicted by 37.26%, 212.37%, and 32.46% when determined from static formula (IS 2911 P1/S2, 2010), Cole and Stroud method (IS 2911 and IRC 78, 2014) and LRFD method (O'Neill and Reese), respectively.
6. The end bearing evaluated using PLAXIS 2D modelling matches fairly with the skin friction derived using the approach of O'Neill and Reese (LRFD method

for IGM). End bearing was found to be over predicted by 754.31%, 864.89%, and 55.04% when determined from static formula (IS 2911 P1/S2, 2010), Cole and Stroud method (IS 2911 and IRC 78, 2014) and LRFD method (O'Neill and Reese), respectively.

7. PLAXIS provided good estimate of load settlement curve based on soil properties and using HS model when findings were compared with the actual load test data.

There is a tendency to terminate full-scale pile load test once ultimate load is found instead of continuing it till failure, which limits this study to some extent. It is desirable that pile load tests are continued till failure. For this, if reaction loading is a limitation than test pile diameter may be reduced which does not result into any appreciable change in soil–structure interaction.

References

1. BIS 2010: Design and Construction of Pile Foundations—Code of Practice. IS 2911 (Part-1/Sec.2) (2010)
2. BIS 2002: Code of Practice for Determination of Bearing Capacity of Shallow Foundations. IS 6403-1981 (R2002) 8
3. Srinivasamurthy, B.R., Pujar, K.L.: Socketing of Bored Piles in Rock. IGC 2009, p. 680 (2009)
4. Bowles, J.E.: Foundation Analysis and Design, 5th edn. McGraw-Hill, New York (1996)
5. AASTHO: AASTHO LRFD Bridge. Highway Subcommittee on Bridges and Structures, Washington DC (2012)
6. O'Neil, M.W., Reese, L.C.: Drilled Shafts: Construction Procedures and Design Methods. FHWA-IF-99-025. Department of Transportation (1999)
7. Nayak, N.V.: Foundation Design Manual for Practicing Engineer. Dhanpat Rai Publication, New Delhi (2001)
8. Brinkgreve, R.B.J., Broere, W.: PLAXIS 3DF Reference Manual, Material Model V1.1. A.A. Balkema Publishers, Netherlands (2004)

Analysis and Design of Micro-pile Foundation for an Extension of a Commercial Building

Rutuj Chheda, Atharva Pisolkar, Chhaya Kandpal, Jigisha Vashi, Aditya Soni, and Rishabh Bakliwal

Abstract Foundations are classified as shallow and deep. They provide support for superstructure by transferring load to layers of soil or rock that have sufficient bearing capacity. However, certain ground conditions and site constraints make it difficult to use these conventional foundations. In such situations, micro-piles are seen as the only alternative. They can be used both as a ground improvement method and structural element designed as soil frictional piles and rock socketed piles either under tension or compression. They can be installed in restricted access sites making it very favorable. The present paper is a case study of use of micro-pile for a commercial building at Chhattisgarh, India, where the access to the construction site is restricted and the ground conditions are unfavorable for conventional foundations. The geotechnical design of micro-pile is carried out. The present paper also discusses the design of group of six micro-piles with a pile cap which were modeled in Plaxis 3D according to substrata conditions observed at a construction site and the deflection parameters were observed.

Keywords Micro-pile · Foundation · Load carrying capacity · Settlement

1 Introduction

Shallow foundations (0.5 m depth) are used for small, light buildings, while deep foundations (20–65 m depth) are for large, heavy buildings. Deep foundations may also be required in conditions where good hard strata are not available at shallow depth. For deep foundations, piles are used. A pile basically is a long cylinder of a strong material such as concrete that is pushed into the ground so that structures can be supported on top of it. Piles are used when there is a layer of weak soil at the

R. Chheda · A. Pisolkar · C. Kandpal · J. Vashi (✉) · A. Soni · R. Bakliwal
Civil Engineering Department, MPSTME, SVKM's NMIMS, Mumbai 40056, India
e-mail: jigisha.vashi@nmims.edu

R. Chheda
e-mail: rutujchheda@gmail.com

surface; this layer cannot support weight of the building, so the loads of the building have to bypass this layer and be transferred to the layer of stronger soil or rock that is below the weak layer. However, certain ground conditions and site constraints make it difficult to use these conventional foundations such as weak soil only present in shallow depths. In such situations, micro-piles are the only alternative. A micro-pile is a pile having smaller diameter than conventional piles, typically less than 300 mm. It is heavily reinforced and carries most of its loading on high capacity steel reinforcement. They can be used both as a ground improvement method and structural element designed as soil frictional piles and rock socketed piles either under tension or compression. They can be installed in restricted access sites making it very favorable [1]. This paper is a case study of use of micro-piles as foundation for a G+10 commercial building at Chhattisgarh, India, where the access to the construction site is restricted and the ground conditions are unfavorable for conventional foundations. Geotechnical design of micro-pile is carried out. Also, a group of six micro-piles with a pile-cap was modeled in Plaxis 3D.

2 Site Investigation

The plan of G+10 building at Chhattisgarh site is shown in Fig. 1. The site at Chhattisgarh having filling material up to 3 m then 3–4 m is fractured rock followed by soft rock up to 15 m. Groundwater is acting at 1.1 m from ground level. The typical subsoil profile is as shown in the bore log Fig. 2. The pile cap arrangement with micro-pile is shown in Fig. 3. After referring to site investigation report and vicinity of the G+10 building, conventional foundation was found unfavorable. Therefore, feasibility of micro-pile foundation was examined and found very convenient and suitable. Hence,
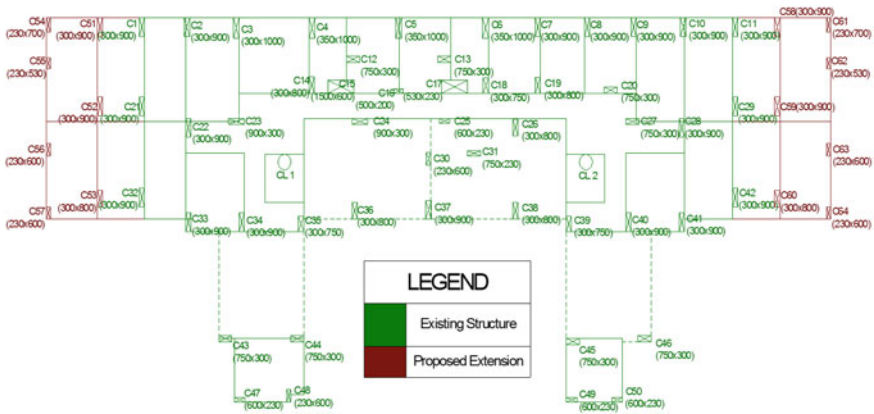

Fig. 1 Layout of proposed extension of existing structure of G+10 building at Chhattisgarh

Type of Boring		Rotary		Job No. : JSPL/SSA/005/14-15
Dia of Hole (mm):		150.00		Bore Hole No.: 03
Depth (M):		0.00-15.00		Co-ordinates :
Commenced on : 28 April 2014		Completed on : 29 April 2014		Ground Bed RL:
Water Struc :		Ground Water : 1.10		Location of Bore Hole :

Description of Strata	Symbol	Thik. (M)	From (M)	To (M)	Sample Depth (M)	Sample Type	Sample Ref. No.	SPT Record 0-150	150-300	300-450	N	Core Rcvry (%)	R.Q.D.	SPT Curve
FILLING MATERIALS		0.00 1.00 2.00 2.90	0.00		1.50	P	SPT-1	12cm in 50 blows, N>50						
FRACTURED ROCK		3.00 4.00												
			4.10		4.00	C	C-1					25.00	0.00	
		5.00			5.50	C	C-2					30.00	0.00	
		6.00 7.00			7.00	C	C-3					40.00	0.00	
		8.00			8.50	C	C-4					42.00	10.00	
SOFT ROCK		9.00 10.00			10.00	C	C-5					44.00	12.00	
		11.00 12.00			11.50	C	C-6					50.00	10.00	
		13.00 14.00			13.00	C	C-7					55.00	18.00	
		15.00		15.00	14.50	C	C-8					60.00	20.00	
					Bore Hole Terminated at : 15.00									

D-Disturbed Sample, U-Undisturbd Sample, P-Standerd Penetration Test, C-Core, W-Water Sample, V-V

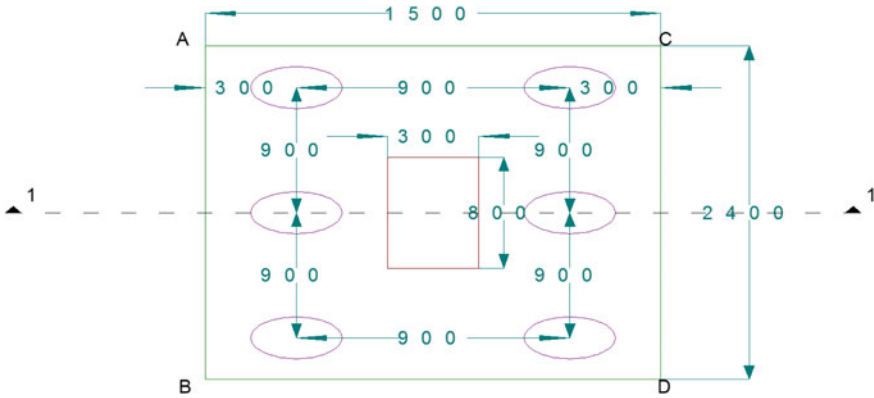**Fig. 2** Bore-log at the site of proposed extension of structure Chhattisgarh

Fig. 3 Micro-pile arrangement at the site of proposed extension of structure

geotechnical aspect of micro-pile was studied, analyzed, and designed in the present study for the structural loads coming on the foundation.

2.1 Geotechnical Calculation

Assessment of vertical load of a single micro-pile based on geotechnical considerations:

- Diameter of pile = 300 mm.
- Multiplication constant for socket length depending on rock strata = 4.
- Socket length = $4 \times 3 = 1.2$ m [2].
- Uniaxial compressive strength of rock = 730 t/m² (as per soil investigation report).
- Depth factor from formula = 1.6 (page 3 of [2]).
- Maximum value of depth factor = 2.
- Actual depth factor = 1.6.
- Area of pile toe = $\pi/4 \times 0.3 \times 0.3 = 0.070686$ m².
- Rock socket slide resistance reduction factor, $\alpha = 0.1$ (From Fig. 1 of [2]).
- Rock socket correction factor, $\beta = 0.4$ (From: Fig. 2 of IS 14593).
- N_j, depending upon the discontinuity in rocks = 0.1 [3].
- Total pile load capacity = 41.28 t.
- Safe load considering neglecting end bearing = 33.02 t.

Assessment of vertical load on micro-pile group based on geotechnical pile capacity:

- Allowable vertical load on pile group = number of piles × vertical load carry capacity of single micro-pile × efficiency factor.

- Vertical load carry capacity of single micro-pile = safe load on single micro-pile = 33 t.
- Minimum center-to-center distance between any two adjacent piles = 3 times diameter of pile = 3 × 0.3 = 0.9 m.
- Group efficiency factor = 1.
- Number of micro-piles in a group = 3, 4, 5, 6, 7, 8

  - 3 group micro-pile group capacity = 3 × 33 × 1 = 99 t
  - 4 group micro-pile group capacity = 4 × 33 × 1 = 132 t
  - 5 group micro-pile group capacity = 5 × 33 × 1 = 165 t
  - 6 group micro-pile group capacity = 6 × 33 × 1 = 198 t
  - 7 group micro-pile group capacity = 7 × 33 × 1 = 231 t
  - 8 group micro-pile group capacity = 8 × 33 × 1 = 264 t.

The ultimate load acting on the foundation was 170 t (based on structural designer) which is less than the ultimate load carrying capacity of six-micro-pile group of 198 t and hence a six-micro-pile group was determined to be sufficient for the column extension. So, future analysis six-micro-pile group is analyzed with Plaxis 3D [4] software.

2.2 Numerical Analysis

It is necessary to review the estimated deflection of the pile under loading conditions and independently check for any geotechnical failure, before it is approved for construction, for this project Plaxis 3D [4] has been used to independently review the design. The model prepared on Plaxis 3D [4] must replicate the physical conditions at the site so that the simulation of the loading conditions give us the expected values of deflection and stresses that will be very close to the actual values that will be observed. For the purpose of this model, a 50 m × 50 m space was considered and a six-micro-pile group was modeled at the center of the space; three layers of the strata were modeled to replicate the conditions at the site namely the top layer (filling material) which was modeled as hardening soil, the intermediate layer (fractured rock) which was modeled as jointed rock, and the bottom layer (soft rock) which was modeled as Hoek–Brown model. The Hoek–Brown failure criterion is an empirical stress surface that is used in rock mechanics to predict the failure of rock, for this model the Hoek–Brown parameters were modeled as uniform basaltic rock which was observed at the site. Table 1 shows the properties of the various layers used in the Plaxis 3D model [4]. The pile was modeled (Fig. 4) as an embedded beam in soil of concrete with properties of M30 grade concrete grout.

Table 1 Properties of the various layers used in the model [1, 4]

Properties	Layers		
	Filling material	Fractured rock	Soft rock
Unit weight saturated (Υ_{sat}) kN/m^3	20	25	26
Unit weight unsaturated (Υ_{unsat}) kN/m^3	17	25	24
Secant stiffness in standard drained triaxial test ($E50^{ref}$) kN/m^2	35×10^3	–	–
Tangent stiffness for primary odometer loading (E_{oed}^{ref}) kN/m^2	35×10^3	–	–
Unloading/reloading stiffness (E_{ur}^{ref}) kN/m^2	105×10^3	–	–
Young's modulus as continuum (E_1) kN/m^2	–	2×10^6	–
Young's modulus (E_{rm}'') kN/m^2	–	–	70×10^6
Young's modulus perpendicular on plane 1 direction (E_2) kN/m^2	–	2×10^6	–
Effective cohesion (C_{ref}') kN/m^2	0	–	–
Effective angle of internal friction (Φ)	33°	–	–
Angle of dilitancy (ψ)	3°	–	–
Drainage type	–	Non-porous	–
Poisson's ratio as continuum (V_1)	–	0.2	–
Poisson's ratio perpendicular on plane 1 direction (V_2)	–	0.2	–
Poisson's ratio (V)	–	–	0.18
Shear modulus perpendicular on plane 1 direction (G_2) kN/m^2	–	833×10^3	–
Uniaxial compressive strength |σ_{ci}| kN/m^2	–	–	7300
Intact rock parameter (M_i)	–	–	25
Geological strength index (GSI)	–	–	80
Disturbance factor (D)	–	–	0
Undrained behavior	–	–	Standard

3 Concluding Remarks

The design of the micro-pile foundation needs to be independently reviewed, and Plaxis 3D was used as a review mechanism. The proposed design was found to achieve the necessary geotechnical capacity without undergoing failure and the deformation of the proposed foundation was found to be 0.06599 mm (Fig. 5) which is very less, accordingly load at which failure occurs corresponding to 12 mm settlement will be much higher than the anticipated load acting on the foundation, hence the proposed designed is deemed safe after the independent review by Plaxis 3D. For the proposed G+10 building, micro-pile was constructed as foundation with 6 bars
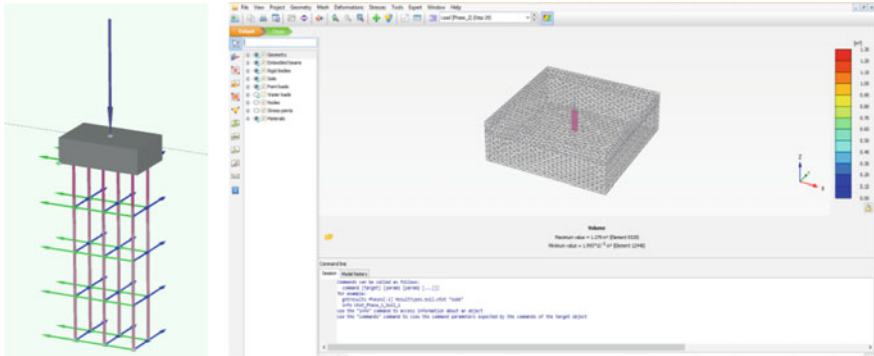
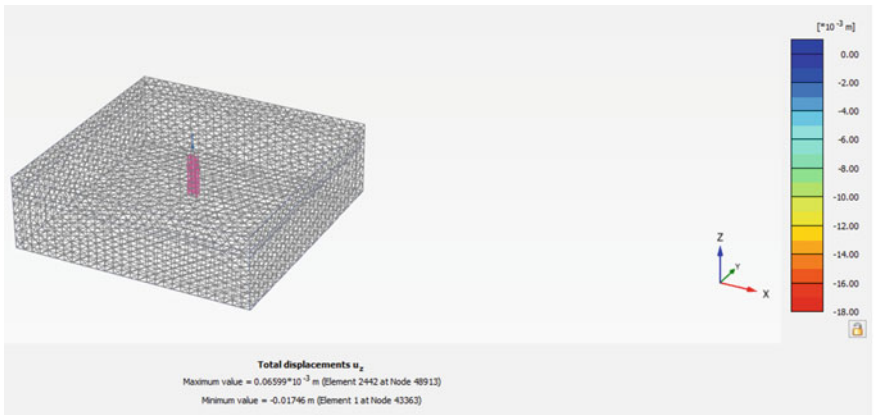**Fig. 4** Model of six-micro-pile group and meshing

Fig. 5 Displacement analysis for six-micro-pile group

of 25 mm diameter and 8 mm stirrups @ 100 c/c specifications (based on design calculation done using [5, 6]).

References

1. Tomlinson, M.J.: Pile Design and Construction Practice, 4th edn. E & FN SPON (1995)
2. IS 14593: Design and construction of bored cast-in-situ piles founded on rocks- Guide-lines (CED 48: Rock Mechanics), 3 (1998)
3. IS 12070: Code of practice for design and construction of shallow foundations on rocks (CED 48: rock mechanics), 6 (1987)
4. Geotechnical Software Suite Plaxis 3D-User's Guide Manual, Version 18 (2016)

5. Bureau of Indian Standards, SP 16, Design aids for reinforced concrete to IS 456456, 47-148-142-171 (1978)
6. IS 456: Plain and reinforced concrete- code of practice (CED2: cement and concrete), 73–94 (2000)

Experimental and Numerical Investigation of Combined Batter Pile–Raft Foundation Embedded in Sand

M. Mahalakshmi, B. Soundara, and C. D. Hashini

Abstract A geotechnical composite foundation system named combined pile–raft foundation (CPRF) is widely used in buildings experiencing colossal loads. Even though raft foundation reduces differential settlement, it tends to cause excessive settlement which can be subsided by using piles. Batter piles are deliberately known for their lateral resistance compared to plumb. The response of CPRF with batter pile under horizontal loading needs enhanced studies. This research focusses on the parametric configuration of combined batter pile–raft foundation embedded in sand. The effect of direction of batter and the angle of batter is studied experimentally under constant relative density. For experimental investigation, model test tank was used and 2×1 solid steel piled raft model was fabricated and used. The basic parametric configuration chosen for the combined batter pile–raft foundation is *L/D*—20, *S/D*—3 and diameter of pile and thickness of the raft was taken as 10 mm. The model is numerically simulated in a comprehensive three-dimensional finite element software ANSYS. The results of the experimental investigation and the numerical simulation are compared. The efficient direction of batter was found to be negative and was carried over for the further studies. The angle of batter taken for the study was 10°, 15°, 20°, 25° and 30° in-battered. The optimum batter angle was found to be in the range from 15° to 20° in-battered. The results from the numerical investigations were found to be in accordance with the experimental results.

Keywords Combined pile–raft foundation · Batter pile · Model test tank · Sand · ANSYS

M. Mahalakshmi (✉) · B. Soundara · C. D. Hashini
Department of Civil Engineering, Bannari Amman Institute of Technology, Sathyamangalam, India
e-mail: mahalakshmice@gmail.com

1   Introduction

The emerging need to accommodate high rise buildings on the problematic ground conditions has drawn a major attention on deep foundation and the one which proves to be significant in such situation is combined pile–raft foundation. CPRF consists of two elements, namely a raft and pile, where the raft acts as a load sharing element and the pile as the settlement reducer. Batter piles are often used in places where they are subjected to lateral and inclined forces such as earthquake, wave currents, off shore structures etc. In this study, an attempt has been made to study the effect of lateral load on the combined pile–raft foundation containing batter pile. Reese [1] developed *p-y* curves for analysis of vertical piles in sand under lateral loads and suggested that the same can be employed for the behaviour prediction of batter pile also. The guidelines for lateral response prediction of fixed head and free head piles were provided by Pise [2, 3]. Chae et al. [4] provided validation for the experimental data using 3D finite element method (FEM) for the lateral resistance of short piles and pile groups located near slopes. The response of piles and pile group by displacement method was analysed by Martin and Chen [5] using FLAC 3D and proposed that the same method can be employed to pile foundation design which undergoes lateral soil movement, and Chen [6] conducted model analysis on the response of batter piles to lateral soil movement using FLAC 3D and inferred that the batter piles experience lesser displacement compared to vertical piles. The resistance mechanism of pile foundations having batter piles has been studied by Vu and Matsumoto [7] by conducting model experiment in sand and stated that the resistance increase was much observed in piled raft having batter piles. Escoffier [8] conducted centrifuge tests on raked piles and noted that the batter pile in pile group induces an increase in the bending moment at the pile cap and axial load at the rear pile compared to the front. Hazzar [9] carried out 3D finite difference parametric analyses on the lateral performance of battered piles in sand and clay and stated that the lateral response is influenced by the batter angle and direction of pile inclination. The lateral resistance of the battered pile groups in the presence of vertical dead load was discussed by Zhang [10] and account that it depends on the pile arrangement, inclination and soil density. The optimum batter angle of 20° was found by Al-Neami [11] when the effect of different batter angle on different relative densities of sand has been studied. Bharathi and Dubey [12] presented the insignificant lateral behaviour of under reamed batter piles. In this paper, the effect of horizontal loading on 2 × 1 combined batter pile–raft is studied experimentally and the same has been numerically analysed using ANSYS software to simulate the response of the system under lateral loading.

2   Experimental Setup and Test Program

The experiment was carried out in a model steel test tank placed under a loading frame supported by four hot rolled steel columns. An automized lateral loading jack

Table 1 Properties of sand

Property	Unit	Value
Specific gravity (G_s)	–	2.77
Young's modulus (E)	kN/m^2	40,000
Poisson's ratio (v)	(no unit)	0.15
Mass density (γ)	kN/m^3	16.3
Angle of internal friction (ϕ)	–	20°
Dilatancy angle (ψ)	–	0°
Cohesion (c)	kN/m^2	10.79

was harnessed on the side columns. The model tank was made as deep as two times the length of the piles in order to avoid stress concentration at the rigid base as stated by Randolph [13] and on the side surface as well. This is done to avoid the influence of boundary on the behaviour and response of the CPRF. The combined piled raft of 2×1 containing batter pile was modelled as solid steel pile having an angle of 10°, 15°, 20°, 25° and 30° and length as 200 mm. The pile diameter was taken as 10 mm, and series of piled raft models were fabricated with a constant thickness of raft as 10 mm. Since the thickness of raft does not make any consequential effect on the response of pile–raft as stated by Oh et al. [14], a constant thickness of 10 mm has been adopted throughout the study. Short or rigid piles behave partially plastic and partially elastic, whereas long or slender piles behave completely as plastic; hence, an optimum *L/D* of 20 was taken for this study.

The sand bed was prepared by filling the tank with sand using rainfall technique by maintaining height of fall as 400 mm in order to achieve a constant relative density of 60%. The sand used for the experimental purpose was collected from the Kodivei River Bank flowing through Sathyamangalam at 11.4731° N and 77.2966° E. Test was done to determine the properties like particle size distribution, specific gravity, density, etc., and the values have been listed in Table 1. The values listed in the table include parameters for the finite element modelling using ANSYS.

Experiments were conducted by varying the batter angle while the direction of batter was kept fixed, i.e. negative batter throughout the test since the experimental results of Albusoda and Alsaddi [15] and Maharaj et al. [16] proved that the negative batter has higher lateral load carrying capacity. Numerical simulation was carried out to prove the negative batter resistance to lateral load. The lateral load was applied gradually in incremental manner on the pile–raft using hydraulic jack. The deflection was measured at the raft top using linear variable differential transformer.

Fig. 1 Effect of direction of
batter
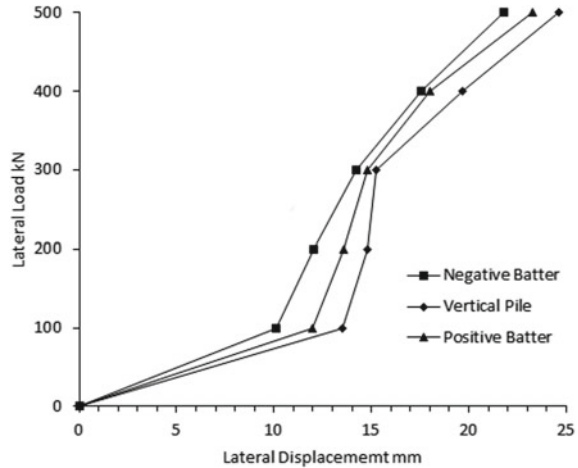
3 Results and Discussion

3.1 Direction of Batter

The effect of direction of batter was numerically simulated. The direction of batter was taken as negative, i.e. in-battered, since the in-battered piles proved to be more significant in the lateral load carrying capacity. The improved resistance to lateral loads is because the loads transferred are tensile in nature compared to the positive batter which transfers loads compressively. The load displacement curve for the numerically simulated in-battered, vertical and out-battered piles is shown in Fig. 1.

3.2 Batter Angle

The combined batter pile–raft with batter angle of 10°, 15°, 20°, 25° and 30° was investigated both experimentally and numerically. It was observed that at a particular angle the lateral stability of combined batter pile–raft system is found to be maximum because a large peripheral surface of the pile encounters the lateral load as compared to other batter angle. The system with batter angle of 15° to 20° was seen to perform well under lateral loading and was considered to be the optimum batter angle. The load displacement curve for the different batter angle which was experimentally investigated is shown in Fig. 2. To verify the experimental values, numerical simulation was done using ANSYS for varying batter angle and it was found to be in accordance with the experimental value and the load displacement curve is shown in Fig. 3.
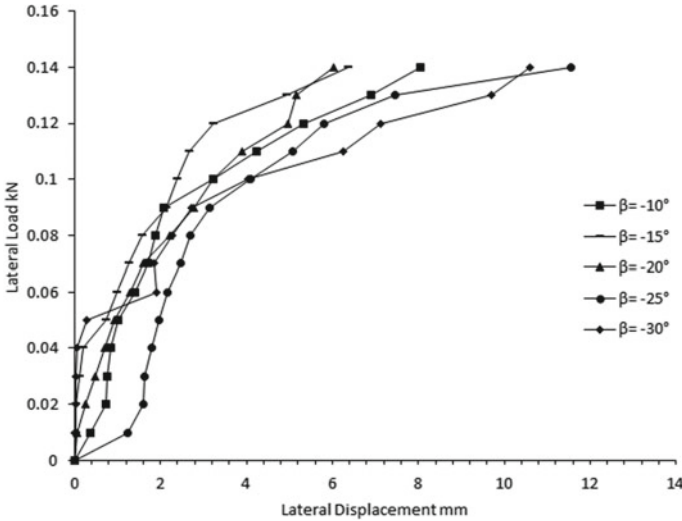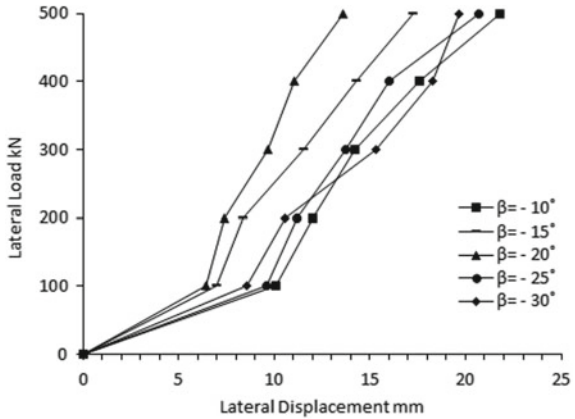
Fig. 2 Experimental result of batter angle

Fig. 3 Numerical simulation result of batter angle

3.3 Comparison Between Experimental Result and Numerical Result

The lateral load and displacement curve for the experimental and numerical results have been shown in Figs. 4 and 5 for an optimum batter angle of 20°.

By comparing the above graph, we can infer that the experimental inadequacy in lateral load application along with measurement of parameters and theoretical assumptions existing in the numerical analysis of ANSYS software might have caused a constant shift in graphical relation of lateral displacement and lateral loads.

Fig. 4 Experimental
displacement curve for 20°
batter angle
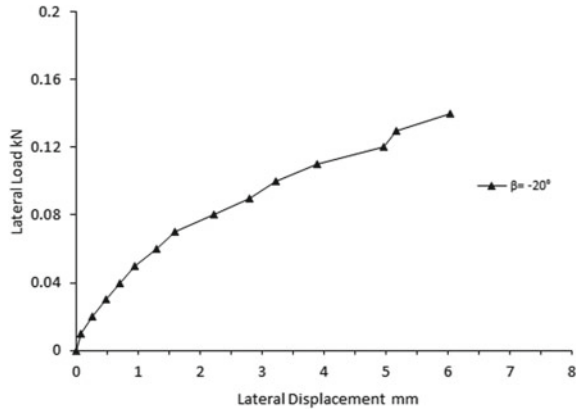
Fig. 5 Numerical
simulation displacement
curve for 20° batter angle
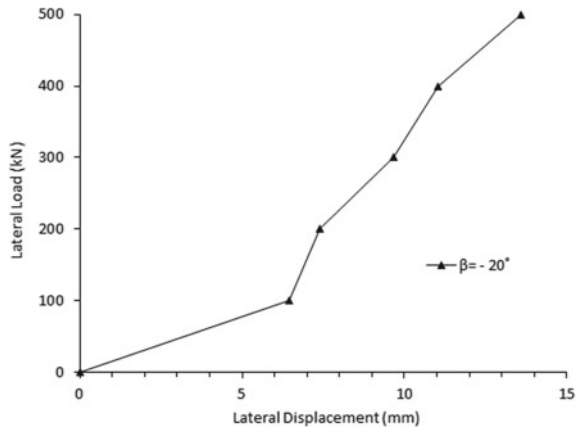
4   Conclusions

The effect of lateral loading on combined batter pile–raft foundation has been studied
in this paper. The following are the conclusions drawn from the experiment and
numerical analysis.

1.   The efficient direction of batter to resist lateral loading is negative battered piles
     compared to vertical and positive battered piles.
2.   The optimum batter angle was found out to be 20° in-battered based on the
     lateral load carrying capacity compared to the other batter angle.
3.   The numerical analysis of combined batter pile–raft shows a similar effect on
     the lateral loading from the experimental test.

References

1. Reese, L.C., Cox, W.R., Koop, F.D., Lawrence–Allison & Associates: Analysis of laterally loaded piles in sand. In: Sixth Annual Offshore Technology Conference, pp. 473–483 (1984)
2. Prabhakar, J.: Pise: lateral response of fixed-head pile. J. Geotech. Eng. ASCE **109**(8), 1126–1131 (1983)
3. Prabhakar, J.: Pise: lateral response of free-head pile. J. Geotech. Eng. ASCE **110**(12), 1805–1809 (1984)
4. Chae, K.S., Ugai, K., Wakai, A.: Lateral resistance of short single piles and pile groups located near slopes. Int. J. Geomech. ASCE **4**(2), 93–103 (2004)
5. Martin, G.R., Chen, C.-Y.: Response of piles due to lateral slope movement. Comput. Struct. **83**, 588–598 (2005)
6. Chen, C.Y., Hsu, H.Q.: Modeling of batter pile behavior under lateral soil movement. In: 2nd International Conference on Civil Engineering and Materials Science 2017, Materials Science and Engineering 216, 012039. IOP Publishing (2017). https://doi.org/10.1088/1757-899X/216/1/012039
7. Vu, A.-T., Matsumoto, T.: Experimental study on pile foundations having batter piles subjected to combination of vertical and horizontal at 1-g. Geotech. Eng. J. SEAGS AGSSEA **48**(3) (2017). ISSN 0046-5828
8. Escoffier, S., Chazelas, J.-L., Garnier, J.: Centrifuge modelling of raked piles. Bull. Earthquake Eng. 689–704 (2008). https://doi.org/10.1007/s10518-008-9094-1
9. Hazzar, L., Hussien, M.N., Karray, M.: Numerical investigation of the lateral response of battered pile foundations. Int. J. Geotech. Eng. (2016). https://doi.org/10.1080/19386362.2016.1224030
10. Zhang, L.M., McVay, M.C., Han, S.J., Lai, P.W., Gardner, R.: Effect of dead loads on the lateral response of battered pile groups. Can. Geotech. J. 561–575. https://doi.org/10.1139/T02-008
11. Al-Neami, M.A., Rahil, F.H., Al-Bayati, K.S.: Bearing capacity of batter piles embedded in sandy soil. Int. J. Geotech. Eng. (2016). https://doi.org/10.1080/19386362.2016.1203094
12. Bharathi, M., Dubey, R.N.: Dynamic lateral response of under-reamed vertical and batter piles. Constr. Build. Mater. **158**, 910–920 (2018)
13. Randolph, M.F.: Design methods for pile groups and piled rafts. In: Proceedings of 13th International Conference on Soil Mechanics and Foundation Engineering, pp. 61–82 (1994)
14. Oh, E.Y.N., Huang, M., Surrak, C., Adame, R., Balasubramaniam, A.S.: Finite element modelling for piled raft foundation in sand. In: Eleventh East Asia-Pacific Conference on Structural Engineering & Construction (EASEC-11), Building Sustainable Environment, pp. 1–8. Taiwan (2008)
15. Albusoda, B.S., Alsaddi, A.F.: Experimental study on performance of laterally loaded plumb and battered piles in layered sand. J. Eng. **9**(23) (2017)
16. Maharaj, D.K., Kumar, D., Gill, S.: Comparison of vertical and battered piles subjected to lateral loads. In: Conference on Recent Innovations in Emerging Technology & Science 2018. ISSN: 2320-2882

An Analytical Parametric Study on Behaviour of Flexible Raft Foundation

Pritam Sinha, Ram Wanare, Parishi Dalal, and Kannan K. R. Iyer

Abstract The understanding of soil–foundation–structure interaction is important for design of flexible raft foundation. For flexible foundation, the behaviour would be influenced by the loading as well as the foundation and soil parameters. The present study attempts to understand the influence of the parameters such as meshing size, loading intensity, magnitude of modulus of subgrade reaction (K_s) and raft thickness on base pressure and settlement of flexible raft foundation using STAAD Pro. A symmetrical multi-storeyed building with 25 columns along with raft foundation has been modelled. The building height is varied as 3-storeyed, 6-storeyed and 10-storeyed to simulate different loading intensity and raft thickness is varied as 0.5 and 0.9 m to understand effect of raft rigidity. K_s values of 2000 and 12,000 kN/m^3 have been considered for the study. Study concludes that 0.5 m mesh size can be utilized for practical foundation modelling purposes. The effect of K_s on base pressure and settlement variation is more prominent as compared to thickness of raft foundation. Further, the base pressure and settlement increase linearly with increase in storey height. The study presents useful guidelines for the foundation engineers for design of flexible raft foundation.

Keywords Flexible raft · Foundation · Soil–structure interaction · Base pressure · Settlement

P. Sinha · R. Wanare · P. Dalal · K. K. R. Iyer (✉)
Department of Civil Engineering, Institute of Infrastructure, Technology, Research and Management, Ahmedabad 380026, India
e-mail: kannaniyer@iitram.ac.in

P. Sinha
e-mail: pritam.sinha.17mc@iitram.ac.in

R. Wanare
e-mail: ram.wanare.19pc@iitram.ac.in

P. Dalal
e-mail: parishi.dalal.18mc@iitram.ac.in

365

1   Introduction

1.1   Soil–Structure Interaction

Behaviour of structure and its foundation depends on soil and the response of soil to pressure experienced from foundation. Hence, understanding the soil–structure interaction (SSI) becomes important for proper and optimum design of foundation. Soil–structure interaction can be understood by defining the appropriate value of modulus of subgrade reaction, which can be defined as the foundation pressure required to cause unit settlement of soil [11]. Soil–structure interaction begins at the initial phase of construction and equilibrium depending on the variable factors can be achieved after some period. Winkler (1867) was the first researcher to address the parameter, modulus of subgrade reaction (K_s), which is an important parameter for soil–structure interaction studies [11]. It has also been stated that soil can be represented as infinite number of springs at the interface between soil and foundation, and the stiffness of the spring can be defined as K_s. Terzaghi [11] has presented a detailed review of modulus of subgrade reaction, K_s which represents deformation characteristics and depends on loaded area which follows Hooks law. According to Larkela et al. [9], K_s is influenced by pseudo-elastic property and it is not a fundamental property of soil. Also, it depends on elastic properties of soil, foundation dimensions, stiffness of foundation and other factors such as depth of foundation below ground surface, and compressible soil layer thickness [1, 10].

Horvath [6] assumed that modulus of elasticity (E) is not constant throughout the depth but it varies, hence affecting K_s. Although K_s has been noted to have less effect in the structural design of foundation, it has an immense effect on the contact pressure distribution and settlement, hence affects the foundation base area. Incidentally K_s is also dependent on the dimensions of the foundation [11]. Eimarakbi and Budkowska [5] reported that K_s obtained for pile foundation by static method has considerable amount of inaccuracy due to discrete modelling based on Winkler approach and highlighted the dependency of K_s on pile width. K_s directly affects the settlement of the foundation, and the settlement distribution depends on other factors such as rigidity of foundation, loading intensity and location and relative stiffness of foundation and soil. As per Briaud [3], modulus of subgrade reaction (K_s) is closely related to the soil properties and degree of compaction. A densely packed soil has high K_s; however, it also depends on the porosity and dry density. Soil with same dry density but different microstructure will have different values of K_s. In fine-grained soil, less water content works as a binder (adhesion) due to suction forces and this adhesion will increase K_s as it develops adhesion effect due to capillary induced suction. But for coarse grained soil K_s increases with increasing water content till a specific limit [3]. The stress history of soil also affects K_s and it has been reported that over consolidated soil has higher K_s than the normally consolidated soil. K_s is inversely proportional to strain level in soil, and higher strain rate enhances the stiffness of the soil hence resulting in higher K_s. For cohesionless soil, K_s has been reported to increase with increase in confining pressure as the soil depth increases.

Barounis et al. [2] used unconfined compression test (UCS) to evaluate K_s and it has been noted that the value of K_s evaluated from this test is very less due to the absence of the confining pressure.

Worku [12] based on their study have reported that Winkler's model, based on the assumption that soil which is represented by springs of certain stiffness below the loaded area is inappropriate, but this approximation can be overcome by appropriate calculation of shear stress of the sub-grade soil. Aristorenas and Gomez [1] have noted that K_s is not a soil property but the contact pressure of foundation which causes deflection in the soil. It depends on elastic properties of soil such as elastic modulus of soil (E_s) and Poisson ratio (ν_s), foundation plan dimensions, foundation stiffness and other indirect factors like depth of foundation below ground surface and compressible soil layer thickness. The various factors affecting modulus of subgrade reaction (K_s) as per Briaud [3] and Dey et al. [4] are packing density and particle arrangement; water content; stress history; confining effect; cyclic loading; type and rigidity of foundation. Although earlier studies have attempted to understand the influence of various factors on modulus of subgrade reaction (K_s), their influence on foundation design parameters such as base pressure and settlement needs further studies. The present study attempts to address these aspects.

1.2 Finite Element Analysis of Foundation Using STAAD Pro.

Present study attempts to understand the effect of various factors such as rigidity of foundation, variation in loading intensity and variation in magnitude of modulus of subgrade reaction, K_s, below foundation. Although the soil is a continuum under the structure but is a reasonable assumption to consider soil as discrete springs supporting the foundation based on Winkler's hypothesis. STAAD Pro V8i (a popular software for soil–structure interaction studies) is utilized in the study for finite element analysis of foundation. Soil can be represented as spring with stiffness defined as per the value of K_s in STAAD Pro. In this study, 12 design alternatives have been studied based on variation of parameters such as mesh size of foundation elements modelled (0.25 m, 0.5 m and 1 m mesh size), loading intensity (3-storey, 6-storey and 10-storeyed building loading), K_s values (2000 and 12,000 kN/m^3) and foundation thickness (0.5 and 0.9 m). The different foundation design parameters such as base pressure and settlement has been obtained and compared for these alternatives. When a foundation is designed as flexible foundation, it is usually acceptable to utilize Winkler's model of representing soil as discrete spring below foundation. In STAAD Pro., the continuity of foundation below the soil springs helps in distribution of load to the springs as per the relative stiffness of raft and spring (soil). Hence, the approach used in STAAD Pro. can be considered as modified Winkler approach. In present study, a multi-storey building design has been adopted and plate elements (element suitable for flexible foundation) have been used to model raft foundation in STAAD
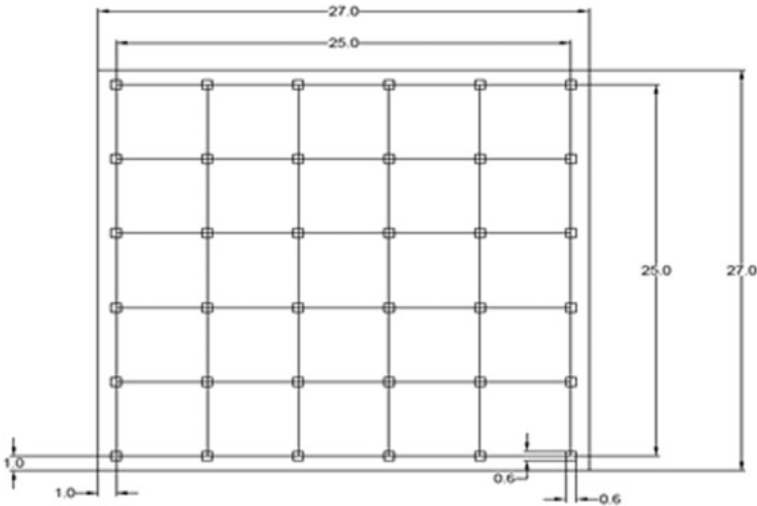
Fig. 1 Plan view of the building and foundation (All dimensions are in metres)

Pro. The supports have been assigned with vertical spring stiffness values in the model. Vertical loads (dead load and live load) on the building were applied as per IS: 875 Part-I [7]. For simplicity, only vertical loads have been considered in the study. The details of the model and the analysis procedure are briefly discussed in this section. Multi-storeyed building (with 5 bays in each direction, 5 m c/c column spacing and 4 m height of each storey) is modelled along with raft foundation. In dead load, the self-weight of all the members is taken as per IS-875 Part-I [7], and the wall load of 20 kN/m as per IS 875 part-I is taken. Building is assumed to be institutional building, and the live load of 4 kN/m^2 is considered as per IS-875 Part-II [8]. Three different mesh sizes of plate element used to model foundation raft have been studied, viz. 0.25 m, 0.5 m and 1 m, to study the effect of mesh size on the foundation base pressure and settlement.

Different alternatives have been generated in STAAD Pro. by varying mesh size, intensity of loading (height of building), values of K_s and thickness of foundation as discussed above. Figures 1, 2 and 3 show the plan view, section view and three-dimensional view of the building with raft foundation.

2 Results from Finite Element Analysis of Foundation in STAAD Pro.

As per the discussed methodology, the analysis of different models were performed in STAAD Pro. Total 12 alternatives were studied with varying mesh size, raft thickness, loading intensity and K_s values. The result obtained in terms of base pressure, total
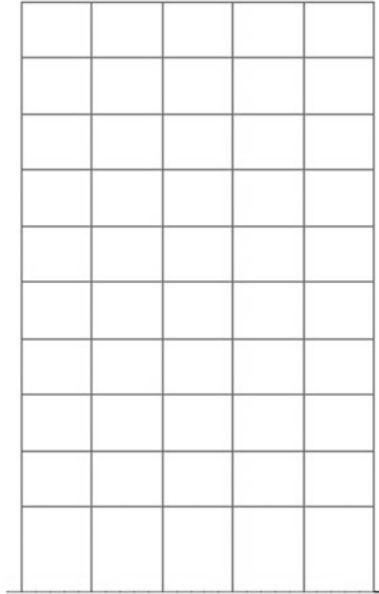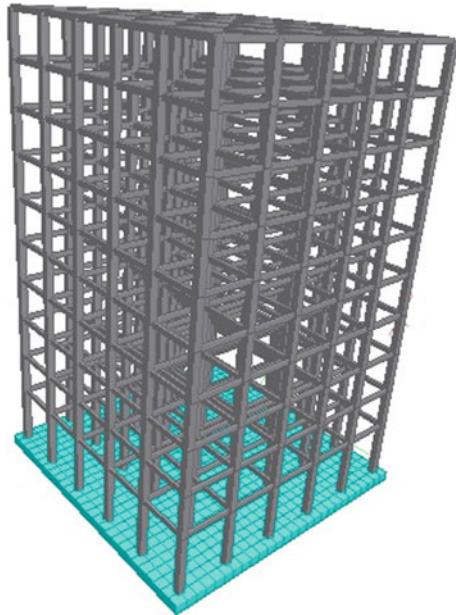
Fig. 2 Section view of model

Fig. 3 Three-dimensional view of 10-storeyed building

settlement and differential settlement is presented in graphical manner and discussed below.

Figures 4 and 5 present the maximum and minimum values of base pressure and settlement, respectively for different cases. Figure 6 presents the variation of differential settlement for different cases. From Fig. 4, it can be observed that the variation in base pressure reduces with increase in mesh size. Further, it can be observed that difference in base pressure is relatively less for mesh size of 0.25 and 0.5 m as compared to 0.5 and 1 m. From Figs. 5 and 6, it can be observed that the total and differential settlement (difference between maximum and minimum settlement within raft foundation) is not affected much by mesh size. It is usually accepted fact that finer mesh size leads to more refinement of results. Hence, for all practical purposes, to achieve accurate results and reduce time of analysis for complex problems, it is recommended to use mesh size of 0.5 m. From Fig. 4, it can also be observed that for $K_s = 12{,}000 \ \mathrm{kN/m^3}$ and raft thickness of 0.5 m, the variation
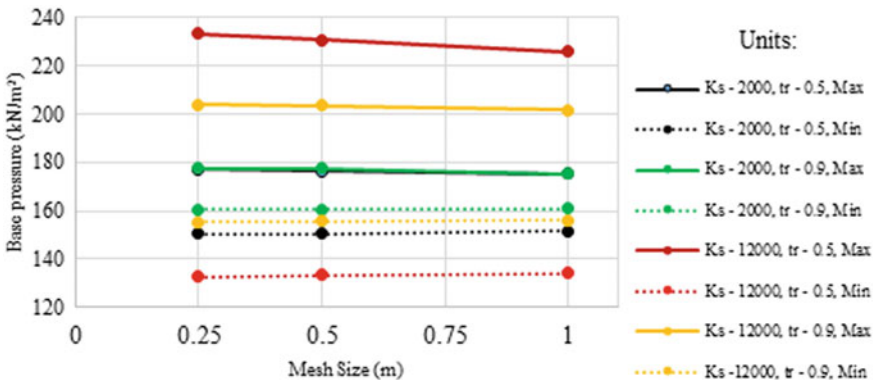
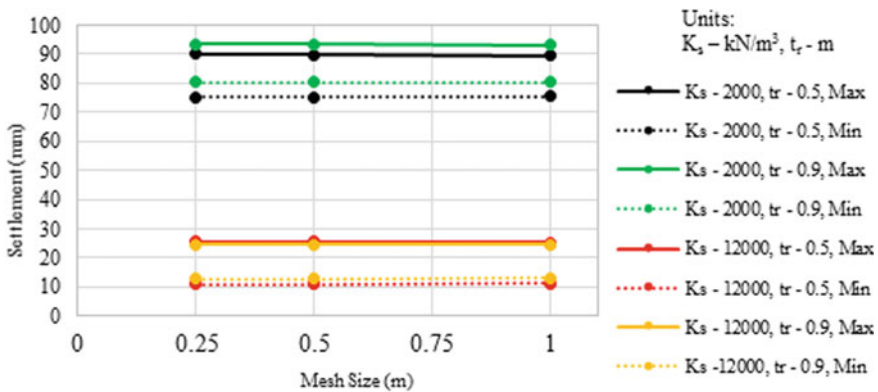**Fig. 4** Variation of maximum and minimum base pressure with mesh size
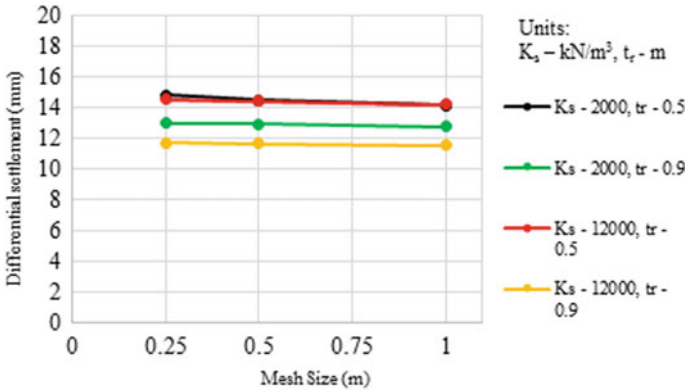

Fig. 5 Variation of settlement with mesh size

Fig. 6 Variation of differential settlement with mesh size

in base pressure is maximum; whereas for $K_s = 2000$ kN/m^3 and raft thickness of 0.9 m, the variation in base pressure is minimum. Further, from Figs. 5 and 6, it can be noted that as expected, the total and differential settlement is lower for higher values of K_s. The effect of K_s on base pressure and settlement variation is more prominent as compared to the effect of raft thickness.

Figure 7 presents the maximum and minimum base pressure for different intensity of loading (viz. 3-storey building, 6-storey building and 10-storey building). It can be seen that base pressure increases linearly with increase in intensity of loading. The
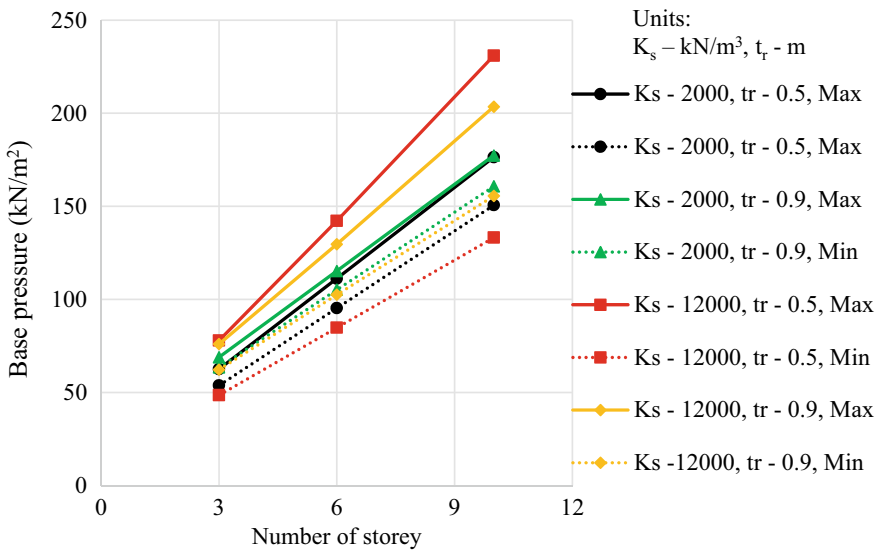

Fig. 7 Variation of base pressure with storey height for uniform distribution of K_s

variation in maximum and minimum base pressure is highest for $K_s = 12,000\,\text{kN/m}^3$ and 0.5 m foundation thickness and lowest for $K_s = 2000\,\text{kN/m}^3$ and 0.9 m foundation thickness. Hence, foundation with higher thickness on relatively less stiff soil results in more uniform base pressure distribution. From Figs. 8 and 9, it can be inferred that settlement as well as differential settlement increases with increase in loading. Further, it can be inferred that the differential settlement for thicker foundation (0.9 m) and stiffer soil ($K_s = 12,000\,\text{kN/m}^3$) is lowest as compared to other cases.
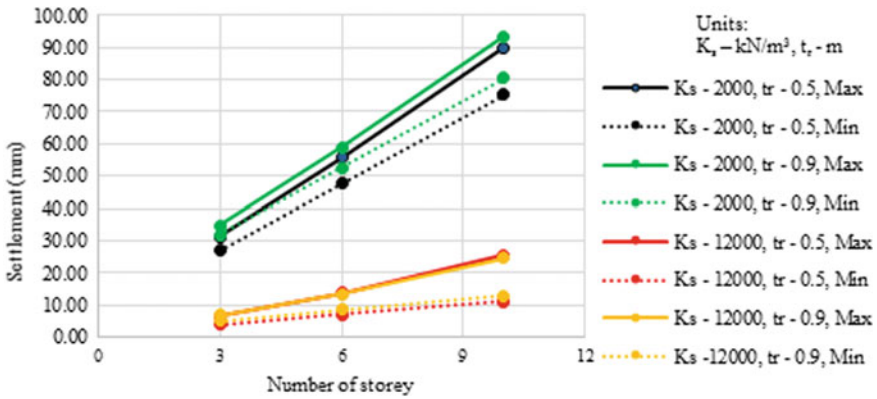

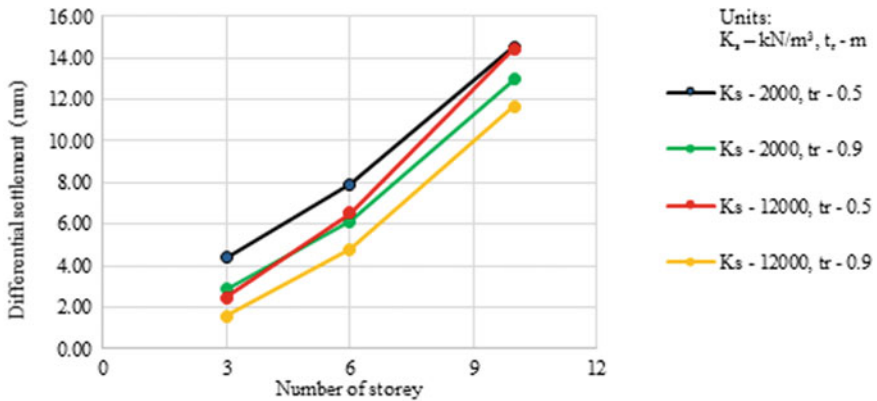**Fig. 8** Variation of settlement with storey height

Fig. 9 Variation of differential settlement with storey height for uniform distribution of K_s

3 Conclusions

The present study evaluated the variation of base pressure, total as well as differential settlement for different foundation mesh size, intensity of loading, K_s values and raft thickness. The following conclusions can be drawn from the study:

1. It can be observed from the study that the variation in base pressure and differential settlement within foundation reduces with increase in mesh size. Further, it can be observed that difference in base pressure is relatively less for mesh size of 0.25 and 0.5 m. For practical purposes, to achieve accurate results and reduce time of analysis, it is recommended to use mesh size of 0.5 m for STAAD Pro. analysis.

2. The base pressure variation for 0.5 m thick foundation on stiff soil ($K_s = 12,000$ kN/m^3) is maximum (40–44% for different mesh sizes), whereas base pressure variation for 0.9 m thick foundation on soft soil ($K_s = 12,000$ kN/m^3) is minimum (8–10% for different mesh sizes). Hence, the relative stiffness of soil–foundation system has significant effect on base pressure variation within the foundation area.

3. The total and differential settlement (viz. difference between maximum and minimum settlement in mm) is minimum for higher values of K_s (12,000 kN/m^3) and higher value of foundation thickness (0.9 m). The differential settlement is maximum for lower foundation thickness (for both $K_s = 2000$ kN/m^3 and $K_s = 12,000$ kN/m^3). However, percentage of differential settlement (viz. percentage difference between maximum and minimum settlement) is observed to be higher for case with higher K_s (12,000 kN/m^3) and lower foundation thickness (0.5 m). Similarly, percentage differential settlement is lower for $K_s = 2000$ kN/m^3 (for foundation thickness 0.5 and 0.9 m). The effect of K_s on base pressure and settlement variation is more prominent as compared to the effect of raft thickness.

4. It can be concluded that base pressure increases with increase in loading. Further, settlement as well as differential settlement increases with increase in loading.

References

1. Aristorenas, G., Gomez, J.: Subgrade Modulus—Revisited. STRUCTURE Magazine (2014)
2. Barounis, N., Orr, T.L.L., McMahon, P.H., Barounis, A.: Modulus of subgrade reaction for foundations on clay from unconfined compression tests. In: 17th International Conference on Soil Mechanics and Geotechnical Engineering (2009)
3. Briaud, J.L.:, Introduction to Soil Moduli, Geotechnical News. BiTech Publishers Ltd, Richmond, B.C., Canada (2001)
4. Dey, A., Basudhar, P.K., Chandra, S.: Distribution of subgrade modulus beneath beams on reinforced elastic foundations. Indian Geotech. J. **41**(2), 54–63 (2011)
5. Eimarakbi, A.M., Budkowska, B.B.: Assessment of modulus of subgrade reaction of sand-sensitivity analysis (2001)

6. Horvath, J.S.: Modulus of subgrade reaction: new perspective. J. Geotech. Eng. **109**, 1591–1596 (1983)
7. IS 875 Part I (1987): Code of Practice for Design Loads (Other than Earthquake) for Buildings and Structures. Part 1: Dead Loads. Bureau of Indian Standards, New Delhi
8. IS 875 Part II (1987): Code of Practice for Design Loads (Other than Earthquake) for Buildings and Structures. Part 2: Imposed Loads. Bureau of Indian Standards, New Delhi
9. Larkela, A., Mengelt, M., Stapelfeldt, T.: Determination of distribution of modulus of subgrade reaction. In: International Conference on Soil Mechanics and Geotechnical Engineering, Paris (2013)
10. Teli, S., Kundhani, P., Choksi, V., Sinha, P., Iyer, K.R.: Analytical study on influence of rigidity of foundation and modulus of subgrade reaction on behaviour of raft foundation. In: International Symposium of International Association for Computer Methods and Advances in Geomechanics (IACMAG), March 2019, IIT Gandhinagar (2019)
11. Terzaghi, K.: Evaluation of coefficients of subgrade reaction. Geotechnique **5**(4), 41–50 (1955)
12. Worku, A.: Winkler's single-parameter subgrade model from the perspective of an improved approach of continuum-based subgrade modeling. J. EEA **26** (2009)

A Case on Engineered Solution for Deep Excavation in Restricted Space

Ajitkumar Kumbhar, Rajay Balwan, and Girish Gokhale

Abstract This paper discusses the methodology adopted in soil support for deep excavation carried out for installation of press foundation in live working mechanical shop with space restriction and variable soil conditions. The method adopted was the cheapest of available alternatives.

Keywords Soil · Stability · Grouting · Excavation · Foundation

1 Introduction

1.1 Plant and Work Description

Mahindra Vehicle Manufacturers Ltd. has its vehicle manufacturing facility located at Chaken near Pune. The manufacturing facility is spread over 700 acre land with number of manufacturing shops and other facilities.

The existing press shop facility was constructed and put to operation in the year 2010 with four press installed at a place. A press is a heavy and huge automatic equipment which gives the required shape to automotive body components and forms an important function in the automobile manufacturing process. Subsequently, under expansion program, another press was proposed to be installed in the existing facility. The existing facility with one press (press no. 1) has numerous activities going on

A. Kumbhar (✉)
Mahindra Vehicle Manufacturers Ltd. Chakan, Pune, India
e-mail: kumbhar.ajitkumar@mahindra.com

R. Balwan
Government Polytechnic, Kolhapur, India
e-mail: rajay64@gmail.com

G. Gokhale
Indospace, Pune, India
e-mail: girish.gokhale@indospace.in

with variable heavyweight dyes, storages and conveyance equipments all around it
which serve as paraphernalia (see Fig. 1).

The challenge was placed before Mahindra Civil Engineers to install another press
(new press) in limited space of 16 m × 16 m available for press foundation raft of
size 11.5 m × 11.5 m to be placed at about 12.50 m depth below existing floor level.
The challenge was twofold, firstly to excavate safely to required depth (about 10 m
deep in filled up ground and another 2.5 m in virgin ground), and secondly, without
interrupting manufacturing process with overhead crane in operation in the area. The
area is continuously subjected to vibration from adjacent press. Dies were also stored
around area to be excavated. Above all, work had to be completed in stipulated time
period of 60 days.

1.2 Soil Condition

The area where the new press foundation was proposed to be installed was made
up ground with murum and boulders. Only top about 1.5 m was compacted. But, it

was not known before as to what extent compaction is done. A loose material with boulders has tendency to slide more easily and very prone to caving (see Fig. 2).

Grain size analysis for a soil sample (depth 0.6 m) worked out and presented in Table 1 and Fig. 3.

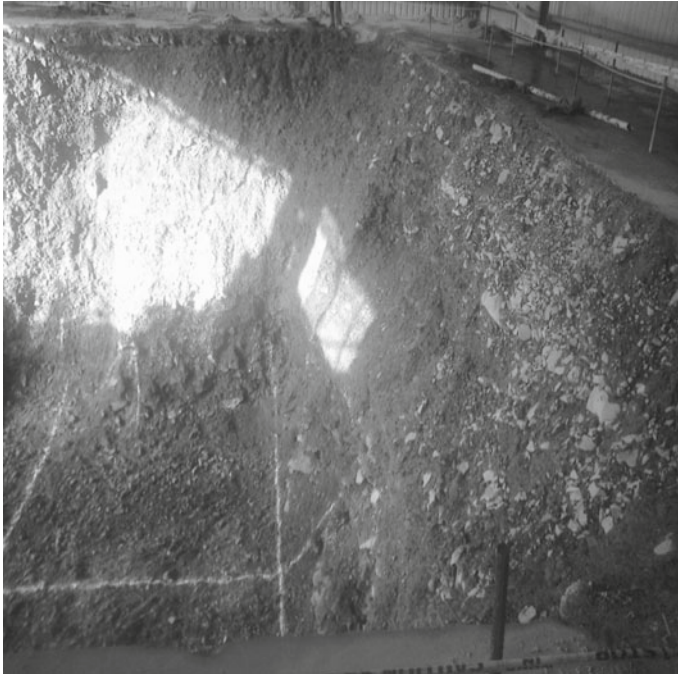Groutability ratio (penetrability of cement in in-situ soil) = 29.91 > 25.

Fig. 2 Soil condition

Table 1 Grain size analysis

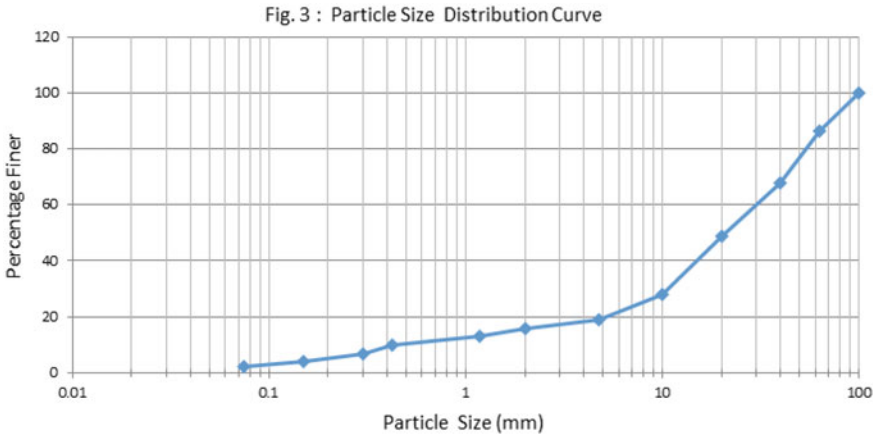| Fraction	Content (%)
Gravel (coarse and fine)	81.00
Sand (coarse, medium and fine)	17.00
Silt and clay	02.00

Fig. 3 Grain size distribution curve

2 Soil Support Methods

2.1 Excavation Without Support

This method consists of excavating pit with sloping sides which the material can stand with and without berm at intermediate level. With side slope of 1V:1.5H, the top size works out to be 47.5 m × 47.5 m at floor level. This option was ruled out due to space constrain and possibility of caving in of side slopes (available space 16 m × 16 m at floor level).

2.2 Excavation by Retaining Soil by Piles

In this option, the first choice was to drive steel piles. Since, soil strata consisted of murum with boulders, driving was not feasible. Therefore, the other option available was to go for bored cast in situ concrete piles. It was decided to provide 600 mm diameter concrete piles in a row along three sides. The fourth side left for access for excavator and for removal of excavated material. Considering 3 m wide working space around 11.5 m^2 area, the plan size required is 21 m × 21 m.

This option again was not attractive due to non-availability of working space for drilling, time required for drilling and casting piles and more cost involved.

2.3 Stabilizing Soil Strata by Grouting

Initially, it was thought to stabilize strata by injection grouting of cement slurry via drilled holes by inserting perforated pipes. Three parallel rows of drill hole were planned. Then, it excavates progressively. Additionally, the excavated surface could be protected by applying mortar. The grout will flow in to void spaces to bind loose particles together, so that grouted portion will act as composite wall which will retain back material.

The area above shear failure plane is unstable. Factor of safety worked out for soil mass will be 0.54 which is unsafe. It is practically not possible to go for any type of open excavation. The unstable soil mass needs to be strengthened and self-supporting too.

In this unstable soil mass, inter-connecting particle bonding was increased by grouting cement slurry in different proportion. The said soil mass was reinforced by providing 32 mm diameter steel reinforcement bars. Thus, the addressed instability of soil mass above shear failure plane, which was retained excavation side nearly in vertical position.

This option looked attractive for the following reasons. One is that it could be done in limited available space, secondly possibility of completing work in stipulated time and cost-effectiveness.

3 Methodology Adopted

To start with the area got cleaned by shifting stored dies, the dies were stored along periphery of area to be excavated due to non-availability of other suitable space for storage. Area was enclosed by providing cladding along three sides and green cloth at top to control the dust. For the movement of machinery, west side access was provided. West side access was made possible by dismantling existing wall resting on ground beam. Ground beam was also had to be removed by cutting it from columns. At lintel level, a structural steel beam was introduced for that bay in order to compensate for the removal of ground beam.

Drilling of 100 mm hole started using wagon drill machine. Drilling could be done without much difficulty up to about 1.50 m depth. Further, the drilling process got struck due to rotation of loose particles at the bottom of cutting edge and side collapses. Since further drilling was not possible, it was decided to inject cement grout from this drilled hole. Accordingly, cement slurry in 1:2 proportion injected under atmospheric pressure. Next day, further drilling tried in the already drilled hole. It was possible to drill further about 1.50 m depth below. This proved that grout helped to bind loose particles together which facilitated further drilling (see Fig. 4).

Based on this experience, it was decided to drill holes along periphery at 2 m spacing in a staggered manner in two rows. Accordingly, drilling of two rows of holes completed up to about 1.5 m depth. Then, the cement slurry injected through
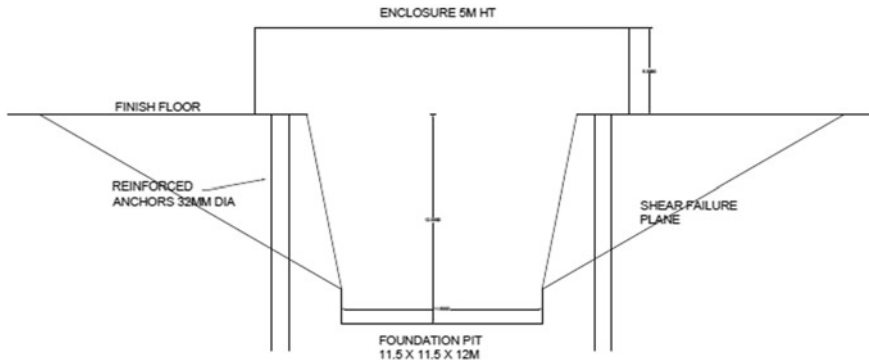
Fig. 4 Line diagram for methodology adopted

all holes. About 1000 L slurry was used per hole up to 6 m depth and 500 L slurry for further depth, this drilling in stages of about 1.5 m and then grouting continued to reach a depth of 10 m. A 32 mm steel rod inserted in each hole and then hole grouted with cement sand mortar in 1:1 proportion. Total number of holes along three sides were 60.

After a gap of 7 days excavation from central size of 11.5 m × 11.5 m started, initially, excavation up to 6 m depth done. During vertical excavation side slope collapses took place. After reaching to 6 m depth, side unstable material removed to get natural slope. In order to stabilize and strengthen this slope further, cement slurry applied along slope and then cement sand mortar in proportion 1:1 applied manually on surface along the slope.

Further excavation then started and reached to 10 m depth where natural ground surface met. After 6 m depth, it was observed that the fill material content was mainly boulders with little murum. The risk of rolling down of boulders here was very much felt. Few boulders came down while excavating lower portion. At northwest corner, a big chunk of fill material collapsed reaching up to grouted line on north side. This collapse also exposed the RCC column pedestal. It was observed that, where filling was done in compacted layers, a horizontal cement slurry layer formed, which improved the inter-layer bonding.

Natural virgin ground met at about 10 m depth. Further, excavation was very much required in order to reach to rock strata. The weight of press along foundation is more than 2000 tons. Such heavy machine foundation had to rest on strong and stable strata. Further, 2 m excavated to reach to rock strata. This 2 m depth excavation was very risky due to the presence of boulders above in fill layer along three sides. Labors were refused to work at that level. Therefore, as an addition measure to safeguard labor and create confidence in their mind, steel mesh was laid all along the slope. Considering risk of boulder collapse, it was decided to excavate partly and immediately fill the excavated portion with plum concrete so that toe of slope of fill material will not remain unsupported for long period. Accordingly, the part excavation was done and filled with plum concrete. Then, the remaining portion excavated and filled with plum

Fig. 5 Mortar application on slope

concrete to complete the square portion. After excavation immediate concreting done, concrete was kept ready while excavation going on. Day-night work continued till got completed. This worked to our satisfaction without any side collapse.

Further, concreting of raft foundation was done by creating a toe support along all four sides. Proper concreting of raft was done after placing reinforcement in square space formed by concrete toe wall (Figs. 5 and 6).

3.1 Cost Comparison

Approximate cost worked out for each method and presented in Table 2.

4 Conclusion

In this work, different solutions were thought as and when difficult situation met with. The work completed within stipulated time without any accident of whatsoever nature and magnitude. The methodology adopted worked out to be the cheapest of the available methods for deep excavation, and the press is presently in working condition.

Fig. 6 Plum concrete laid in part area

Table 2 Cost comparison

Method	Cost Rs.
Open excavation	101.27 lakh
Retaining by piles	153.14 lakh
Injection grouting method	25.57 lakh

Response of Laterally Loaded Monopile Using Three-Dimensional Finite Element Analysis

Jithin P. Zachariah and Jagdish Prasad Sahoo

Abstract The increase in need for energy in the developing world boosted the search for efficient energy sources. Most of the current energy sources in the past decades were not sustainable. The growing concern on the existence of earth leads to find an alternative sustainable energy source. The right proportion of energy need in many developed countries is obtained using offshore wind energy. Offshore wind turbine (OWT) produces renewable and efficient energy in this era, which is supported on large-diameter monopiles. These monopiles are subjected to very high lateral and moment loads. This paper deals with the response of a bottom fixed monopile under lateral loads taking into account varying soil strata and pile diameter. The analysis was performed using a three-dimensional finite element approach for the pile embedded in three types of soils, that is, clay, sand, and layered soil. By varying the diameter of the monopile, it is observed that large-diameter monopile in any soil tends to behave like a rigid system having a minor deflection. However, the soil profile influences the behavior of monopile considerably with considerable length to diameter ratios.

1 Introduction

Wind energy, a renewable source of energy, is expected to satisfy the right proportion of electricity demand in the coming generation. In comparison with onshore wind, offshore wind is more steady and robust [4]. In shallow waters, offshore wind turbines are supported on monopiles, which are connected through transition piece [1]. Monopiles are tubular piles with large diameter which carry lateral loads and

J. P. Zachariah (✉)
Civil Engineering Department, MBC CET, Kerala 685531, India
e-mail: jithinp.olickal@gmail.com

J. P. Sahoo
Civil Engineering Department, IIT Roorkee, Roorkee 247667, India
e-mail: sahoofce@iitr.ac.in

moment loads from ocean waves and wind energy. It also gives the weight of the tower and turbine in the form of axial loads [7].

Generally, monopiles have a diameter of 4–6 m having a slenderness ratio of less than 10. However, monopiles with diameter 7.5 m are also used for more giant wind turbines [2, 10, 14]. The lateral load acting on the monopiles are transferred to the soil by way of bending action [13]. An overturning moment is applied to the monopile foundation by the effect on wind force. In calculating the overturning moment acting on the monopile, the wind load has a higher lever arm, which results in more significant loading condition. For instance, in the northern sea environment, about 75% of the overturning moment is caused by a horizontal force developed by wind force [6]. Torsional moments acting on monopiles are negligible, and the lateral loads cause high bending moment and control the design of monopile. The wind and wave loading causes horizontal forces and bending moments, which are transferred to the earth by cantilever action [12].

The design parameters of a monopile depend on the amount of energy to be produced from that windmill. However, it also depends on the environmental conditions and soil profile. As a design criterion, the limiting value for maximum horizontal deflection of a monopile under field condition is 120 mm [3, 16]. The *p-y* design methodology is currently used for the design of monopiles using American Petroleum Institute (API 2000) and DNV 2011 codes. The method deals with the nonlinear relationship between soil reaction (*p*) and the lateral deflection (*y*) of the monopile. The monopile is considered as a Winkler beam resting on soil represented as uncoupled nonlinear elastic springs [5]. The presence of different types of soil in the sea basins has been reported in various locations around the globe. This makes the importance of the study on the behavior of monopile in different soil conditions. The effect of change in length and diameter was also considered in the present study. Keeping the length to diameter ratio constant, the diameter and length of the monopile are changed to obtain the response of monopile on extreme static loading conditions.

In this paper, the response of a bottom fixed monopile supporting an offshore wind turbine subjected to extreme static loading conditions has been studied. The loads on the monopile are in the form of horizontal force by the action of ocean waves and currents and moment by the action of massive wind force on the tower. The response was obtained in the form of lateral deflection of the monopile from the initial position and bending moment, along with the depth of the monopile. A comparison has been made by changing the soil profile (soft clay, medium dense sand, and layered soil) and properties. Also, the lateral response has been studied by varying the penetration depth and diameter of the monopile keeping the slenderness ratio (length to diameter ratio) within a range of 4–6.

Table 1 Size of monopiles for different conditions	l/d ratio	d (when l is unchanged) (m)
	4	5.5
	5	4.4
	6	3.6

2 Finite Element Modeling

Three-dimensional finite element analysis (3D FEA) has been attempted to study the response of laterally loaded monopile in different soil conditions (clay, medium dense sand, and layered profile). Mohr–Coulomb failure criterion is employed to simulate the soil profiles. The analysis was carried out using the finite element tool ABAQUS CAE.

2.1 Monopile Modeling

Monopiles are open-ended tubular piles with large diameter subjected to the combined action of lateral and moment loads. The presence of heavy wind load and wave load contributes to the bending of monopile as a flexible pile. However, in some cases, monopiles are considered as rigid, which results in rotation and translation action.

A monopile of 4.5 m diameter and an overall length of 22 m is chosen for the numerical study. The monopile is composed of a steel (linearly elastic material) with Young's modulus (E) of 210 GPa and Poisson's ratio (υ) 0.3. The density of steel is taken as 7850 kg/m³. The tubular pile is replaced with a solid cylinder with the same diameter in such a way that the bending stiffness of the two monopiles is kept unchanged. The bottom of the monopile is kept fixed and restricted to any deflection.

The effect of change in diameter and length of the monopile was also considered in the numerical study. The response was obtained by changing the length and diameter of the monopile, keeping the length to diameter (l/d) ratio constant. The length and diameter of the monopile corresponding to l/d ratio are shown in Table 1. The monopile was constructed using eight-noded linear brick element with reduced integration and hourglass control and six-noded linear triangular wedge prism toward the center. A global mesh size of 0.5 was adopted for modeling.

2.2 Soil Modeling

Three different soil conditions were taken for the study. The overall diameter of the model was considered to be 20D, where D is the diameter of the monopile. The

bottom of the soil mass is restricted to translate in all directions. A mesh sensitivity analysis has been carried out to fix the mesh density.

During the load application, clay exhibits an undrained behavior due to its low permeability. Clayey soil with an undrained shear strength (C_u) of 75 kPa and plasticity index (PI) of 40%, which represents the actual clay obtained from sea bed is considered for the study. The soil is defined by Young's modulus (E_c), Poisson's ratio (υ_c), and undrained shear strength. The homogeneous and isotropic clay are assumed to be normally consolidated with an unchanged C_u and E_c throughout its depth. The value of E_c is calculated using the relation,

$$E_c = K_c.C_u \tag{1}$$

where K_c is the correlation factor depending on the plasticity index and over consolidation ratio of the clay. Figure 1 shows the value of K_c of clay with C_u 75 kPa and OCR 1.

The second soil profile is a dense sand medium with an effective unit weight (γ') of 11 kN/m^3.

A layered soil profile with different properties at different levels is also considered for the study. This layered stratum represents the existing geotechnical conditions of the offshore soil bed. The profile chosen for the study was taken for Windmill Park at Horns Rev, Denmark [9]. The geotechnical properties of soil profiles at different levels are presented in Table 2.
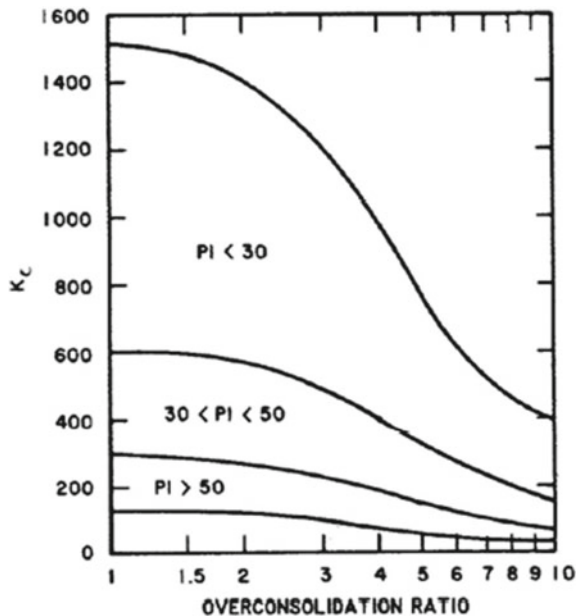
Fig. 1 Kc for clays [15]

Table 2 Different properties of the soil profile

Soil layer	Name	Depth (m)	Young's modulus, E (kN/m^2)	Effective unit weight, γ' (kN/m^3)	Angle of internal friction, Φ (deg.)	Dilatancy angle, Ψ (deg.)	Poisson's ratio, ν
Clayey soil	Clay	41.8	33,525	8	13.87	0.0	0.495
Dense soil	Sand	41.8	32,000	11	35	5.0	0.25
Layered profile							
Layer 1	Sand	1.0	31,800	10	42.0	12.0	0.3
Layer 2	Sand	3.5	57,100	10	43.5	13.5	0.3
Layer 3	Sand	5.5	52,534	10	42.5	12.5	0.3
Layer 4	Sand	6.5	44,100	10	41.7	11.7	0.3
Layer 5	Sand	7.0	58,200	10	43.2	13.2	0.3
Layer 6	Sand	8.5	72,170	10	44.3	14.3	0.3
Layer 7	Sand	10.0	52,950	10	43.1	13.1	0.3
Layer 8	Sand	11.5	35,400	10	40.3	10.3	0.3
Layer 9	Sand	12.5	23,530	10	37.2	7.2	0.3
Layer 10	Sand	13.5	13,600	10	33.8	3.8	0.3
Layer 11	Org. Sand	20.0	3135	7	21.6	0.0	0.3
Layer 12	Org. Sand	21.04	12,950	7	31.2	1.2	0.3
Layer 13	Sand	41.80	36,800	10	37.8	7.8	0.3

3   Soil–Monopile Interaction

. Soil–monopile interaction defines the modeling of contact behavior of soil and monopile. The interaction surface is defined by the general surface between the contact surfaces. The contact is constrained in normal and tangential directions with reference to Haiderali [8]. The maximum friction angle (δ_{peak}) between the monopile and clay is observed when the monopile is subjected to its maximum capacity. Figure 2 gives the value of friction coefficient μ between monopile and clay [8]. For sandy strata, the soil–monopile interaction is modeled by considering the friction angle (δ) as two-third of the frictional angle φ. The contact stress is deemed to be zero when a gap is produced between soil and monopile in the normal direction.
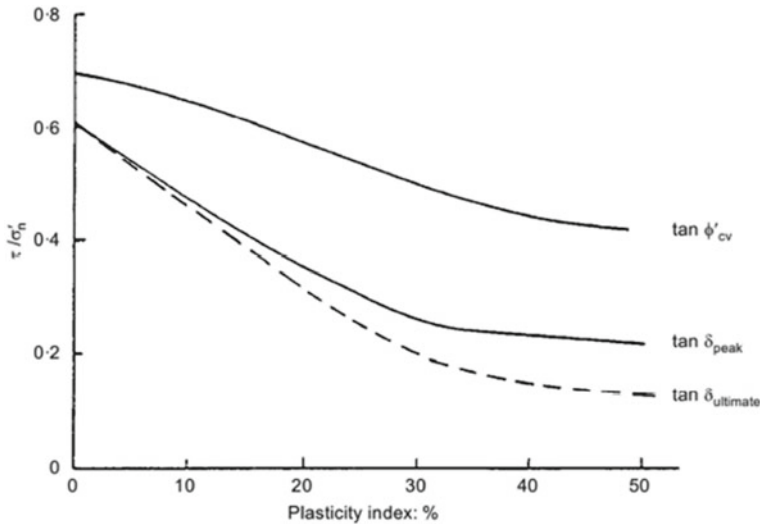
Fig. 2 Pile–clay interaction factor [11]

4 Loading

An offshore wind turbine, in its lifetime, is subjected to various loading conditions like wind, wave, ice, seismic load, etc. The effect of wind, waves, and currents are the most predominant examples of these loads. These loads are transferred to the monopiles in the form of significant bending moments and lateral loads. A typical loading pattern on an OWT is shown in Fig. 3.

In the present study, the monopiles have been analyzed by applying extreme static loading. The analysis was performed for a static horizontal force of 2503 kN and
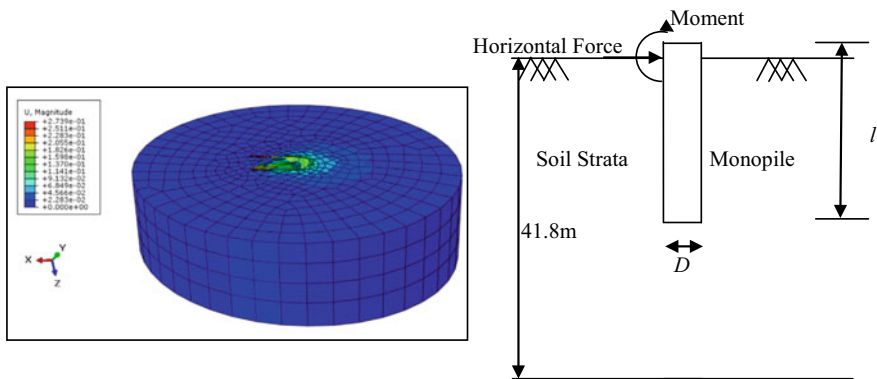
Fig. 3 Meshing and schematic loading diagram of an OWT supporting monopile

moment of 89,483 kN-m as reported by Kallezi and Hansen [9] for the foundation of a windmill at Horns Rev, Denmark with depth of water varying from 9 to 17 m. The windmill was located about 30 km away from the shore with a wind speed of 10 m/s. This load accounts for the effect of wind load acting on the blades and the ocean waves on the base of the tower.

5 Results and Discussion

The response of monopile subjected to extreme static loading conditions is discussed in this section. Firstly, the monopile is of diameter 4.5 m and length 22 m (21 m embedded length) and is analyzed in various soil conditions, i.e., clayey soil, medium dense soil, and a layered stratum. The response is plotted in terms of lateral deflection and a bending moment of the monopile along the length. Further, the effect of length to diameter ratio on the monopile is also studied. The various length to diameter ratio is achieved by two conditions, as discussed in the previous sections.

5.1 Effect of Soil Profile

Figure 4a shows the lateral deflection and bending moment of the monopile in various soil conditions. The deflection of the monopile is negligible at the bottom tip and shows a gradual increase to the pile head. The maximum lateral deflection is observed at the pile head. The deflection pattern of the monopile along the length reflects the bending nature of the pile. A similar trend is observed in the case of all three soil types. Moreover, the variation in the magnitude of lateral deflection for monopiles embedded in different soil conditions is negligible.

The bending moment induced in the monopile is presented in Fig. 4b. The maximum bending moment in all the cases is concentrated at the bottom end of the monopile. This is due to the restriction of monopile at the bottom of the pile for any movement. The magnitude of bending moment also follows a similar pattern to deflection. Even though the values of bending moment are very close, the quantity is less in case of layered strata and increased for clay and for medium dense sand. The magnitude of lateral deflection and maximum bending moment in the monopile is tabulated in Table 3.

5.2 Effect of Pile Diameter

The influence of pile diameter on the monopile is studied by changing the *l/D* of the monopile, keeping the constant length 22 m. The results were analyzed for *l/D* ratios
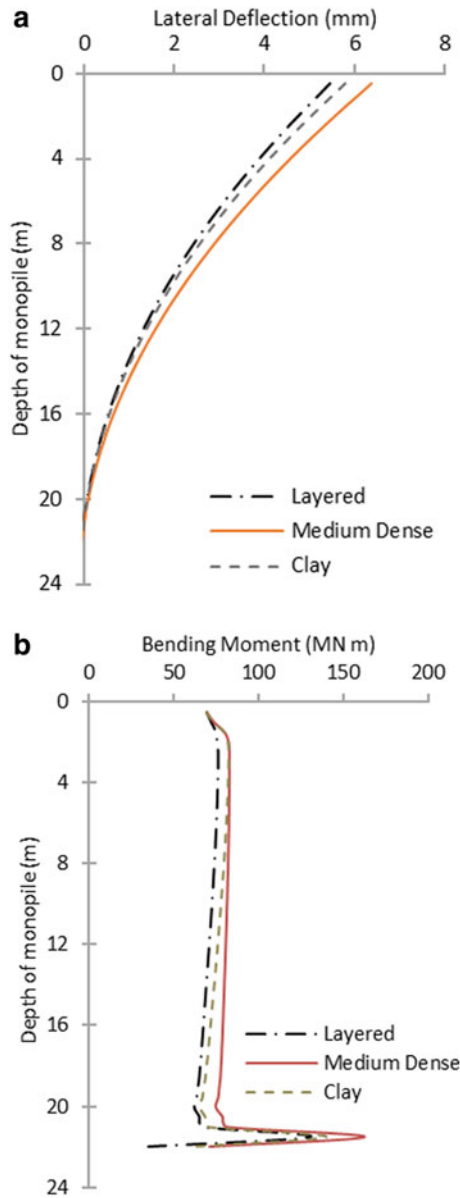
Fig. 4 **a** Lateral deflection of monopile along with depth embedded in different soil. **b** Bending moment of monopile along with depth embedded in different soils

Table 3 Maximum lateral deflection and bending moment of monopile in different soil profiles

Soil type	Maximum lateral deflection (mm)	Maximum bending moment (kN-m)
Clay	5.80	140,296.542
Medium dense sand	6.39	162,220.597
Layered profile	5.44	131,049.364

4, 5, 6 in terms of lateral deflection and bending moment of the monopile along the length. The diameter of the monopile is reduced with an increase in the *l/D* ratio.

The results show a similar trend in deflection, as shown in Fig. 5a–c. The lateral deflection of the monopile is observed to be small, with an increase in diameter of the monopile. The lateral deflection is increased 2–4 times corresponding to *l/D* = 5 and *l/D* = 6 when compared to monopile with *l/D* = 4. This implies that the monopiles with larger diameter has a tendency to behave like a rigid pile.

Unlike the pattern followed in the primary model, the monopile embedded in clay has a lesser deflection from its initial state. Since the deflection is not much critical in large-diameter monopiles, they have a negligible difference in different soil profiles. With the decrease in diameter, the monopile tends to bend more and shows a considerable variation of the maximum lateral deflection. The monopiles with different diameters tend to deflect 10–30% when embedded in different soil strata. It may be noted that the layered soil is having low stiffness when compared
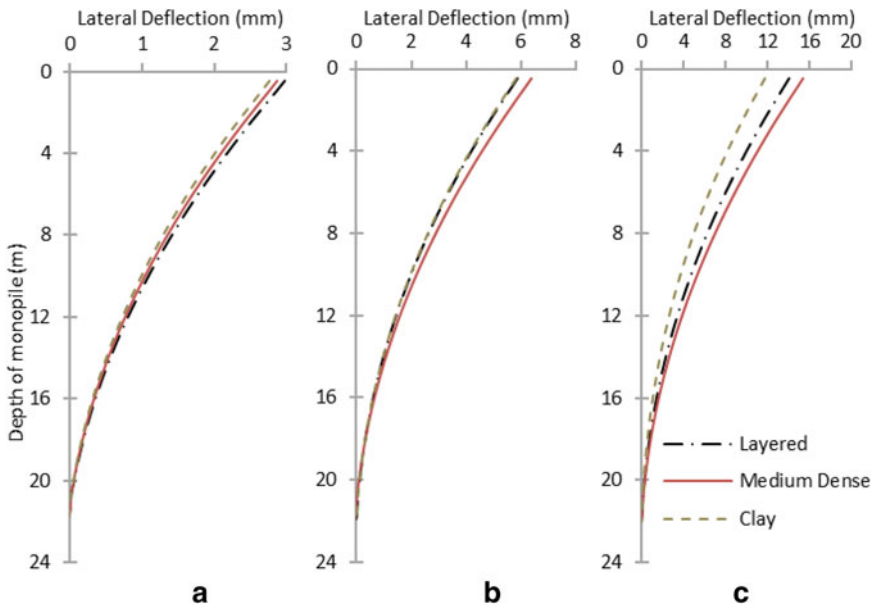

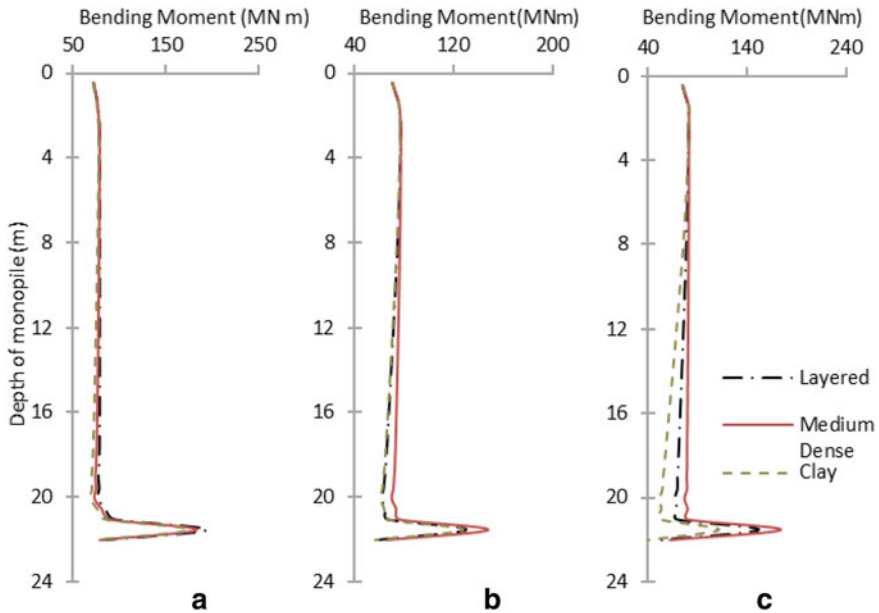**Fig. 5** Lateral deflection of monopile along with depth embedded in different soils for **a** R4, **b** R5, and **c** R6

Fig. 6 BM of monopile along with depth embedded in different soils for **a** R4, **b** R5, and **c** R6

to the other two soil profiles. The deflection pattern reflects a similar trend in the analysis.

The bending moment follows a similar trend as the primary model of monopile. The maximum bending moment is concentrated at the bottom of the pile. The results are shown in Fig. 6a–c. It is observed that the diameter of monopile is not heavily influencing the bending moment because the magnitude of bending moment in various diameters does not show a huge fluctuation. It is thus concluded that the bending stress is the driving factor for bending moment than the moment of inertia (I) and deflection of monopile (y) in the bending equation.

It is also seen that the monopile embedded in medium dense sand is subjected to a more bending moment. Like deflection, large-diameter monopiles have lesser fluctuation in bending moment for different types of soil. With the decreasing diameter, the bending moment shows a considerable variation in the results. About 20% of increase in bending moment is observed for monopiles in medium dense than that for clay and layered soil for different diameters of monopiles. The maximum lateral deflection and bending moment of monopile in different soil profiles is tabulated in Table 4.

Table 4 Maximum lateral deflection and bending moment of monopile in different soil profiles (for a constant length of monopile)

Soil type	Maximum lateral deflection (mm)			Maximum bending moment (kN-m)		
	R4	R5	R6	R4	R5	R6
Clay	2.76	5.81	11.73	174,769.26	127,884.17	111,710.63
Medium dense sand	2.86	6.40	15.42	183,656.72	147,784.72	174,339.61
Layered profile	2.97	5.86	14.08	193,681.85	129,707.50	151,297.77

6 Conclusions

The response of a monopile under different loading conditions has been studied in the present study using finite element-based software ABAQUS. The responses were presented in the form of lateral deflection and bending moment of the monopile. The monopile is embedded in three different soil conditions, clay, medium dense sand, and layered profile.

The following conclusions were derived on the basis of the present analysis.

1. The monopile tends to bend when it is subjected to a combination of lateral and moment load. Also, a maximum lateral deflection is observed at the pile head.
2. When a monopile is restrained at the bottom edge, the maximum bending moment is found near the pile bottom.
3. The monopile does not show a tendency of bending for higher diameters and deflects a considerable amount with a reduction in diameter.
4. The difference in the behavior of monopiles for large and small diameter reflects the importance of pile geometry. A considerable variation in response is observed for small diameter monopiles when embedded in different soil types.

References

1. Abhinav, K.A., Saha, N.: Dynamic analysis of monopile supported offshore wind turbines. Proc. Inst. Civ. Eng. Geotech. Eng. **170**, 428–444 (2017)
2. Achmus, M., Kuo, Y.-S., Abdel-Rahman, K.: Behaviour of monopile foundations under cyclic lateral load. Comput. Geotech. **36**(5), 725–735 (2009). https://doi.org/10.1016/j.compgeo.2008.12.003
3. Arshad, M., O'Kelly, B.C.: Analysis and design of monopile foundations for offshore wind-turbine structures. Marine Georesour. Geotechnol. **34**(6), 503–525 (2016). https://doi.org/10.1080/1064119X.2015.1033070
4. Bilgili, M., Yasar, A., Simsek, E.: Offshore wind power development in Europe and its comparison with onshore counterpart. Renew. Sustain. Energy Rev. **15**, 905–915 (2011). https://doi.org/10.1016/j.rser.2010.11.006

5. Brodbaek, K.T., Moller, M., Sorensen, S.P.H., Augustesen, A.H.: Review of p-y relationships in cohesionless soil. DCE Technical Report No. 57, Department of Civil Engineering, Aalborg University, Aalborg, Denmark (2009)

6. Byrne, B.W., Houlsby, G.T.: Foundations for offshore wind turbines. Philos. Trans. R. Soc. Lond. **361**(1813), 2909–2930 (2003)

7. Doherty, P., Gavin, K.: Laterally loaded monopile design for offshore wind farms. In: Proceedings of the ICE—Energy 165(EN1), pp. 7–17 (2011)

8. Haiderali, A., Madabhushi, G.: Three-dimensional finite element modelling of monopiles for offshore wind turbines. In: The 2012 World Congress on Advances in Civil, Environmental, and Materials Research (2012)

9. Kellezi, L., Hansen, P.B.: Static and Dynamic Analysis of an Offshore Mono-Pile Windmill Foundation. GEO-Danish Geotechnical Institute, Lyngby, Denmark (2003)

10. LeBlanc, C., Houlsby, G.T., Byrne, B.W.: Response of stiff piles in sand to long-term cyclic lateral loading. Geotechnique **60**(2), 79–90 (2010). https://doi.org/10.1680/geot.7.00196

11. Lehane, B.M., Chow, F.C., McCabe, B.A., Jardine, R.J.: Relationships between shaft capacity of driven piles and CPT end resistance. Proc. Inst. Civ. Eng. Geotech. Eng. **143**, 93–101 (2000)

12. Malhotra, S.: Design and construction considerations for offshore wind turbine foundations in North America. In: Fratta, D.O., Puppala, A.J., Muhunthan, B. (eds.) Proceedings Geo- Florida 2010: Advances in Analysis, Modelling and Design, West Palm Beach, Florida, USA, February 20–24th, 2010, vol. 2, pp. 1533–1542, GSP 199. Curran Associates, Inc., Red Hook, NY, USA (2011)

13. Schaumann, P., Boker, C.: Can jackets and tripods compete with monopiles? In: Proceedings of Copenhagen Offshore Wind, COW05, Copenhagen, Denmark. European Wind Energy Association, Brussels, Belgium

14. Tomlinson, M.J.: Foundation Design and Construction, 7th edn. Pearson Education, Harlow, England (2001)

15. USACE: Engineering and Design—Settlement Analysis. Engineer Manual 1110-1-1904. U.S. Army Corps of Engineers (1998)

16. Zachariah, J.P., Sahoo, J.P., Ghosh, S.: Influence of length to diameter ratio on strength parameters of offshore monopiles. In: Agnihotri, A., Reddy, K., Bansal, A. (eds.) Environmental Geotechnology. Lecture Notes in Civil Engineering, vol .31, pp. 201–208. Springer, Singapore (2019). https://doi.org/10.1007/978-981-13-7010-6_19

Influence of Combined Vertical and Lateral Loading on Lateral Response of Piled Raft Foundation

Plaban Deb and Sujit Kumar Pal

Abstract Due to the complexity involved in analysing the piled raft foundation under combined loading, the existing design practice for the piled raft assumes that the influence of vertical and lateral loads is independent of each other and the experimental tests on the behaviour of piled raft foundation under the action of combined vertical and lateral loads are relatively scarce. Therefore, the objective of the present study is to examine the behaviour of piled raft foundation subjected to pure lateral loads and combined vertical and lateral loads through laboratory model tests. The experimental programme includes the prototype model test on raft braced by 2×2 and 3×3 pile groups. The laboratory tests are performed in silty-clay soil underlain by sandy soil. Initially, the response of the piled raft foundation under pure lateral load is performed through laboratory model test and to understand the response of the piled raft foundation under combined loads, and the influence of vertical loads equal to $0.25V_u$, $0.5V_u$, $0.75V_u$ and $0.9V_u$ are considered. The ultimate vertical load capacity (V_u) corresponding to the settlement of 10% of raft width is evaluated by a separate vertical load test. The results of the experiments have shown the significant influence of vertical loads on a pile's lateral response. For the structural design of piled raft, it is important to find out the bending moment developed in the pile in piled raft. Therefore, the influence of combined loading on the bending moment developed in the pile has been examined from the laboratory model test.

Keywords Piled raft · Combined vertical and lateral loading · Ultimate vertical load capacity · Bending moment

P. Deb · S. K. Pal (✉)
Civil Engineering Department, NIT Agartala, Agartala, Tripura, India
e-mail: skpal1963@gmail.com

P. Deb
e-mail: plaban930@gmail.com

1 Introduction

Piled raft foundations are generally used when the isolated footing covers more than 70% of area under a super-structure and these are being used in several countries to sustain different kinds of super-structures, like buildings, bridges or industrial plants in various types of sub-soil. Using these foundation systems, differential settlement can be lowered to a great extent as piles improve the load carrying capability of the raft. In the piled raft foundation technique, the raft is directly contacted with the sub-soil and hence a greater number of load exerts on the raft; thereby, making the method very tedious and also leads to the over design of the foundation. Although considering the settlement reduction, piled raft is a widely used foundation technique in today's world. The idea of using the pile as a settlement reducer was suggested by Burland et al. [1]. According to Horikoshi and Randolph [2] and Reul and Randolph [3] the strategic placement of the piles under the centre of the raft can effectively decrease differential settlement under uniform loading condition. The effect of the variation in pile and raft geometry to determine the piled raft stiffness was studied through the centrifuge test on the piled raft system [4]. Furthermore, the analysis methods of the piled raft foundation are systematically summarized by Poulos [5] and a lot of experimental and numerical studies and field measurements on piled raft foundations have been accompanied to explore the settlement behaviour and the load sharing behaviour between raft and piles for vertical loading [6, 7]. All of the above research works are mainly concerned with piled raft foundations subjected to vertical loads only. A few researches have been worked on the behaviour of piled rafts subjected to lateral load. Pastsakorn et al. [8] performed small-scale laboratory model test on the piled raft foundation under the action of horizontal loading in a 1 g field. Hamada et al. [9] carried out large-scale cyclic lateral loading test on the piled raft foundation to investigate the effect of vertical load during earthquake. Horikoshi et al. [10] performed a series of static vertical and horizontal load test on the piled raft foundation using a geotechnical centrifuge. Zhu et al. [11] studied the influence of vertical loading on the horizontal response of the disconnected piled raft through a series of 1 g model test.

In the conventional design concept for pile groups, it is assumed that all lateral loads are carried by the piles only. But in the case of the piled raft foundation, the fact is that some of the load is transferred to the soil through the raft by friction. In the case of the piled raft subjected to the combined vertical and lateral loading, the bending moment developed in the piles is not only due to the shear force at pile heads but also due to the ground displacement caused by the raft friction. From the previous research works, it is understood that the behaviour of the piled raft foundation under the combined vertical and lateral load is rather limited. According to the current design practice of foundation in the field of geotechnical engineering, it is more rationally required to understand the behaviour of piled raft foundation subjected to combined load. Therefore, the main objective of the present study is to observe the effect of vertical load on the lateral response of the piled raft foundation.

Table 1 Physical and geotechnical properties of sand

Physical properties	Test results
Specific gravity (G_s)	2.64
Effective grain size, D_{10} (mm)	0.37
Mean grain size, D_{50} (mm)	0.85
Coefficient of curvature (C_c)	1.02
Coefficient of uniformity (C_u)	2.57
Unified soil classification system	SP
Minimum void ratio (e_{min})	0.59
Maximum void ratio (e_{max})	0.86
Void ratio at placement density ($e_{exptl.}$)	0.67
Minimum dry density, γ_{min} (kN/m^3)	14.20
Maximum dry density, γ_{max} (kN/m^3)	16.60
Placement dry density, $\gamma_{exptl.}$ (kN/m^3)	15.80
Relative density, I_D (%)	70

2 Materials, Test Setup and Test Procedure

2.1 Sub-soil Materials

In this study, silty-clay and sand are used as sub-soil materials. The physical and geotechnical properties of both the soil are evaluated according to ASTM codes. The index properties of silty-clay soil are obtained as liquid limit 46%, plastic limit 24% and plasticity index 22%. According to the unified soil classification system (USCS), the silty-clay soil sample is categorized as low plasticity clay (CL). By performing several UCS test, the undrained shear strength (S_u) of silty-clay sample is found to be 10 kPa at the water content of 35% and corresponding soil density ($\gamma_{exptl.}$) is found around 17.5 kN/m^3. The physical and geotechnical properties of clean dry sand are listed in Table 1 and the particle size distribution curve for both the soil is shown in Fig. 1.

2.2 Model Raft and Pile

Mild steel plate of dimensions 250 mm × 250 mm × 10 mm are used as a model raft and steel hollow pipes with outer diameters of 20 mm is used as a model pile. The embedded length of the pile is 300 mm. Each pile is instrumented with six pairs of strain gauges to measure the axial strain and bending moment. Each strain gauge has a gauge factor of 2, and resistance of 350 Ω. Shear strain gauges are pasted near the each pile head for measuring the lateral load carried by the pile head. Epoxy resin is
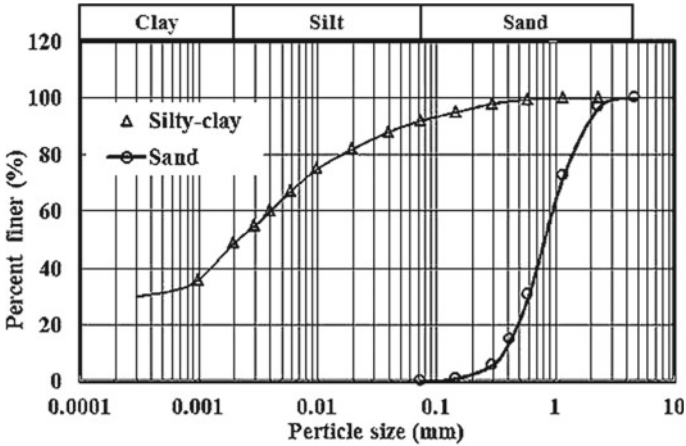
Fig. 1 Particle size distribution curve

used to paste each strain gauge on the surface of pile. A waterproof coating of silica gel is used to cover the strain gauges. The location of each pair of strain gauge and shear strain gauge is shown in Fig. 2. Each pile head is provided with a bolt of 20 mm in diameter and 10 mm in length. To fix the pile into the raft surface, screwed holes
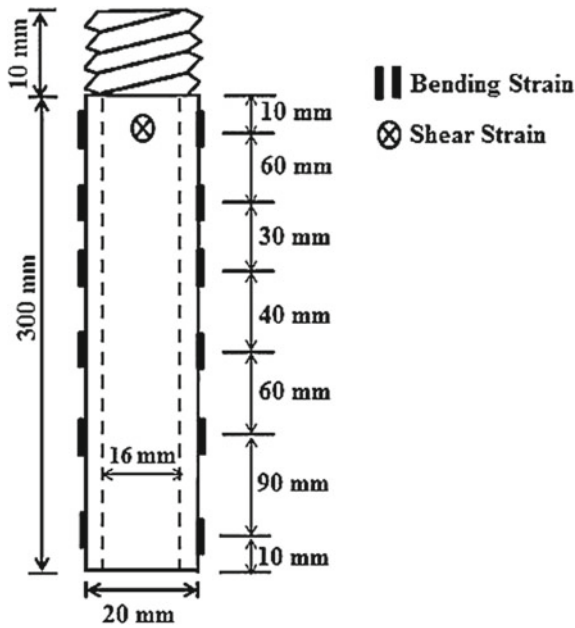

Fig. 2 Model pile and location of the each pair of strain gauge

are provided in the raft surface with diameter equal to the outer diameter of the pile which ensures the rigid connection between the pile and raft.

2.3 Testing Tank and Test Setup

Testing tank is made of translucent Perspex sheet and steel plates. To minimize the boundary effect of testing tank, the lateral boundary is taken 3.6 times the raft width and vertical boundary is taken around 2 times the embedded pile length. Therefore, the dimension of the testing tank is 90 cm long, 90 cm wide and 65 cm high. Four horizontal stiffeners are attached at the four side wall of the testing tank to avoid any bulging of the tank during the loading process. The combined vertical and lateral load test setup is represented in Fig. 3. The vertical load is applied in the piled raft through a 5-ton capacity hydraulic jack and the lateral load is applied through a winch and a wire rope. A calibrated 30 kN capacity compressive load cell is attached to the hydraulic jack for measuring the applied vertical load, and two calibrated LVDTs are used to measure the vertical deformations. The lateral load is measured using a calibrated 2 kN load cell and the lateral displacement is measured by two calibrated LVDTs.
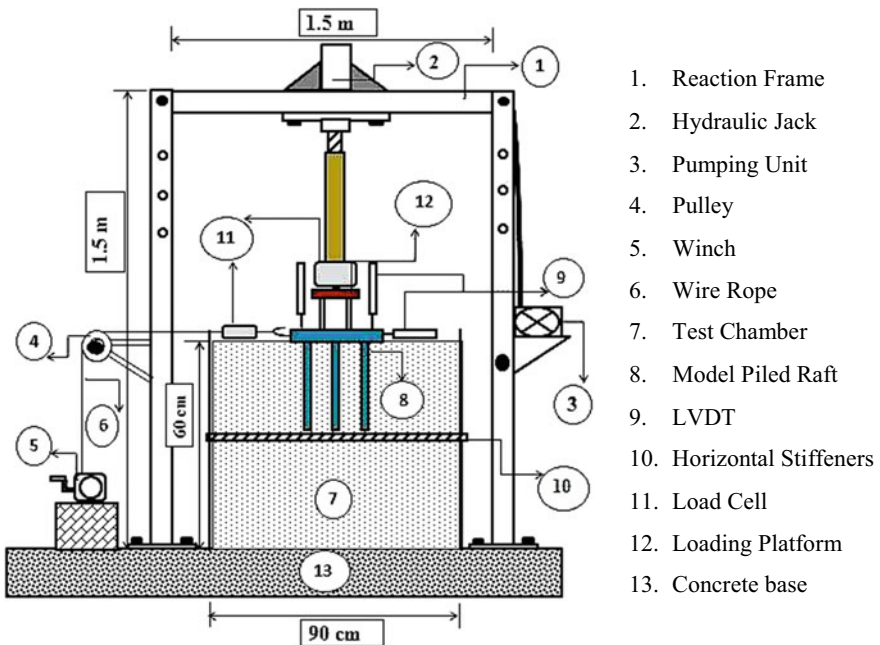

1. Reaction Frame
2. Hydraulic Jack
3. Pumping Unit
4. Pulley
5. Winch
6. Wire Rope
7. Test Chamber
8. Model Piled Raft
9. LVDT
10. Horizontal Stiffeners
11. Load Cell
12. Loading Platform
13. Concrete base

Fig. 3 Model test setup

Table 2 Laboratory test programme on piled raft foundation

SI. No.	Model configuration	s/d	Loading sequence	
			Vertical load	Lateral load
1	Raft + 4 piles	4	Up to failure	–
			–	Up to failure
			$0.25V_u$, $0.5V_u$, $0.75V_u$ and $0.9\ V_u$	Up to failure
2	Raft + 9 piles	4	Up to failure	–
			–	Up to failure
			$0.25V_u$, $0.5V_u$, $0.75V_u$ and $0.9\ V_u$	Up to failure

2.4 Test Programme

A series of laboratory tests are performed to understand the effect of vertical load on the lateral behaviour of piled raft foundation. The 2×2 and 3×3 pile configuration with pile spacing to pile diameter ratio of 4 is used under the model raft to perform the laboratory test. The laboratory tests are performed in silty-clay soil underlain by sandy soil. Initially, the response of the piled raft foundation under pure lateral load is performed through laboratory model test and to understand the response of the piled raft foundation under combined loads, and the vertical loads equal to $0.25V_u$, $0.5V_u$, $0.75V_u$ and $0.9V_u$ are considered. The ultimate vertical load capacity (V_u) corresponding to the settlement of 10% of the raft width is evaluated by a separate vertical load test. Therefore, the total 12 tests are conducted in the laboratory. The programme of laboratory model test on piled raft foundations is presented in Table 2.

2.5 Test Procedures

1. Each experimental test started with placing the sand in the testing chamber in layers (each of about 50 mm thick) by sand raining technique and the sand is poured up to a height of 450 mm. The sand is placed in the chamber with uniform relative density of 70%.
2. After the placing of sand, the silty-clay soil is placed in the test chamber up to a height of 600 mm at a constant density and water content. Dry silty-clay soil is thoroughly mixed with water content of 35% to get the required consistency ($I_c = w_L − w/I_p = 0.49$) of silty-clay lump. The mixed silty-clay lump is then placed in the testing chamber in 50 mm thick layers and tamped with a steel template to attain the required bulk density of 17.5 kN/m^3. After the completion of silty-clay bed preparation, the soil bed is covered with plastic sheet and is permitted to set at room temperature for about 24–30 h to confirm the uniform circulation of the moisture content.

3. As the piles used in the piled raft are non-displacement piles, at first, the soil is placed up to the tip of the piles. After that, the model piled raft is kept in the centre of the test chamber and again soil is packed in the chamber up to the required height keeping the model piled raft in vertical position.

4. After that, the vertical load is applied to model piled raft through hydraulic jack at a loading rate of 1 mm/min and vertical displacement is measured with the help of LVDTs. After the application of required level of vertical load, the lateral load is applied through a winch and a wire rope at a displacement rate of 0.25 mm/min. The lateral displacement is then recorded with the help of two horizontally placed LVDTs.

5. After completion of one test, all the piles, raft and the soil from the testing chamber are removed and the similar method is repeated for the consecutive tests.

3 Results and Discussion

3.1 Pure Vertical and Pure Lateral Load Test on Piled Raft

Figure 4 shows the load-settlement response of different piled raft foundations under pure vertical load. From this load-settlement response, the ultimate vertical load corresponding to the settlement of 10% of raft width for each piled raft configuration is evaluated. From the figure, it is observed that as the number of pile beneath the raft increases the vertical load carrying capacity is also increases. To understand the lateral response of piled raft foundation, the lateral load is applied up to the lateral deflection corresponding to 10% of the pile diameter. The lateral load vs. normalized lateral deflection $(y/d = 0.1)$ of different piled raft foundation subjected to pure lateral load is presented in Fig. 5. It is observed from the figure that for same normalized lateral deflection, the raft with 9 piles exhibits higher lateral load as compared to the raft with 4 piles.

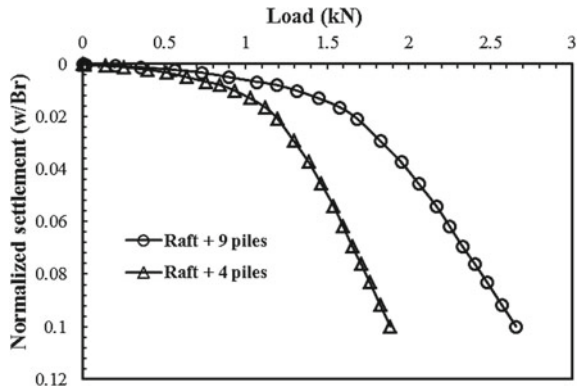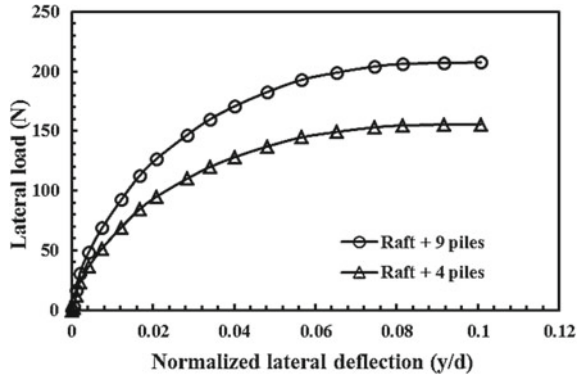**Fig. 4** Vertical load versus settlement curve

Fig. 5 Lateral load versus normalized lateral deflection curve

3.2 Effect of Vertical Load on the Lateral Response of Piled Raft

To observe the effect of vertical load on the lateral response of the piled raft foundation, the lateral responses of piled raft foundation at different level of vertical load are shown in Figs. 6 and 7. Form the figures, it can be concluded that at certain normalized lateral deflection, and the lateral load carrying capacity of the piled raft foundation increases with the increase of the vertical load level. This increase is due to the increase in the confining stress developed in the soil below the raft with the continuous increase of the vertical load. When the applied vertical load is 90% of the ultimate vertical load, the lateral load carrying capacity of model configuration (raft + 9 piles) is increased about 46% as compared to pure lateral load and the lateral load carrying capacity of model configuration (raft + 4 piles) is increased by 30%.
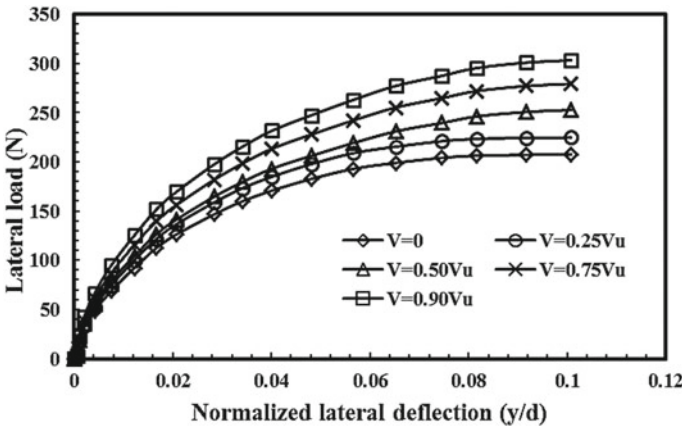
Fig. 6 Lateral responses of piled raft (raft + 9 piles) at different vertical loads

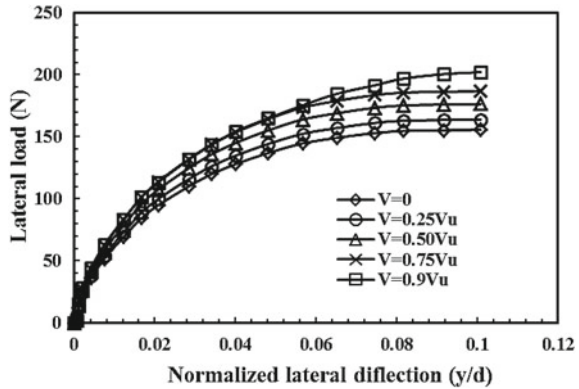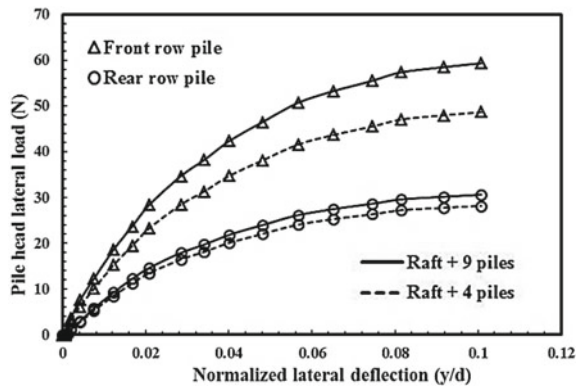**Fig. 7** Lateral responses of piled raft (raft + 4 piles) at different vertical loads

Fig. 8 Pile head lateral load versus normalized lateral deflection for each row pile

The lateral load carried by front row pile and rear row pile with the normalized lateral deflection for both the model configuration under pure lateral loading condition is shown in Fig. 8. From the figure, it is found that the front row pile carries much higher lateral load as compared to the rear row pile. For the model configuration (raft + 9 piles), the front row pile takes about 41% to 45% of the total lateral load carried by the pile group, whereas in the case of (raft + 4 piles), the front row pile carries around 55–61% of the total lateral load carried by the pile group.

3.3 Bending Moment in the Pile

The bending moment developed in the pile can be evaluated as

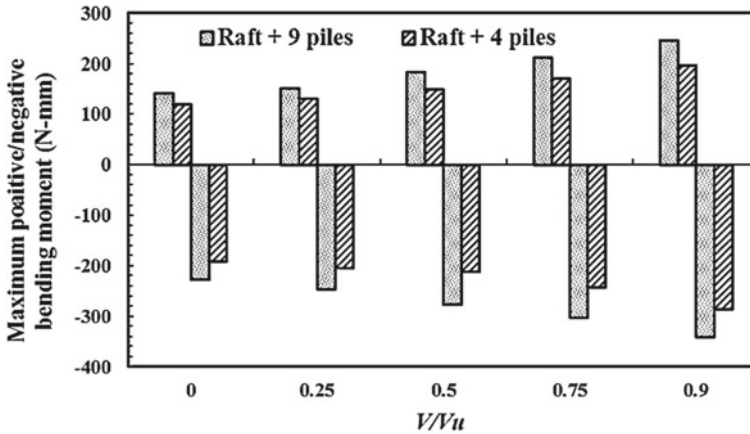$$M = \frac{E_P I_P (\varepsilon_t - \varepsilon_c)}{d}$$

Fig. 9 Variation of maximum positive and negative bending moment for different vertical loads

where E_P is the modulus of elasticity of pile, I_P is the moment of inertia of pile, d is the pile diameter and $(\varepsilon_t - \varepsilon_c)$ is the difference between the strain in tension and compression face. The maximum positive and negative bending moment for different vertical loads is shown in Fig. 9. It is observed from the figure that the maximum positive and negative bending moment for both the model configuration increases with the increase of vertical load. The variation of the bending moment developed along the front row pile and rear row pile under pure lateral load is presented in Fig. 10. The result obtained from the figure reveals that the bending moment is higher in the case of front row pile as compared to the rear row pile for both the model configuration. It is also observed from the figure that the maximum positive bending moment is developed almost at a depth of 0.5 times the embedded length of the pile from the pile head and the maximum negative bending moment is developed at the pile head.

4   Conclusions

From the results of the experimental investigation on the behaviour of the piled raft foundation subjected to combined vertical and lateral loading condition, the following conclusions may be drawn:

1.   Due to the increase of confining stress in the soil below the raft, the lateral load carrying capacity of piled raft foundation increases with the increase of vertical load. When the applied vertical load is equal to 90% of the ultimate vertical load, the lateral load carrying capacity of (raft + 9 piles) and (raft + 4 piles) is increased about 46% and 30%, respectively, as compared to pure lateral load

Fig. 10 Variation of bending moment for each row pile
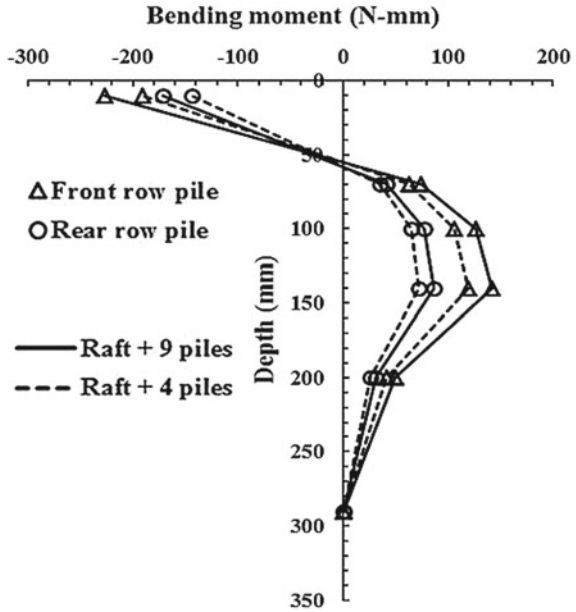
and the lateral load carrying capacity of piled raft foundation get enhanced by adding the number of piles below the raft.

2. The lateral load carrying capacity of the front row pile in model configuration (raft + 9 piles) is around 41–45%, and model configuration (raft + 4 piles) is about 55–61% of the total lateral load carried by the pile group.

3. The maximum positive and negative bending moment increases with the increase of vertical load and the maximum positive bending moment is developed almost at a depth of 0.5 times the embedded length of the pile from the pile head, whereas the maximum negative bending moment is developed at the pile head.

References

1. Burland, J.B., Brooms, B.B., de Mello, V.F.B.: Behavior of foundations and structures. In: Proceedings of 9 ICSMFE, Tokyo 2, pp. 495–546 (1977)
2. Horikoshi, K., Randolph, M.F.: Centrifuge modelling of piled raft foundation on clay. Geotechnique **46**(4), 741–752 (1996)
3. Reul, O., Randolph, M.F.: Design strategies for piled rafts subjected to nonuniform vertical loading. J. Geotech. Geoenviron. Eng. **130**(1), 1–13 (2004)
4. Conte, G., Mandolini, A., Randolph, M.F.: Centrifuge modeling to investigate the performance of piled rafts. In: Van Impe, W.F. (ed.) Proceedings of the 4th International Geotechnical Seminar on Deep Foundations on Bored and Auger Piles, pp. 359–366. Millpress, Rotterdam (2003)

5. Poulos, H.G.: Piled raft foundations: design and applications. Geotechnique **51**(2), 95–114 (2001)
6. Katzenbach, R., Arslan, U., Moormann, C.: Piled raft foundation projects in Germany. In: Design Applications of Raft Foundations (2000)
7. Yamashita, K., Hamada, J., Onimaru, S., Higashino, M.: Seismic behavior of piled raft with ground improvement supporting a base-isolated building on soft ground in Tokyo. Soils Found. **52**(5), 1000–1015 (2012)
8. Pastsakorn, K., Hashizume, Y., Matsumoto, T.: Lateral load tests on model pile groups and piled raft foundations in sand. In: Proceedings of International Conference Physical Modelling in Geotechnics, pp.709–714 (2002)
9. Hamada, J., Tsuchiya, T., Tanikawa, T., Yamashita, K.: Lateral loading tests on piled rafts and simplified method to evaluate sectional forces of piles. Geotech. Eng. J. SEAGS AGSSEA **46**(2), 29–42 (2015)
10. Horikoshi, K., Matsumoto, T., Hashizume, Y., Watanabe, T., Fukuyama, H.: Performance of piled raft foundations subjected to static horizontal loads. Int. J. Phys. Model. Geotech. **3**(2), 37–50 (2003)
11. Zhu, X.J., Fei, K., Wang, S.W.: Horizontal loading tests on disconnected piled rafts and a simplified method to evaluate the horizontal bearing capacity. Adv. Civ. Eng. (2018)

Interpretation of Load-Settlement Curves from Graphical Methods

Naga Sireesha Ghanta and Sujit Kumar Pal

Abstract Bearing capacity of pile depends mainly on the type of soil through which it rests and on the method of installation. Many empirical and analytical formulae developed based on the field and laboratory experiments to estimate the pile group bearing capacity. The present investigation is carried out to get the load-settlement characteristics of different configurations of pile groups, such as 1×1, 2×2 and 3×3. In many projects, some of the manufactured piles are loaded to determine the pile bearing capacity. This is the most reliable way to determine the pile capacity. However, it is not easy to determine the point where the pile has reached its ultimate capacity on the load-settlement curve. By using different graphical methods, the ultimate bearing capacity is calculated from load-settlement data. Among these methods, there are considerable differences between the graphical ultimate bearing capacities of the piles which decrease to 35% for the piles loaded up to the collapse load and increases up to 120% for the piles loaded to the failure load. Improvement ratio and settlement ratio are calculated using load-settlement curves. Model plate load test is used to determine the load-settlement curves. It is time and cost efficient, easy to perform and reliable. Experiments are conducted on dry, clean and poorly graded sand. Steel pipe piles of length 30 cm, diameter 2 cm, 2.5 cm are used in this experiment. The spacing between the piles is taken as 3d.

Keywords Pile group · Bearing capacity · Settlement ratio

N. S. Ghanta · S. K. Pal (✉)
Department of Civil Engineering, National Institute of Technology Agartala, Agartala, Tripura, India
e-mail: skpal1963@gmail.com

N. S. Ghanta
e-mail: sireeshaghanta77@gmail.com

1   Introduction

Increase in population growth in the current scenario has led to increase in the need of housing and infrastructure and the availability of space is becoming very less. So, many agencies are forced to exploit the poor soil condition; this has led to the development of pile foundation and pile driving system. Pile driving into long depths, due to non-homogeneity of soil and lack of suitable analytical method, the determination of bearing capacity is complex. The designer should know the pile bearing capacity and settlement before starting construction. Many empirical formulae and experimental methods are available to find ultimate bearing capacity, but soil conditions should be predictable to find the ultimate bearing capacity from empirical methods. To determine accurate capacity values large-scale load tests which represent the actual pile behaviour are available. However, the ultimate bearing capacity values obtained from load tests are distinct; so, many interpretive methods are available to find the ultimate bearing capacity.

1.1   Different Interpretation Methods to Find Ultimate Bearing Capacity

Davisson Off-Set Limit Load Method
Davisson proposed an off-set limit load method [1] to interpret the ultimate bearing capacity. It is widely used in western countries, Canada and USA. Q_u is the load at which the settlement exceeds the elastic compression (QL/AE) of a pile by the value of 0.15 in. (4 mm) plus the value of $D/120$, where $Q =$ load, $L =$ length of pile, $A =$ area of the pile, $E =$ Young's modulus of pile, $D =$ diameter of pile in inches.

Brinch Hansen 80% Method
According to Brinch Hansen method [2], the ultimate load as the load that corresponding to four times the settlement as obtained for 80% of that load. In this method, an ultimate load can be calculated directly from load-settlement curves. To determine accurate loads, this method can be plotted as a square root of settlement value divided by its load value and plotted against the settlement. The ultimate bearing capacity of foundation is represented as

$$Q_u = \frac{1}{2\left(\sqrt{C_1}\sqrt{C_2}\right)} \tag{1}$$

where $Q_u =$ ultimate bearing capacity; $C_1 =$ slope of the straight line; and $C_2 =$ y-intercept of the straight line.

Chin-Konder Method
According to Chin-Konder method [3], the graph is plotted between load divided by settlement against load values. The points on a graph show a linear trend at a

particular point. The inverse of the slope ($1/C_1$) of that linear line gives the ultimate bearing capacity.

Tangent Intersection Method
In the tangent intersection method [1], two tangents are drawn from initial and final points of the load-settlement curve. The intersection point of these two tangents gives the ultimate bearing capacity.

Fuller and Hoy Method
According to Fuller and Hoy method [4], the ultimate bearing capacity is determined at a point, where the line has slope of 0.127 mm/kN.

2 Materials and Methodology

The experimental work starts with the collection of sand, piles and pile cap. Model experiments are carried out in the laboratory to measure the pile behaviour under static vertical load. Models are properly scaled down so that the bearing behaviour of pile measured from the small-scale models that can be used to interpret the behaviour of prototype pile foundations. The materials which are used in this work are discussed below.

2.1 Sand

Dry sand is used in the experiment. Sand is collected from the Haora River. Specific gravity, sieve analysis, relative density and direct shear tests are conducted on the three sand samples. The tested properties of the sand used in the present experiment are shown in Table 1.

2.2 Model Piles

The model piles used in this experiment are smooth, hollow steel pipe of length 30 cm with two different diameters 20 mm and 25 mm. Different types of configuration of piles such as single pile 2 × 2 and 3 × 3 are used.

Table 1 Physical properties of the sand

SI. No.	Property	Value
1	Effective size (D_{10}), mm	0.16
2	Uniformity coefficient (C_u)	2.187
3	Coefficient of curvature (C_c)	1.4
4	IS classification	SP
5	Mean specific gravity	2.62
6	Maximum dry density	1.785
7	Minimum dry density, gm/cc	1.51
8	Relative density of sand (%)	65
9	Optimum moisture content	11.2
10	Angle of internal friction (in degree)	32

SP—Poorly graded sand

2.3 Pile Cap

Mild steel plate is used as a pile cap. Different sizes of pile caps are used in this experiment. The spacing between the piles is maintained as three times the diameter of pile.

2.4 Test Procedure

The soil tank of size 700 mm × 700 mm × 600 mm that is made of iron and glass fibre is used in the experiment. The test is conducted by following IS: 2911 Part IV (1979). As per code, vertical loads are applied in small increments on pile cap. Load is applied using hydraulic jack which is mounted on pile cap, and the other end of hydraulic jack is fixed to loading frame. Strain gauges of sensitivity 0.02 mm are used to measure the settlement. The loading is continued to twice the design load (3.5 kN).

3 Experimental Load-Settlement Curves

Figures 1, 2 and 3 show the load-settlement curves of different configurations of pile groups; those are single pile, 2 × 2 pile group and 3 × 3 pile group, respectively. Diameter and length of piles used in the experiment are 2 cm and 30 cm, respectively. Loads are applied on the pile cap up to twice the safe load as per IS: 2911 Part IV (1979).
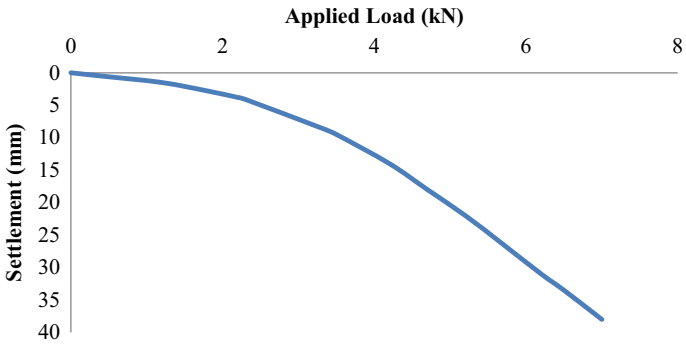
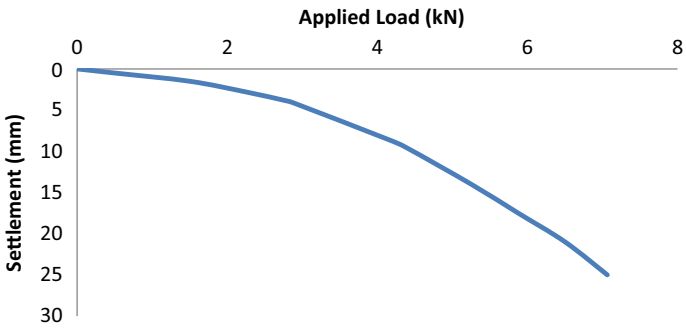**Fig. 1** Load-settlement curve for a single pile of 25 mm diameter

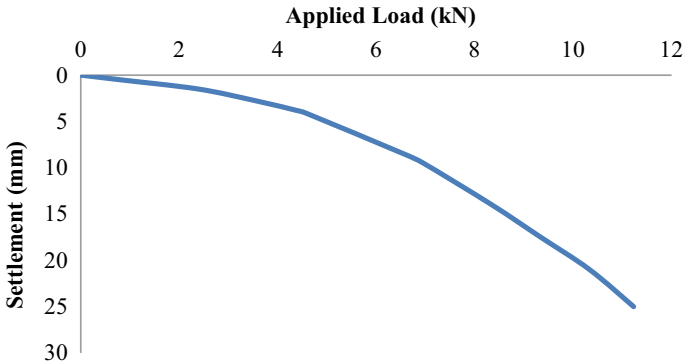**Fig. 2** Load-settlement curve of 2 × 2 pile group

Fig. 3 Load-settlement curve of 3 × 3 pile group

4 Discussions of Experimental Results

Load versus settlement curves drawn from experiments are nonlinear. These curves are not showing peak behaviour that means with increase in pile settlement the vertical load increases. Hence, by using pile load test data, it is not possible to find the failure loads. So, there are many interpretation methods available to find the failure loads, which are already mentioned above.

Load improvement ratio is calculated from experimental results. It is a non-dimensional parameter which shows the variation in load carrying capacity with the change in the number of piles in a group. From experimental results, it is concluded that the load improvement ratio (LIR) increases with the increase in the number of piles. As it is found that the LIR obtained as 3.57 for 2×2 pile group and increases to 8.55 for 3×3 pile group.

The settlement ratio of a pile group is defined as the total settlement of a pile group divided by the settlement of a single pile at the same average load per pile. The settlement ratio decreases with the increase in the number of piles in a group.

5 Interpretation of Ultimate Bearing Capacity from Graphical Methods

Figures 4, 5, 6, 7 and 8 show the load-settlement curves of 25 mm diameter single pile which are plotted based on the pile load test data. There is no specific procedure to find the bearing capacity of piles. Different interpretation methods available to find ultimate bearing capacity; so, the average load is considered as the ultimate bearing capacity (Table 2).

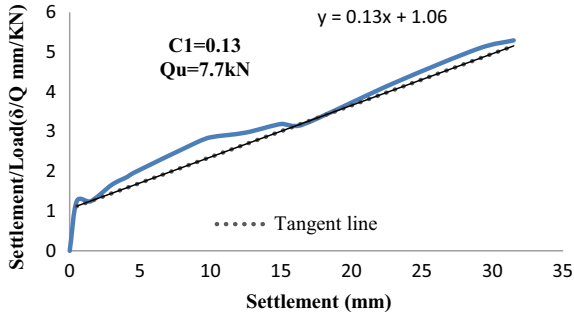**Fig. 4** Load-settlement curves by Davisson's off-set limit load method
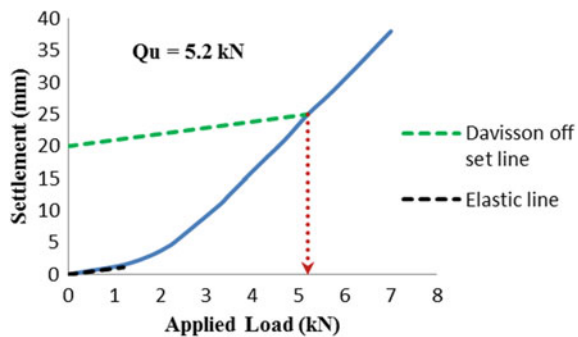
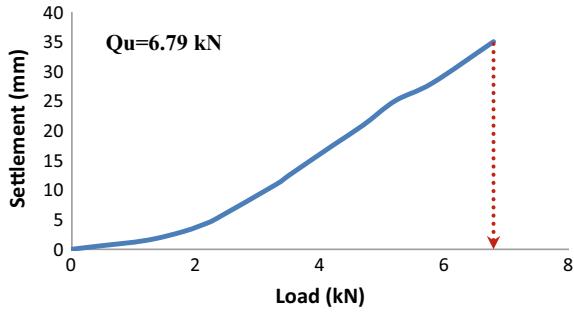**Fig. 5** Load-settlement curves by Chin-Konder method

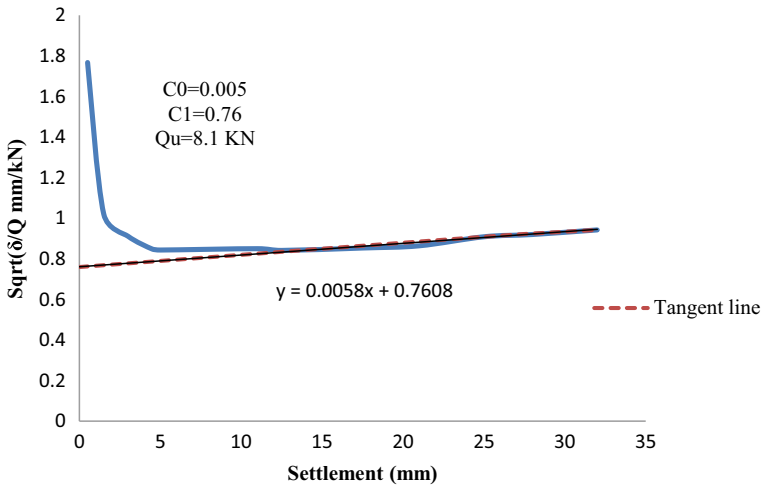**Fig. 6** Load-settlement curves by Fuller and Hoy method

Fig. 7 Load-settlement curves by Brinch Hansen method

Fig. 8 Load-settlement
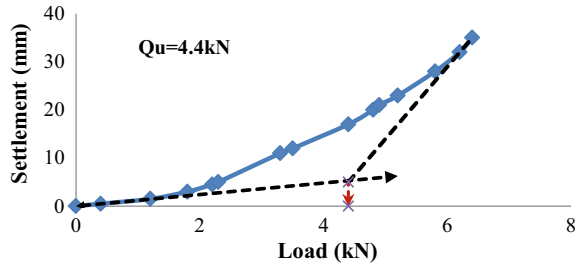curves by tangent
intersection method

Table 2 Failure loads for different configurations of pile groups

Bored piles	Diameter of pile (mm)	Failure loads (kN)				
		Brinch Hansen [5]	Chin-Konder [3]	Fuller and Hoy [4]	Davisson's off-set [6]	Tangent [7]
Single pile	25	8.1	7.7	6.8	5.2	4.4
2 × 2		28.4	27.3	24.3	17.8	15.1
3 × 3		68.2	65.4	58.2	44.6	37.7
Single pile	20	6.5	6.2	5.4	4.2	3.5
2 × 2		22.7	21.8	19.4	14.3	12.1
3 × 3		54.5	52.4	46.6	35.7	30.2

6 Discussions About Ultimate Bearing Capacities Obtained from Graphical Methods

Table 3 shows the Q_g/Q_m values based on different methods, where Q_g = graphical ultimate bearing capacity and Q_m = measured ultimate bearing capacity. From graphical methods, the following discussions are drawn.

1. The average of Q_g/Q_m varies from 1.2 to 0.65 for the Brinch Hansen and tangent intersection method, respectively.
2. Fuller and Hoy method estimated the accurate failure loads. The ratio of Q_g/Q_m value nearly to 1. This shows that the interpreted and measured failure loads are same.
3. Brinch Hansen and Chin-Konder methods show more failure loads, first one shows the relatively more failure loads compare to later.

Table 3 Q_g/Q_m ratios for different configuration of pile groups

Interpreted methods	Single pile (Q_g/Q_m)		2 × 2 (Q_g/Q_m)		3 × 3 (Q_g/Q_m)	
	25 mm dia.	20 mm dia.	25 mm dia.	20 mm dia.	25 mm dia.	20 mm Dia
Brinch Hansen	1.22	1.22	1.19	1.19	1.19	1.16
Chin-Konder	1.10	1.1	1.09	1.09	1.09	1.05
Fuller and Hoy	0.97	0.97	0.97	0.98	0.97	0.99
Davisson's off-set	0.74	0.74	0.71	0.71	0.74	0.71
Tangent intersection	0.68	0.68	0.63	0.63	0.66	0.63

7 Conclusions

Following conclusions are drawn from the pile load test, load-settlement curves, and from five different graphical methods (i.e., Brinch Hansen, Chin-Konder, Fuller and Hoy, Davisson's off-set and tangent intersection method).

1. The behaviour of load versus settlement curve is shown nonlinear. All tests indicate that the load-settlement curves do not show a peak behaviour, i.e., with increase in pile settlement, the vertical load increases.
2. The maximum failure load varies from 7 to 50 kN from a single pile (25 mm diameter) to 3 × 3 pile group.
3. Load improvement ratio is 8.55 for 3 × 3 pile group and it is 3.57 for 2 × 2 pile group.
4. Settlement ratios are decreasing with increasing in the number of piles in a group. Settlement ratio for 2 × 2 pile group to 3 × 3 pile group decreases from 0.66 to 0.25.
5. Comparison of interpreted and measured failure loads showed that the Brinch Hansen and Chin-Konder over-estimate the failure load; remaining three methods under-estimate the failure loads.
6. Fuller and Hoy method approximately gives the same interpreted and measured failure loads.
7. Considerable differences are observed between the graphical ultimate bearing capacities of the piles which decrease to 35% for the piles loaded up to the collapse load and increases up to 120% for the piles loaded to the failure load.
8. Davisson's off-set method gives the poorer results compared to remaining all methods after tangent intersection method.

References

1. Hirany, A., Kulhawy, F.H.: Conduct and interpretation of load tests on drilled shaft foundations. J. Geotech. Geoenviron. Eng. **121**(5) (1988)
2. Hansen, J.B.: Discussion of hyperbolic stress-strain response in cohesive soils. J. SMFD **89**(4), 241–242 (1963). https://doi.org/10.21660/2016.19.20111
3. Chin, F.K.: Estimation of the ultimate load of piles not carried to failure. Proc. Second Southeast Asian Conf. Soil Eng. Singapore **1**, 81–90 (1970)
4. Fuller, F.M., Hoy, H.E.: Pile load tests including quick-load test method conventional methods and interpretations. HRB **333**, 78–86 (1970)
5. Brinch Hansen, J.: Discussion of hyperbolic stress-strain response: cohesive Soil. by Robert L. Kondner. J. Soil Mech. Found. Div. ASCE **89**(4), 241–242 (1963)
6. Davisson, M. T.: High capacity piles. Proc. innovations in found. Const. **52**, (1972)
7. Deb, P., Pal, S. K.: Load-settlement and load-sharing behaviour of a piled raft foundation resting on layered soils. Acta Geotech. Slov. **17**(1), 71–86 (2020)

Behavior of Rigid Footing Rested on a Group of Stone Column

Mrinal Bhaumik, Suresh Prasad Singh, and Megha Biswas

Abstract Raft foundation often adopted for structures constructed on highly compressible soil. Sometimes raft footings are preferred on stone column-improved ground. The current FEM-based numerical study investigated the behavior of a rigid square footing model resting on the surface of a soft ground improved with a group of stone column. To analyze the behavior of the rigid footing, a group of fully penetrating stone columns was constructed beneath the rigid footing. Various parameters such as area replacement ratio, column spacing and relative position of column have been studied. Performance of rigid footing enhances with the increment of area replacement ratio. Bearing capacity improvement was found to be higher at lower settlement level. And a better settlement improvement was observed when footing is acted upon by a higher loading. For larger size raft footing, stone columns arrangements have a significant effect on load-settlement behavior. When stone columns are placed near to the center of the footing, it shows a better improvement in term of settlement and load carrying capacity. A single stone column of equivalent area ratio constructed at the center shows similar behavior as a group of stone column. Different types of failure mechanism were observed for the stone columns placed at different position. Stone columns constructed near the edge of the footing failed by the combined action of bulging and buckling. Whereas, central columns mainly failed by bulging near the top.

Keywords Stone column · Rigid footing · Bearing capacity improvement · Stone column arrangement

M. Bhaumik · S. P. Singh (✉) · M. Biswas
Civil Engineering Department, NIT Rourkela, Rourkela 769008, India
e-mail: spsingh@nitrkl.ac.in

M. Bhaumik
e-mail: mrinal.bhaumik2012@gmail.com

M. Biswas
e-mail: 218ce1019@nitrkl.ac.in

417

1 Introduction

Ground improvement using vibro stone column is one of the most widely accepted techniques adopted in improving soft soil deposit like marine clay [6–10]. It provides a relatively stiffer medium that improves the load carrying capacity of soft soil and accelerates the consolidation settlement by reducing the drainage path. The structures (like embankment, storage tank, lightweight structure, etc.) that can tolerate a few amounts of settlement are preferred to construct on stone column improvement ground. Recently, stone columns are also employed beneath a rigid footing [2–5, 7, 14, 15]. Further, rigid foundation for oil storage tanks is often constructed on stone column-improved ground near the seashore [4]. In these cases, the ground is subjected to a uniformly distributed load. The performance of the stone columns depends upon all-round confinement of the surrounding soil. Sometimes the function of the stone column becomes limited due to low confinement. When stone columns are installed in a large area, one single stone column can be idealized as a unit cell. But, the individual behavior of stone columns beneath a rigid footing is different. The footing near the edge of the raft tends to shift outwards upon loading [5]. Das and Deb [4] presented an analytical solution to understand the behavior of circular rigid raft footing constructed on stone column-improved ground. They idealized the surrounding soil and stone column as a Pasternak shear layer and nonlinear spring system. Castro [2] performed a numerical 2D and 3D analysis on the performance of a group of stone column beneath a rigid square footing. Configuration and arrangement of stone column with different area ratio were studied in this study. A new simplified model suggested where a group of stone column can be replaced with a single central stone column of equal area replacement ratio. Zhou et al. [16] evaluated the failure modes and ultimate bearing capacity of strip footing constructed on stone column reinforced ground. A parametric analysis is conducted by varying aspect ratio, area replacement ratio and surcharge load. El-Garhy and Elsawy [5] also carried out a 3D finite element analysis to investigate the influence of various parameters on the load-settlement behavior of a rigid footing constructed on the granular pile. The settlement improvement achieved and bending moment generated in the rigid raft by the various configuration of stone columns. Castro [3] studied the performance of a group of encased stone column beneath a rigid footing. A 2D and 3D finite element analysis is carried out and presented the concept of critical length of encasement as well as column length. The influences of several parameters such as length of the column, length of the encasement, column arrangement are investigated in the load-settlement response of the rigid raft footing.

However, a scarce of information is available on the performance of raft footing on stone column-improved ground. This numerical study presents a 3D finite element model to investigate the influence of various parameters on the bearing capacity improvement as well as settlement improvement.

2 Numerical Models

A 3D finite element model was developed using FEM program Plaxis 3D. A rigid square footing was assumed to be constructed over a soft clay layer of 20 m thickness. A sand blanket was provided on the top surface of the clay layer. For the sake of simplicity, water table was considered at the top of the clay layer. A 50 m × 50 m clay surface was taken to avoid boundary constraint on the load-settlement behavior of footing. A schematic diagram of the used model is presented in Fig. 1. Finite element discretization was done using ten noded tetrahedral elements. To avoid the complexity of the model and to reduce calculation time, the load-settlement analysis was carried out with an axisymmetric part of the rigid footing (Fig. 2). Only the vertical movement was allowed along the side of the model, and the movement of the base was kept restrained. Raft footing was idealized as a plate element available in the program.
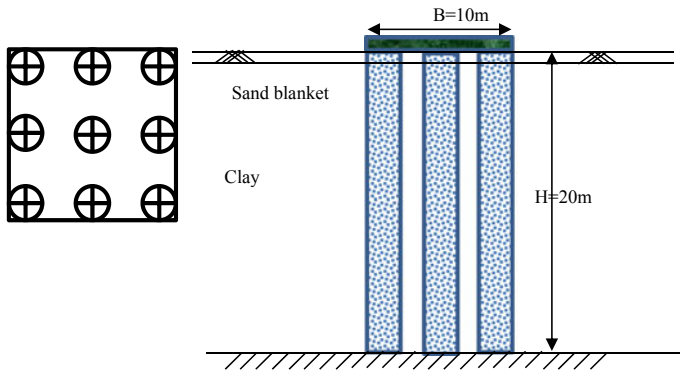

Fig. 1 Layout of a rigid footing on a group of stone columns in the clay layer of 20 m thickness
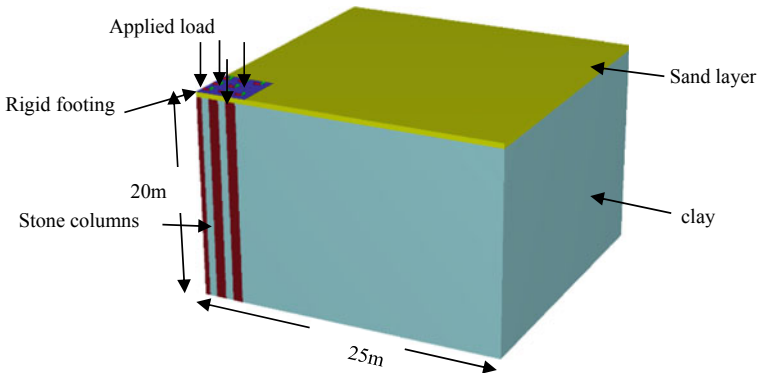

Fig. 2 Layout of the 3D reference model

Table 1 Material properties [1]

Materials	E (kPa)	Cu (kPa)	Φ (°)	Ψ (°)	μ	Υ_{dry} (kN/m^3)	Υ_{bulk} (kN/m^3)
Clay	2,150	7	0	0	0.47	13.6	18.3
Sand	20,000	0.3	30	5	0.3	15.5	18.5
Stone	55,000	0.3	43	10	0.3	16.62	20.1

Long-term behavior of clay can be modeled by two methods: (i) drained analysis using effective stress parameters, (ii) using undrained condition and effective stress parameters followed by consolidation [7]. The study was carried out after a sufficient time lapsed after loading and considering the consolidation of the clay layer already occurred by drainage of excess pore water through stone columns. A drained analysis was carried out by assuming all the pore pressure was dissipated. Considering the elasto-plastic behavior of the materials, Mohr–coulomb failure criteria were adopted [1, 3, 11–13]. Assuming perfect bonding between the column and soil, no interface element was considered.

3 Reference Case

Loading was applied through a rigid footing of size 10 m × 10 m. Table 1 shows the properties of the clay layer and column material adapted from well-established literature. In the case of stone and sand, a small value of cohesion was assumed to avoid calculation difficulty. A 0.5 m thick sand layer was provided at the top of the clay layer. In this reference case, the stone columns are extended through the clay layer. Although stone column having length more than critical length does not indicate any further significant improvement in load carrying capacity, it may be effective as a vertical drain to accelerate consolidation. As this numerical analysis is based on the long-term behavior of surrounding soil, both the stone columns (floating type and end bearing) of length more than the critical length will not affect the results discussed here. Stone columns of diameter 1 m were constructed in a square grid pattern beneath the rigid raft.

4 Result and Discussion

The load-settlement behavior of rigid raft on unreinforced soil and reinforced with group of end bearing stone column was studied using FEM program Plaxis 3D. The influence of area replacement ratio, column configuration, column spacing and modes of failure of individual stone columns in the group has been investigated.

4.1 Area Replacement Ratio (A_r)

Area replacement ratio (A_r), i.e., the quantity of soil replaced by granular materials is a very significant parameter to control the degree of improvement. Here, A_r is calculated as the ratio between the sums of area of columns to the area of raft footing. As uniformly distributed load was applied on the footing, hence the loaded area and the raft area are same. The effect of area replacement ratio on both bearing capacity improvement and settlement improvement was studied. Bearing capacity improvement is presented here as the ratio of bearing capacity of reinforced ground to that of the unreinforced one. Further, settlement improvement was calculated at different loading level as well as at ultimate load carrying capacity of footing on unreinforced soil. Settlement improvement ratio is presented as the ratio between the settlement of unreinforced ground and settlement of reinforced ground at that load. To study the effect of area replacement ratio, stone column of group 2×2, 3×3, 4×4, 5×5, 6×6, 7×7 was constructed beneath the footing. Figure 3 shows the column arrangements for which the improvement factors were calculated, and in all cases, diameter of column was same.

Figure 4 presents the bearing capacity improvement with inverse area ratio. Here, improvement was calculated at different settlement level (i.e., 50, 100, 150 and 200 mm). A rapid change of improvement was observed when inverse area replacement ratio is less than 15. Further, the bearing capacity improvement was found to be higher at lower settlement. Figure 5 presents the variation of settlement improvement with inverse area ratio at different applied stress (i.e., 25, 30, 35 kPa and ultimate load carrying capacity of unreinforced ground). Settlement improvement decreases with the increase of inverse area replacement ratio. Further, the rate of reduction is higher when inverse area replacement ratio is less than 15. It was observed that the settlement improvement was higher at higher loading. In all cases, stone columns are equally distributed beneath the rigid footing. This improvement depends upon the arrangement of the stone columns which is discussed in the following sections.
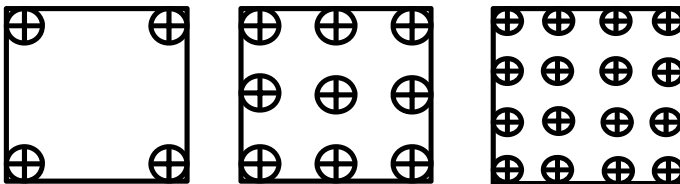

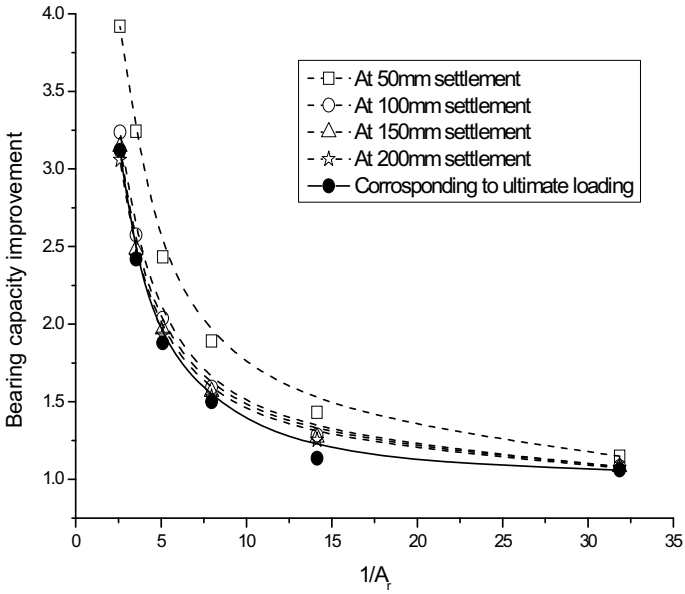**Fig. 3** Column configuration adopted to study the effect of area ratio

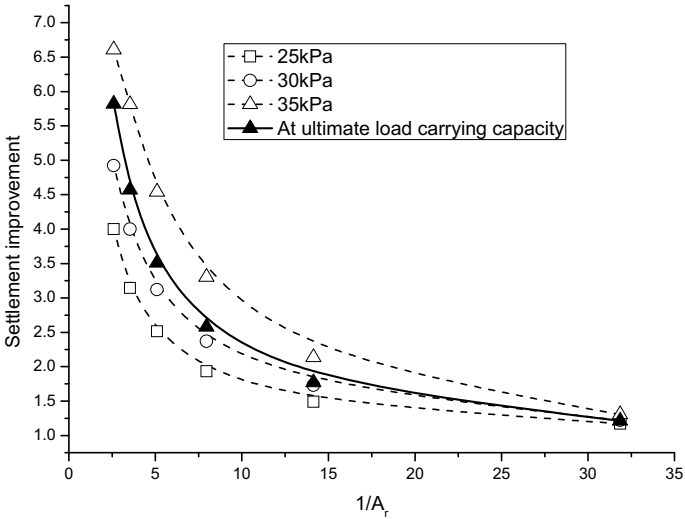**Fig. 4** Variation of bearing capacity improvement with inverse area ratio

Fig. 5 Variation of settlement improvement with inverse area ratio

4.2 Column Position

When large numbers of stone columns are constructed in a group, then the behavior of interior columns is nearly same, and they can be approximated as a single stone column in a unit cell. But when stone columns are constructed beneath a rigid footing, the all-around confinement generated due to the overburden pressure is not identical except the central column. The load-settlement performance of the footing significantly depends upon the increased confinement around the stone columns during loading. So, in this case, relative position of column is more meaningful than the spacing of stone columns. In this study, a group of 4, 9, 16, 25 and 36 numbers of stone columns were taken. In each case, relative column position was shifted toward the center by keeping area ratio constant. The detailed information of the study is shown in Table 2.

Relative bearing capacity improvement and settlement improvement of reinforced ground were calculated over an unreinforced ground. The position of the columns was shifted toward the center of the raft from the edge by reducing their center to center spacing, and finally, one single stone column was constructed at the center of equivalent area replacement ratio. Figure 6 shows the studied relative column positions beneath the rigid footing.

Figures 7 and 8 shows the performance of the footing gets improved when stone columns are placed near to the center. Two main criteria play behind this characteristic: (1) as the rigid footing constructed on the granular layer, then the stress accumulation will be there near to the center, so the presence of stone column near to the center improves the performance. (2) On the other hand, stone columns near to the center experience higher lateral confinement increased due to overburden pressure of the rigid footing. By maintaining constant area ratio, spacing between the columns was subsequently decreased, and column group shifted toward the center. A clear enhancement of the performance was found when columns are toward center. For this particular case, this increment was observed up to a distance between the exterior column and center of the raft decreased to 3 m. So, a minimum edge distance of 1–1.5 times the diameter of column is effective for a constant area replacement ratio. The bearing capacity and the settlement of a group of stone column were compared with the single central column of equivalent area ratio, and the results were found to be similar in both cases.

4.3 Failure Mechanism

Failure mechanism of stone columns beneath a rigid footing is quite different than the stone columns constructed in an infinite group. Bulging type failure is predominant in both cases. The central column senses symmetrical all-round confinement developed due to overburden pressure from raft footing, whereas, the columns other than the central column, are acted upon a higher lateral pressure inside the footing area. As a

Table 2 Detailed information of the studied case

Case no.	Number of column	A_r (%)	s/d	D_c (m)	Edge distance (m)
1	4	0.031	9	4.5	0.5
			7	3.5	1.5
			6	3	2
			4	2	3
			2	1	4
			0	0	5
2	9	7.07	4.5	4.5	0.5
			3.5	3.5	1.5
			3	3	2
			2	2	3
			0	0	5
3	16	12.57	3	4.5	0.5
			2.33	3.5	1.5
			2	3	2
			1.67	2.5	2.5
			0	0	5
4	25	19.63	2.25	4.5	0.5
			1.75	3.5	1.5
			1.5	3	2
			1.25	2.5	2.5
			0	0	5
5	36	28.27	1.8	4.5	0.5
			1.4	3.5	1.5
			1.2	3	2
			0	0	5

Where s/d spacing to diameter ratio, D_c distance of the exterior column from the center of the raft

result, bulging and buckling happens simultaneously in the peripheral columns. And this phenomenon is more predominant in the stone columns near the edge. Figure 9 shows the different failure pattern of the individual stone columns placed at different position. Again when columns are constructed more close to center, load bearing capacity also increase due to better confinement.

Bulging depth of the individual stone columns also differs with the relative position. A central column experiences bulging at higher depth than the columns away from the center.
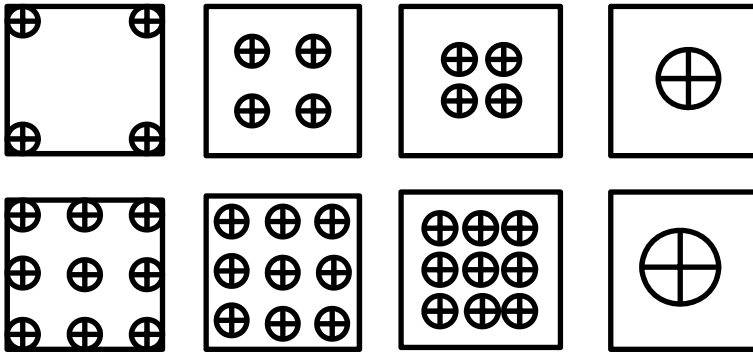
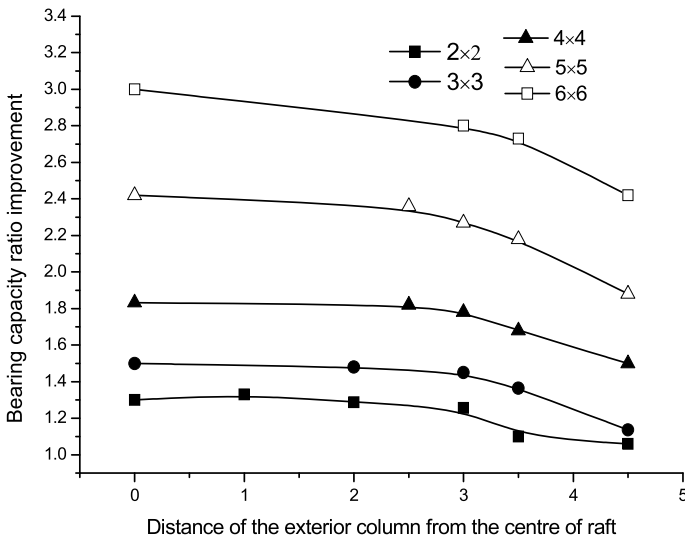**Fig. 6** Column arrangement for 2 × 2 and 3 × 3 group of stone column

Fig. 7 Bearing capacity improvement at different column arrangement

5 Conclusions

The performance of a square rigid footing on a stone column reinforced soft ground has been studied in this analysis. A full scale 3D finite element analysis of the stone column treated soil and untreated soft ground was investigated using Plaxis program. A series of parametric study was conducted to examine the effect of various design parameters such as area replacement ratio (A_r), spacing and different arrangement of granular pile, edge distance from the exterior column and diameter of stone column (d). Influence of these parameters on settlement improvement and load carrying
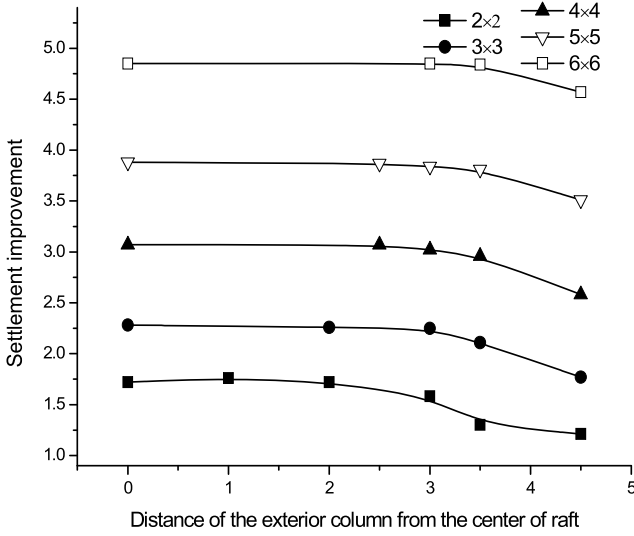
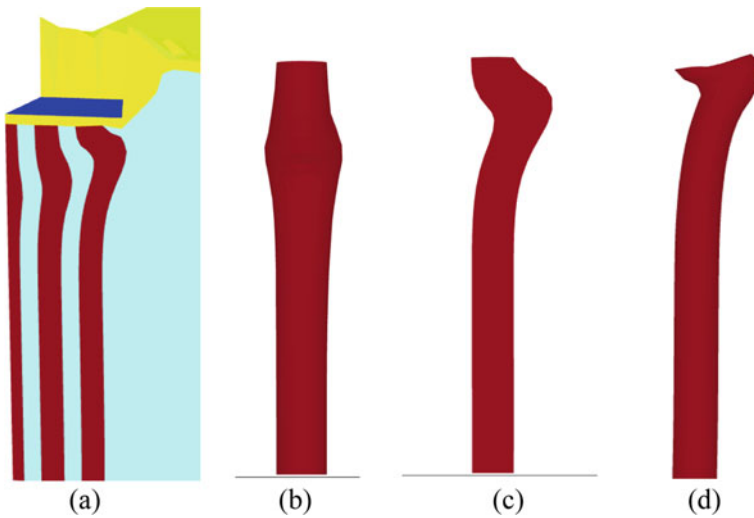**Fig. 8** Settlement improvement factor at different column arrangement

Fig. 9 Failure pattern of stone columns: **a** at group, **b** central column, **c** intermediate column, **d** column near edge

capacity improvement of the rigid raft was investigated. Based on the results obtained, the following conclusions can be drawn:

Settlement improvement as well as load carrying capacity improvement was observed to be increased with area replacement ratio. A higher load carrying

capacity improvement was found at lower settlement level. Further, a better settlement improvement of the reinforced ground was observed when higher loading is applied on the footing. A rapid change of the improvement factor is noticed when inverse area ratio is less than 15. Relative column position has a significant effect on performance of rigid footing. Stone columns placed closer to the center show better improvement in performance than placed near the edge. For a group of stone columns, a minimum edge distance of $1–1.5D$ is found to be more effective for a particular area replacement ratio. Failure mechanism of individual stone columns depends upon their relative position. Only the central column failed by uniform bulging near the top. Whereas the stone columns other than central column failed by non-uniform bulging, due to uneven lateral pressure. Therefore, stone columns near the edge mainly failed by combined action of bulging and buckling.

References

1. Ambily, A.P., Gandhi, S.R.: Behavior of stone columns based on experimental and FEM analysis. J. Geotech. Geo-Environ. Eng. **133**(4), 405–415 (2007)
2. Castro, J.: Numerical modelling of stone columns beneath a rigid footing. Comput. Geotech. **60**, 77–87 (2014)
3. Castro, J.: Groups of encased stone columns: influence of column length and arrangement. Geotext. Geomembr. **45**(2), 68–80 (2017)
4. Das, A.K., Deb, K.: Modeling of uniformly loaded circular raft resting on stone column-improved ground. Soils Found. **54**(6), 1212–1224 (2014)
5. El-Garhy, B., Elsawy, M.: Effect of different parameters on the behavior of strip footing resting on weak soil improved by granular piles. Int. J. Geo-Eng. **8**(1), 4 (2017)
6. Elshazly, H., Hafez, D., Mossaad, M.: Settlement of circular foundations on stone-column-reinforced grounds. Proc. Inst. Civ. Eng.-Ground Improv. **11**(3), 163–170 (2007)
7. Greenwood, D.A.: Mechanical improvement of soils below ground surface. In: *Proceedings of Ground Improvement Conference*, Institute of Civil Engineering, pp. 9–29 (1970)
8. Killeen, M.M., McCabe, B.A.: Settlement performance of pad footings on soft clay supported by stone columns: a numerical study. Soils Found. **54**(4), 760–776 (2014)
9. Lee, J.S., Pande, G.N.: Analysis of stone-column reinforced foundations. Int. J. Numer. Anal. Meth. Geomech. **22**(12), 1001–1020 (1998)
10. Madhav, M.R., Vitkar, P.P.: Strip footing on weak clay stabilized with a granular trench or pile. Can. Geotech. J. **15**(4), 605–609 (1978)
11. Madhav, M.R., Sharma, J.K., Sivakumar, V.: Settlement of and load distribution in a granular piled raft. Geomech. Eng. **1**(1), 97–112 (2009)
12. McKelvey, D., Sivakumar, V., Bell, A., Graham, J.: Modelling vibrated stone columns in soft clay. Proc. Inst. Civ. Eng.-Geotech. Eng. **157**(3), 137–149 (2004)
13. Mitchell, J.K., Huber, T.R.: Performance of a stone column foundation. J. Geotech. Eng. **111**(2), 205–223 (1985)
14. Ng, K.S., Tan, S.A.: Design and analyses of floating stone columns. Soils Found. **54**(3), 478–487 (2014)
15. Ng, K.S., Tan, S.A.: Simplified homogenization method in stone column designs. Soils Found. **55**(1), 154–165 (2015)
16. Zhou, H., Diao, Y., Zheng, G., Han, J., Jia, R.: Failure modes and bearing capacity of strip footings on soft ground reinforced by floating stone columns. Acta Geotech. **12**(5), 1089–1103 (2017)

Design and Construction of Rock Socketed Pile Foundation for Bridges—Case Study on Road Project in Madhya Pradesh, India

Avik Kumar Mandal, S. Sailesh, and Pradyot Biswas

Abstract The design and construction of rock socketed pile foundation involve finalization of required length of rock socket based on the detailed study of the founding rocky strata and also include the establishment the safe load carrying capacities of pile foundations corresponding to its rock socket. Such detailed assessment of safe and allowable load carrying capacities of rock socketed bored cast-in-situ pile foundations is done for the new widened bridges of four-lane configuration along the project corridor in between Biaora and Dewas section of NH3 in the state of Madhya Pradesh. Those bridge structures along the project road are founded over the bored cast-in-situ concrete pile shaft which was penetrated through the overburden soil layers and then finally socketed inside the underlying highly to moderately and slightly weathered basaltic rock of varying depth. This paper presents the above-said typical project case study on the details of geotechnical design assessment of rock socketed pile foundation covering its safe vertical and lateral load carrying capacities for the bridges. The different types of field load test namely "Vertical and Lateral Pile Load Tests" over the "Test Pile" and "Working Pile" are conducted to establish the estimated safe load carrying capacity of rock socketed pile foundation. The results of these pile load tests are also reported here in this paper. The required "Pile Penetration Ratio (PPR)" of the desired socket length inside the founding rocky strata is fixed based on the nature of rock as explored through investigation. This pre-decided "PPR" is adopted during installation of pile foundation inside the underlying rocky strata.

Keywords Bored cast-in-situ concrete (RCC) pile foundation · Rock socketing of pile · Pile capacity

A. K. Mandal (✉) · S. Sailesh · P. Biswas
LEA Associates South Asia Pvt. Ltd., New Delhi, India
e-mail: avik@lasaindia.com

S. Sailesh
e-mail: sailesh@lasaindia.com

P. Biswas
e-mail: pradyotbiswas@lasaindia.com

429

1   Introduction

There are numbers of major river bridges and railway over bridges (ROB) along the project road of 140 km stretch starting from Biaora to Dewas in the state of Madhya Pradesh. The project road is part of important Agra–Mumbai section of the National Highway No. 3 (i.e., NH-3). Some of the major river bridges and one ROB structure along the said project road were built over the group of bored cast-in-situ concrete (RCC) pile shaft of 1200 mm diameter which was founded through the overlying soil strata of variable thickness and finally socketed into the weathered basaltic rock. The pile foundations of the said bridges and ROB are designed to resist vertical and horizontal forces due action of the different types of loads namely dead loads, live loads, seismic loads, wind loads, water current forces (in case of river bridges) and other loads over those structures. The river bridges have varying unsupported pile lengths due to the occurrence of scour of loose unconsolidated channel bed material of silty/clayey as well as sandy nature overlying the weathered basalt rock. Due to the unsupported pile shaft lengths of the major river bridges in scour condition, there is possibility of occurrence of large deflections under the applied horizontal loads in addition to the large amount of vertical loads in static as well as in seismic condition. In case of ROB structure, the pile foundations are subjected to higher vertical and horizontal loads due to increased height of piers and abutments supporting the long span of the superstructure. So, the pile foundations of the above-said major river bridges and ROB structures require adequate socketing inside the underlying rock layer after penetrating through the overlying soil strata to provide stability and achieve satisfactory pile capacities to sustain the high vertical and lateral loadings. Again due to the variable depth of underlying rock layer and its engineering quality, the design of socket length of pile shaft inside the rock and finalization of the termination level of pile tip are very much challenging tasks.

The present paper describes the above-said one typical project case study on the details of geotechnical design assessment and construction aspects of rock socketed pile foundation for one typical major river bridge and ROB structure.

2   Geotechnical Investigation and Subsurface Stratifications

To characterize and assess the subsurface conditions, a comprehensive geotechnical exploration work covering detailed field and laboratory investigation had been carried out at each and every pier and abutments of the river bridges and ROB structures. The field investigation work was comprised of soil borings and rock drillings, performing in-situ tests, obtaining and preserving soil, rock and water samples and field observations of the subsurface conditions and special phenomenon including groundwater table. The laboratory-testing program included testing samples (soil, rock, water) as collected from site to characterize the geotechnical/geological properties. The field and laboratory-testing works had been performed as per provision of latest version of related guidelines like Bureau of Indian Standards (BIS), Indian Road

Congress (IRC) namely IRC:78-2014 [1] and Ministry of Road Transport and Highways (MORT&H) Specifications for Road and Bridge Works (Fifth Revision) [2]. The exploratory boreholes at pier and abutments locations of the river bridges and ROB structures were terminated by extending up to 10.00 m inside the underlying rock layer. The general geology of the area, position of groundwater table (GWT) and site-specific subsurface conditions are described in the subsequent sections briefly.

2.1 General Geology of Project Area

The oldest group of rocks comprising Archaeans and Proterozoic formation constitutes nearly 45% area of the State of Madhya Pradesh (MP). The next younger formation of Carboniferous to lower Cretaceous comprising Gondwana Super Group covers 10% area while the formation of Cretaceous to Paleocene comprising mostly Deccan Trap basalt constitutes 38% area of the State of MP. In the studied project area in between Biaora and Dewas, the Deccan Trap basalt is observed.

Biaora and Dewas both the locations are part of Chambal river basin. Biaora is a part of Rajgarh District, and Dewas is a part of Dewas District of Madhya Pradesh. Rajgarh District forms the part of Malwa plateau generally an undulating topography. The Vindhyan hill range occupies the south-eastern part of the district. The basaltic rocks of Malwa plateau occupy almost entire district except south-eastern part. The Vindhyans are having Shale and Sandstone with thin layer of alluvium. The Dewas District lies in the central part of the state. The city is located on the level plains of the Malwa plateau; to the south, the land rises gently to the Vindhya Range, which is the source of the Chambal and Kali Sindh Rivers.

2.2 Location of Groundwater Table

The recorded depth of "Groundwater Table (GWT)" in various explored boreholes in the bridge and ROB structures along the project road was varying from 3.40 to 11.50 m from the exiting ground level (EGL) or bed level. For designing of pile foundation of structures, the water table was considered at ground level anticipating the fluctuations in the measured water levels due to seasonal variation and corresponding to the critical condition which may arise during or immediately after the monsoon during the serviceability life of the structures.

2.3 Subsurface Stratifications

The site-specific subsurface conditions at the major river bridges and ROB structure sites have been characterized using the field and laboratory-testing data obtained during geotechnical exploration. Broadly, the foundation profile comprises following major strata as found in the investigation at the major river bridge and ROB structure locations.

1. Medium Stiff to Hard Silty Clay/Clayey Silt with low to high plasticity (CL/CI/CH) of variable thickness (0.00–17.00 m)
2. Medium Dense to Dense/Very Dense Silty Sand/Poorly graded Sand (SM/SP) having 0.00–4.50 m thickness
3. Completely weathered rock in the form of disintegrated granular material (residual soil) having thickness maximum up to 1.50 m
4. Highly Weathered Fractured/Highly to Moderately Weathered/Moderately Weathered/Slightly Weathered Moderately Strong Bed Rock (basalt) with varying engineering quality and explored thickness maximum up to 10.00 m.

The top level of the underlying rock and its engineering quality as encountered was widely varying in all the boreholes in any particular structure location. Intermediate bands of highly weathered rock layers were also found within the moderately to slightly weathered rock in some of the boreholes of the structures. The range of variations of encountered depth of rock top level from existing ground level (EGL), explored thickness, total core recovery (TCR), rock quality designation (RQD), rock crushing strength, rock mass rating (RMR) and the class of rock layers as per its RMR as explored in case of one typical major river bridge and ROB are shown in Table 1.

Table 1 Range of engineering properties of rock

Name of structure	Bore hole location and number	Encountered depth from EGL (m)	TCR (%)	RQD (%)	Rock crushing strength (ton/m^2)	Rock mass rating (RMR)	Class of rock
Major bridge over river Kalisindh	BH-A1	17.00–27.00	43.33–93.33	0.00–93.33	3104–6638	19–67	Very poor to good
	BH-P1	12.50–18.50	40.00 - 98.67	0.00 - 94.00	5974 - 7440	19 - 67	Very poor to good
	BH-P2	17.00–24.00	11.00–99.33	0.00–84.66	3190–7285	9–61	Very poor to good
	BH-P3	16.50–22.50	41.33–99.33	0.00–92.00	4367–6290	9–74	Very poor to good
	BH-P4	7.00–16.00	25.00–96.00	0.00–88.66	4996–7115	19–64	Very poor to good

Table 1 (continued)

Name of structure	Bore hole location and number	Encountered depth from EGL (m)	TCR (%)	RQD (%)	Rock crushing strength (ton/m^2)	Rock mass rating (RMR)	Class of rock
	BH-P5	9.00–15.00	28.66–98.00	0.00–97.00	6306–7596	22–67	Poor to good
	BH-P6	6.00–12.00	13.00–94.00	0.00–94.00	4052–6446	9–67	Very poor to good
	BH-P7	11.50–20.00	8.00–93.34	0.00–90.00	3888–7619	5–74	Very poor to good
	BH-A2	12.00–22.00	26.67–94.67	0.00–86.00	4372–6205	19–55	Very poor to fair
ROB @ 256 + 730 km	BH-A1	7.00–17.00	41.33–98.00	0.00–69.00	2186–3544	15–64	Very poor to good
	BH-P1	8.00–18.00	29.00–83.00	0.00–83.00	2522–5790	12–56	Very poor to fair
	BH-A2	6.40–16.50	32.00–85.00	0.00–69.00	2467–5464	18–50	Very poor to fair

From the above table of engineering properties of underlying rock layers, it can be noted that the TCR is varying from 8 to 99.33%, and RQD is varying from 0 to 97%. The rock crushing strength of the explored rock layers ranges from 2186 ton/m^2, i.e., 21.86 MPa to 7619 ton/m^2, i.e., 76.19 MPa. At the top part of the rock layer where the RQD is 0% with core recovery, the equivalent rock crushing strength corresponding to the "Point Load Strength Index (PLI)" of the tested rock specimen is reported. In case of rock sample having RQD, the crushing strength is reported as per the "Uniaxial Crushing Strength (UCS)" value of the rock layer. The engineering quality of explored rock layers is varying from "Very Poor/Poor" to "Fair/Good" nature as per the overall rating of rock mass based on the guidelines given in IS 13365 (Part I) [3], in accordance with the "Geo-mechanics Rock Mass Classification System (after Bieniawski 1998)". At top part of the explored rock layers mostly within 2.00–3.00 m of depth immediately below the overlying granular residual soil is highly fractured, moderately strong and of "Very Poor/Poor" nature. However, the quality of underlying bed rocks becomes stronger and moderately to slightly fractured and of "Fair" to "Good" nature with increase in depth below.

3   Geotechnical Design of Rock Socketed Pile Foundation

Deep foundations in the form of "Bored Cast-in-situ RCC Pile Foundations" of 1.20 m diameter having shaft length varying from 8.25 to 16.60 m were adopted in the design for the structures namely bridges over major rivers and ROB. The selection of foundation was based on the considerations of availability of suitable load bearing strata in the form of underlying rock layers having adequate vertical compression and uplift capacity and also the required horizontal resistance against the various kinds of applied loads which can ensure enough stability of the structure. The penetration of single pile shaft inside the underlying weathered basalt rock, i.e., designed rock socket length of the pile shaft was varying from 1.86 to 2.40 m in case of bridges over major rivers and 2.40 to 3.18 m for the ROB structure satisfying the availability of adequate resistance, i.e., vertical and horizontal load carrying capacity.

The geotechnical design of pile foundations socketed into the underlying rock includes finalization of socket length inside the rock layer for carrying maximum applied horizontal loads and moments at rock top in addition to the provision of adequate vertical compression and uplift load carrying capacity.

3.1   Length of Rock Socket for Carrying Horizontal Load and Moments at Rock Top

The capacity of the rock socketed pile to withstand the lateral loads depends on the rigidity of the pile as well as the load deformation characteristics, thickness of the soil and rock strata in which the pile is rock socketed. The lateral load carrying capacity and corresponding moment carrying capacity of the single pile have been done with due consideration of the lateral resistance offered by the surrounding soil above the rock socketing portion up to the scour level or pile cut-off level whichever is lower, in addition to the resistance offered by the portion of rock socket. The effect of lateral resistance of the surrounding soil above the rock socket is considered in the form of reducing the "Free Cantilever Moment" at top of rock socket depending upon the ratio of the free, i.e., unsupported length of pile shaft below the pile cut-off, i.e., "L_1" and stiffness factor namely "R" or "T" of the surrounding soil, i.e., (L_1/T) or (L_1/R) corresponding to the pile head conditions namely "Free Headed Pile" for single row of piles and "Fixed Headed Pile" for multiple rows of piles under any group, as per the guidelines given in "Clause No. C-4.3 of Appendix-C of IS 2911 (Part 1/Sec 2): 2010 [4]".

The rock socket length, i.e., "L_s" of pile having the pile tip as fixed into rock, is satisfied corresponding to the "Moment Carrying Capacity of Pile" as per the following equation given in "Clause no. 9.2 of Appendix-C of IRC:78-2014 [1]".

$$L_s = 2 * H/(\sigma_1 * D) + \text{SQRT}[\{4 * H^2/(\sigma_1^2 * D^2)\} + \{6 * M/(\sigma_1 * D)\}] \quad (1)$$

where

1. "*D*" is the diameter of the pile shaft.
2. "*H*" is the maximum horizontal force at top of the rock socket.
3. "*M*" is the maximum actual moment at top of the rock socket which is obtained from the maximum "Free Cantilever Moment (*M′*)" by multiplying it with the "Moment reduction Ratio (*m*)" as per the guidelines of IS: 2911 (Part 1/Sec2) [4], i.e., $M = M' \times$ Moment Reduction Ratio (*m*).
iv. "σ_1" is the permissible compressive strength in rock socket which is lesser of 30 kg/cm^2 or $0.33 * q_c$, "q_c" being the average unconfined, i.e., uniaxial compressive strength of rocks in the socket. The permissible compressible strength in rock socket under wind and seismic conditions is taken as 25% more of its value under static condition, i.e., $(1.25 * \sigma_1)$.

The maximum horizontal force (*H*) and corresponding maximum moment (*M*) at top of rock socket under static, wind and seismic conditions, diameter (*D*) of pile shaft, permissible compressive strength (σ_1) in rock socket and the corresponding minimum required socket length (L_s) for the pile shaft under the piers and abutments as estimated using the above equation no. 1 for one typical major river bridge and ROB are shown in Table 2.

Table 2 Required minimum length of rock socket for resisting horizontal loads and moments as per IRC:78-2014 [1]

Name of structure	Pier (P)/Abutment (A)	Pile diameter (m)	Maximum horizontal force at top of rock socket (ton)	Maximum actual moment at top of rock socket (ton-m)	Permissible compressive strength in rock socket (ton/m^2)	Minimum required length of rock socket (m)
Major bridge over river Kalisindh	A1	1.20	41	175	375	1.72
	P1	1.20	34	217	375	1.90
	P2	1.20	32	265	375	2.03
	P3	1.20	34	263	375	2.03
	P4	1.20	45	191	375	1.81
	P5	1.20	44	203	375	1.85
	P6	1.20	57	185	375	1.84
	P7	1.20	35	213	375	1.89
	A2	1.20	43	220	375	1.91
ROB @ 256 + 730 km	A1	1.20	74	210	375	2.03
	P1	1.20	20	60	375	1.00
	A2	1.20	83	231	375	2.16

From the above-tabulated summary, it is observed that the minimum required rock socket length was varying from 1.72 to 2.03 m, i.e., around 1.5 times of pile diameter and even more than that in case of the major river bridge. Similarly, the minimum rock socket length was required as 1.00 m, i.e., around one diameter of pile shaft under the pier and 2.03–2.16 m, i.e., around 2.0 times of pile diameter for the abutments of the ROB structure.

As per the guidelines given in IRC:78-2014 [1], in case of rock socketed pile, for the satisfactory performance of the socket as fixed tip, the rotation of pile shaft at the top of rock socket for the fixed condition should be very limited and does not exceed 5% of the pile shaft rotation for the pinned condition at the top of socket. The virtual depth of fixity of the pile shaft was designed as located inside the middle of the length of rock socket to satisfy the above-said IRC:78-2014 [1] criteria of pile shaft rotation and corresponding permissible pile top deflection maximum up to 1% of pile diameter of 1.20 m, i.e., 12 mm. The rock socket length as decided based on the requirement of resisting the maximum horizontal load and moments at top of rock socket was also verified against the maximum applied vertical loads for any single pile shaft in the group.

3.2 Vertical (Axial Compressive) Load Carrying Capacity

The total vertical, i.e., axial compressive load carrying capacity of pile foundation is usually a combination of skin friction along the pile shaft surface and end bearing resistance at pile tip. However, as per IS 14593:1998 [5] and IRC:78-2014 [1] guidelines, the vertical compressive load carrying capacity of pile foundation socketed in rock is estimated from the side friction along the pile shaft only in rock socket portion and the end bearing resistance of rock at the proposed pile tip. As per the above-mentioned IS and IRC guidelines, the side friction along the pile shaft in the overburden soil portion has not been considered. As per the available guidelines, the important factors which influence the load carrying capacity of rock socketed pile shaft are the available strength inside socket, extent of fracturing and deformation modulus of rock mass, the condition of the walls and base of the rock socket and the geometry of the rock socket.

Since the underlying rock encountered in the project site was weathered "Basalt" of sound nature where cores were obtained mostly with RQD > 0% and uniaxial crushing strength of the rock mass was determined directly from the UCS test, so the method based on the "Uniaxial Compressive Strength of Rock" as per the "Clause No. 6.5.1.1 of IS 14593:1998 [5]" was used for the determination of safe vertical (axial) compressive load carrying capacity of the single pile shaft socketed into the rock. As per the IS 14593:1998 [5] guidelines, the expression for the determination of safe vertical load carrying capacity (Q_s) of the rock socketed bored concrete pile foundation based on the uniaxial compressive strength is given below.

$$Q_s = \left(q_c * N_j * N_d * A_p\right) + \left(q_c * A_s * \alpha * \beta\right) \tag{2}$$

where

1. "q_c" is the uniaxial compressive strength of rock ("q_c" is at pile tip, and "q_s" is along pile socket)
2. "N_j" is the empirical coefficient based on "spacing of discontinuities" in rock mass as per "Fig. 2" or "Table 4" of IS:12070-1987 [6]
3. "N_d" is the depth factor, i.e., "N_d" = [0.80 + 0.20 * (Length of rock socket/Diameter of pile shaft inside rock socket)] ≤ 2.00
4. "A_p" is the base area of pile shaft inside rock, i.e., A_p = pi() * D^2/4, where "D" = Pile shaft diameter
5. "α" is the rock socket slide resistance reduction factor based on rock strength as per "Fig. 1" of IS 14593:1998 [5]
6. "β" is the rock socket correction factor based on rock mass reduction factor (j) as per "Fig. 2" of IS 14593:1998 [5]
7. "A_s" is the surface area of pile shaft inside rock, i.e., A_s = pi() * Pile shaft diameter inside rock socket (D) * Length of rock socket (L_s).

The value of "q_c" was taken as the average value of uniaxial crushing strength of rock mass present along the side wall of socket for estimating the side socket shear resistance. For estimating the point, i.e., end bearing resistance of pile socket tip, the average value of uniaxial crushing strength (q_c) of rock available at pile tip was considered. The average value of uniaxial crushing strength of rock mass for estimating the load carrying capacity pile shaft socketed into rock should preferably be restricted maximum up to the ultimate value of unconfined, i.e., uniaxial crushing strength of the grade of pile concrete from the consideration of pile concrete and rock interaction behavior as it is recommended in many popular guidelines namely FHWA (1999) [7], NAVFAC DM-7.2 (1982) [8] and AASHTO (1996) [9] design methods. In conservative way, the uniaxial crushing strength of rock mass inside socket may also be restricted to the safe strength of grade of pile concrete as per the guidelines of IS 14593:1998 [5].

The concrete grade for the pile shaft adopted was M35 having 28 days characteristics strength (f_{ck}) as 35 MPa, i.e., 3500 ton/m^2 and safe value of direct compressive strength as (0.36 * 35), i.e., 12.60 MPa, i.e., 1260 ton/m^2 as per the guidelines of IRC:112-2011 [10].

Since the encountered rock was highly to moderately/slightly weathered and fractured in the socket portion, so the value of "N_j" was taken as 0.10 as per "Table 4" of IS:12070 [6], based on the consideration of moderately close spacing of discontinuities in between 0.30 and 1.00 m and aperture (opening) of discontinuities as less than 10 mm. The value of "α", i.e., rock socket side resistance reduction factor was considered as 0.03 from the "Fig. 1" of IS 14593 [5] based on the average crushing strength of rock along the wall of the socket. Similarly, the value of "β", i.e., rock socket correction factor was taken as 0.40 as per "Fig. 2" of IS 14593 [5] based on rock mass reduction factor (j) corresponding to the quality of rock present in the wall of socket.

The pile diameter (D), length of rock socket (L_s) and corresponding value of depth factor (N_d), uniaxial crushing strength (q_c) of rock mass present along the

side wall and tip of socket, ultimate crushing strength, i.e., 28 days characteristics strength (f_{ck}) of the design grade of pile concrete and the safe vertical compressive load carrying capacity (Q_s) of pile shaft as estimated using the above equation no. 2 under different piers and abutments in case of one typical major river bridge and ROB are shown in Table 3.

Table 3 Summary of estimated safe vertical load carrying capacities of single pile as per IS 14593:1998 [5]

Name of structure	Pier (P)/Abutment (A)	Pile diameter (m)	Length of rock socket (m)	Values of "N_d"	Uniaxial crushing strength of rock at wall of socket (ton/m^2)	Uniaxial crushing strength of rock at tip of socket (ton/m^2)	Uniaxial crushing strength of pile concrete (ton/m^2)	Safe vertical load carrying capacity (ton)	
								As per rock crushing strength	As per concrete crushing strength
Major bridge over river Kalisindh	A1	1.20	2.40	1.20	2554	4533	3500	893	752
	P1	1.20	1.92	1.12	2283	5974	3500	955	642
	P2	1.20	2.10	1.15	2220	4342	3500	776	666
	P3	1.20	2.10	1.15	2809	4367	3500	835	722
	P4	1.20	1.86	1.11	3123	5464	3500	949	702
	P5	1.20	1.86	1.11	3778	6306	3500	1110	734
	P6	1.20	1.86	1.11	2651	4728	3500	817	662
	P7	1.20	1.92	1.12	2106	3433	3500	618	–
	A2	1.20	1.92	1.12	2811	3871	3500	734	688
ROB @ 256 + 730 km	A1	1.20	3.18	1.33	2166	2919	3500	751	–
	P1	1.20	2.40	1.20	1886	2522	3500	547	–
	A2	1.20	3.18	1.33	2226	2714	3500	728	–

From the above summary table, it is seen that the estimated safe vertical (compressive) load carrying capacities of the single pile shaft under the piers and abutments were varying from 642 to 1110 ton in case of the major river bridge. Similarly, the estimated safe vertical (compressive) load carrying capacities of the single pile shaft under the pier and abutments were in between 547 and 728 ton for the ROB structure.

The safe vertical, i.e., axial (compressive) load carrying capacities of the single pile shaft were also estimated by using the "Method 1" following the approach given under "Clause No. 9.1 of Appendix-5 of IRC:78-2014 [1]" due to the availability of moderately strong "Basalt" rock of igneous nature having uniaxial crushing strength of the rock mass as more than 10 MPa, i.e., 1000 ton/m^2 in socket portion with RQD > 0% and (CR + RQD)/2 > 30% at the pile socket bottom. The safe vertical load carrying capacity (Q_s) of the rock socketed bored concrete pile foundation was determined using the following expression as given under "Method 1" of IRC:78-2014 [1] based on the uniaxial compressive strength.

$$Q_s = \left(q_c * K_{sp} * d_f * A_b\right)/\text{FOS as } 3 + (C_{us} * A_s)/\text{FOS as } 6 \qquad (3)$$

where

1. "q_c" is the uniaxial, i.e., unconfined compressive strength of rock in MPa
2. "K_{sp}" is the empirical coefficient whose value ranges from 0.30 to 1.20 corresponding to the values of (CR + RQD)/2 varying in between 30 and 100% of the rock mass at pile tip, i.e., base of pile shaft
3. "d_f" is the depth factor, i.e., "d_f" = [1.00 + 0.40 * (Length of rock socket/Diameter of pile shaft inside rock socket)] ≤ 1.20
4. "A_b" is the base area of pile shaft inside rock, i.e., A_b = pi() * D^2/4, where "D" = Pile shaft diameter
5. "C_{us}" is the ultimate shear strength of rock along socket length = 0.225 * SQRT (q_c), but restricted to the shear capacity of concrete of the pile to be taken as 3 MPa, i.e., 3000 ton/m^2 for M35 grade of concrete in confined condition, which of other strength of concrete can be modified by a factor SQRT (28 days characteristics strength, i.e., f_{ck}/35)
6. "A_s" is the surface area of pile shaft inside rock, i.e., A_s = pi() * Pile shaft diameter inside rock socket (D) * Length of rock socket (L_s)
7. FOS is the "Factor of Safety" as recommended to be applied over the corresponding ultimate value.

The average value of uniaxial crushing strength (q_c) of rock available at pile tip within the depth twice the diameter, i.e., 2D depth of pile shaft from its base was considered for estimating the end bearing resistance of pile socket as per the guidelines given in IRC:78-2014 [1]. The average value of uniaxial crushing strength of rock mass for estimating the end bearing component of the load carrying capacity pile shaft socketed into rock may be restricted maximum up to the 28 days characteristic crushing strength of the grade of pile concrete. However, the allowable end bearing component after dividing by factor of safety (i.e., FOS as 3) shall be restricted to maximum value of 5 MPa, i.e., 500 ton/m^2 by following the guidelines of IRC:78-2014 [1].

Similarly, the average value of unconfined, i.e., uniaxial compressive strength (q_c) of rock available along the surrounding wall of socket was taken into consideration for finalizing the value of "C_{us}" as said above following stipulations of IRC:78-2014 [1] while estimating the rock socket side resistance. Again, for evaluation of the side socket friction capacity, the top 300 mm depth of rock socket was neglected, and the side socket friction capacity was further limited to the maximum socket depth six times diameter of pile shaft as per the guidelines of IRC:78-2014 [1]. Since the encountered rock in the project area was highly to moderately weathered nature, so the socket depth inside such weathered rock was provided more than the minimum requirement of 0.50 times of diameter of pile shaft following IRC:78-2014 [1] criteria.

The value of empirical coefficient, i.e., "K_{sp}" was taken as 0.30 corresponding to the minimum value of (CR + RQD)/2 as 30% due to the weathered and fractured nature of encountered rock mass inside the socket in the project area.

By following the above-stated approach of IRC:78-2014 [1] and using equation no. 3, the estimated safe vertical (axial) compressive load carrying capacity (Q_s)

of pile shaft corresponding to the pile diameter (D), length of rock socket (L_s) and corresponding value of depth factor (d_f), uniaxial crushing strength (q_c) of rock mass at bottom of socket, ultimate shear strength of rock along socket length (C_{us}), 28 days characteristics strength (f_{ck}) of the design grade of pile concrete under piers and abutments for one major river bridge as well as for one ROB are summarized below in Table 4.

Table 4 Summary of estimated safe vertical load carrying capacities of single pile as per IRC:78-2014 [1]

Name of structure	Pier (P)/Abutment (A)	Pile diameter (m)	Length of rock socket (m)	Values of "d_f"	Ultimate shear strength of rock along socket (ton/m^2)	Uniaxial crushing strength of rock at tip of socket (ton/m^2)	Uniaxial Crushing strength of pile concrete (ton/m^2)	Safe vertical load carrying capacity (ton)	
								As per rock crushing strength	As per concrete crushing strength
Major bridge over river Kalisindh	A1	1.20	2.40	1.20	114	4533	3500	716	625
	P1	1.20	1.92	1.20	108	5974	3500	675	584
	P2	1.20	2.10	1.20	106	4342	3500	685	595
	P3	1.20	2.10	1.20	119	4367	3500	700	610
	P4	1.20	1.86	1.20	126	5464	3500	689	598
	P5	1.20	1.86	1.20	138	6306	3500	701	611
	P6	1.20	1.86	1.20	116	4728	3500	679	589
	P7	1.20	1.92	1.20	103	3433	3500	571	–
	A2	1.20	1.92	1.20	119	3871	3500	647	596
ROB @ 256 + 730 km	A1	1.20	3.18	1.20	105	2919	3500	586	–
	P1	1.20	2.40	1.20	98	2522	3500	472	–
	A2	1.20	3.18	1.20	106	2714	3500	560	–

As per the above summary table, it can be noted that the estimated safe vertical (compressive) load carrying capacities of the single pile shaft under the piers and abutments were in between 571 and 716 ton for the river bridge. In case of the ROB, the estimated safe vertical (compressive) load carrying capacities of the single pile shaft under the piers and abutments were ranging from 472 to 586 ton.

By comparing the estimated safe vertical load carrying capacities of single pile shafts as summarized under Tables 3 and 4, it can be seen that the safe capacity evaluated using the approach of IRC:78-2014 [1] was lesser than the safe value derived as per the method prescribed in IS 14593:1998 [5]. This is due to the reason of consideration of the restricted side socket shear resistance as predicted in the suggested method of estimation in IRC:78-2014 [1].

By limiting the uniaxial crushing strength of rock mass inside socket maximum up to the safe strength of adopted M35 grade of pile concrete following the guidelines of IS 14593:1998 [5], the safe vertical load carrying capacities of the single pile shaft were reduced to the minimum value of 264–308 ton for the different piers and abutments of the major river bridge and 308–371 ton under the pier and abutments for the ROB. However, these evaluated minimum values of safe vertical (compressive) load

carrying capacities were also found satisfactory to the required maximum vertical structural load to be carried by the single pile shaft of the group for those respective structures.

3.3 Uplift Load Carrying Capacity

The uplift load carrying capacity of pile shaft was derived only from the side socket resistance component of the vertical compressive load carrying capacity. No side friction along the pile shaft in the overburden soil portion above the rock socket was considered in uplift capacity. Since the self-weight of the pile shaft acts against the uplift load, so the self-weight of the pile shaft was also added with the side socket resistance component to get the total uplift load carrying capacity of pile shaft as per the available IS and IRC guidelines. The entire part of the available side socket resistance of the vertical compression was considered in case of uplift load resistance capacity of the pile shaft as per IS guidelines, whereas only the 70% of the ultimate shaft side socket resistance for compression was taken in the estimation of uplift load carrying capacity of pile shaft following the guidelines of "Clause No. 709.3.6.2 of IRC:78-2014 [1]". A factor of safety, i.e., FOS as 6 was also applied over the ultimate shaft side socket resistance to get its safe value in estimation of uplift resistance like vertical compression as per the stipulations of IRC:78-2014 [1].

The estimated safe uplift load carrying capacity [$(Q_s)_{uplift}$] of pile shaft corresponding to the pile diameter (D), total length of pile shaft (L_p) and the corresponding self-weight of pile shaft (W_p), length of rock socket (L_s) and the corresponding safe side socket resistance in uplift as per the IS 14593:1998 [5] and IRC:78-2014 [1] guidelines for the different piers and abutments of one typical major river bridge as well as for one ROB are summarized in Table 5.

Table 5 Summary of estimated safe uplift load carrying capacities of single pile

Name of structure	Pier (P)/Abutment (A)	Pile diameter (m)	Total pile length (m)	Length of rock socket as provided (m)	Self-weight of pile (ton)	Safe side socket shear capacity in uplift (ton)		Safe uplift load carrying capacity (ton)	
						As per IS 14593	As per IRC:78	As per IS 14593	As per IRC:78
Major Bridge over River Kalisindh	A1	1.20	16.60	2.40	47	277	105	324	152
	P1	1.20	15.32	1.92	44	198	76	242	120
	P2	1.20	19.54	2.10	55	211	84	266	139
	P3	1.20	18.36	2.10	52	267	94	319	146
	P4	1.20	10.33	1.86	29	263	86	292	115
	P5	1.20	11.11	1.86	31	318	95	349	126
	P6	1.20	8.35	1.86	24	223	79	247	103
	P7	1.20	14.73	1.92	42	183	73	225	115
	A2	1.20	12.14	1.92	34	244	85	278	119
ROB @ 256 + 730 km	A1	1.20	8.77	3.18	25	311	133	336	158
	P1	1.20	8.27	2.40	23	205	91	228	114
	A2	1.20	8.77	3.18	25	320	135	345	160

From the above tabulation, it can be noted that the safe uplift load carrying capacity evaluated using the approach of IRC:78-2014 [1] was lower in comparison with the safe uplift load value estimated as per the method given in IS 14593:1998 [5]. The required maximum design uplift loads for the single pile shaft in the group under the respective pier and abutments of the structures were duly satisfied with corresponding minimum of the safe available capacities as estimated by the above-stated methods.

4 Construction of Pile Foundation

The pile foundations with the designed depth of socketing inside the underlying rock for the structures were successfully executed in the said project area. Adequate numbers of computerized hydraulic rotary type pile drilling rig having model number "BG-28" of M/s. BAUER, Germany, were used in the project. The Photograph 1 as shown here was the typical piling rig actually deployed in the project site. The plant made ready mix concrete, i.e., RMC of M35 grade was used for concreting of pile shaft and pile cap. The output of pile construction including its quality was

Photograph 1 Piling rig deployed in site

quite satisfactory. All the checklists related to the different phases of piling work namely the fixing of pile position, casing driving and pile boring, drilling through the underlying rock and termination of pile shaft with required socketing inside the rock as designed, recording of the pile history sheet, pile reinforcement and cage lowering, pile concreting including the "Tremie Chart" and "Piling Pour Card" were regularly maintained under quality control program. The safety measures for all the engineers and construction workers were taken care. There were some cases of less consumption of concrete observed during pile foundation construction. The remedial measures were undertaken in various ways namely by introduction of high plastic bentonite, doing construction time management and maintaining the viscosity of pile boring fluid, providing increased diameter of cutting tools, etc. Bottom sampler was also used to confirm the proper cleaning of pile bore bottom after adequate and profuse flushing and before start of pile concreting.

The termination of pile shaft was done after socketing the adequate length of pile shaft inside the underlying founding rock as per the design recommendations. In field construction, the termination including the rock socketing of the pile shaft was finalized using the energy criteria which is based on the actual energy consumed while drilling through the founding rock strata and is measured as "Pile Penetration Ratio (i.e., PPR)" following guidelines given in IRC:78-2014 [1]. The "Pile Penetration Ratio (PPR)" is defined as the energy in ton-meter required to advance the pile bore of one square-meter of cross-sectional area by 1 cm. For standard penetration test (SPT), the "PPR" corresponding to the "N" number of blows for 300 mm penetration can be determined as $(0.747 * N)$. Since the encountered rock in the said river bridge and ROB was highly to moderately weathered, fractured and moderately strong in nature, so the approximate equivalent SPT, "N" value corresponding to rock classification at beginning of pile socketing zone was taken as minimum as 600 as per the guidelines given in IS 2911 (Part 1/Sec 2):2010 [4]. The minimum required value of PPR corresponding to the SPT (N) value of 600 for the weathered basalt rock was derived as 448 say around 500 ton-m/m^2/cm. Now, the "PPR" for the hydraulic rotary type piling rig, as it was used in the structure locations of the project, was determined by following the stipulation of IRC:78-2014 [1] and using the equation no. 4 given below.

$$PPR = (2 * \pi * n * T * t)/(A * P) \tag{4}$$

where "n" is rotation in "rpm", i.e., revolution per minute, "T" is the torque in "ton-meter" corresponding to "n", "t" is the time in minutes, "A" is area of pile shaft in "m^2" and "P" is penetration in "cm".

All the above-stated values of rotation, torque, penetration and time required for the depth of penetration were recorded all through the depth of boring in soil and drilling in rocky strata in every pile point shaft, and the corresponding value of PPR was also calculated. The required depth of rock socketing for the pile shaft was provided from the level of moderately strong rock based on its estimated value of the PPR satisfying with the minimum required value of around 500 ton-m/m^2/cm.

5 Load Testing of Pile Foundation

The required numbers of different types of pile load tests namely "Initial Load Test" over the "Test Pile" and "Routine Load Test" over the "Working", i.e., "Service Pile" both in vertical and horizontal direction were conducted to establish the estimated safe pile capacities of the single shaft. The pile load test was conducted as per the guidelines given in IS 2911 (Part 4):2013 [11] and IS 14593:1998 [5]. The "Maintained Load Test" procedure comprising gradual continuous loading and then unloading in stages after reaching up to the test load was adopted in the project for conducting the pile load test as per the relevant IS guidelines. The gross settlement at every stage of loading and then net settlement for each stage of gradual unloading were recorded during vertical and horizontal pile load tests. The locations of "Test Piles" were selected based on the variation in subsurface stratifications especially the founding rock level actually encountered in the structure. The typical photographs of conducting vertical (compression) pile load test are shown under Photographs 2 and 3. The vertical load versus pile head deflection curve of "Initial Load Test" from the "Test Pile" as obtained for the river bridge and ROB is shown below in Fig. 1. The maximum applied test load over the "Test Pile" in "Initial Load Test" was limited to the 2.5 times of the maximum required safe design load for the single pile shaft. The recorded gross settlement was varying from 2.63 to 5.93 mm, and the ranges of applied test load as recorded were in between 570 and 1030 ton as per the vertical load-deflection behavior of "Test Pile" for the major river bridge and ROB. The "Working Piles", as selected based on its history, i.e., records of construction, were loaded up to the 1.5 times of the maximum required safe design load for the single pile shaft under "Routine Load Test". The gross vertical settlement of the pile head as observed in "Routine Load Test" was in between 3.53 to 4.03 mm, and the applied test load as noted was varying from 309 ton to 550 for the said structures. The graphs of the applied vertical load versus pile top deflection curve of "Routine

Photograph 2 Setup of vertical pile load test

Photograph 3 Jacks and dial gauges in load test

Fig. 1 Results of initial vertical pile load test
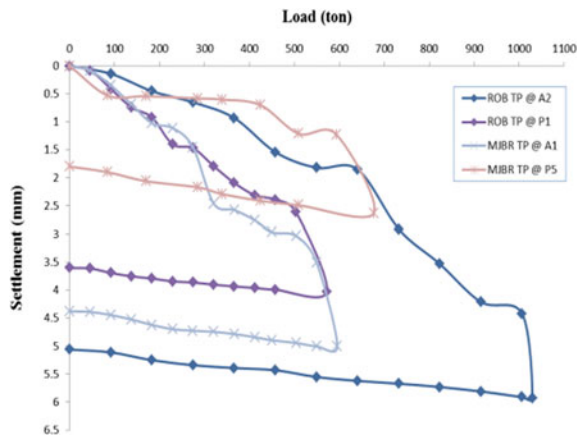
Load Test" as conducted over the "Working Pile" for the said river bridge and ROB are shown below in Fig. 2. The maximum permissible total settlement of pile under the test load was considered as 12 mm and 8 mm, respectively, for "Initial Load Test" and "Routine Load Test" as per the guidelines of "Clause No. 9.2 of IS14593:1998 [5]".

The pile head vertical displacement, i.e., settlement was also estimated corresponding to the applied different stages of loads of "Initial Load Test" by following guidelines as given in "Clause no. 6.6 of IS 14593:1998 [5]" and also in "Clause No. 9.1 of IS:8009 (Part II)-1980 [12]". It was noted that the recorded settlement was almost in line with the estimated value up to the test load applied in site. So beyond the test load of 2.5 times of safe required design load as actually applied and for the total load corresponding to the 2.5 times of safe estimated pile capacity, i.e., up to say 1650 ton, the anticipated maximum value of settlement as per the IS guidelines
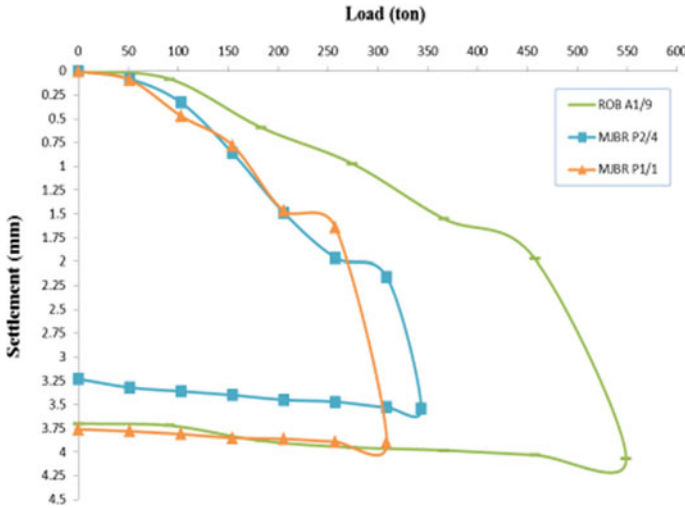
Fig. 2 Results of routine vertical pile load test

was derived as 9.60 mm which is found as less than permissible value of 12 mm for the single pile shaft under the structures of the project. Hence, the estimated safe pile capacity in the range of 600–650 ton was also achievable within the limit of allowable settlement as per IS guidelines. This comparison in between estimated and observed settlement under the vertical loads of "Initial Test" for the said river bridge and ROB is shown here in Fig. 3.
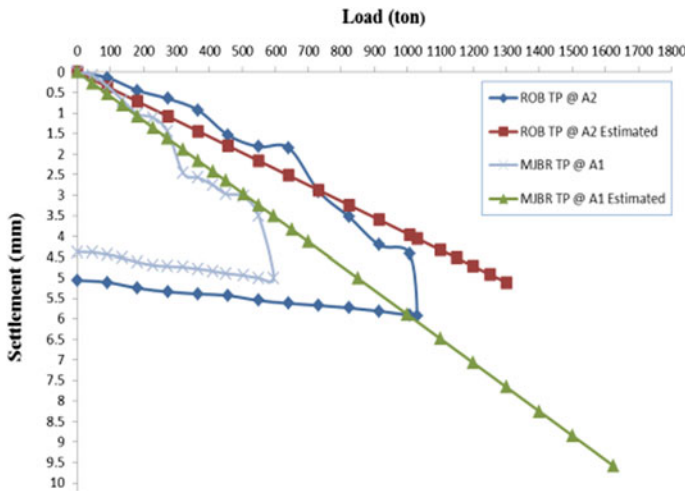
Fig. 3 Comparison of observed and estimated settlement under vertical loads of initial pile test

Similarly, the results of "Initial Lateral Pile Load Test" and "Routine Lateral Pile Load Test" for the major river bridge and ROB structures are shown, respectively, in Figs. 4 and 5. The recorded gross horizontal deflection was in between 2 and 3 mm, and the applied lateral test load was varying from 19 to 90 ton as per the lateral load-deflection behavior of "Test Pile" in "Initial Load Test" for the major river bridge and ROB. The observed total horizontal deflection of the pile head in "Routine Load Test" was varying in between 2.14 and 3.38 mm, and the applied test load was ranging from 40 and 57 ton for the river bridge and ROB structures. The maximum permissible total horizontal deflection of pile head under the lateral test load was considered as 8 mm and 4 mm, respectively, for "Initial Load Test" and "Routine Load Test" as per stipulations of "Clause No. 9.3 of IS14593:1998 [5]".
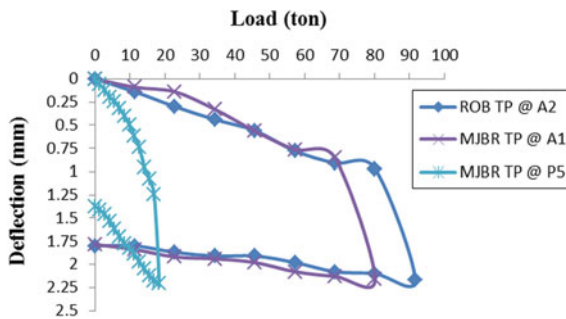
Fig. 4 Results of initial lateral pile load test
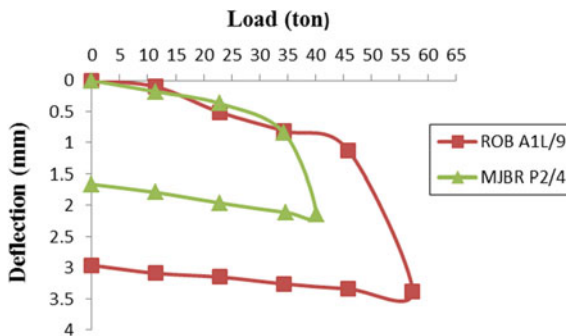
Fig. 5 Results of routine lateral pile load test

6 Conclusions

This paper discusses about the detailed design philosophy and construction methodology of the pile foundation socketed into the underlying rock as per the available IS and IRC guidelines and technical specifications which was adopted for the major river bridge and ROB structures along the Biaora and Dewas project road (a section of NH3) in the state of Madhya Pradesh. It was quite challenging situation for installing the pile foundations penetrating through the overburden soil layers and then finally socketed inside the underlying highly to moderately and slightly weathered basaltic rock of varying depth. The socket length of pile shaft was decided with provision of adequate resistance against the maximum applied horizontal loads and corresponding moments and also by satisfying the required maximum vertical compression and uplift loads to be carried by the single pile shaft. The socket length of pile shaft as

Photograph 4 Major river bridge

Photograph 5 Railway over bridge (ROB)

designed was also executed in site by using the hydraulic rotary piling rig based on the criteria of minimum required "Pile Penetration Ratio (PPR)" for the founding basalt rock of highly to moderately weathered and fractured nature following the guidelines of IRC:78-2014. The required maximum safe design vertical and horizontal loads for the single pile shaft were also established by conducting the adequate numbers of actual field pile load tests over the "Test Pile" as well as over the identified "Working Pile". The Photographs 4 and 5 shown here are, respectively, the completed major river bridge and ROB structure which are already open to the road traffic.

References

1. IS 14593:1998: Indian Standard Design and Construction of Bored Cast-in-Situ Piles Founded on Rock—Guidelines
2. IS 2911 (Part 1/Sec2):2010: Indian Standard Design and Construction of Piles Foundation—Code of Practice, Part 1 Concrete Piles, Section 2 Bored Cast in-situ Concrete Piles (Second Revision)
3. IS 2911 (Part 4):2013: Indian Standard Design and Construction of Piles Foundation—Code of Practice, Part 4 Load Test on Piles (Second Revision)
4. IS:12070-1987 (Reaffirmed 2005): Indian Standard Code of Practice for Design and Construction of Shallow Foundations on Rock
5. IS 13365 (Part 1):1998 (Reaffirmed 2003): Indian Standard Quantitative Classification Systems of Rock Mass—Guidelines, Part 1 Rock Mass Rating (RMR) for Predicting Engineering Properties
6. IS:8009 (Part II)-1980 (Reaffirmed 1985): Indian Standard Code of Practice for Calculations of Settlement of Foundations, Part II Deep Foundations Subjected to Symmetrical Vertical Loading
7. IRC:78-2014: Standard Specifications and Code of Practice for Road Bridges, Section: VII Foundations and Substructure (Revised Edition)
8. FHWA: Drilled Shafts: Construction Procedures and Design Methods. FHWA Publication No. FHWA-IF-99-025. Department of Transportation, Federal Highway Administration, Office of Implementation, McLean, VA (1999)
9. AASHTO: Standard Specifications for Highway Bridges, 4th edn. American Association of State Highway and Transportation Officials, Washington, D.C. (1996)
10. Specification of Road and Bridge Works, Indian Road Congress (IRC), Ministry of Road Transport and Highways (MORT&H), Govt. of India, Fifth Revision (2013)
11. NAVFAC: Foundation and Earth Structures (Design Manual 7.2). Department of the Naval Facilities Engineering Command (1982)
12. IRC:112-2011: Code of Practice for Concrete Road Bridges, Indian Road Congress (IRC), New Delhi

Evaluation of Bearing Capacity of Ground in Transition Zone

Sreevar Ramesh, R. V. Suman, M. Yashwanth, and S. K. Prasad

Abstract The determination of ultimate bearing capacity in transition zone by classical theory is not clearly explained (IS: 6403-1981: Code of Practice for the Determination of Bearing Capacity of Shallow Foundation, first revision, New Delhi, 1981 [1]) (Murthy in Soil Mechanics and Foundation Engineering. Marcel Dekker Inc. New York [2]; Punmia and Jain in Soil Mechanics and Foundations, 17th edn. Laxmi Publications, New Delhi, India [3]). Most of them including IS: 6403-1981 suggest a linear interpolation between general and local shear failure in transition zone with no further explanation. Practicing engineers do not have consistency in calculation of bearing capacity in the transition zone. More often, they are likely to encounter the situation of the angle of internal friction lying between 28° and 36°. Many a times, it is felt that the baring capacity is overestimated. Therefore, an attempt is made in this paper to determine the ultimate bearing capacity by different methods in the transition zone and to give more precise calculation procedure for the determination of bearing capacity in the transition zone. For this purpose, Terzaghi's bearing capacity factors are used in the analysis. An attempt is made to present bearing capacity factors as a function of angle of internal friction of soil considering local shear zone, transition zone and general shear zone. Three methods to determine the ultimate bearing capacity of soil in transition zone are discussed, and their relative conveniences are brought out.

S. Ramesh (✉) · R. V. Suman · M. Yashwanth
Civil Engineering, Sri Jayachamarajendra College of Engineering, Mysuru 570006, India
e-mail: sreevarramesh95@gmail.com

R. V. Suman
e-mail: sumanrv342@gmail.com

M. Yashwanth
e-mail: myashwanth88@gmail.com

S. K. Prasad
Professor and Head of Civil Engineering, Vidyavardhaka College of Engineering, Mysuru 570006, India
e-mail: prasad_s_k@hotmail.com; skprasad@vvce.ac.in

1 Introduction

The determination of bearing capacity of soil is the most important requirement
of foundation design. Depending on strength and stiffness of soil, bearing capacity
failures can be broadly divided into three modes, namely general shear failure when
the angle of internal friction of soil, $\phi > 36°$, mixed or transition zone when $28° < \phi < 36°$ and local shear failure when $\phi < 28°$. Local shear failure generally occurs in
loose sand, while general shear failure occurs in dense sand [3–1]. For general shear
failure conditions, bearing capacity equations are available, and for local shear failure
conditions, same equations are reduced by considering reduced shear parameters.
However, for intermediate values of ϕ, in mixed or transition state between local and
general shear failure, no separate equations are available. As ϕ increases above 28°,
there is a need for gradual transition from local to general shear failure. IS: 6403-1981
suggests interpolation between local and general shear failure for determination of
bearing capacity in transition zone with no further explanation. The curve obtained
by plotting ultimate bearing capacity versus friction angle (ϕ) is not smooth. Terzaghi
and Peck [4] suggested that linear interpolation is made to evaluate ultimate bearing
capacity for soil with ϕ lying between 28° and 36°. Punmia (2005) indicates that no
separate equation is available for intermediate values of ϕ in mixed zone and that
there should be gradual transfer from local to general shear failure.

2 Methods for Determination of Bearing Capacity
in Transition Zone

Ultimate bearing capacity of soil according to Terzaghi's method of analysis is as
follows.

For general shear failure ($\phi > 36°$),

$$Q_{\mathrm{f}} = cN_{\mathrm{c}} + \gamma D N_{\mathrm{q}} + 0.5\gamma B N_{\gamma} \tag{1}$$

For local shear failure ($\phi < 28°$),

$$Q_{\mathrm{f}} = c_{\mathrm{m}} N c' + \gamma D N_{\mathrm{q}}' + 0.5\gamma B N_{\gamma}' \tag{2}$$

Here, c is cohesion of soil, γ is unit weight of soil, D is depth of footing, B is
width of footing N_{c}, N_{q} and N_{r} are Terzaghi's bearing capacity factors that depend
on soil friction angle, ϕ. Bearing capacity factors corresponding to the local shear
failure N_{c}', N_{q}', N_{γ}' are reduced in Eq. 2 (tan $\phi_{\mathrm{m}} = 2/3$ tan ϕ, $c_{\mathrm{m}} = 2/3\ c$). Let us
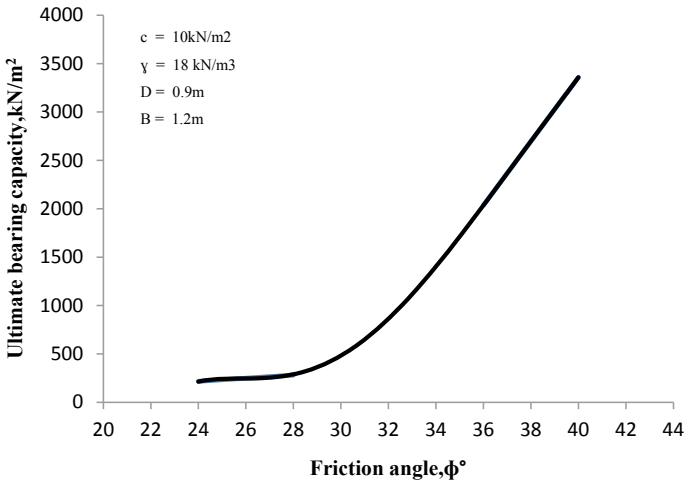
Fig. 1 Variation of ultimate bearing capacity with friction angle considering best fit curve in transition zone

consider a strip footing of width 1.2 m and depth 0.9 m, in a homogenous soil having cohesion $c = 10$ kN/m^2, and unit weight $\gamma = 18$ kN/m^3. Let Q_f be the ultimate bearing capacity of a given soil mass in kN/m^2. Let us consider a smooth curve to connect from ultimate bearing capacity at 28° to ultimate bearing capacity at 36° for which a best fit curve is drawn by taking a fifth order polynomial as shown in Fig. 1.

2.1 Method-1 (As Suggested by IS: 6403-1981 by Interpolation Method)

2.1.1 Procedure

1. For various values of ϕ, ultimate bearing capacity for local and general shear failures is determined by Eqs. 1 and 2.
2. In transition zone, ultimate bearing capacity is calculated by linear interpolation between local and general shear failure.
3. A graph is plotted, taking ultimate bearing capacity along y-axis and friction angle (ϕ) along x-axis.
4. It is compared with the best fit curve as shown in Fig. 2.
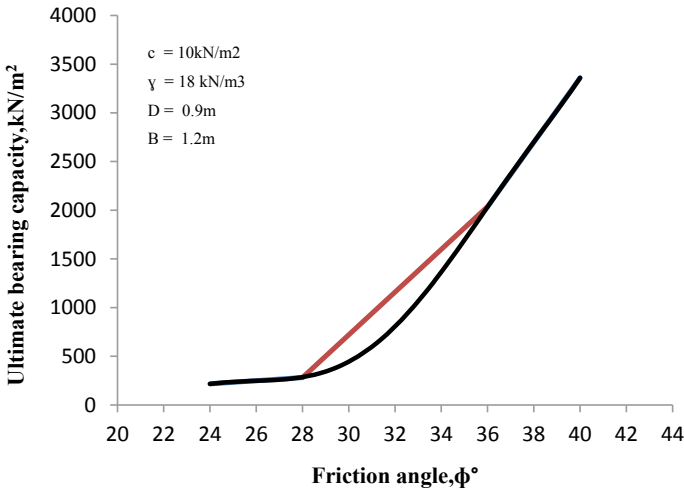
Fig. 2 Variation of ultimate bearing capacity with friction angle considering linear interpolation of Method-1 in transition zone

Table 1 Ultimate bearing capacity in local and general shear failure zones

Failure zone	$\phi°$	Reduced $\phi°$	Reduced c (kN/m^2)	Q_f (kN/m^2)
Local shear failure	28°	19.52°	6.67	281.51
General shear failure	36°	36°	10.00	2036.95

2.1.2 Example

For $\phi = 32°$, ultimate bearing capacity is determined by linearly interpolating between the ultimate bearing capacities of $\phi = 28°$ and 36°, respectively, as (Q_f) $32° = 1159.23$ kN/m^2 (Table 1).

2.2 Method-2

2.2.1 Procedure

1. For various values of ϕ in local and general shear zones, ultimate bearing capacities of soil are determined by Eqs. 1 and 2.
2. Ultimate bearing capacity of a soil in mixed zone is determined by assuming the linear interpolation at the given ϕ in between local and general shear failure for same value of ϕ.
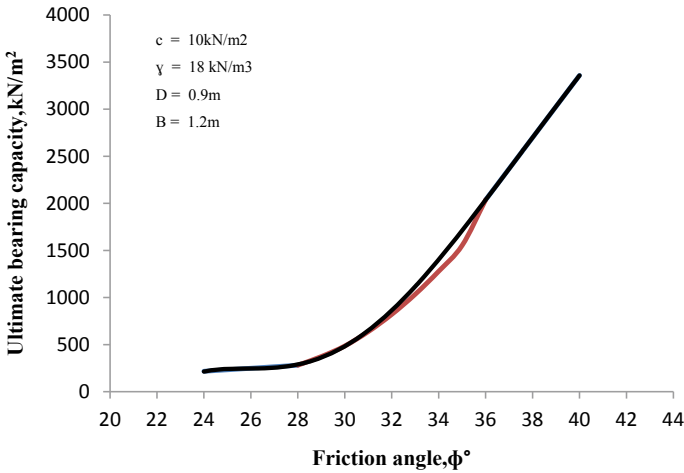
Fig. 3 Variation of ultimate bearing capacity with friction angle considering interpolation at the given ϕ of Method-2 in transition zone

3. Hence, for given values of ϕ ($28° < \phi < 36°$), ultimate bearing capacity is calculated for both local and general shear failure and interpolated between them by Eq. 3.
4. The graph of ultimate bearing capacity along y-axis and friction angle (ϕ) along x-axis plotted in this condition is compared with best fit curve as shown in Fig. 3.

$$Q_f'' = Q_f' + \left(Q_f - Q_f'\right)/(36 - 28) * (\phi - 28) \tag{3}$$

Here

Q_f'' Ultimate bearing capacity for a given value of ϕ in transition zone.

Q_f Ultimate bearing capacity for a same value of ϕ, considering soil to undergo general shear failure.

Q_f' Ultimate bearing capacity for a same value of ϕ, considering soil to undergo local shear failure.

2.2.2 Example

For $\phi = 32°$, assuming that the soil in transition zone may undergo mixed shear failure, i.e., it may undergo both local and general shear failure for same value of ϕ. Value of ultimate bearing capacity, considering local shear failure (Q_f) $32° = 389.156$ kN/m^2 and general shear failure (Q_f) $32° = 1252.196$ kN/m^2. Therefore, ultimate bearing capacity at $\phi = 32°$ from Eq. 3 is (Q_f) $32° = 820.676$ kN/m^2.
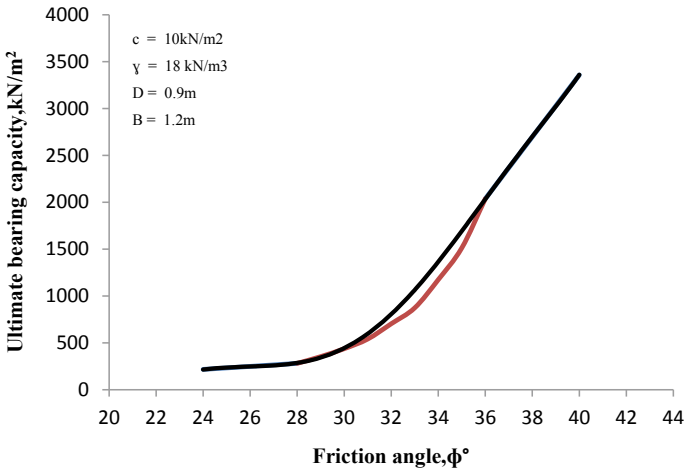
Fig. 4 Variation of ultimate bearing capacity with friction angle considering gradual transition of Method-3 in transition zone

2.3 Method-3

2.3.1 Procedure

1. For various values of ϕ, ultimate bearing capacity for local and general shear failures is determined by Eqs. 1 and 2.
2. In transition zone, ultimate bearing capacity of a soil is determined by gradually varying the reduction factor for cohesion and friction angle from 2/3 to 1 (i.e., from 28° to 36°).
3. A graph is plotted, taking ultimate bearing capacity along y-axis and friction angle (ϕ) along x-axis, and the results are compared with best fit curve as shown in Fig. 4.

2.3.2 Example

For $\phi = 28°$, c and $\tan \phi$ are reduced to 2/3 (c) and 2/3 * ($\tan \phi$), respectively. Similarly for $\phi = 29°$, c and $\tan \phi$ are reduced to (2/3 + 1/24) times and so on. At 36°, there is no reduction in c and ϕ.

For $\phi = 32°$, c and ϕ become 8.33 kN/m² and 27.51°, respectively. Therefore, ultimate bearing capacity at $\phi = 32°$ is (Q_f) 32° = 703.99 kN/m².
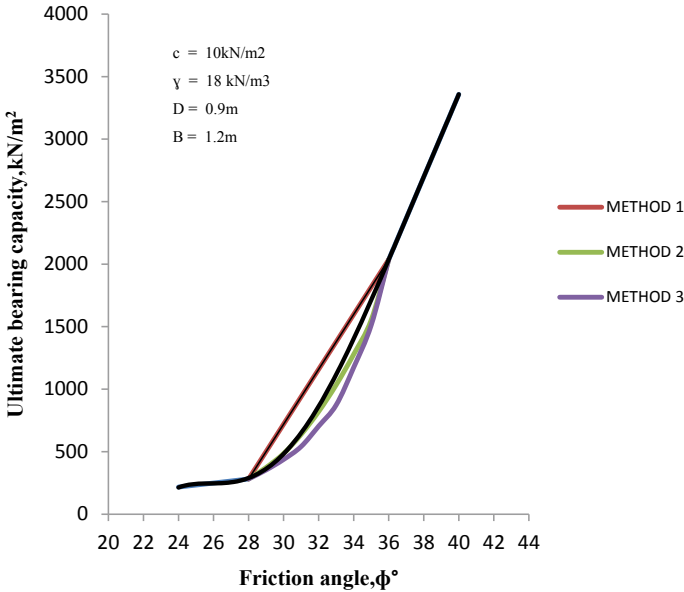
Fig. 5 Variation of ultimate bearing capacity with friction angle considering all three methods in transition zone

3 Comparison of Ultimate Bearing Capacity by Three Methods

For various values of ϕ, ultimate bearing capacity determined by above three methods is plotted in the same graph as shown in Fig. 5.

4 Conclusion

A number of problems are solved, and the results are presented in Table 2 corresponding to the determination of ultimate bearing capacity in transition zone. From the above analysis, the inference is made as follows. From Fig. 2, it is evident that the ultimate bearing capacity obtained under transition zone using Method-1 is overestimated compared to the capacity according to that of best fit curve. From Fig. 3, it is evident that the ultimate bearing capacity obtained under transition zone using Method-2 is underestimated compared to the capacity according to that of best fit curve. From Fig. 4, it is evident that the ultimate bearing capacity obtained under transition zone using Method-2 is underestimated compared to the capacity according to that of best fit curve. From Table 2, it is evident that the error is minimum in Method-2. Further, the method underestimates the ultimate bearing capacity which is on the safer side. Hence, it is concluded that Method-2, which is easy to compute

Table 2 Percentage difference in area between best fit curve and the values obtained by different methods

Problem No.	Problem description	Percentage error (%)		
		Method-1	Method-2	Method-3
1	Strip footing $c = 0$ kN/m^2, $\phi = 16$ kN/m^3, $B = 1.5$ m, $D = 0.8$ m	−21.58	+04.73	+11.66
2	Strip footing $c = 10$ kN/m^2, $\phi = 18$ kN/m^3, $B = 1.2$ m, $D = 0.9$ m	−18.30	+ 03.89	+10.64
3	Strip footing $c = 20$ kN/m^2, $\phi = 17$ kN/m^3, $B = 1.7$ m, $D = 1$ m	−17.86	+03.43	+10.27
4	Square footing $c = 0$ kN/m^2, $\phi = 16$ kN/m^3, $B = 1.5$ m, $D = 0.8$ m	−21.66	+04.24	+11.08
5	Square footing $c = 10$ kN/m^2, $\phi = 18$ kN/m^3, $B = 1.2$ m, $D = 0.9$ m	−16.18	+04.72	+11.33
6	Square footing $c = 20$ kN/m^2, $\phi = 17$ kN/m^3, $B = 1.7$ m, $D = 1$ m	−14.83	+ 04.97	+11.61
7	Circular footing $c = 0$ kN/m^2, $\phi = 16$ kN/m^3, $B = 1.5$ m, $D = 0.8$ m	−21.89	+03.52	+10.24
8	Circular footing $c = 10$ kN/m^2, $\phi = 18$ kN/m^3, $B = 1.2$ m, $D = 0.9$ m	−17.29	+03.36	+09.98
9	Square footing Groundwater table at 0.6 m from GL $c = 10$ kN/m^2, $\phi = 18$ kN/m^3, $B = 1.2$ m, $D = 0.9$ m, $R_{w1} = 0.833$, $R_{w2} = 0$	−14.96	−14.96	+11.20
10	Circular footing Groundwater table at 1.5 m from GL $c = 10$ kN/m^2, $\phi = 18$ kN/m^3, $B = 1.2$ m, $D = 0.9$ m, $R_{w1} = 1$, $R_{w2} = 0.75$	−15.46	+04.51	+10.98

Note Positive sign is considered for underestimated value and negative sign for overestimated value
Percentage error $= (A_B - A)/A_B * 100$, where A_B = Area under the best fit curve in transition zone and A = Area under the curve by method 1, 2 or 3 in transition zone. Area is found out by integration of piecewise linear curves.

also in addition to being most accurate, is the best suited to determine the ultimate bearing capacity of soil in the transition zone.

References

1. IS: 6403-1981: Code of Practice for the Determination of Bearing Capacity of Shallow Foundation, first revision, New Delhi (1981)
2. Murthy, V.N.S.: Soil Mechanics and Foundation Engineering. Marcel Dekker Inc., New York (2002)
3. Punmia, B.C., Jain A.K.: Soil Mechanics and Foundations, 17th edn. Laxmi Publications, New Delhi, India (2008)
4. Terzaghi, K., Peck, R.B.: Soil Mechanics in Engineering Practice. Wiley (1967)

Behavior of Rectangular and T-Shaped Diaphragm Wall Panels in Mixed Soil Conditions: A Case Study

C. Vimala and Madan Kumar Annam

Abstract In urban areas, properly designed deep excavation support systems are essential for any new underground construction adjacent to the existing buildings. Diaphragm walls are widely used in India as deep excavation support system to facilitate strut-free excavation as well as to limit the soil movement of surrounding areas due to excavation. In this paper, a ten-story new commercial development required a three-level basement excavation of 12.5 m (max.) from the existing ground level (EGL). Project site consists of mixed soil condition with silty clay of varying consistency followed by dense sand underlain by a weathered rock layer. A 600 mm thick rectangular D wall panel with temporary ground anchors was used to support deep excavation wherever sufficient setback is available. In the same site, one of the corners has a restricted setback which demanded 8 m cantilever wall with high structural rigidity. Hence, T-shaped diaphragm wall panels of 600 mm thick were adopted as a permanent cantilever wall. Numerical modeling of the retention system was analyzed using WALLAP and PLAXIS 2D software. The wall deflections were monitored through inclinometers. This paper reviews the performance of cantilever diaphragm wall and rectangular panel wall with single anchor for 8 m excavation depth. Cantilever T-shaped diaphragm wall proved to be effective and stable system, where tie back is not feasible.

Keywords Diaphragm wall · T panel · PLAXIS 2D · WALLAP · Inclinometer · Deflection

C. Vimala (✉) · M. K. Annam
Keller Ground Engineering India Pvt Ltd, Chennai 600024, India
e-mail: vimala@kellerindia.com

M. K. Annam
e-mail: madankumar@kellerindia.com

461

1 Introduction

Land has become scarce and expensive in the developing cities of India due to urbanization, and this demands high-rise buildings with underground structures to meet the increasing space requirements. A ten-story commercial building requires a deep excavation of 12.5 m for three-level underground car parking in a busy area. The site has enough setback distance of about 10–12 m in majority portion, whereas very limited setback (less than 2 m from boundary) is available in one of the corners. The subsoil consists of silty clay with varying consistency followed by silty sand underlain by weathered rock. The surrounding constraints of the sites are residential buildings, highway on one side and commercial multi-storied buildings on one side. Based on the site constraints and available setback distance, diaphragm wall with two-level inclined ground anchors has been adopted as a retention system to facilitate 12.5 m deep excavation. Cantilever T-shaped diaphragm wall was adopted for a small length having maximum excavation depth 8.0 m and a limited setback distance of 2 m. This paper reviews the performance of cantilever T panel in comparison with the rectangular diaphragm wall panels with single-level anchor for 8 m excavation.

2 Necessity of T Panel

The northeast corner of the site has limited setback of 2 m, and anchors are not allowed to encroach into neighboring properties. Also, this part of the site is proposed with a utility tank wall of about 8 m deep. So, in the permanent condition, there will not be any structural slabs connection to the diaphragm wall as a prop. Also, there are issues of inadequate space between the diaphragm wall and permanent wall for facilitating de-stressing the anchors if provided in the retention system. Various options were reviewed during design stage, and cantilever T-shaped diaphragm wall was considered, which is structurally rigid to act as a permanent cantilever wall. Also, side friction will develop in the buttress portion of the T panel that will provide additional passive resistance to the wall [1]. The proposed cantilever portion of the retention system is shown in Fig. 1.

3 Soil Stratigraphy

The subsoil in cantilever wall location consists of silty clay with varying consistency followed by dense silty sand up to the depth of 18–19 m underlain by weathered rock. The groundwater table was at 3–4 m below EGL during the time of soil investigation. The design soil parameters were arrived based on the confirmatory soil investigation. Groundwater table at 2 m below EGL was considered for the analysis.
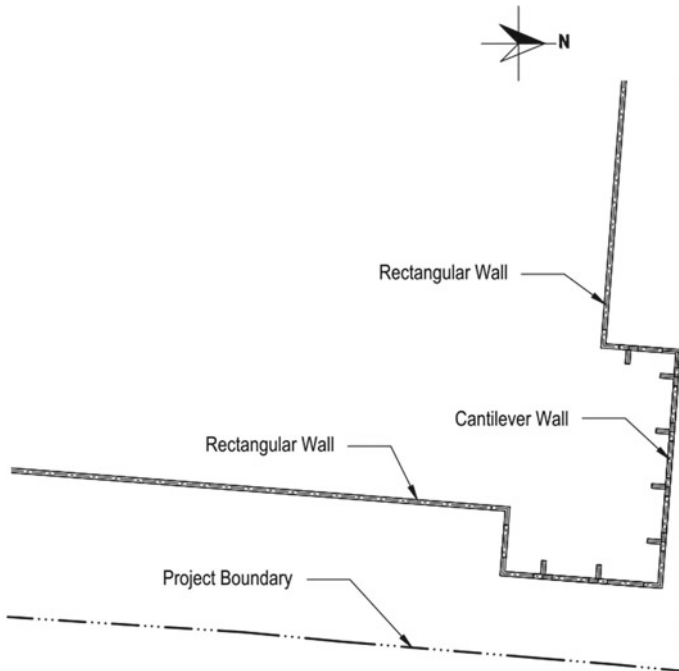
Fig. 1 Proposed cantilever portion of the wall

4 Numerical Analysis of Retention System

The preliminary analyses were carried out using WALLAP which is fast and widely used software. Earth pressures are calculated using active and passive earth pressure coefficients based on the wall and soil interface friction. In WALLAP analysis, the wall and soil interaction is modeled as a beam and spring analogy. The final design was carried out with plain strain model of 15 nodded elements using PLAXIS 2D. These two analyses were carried out for both rectangular and T panel cantilever wall.

4.1 Rectangular Wall Panels

A 600 mm thick diaphragm wall of 19 m deep with two-level ground anchors was finalized to support 12.5 m excavation for the majority of the project site where enough setback distance is available. The first level of ground anchor was proposed at 6.5 m below EGL, and the second level was at 10 m below EGL. The analysis model and predicted deflection profile for 8 m excavation using WALLAP and PLAXIS 2D are presented in Fig. 2. Magnitude of the deflection of wall is almost same; however,
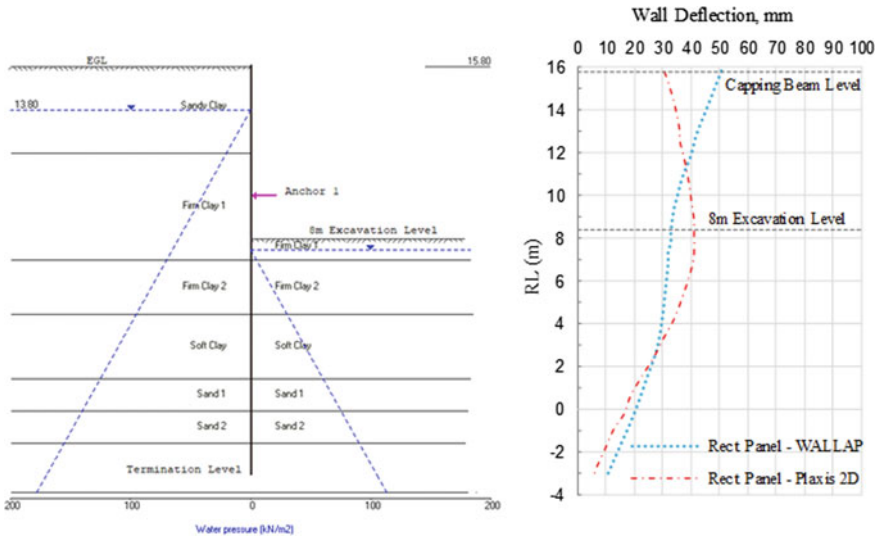
Fig. 2 Typical WALLAP model and predicted wall deflections of rectangular panels

WALLAP indicates at top, whereas it is seen at middle of the wall excavation in PLAXIS 2D.

4.2 T-Shaped Panels

The behavior of T panel is three-dimensional problem which is having interaction between subsoil, buttress portion and rectangular panels. A 3D analysis, being complex and expensive and 2D analysis were carried out using combination of different structural elements available in the program, at the same time providing a geometry close to 3D.

T-shaped walls can be modeled in 2D software using two approaches. The first approach is to estimate equivalent wall stiffness of rectangular and buttress portion of the wall [1]. This approach will provide total bending moment and shear force of both rectangular and buttress walls. WALLAP uses this approach to design T panels (Fig. 3).

The second approach uses two different elements, plate elements to simulate the rectangular panel and embedded beam rows to simulate buttress wall. This approach can be used in PLAXIS 2D. Using this method, the bending moment and forces on the wall and buttress portion can be estimated separately. In PLAXIS 2D, T panel design was modeled using these two approaches. PLAXIS 2D model indicating these two approaches is illustrated in Fig. 4.

T panel design was carried out with different cross-sectional dimensions and finalized with 1.9 m web depth and 2.5 m flange length of 0.6 m thick as an optimized

Fig. 3 Typical T panel
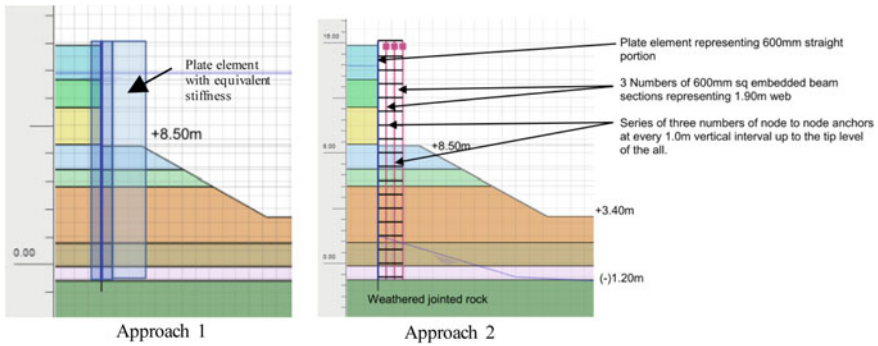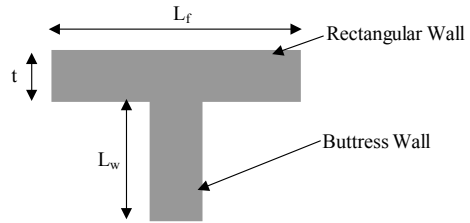
Fig. 4 Typical T panel model (PLAXIS 2D)

solution for the proposed cantilever wall portion. As per the design, the T panels are required to be installed between rectangular panels and are connected with the capping beam at top so that it will act as monolithic element. The estimated deflection of T panels for 8 m excavation using WALLAP and PLAXIS 2D is illustrated in Fig. 5. Similar trend is seen for the predicted deflection in both WALLAP and PLAXIS 2D. This confirms cantilever wall behavior, and maximum deflection is around 50 mm at top.

T panels shall be constructed as a single panel to form an integral unit which will ensure the perfect structural rigidity between the buttress wall and rectangular panels [2]. Construction of monolithic T panel requires more care with special lifting hook and hangers. The T panel shall be restrained on stiff/dense soil to reduce the wall deflections [2] (Fig. 6).

5 Performance of Executed Wall

Precise instruments like inclinometer, piezometers and deflection markers were installed at site to assess wall deflection and groundwater table. This continuous monitoring system helped to assess the executed wall performance throughout the excavation and basement construction period. One inclinometer was installed in cantilever portion of the wall to observe T panel behavior during excavation.

Fig. 5 Predicted deflection
of cantilever T panel wall
(8 m excavation)
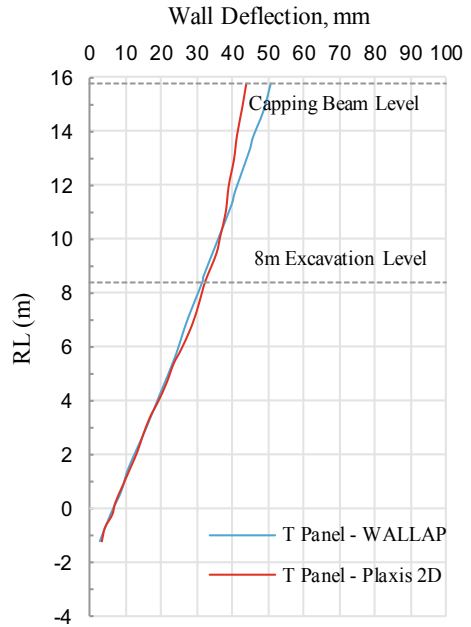
Fig. 6 Rectangular and cantilever wall

Also, another inclinometer was installed in rectangular panels which is close to the cantilever portion to compare the estimated results. The maximum deflection at T panel is observed as 50 mm, whereas in rectangular panel, the maximum observed deflection is about 36 mm. In T panel, the wall deflections are controlled by the
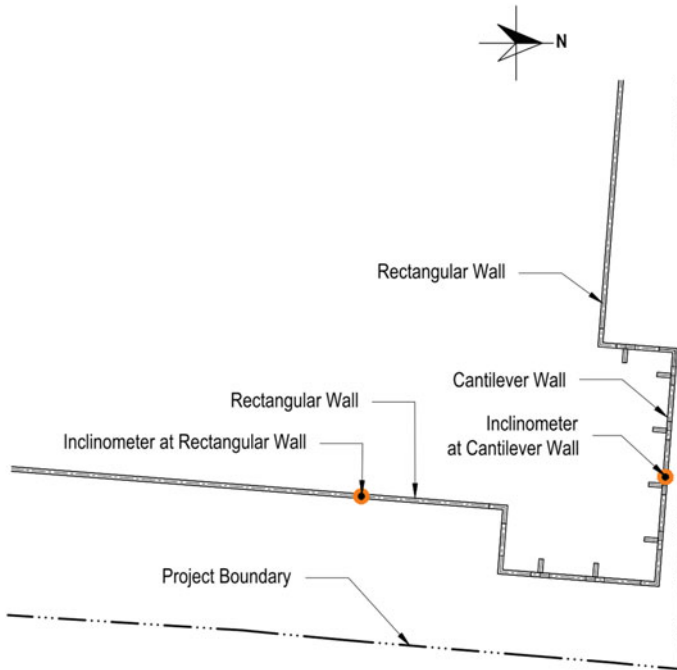
Fig. 7 Location of inclinometers at T-shaped cantilever and rectangular wall

combined stiffness of web and flange portion [3]. This proves that the T panels provide increased wall stiffness as well as worked as a prop to the D'wall to control wall deflections [4]. The locations of inclinometers and observed wall deflections are shown in Figs. 7 and 8, respectively.

6 Comparison of Wall Deflections

The estimated wall deflections of T panel with 8 m cantilever wall and rectangular panel wall with one-level anchor of 8 m excavation are compared with respective actual field measurements. Deflection patterns are presented in Fig. 9.

The observed deflection of cantilever T panels is almost matching with the estimated deflections which indicates that the design assumptions are reasonable and are accorded with actual site condition. In rectangular panels, the observed deflection and predicted WALLAP deflections are similar line and the magnitude of wall deflection is 36 mm, whereas the predicted values are in the range of 50 mm (max.).

Fig. 8 Observed deflections
of rectangular and T panels
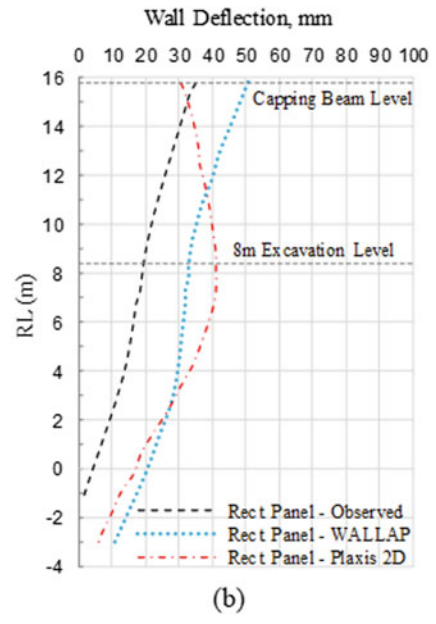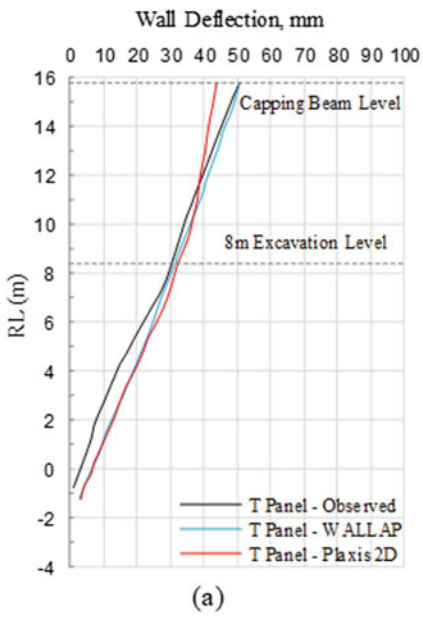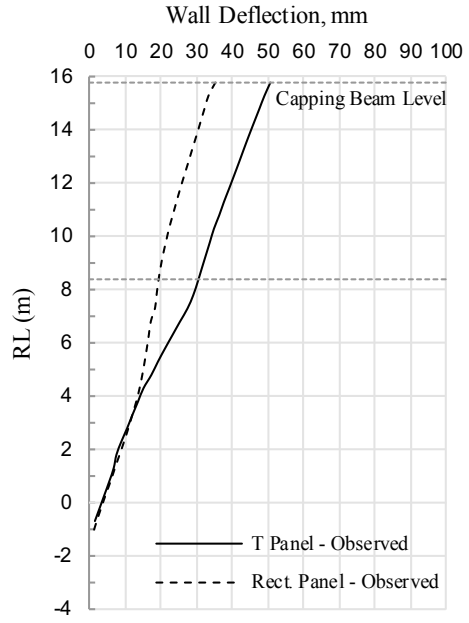
Fig. 9 Predicted and observed wall deflections of **a** T panel and **b** rectangular panel

7 Conclusions

Various retention system proposals based on the available setback and site constraints are proposed and executed. T panel behavior can be modeled in 2D software with appropriate assumptions to simulate the 3D behavior. Different approaches of modeling of T panels are described and indicate that the analysis results are comparable. The estimated and observed field behaviors of cantilever T panel are matching. This proves that the design assumptions made for the simulation of 3D problem into 2D model and design soil parameters are reliable and reflect the actual site conditions. The actual performance of rectangular panels with one-level anchor indicates that wall deflection is well within the predicted limits. Since the rectangular panel wall is designed for 12.5 m deep excavation and provides more stiffness, resulted in less wall deflection.

References

1. Hsieh, H.-S., Li-Hua, Wu., Lin, T.-M., Cherng, J.-C., Hsu, W.-T.: Performance of T-shaped diaphragm wall in a large-scale excavation. J. GeoEng. **6**(3), 135–144 (2011)
2. Ou, C.-Y., Teng, F.-C., Seed, R.B., Wang, I.-W.: Using buttress walls to reduce excavation-induced movements. Proc. Inst. Civ. Eng. Geotech. Eng. **161**(GE4), 209–222 (2008)
3. Ou, C.-Y., Hsieh, P.-G.: Use of rigid support system to reduce movements in deep excavations. In: Proceedings of the 19th International Conference on Soil Mechanics and Geotechnical Engineering, Seoul (2017)
4. Hwang, R., Moh, Z.-C.: Evaluating effectiveness of buttresses and cross walls by reference envelopes. J. GeoEng. **3**(1), 1–11 (2008)

Bearing Capacity of Eccentrically Loaded Circular Footing Supported on Reinforced Sand

Srikalpa Rajguru Mahapatra and Rupashree Ragini Sahoo

Abstract In the recent past, investigators have given less attention on circular foundation. Thus, this research deals with the strength of circular foundation on reinforced sand. There are total 48 numbers of tests conducted on model footings of radius 10 and 5 cm and eccentricities varying from 5 to 15 mm with an increment of 5 mm. Square shaped geonet is used as reinforcing material having aperture size of 1.637 mm. There are three layers of reinforcement used, i.e., from 0 to 2, where the distance between reinforcing layer and base of foundation is 0.35D and distance between two reinforcing layers is 0.25D. The test tank has size of 0.60 m × 0.60 m × 0.30 m. This test is carried out on dense and medium dense sand. Relative density is 71% for dense sand and 51% for medium dense sand, calculated as per IS code method. Load-settlement curve of each experiment is done from which bearing capacity is calculated by tangent intersection method. The result showed that rise in reinforcing layer increases the bearing capacity, whereas rise in eccentricity has decreased bearing capacity. The results are also compared with different existing theories, with unreinforced and reinforced dense and medium dense single entities and bearing capacity ratio (BCR) which are calculated.

Keywords Circular footing · Eccentricity · Reinforcement

S. R. Mahapatra (✉) · R. R. Sahoo
Civil Engineering Department, VSSUT, Burla, Odisha, India
e-mail: srm.kalpa@gmail.com

R. R. Sahoo
e-mail: rupashreesec@gmail.com

1 Introduction

Structural foundations are the sub-structure elements which transmit the structural load to the earth in such a way that the supporting soil is not overstressed and not undergo deformations that would cause excessive settlement of the structure. Hence, the properties of the supporting soil must be expected to affect vitally the choice of the type of structural foundation suitable for a structure. The bearing capacity and settlement of foundations have been proven a function of the shape of the footing, foundation soil parameters and conditions. Footing is subjected to moments and vertical loads (like wind, water, earthquake, earth pressure, etc.) [1]. Due to this load eccentricity, the overall stability of foundation decreases along with differential settlement, tilting of foundation, heaving the supporting soil which reduces the bearing capacity [2]. To avoid such scenario, we must reduce the contact pressure using larger dimension of footing, which leads to uneconomical design. This can be achieved by increasing the bearing capacity of soil by appropriate reinforcing techniques [3]. Several theories have been established to calculate the bearing capacity and settlement of strip, square and circular footings. In 1943, Terzaghi published the landmark theory for estimation of the ultimate bearing capacity of shallow foundation subjected to vertical centric loading on a $c–\varphi$ soil. Since then, many researchers extended their study on this topic based on theoretical and experimental approach. Sometimes, eccentrically inclined loads are encountered in strip foundations, which act inclined toward the center line of strip foundation and were reefed to as partially compensated. Many model tests are conducted with eccentric inclined load on strip foundation [4, 5]. Comprehensive mathematical formulations to calculate bearing capacity of continuous foundation were developed by Prakash and Saran [6]. Population explosion resulted a huge demands of lands for providing basic needs like road, train, metro, homes, etc. Shortage of lands provided an opportunity to use unfavorable lands with proper ground improvement. Thus, various soil improvement techniques like soil reinforcement, replacing unfavorable soils, compaction, dewatering procedures, etc., got popular. During few decades, researchers emphasized more on the bearing capacity of shallow foundations with multi-layered reinforced layers [6]. Small-scale laboratory model tests on strip foundation have been a popular area of research in most cases [6, 7]. Large number of studies on geosynthetic reinforced soil foundations found that it forms a soil failure wedge beneath the soil layer. There is substantial improvement in surface heaving, and bearing capacity is found when model tests are performed on granular fill overlaying soft clay beds [8, 9]. Circular footing behavior beneath the reinforcement layers of geogrid and geocells improves the bearing capacity [10, 11]. A numerical model approach to predict footing size effect and bearing capacity ratio values developed by Murat et al. [12]. It is clear from the literature review that most of the studies concentrated on behavior of circular footing on vertical and inclined loading arrangement. Thus, objective of these studies is to witness the behavior of eccentrically loaded model footings of eccentricity varying from 0 to 15 mm with increment of 5 mm, relative density and reinforcement layers and their effect on bearing capacity of soil.

2 Materials and Equipment

Dry sand of dense ($I_D = 71\%$) and medium dense ($I_D = 51\%$) sand layer is used as the geomaterial, and biaxial geonet is used as the reinforcement material. The tests are performed on circular model footings of mild steel, sizes of 100 and 50 mm, with varying eccentricities from 0.05 to 0.15 cm with an increment of 0.05 mm. The thickness of footing was 4 mm. The detail about biaxaial geonet is given in Table 2. The bearing capacity and settlement were interpreted from each test and analyzed. All the model tests were performed in a cement concrete tank measuring 0.60 m × 0.60 m × 0.30 m (Table 1; Fig. 1).

Geonet, as a reinforcing material, is placed horizontally after levelling the surface at preferred depth, keeping (u/D) = 0.35 and (h/D) = 0.25 as shown in Figure 5. Total 48 numbers of model tests are carried out on model footings. Model test series summarized in Table 3 (Figs. 2, 3 and 4).

Table 1 Geotechnical parameters of sand

Geotechnical parameters	Value
Sp. gravity (G)	2.60
Eff. particle size (D_{10})	320 μ
Particle size (D_{30})	480 μ
Mean particle size (D_{60})	780 μ
Uniformity coefficient (C_u)	2.43
Working dry density (γ_d)	13.82 kN/m^3
Maximum unit weight (γ_{dmax})	14.10 kN/m^3
Minimum unit weight (γ_{dmin})	13.10 kN/m^3
Relative density (D_r)	71% (dense sand), 51% (medium dense sand)
Internal angle of friction (φ)	42.3° (dense sand), 39.8° (medium dense sand)

Table 2 Physical parameters of reinforcing material

Material type	Synthetic fabrics
Aperture shape	Square
Aperture size	1.6 × 1.6
Mesh size	1.243 mm
Ultimate tensile strength (kN/m)	7.6
Failure strain (%)	2.5
/Mass per unit area (g/m^2)	139

Fig. 1 Grain size
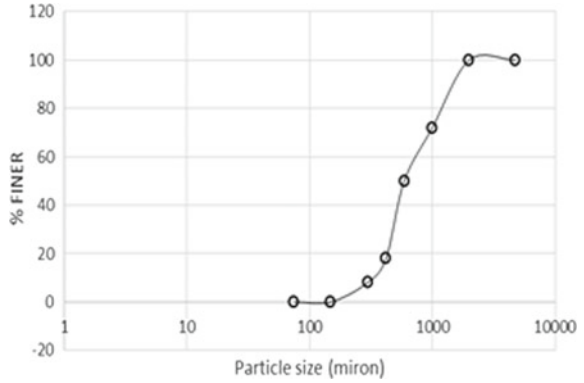distribution of sand

Table 3 Model test series

Number of test	Diameter of footing (cm)	Density of sand	Unit weight (kN/m³)	Relative density (I_D) (%)	Shearing angel (φ)	Reinforced layers	Eccentricity (mm)
1–12	10	Dense	13.80	71	42.3°	0, 1, 2	0, 5, 10, 15
12–24	5	Dense	13.80	71	42.3°	0, 1, 2	0, 5, 10, 15
24–36	10	Medium dense	11.36	51	39.8°	0, 1, 2	0, 5, 10, 15
36–48	5	Medium dense	11.36	51	39.8°	0,1,2	0, 5, 10, 15

Fig. 2 Typical geonet
material

Fig. 3 Model circular footing

Fig. 4 Model test tank
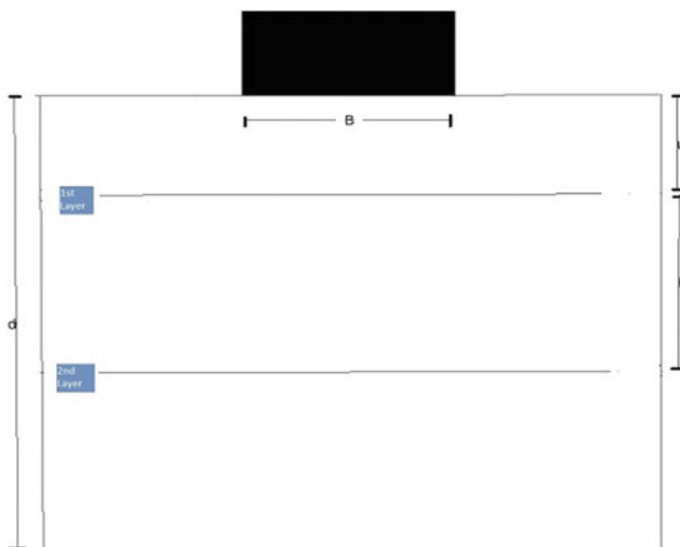
Fig. 5 Placement of reinforcing layer

3   Experimental Result and Analysis

The loading arrangement is shown in Fig 6 where the loading on eccentrically loaded footing is defined. It is seen from figure clearly that load on footing deflects according to the eccentricity of footing from center. The laying of reinforced layer is clear from Fig. 5. After all the arrangements, i.e., reinforcement layer and loading pattern, are done, load-settlement data is noted which is penned according to Fig. 7. The bearing capacity of each footing on different conditions is calculated as per tangent intersection method; here, two straight lines are drawn from two opposite corners of graph, and their intersection point on loading directions gives us the required bearing capacity of respective condition.

Fig. 6 Eccentrically loaded circular footing ($B =$ diameter of footing)
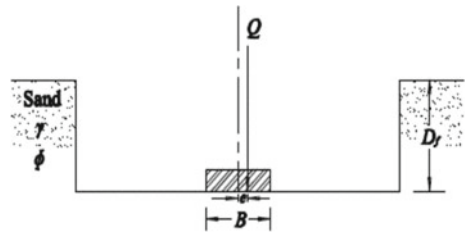
Fig. 7 Interpretation of ultimate bearing capacity of 5 cm diameter footing on dense unreinforced sand bed by tangent intersection method at $e = 0$
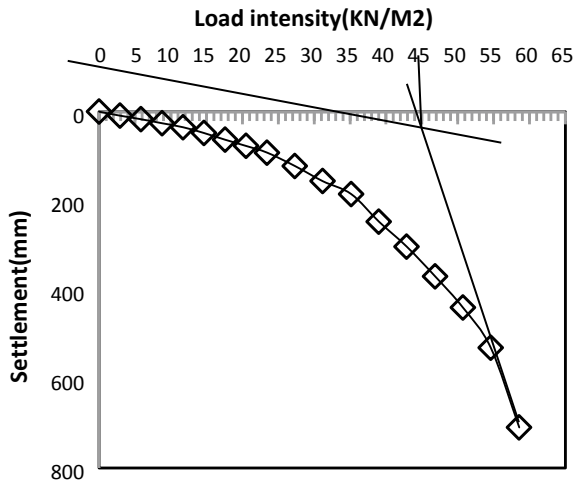
From Figs. 8, 9, 10, 11, 12 and 13, the load deformation curve of eccentrically loaded footing with varying eccentricity is compared, whereas Figs. 14, 15, 16 and 17 compares eccentrically loaded footing in accordance to reinforcing layer. In Figs. 18 and 19, bearing capacity ratio at different conditions is shown, where bearing capacity ratio is given by,
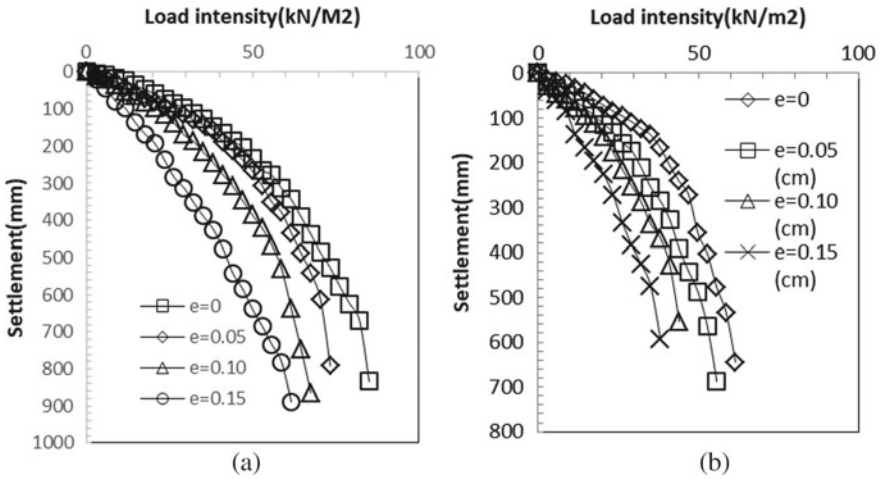
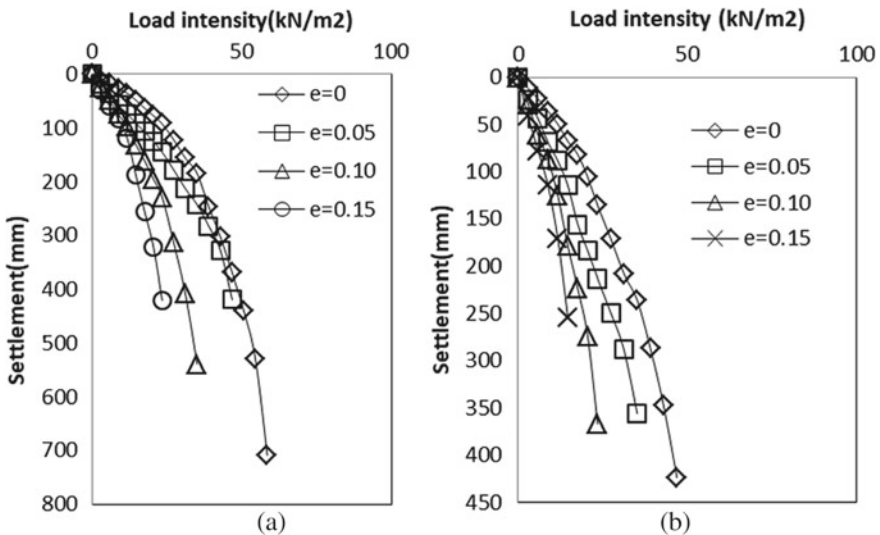Fig. 8 Load-settlement curve of eccentrically loaded 10 cm footings on unreinforced **a** dense sand **b** medium dense sand

Fig. 9 Load-settlement curve of eccentrically loaded 5 cm footings on unreinforced **a** dense sand **b** medium dense sand
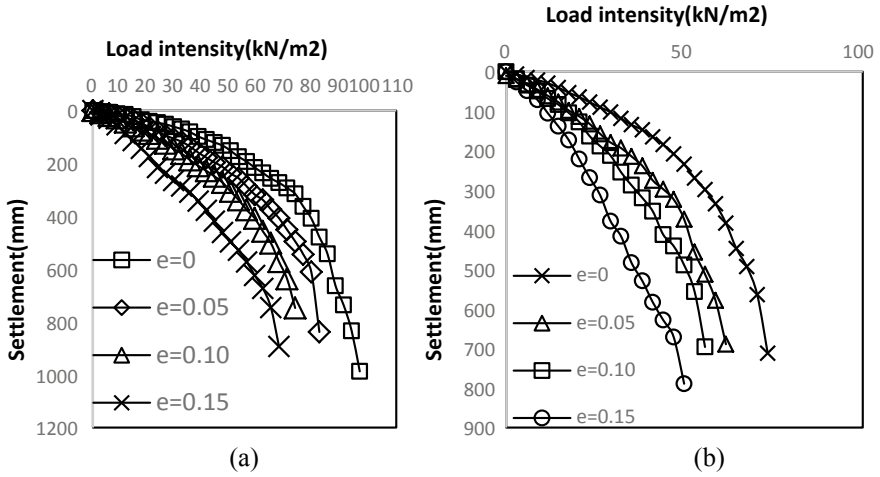
Fig. 10 Load-settlement curve of eccentrically loaded 10 cm footings on **a** dense sand **b** medium dense sand at $N = 1$
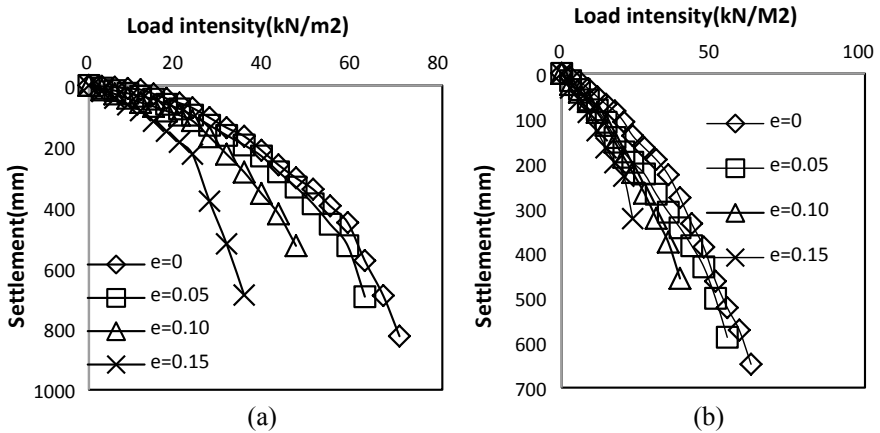
Fig. 11 Load-settlement curve of eccentrically loaded 5 cm footings on **a** dense sand **b** medium dense sand at $N = 1$

$$\text{Bearing capacity ratio} = \text{BCR} = Q_{u(\text{Reinforced})}/Q_{u(\text{un - Reinforced})} \tag{1}$$

It is seen from the graph that in dense sand, there is greater bearing capacity which is observed as compared to medium dense sand. But if we discuss the other side of it, we can say that the settlement is more in case of medium dense sand, and the load bearing capacity of dense sand is higher. Hence, it can be clear that the variation of relative densities or denseness aspect of the soil has great influence on the bearing pressure. From the discussed graphs with varying densities of sand, there is
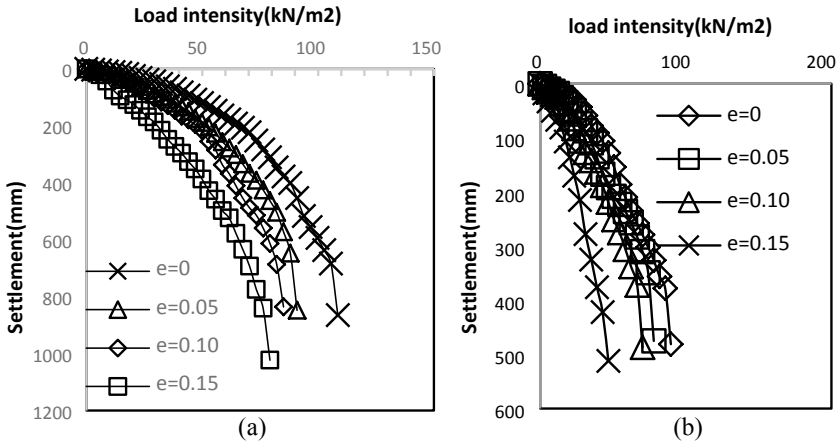
Fig. 12 Load-settlement curve of eccentrically loaded 10 cm footings on **a** dense sand **b** medium dense sand at $N = 2$
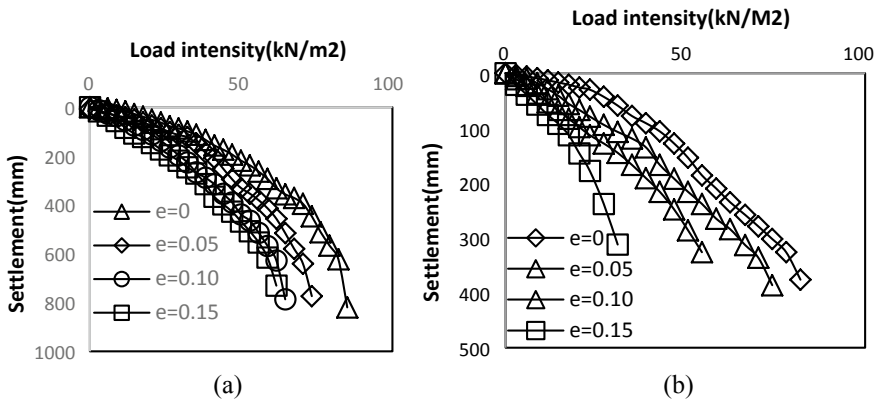

Fig. 13 Load-settlement curve of eccentrically loaded 5 cm footings on **a** dense sand **b** medium dense sand at $N = 2$

no clear evidence found that the reinforcement is the sole reason behind the increase of the ultimate bearing capacity. To know more about the outcome of reinforcement on the bearing capacity of circular footing, with various eccentricities and varying reinforcement layer (N), comparison is done from figure. In this, we will discuss how the load-settlement curve changes according to change in relative densities of soil. The change in relative densities with variation of reinforcement layer gives a clear indication of how the circular footings behave in this case.
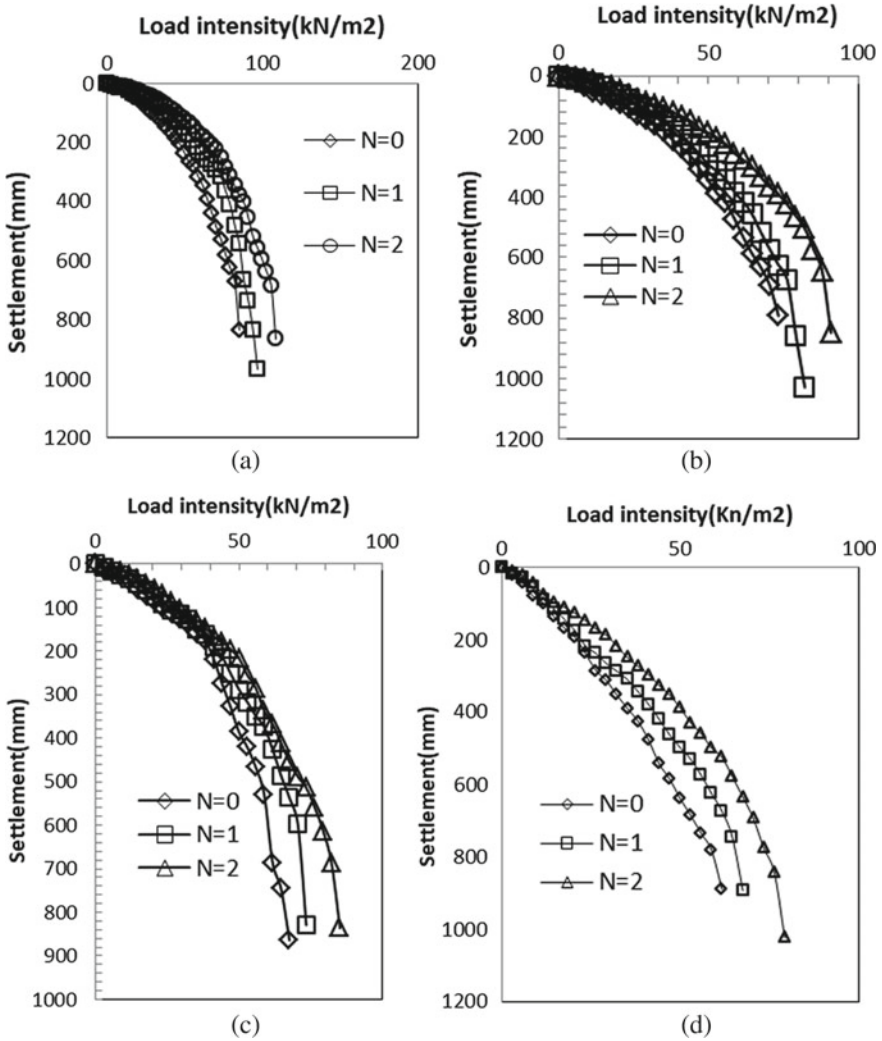
Fig. 14 Comparison of load-settlement curve of 10 cm footing on dense sand of **a** $e = 0$ **b** $e = 0.05$ cm **c** $e = 0.10$ cm **d** $e = 0.15$ cm varying reinforcement layer
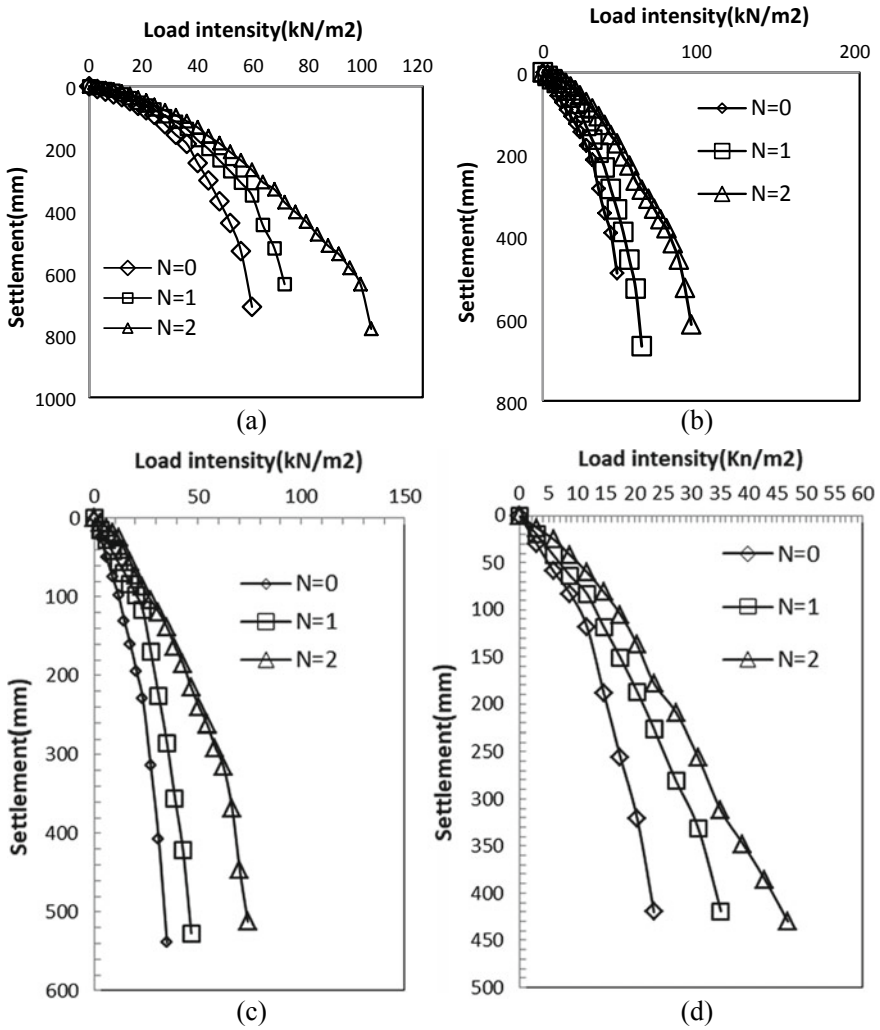
Fig. 15 Comparison of load-settlement curve of 5 cm footing on dense sand bed **a** $e = 0$ **b** $e = 0.05$ cm **c** $e = 0.10$ cm **d** $e = 0.15$ cm at varying reinforcement layer
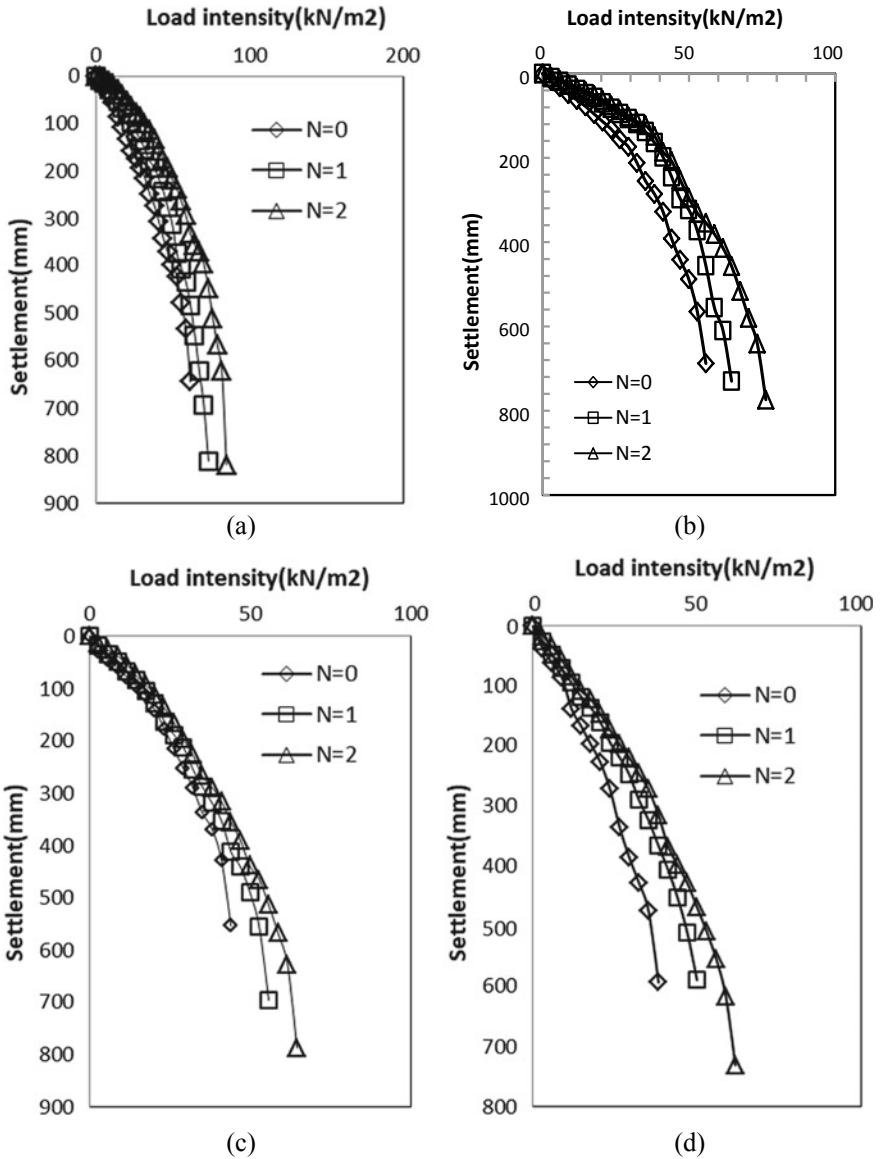
Fig. 16 Comparison of load-settlement curve of 10 cm footing on medium dense sand bed **a** $e = 0$ **b** $e = 0.05$ cm **c** $e = 0.10$ cm **d** $e = 0.15$ cm at varying reinforcement layer at varying reinforcement layer
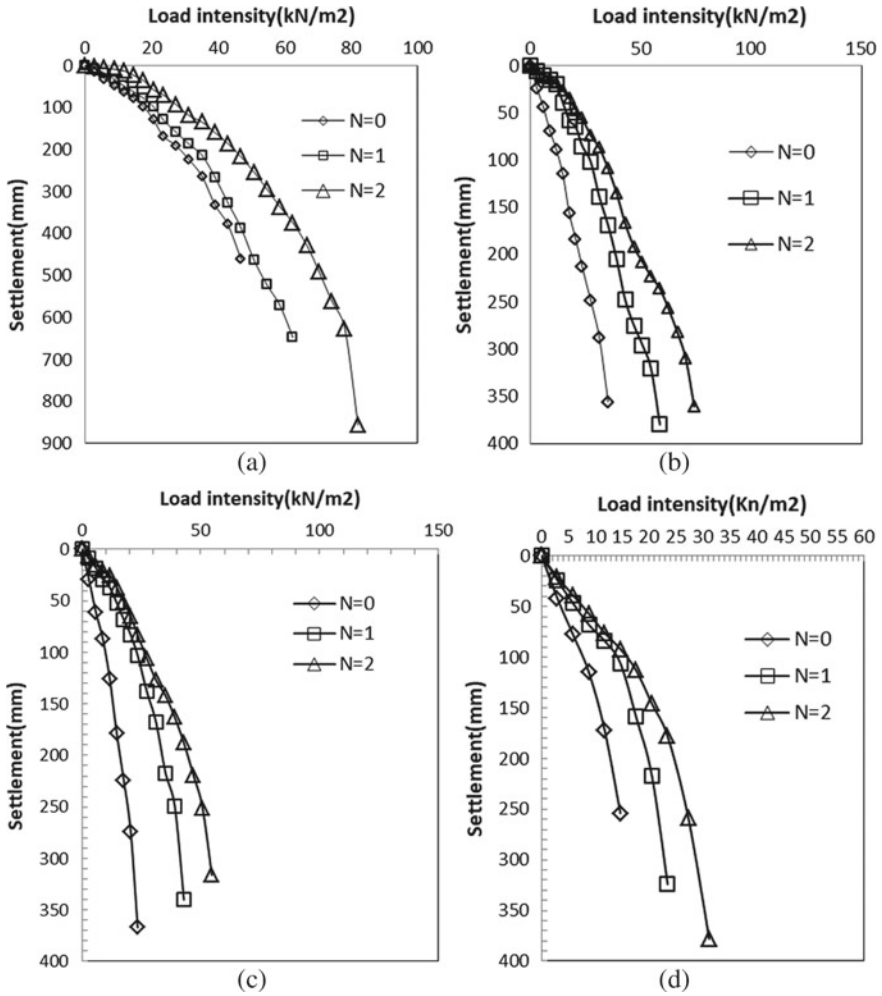
Fig. 17 Comparison of load-settlement curve of 5 cm footing on **a** $e = 0$ **b** $e = 0.05$ cm **c** $e = 0.10$ cm **d** $e = 0.15$ cm medium dense sand bed at varying reinforcement layer
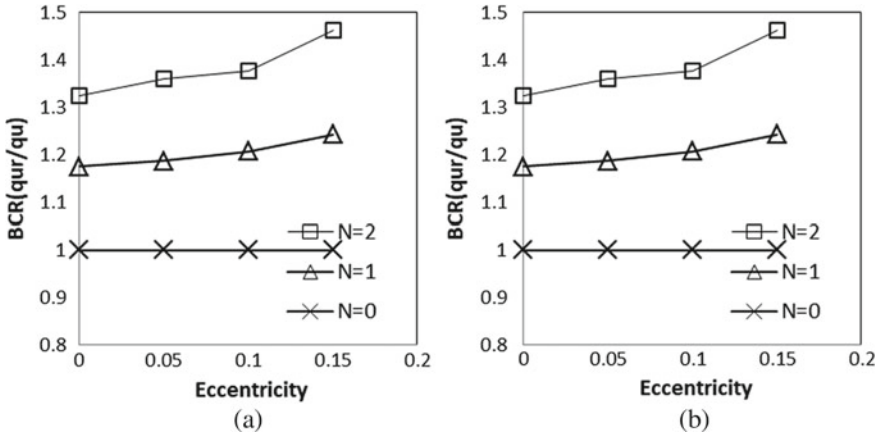
Fig. 18 BCR of 10 cm footing: **a** on dense sand **b** medium dense sand with varying reinforcing layer
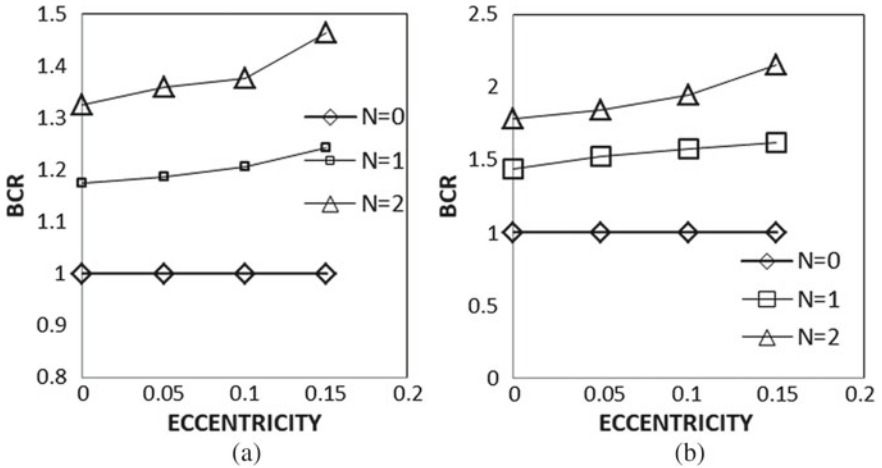

Fig. 19 BCR of 10 cm footing: **a** on dense sand **b** medium dense sand with varying reinforcing layer

The effect of number of geonet layers and variation of densities of sand on settlement and load bearing pressure is clearly visible in these figures. It is observed that with increase in reinforcement, bearing pressure increases at any eccentricity of load application for any level of settlement. On the contrary, settlement of footings decreases with increase in reinforcing layer for any type of load bearing pressure.

4 Conclusion

As per these experimental results and within the range of parameters, the following conclusions are made:

- Relative density increased had a positive effect on bearing capacity of soil, but the final settlement is more or less same.
- Settlement decreases in decreasing rate with increase in reinforcement layer.
- Increasing in reinforcement layer resulted substantial increase in BCR value, although considerable settlement improvement is not observed.
- For reinforced condition, it is observed that with increase in footing size, bearing capacity ratio decreases, but increases with increase in eccentricity, and latter bearing capacity ratio values become steady.

References

1. Meyerhof, G.G.: Some recent research on the bearing capacity of foundation. Can. Geotech. J. **1**(1), 16–26 (1963)
2. Patra, C., Behara, R., Sivakugan, N., Das, B.: Ultimate bearing capacity of shallow strip foundation under eccentrically inclined load. Part II Int. J. Geotech. Eng. **6**(4), 507–514 (2012)
3. Dewaikar, D.M., Guptha, K.G., Chore, S.H.: An experimental study into behaviour of circular footing on reinforced soil. In: International Scientific Conference, pp. 630–634 (2011)
4. Das, S.K.: Artificial neural networks in geotechnical engineering: modeling and application issues. In: Yang, X., Gandomi, A.H., Talatahari, S. (2013)
5. Meyerhof, G.G.: The bearing capacity of foundations under eccentric and inclined loads. In: Proceedings of 3rd International Conference on Soil Mechanics, Zurich, vol. 1, pp. 440–45 (1953)
6. Prakash, S., Saran, S.: Bearing capacity of eccentrically loaded footings. J. Soil Mech. Found. Div. ASCE **97**, 95–118 (1971)
7. Sireesh, S., Sitharam, T.G., Dash, S.K.: Bearing capacity of circular footing on geocell–sand mattress overlying clay bed with void. Geotext. Geomembr. **27**, 89–98 (2009)
8. Alwaji, H.A.: Settlement and bearing capacity of geogrid reinforced sand over collapsible soil. Geotextiles Geomembr. **19**, 75–88 (2001)

9. Adam, M.T., Collin, J.G.: Large model spread footing tests on geosynthetic reinforced soil foundations. J. Geotech. Geoenviron. Eng. Div. ASCE **123**(1), 66–72 (1997)
10. Dash, S.K., Sireesh, S., Sitharam, T.G.: Model studies on circular footing supported on geocell reinforced sand underlain by soft clay. Geotextiles Geomembr. **21**, 197–219 (2003)
11. Boushehrian, J.H., Hataf, N.: Experimental and numerical investigation of the bearing capacity of model circular and ring footings on reinforced sand. Geotextiles Geomembr. **21**(4), 241–256 (2003)
12. Murat, O., et al.: Numerical analysis of circular footings on natural clay stabilized with a granular fill. Acta Geotech. Slov. (2012)
13. Suman, S., Das, S.K., Mohanty, R.: Prediction of friction capacity of driven piles in clay using artificial intelligence techniques. Int. J. Geotech. Eng. (2016). https://doi.org/10.1080/19386362.2016.1169009
14. Basudhar, P.K., Saha, S., Deb, K.: Circular footings resting on geotextile reinforced sand bed. Geotextiles Geomembr. **25**, 377–384 (2007)
15. Terzaghi, K.: Theoretical Soil Mechanics. Wiley, New York (1943)
16. Cerato, A.B., Lutenegger, A.J.: Bearing capacity of square and circular footings on a finite layer of granular soil underlain by a rigid base. J. Geotech. Geoenviron. Eng. ASCE **132**(11), 1496–1501 (2006)
17. Karthigeyan, S., et al.: Influence of vertical loads on the lateral response of piles in sand. Comput. Geotech. **33**, 121–131 (2006)
18. DeBeer, E.E.: Experimental determination of the shape factors and the bearing capacity factors of sand. Geotechnique **20**(4), 387–411 (1970)
19. Taiebat, H.A., Carter, J.P.: Bearing capacity of strip and circular foundation on undrained clay subjected to eccentric loads. Geotechnique **52**(1), 61–64 (2002)
20. Vesic, A.S.: Bearing capacity of shallow foundations. In: Geotechnical Engineering (1975)
21. Meyerhof, G.G.: Ultimate bearing capacity of footings on sand layer overlying clay. Can. Geotech. J. **11**, 223–229 (1974)
22. Purkayastha, R.D., Char, R.A.N.: Sensitivity analysis for eccentrically loaded footings. J. Geotech. Eng. Div. ASCE **103**(6), 647 (1977)
23. Erickson, H.L., Drescher, A.: Bearing capacity of circular footings. J. Geotech. Geoenviron. Eng. 34–43 (2002)

Seismic Bearing Capacity of Shallow Footing in Layered Soil

Smita Tung [ID]**, Sibapriya Mukherjee, Narayon Roy, and Somenath Mukherjee**

Abstract Ultimate bearing capacity of a footing resting on a stratified deposit reduces under a seismic excitation as soil stiffness degrades during a shaking. Ultimate bearing capacity depends on the shear strength parameters (cohesion and angle of internal friction) of subsoil, along with shape and size of footings. An attempt has been made to study the bearing capacity of shallow circular and strip footings in a layered cohesionless soil under static and seismic conditions. The subsoil conditions resemble that of a site located at Rajarhat, Kolkata, West Bengal, India. The modeling has been done using finite element method. The analysis has been carried out for footing width (B) of 2.0 m and depth (D_f)-to-width ratio (D_f/B) of 0.5 and 1.0. For each D_f/B ratio, the analysis has been repeated for three different ratios of layer thickness [top layer (weaker): bottom layer (stronger)] which are 0.33, 1 and 3. For seismic condition, pseudo-static analysis has been performed for horizontal seismic acceleration 0.1–0.3 g. It has also been confirmed from the initial evaluation of liquefaction potential based on the SPT data for the site that the cohesionless soil layers considered here are not prone to liquefaction. It has been observed that due to variation of layer thickness ratio from 0.33 to 3, the ultimate bearing capacity decreases up to 20.00% under static case, whereas for seismic case, decrement of bearing capacity is about 18.00% under similar condition. It has also been found that with the increase in horizontal seismic acceleration from 0.1–0.3 g, the seismic bearing capacity factors N_q and N_γ reduce appreciably by 30% and 60%, respectively. Further attempt has been made to find the effect of shape of footing on seismic

S. Tung (✉) · S. Mukherjee · N. Roy
Civil Engineering Department, Jadavpur University, Kolkata 700032, India
e-mail: smita1989smita@gmail.com

S. Mukherjee
e-mail: sibapriya.mukherjee@gmail.com

N. Roy
e-mail: narayan.roy04@gmail.com

S. Mukherjee
Geotechnical, C E Testing Company Pvt Ltd, Kolkata 700092, India
e-mail: somenath2004@gmail.com

bearing capacity. The paper presents the importance of seismic effect, on layered soil and shape and size of footing in terms of ultimate bearing capacity.

Keywords Ultimate bearing capacity · Layered soil · Finite element method · PLAXIS 2D

1 Introduction

Foundation of structure is designed to transfer and distribute the load of the super-structure to the underlying soil without overstressing it. The general bearing capacity theories proposed by Terzaghi [10], Meyerhof [4] and Hansen [1] are routinely used in foundation design. But, in actual practice, soil is non-homogeneous and anisotropic in nature. Richards et al. [7] observed seismic settlements of foundations on partially saturated dense or compacted soils in terms of seismic bearing capacity reduction. He investigated that settlements were not associated with liquefaction or densification. Many researchers worked on the problem and have studied the seismic bearing capacity of strip footing [2, 3, 5, 9]. Saadda et al. [8] investigated kinematic approach of seismic bearing capacity using limit analysis theory. The analysis focuses on evaluating the reduction in bearing capacity induced by seismic loading. Due to seismic loading, foundations may experience a reduction in bearing capacity and increase in settlement. Although several studies have been carried out to study the seismic bearing capacity but the study of seismic bearing capacity on layered soil is limited. And this paper attempts to include the effect of layer thickness ratio in ultimate bearing capacity under static and seismic conditions. The paper uses pseudo-static approach to determine bearing capacity of the foundations subjected to seismic loads in non-liquefying soils, considering also the depth effects for an embedded footing. In dynamic response, dynamic nature of the load and other factors are not being considered. In the present paper, bearing capacity of strip footings has been estimated on sandy soil which satisfies Mohr–Coulomb strength criterion. The analyses are based on pseudo-static method. The commercially available code, PLAXIS 2D, is used for the finite element analyses. The analysis has been carried out for footing width (B) of 2.0 m and depth (D_f)-to-width ratio (D_f/B) of 0.5 and 1.0 considering three different ratios of layer thickness [top layer (weaker): bottom layer (stronger)] which are 0.33, 1 and 3. In this present study, the effects of the depth-to-width ratio (D_f/B), layer thickness ratio and seismic acceleration on bearing capacity have been investigated.

2 Mathematical Background

The ultimate load that the foundation soil can sustain is expressed by the linear combination of the three bearing capacity factors N_c, N_q and N_γ. The bearing capacity

evaluation is based on the assumption that a failure surface can develop beneath the foundation, by the limit equilibrium method or by the limit analysis. The ultimate bearing capacities for strip foundations in granular soil for static condition are expressed in Eq. 1 and for seismic condition Eq. 2.

$$qu = qN_q + \frac{1}{2}\gamma B N_\gamma \tag{1}$$

Earthquake conditions:

$$Qu = qN_{qE} + 1\,2\gamma B N_{\gamma E} \tag{2}$$

where

$N_q, N_\gamma, N_{qE}, N_{\gamma E}$ bearing capacity factors
$N_{qE}, N_{\gamma E}$ $f(\phi, \tan\theta)$.

The settlement of a strip foundation due to an earthquake [7] is presented in Eq. 3,

$$SEq = (m) = \frac{0.174V^2}{A\,g} \frac{k_h}{A}^{-4} \tag{3}$$

where

V peak velocity for the design earthquake (m/s)
A acceleration coefficient for the design earthquake
g acceleration due to gravity (m/s^2).

3 Present Study

The present study has been formulated to determine the ultimate bearing capacity for strip footing of width $(B) = 2.0$ m depth (D_f)-to-width ratio (D_f/B) of 0.5 and 1.0. For each D_f/B ratio, the analysis has been repeated for three different ratios of layer thickness [Top layer (weaker): bottom layer (stronger)] which are 0.33, 1 and 3. For seismic condition, pseudo-static analysis has been performed for horizontal seismic acceleration 0.1–0.3 g. The soil profile of Rajarhat, West Bengal site, is shown in Table 1.

Table 1 Soil profile at Rajarhat site, West Bengal

Stratum No.	Description	Properties
I	Medium brownish gray sandy clayey silt (0.00–5.50 m)	Submerged density = 8.00 kN/m^3 Cohesion = 5 kPa Friction angle = 30° Specific gravity = 2.65
II	Loose brownish gray sandy silt with mica (5.50–18.00 m)	Submerged density = 8.50 kN/m^3 Friction angle = 33° Specific gravity = 2.60
III	Dense brownish gray silty fine sand with mica (18.00–49.00 m)	Submerged density = 9.20 kN/m^3 Friction angle = 34° Specific gravity = 2.65 Corrected N = 44

4 Methodology and Modeling PLAXIS 2D

An attempt has been made to carry out numerical analysis of the present study by finite element method using PLAXIS 2D software. Two-dimensional plane strain condition has been considered for all the analyses. Material nonlinearity has been considered to model the soil using Mohr–Coulomb failure theory and elastic-perfectly plastic behavior of soil. In the finite element analysis, the entire domain has been discretized by 15 nodded triangular elements. Soil nonlinearity was considered. Soil was idealized as elastic-perfectly plastic material satisfying Mohr–Coulomb criterion. Shear failure criterion has been used only, no settlement criterion has been considered. Figure 1 also shows the model discretization, loading and boundary conditions adopted in this study. Each node of the element has two degrees of freedom, displacement u in the horizontal direction (x) and displacement v in the vertical direction (y).

The generalized displacement vector (u) at a point within an element is related to the nodal displacement vector (q) by shape function matrix [N]
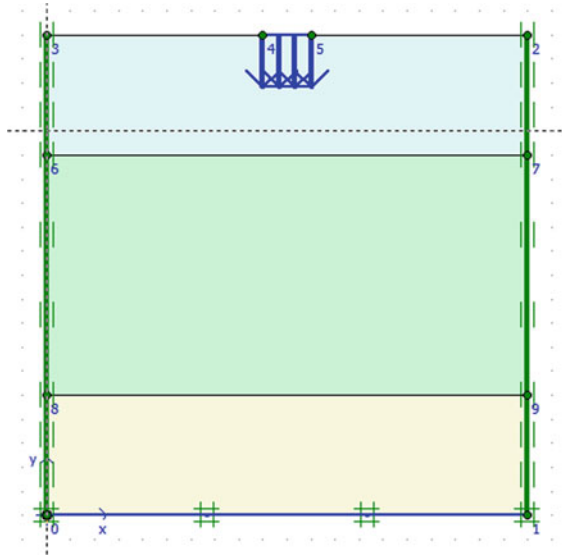
Fig. 1 Boundary and geometry conditions of the footing (seismic boundary condition)

$$As\{u\} = \begin{Bmatrix} u \\ v \end{Bmatrix} = [N]\{q\} \tag{4}$$

where $\{u\}$ = displacement vector at the point within an element,

$$\{q\}T = \{u_1, v_1, u_2, v_2, \ldots, u_{15}v_{15}\} \tag{5}$$

A pseudo-static approach is adopted to account for the earthquake effects for the seismic bearing capacity evaluations. The loading of rigid strip footing has been modeled by applying stresses at the surface nodes below the footing base. The loading process has been continued incrementally until the nodal out of balance forces was solved. Figures 2 and 3 represent deformed mesh for D_f/B ratio = 0.5 with and without seismic condition.

5   Results and Discussions

5.1   Load Settlement Criteria

Typical pressure–settlement graph for static and seismic condition for a fixed D_f/B ratio = 1 with varying layer thickness ratios of 0.33, 1 and 3.0 has been shown in Figs. 4 and 5 respectively. The results have been presented for both static and seismic

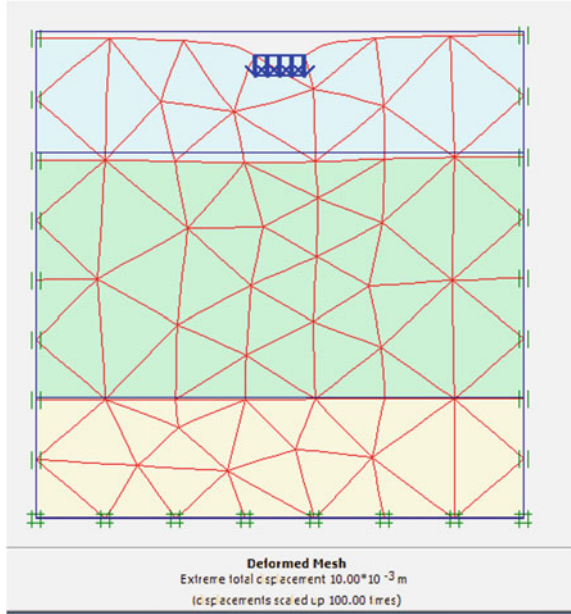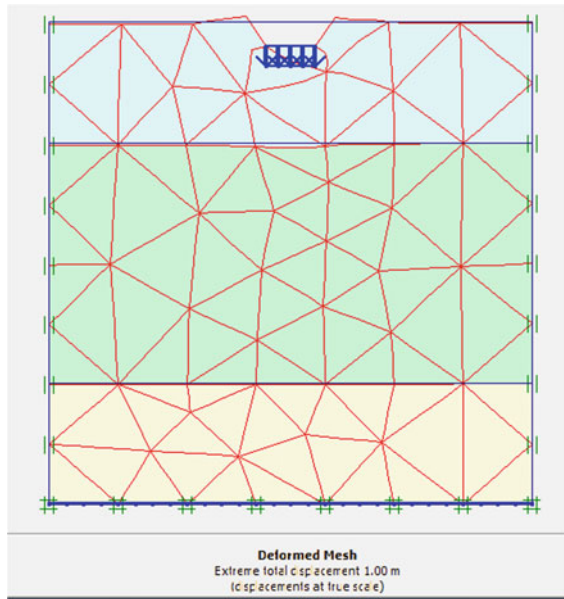**Fig. 2** Deformed mesh of 2 m wide strip footing ($D_f/B = 0.5$) static condition

Deformed Mesh
Extreme total displacement 10.00*10^{-3} m
(displacements scaled up 100.00 times)

Fig. 3 Deformed mesh of 2 m wide strip footing ($D_f/B = 0.5$) for seismic condition for 0.3 g

Deformed Mesh
Extreme total displacement 1.00 m
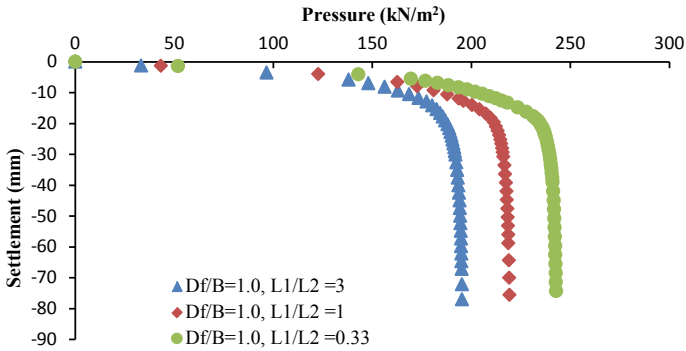(displacements at true scale)

Fig. 4 Pressure versus settlement graph for D_f/B ratio $= 1$ for layer thickness ratio $= 0.33$, 1 and 3.0 (static case)
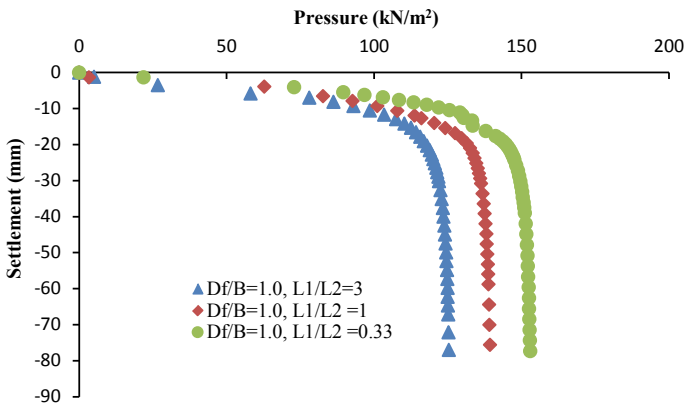

Fig. 5 Pressure versus settlement graph for D_f/B ratio $= 1$ for layer thickness ratio $= 0.33$, 1 and 3.0 (seismic case at 0.1 g acceleration)

conditions for D_f/B ratio $= 1$ for layer thickness ratio $= 0.33$, 1 and $3.0 = 0$, 1 and 3.0.

It has been shown that for a fixed D_f/B ratio, bearing capacity decreases due to increase of thickness ratio. Hence, the results show that the layering effect of foundation has a good effect on the bearing capacity (Fig. 6).

Comparison of seismic bearing capacity factors obtained by the present numerical study with IS: 6403 for static case and Richard et al. [7] obtained for layered soil of ($\varphi_{top} = 30°$ and $\varphi_{bottom} = 33°$) is shown in Figs. 7 and 8. It has been evident that results match well.
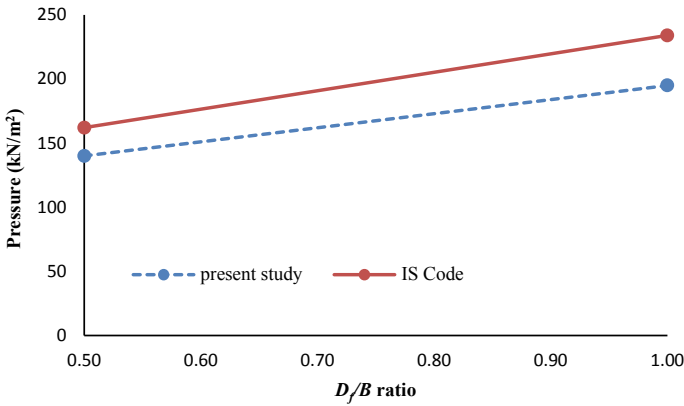
Fig. 6 Pressure versus settlement graph for D_f/B ratio $= 1$ for layer thickness ratio at static case. *Source* IS 6403 : 1981 (Reaffirmed 2002): Code of Practice for Determination of Breaking Capacity of Shallow Foundations
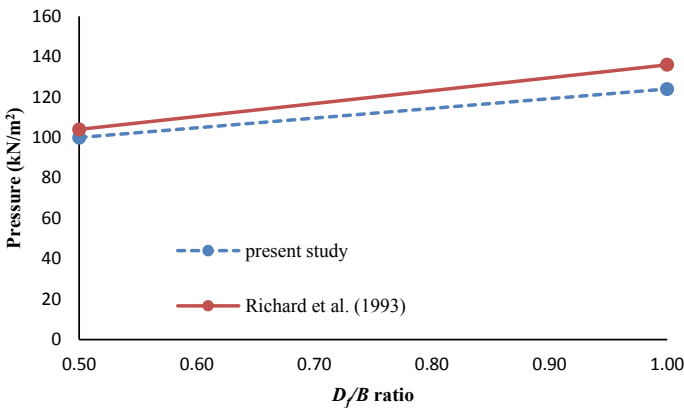

Fig. 7 Pressure versus settlement graph for D_f/B ratio$= 1$ for layer thickness ratio $= 1$ (seismic case at 0.1 g acceleration)

5.2 Effect of Thickness Ratio and D_f/B Ratio

A typical graph for D_f/B ratio $= 0.5$ and 1, with varying layer thickness ratios of 0.33, 1 and 3.0, at static and seismic conditions is shown in Fig. 8. It has been shown that when D_f/B ratio increases, bearing capacity also increases on an average by 15.00% for static condition and 20% for seismic condition. Hence, the results show that the foundation depth has a remarkable effect on the seismic bearing capacity. It has been observed that due to variation of layer thickness ratio from 0.33 to 1, the ultimate bearing capacity decreases up to 11.00% under static case, whereas for seismic case, decrement of bearing capacity is about 12.00% for a D_f/B ratio of 1. A decrease in
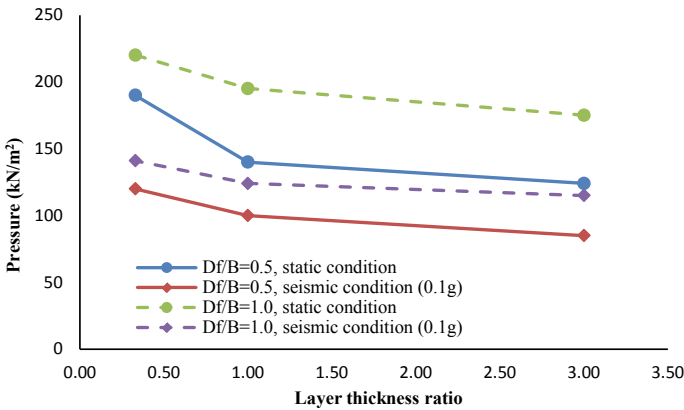
Fig. 8 Load versus settlement graph for D_f/B ratio= 1 for layer thickness ratio = 0.33, 1 and 3.0 (seismic case at 0.1 g acceleration)

ultimate bearing capacity of 26% and 16% are observed under static and seismic cases, respectively for a D_f/B ratio of 0.5. It has been observed that due to variation of layer thickness ratio from 0.33 to 3, the ultimate bearing capacity decreases up to 20.00% under static case, whereas for seismic case, decrement of bearing capacity is about 18.00% for a D_f/B ratio of 1. A decrease in ultimate bearing capacity of 34% and 29% are observed under static and seismic cases, respectively for a D_f/B ratio of 0.5. Further, it has been observed that reduction of bearing capacity due to seismic effect is on an average 35.00%.

5.3 Determination of Bearing Capacity Factors N_Υ and N_q

An attempt has been made to generate bearing capacity factors, N_γ and N_q numerically, using PLAXIS 2D, for broad comparison with those found in the literature. To study the contribution of the soil wedge beneath the footing to the bearing capacity of the soil, unit soil weight (γ) of 18 kN/m^3 was used, cohesion c was set to null and no surcharge load was applied, by determining bearing capacity factor, N_γ. Secondly, another bearing capacity factor, N_q was found by setting soil unit weight and cohesion to null and applying a surcharge load. The seismic bearing capacity of saturated sands is redefined with new seismic bearing capacity factors, N_q and N_γ. Figures 9 and 10 represent variation of N_{qE} and $N_{\gamma E}$ with D_f/B ratio. It has been shown from Figs. 9 and 10, that for a fixed layer thickness ratio and fixed D_f/B ratio, bearing capacity factor in case of seismic condition N_{qE} and $N_{\gamma E}$ value less than static case. It has been also observed that N_{qE} value increases linearly with D_f/B ratio.

It has been observed from Figs. 9 and 10 that the equivalent bearing capacity factor N_{qE} for two-layered cohesionless soil system [strong soil overlaid by a weak soil deposit, i.e., top layer (weaker): bottom layer (stronger) $\geq$ 1] decreases with

Fig. 9 Variation of N_{qE} with D_f/B ratio with varying layer thickness at static condition

Fig. 10 Variation of N_{qE} with D_f/B ratio with varying layer thickness at seismic condition

increase in the thickness of the top layer. N_{qE} is also found to increase with increase in relative frictional strength between two layers. The curves are more or less linear which eases in using interpolated values of N_{qE} for any thickness of the top layer (h) during investigation of bearing capacity of strip footing. It has been observed that with variation of D_f/B ratio, the increase of equivalent bearing capacity factor N_{qE} is approximately 11.00% for static case and 10.00% for seismic condition. It has been further observed that for the decrease of layer thickness ratio, equivalent bearing capacity factor N_{qE} increases on an average by 25.00%.

It has been observed from Figs. 11 and 12 that the equivalent bearing capacity factor $N_{\gamma E}$ for two-layered cohesionless soil system [strong soil overlaid by a weak soil deposit, i.e., top layer (weak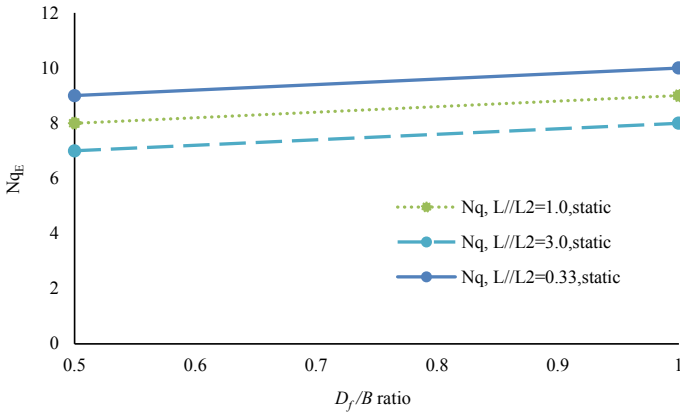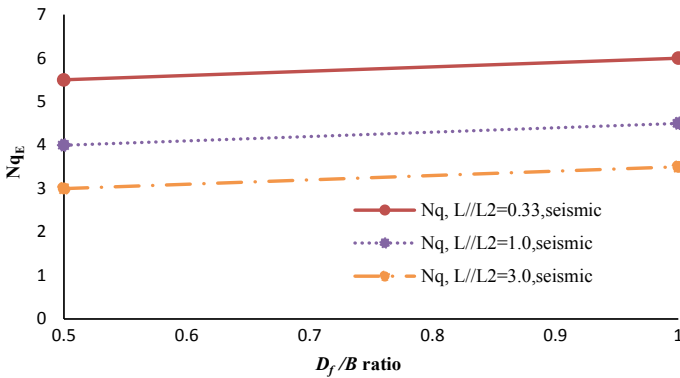er): bottom layer (stronger) $\geq$ 1) decreases with increase in the thickness of the top layer. $N_{\gamma E}$ is also found to increase with increase in relative frictional strength between two layers. The curves are more or less linear
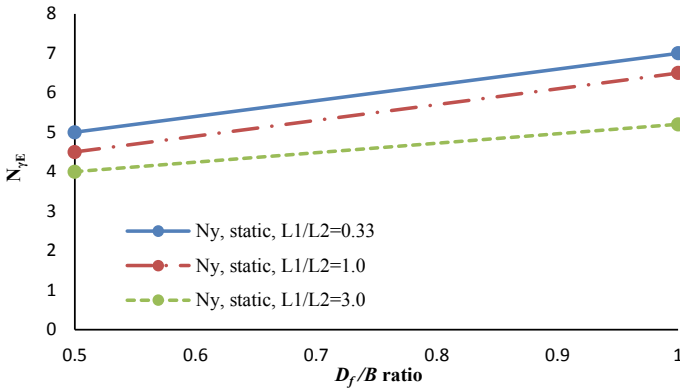
Fig. 11 Variation of $N_{\gamma E}$ with D_f/B ratio with varying layer thickness at static condition
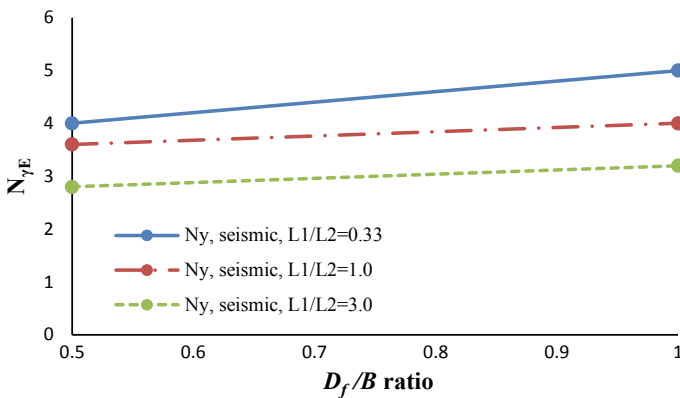

Fig. 12 Variation of $N_{\gamma E}$ with D_f/B ratio with varying layer thickness at seismic condition

which eases in using interpolated values of N_{qE} for any thickness of the top layer during investigation of bearing capacity of strip footing. It has been observed that with variation of D_f/B ratio, the increase of equivalent bearing capacity factor $N_{\gamma E}$ is approximately 40.00% for static case and 25.00% for seismic condition. It has been further observed that for the decrease of layer thickness ratio, equivalent bearing capacity factor $N_{\gamma E}$ increases on an average by 30.00%.

Figures 13 and 14 represent the variation seismic bearing capacity factors, N_{qE} and $N_{\gamma E}$ with seismic acceleration = 0.1–0.3 g, at D_f/B ratio = 1. It has been observed that seismic bearing capacity factors, N_{qE} and $N_{\gamma E}$, decrease with increase of seismic acceleration from 0.1 to 0.3 g. Numerical analysis shows that by considering pseudo-static seismic forces, design solutions can be found for the computing of seismic bearing capacity factors for shallow foundations. It has been found that for the increase of seismic acceleration = 0.1–0.3 g, decrease of equivalent bearing
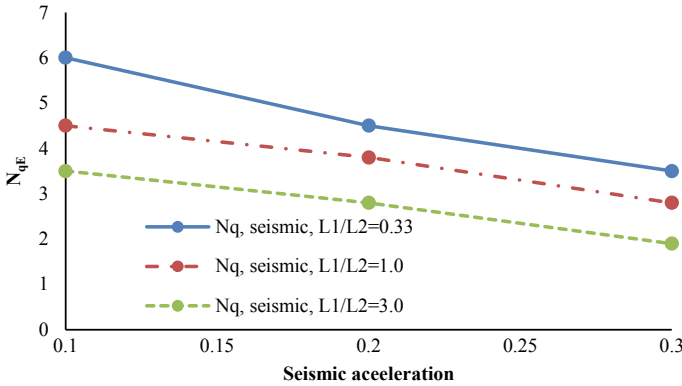
Fig. 13 Variation of N_{qE} for D_f/B ratio $= 1$, with varying layer thickness at seismic acceleration (0.1–0.3 g)
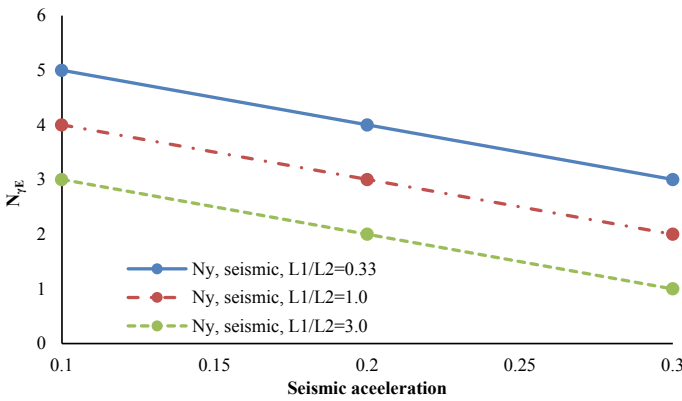
Fig. 14 Variation of $N_{\gamma E}$ for D_f/B ratio $= 1$, with varying layer thickness at seismic acceleration (0.1–0.3 g)

capacity factor $N_{\gamma E}$ is approximately 60.00% for and 30.00% for N_{qE}. The reduction of seismic bearing capacity is due to the fact of the soil inertia (kinematic effect).

6 Conclusions

From the current investigations, the following conclusions may be drawn:

1. The analysis shows that by considering pseudo-static seismic forces, design solutions can be obtained for the computing of seismic bearing capacity factors for shallow foundations. It has been observed that with the increase in D_f/B ratio,

bearing capacity also increases on an average by 15.00% for static condition and 20% for seismic condition.

2. It has also been observed that due to variation of layer thickness ratio from 0.33 to 3, the ultimate bearing capacity decreases up to 20.00% under static case, whereas for seismic case, decrement of bearing capacity is about 18.00% under similar condition. It has also been found that with the increase in horizontal seismic acceleration from 0.1 g to 0.3 g, the seismic bearing capacity factors N_q and N_γ reduce appreciably nearly by 30% and 60%, respectively.

3. With the variation of D_f/B ratio, the increase of equivalent bearing capacity factor N_{qE} is approximately 11.00% for static case and 10.00% for seismic condition. It has been further observed that for the decrease of layer thickness ratio, equivalent bearing capacity factor N_{qE} increases on an average by 25.00%.

4. The analysis further shows that with variation of D_f/B ratio, the increase of equivalent bearing capacity factor $N_{\gamma E}$ is approximately 40.00% for static case and 25.00% for seismic condition. It has been further observed that for the decrease of layer thickness ratio, equivalent bearing capacity factor $N_{\gamma E}$ increases on an average by 30.00%.

5. It can further be observed that for the increase of seismic acceleration = 0.1–0.3 g, decrease of equivalent bearing capacity factor $N_{\gamma E}$ is approximately 60.00% for and 30.00% for N_{qE}. The reduction of seismic bearing capacity is due to the fact of the soil inertia (kinematic effect).

References

1. Brinch Hansen, J.A.: Revised and extended formula for bearing capacity. Bulletin no. 28, Danish Geotechnical Institute Copenhagen, pp. 5–11 (1970)
2. Chaudhury, D., Subba Rao, K.S.: Seismic bearing capacity of shallow strip footings. Geotech. Geol. Eng. **23**(4), 403–418 (2005)
3. Lotfizadeh, M.R., Kamalian, M.: Estimating bearing capacity of strip footings over two-layered sandy soils using the characteristic lines method. Int. J. Civil Eng. **14**(2B), 107–116 (2016)
4. Meyerhof, G.G.: Some recent research on the bearing capacity of foundations. Can. Geotech. J. **1**, 16–26 (1963)
5. Mosallanezhad, M., Moayedi, H.: Comparison analysis of bearing capacity approaches for the strip footing on layered soils. Arab. J. Sci. Eng. **42**, 3711–3722 (2017)
6. PLAXIS BV.: User's manual of PLAXIS, A.A. Balkema Publishers (2002).
7. Richards, R., Jr., Elms, D.G., Budhu, M.: Seismic bearing capacity and settlement of foundations. J. Geotech. Eng. ASCE **119**(4), 662–674 (1993)
8. Saada, Z., Maghous, S., Garnier, D.: Seismic bearing capacity of shallow foundations near rock slopes using the generalized Hoek-Brown criterion. Numer. Anal. Methods Geomech. **35**, 724–748 (2011)
9. Sarma, S.K., Iossifelis, I.S.: Seismic bearing capacity factors of shallow strip footings. Geotechnique **40**(2), 265–273 (1990)
10. Terzaghi, K.: Theoretical Soil Mechanics. Wiley, New York (1943)

Ground Improvement by Granular Anchor Pile Foundation in Cohesive Soil Under Axial Pullout Loads

Heena Malhotra and **Sanjay Kumar Singh**

Abstract Due to rapid urbanization and increase of population, the demand of construction has increased significantly during the last few decades and thus resulting in scarcity of land. So, to eradicate this problem, geotechnical engineers are using several ground improvement techniques such as use of geosynthetics, stabilization of soil, vibro-compaction, stone column, blasting, compacting piles and granular anchor pile foundation to construct buildings on weak subsoil strata for the optimum usage of land. These techniques are used to improve the soil bearing capacity to withstand compressive as well as uplift forces imposed on the structure. The adoption of suitable type of foundation technique will depend upon various factors such as nature of soil, type of loading and type of structure. Granular anchor pile foundation is the innovative technique used to sustain the compressive and pullout loads over weak subsoil. In this paper, the laboratory experiments were conducted to understand the behavior of axial pullout load of granular anchor pile foundation in cohesive soil. The parameters studied were length of the pile, diameter of the pile, L/D ratio and size of the granular fill material. The test results indicate that the pullout capacity decreases with the increase in L/D ratio from 7.5 to 12.5. There was an increase in the pullout load resistance, when the diameter of the pile increases. Moreover, pullout load capacity increases when size of the granular fill increased.

Keywords Granular anchor pile foundation (GAPF) · Pullout load · Cohesive soil

H. Malhotra (✉) · S. K. Singh
Civil Engineering Department, Punjab Engineering College (Deemed to be University),
Chandigarh 160012, India
e-mail: malhotraheena16@gmail.com

S. K. Singh
e-mail: sksingh@pec.ac.in

1 Introduction

There are many structures such as television and transmission towers, tall chimneys, tension cable for suspension bridges and marine structures such as floating platforms, bridge abutments, retaining walls, bulkheads, avalanche control structures (snow nets, umbrella system) and tall buildings whose foundations are subjected to large uplift forces. The conventional shallow foundation in cohesive soil may not be sufficient to withstand the uplift forces, and such cases required deep foundations such as concrete pile, under-reamed pile foundations and belled pier foundations. The structures are subjected to compressive vertical load, uplift loads (tension forces), lateral loads or a combination of all these to make resultant load oblique. Granular piles (GPs) were developed initially to resist compressive loads through predominantly pile action. Granular piles, also known as stone columns, have been extensively used in soft clays and loose sands to rectify their geotechnical properties [1, 2]. However, the capacity of single or small groups of GPs was restricted due to bulging near the upper end of pile. It can be installed in wide variety of soils, ranging from loose to medium sands, soft to medium clays and organic soils but is deficient in taking uplift loads. The failure mechanism of GP under uplift loads demonstrates the granular material displacing out from the sides of the pile–soil interface. Hence, any pressure bulb is not formed, thus restricting its uplift capacity near the bottom of the pile. This deficiency of granular pile may be improved by providing an anchor plate at the base of the granular pile with a rod attached to the bottom of foundation to resist pullout loads [3–6]. The granular anchor pile (GAP) is much superior to that of solid piles as the load is directly transferred to the tip where the bulging capacity is the highest [7]. Therefore, the behavior of GAP is required to be studied in the case of non-expansive clayey soil also. Therefore, for a thorough understanding of pile–soil interaction, it is necessary to study the behavior of a granular anchor pile foundation by varying different parameters subjected to pullout loads embedded in cohesive soil. In this paper, extensive experimental tests were conducted on laboratory-scale GAP installed in clayey soils under uplift loads by varying different pile parameters.

2 Concept of Granular Anchor Pile

Granular anchor pile (GAP) is a new ground improvement technique used widely for improving the settlement and strength characteristics of cohesive soils for shallow foundation. A granular anchor pile is the one in which the foundation is anchored at the bottom of the granular pile to a mild steel plate through a central mild steel rod (Fig. 1). This serves to hold the particulate granular medium and prevents the granular pile from being sheared away and is thus instrumental in mobilizing the frictional resistance to the uplift force on the foundation.

Fig. 1 Concept of granular pile anchor
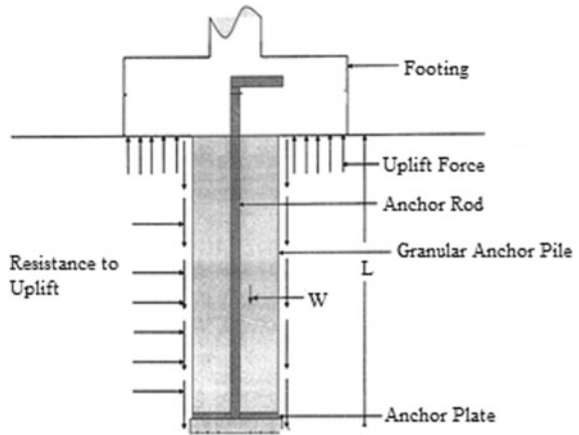
3 Materials

The soil used in pullout tests was collected from Village Sarsod, District Hisar, Haryana (India). Table 1 shows the index properties of the soil. Based on the index properties, the soil was classified as CI as per IS 1498:1970 [8]. The soil had a maximum dry unit weight of 15.1 kN/m^3 at optimum moisture content (OMC) of 18% as determined from the standard Proctor compaction test IS:2720-PART 7 [9]. The grain size distribution curve is shown in Fig. 2.

Granular anchor piles were installed in the soil beds using a granular material that was a mixture of particle size of coarse aggregates which varies between 3 to 6 mm and 8 mm to 10 mm. All the granular anchor piles studied in this laboratory test program were compacted by ramming the granular material into equal parts up to the required height. The maximum and minimum densities of the granular material from relative density test are 20.1 kN/m^3 and 14.1 kN/m^3, respectively. Granular material was filled in the pile at 60% relative density, i.e., 17 kN/m^3.

Table 1 Index properties of the soil

Properties	Value	IS Code
Specific gravity	2.71	IS:2720-PART 3 [10]
Sand (%)	3	
Silt (%)	67	
Clay (%)	30	
Liquid limit (%)	46	IS: 2720-PART 5 [11]
Plastic limit (%)	23	IS: 2720-PART 5 [11]
Plasticity index (%)	23	
Free swell index, FSI (%)	22.7	IS: 2720 PART 40 [12]
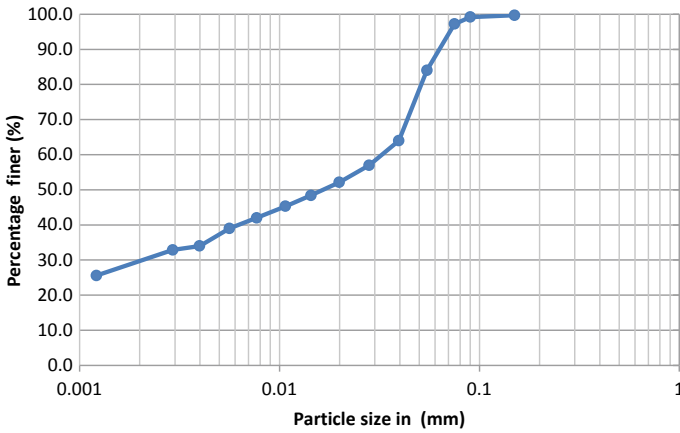
Fig. 2 Grain size distribution curve of soil

In order to study the effect of pullout loads on granular anchor pile foundation (GAPF), the steel anchor piles were fabricated as shown in Fig. 5.The circular anchor plate of diameter equal to diameter of pile has been welded to the bottom of the tie rod, thus making a rigid bond for embedded lengths as 250 mm, 350 mm and 450 mm for L/D ratio 7.5, 10 and 12.5. The hook was made at the top of the pile to connect the loading wire and apply the uplift load on the granular anchor pile (Figs. 3 and 4).

Fig. 3 Granular material of size 3 to 6 mm

Fig. 4 Granular material of size 8 to 10 mm

Fig. 5 Anchor piles used in laboratory tests

4 Experiment Program

The laboratory tests were performed on soil to study the uplift capacity of a GAPF system. The aim of the study was to investigate the behavior of the granular anchor pile foundation system as a new foundation technique used in improvement of cohesive soils. Various tests have been conducted by varying different pile parameters to understand the behavior of granular anchor pile foundation. The parameters such as pile length, pile diameter, L/D ratio, load inclination, group pile, encasing of pile periphery with geotextile and geonet, and spacing of piles have been studied.

4.1 Model Test Setup

The rectangular tank of size 900 mm $(L) \times 900$ mm $(B) \times 600$ mm (H) was fabricated to perform model laboratory test. The wall thickness of the metal tank was kept 5 mm. The experimental setup is shown in Fig. 6. The soil was filled in the tank at MDD, i.e., 15.1 kN/m^3, and weight of the soil required to fill the tank was calculated. The tank was divided into convenient number of equal parts, and each part is having to be compacted for desired unit weight so as to achieve the required density. A total of nine no. GAP piles were casted simultaneously at c/c distance of 225 mm. A steel tie rod with a circular plate of diameter equal to that of GAP was welded and placed

Fig. 6 Preparation of test bed and construction of GAP

vertically at the bottom of the test tank at the required position with c/c spacing of 225 mm distance from each pile w.r.t tank dimensions. This spacing was adopted by considering the uplift load influence on the pile surface. The anchor rod and pile casing were held in position with the help of the steel bars placed on the top of the tank, tied with the binding wires as shown in Fig. 6. The soil was filled in layers of 50-mm thickness in the tank. Each part of the soil was carefully placed in the tank such that it abstains from entering the casing pipe and thus compacting with the rammer up to the required height of the test tank The amount of the granular pile material required to be filled at uniform density was filled in layers of equal thickness with simultaneous removal of casing pipe.

After the test bed and construction of GAP were ready, the top end of the MS anchor rod was connected to the loading arrangement with the help of a specially designed and fabricated attachment provided at the top to transfer the uplift force to the GAP system. After compaction, the loading frame was placed over the granular anchor pile centrally, and the side frame was fastened with the nut bolt with the test tank to resist the upward thrust on the loading frame. The pullout load was applied at the center of the pile axis with the properly designed load arrangement, which consists of the steel frame, a flexible steel wire rope (10 mm dia) and 3 nos. of frictionless pulleys, a loading platform and dead weights. A special fabricated 6 mm dia steel hook was made to attach the loading setup with the granular anchor pile from which the pullout load was transferred to the GAP. On the other hand, a steel wire was connected with the U-shaped hook fastened with nut bolt to make its connection with the loading platform. The pullout dead loads were applied with respect to axis of granular pile, by taking steel wire rope through pulleys and placing loading setup at accurate position from the granular pile. In each case, this was achieved by placing the loading setup at calculated position, attaching wire rope with granular anchor pile and putting 8 kg weight on the loading platform for straightening of the wire rope. The tank was fabricated for load carrying capacity of 650 kg. Incremental loading was provided in 10–15 increments by putting known dead weights in the loading platform, till granular anchor pile is completely pulled out of the clay bed. For measuring the upward displacements in vertical direction, an L-shaped steel plate was welded with the steel hook attachment from which the pullout load was applied, and two dial gauges were placed on the steel plate to measure the upward movements. The average displacement found from the two dial gauges was considered to be the final uplift movement.

5 Results and Discussion

The results of pullout test on single GAP by varying different parameters such as length of piles, diameter of piles, *L/D* ratio and size of granular fill are discussed in terms of pullout load–uplift displacement behavior. To study the effect of pullout load, the graphical representation of results is presented showing the applied uplift

load (N) on *x*-axis and the axis and the corresponding upward displacement (mm) on *y*-axis.

5.1 Effect of Length and Diameter on Granular Anchors Pile Foundation

The effect of vertical pullout load-upward displacement curve for GAP of different length and diameters with L/D ratio 10 is shown in Fig. 7. The curves indicate that at all stages of loading, the upward load required to be applied on the GAP to cause a given upward movement increased with increase in length of GAP. The ultimate capacity of pile is evaluated using the double tangent intersection method. In this method, two tangents are drawn; one from the initial flatter position and second through the final steeper portion of load–displacement curve. The load corresponding to intersection point of two tangents is considered to be the ultimate capacity of pile. Figure 7 shows the ultimate pullout load from double tangent intersection method for length $L = 250$ mm. The ultimate pullout load for all the cases of GAP is calculated and mentioned in Table 2.

In Fig. 8, pullout behavior of the curve reflects the effect of diameter of GAP on pullout behavior. The applied upward load was observed to increase with increasing
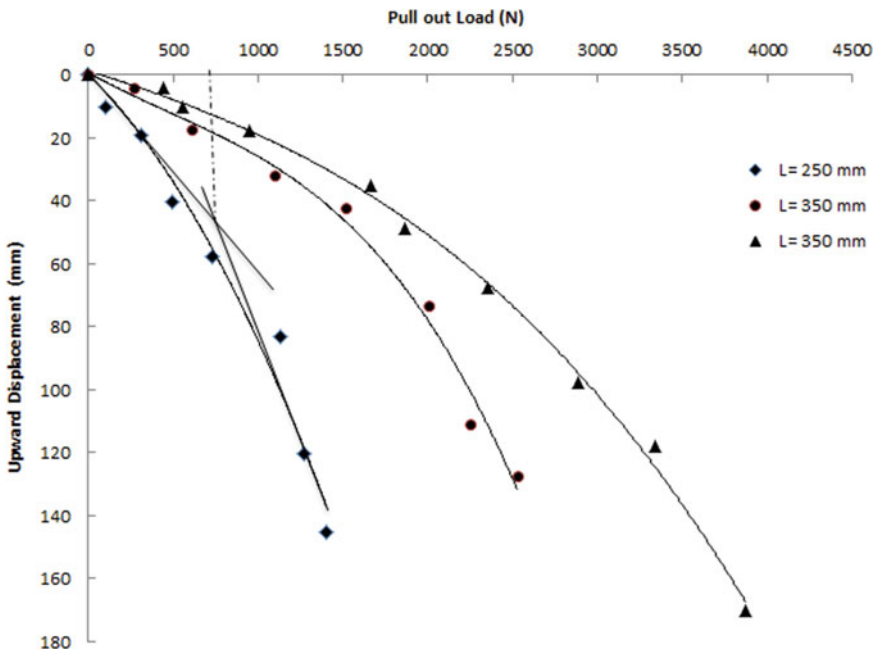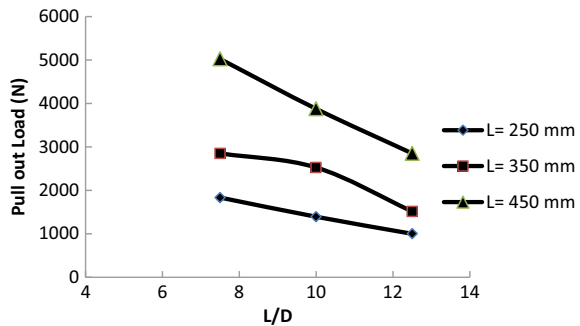

Fig. 7 Pullout deformation curves for $L/D = 10$

Table 2 Ultimate pullout capacity of single GAP for length 250 mm, 350 mm and 450 mm

Length of pile (mm)	L/D	Ultimate pullout capacity of clay (N)
250	7.5	820
	10	641
	12.5	457
350	7.5	1310
	10	1161
	12.5	697
450	7.5	2490
	10	1921
	12.5	1413

Fig. 8 Pullout deformation curve of *L/D* versus pullout load

diameter of the GAP at all stages of the test as the resistance to uplift increased with increasing surface area of the pile–soil interface. It has also been observed from the results that as the L//D ratio of GAP increases, the pullout load decreases. Therefore, the uplift resistance depends upon the frictional characteristics and the surface area of the interface. The higher the surface area of the interface, the greater the uplift resistance. Increasing the diameter increases the surface area and pile anchor weight and consequently uplift resistance and results in increased failure pullout load.

5.2 Effect of Size of the Granular Material Fill on Pullout Load Capacity

The influence of size of granular material on ultimate pullout capacity of GAP was studied for two sizes of granular material, i.e., 3–6 mm and 8–10 mm. Table 3 presents the results of ultimate pullout capacity of granular anchor pile. It is observed from Table 3 that with increase in the size of the aggregates, the ultimate pullout capacity of GAP is increased. This is because the movement of aggregate in soil is restricted, thus

Table 3 Ultimate pullout capacity of single GAP for varying sizes of granular material

Length (mm)	L/D	Pullout load (N)		Percentage increase
		Agg size (3–6 mm)	Agg size (8–10 mm)	
250	7.5	820	941	14.8
	10	641	708	10.5
	12.5	457	493	7.8
350	7.5	1310	1425	8.8
	10	1161	1235	6.4
	12.5	697	758	8.7
450	7.5	2490	2680	7.6
	10	1921	1970	2.5
	12.5	1413	1546	9.4

making large pressure bulb in comparison with smaller aggregates. Also, with the increase in size of the granular fill, the weight of the granular anchor pile increases, thus resulting in resistance to uplift load due to self-weight of the pile. As shown in Table 3, the percentage increase in pullout capacity is more in case of length $L = 250$ mm with increase in aggregate size.

6 Conclusions

A comprehensive laboratory test program was performed to study the pullout load response of GAP embedded in non-expansive clayey soil. The test program studied pullout load-upward movement behavior of GAP embedded in soil with varying parameters. The following conclusions can be drawn from the present study.

1. The uplift load increases with the increase in diameter of the GAP. The resistance to uplift force increases with increasing surface area of the pile–soil interface consequent upon increase in the diameter.
2. For a given L/D ratio, the failure pullout load increased with increasing length of the GAP. Similarly, for a given length of the GAP, the failure pullout load increased with decreasing L/D ratio. Increasing diameter increases the surface area and consequently the uplift resistance and results in increased failure pullout load.
3. With the increase in size of the granular material, resistance to uplift load increases due to formation of large pressure bulb in case of large aggregates as compared to smaller aggregates.

References

1. Kumar, P., Ranjan, G.: Pullout capacity of granular piles: a field study. In: Proceedings of Indian Geotechnical Conference Indian Geotechnical Society, Vadodara Chapter, India, 349–352 (2007)
2. Kumar, P., Ranjan, G.: Granular pile system for uplifting loads: a case study. In: Proceedings of International Conference on Offshore Engineering and Nearshore Engineering (GEOSHORE), Oxford & IBH, New Delhi, India, pp. 427–432 (1999)
3. Phanikumar, B., Prasada, G., Srirama, A.: Use of anchored granular column in minimizing swell in expansive clay. In: Proceedings of Indian Geotechnical Conference, Warangal, India, pp. 61–65 (1995)
4. Phanikumar, B.R.: A study of swelling characteristics of granular pile-anchor foundation system in expansive soils. Ph.D. thesis, Jawaharlal Nehru Technological Univ, Hyderabad, India (1997)
5. Srirama, A., Phanikumar, B., Dayakar, R.: Pullout behavior of granular pile-anchors in expansive clay beds in-situ. Geotech. Geoenviron. Eng. **133**(5), 531–538 (2007)
6. Kranthikumar, A., Sawant, V., Shukla, S.: Numerical modeling of granular anchor pile system in loose sandy soil subjected to uplift loading. Int. J. Geosynth. Ground Eng. **2**(15), 1–7 (2016)
7. Madhav, M.R.: Granular Piles—Recent Contributions. Workshop On Ground Improvement with Geotextiles and Stone Columns, Calcutta (1994)
8. IS 1498: Classification and identification of soils for general engineering purposes. Bureau of Indian Standards, New Delhi (1970)
9. IS 2720 Part 7: Methods of test for soils—determination of water content-dry density relation using light compaction. Bureau of Indian Standards, New Delhi (1980)
10. IS 2720 Part 3: Methods of Test for Soils—Determination of Specific Gravity Bureau of Indian Standards, New Delhi (1980)
11. IS 2720 Part 5: Methods of Test for Soils—Determination of Liquid Limit and Plastic Limit. Bureau of Indian Standards, New Delhi (1985)
12. IS 2720 Part 40: Methods of Test for Soils—Determination of Free Swell Index of Soils. Bureau of Indian Standards, New Delhi (1977)

Seismic Bearing Capacity of Strip Footing Embedded in Slope Situated Below Water Table

Litan Debnath, Rohan Deb, Prasanta Das, and Sima Ghosh

Abstract An attempt is made to give a formulation of the pseudo-static bearing capacity coefficient of a shallow strip footing embedded in slope in c-φ nature of the soil in terms of a single coefficient ($N_{\gamma e}$) using limit equilibrium method which is subjected to groundwater flow. Failure surface is assumed linearly varying with cohesion, surcharge and unit weight of the soil. Iteration technique has been applied to optimize the solution. The ultimate bearing capacity equation was derived as a function of different properties of soils and footing, i.e., width of footing, depth of footing, the cohesion of soil, unit weight of soil and depth of water table. Various parametric studies have been studied to show the variation of bearing capacity coefficient with different parameters. Design chart of table has been shown for various ranges of parameters.

Keywords Bearing capacity · Pseudo-static · Water table · Limit equilibrium · c-φ soil

1 Introduction

The very first researches were done based on the static method of analysis in which bearing capacity coefficients were calculated on the basis of static loads on the footings and the weight of the soil mass in both active and passive conditions. The critical bearing capacity theories started from Rankine [1], Prandtl [2], Terzaghi [3], Saran et al. [4] and many others who have extensively studied the bearing capacity of shallow footings for static loading case. Terzaghi bearing capacity theory (1943) was the first general theory for the bearing capacity of soils under a strip footing. The seismicity effect was not considered in the analysis and hence the name static. Meyerhof and Adams [5], Rowe and Devis [6, 7], Subha Rao and Kumar [8] worked on the ultimate uplift capacity of foundations under static condition by using different methods of analysis (limit equilibrium, nonlinear finite element method,

L. Debnath (✉) · R. Deb · P. Das · S. Ghosh
National Institute of Technology, Agartala, India
e-mail: litandbnth4@gmail.com

method of characteristics). The effects of dynamic loadings like seismic forces were not considered in the static analysis. Severe earthquakes such as the Kobe earthquake (1995), Santa Barbara (1925), Nigata (1964) and Loma Prieta (1989) have earmarked the necessity of seismic design of structures. The dynamic loading of the earthquake has caused catastrophic effects due to foundation failure as well as anchor failure, creating an urgent need for seismic design of foundations and anchors under different conditions it can be subjected to. Since a dynamic load is repetitive in nature, there is a need to determine the displacement of the foundation due to earthquakes and their damage potential.

In pseudo-static analysis, the seismic loadings are considered to be as equivalent inertia forces, i.e., the weight of the wedge is multiplied with the acceleration coefficient (horizontal and vertical) and the inertia forces are found out on the basis of the static equilibrium considerations.

Mononobe and Okabe (M–O) [9] was the pioneer in the inclusion of "seismicity" in the design of structures (in this case retaining walls). IS 1893:1984 has also adopted the M–O method for the determination of seismic active and passive earth pressure behind the retaining walls. Among the limited literature available on the seismic bearing capacity, the earliest is the Meyerhof's [10] method, where the seismic forces were considered as inclined pseudo-static loads applied at the structure. Then, Sarma and Lossifelis [11], Richards et al. [12], Buddhu and Al-Karni (1993) and Kumar and Kumar (2003) considered the seismic forces both on the structure and on the supporting soil mass which was not considered by Meyerhof. Researchers like Sarma and Lossifelis [11], Buddhu and Al-Karni [13], Richards et al. [12], Dormieux and Pecker [15], Paolucci and Pecker [16], Soubra [17, 18], Kumar and Rao [19], Kumar [20] and Choudhury and Subha Rao [21] had studied the seismic bearing capacity of shallow footings for horizontal ground. But the study for the sloping ground is very limited. Sawada et al. [22], Sarma [23] and Askari and Farzaneh [24] had given the solution for seismic bearing capacity of shallow foundations near the sloping ground; again, some works for surface footing on the sloping ground were carried out by Zhu [25], Kumar and Kumar [14], Kumar and Rao [26], by limit equilibrium analysis, method of characteristic, etc., but for foundations embedded in sloping ground, research is still limited. Choudhury and Rao [27], Chakraborty and Kuamr [28] determined the seismic bearing capacity of a shallow foundation embedded in a sloping ground surface by using the theorems of limit equilibrium method and limit analysis in conjunction with finite elements and nonlinear operations, respectively. Larkin [29] presented a method of assessing the probability of failure of shallow foundations in saturated fine-grained soil under multi-directional seismic loading. Then, Massiah and Soubra [30] presented a reliability-based approach for the analysis and design of a shallow strip footing subjected to a vertical load with or without pseudo-static seismic loading. The computation of bearing capacity of foundations in the presence of groundwater flow is not straightforward. Because footings are generally impervious, the ground flow patterns beneath and around the foundation base may experience a change attributable to the construction of the footing. The effect of groundwater flow has been given less consideration in the literature. Very recently, the bearing capacity of foundations

subject to groundwater flow has been presented by Veiskaramiand Kumar [31] and Kumar and Chakraborty [32] by which the ultimate bearing capacity of strip foundations was calculated subjected to horizontal groundwater flow with the help of the stress characteristics method and lower bound finite element method, respectively.

2 Method of Analysis

A shallow strip footing of width (B) resting below the ground surface at a depth of (D_f) over which a load (P_L) acts. For shallow foundation ($D_f \leq B$), the overburden pressure is idealized as a triangular surcharge load over the slope line which acts about a length EY at a slope angle of i. The failure surface has two main regions, the active and the passive wedge, and thereby is assumed to be a simple Coulomb failure mechanism as shown in (Fig. 1). The detailed free body diagram of active zone AMC and passive zone MCF, respectively, is shown in (Fig. 2). The water table is taken at a depth of D_w from the ground level (first case) see (Fig. 1). And the water table is taken at a depth of D_w from the base of the footing (second case) see (Figs. 3 and 4). H is the depth of the failure wedge from the base of the footing, h is the depth from the level of the water table up to the end of the failure zone, and H is the total depth of the failure mechanism from the ground level to the end of the failure zone.

The hydrostatic force due to the presence of the water is given by:

$$P_{\text{stat}} = \frac{\gamma_w}{2} h^2 \tag{1}$$

which acts at a height of $h/3$ from the base of the system.

As given by Ebeling and Morrison (1992) is replaced by such as:

$$\gamma_{we} = \gamma_w + (\overline{\gamma} - \gamma_w) r_u \tag{2}$$
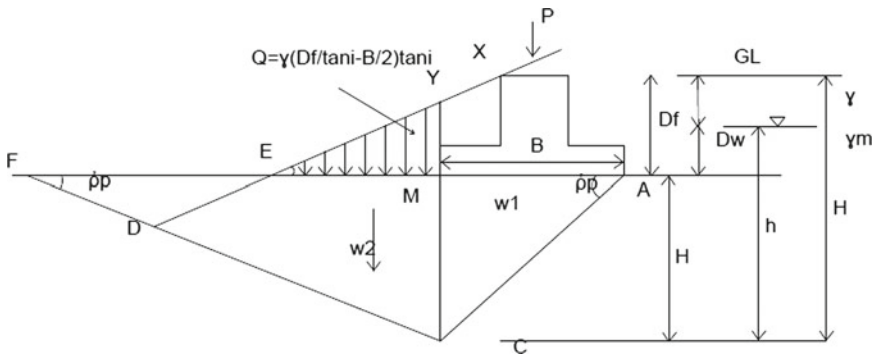

Fig. 1 First condition (water table above the base of footing)
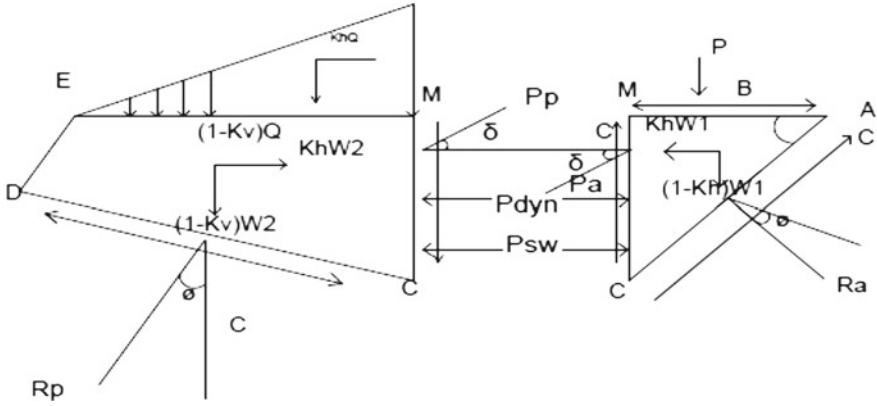
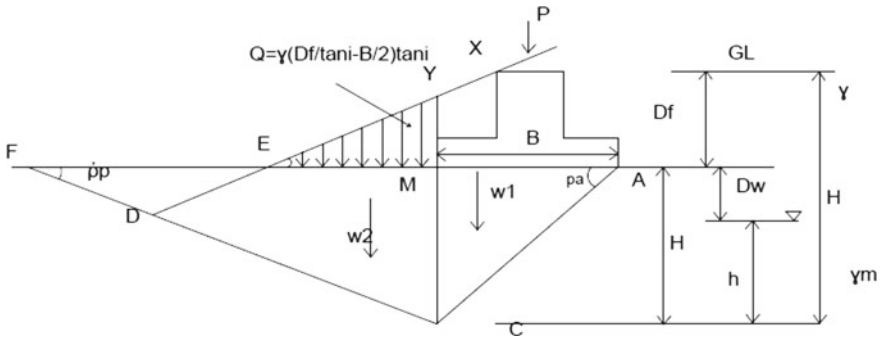**Fig. 2** Free body diagram of forces under pseudo-static approach

Fig. 3 Second condition (water table below the base of the footing)
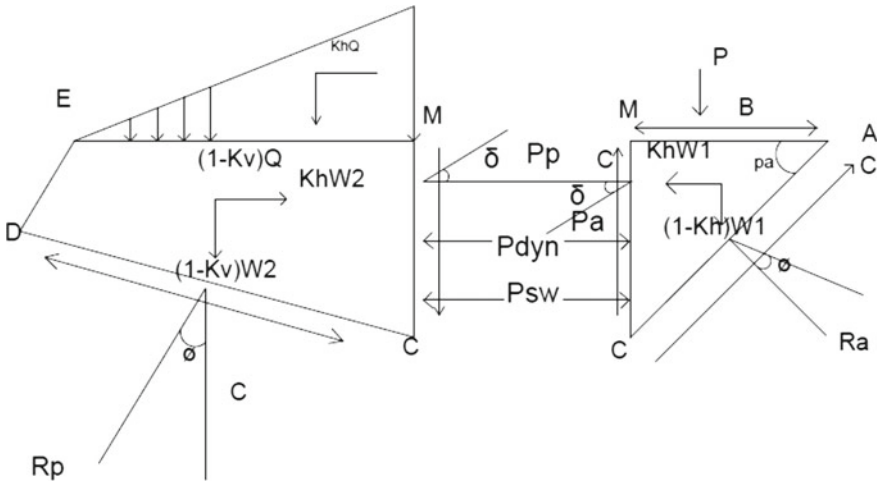

Fig. 4 Free body diagram of forces under pseudo-static approach

The hydrostatic force, i.e., under seismic condition, is calculated by using. Westergaard's approach(1993):

$$P_{\text{dyn}} = \frac{7}{12} k_h \gamma_w h^2 \tag{3}$$

which acts at a height of $0.4h$ from the base of the system.

Pseudo-Static analysis:

First condition (water table above the base of the footing).

Active region:

Let width of the footing AM $= B$.

The angle of inclination of the active wedge with the horizontal is ρ_a, and therefore, the height of the wall MC $= B \tan(\rho_a)$which is considered as H say.

Applying the limit equilibrium conditions in the triangular region AMC, i.e., summation.

of horizontal forces and vertical forces equal to zero, we get:

$$\sum H = 0 \Rightarrow P_A \cos \delta = R_A \sin(\rho_a - \Phi)$$
$$- \frac{cB}{\cot \rho_a} \cot \rho_a + (W_1 + P)k_h - P_{\text{hyd}} - P_{sw} \tag{4}$$

$$\sum V = 0 \Rightarrow P_A \sin \delta = -R_A \cos(\rho_a - \Phi) + (W_1 + P)(1 - k_v) - 2cB \, \tan \rho_a \tag{5}$$

$$P_A = f(k_h, k_v, \rho_a, \phi, \delta, D_w) \tag{6}$$

Passive region:

Applying the limit equilibrium condition in the polygonal region MCDE, i.e., summation of horizontal forces and vertical forces equal to zero, we get:

$$\sum H = 0 \Rightarrow P_P \cos \delta = R_P \sin(\rho_p + \Phi) + \frac{c \cos \rho_p}{\sin \rho_p} \times B$$
$$\times \left[\tan \rho_a - \left(\frac{\tan \rho_a}{\tan \rho_p} - \frac{n}{\tan i} + \frac{1}{2} \right) \times \left(\frac{\sin \rho_p \, \sin i}{\sin(i + p)} \right) \right]$$
$$+ (W_2 + Q)k_h - P_{\text{hyd}} - P_{sw} \tag{7}$$

$$\sum V = 0 \Rightarrow P_P \sin \delta = R_P \cos(\rho_p + \Phi) - cB \tan \rho_a - cB$$
$$\times \left[\tan \rho_a - \left(\frac{\tan \rho_a}{\tan \rho_p} - \frac{n}{\tan i} + \frac{1}{2} \right) \times \left(\frac{\sin \rho_p \, \sin i}{\sin(i + p)} \right) \right]$$
$$+ (W_2 + Q)(1 - k_v) \tag{8}$$

$$P_P = f(k_h, k_v, \rho_a, \phi, \delta, D_w)$$

From the equilibrium of two wedges, the active pressure and passive pressure will be equal. Thus, we can find out maximum load (P_L) acting on the foundation from the equilibrium of the two wedges.

So,

$$P_A = P_P \tag{9}$$

$$P_L = \frac{1}{2} \gamma B N_{\gamma e} \tag{10}$$

Second Condition (water table below the base of the footing)
Active region
Similarly, as in the first condition.
Applying the limit equilibrium condition in the triangular region AMC, i.e., summation of the horizontal forces and the vertical forces equal to zero, we get:

$$\sum H = 0 \Rightarrow P_A \cos \delta = R_A \sin(\rho_a - \Phi) - \frac{cB}{\cot \rho_a} \cot \rho_a$$
$$+ (W_1 + P)k_h - P_{hyd} - P_{sw} \tag{11}$$

$$\sum V = 0 \Rightarrow P_A \sin \delta = -R_A \cos(\rho_a - \Phi)$$
$$+ (W_1 + P)(1 - k_v) - 2cB \tan \rho_a \tag{12}$$

$$P_A = f(k_h, k_v, \rho_a, \phi, \delta, D_w) \tag{13}$$

Passive region.
Applying the limit equilibrium condition in the polygonal region MCDE, i.e., summation of the horizontal forces and the vertical forces equal to zero, the authors get:

$$\sum H = 0 \Rightarrow P_P \cos \delta = R_P \sin(\rho_p + \Phi) + \frac{c \cos \rho_p}{\sin \rho_p} \times B$$
$$\times \left[\tan \rho_a - \left(\frac{\tan \rho_a}{\tan \rho_p} - \frac{n}{\tan i} + \frac{1}{2} \right) \times \left(\frac{\sin \rho_p \sin i}{\sin(i + p)} \right) \right]$$
$$+ (W_2 + Q)k_h - P_{hyd} - P_{sw} \tag{14}$$

$$\sum V = 0 \Rightarrow P_P \sin \delta = R_P \cos(\rho_p + \Phi) - cB \tan \rho_a - cB$$
$$\times \left[\tan \rho_a - \left(\frac{\tan \rho_a}{\tan \rho_p} - \frac{n}{\tan i} + \frac{1}{2} \right) \times \left(\frac{\sin \rho_p \sin i}{\sin(i + p)} \right) \right]$$
$$+ (W_2 + Q)(1 - k_v) \tag{15}$$

$$P_P = f(k_h, k_v, \rho_a, \phi, \delta, D_w) \tag{16}$$

From the equilibrium of two wedges, the active pressure and passive pressure will be equal. Thus, we can find out maximum load (P_L) acting on the foundation from the equilibrium of the two wedges.

So,

$$P_A = P_P \tag{17}$$

$$P_L = \frac{1}{2}\gamma B N_{\gamma e} \tag{18}$$

3 Results and Discussion

The bearing capacity coefficient $N_{\gamma e}$ is optimized with respect to ρ_A, ρ_p by iterative technique. From the global concave curve, the minimum value is taken as optimum value. Tables and parametric studied have been determined for pseudo-static values of strip footing which has been subjected to water condition under seismic criteria. Design charts are shown in Table 1.

Parametric study

A detailed parametric study has been conducted using the results that are obtained from the optimizing spread sheet which gives the optimum reduced seismic bearing capacity coefficient $N_{\gamma e}$, and discussions are made for the different variation of parameters for all the two different mechanisms adopted in the work, i.e., limit equilibrium principle: pseudo-static method.

From the graph, it can be seen that the bearing capacity coefficient $\left(N_{\gamma e}\right)$ increases with the increase in the soil friction angle (Φ). Increase in Φ increases the strength of the soil (or the internal resistance of the soil) against the shearing resistance.

Figure 5a, b shows the variation of bearing capacity coefficient with respect to seismic acceleration (k_h) for different soil friction angles ($\varphi = 20°, 30°, 40°$) at $\delta = \frac{\varphi}{2}$, $k_v = \frac{k_h}{2}$, $r_u = 0.2$, $\frac{D_w}{B} = 0.25$, $\frac{D_f}{B} = 0.5$, $\frac{2c}{\gamma B} = 0.5$, $i = 15°$.

Figure 2 a, b has done for a particular case, $k_h = 0.2$, when φ increases from 30° to 40°, $N_{\gamma e}$ increases by pseudo-static analysis: first condition—133%, second condition—147%, respectively, which may be due to the fact that increase in φ increases the strength of the soil against shearing resistance.

Figure 6 shows that it can be seen that $N_{\gamma e}$ decreases with the increase in depth of water level (D_w) for water table both above and below the base of the footing as the soil looses its strength with increase in the content of water. From Fig. 3, for a particular case, $k_h = 0.2$, when D_w increases from 0.5 m to 1.0 m, $N_{\gamma e}$ decreases by pseudo-static analysis: first condition—17%, second condition—2%, respectively.

Table 1 Pseudo-static bearing capacity coefficients ($N_{\gamma e}$) for $k_h = 0.1$, $D_w/B = 0.25$

| ϕ	δ	$2c/\gamma B$	$K_v = 0$				$K_v = k_h/2$			
			D_f/B				D_f/B			
20	0	0	7.6	8.7	10.4	12.4	8.0	8.9	10.5	12.5
		0.25	10.16	11.39	13.21	15.33	10.45	11.66	13.47	15.60
		0.5	12.57	14.03	16.05	18.31	12.97	14.42	16.42	18.72
	$\phi/2$	0	8.57	9.90	12.08	14.69	8.75	10.04	12.211	14.832
		0.25	15.52	13.20	15.61	18.44	11.83	13.49	15.91	18.74
		0.5	14.32	16.33	19.01	22.06	14.76	16.75	19.45	22.53
	ϕ	0	9.462	11.29	13.97	17.30	9.65	11.35	14.11	17.45
		0.25	13.01	15.23	19.36	22.07	13.35	15.55	18.59	22.53
		0.5	16.3	19.09	22.51	26.49	16.80	19.49	23.01	27.03
30	0	0	15.68	17.86	20.98	24.57	15.95	18.07	21.12	24.72
		0.25	19.32	21.80	21.32	25.077	19.25	22.18	25.08	29.29
		0.5	22.84	25.92	29.22	31.24	23.42	25.27	29.75	29.99
	$\phi/2$	0	20.02	23.03	28.01	34.31	20.30	23.84	28.71	36.71
		0.25	24.84	28.85	34.92	40.41	20.19	25.7	34.71	40.89
		0.5	29.51	34.15	39.89	46.41	30.2	34.79	40.55	47.08
	ϕ	0	26.09	32.04	39.93	49.11	26.37	32.26	40.05	49.21
		0.25	33.07	39.93	48.59	58.48	33.62	40.44	49.10	58.97
		0.5	39.82	47.58	57.01	67.60	40.63	48.40	57.85	68.48
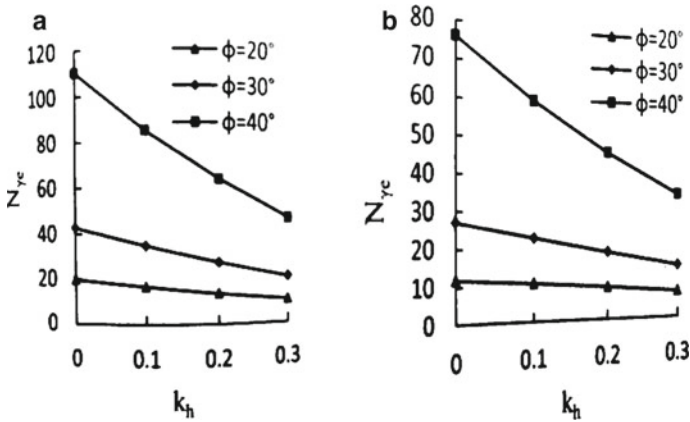
Fig. 5 **a** First condition (pseudo-static analysis), **b** Second condition

Fig. 6 **a** First condition, **b** Second condition

Figure 6a, b shows the variation of bearing capacity coefficient with respect to seismic acceleration (k_h) at different depths of water table (D_w in m) at $\delta = \frac{\varphi}{2}$, $k_v = \frac{k_h}{2}$, $r_u = 0.2$, $\frac{D_w}{B} = 0.25$, $\frac{D_f}{B} = 0.5$, $\frac{2c}{\gamma B} = 0.5$, $i = 15°$.

From Fig. 7, it can be seen that $N_{\gamma e}$ decreases with the increase in the width of the footing (B) with increasing seismic acceleration for the water table lying both above and below the base of the footing. This is due to the stress effect, i.e., the stress dependency—smaller footing will have smaller stress, whereas the larger footing will have higher stress and hence smaller bearing capacity coefficient. For a particular case, $k_h = 0.2$, when B increases from 2 m to 2.5 m, $N_{\gamma e}$ decreases by pseudo-static analysis: first condition—17%, second condition—23%, respectively.

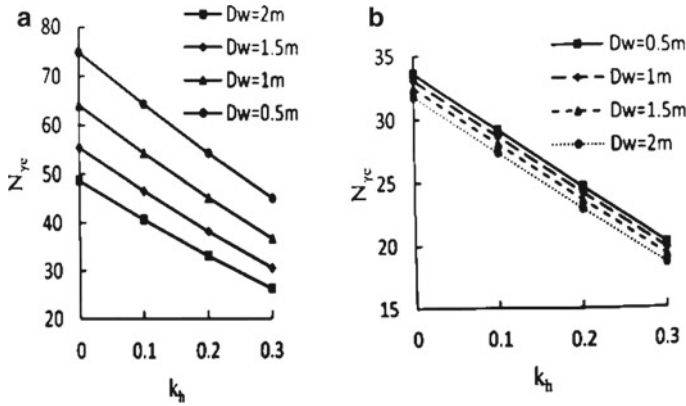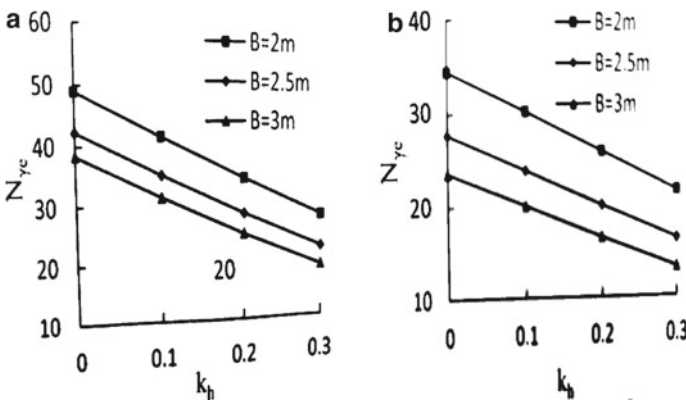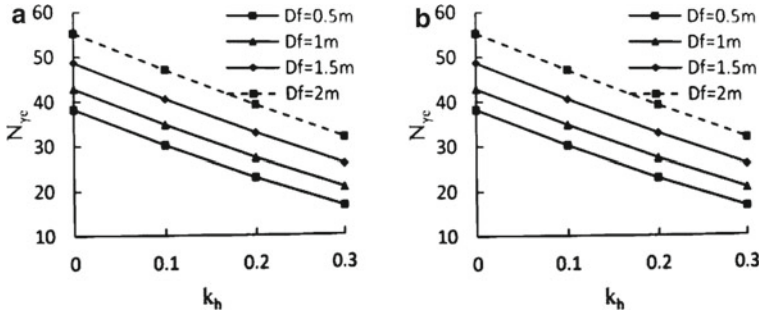**Fig. 7** **a** First condition, **b** Second condition

Fig. 8 **a** First condition, **b** Second condition

Figure 7a, b shows the variation of bearing capacity coefficient with respect to seismic acceleration (k_h) for different widths of footing at $\varphi = 30° \, at \, \delta = \frac{\varphi}{2}$, $k_v = \frac{k_h}{2}$, $r_u = 0.2$, $\frac{D_w}{B} = 0.25$, $\frac{D_f}{B} = 0.5$, $\frac{2c}{\gamma B} = 0.5$, $i = 15°$.

Figure 8 shows that $N_{\gamma e}$ increases with the increase in the depth of foundation (D_f) for the case of both water tables which lies below and above the base of the footing. The effect of increase in depth on increase in bearing capacity coefficient is predominant due to increase in surcharge weight, thus causing maximum passive resistance which governs the safe bearing capacity of the soil. For a particular case, $k_h = 0.2$, when D_f increases from 0.5 m to 1.0 m, $N_{\gamma e}$ increases by pseudo-static analysis: first condition—19%, second condition—39%, respectively.

Figure 8a, b shows the variation of bearing capacity coefficient with respect to seismic acceleration (k_h) for different depths of footing (D_f in m) at $\varphi = 30°$ at $\delta = \frac{\varphi}{2}$, $k_v = \frac{k_h}{2}$, $r_u = 0.2$, $\frac{D_w}{B} = 0.25$, $\frac{D_f}{B} = 0.5$, $\frac{2c}{\gamma B} = 0.5$, $i = 15°$.

Figure 9 shows the variation of $N_{\gamma e}$ under seismic condition, i.e., k_h at different values of cohesion ($c = 0$ kN/m^2,5 kN/m^2,10 kN/m^2). Seismic bearing capacity coefficient increases as cohesion increases, which causes increase in intermolecular attraction among the soil particle, thus offering more bearing capacity for the conditions where table lies both below and above the base of the footing. For a particular case, $k_h = 0.2$, when c increases from 0 kN/m^2 to 5 kN/m^2, $N_{\gamma e}$ increases by pseudo-static analysis: first condition—29%, second condition—53%, respectively.

Figure 9a, b shows the variation of bearing capacity coefficient with respect to seismic acceleration (k_h) for different values of cohesion for $\varphi = 30°$ at $\delta = \frac{\varphi}{2}$, $k_v = \frac{k_h}{2}$, $r_u = 0.2$, $\frac{D_w}{B} = 0.25$, $\frac{D_f}{B} = 0.5$, $\frac{2c}{\gamma B} = 0.5$

Figure 10 shows the variation of bearing capacity coefficient with respect to seismic acceleration (k_h) for different unit weights of soil (γ in kN/m^3) at

$$\varphi = 30° \text{ at } \delta = \frac{\varphi}{2}, \, k_v = \frac{k_h}{2}, \, r_u = 0.2, \, \frac{D_w}{B} = 0.25, \, \frac{D_f}{B} = 0.5, \, \frac{2c}{\gamma B} = 0.5, \, i = 15°$$

Figure 10a, b shows the variation of $N_{\gamma e}$ with respect to horizontal seismic acceleration (k_h) at three different values of unit weight of soil (γ), and seismic bearing
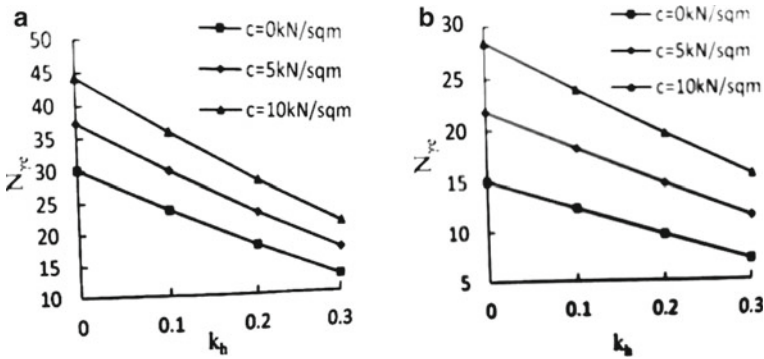
Fig. 9 **a** First condition, **b** Second condition
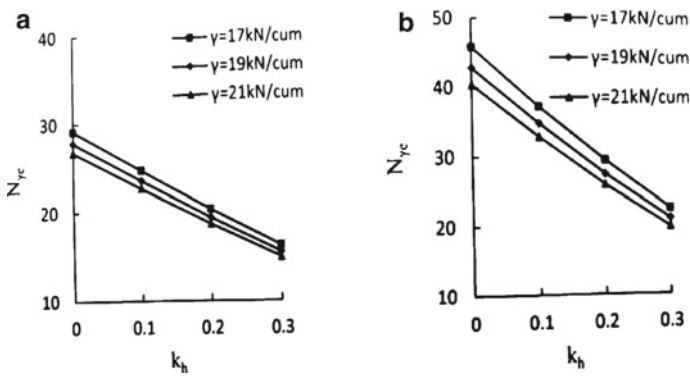
Fig. 10 **a** First condition, **b** Second condition

capacity factor will be decreased because the $(2c/\gamma B)$ portion decreases in the expression of $N_{\gamma e}$. For a particular case, $k_h = 0.2$, when γ increases from 17 kN/m³ to 19 kN/m³, $N_{\gamma e}$ decreases by pseudo-static analysis: first condition—07%, second condition—53%, respectively.

The change in bearing capacity coefficient due to increase in pore water pressure is found to be very minimal for both the cases of water table above and below the base of the footing and pseudo-static analysis.

4 Conclusions

An effort has been built to assess the pseudo-static bearing capacity of shallow strip footing embedded in slope in c-φ nature of soil in terms of a single coefficient $(N_{\gamma e})$ using limit equilibrium method which is subjected to groundwater flow. In the

analysis, coincident resistance of unit weight, surcharge and cohesion is taken into account to calculate the pseudo-static bearing capacity coefficients in which linear failure surface is considered. From the parametric study, it has been observed that ultimate bearing capacity decreases by increasing depth of water table; seismic coefficients and bearing capacity increase by increasing width of the footing, cohesion and unit weight of the soil. Design chart is represented in table which can be applied in practical field.

References

1. Rankine, W.J.M.: On the stability of loose Earth. Phil. Tras. Royal Society (London) (1857)
2. Prandtl, L.: Umber die eindringungkeit plasticizer baustoffe und die festigkeit von schneiden. zeitschrift Fur Angewandt Mathematik Und Mechanik **1**(1), 15–30 (in German) (1921)
3. Terzaghi, K.: Theoretical soil Mechanics. Wiley (1943)
4. Saran, S., Sud, V.K., Handa, S.C.: Bearing capacity of footings adjacent to slopes. J. Geotech. Eng. **115**(4), 553–573 (1989)
5. Meyerhof, G.G., Adams, J.I.: The ultimate uplift capacity of foundations. Can. Geotech. J. **5**(4), 225–244 (1968)
6. Rowe, R.K., Davis, E.H.: The behavior of anchor plates in clay. Geotechnique **32**(1), 9–23 (1982)
7. Rowe, R.K., Davis, E.H.: The behavior of anchor plates in sand. Geotechnique **32**(1), 25–41 (1982)
8. Subba Rao, K.S., Kumar, J.: Vertical uplift capacity of horizontal anchors. J. Geotech. Eng. ASCE **120**(7), 1134–1147 (1994)
9. Mononobe, N., Matsuo, H.: On the determination of earth pressure during earthquakes. In: Proceedings of the World Engineering Congress, Tokyo, 9, pp. 179–187 (1929)
10. Meyerhof, G.G.: Some recent research on the bearing capacity of foundations. Can. Geotech J. **1**(1), 16–26 (1963)
11. Sarma, S.K., Lossifelis, I.S.: Seismic bearing capacity factors of shallow strip footings. Geotechnique **402**, 265–273 (1990)
12. Richards, R., Elms, D.G., Budhu, M.: Seismic bearing capacity and settlements of Foundations. J. Geotech. Eng. ASCE **119**(4), 662–674 (1993)
13. Budhu, M., Al-Karmi, A.: Seismic bearing capacity of soils. Geotechnique **43**(1), 181–187 (1993)
14. Kumar, J., Kumar, N.: Seismic bearing capacity of rough footings on slopes using limit equilibrium. Geotechnique **53**(3), 363–369 (2003)
15. Dormieux, L., Pecker, A.: Seismic bearing capacity of foundations on cohesionless soil. J. Geotech. Eng. ASCE **121**(3), 300–303 (1995)
16. Paolucci, R., Pecker, A.: Seismic bearing capacity of shallow strip foundations on dry soils. Soils Found **37**(3), 95–105 (1997)
17. Soubra, A.H.: Sesmic bearing capacity of shallow strip footings in seismic conditions. Proc. Instn. Civil Engrs, Geotech. Engr. **125**(4), 230–241 (1997)
18. Soubra, A.H.: Upper bound solutions for bearing capacity of foundations. J. Geotech. Geoenviron. Eng. ASCE **125**(1), 59–69 (1999)
19. Kumar, J., Rao, V.B.K.M.: Sesmic bearing capacity factors for spread foundations. Geotechnique **52**(2), 79–88 (2002)
20. Kumar, J.: Nγ for rough strip footing using the method of characteristics. Can. Geotech. J. **40**(3), 669–674 (2003)
21. Choudhury, D., Subba Rao, K.S.: Seismic bearing capacity of shallow strip footings. Geotech. Geol. Eng. **23**(4), 403–418 (2005)

22. Sawada, T., Nomachi, S.G., Chen, W.F.: Seismic bearing capacity of a mounded foundation near a downhill slope by pseudo-static analysis. Soils Found **34**(1), 11–17 (1994)
23. Sarma, S.K.: Seismic bearing capacity of shallow strip footings adjacent to a slope. In: Proceedings of 2nd International Conference Earthquake Geotechnical Engineering, Lisbon, Portugal, Balkema, Rotterdam, The Netherlands, pp. 309–313 (1999)
24. Askari, F., Farzaneh, O.: Upper-bound solution for seismic bearing capacity of shallow foundations near slopes. Geotechnique **53**(8), 697–702 (2003)
25. Zhu, D.Y.: The least upper bound solutions for bearing capacity factor N_γ. Solid Found **40**(1), 123–129 (2000)
26. Kumar, J., Rao, V.B.K.M.: Seismic bearing capacity of foundations on slopes. Geotechnique **53**(3), 347–361 (2003)
27. Choudhury, D., Subba Rao, K. S.: Seismic bearing capacity of shallow strip footings embedded in slope. Int. J. Geomech. **6**, 176–184 (2006)
28. Chakraborty, D,, Kumar, J.: Seismic bearing capacity of shallow embedded foundations on a sloping ground surface. Int. J. Geomech. ASCE, ISSN, 1532-3641/04014035(8) (2014)
29. Larkin, T.: Reliability of shallow foundations subjected to multidirectional seismic loading. J. Geotech. Geoenviron. Eng. **132**(6), 685. https://doi.org/10.1061/(ASCE)1090-024 (2006)
30. Massih, D.S.Y.A., Soubra, A.H., Low, B.K.: Reliability-based analysis and design of strip footings against bearing capacity failure. J. Geotech. Geoenviron. Eng. **134**(7), 917 https://doi.org/10.1061/(ASCE) 1090-024 (2008)
31. Veiskarami, M., Kumar, J.: Bearing capacity of foundations in the presence of groundwaterflow. Geomech. Geoeng. Int. J. **7**(4), 293–301 (2012)
32. Kumar, J., Chakraborty, D.: Bearing capacity of foundations in the presence of groundwaterflow. Geotechnique (in press) (2013)

Study on Piles Subjected to Axial and Lateral Loading

V. K. Stalin, A. Priyadharshini, P. Deepan, and A. Abudaheer

Abstract Piles are often subjected to combination of vertical and lateral loading in places like bridge piers, offshore structures, retaining walls, etc. The behaviour of piles under biaxial loading is much more complex when piles are embedded in layered soil system. In this paper, an attempt is made to study behaviour of pile subjected to vertical and lateral loading for varying soil layers. Model pile load tests have been conducted in a model tank filled with sand, clay and clay–sand medium to examine the behaviour of single pile and pile group under vertical and lateral loading. Both single and pile group (2×2) have been subjected to axial compressive loads and lateral loads, for varying type of soil medium, combinations of loading, number of pile and L/D ratio. Result indicated that the vertical load capacity of pile increases with L/D ratio and number of piles at any given settlement, but however, the vertical capacity of sand medium is always higher compared to clay or clay–sand medium. Similar trend is observed on the lateral load capacity also. At the given deflection, lateral capacity increases with L/D ratio and number of piles relatively on the higher magnitude for sand medium but less noticed for clay and clay–sand bed. Under the influence of ultimate vertical load, the lateral capacity of pile is much lower than the lateral capacity of pile without vertical load, for single pile irrespective of the settlement and for pile group at specified settlement values.

Keywords Pile foundation · Combined loading · L/D ratio

1 Introduction

Normally, vertical piles are used to carry vertical compression loads coming from super structures such as tall buildings, bridges, etc. Piles used in tall chimneys, hill

V. K. Stalin · A. Priyadharshini · P. Deepan (✉) · A. Abudaheer
Department of Civil Engineering, College of Engineering, Anna University, Chennai 600025, India
e-mail: deepangeotech95@gmail.com

A. Priyadharshini
e-mail: priyavanaja606@gmail.com

retaining wall, high-rise buildings, offshore structures, etc. are normally subjected by high lateral load. The piles are commonly used to carry vertical compressive load to resist uplift also as to resist lateral and inclined load. These piles are used to support vertical loads, lateral loads and combinations of vertical and lateral loads. However, in view of the complexity involved in analysing the piles under combined loading, the current practice is to analyse the piles independently for vertical loads to determine their bearing capacity and settlement and for the lateral load to determine their flexural behaviour. Since the piles are not often adequately designed to resist lateral loads, the response of piles under lateral load in the presence of vertical loads is more critical and interesting for the design engineers. Zhang and Small [5] presented a method of analysis for a ground and cap supported by piles embedded in a layered soil and subjected to horizontal and vertical loads. Rajagopal and Karthigeyan [3] analysed the pile behaviour subjected to combined vertical and lateral loads. It is concluded that the presence of a vertical load marginally reduces the lateral load capacity of piles in clayey soils for vertical load level up to 0.6Vult and by as much as 20% for higher vertical load level. Karthigeyan and Rajagopal [1] presented some numerical results on the effect of vertical load over the lateral capacity of 2×2 pile group in homogeneous sand. Miyamoto [2] carried out dynamic centrifuge tests performed on a four-pile group foundation model embedded in saturated fine sand layers. It is concluded that the proposed model well represented the pile foundation response in liquefied soil. Zamri et al. [4] carried out 3D finite element analysis of the behaviour of single pile under pure lateral and combined loading with different water table elevations. They found that dry soil condition yielded higher lateral resistance than fully saturated soil condition. The present investigation focuses on the effect of L/D ratio, number of piles and various soil types on the load carrying capacity of pile and pile groups under vertical and lateral loading combination.

2   Materials

River sand collected from nearby site is washed and air-dried before the same is used for laboratory testing. The river sand has coarse sand, medium sand and fine sand of 14%, 65% and 21%, respectively. Based on the Cc and Cu values, the sand is classified as poorly graded sand (SP). Natural clay is collected from west Tambaram, Chennai, Tamil Nadu. The soil is having clay, silt and fine sand of 64%, 20% and 16%, respectively. As per Indian Standard of Classification, the soil is classified as clay of high plasticity (CH). Model hollow aluminium piles with an outer diameter of 10 mm, inner diameter of 4 mm and thickness of 3 mm plugged at both ends are used. The length-to-diameter ratio (L/D ratio) of the piles of 12 and 24 is selected to study the short rigid piles and long flexible piles based on the stiffness factor, T of the pile system as per IS 2911 (Part 1/Sec1), 2010. Aluminium plate of 5 mm thickness and size 45 mm × 45 mm is used as pile cap. For 2×2 pile group, the pile cap is welded on the top of the piles with 3D centre - centre spacing between the piles. Steel square tank of 500 mm × 500 mm of breath and width and height 700 mm is used

Table 1 Index properties of sand

Properties	Value
Maximum dry unit weight, Y_{dmax}	17.24 kN/m^3
Minimum dry unit weight, Y_{dmin}	15.50 kN/m^3
Maximum void ratio, e_{max}	0.65
Minimum void ratio, e_{min}	0.58
Specific gravity, Gs	2.67
Coarse sand	14%
Medium sand	65%
Fine sand	21%
Coefficient of uniformity, Cu	4.55
Coefficient of curvature, Cc	1.32
Soil classification	Poorly graded sand (SP)

Table 2 Index properties of clay

Properties	Value
Clay	64%
Silt	20%
Fine sand	16%
Liquid limit, W_L	77%
Plastic limit, W_P	33%
Plasticity index, I_P	45%
Shrinkage limit, Ws	8%
Specific gravity, Gs	2.68
Free swell index	100%
Soil classification	Clay of high plasticity (CH)

in the experiments. These dimensions are arrived based on significant depth (0.1q) for pile foundation, which is sufficiently large enough to avoid boundary effect. The test tank contains a pulley with frame attached at the side of the tank to apply lateral load using loading frame hinged using string (Tables 1 and 2).

3 Methods

3.1 Model Tank

The schematic view of the model tank along with provisions for applying vertical load and lateral load is shown in Fig. 1. A steel square tank of 500 mm × 500 mm of breath and width and height 700 mm is used in the experiments. Figure 2 shows

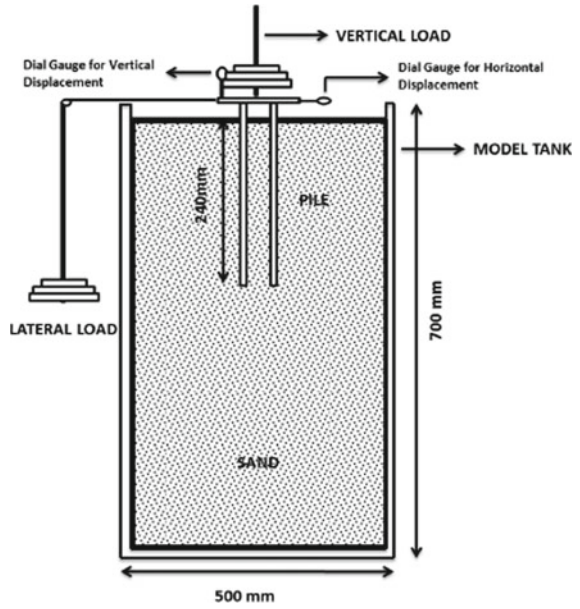**Fig. 1** Schematic view of vertical and lateral load test in model tank

Fig. 2 View of model tank with provision apply vertical and lateral load

the photographic view of model load test setup. The dial gauges used for taking measurement of lateral deflection and vertical measurement have the least count of 0.002 mm.

3.2 Vertical Load Test on Pile

There is a provision to apply static vertical load on the top of the pile head, see Fig. 1, and corresponding settlement. The load is applied to estimate load settlement curve, until the failure load is reached in both single-pile and four-pile group (2×2). The vertical load test is conducted for varying L/D ratio, soil medium and number of piles. This ultimate failure load is used as a reference to apply lateral load. The vertical load is varied as 0.3, 0.5 and 0.8 times of ultimate failure load to analyse lateral load capacity of model piles. IS 2911 (part 4), 1985 Section 6.2. Maintained Load Method was followed with regard to application of load increment.

3.3 Lateral Load Test on Pile

In the model load test setup, see Fig. 1, there is a provision to apply lateral load and to measure the corresponding deflection. For a given vertical load, the static lateral load is also applied until the failure load is reached, to analyse the lateral capacity of pile and pile groups.

3.4 Experimental Procedure Adopted to Carry Out Vertical and Lateral Load Capacity of Piles'

The tank of 500 mm × 500 mm × 700 mm is filled with sand layer for several layers; see Fig. 1. Sand layer is approximately 500 mm thickness and tamped with flat plate to achieve 60% relative density. In the case of clay bed, the hand remoulded clay sample is carefully placed at an initial moisture content of 68% and corresponding consistency of 0.2. During filling the tank with either sand bed or clay bed and clay–sand bed, the aluminium model piles (2 Nos. or 4 Nos.) are placed as the approximate location and soil layers are placed surrounding the model piles. After filling the tank completely with sand or clay bed to a embedded length 700 mm, a free head of 20 mm is provided in all medium. To facilitate lateral loading, pile is connected to loading frame using high-tension wire. The vertical or lateral load and pile head displacement are recorded at regular interval up to failure for both vertical and laterally loaded pile and pile group using dial gauge. For each test, separate soil bed is prepared. For clay–sand layer bed, clay is filled up to the L/2 of the embedded length of the pile

used followed by sand till the bottom of the model tank. In the analysis of vertical and laterally loaded piles, the main parameters involved are ultimate pile capacity and displacement. Herein, the vertical and lateral load capacity are arrived for known settlement of 2 mm, 4 mm and 6 mm in case of vertical loaded piles and deflection of 1.5 mm, 3 mm and 4.5 mm for lateral loaded piles.

4 Results and Discussions

4.1 Vertical Load Carrying Capacity of Pile

The vertical load capacities of pile for L/D ratio 12 and 24 for single- and 2×2 pile group are analysed for varying soil medium. Similarly, for a given soil medium, the effect of L/D ratio and number of pile on the vertical capacity of pile are also analysed in this section.

Effect of soil medium. Figures 3 and 4 present the vertical load—settlement behaviour of single pile for varying soil medium and L/D ratio. These curves are not showing a typical parabolic shape with single peak. Hence, the vertical load capacity is arrived for a known settlement of 2 mm, 4 mm and 6 mm.

Similar trend of vertical load settlement curve, see Figs. 3 and 4, has been observed in case of 2×2 pile group subjected to a pure vertical load.

at 6 mm settlement

Effect of L/D ratio. The results indicate that, from Figs. 5 and 6 and Table 3, it is thus inferred that for a single pile in sand, clay and clay–sand medium, when L/D ratio increases the vertical load capacity also increases irrespective of settlement. Similarly, in the case of four pile group, the vertical load capacity increases with increase in L/D ratio for any known settlement value of 2 mm, 4 mm and 6 mm.

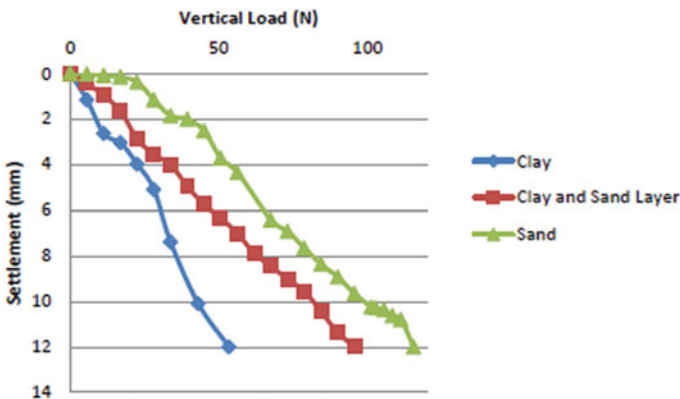**Fig. 3** Vertical load—Settlement curve of single pile for varying soil medium for L/D ratio 12
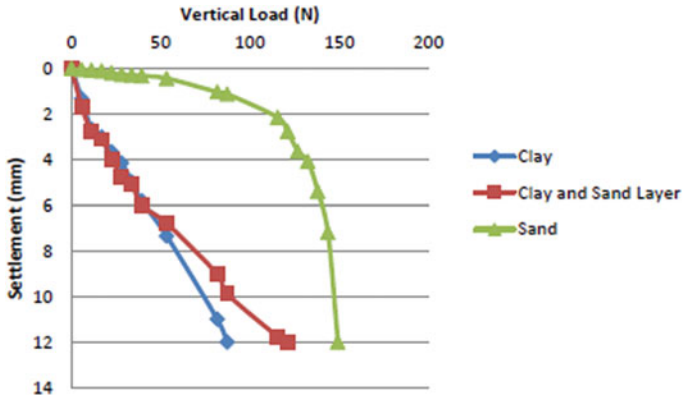
Fig. 4 Vertical load—Settlement curve of single pile for varying soil medium for L/D ratio 24
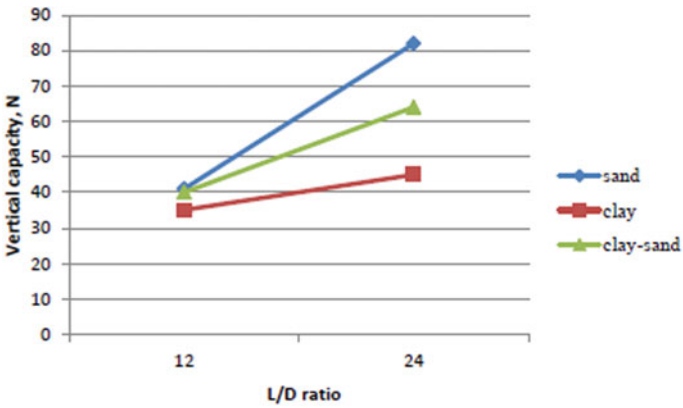

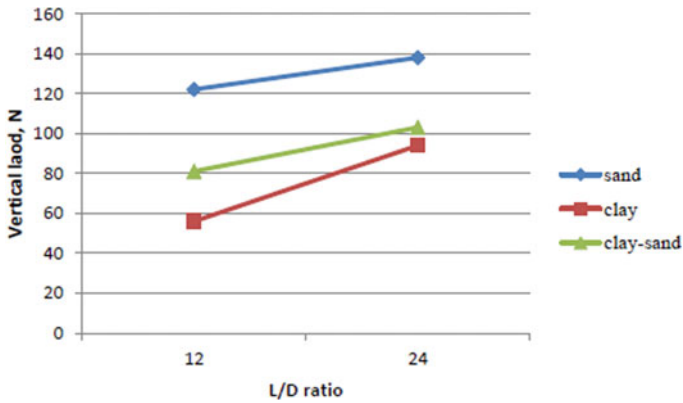**Fig. 5** Vertical Load—L/D Ratio variation of single pile for different soil medium at 6 mm settlement

Fig. 6 Vertical Load—L/D Ratio variation of 2×2 pile group for different soil medium

Table 3 Vertical load capacity of single pile and 2×2 pile group for varying settlement

Soil medium	L/D ratio	Load, N					
		Single pile			2×2 pile group		
		2 mm	4 mm	6 mm	2 mm	4 mm	6 mm
Sand bed	12	22	24	41	47	96	122
	24	35	51	82	115	127	138
Clay bed	12	6	23	35	17	35	56
	24	13	51	45	34	65	94
Clay–sand layer	12	11	23	40	23	39	81
	24	22	28	64	36	89	103
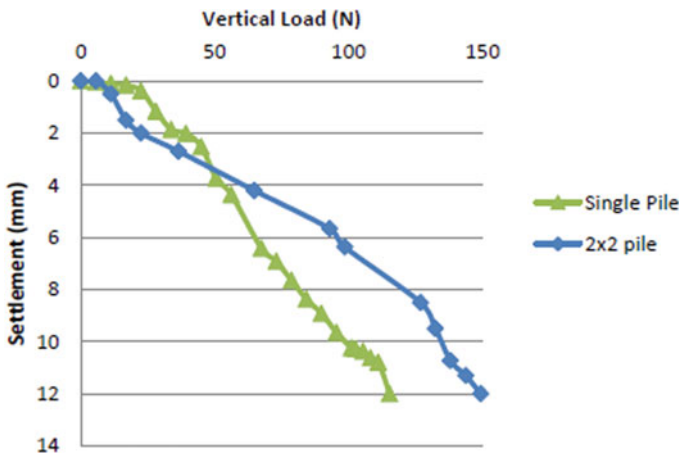
Fig. 7 Vertical load—Settlement curve for number of piles (L/D Ratio = 12) in Sand

Effect of number of pile. Figures 7, 8, 9 and 10 show the vertical capacity of pile for single-pile and four-pile group for varying settlement for sand, clay and clay–sand medium. It is observed that the pile capacity increases with number of piles irrespective of soil medium and L/D ratio, but the influence of number of pile is very significant in sand medium. Almost three times increase is found on vertical capacity of four pile group compared to single pile; refer Table 3.

4.2 Lateral Load Capacity of Pile

Lateral pile load test for single-pile and four-pile group (2×2) was conducted for varying soil medium (sand, clay and clay–sand bed), L/D ratio and number of piles.
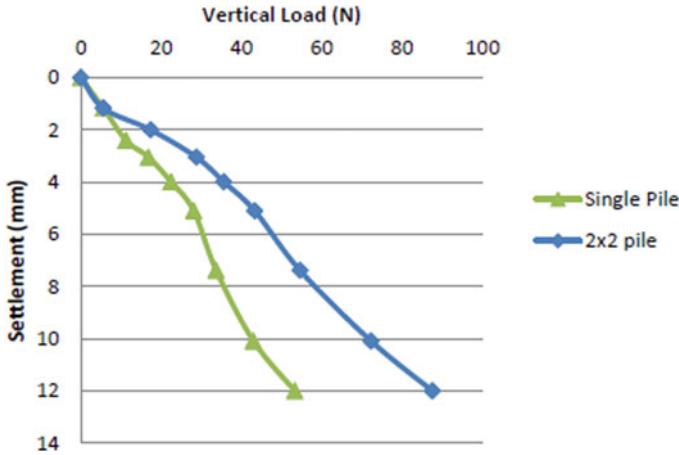
Fig. 8 Vertical load—Settlement curve for number of piles (L/D Ratio = 12) in Sand
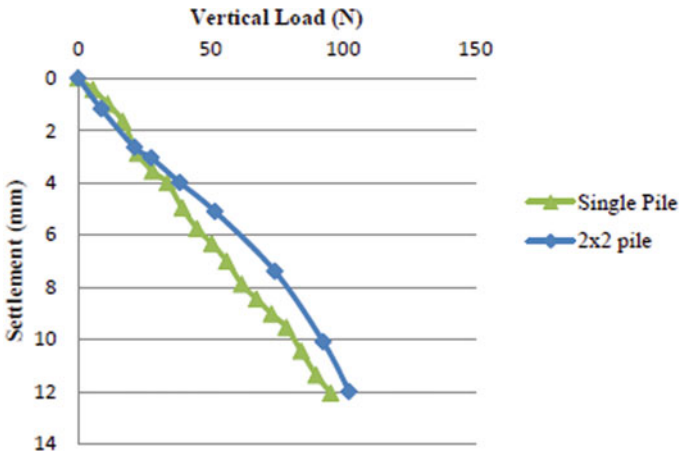
Fig. 9 Vertical load—Settlement curve for number of piles (L/D Ratio = 12) in Clay- Sand Bed

The lateral load is applied independently without vertical load on model pile head, and results are discussed below.

Effect of soil medium. The variation of lateral load capacity with deflection of pile is without any vertical load for varying L/D ratio 12 and 24 for single-pile and four-pile group. The lateral load–deflection curve also did not show a typical parabolic shape with single peak; see Figs. 11 and 12. Hence, the lateral load capacity of pile is considered corresponding to the known deflection of 1.5 mm, 3 mm and 4.5 mm for analysis.

Similar trend of lateral load and deflection curve as shown in Figs. 11 and 12 has been observed in case of clay and clay–sand bed subjected to a pure lateral load.
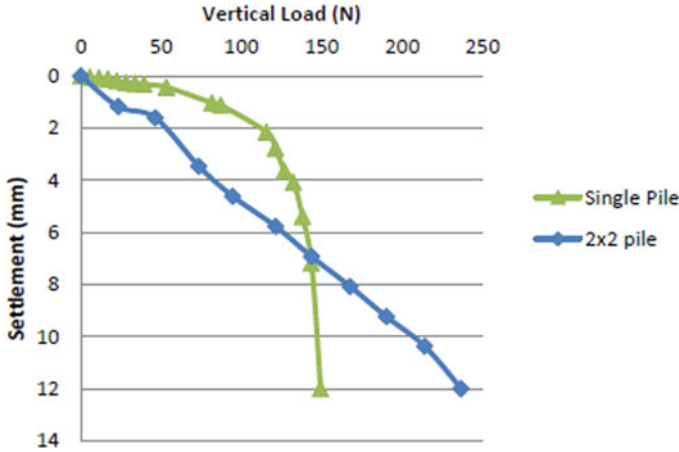
Fig. 10 Vertical load—Settlement curve for number of piles (L/D Ratio = 12)
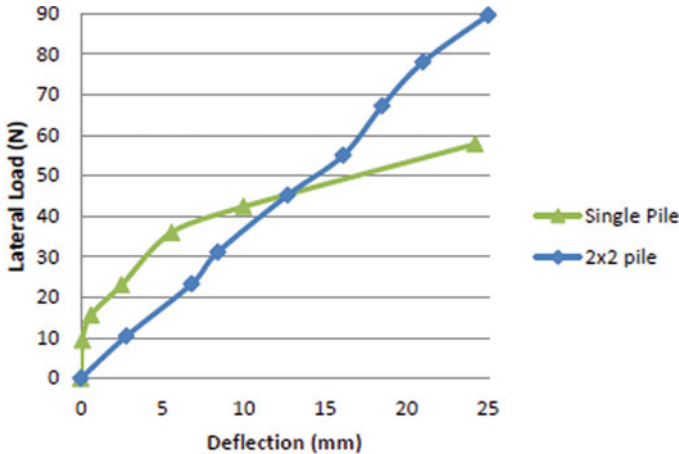
Fig. 11 Lateral load—Deflection curve for varying number of piles (L/D Ratio = 12) in Sand

From Table 4, it is seen that for any given deflection, the lateral load is always higher for sand bed compared to clay bed or clay–sand bed. For L/D = 24, the lateral load capacity of pile is 1.79, 2.3 and 1.4 times higher than that of L/D = 12, respectively for sand, clay and clay–sand medium. However, for single pile with either L/D = 12 or L/D = 24 in sand bed yielded higher lateral load capacity, but considering the rate of increase, in the lateral capacity is high for clay bed compared to sand or clay–sand bed. Similarly, for the four-pile group the lateral capacity of sand bed is always higher irrespective of deflection, L/D ratio and number of piles compared to clay or clay–sand bed.
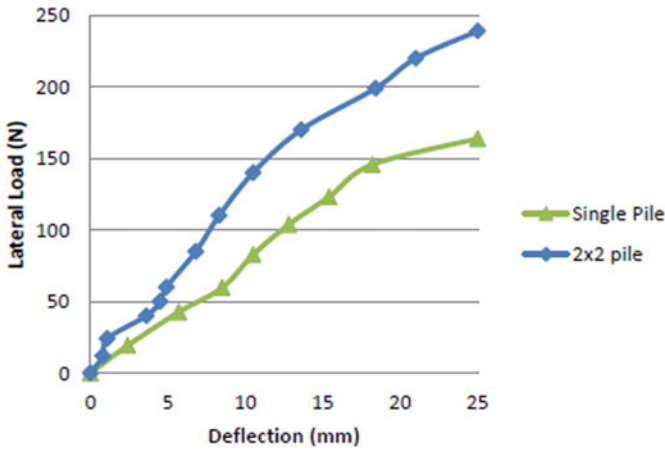
Fig. 12 Lateral load—Deflection curve for varying number of piles (L/D Ratio = 24) in Sand

Table 4 Lateral load capacity of single-pile and 2 × 2 pile group for varying deflection (without vertical load)

Soil medium	L/D ratio	Load, N					
		Single pile			2 × 2 pile group		
		1.5 mm	3 mm	4.5 mm	1.5 mm	3 mm	4.5 mm
Sand bed	12	16	25	34	9	13	19
	24	17	22	61	26	39	50
Clay bed	12	6	8	13	5	9	13
	24	14	26	30	15	29	38
Clay–sand layer	12	18	23	29	9	11	15
	24	16	33	42	13	29	41

Effect of number of pile. Table 4 shows the variation of lateral capacity for single-pile and four-pile group for deflection values of 1.5 mm, 3 mm and 4.5 mm with varying soil medium and inferred that the lateral load capacity decreases with number of piles. Similar trend is observed for clay–sand medium irrespective of deflection on L/D ratio. Figure 13 presents the variation of lateral load with number of piles for varying L/D ratio for 4.5 mm deflection. However, the lateral load capacity noted against 25 mm deflection showed a reverse trend; see Fig. 14.

In the case of L/D = 24, the rate of increase in lateral capacity of four pile group is 1.2 to 1.5 times higher than that of single pile and out of which higher value is obtained for sand bed and lower value for clay–sand bed; refer Table 4.
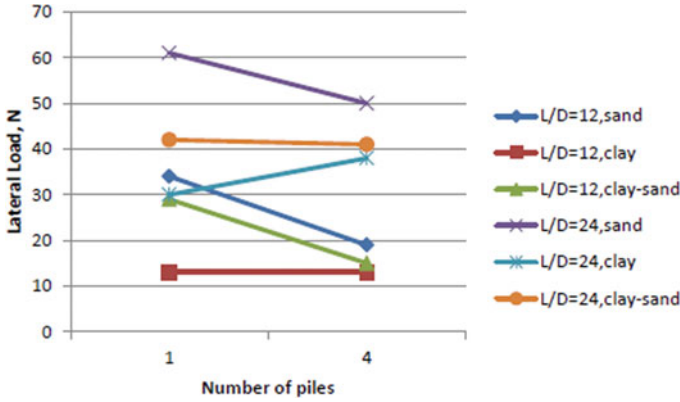
Fig. 13 Lateral Load—number of piles variation of piles for different soil medium and L/D ratio for 4.5 mm deflection
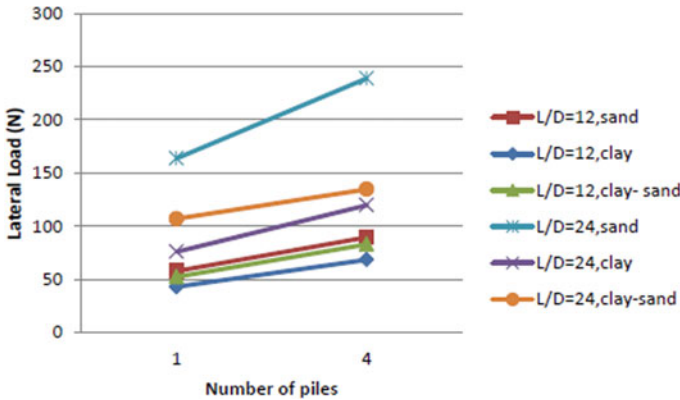
Fig. 14 Lateral Load—number of piles variation of piles for different soil medium and L/D ratio for 25 mm deflection

4.3 Lateral Load Capacity of Piles Under the Influence of Vertical Load

In order to find the influence of ultimate vertical load on the lateral load capacity, lateral load tests were conducted for varying L/D ratio, number of piles and soil medium, keeping the vertical load as that of ultimate vertical failure load. From Table 5, it is evident that, for single pile irrespective of soil medium, the lateral load increases with L/D ratio for any given deflection value, under the influence of ultimate vertical load. But, the lateral load decreases with increasing number of piles only for clay medium and that too for L/D = 24 at 4.5 mm deflection. Further, lateral load is almost higher for clay layer with number of piles for L/D = 12 at

Table 5 Lateral load capacity of single-pile and 2 × 2 pile group for varying deflection, L/D ratio and soil medium under the influence of vertical loading

Soil medium	L/D ratio	Load, N					
		Single pile			2 × 2 pile group		
		1.5 mm	3 mm	4.5 mm	1.5 mm	3 mm	4.5 mm
Sand bed	12	7	16	19	15	37	49
	24	25	29	41	22	43	52
Clay bed	12	12	17	23	9	11	24
	24	25	30	36	12	19	25
Clay–sand layer	12	7	14	18	9	22	36
	24	24	28	32	19	27	42
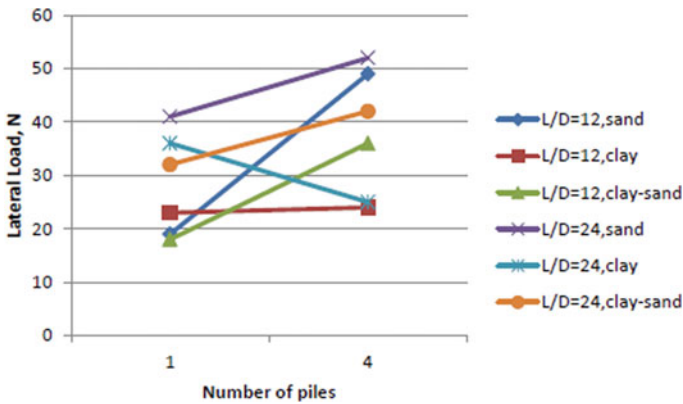
Fig. 15 Variation of Lateral Load – Number of piles for different soil medium and L/D ratio at 4.5 mm deflection

same deflection. But, in all the other cases, there is a considerable increase in lateral capacity irrespective of L/D ratio and soil medium. This could be due to the fact that the shaft resistance would have mobilized under the influence of vertical load and consequence of which the lateral load did not show progressive change on lateral capacity (Fig. 15).

4.4 Comparison of Experimental and Theoretical Values of Ultimate Vertical Load Capacity of Single Pile in Sand, Clay and Clay–Sand Bed (for 12 mm Settlement)

The theoretical ultimate vertical load capacities of single pile embedded in sand, clay and clay–sand bed computed based on IS 2911—part 1/ Section 1 (2010) clause

6.3.1.1 are 2.5 to 5 times lesser than that of experimental ultimate vertical load capacity of short pile and 1.5–5 times lesser than that of experimental ultimate vertical load capacity of long pile.

4.5 Comparison of Experimental and Theoretical Values of Lateral Load Capacity of Single Pile in Uniform Sand and Clay (for 1.5 mm, 3 mm and 4.5 mm Deflection)

The theoretical ultimate lateral load capacities of single pile embedded in sand bed computed based on Brom's (1965) method are 4–8.5 times lesser than that of experimental ultimate lateral load capacity for both short and long piles. Similarly, for clay bed the theoretical ultimate lateral capacity is 20 to 43 times lesser than that of experimental ultimate lateral load capacity for both short and long piles.

5 Conclusions

Based on the analysis of vertical, lateral and combination of vertical and lateral load test results of model piles for varying L/D ratio, number of piles and soil medium, the following general conclusions are drawn.

- Vertical load capacity of pile increases with number of piles, L/D ratio predominantly for sand bed compared to clay bed or clay-sand bed for a given settlement.
- Lateral load capacity of pile increases with L/D ratio irrespective of sand, clay and clay–sand medium for a known deflection. However, the lateral capacity decreases with number of piles when deflection is less than 4.5 mm and the same increases with number of piles corresponding to 25 mm deflection.
- The vertical and lateral load capacity of piles embedded in clay–sand layer gives 1.4–2.7 times higher than that of the vertical and lateral load carrying capacity of piles embedded in uniform clay bed.
- Under the influence of ultimate vertical load, the lateral capacity of single pile decreases compared to the case of lateral capacity of piles without any vertical load irrespective of settlement, whereas in case of pile group the lateral capacity decreases at specified settlement values.
- The effect of combined loading on lateral response of the piles is more pronounced in uniform clay bed rather than sand bed or clay–sand bed.

References

1. Karthigeyan, S., Rajagopal, K.: Lateral Response of 2×2 pile group under combined axial and lateral loading. In: International Geotechnical Conference, pp. 665–669 (2009)
2. Miyamoto, Y.: Pile response during earthquake and performance evaluation of pile foundation. Kobori Research Complex, Kajima Corporation, Tokyo, Japan, pp. 01–09 (2000)
3. Rajagopal, K., Karthigeyan, S.: Influence of combined vertical and lateral loading on the lateral response of piles. International Association for Computer Methods and Advances in Geomechanics (IACMAG), pp. 3272–3282 (2008)
4. Zamri, H., Chik, Jasim, M., Abbas, Taha, M.R.: Lateral behavior of single pile in cohesionless soil subjected to both vertical and horizontal loads. Eur. J. Sci. Res. **29**, 194–205 (Research Gate) (2009)
5. Zhang, H.H., Small, J.C.: Analysis of capped pile groups subjected to horizontal and vertical loads. Comput. Geotech. 01–21 (2000)

Experimental Study of Pile Resting on Sloping Ground Subjected to Cyclic Lateral Loading

Dinesh Bishnoi, M. Upendra, and Jignesh B. Patel

Abstract Pile foundation has to resist lateral loads coming from moving trains, winds, etc. Due to presence of sloping ground, there is reduction in lateral capacity of pile because of reduction in passive resistance offered by soil. The nature of forces is dynamic, and a very limited study has been done to determine the effect of dynamic lateral loading on piles resting on sloping ground. In present study, small-scale physical model tests were performed on sand to determine the reduction in lateral capacity of pile when subjected to 50 numbers of cycles. The relative density (30% and 60%) and ground slope (0° and 20°) were the variables. Initially, the static lateral capacity was determined for both the horizontal and sloping grounds. The load corresponding to 5 mm lateral displacement is the lateral capacity of pile. In second phase, cyclic loading was given to the pile and after that its capacity was determined same as in static case, and the results were compared. In static case due to presence of slope, only the reduction in lateral capacity is 20%–30% depending on the relative density. Due to application of cyclic loading, the reduction in lateral capacity was greater than 50%. This study shows that pile resting on sloping ground and subjected to cyclic lateral loading becomes critical case and needs to be considered while designing pile foundation.

Keywords Lateral capacity · Sloping ground · Cyclic loading

D. Bishnoi (✉) · M. Upendra · J. B. Patel
Applied Mechanics Department, SVNIT Surat, Surat 395007, India
e-mail: dineshbishnoi664@gmail.com

M. Upendra
e-mail: upendarjntuk@gmail.com

J. B. Patel
e-mail: jig8107@gmail.com

1   Introduction

Indian Railways is planning a 'Make in India' touch to the super-fast bullet train project connecting Mumbai with Ahmedabad. The introduction of the bullet train, capable of hitting a speed of up to 350 kmph, will mark the country's shift from an era of slow-speed trains to high-speed ones. These super-fast trains will travel over the bridges, exerting large lateral forces on the foundation system. He et al. (2013) [2] found out that the lateral force exerted due to these high-speed trains can be up to 50 kN. Pile foundations are generally the preferred foundation system for the bridges and designed to resist vertical structural loads. However, the pile should also be able to withstand the lateral loads, which may be caused by wind, wave action, earthquakes, or, in the case of bridges, traffic. The problem of laterally loaded piles is of particular interest, where, the ratio of lateral to vertical load is significant as in the bullet trains. The lateral resistance of a pile foundation is dependent on both the structural properties of the pile and the properties of the surrounding soil. In many practical situations, structures subject to lateral loading are located near excavated slopes or embankments. Bridge abutments, in most circumstances, are constructed on or near a slope crest to accommodate grade separations or geographical feature. Development in hilly regions often involves construction of buildings and bridges on slopes which are to be supported by piles. This situation may become critical case for the bullet train if not properly taken into consideration.

Several researchers investigated the effects of soil slope and cyclic loading separately on the lateral capacity of piles using small-scale model testing, centrifuge testing and finite element analysis. Mezazigh et al. (1998) [4] performed an extensive program of centrifuge tests to study the effect of slopes on P–Y curves in dry sand. The program of tests on piles near slopes was given. It includes studies of the effect of distance to the slope, slope angle and soil properties. Sample preparation method, model piles and the lateral loading device were described. Deflection versus load curves, bending moment curves and derived P–Y curves for piles close to slopes are compared to horizontal ground response. Rosquoet et al. [6] examined the behaviour of instrumented flexible piles in dry sand under lateral cyclic loading using centrifuged models. Considering load service conditions, the influence of the number of cycles of their amplitude and of the soil density on the pile cap displacement and the maximum bending moment of the pile was examined. The cyclic loading sequences were characterized by the number of cycles, the maximum applied load and the cycle amplitude. Muthukkumaran et al. [5] performed detailed laboratory experimental model tests to study the effect of slope on laterally load pile capacity and p–y curves. The study concerns the method developed by a series of laboratory model tests (27 lateral load tests) to experimentally determine p–y curves. The study includes the effect of ground slope, relative density and embedment length on lateral load capacity, bending moment, lateral soil resistance, lateral deflection and p–y curves.

From the literature, it has been found that a lot of work is done on the lateral capacity of pile for both static and dynamic loading conditions. Also static lateral

capacity of pile on slopes is done, but the study on the lateral capacity of pile on slopes subjected to dynamic cyclic loading is very limited. Thus, the lateral capacity of pile under dynamic cyclic loading will be studied, and the effect of loading direction will also be considered.

2 Physical Modelling

In the present study, we performed physical modelling under normal gravity (1-g model tests) to study the behaviour of pile subjected to static and cyclic lateral loads on the sloping grounds.

2.1 Materials and Equipment

The details about the materials and equipment used for testing will be discussed in this section.

Sand. Relatively uniform sand was used in the study. The specific gravity of the soil is 2.611. Physical properties of the sand are shown in Table 1. The sand is classified as poorly graded sand (SP) according to USCS classification system. All the tests were performed as per Bureau of Indian Standards (BIS).

Model pile. The current project considers prototype pile made up of concrete having diameter and length of 0.5 m and 10 m respectively. The modulus of elasticity of concrete was assumed equals to 30 GPa. Wood [7] mentioned that correct physical modelling can be obtained for piles under lateral loading if we maintain the dimensionless ratio φ identical for model and prototype, where

$$\phi = \frac{GL^4}{EI}$$

$G =$ Shear modulus of soil, $L =$ Length of pile, $EI =$ Flexural rigidity of pile.

Table 1 Physical properties of soil

Property of sand	Value	Property of sand	Value
Specific gravity (G)	2.61	Coefficient of curvature (Cc)	0.76
Effective size of particle (D10), mm	0.21	USCS[a] classification	SP
Mean size of particle (D50), mm	0.70	Minimum unit weight (γ_{min}),kN/m^3	14.87
Coefficient of uniformity (Cu)	4.76	Maximum unit weight (γ_{max}), N/m^3	17.87

[a]unified soil classification system
[b]poorly graded sand

Fig. 1 Concrete model piles
with mould

Assuming soil stiffness *G* identical in model and prototype and considering length scale (nl) equals to 30, we get a concrete model pile having length and diameter equals to 0.33 m and 0.016 m, respectively. The pile casted is shown in Fig. 1. As concrete model piles takes time for curing and also a single pile can only be used once due to formation of cracks, thus alternative pile made up of CPVC is used in present study as shown in Fig. 2. The detail of model and prototypes decided by performing calculations is shown in Table 2. Due to unavailability of solid section, the hollow section of PVC was used for testing purpose.

Model Box. A cubical box of size 610 mm × 610 mm × 610 mm was prepared to conduct lateral test on piles. The dimensions of the box were selected by considering the boundary effects from the pile. Three sides were made up of steel plates (1.02 mm thickness) and fourth side was made up of acrylic glass sheet (6 mm thickness) to check the relative density distribution throughout the depth.

Shake table. Uni-directional shake table was used to generate cyclic displacement to the pile. It can traverse distance from −50 mm to +50 mm with maximum vibratory motor frequency of 50 Hz. The frequency of vibration of table and rotating motor was different; thus, calibration chart was prepared for various ranges of frequencies of shake table. This chart was used to determine the required vibration frequency of table. The wave pattern was found out to be linearly varying. In the present study, table frequency of 0.5 Hz was used so that inertia effect can be avoided.

Fig. 2 CPVC model piles
used in testing

Table 2 Detail of model and prototype considered for study

Type	Material	E (GPa)	μ	Length (m)	Diameter (m)	Thickness (m)
Prototype	Concrete	30	0.150	10	0.5	–
Model	Concrete	30	0.150	0.33	0.016	–
Model	CPVC	2	0.386	0.578	0.029	–
Model (Hollow)	CPVC	2	0.386	0.578	0.0325	0.0035

2.2 Methodology

In the previous section, we discussed the materials and equipment used for the testing purpose; in this section, we will discuss the methodology adopted for testing. The following section will cover the sand placemesnt method, test set-up for static and cyclic loading.

Methodology for placement of sand. The sand bed was prepared by weight–volume method. The sand was filled in layers of thickness 5 cm and compacted by using roller of 2.16 kg. A total of 11 layers were constructed by this method for each test. The detail of procedure is shown in Table 3. The density for each relative density was determined from

$$\text{R.D.} = \left(\frac{1}{\gamma_{\min}} - \frac{1}{\gamma} \right) \bigg/ \left(\frac{1}{\gamma_{\min}} - \frac{1}{\gamma_{\max}} \right)$$

Table 3 Detail of weights for sand placement

Relative density (%)	Unit weight (kg/m^3)	Volume of each layer (m^3)	Weight of soil for each layer (kg)	Weight of soil to be removed for 20° slope (kg)
30	1566.73	0.0186	29.15	15.39
45	1609.34	0.0186	29.93	16.07
60	1654.33	0.0186	30.77	16.62

For generating sloping ground, calculated amount of sand was removed after filling the whole tank. The detail of sand quantity is shown in Table 3.

Static loading. After preparation of sand bed, the pile was inserted into the sand by providing blows with hammer having weight of 5 kg. For the case of sloping ground, the pile was first inserted and then the sand was removed to generate slope. In slopes, the pile was inserted at a distance of 50 mm from the crest of the slope to avoid any disturbance to the pile while removing sand.

The static lateral capacity of pile was determined by measuring the load corresponding to lateral deflection of 5 mm as mentioned in IS 2911 [1]. The test set-up used to measure lateral capacity is shown in Fig. 3. A multi-speed loading frame having load cell of capacity 1-ton capacity with precision of 0.1 kg was used for applying lateral load to pile. A linear variable displacement transducer (LVDT) having precision up to ±0.01 mm was used to measure the lateral deflection of
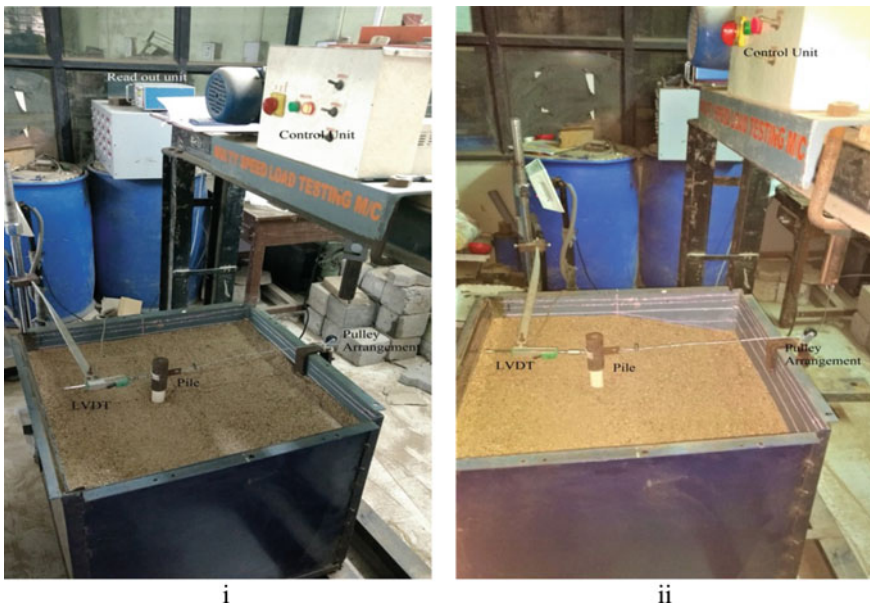

i ii

Fig. 3 Static loading test set-up for (i) horizontal ground and (ii) sloping ground

Fig. 4 Cyclic loading test arrangement with connections

pile. The vertical movement of loading shank is converted into lateral motion with the help of pulley and steel wire arrangement.

Cyclic loading. Displacement controlled lateral loading was given to the pile head with the help of shake table. Long, J H and Geert Vanneste [3] mentioned that effect of cyclic loading is greatest for the first cycle and with consequent loading the effect of cycles reduces. Considering the mentioned finding, 50 numbers of cycles were decided. The frequency of vibration considered is such that the effect of repeated loads is important and effect of inertia is minimal. Two types of loading conditions are studied, i.e. one-way loading and two-way loading. In one-way loading, the displacement varies from 0 to 5 mm linearly, and in two-way, the displacement varies from −5 mm to 5 mm linearly.

The test set-up used to perform cyclic loading is shown in Fig. 4. The sand placement method and pile installation method are same as in static loading. The lateral cyclic movement of shake table is transferred to the pile head with the help of rigid bar which is bolted firmly to the shake table and pile head. It was ensured that the rigid bar only moves to and fro, and there is no rotation of the bar so that the piles moves the exact distance as the input given to shake table. During testing, the shaking of the test box was not observed ensuring the suitability of box dimensions for preventing the boundary effect.

After the pile was subjected to desired number of cycles, the pile was disconnected from the shake table by loosening the bolts. The degradation in the lateral capacity of pile was determined by making alternative arrangement as shown in Fig. 5. The displacement and load were measured with LVDT and load cell. As loading frame was not available to generate loading, sand was used to give load to the pile head. The sand was poured into the plastic container with the help of special pouring apparatus as shown in Fig. 6, so that uniformity in pouring can be obtained with

Fig. 5 Test arrangement after cyclic loading

proper measurement from LVDT and load cell. The sand was filled until the lateral deflection reached 5 mm which is the lateral capacity of pile after the cyclic loading.

3 Results and Discussions

3.1 Static Test Results

The static lateral capacity of pile was determined first as mentioned in Sect. 2.2. A total of four numbers of tests were performed as shown in Table 4.

Fig. 6 Sand pouring
cylinder

Table 4 Parameters for static
loading

Relative density (%)	Slope of ground (°)
30%	0°
	20°
60%	0°
	20°

The load–deflection curve of pile head for 30% and 60% relative density is shown in Figs 7 and 8.

From the curves, it can be seen for both the relative densities that there is reduction in lateral capacity due to sloping ground. The main reason for this reduction is less passive resistance offered by the sloping ground due to unavailability of soil. The reduction in capacity of pile for 30% and 60% relative density due to slope, considering the 5 mm failure criteria, is 21.33% and 31.57%, respectively. It is observed that for medium dense sand, there is more reduction in capacity compared to the loose sand.

3.2 Cyclic Results

The cyclic tests were performed as mentioned in Sect. 2.2 with the help of shake table. The detail about the shake table and methodology of testing adopted is already

Fig. 7 Load–deflection curve for 30% relative density for horizontal and sloping ground
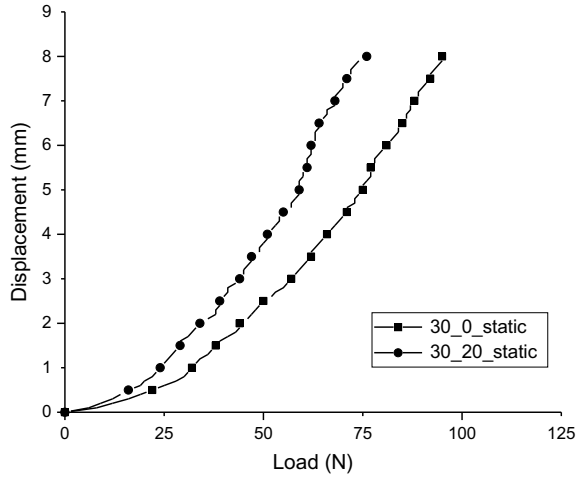
Fig. 8 Load–deflection curve for 60% relative density for horizontal and sloping ground
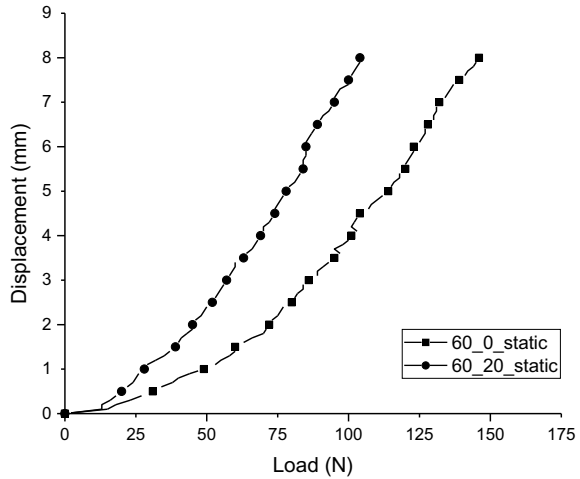
discussed in Sect. 2. The parameters considered for cyclic tests are shown in Table 5. A total of ten cyclic tests were performed for current study.

The results for the mentioned parameters are shown in Figs. 9 and 10 for 30% and 60% relative density, respectively. These results are for both horizontal and sloping ground when subjected to 50 numbers of cycles with one-way and two-way loading. The format used to depict the different combination is as follows,

Relative density_Slope_Loading type.

Thus 30_20_1 means piles in 30% relative density having sloping ground of 20° and subjected to two-way cyclic loading.

It can be observed from the load–deflection curve that for horizontal ground, there is slight effect of loading type. The lateral capacity for two-way loading is

Table 5 Parameters considered for the cyclic tests

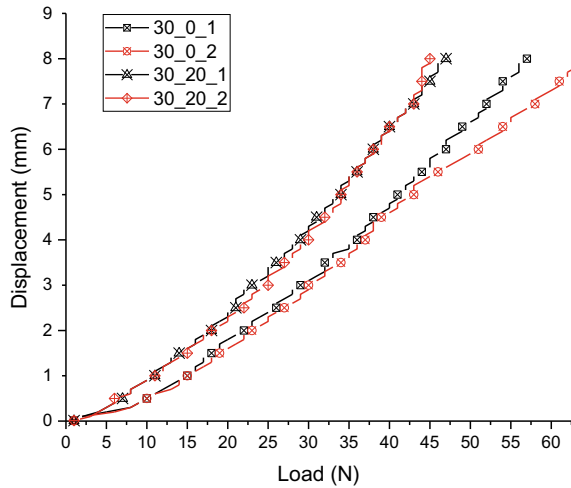| Relative density (%)	Slope of ground (°)	No. of cycles	Loading type
30%	0°	50	One-way, two-way
	20°	50	One-way, two-way
60%	0°	50	One-way, two-way
	20°	50	One-way, two-way
	0°	500	Two-way
	20°	500	Two-way

Fig. 9 Load–deflection curve for 30% relative density for cyclic tests

higher than the one-way loading for both relative densities, but for sloping ground the effect of loading type is insignificant. This shows that the characteristics of load can be a significant parameter when behaviour of piles subjected to cyclic loading is considered. The reason for higher reduction in case of one-way loading is greater cumulative deformations compared with two-way loading. Due to absence of sand because of slope, the accumulated deformations are same for the one-way and two-way loading; therefore, the difference is insignificant.

The reduction in capacity due to slope and the nature of cyclic loading is summarized in Table 6. It shows the lateral capacity of pile corresponding to 5 mm deflection for all the static and cyclic tests performed. The percentage reduction is found out with reference to lateral capacity for horizontal ground and under static loading. It can be concluded from the data that the reduction in capacity is much significant for medium dense sand compared with the loose sand. The critical case becomes when

Fig. 10 Load–deflection curve for 60% relative density for cyclic tests
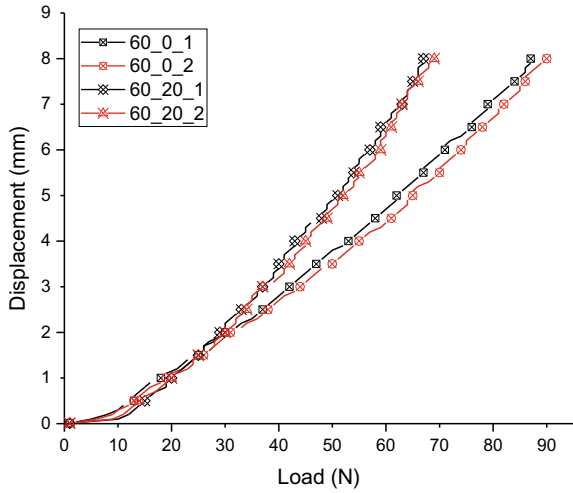
Table 6 Summary of the reduction in lateral capacity for tests performed

Relative density (%)	Slope (°)	Loading type	Lateral capacity (Newton)	Percentage reduction (%)
30	0	Static	75	–
	0	Two-way	43	42.66
	0	One-way	41	45.33
	20	Static	59	21.33
	20	Two-way	34	54.66
	20	One-way	34	54.66
60	0	Static	114	–
	0	Two-way	65	42.98
	0	One-way	62	45.61
	20	Static	78	31.57
	20	Two-way	52	54.38
	20	One-way	51	55.26

the pile is installed near sloping ground and subjected to one-way cyclic loading. The static lateral capacity method overestimates the pile capacity, and cyclic or dynamic nature of load needs to be considered for proper design of pile foundations.

4 Conclusions

In present study, small-scale physical modelling of pile constructed near slopes subjected to static and cyclic loading was done. From the results, we can conclude the following:

- The presence of slope causes reduction in lateral capacity of pile, and due to absence of soil, there is less passive resistance offered by soil to pile. The reduction in capacity due to slopes compared to horizontal ground can be 20% to 30% depending on the relative density.
- The pile subjected to dynamic lateral forces can reduce the lateral capacity by 56% depending on the ground slopes and relative density.
- The nature of cyclic loading (one-way and two-way loading) also influences the lateral capacity of pile.

High-speed trains can exert large lateral force with cyclic nature which may cause damage if pile is not designed considering its dynamic nature. The situation worsens if slope is also present as in abutments; thus, further study such as more number of tests with variable slope is required for better design.

References

1. Bureau of Indian Standards 'Code of practice for design and construction of pile foundations. Part 4: Load test on piles', IS:2911 (Part 4) (1985)
2. He, X., Kawatani, M., Hayashikawa, T., Matsumoto, T.: Three-dimensional numerical analysis on site vibration around shinkansen viaducts under high-speed running bullet train. J. Struct. Eng. **59**, 290–298 (2013)
3. Long, J.H., Vanneste, G.: Effects of cyclic lateral loads on piles in sand. J. Geotech. Eng. ASCE **120**(1), 225–244. https://doi.org/10.1061/(ASCE)0733-9410(1994)120:1(225) (1994)
4. Mezazigh, S., Levacher, D.: Laterally loaded piles in sand: slope effect on p-y reaction curves. Can. Geotech. J. **35**(3), 433–441. https://doi.org/10.1139/t98-016 (1998)
5. Muthukkumaran, K., Almas Begum, N.: Experimental investigation of single model pile subjected to lateral load in sloping ground. Geotech. Geol. Eng. **33**(4), 935–946. https://doi.org/10.1007/s10706-015-9875-7 (Springer International Publishing) (2015)
6. Rosquoet, F., Thorel, L., Garnier, J., Canepa, Y.: Lateral cyclic loading of sand-installed piles. Soils Foundations **47**(5), 821–832. https://doi.org/10.3208/sandf.47.821 (2007)
7. Wood, D.M.: Geotechnical Modelling. doi: https://doi.org/10.1201/9781315273556 (2004)

A Study of Piled Raft Foundation

Riddhi M. Gupta, Jaykumar C. Shukla, and Nitin H. Joshi

Abstract Nowadays, piled raft foundation is increasingly being used not only in developed countries but also in developing countries like India. This paper is based on the study of piled raft foundation constructed in Uttarakhand, India, with the help of finite element software ELPLA and finite difference software GROUP. In analysis with ELPLA methods considered are linear as well as nonlinear methods such as hyperbolic stress–strain function and method as per DIN (4014) standard. The software is validated with results of the on-site pile load–settlement test conducted on individual pile. The results are compared also with analysis performed using PLAXIS 3D.

Keywords Piled raft · ELPLA · GROUP · Nonlinear hyperbolic stress–strain function for soil and DIN (4014) standards · Plaxis3D

1 Introduction

It is a general practice in design of the pile foundation to consider the upcoming super structure load is resisted by piles only. The contribution of raft in sharing the load is usually neglected. The overall factor of safety is based on load transmitted by piles only. A piled raft system is combination of both the load bearing structures, i.e., pile foundation and raft foundation. The advantage of piled raft foundation is that it is

---

R. M. Gupta (✉) · N. H. Joshi
Applied Mechanics Department, FTE, MSU Baroda, Baroda 390002, India
e-mail: riddhigupta95@gmail.in

N. H. Joshi
e-mail: nhjoshi-appmech@msubaroda.ac.in

J. C. Shukla
Geo Dynamics, Baroda 390002, India
e-mail: shukla.jc@gmail.com

N. H. Joshi
Applied Mechanics Department, FTE, MSU Baroda, Gujarat 390002, India

effective in reducing overall and differential settlements. Moreover, it helps economically by improving bearing capacity of shallow foundation. This paper is about analyzing the re-designed piled foundation, on which an Industrial RCC Building of about 35 m height is to be constructed. The site is situated in Uttarakhand, India. The revised foundation design has been analyzed using the finite-element-based software ELPLA [1] and finite difference software GROUP [2]. The obtained results are compared with finite element software PLAXIS 3D [3]. The analysis carried out with above software is based on soil data provided by geotechnical investigation report.

The effectiveness of piles and raft as a combined system in reducing the overall settlement and improving bearing capacity depends on the factors such as the subsoil characteristics, the geometric profile of the structural elements, i.e., pile and raft and location of upcoming loading [4]. For the same ground condition and raft area, the strategical arrangement of piles and length of piles can lead to variation in piled raft coefficient value [5]. This combined piled raft system is in practice by more than six decades globally. Many authors including few listed as Zeevaert [6], Davis and Poulos [7], Hooper [8], Burland et al. [9], sommer et al. [10], Price and Wardle [11] and Franke [12], among others have made assumption related to behavior of piled raft system.

2 Site Soil Condition

As per report, soil investigation involved the drilling of the three boreholes. Standard penetration test was also carried out. From which it is concluded that site is predominantly consists of clayey silt to sandy silt layers with few interbedded layers of sand. However, in most of the cases, % of silt fraction is more than 50, which indicates that strength behavior of these silt layer can be conservatively estimated as fine grained soil in presence of free water, i.e., below water table/saturated conditions. In absence of sufficient laboratory tests data for drained and undrained soil strength assessment, pile capacity calculations in the soil investigation data largely depend upon the SPT N-values. Top 3 m soil will be excavated and removed from the foundation thereby reducing severity of the liquefaction susceptibility on the foundation as whole. The geotechnical properties of each layer are given in Table 1. Figure 1 indicates borehole data considered for numerical analysis. The saturated unit weight for all layer expect layer no 10 is taken as 20 kPa. For layer no 10, it is taken as 21 kPa. Moreover, for sand/ sandy silty type of soil drain soil model is considered, and for the rest undrained soil model is considered for analysis.

3 Loading Details

There are structures in utility building within the construction site of area 40 m × 30 m. Bored cast-in-situ piles are selected for all structures as per the soil investigation

Table 1 Geotechnical properties for soil layers

Sr. No.	Depth (m)	Thickness (m)	Soil type	Bulk unit weight (kN/m³)	Cohesion (kPa)	Friction angle ϕ	Young's modulus (MPa)	Poisson's ratio (μ)
1	3	3	Fill (Ignored)	19	0	32	40	0.32
2	4.5	1.5	Silty clay	19	0.00	30	40	0.32
3	6	1.5	Clayey silt	18.63	30.00	0	8	0.35
4	7.5	1.5	Silty clay	18.63	40.00	0	10	0.49
5	9	1.5	Silty clay	19.03	55.00	0	15	0.35
6	12	3	Silty clay	19.03	30.00	0	8	0.4
7	15	3	Silty clay	19.03	50.00	0	20	0.3
8	18	3	Sandy silty	19.22	0.00	32	40	0.33
9	21	3	Silty clay	19.62	140.00	0	80	0.4
10	24	3	Silty clay	20.01	90.00	0	60	0.42
11	27	3	Silty clay	20.5	90.00	0	60	0.42
12	29	2	Silty fine dense sand	20.5	0.00	32	40	0.32
13	32	3	Very stiff low plastic clay	20.5	100.00	0	70	0.42
14	40	8	Fine sand with gravel	20.5	0.00	34	80	0.3

Fill layer is ignored while routine pile load tests validation

report. More than 90% of the piles were misaligned (minor to major, leading to severe eccentricity of loading) during the construction process which indicates poor construction supervision and inappropriate construction methods were practiced at site (or there may be wrong layout reference for pile construction). The thickness of raft for utility area is kept as 1.0 m. The utility building is divided into chiller building (PC 2 to 21) and office building (PC 4A,4B,5 and 6), in which the pile length of chiller building is 15 m, whereas of office building is of 18 m. There are total of 12 pile caps in the chiller building area and 4 in the office building area; the loading details of the foundation of utility area are shown in Table 2.
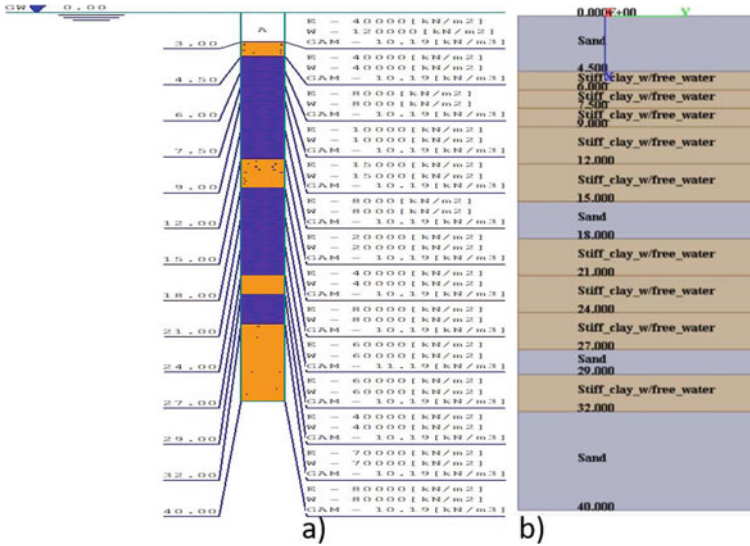
Fig. 1 Borehole data considered for numerical analysis **a** ELPLA borehole data and **b** group borehole data

4   Field Routine Compression Load Test on Pile and Validation of ELPLA Model

On the site routine compression, pile load tests conducted are validated with the developed numerical model in order to simulate actual field condition, and four numbers of vertical pile load tests were conducted at the site as per IS 2911:part 4 [13], on bored cast-in-situ pile of diameter 600 mm and length 18 m. The tests were conducted up to test load of 930 kN. All the four pile load tests attained different settlement levels at the same load of 930 kN. To decide the reliability of the output using a computer-based method, model of single pile is analyzed with ELPLA software in order to simulate field test results. A single pile was modeled considering raft of zero mm thickness and zero-unit weight. The load–settlement curve developed by using ELPLA is on the conservative side when compared with Test-1 and Test-3. However, the developed curve is clearly validating with the worst-case scenario, i.e., Test-1 up to working load. Hence, it can be established that numerical model simulated in ELPLA is in close agreement with the test load result both qualitatively and quantitatively as compared to field condition, Fig. 2.

Table 2 Loading details considered in the present study

| PC	Col. No	Force (kN)			Moment (kN.m)		
		FX	FY	FZ	Mx	My	Mz
2	C4	−70	13.75	−556	−13.34	−74.47	1.16
7	C5	213.5	143.4	−971.18	−89.19	281.94	23.912
8	C6	−24.76	−130.28	−2204	444.24	−104.67	13.57
9	C7	−34.45	136.67	1434.48	−478.38	−117.44	5.45
10	C8	0.04	133.93	−1337.2	−480.92	−2.284	0.223
11	C9	37.37	127.51	−1338.4	−456.18	118.78	10.45
12	C10	116.38	38.802	−1031.8	−126.86	383.46	1.77
13	C11	−45.9	−70.86	−926.79	−15.71	138.01	−1.36
14	C12	27.57	147.45	−1593.2	−313.63	99.559	−0.517
15	C13	−14.7	31.88	−945.45	80.39	46.73	0.09
16	C14	−44.55	161.84	−1701.4	330.02	−142.96	−12.92
17	C15	36.03	−125	−1448	434.69	116.9	−11
18	C16	−41.82	−138	−1436.2	485.45	−137.74	−4.118
19	C17	−3.382	−134.2	−1403.1	482.2	−10.67	0.722
20	C18	38.06	−126.7	−1457	453.99	122.06	11.77
21	C19	126.34	−35.61	−1114	115.69	−416.5	5.39
4	C21	134.79	8.275	−727	−16.85	297.86	−1.26
4	C2	158.51	7.54	−568.84	−2.12	−333.98	−6.79
5	C14	111.61	6.73	−737.83	−16.25	−256.82	−0.26
6	C7	239.22	42.46	−543.74	−48.71	−354.94	5.77
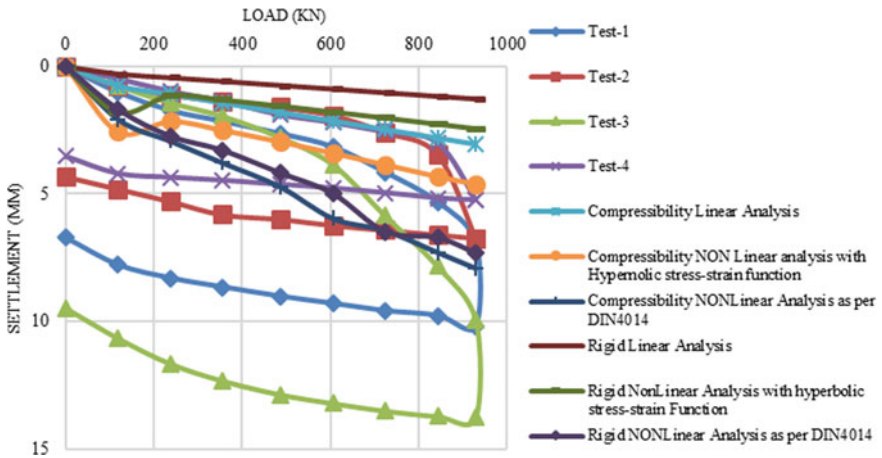
Fig. 2 Load–settlement curve comparison for single pile b/w field and numerical analysis with ELPLA

5   Numerical Methods and Assumptions for Analysis

The numerical model ELPLA (**E**lastic **P**late by M. El Gendy and A. El Gendy [14]) is used to evaluate the behavior of the piled raft foundation based on applied conditions. In analysis with ELPLA, it is considered that each node of plate elements has three degrees of freedom, i.e., vertical displacement and two rotations. The present analysis with ELPLA methods is as per continuum model (Ohde, 1942). In continuum model [15], the settlement at a point will occur not only occur under the loaded area, but it also influences area outside the loaded area. The elemental length of pile for ELPLA varies between 1 and 2 m, and the approximate size of the grids varies between 0.2 m minimum and 0.5 m. In present paper in analysis with ELPLA, various soil–raft combinations are considered which include the raft rigidity and compressibility, soil linear and nonlinear behavior, methods based on DIN(4014) for piled raft behavior, hyperbolic stress–strain function, i.e., soil model. For each piled raft system configuration, the above-described variations are applied and results are compared in order to understand the different behavior in varying conditions.

The program **GROUP** (by Lymon C. Reese, Shin-Tower Wang, Luis Vasquez for ENSOFT, INC, May 2016) was adopted to evaluate the behavior of pile group, without considering the contribution of pile cap in load bearing capacity evaluation. The cap is assumed to act as a rigid body. The cap may settle and rotate as per the applied loading and subsoil profile. As the group software is based on finite difference equation, same are applied in order to establish compatibility between pile displacement and load transfer along a pile. Similar conditions are applied for displacement and resistance at the tip of the pile. The finite difference software GROUP has six degrees of freedom, i.e., it assumes all three-direction displacement and three rotations.

The unit weight of concrete, Young's modulus and Poisson's ratio considered is 25 KN/m^3, 27,390,000 kPa and 0.15 for both pile cap and piles.

6   Results

The values of axial support reaction obtained with all six methods of ELPLA, GROUP and PLAXIS 3D are compared. Bar chart for all piled raft with pile cap notation is shown in Fig. 4. The layout of respective piled raft is shown beside each graph. The modeling in ELPLA (top view) and GROUP (3D) is shown in Fig. 3 side by side for respective structures.
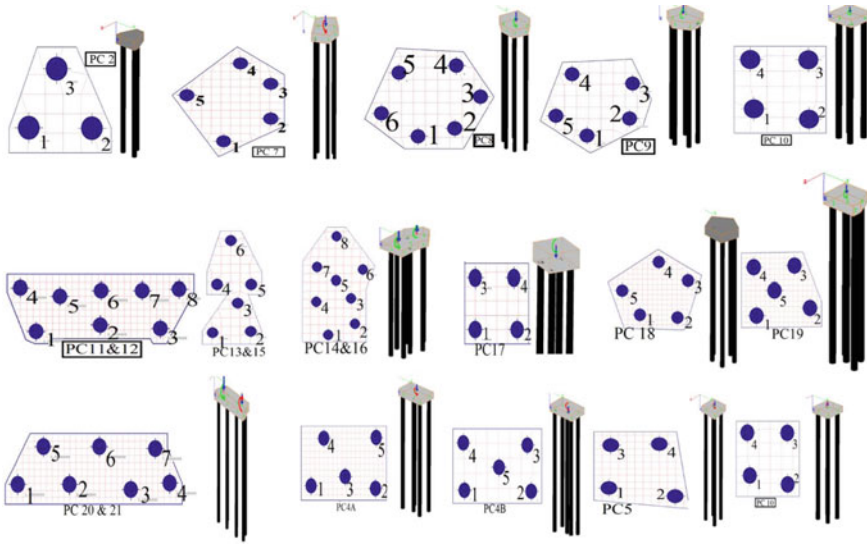
Legends:

Fig. 3 Modeling of piled raft in ELPLA (plane view) and GROUP (3D modeling)

▩ Method 1	Method 1	PLAXIS3D
▩ Method 2	Method 2	Rigid RAFT Non-Linear Analysis with DIN (4014)-ELPLA
▩ Method 3	Method 3	Compressible RAFT Non-Linear Analysis with DIN (4014)- ELPLA
	Method 4	Compressible RAFT Linear analysis- ELPLA
▢ Method 4	Method 5	Compressible RAFT Non-Linear analysis using Hyperbolic stress-strain function-ELPLA
▢ Method 5		
▩ Method 6	Method 6	Rigid RAFT Linear analysis-ELPLA
▩ Method 7	Method 7	Rigid RAFT Non-Linear analysis using Hyperbolic stress-strain function- ELPLA
▩ Method 8	Method 8	Analysis with GROUP

Table 3 shows piled raft coefficient (bearing factor) αkpp derived with all six ELPLA methods. The bearing capacity factor αkpp indicates the percentage of load sharing, i.e., percentage total load and load taken by piles.

7 Conclusion

(1) The load–settlement curve developed by using PLAXIS 3D; ELPLA is on the conservative side when compared with Test-1 and Test-3. Hence, it can be established that numerical models simulated in PLAXIS 3D and ELPLA are in close agreement with the test load results both qualitatively and quantitatively as compared to field condition.

(2) The percentage variation in vertical support reaction b/w methods 2 and method 3 is marginally 5% for PC2, PC7, PC9, PC10, PC 11 &12, PC13 & 15, PC14&16, PC17, PC20 &21, PC4A, PC4B, PC5, PC6. This variation for PC8,

PC18 and PC19 is 17%, 12% and 20%, respectively. From this, it can be said that analysis with DIN (4014) method gives almost same results whether piled raft is considered as rigid or flexible, for small piled rafts.

(3)   When vertical support reaction obtained with method 4 is compared with method 5, there is marginally 5% variation b/w results of these two methods
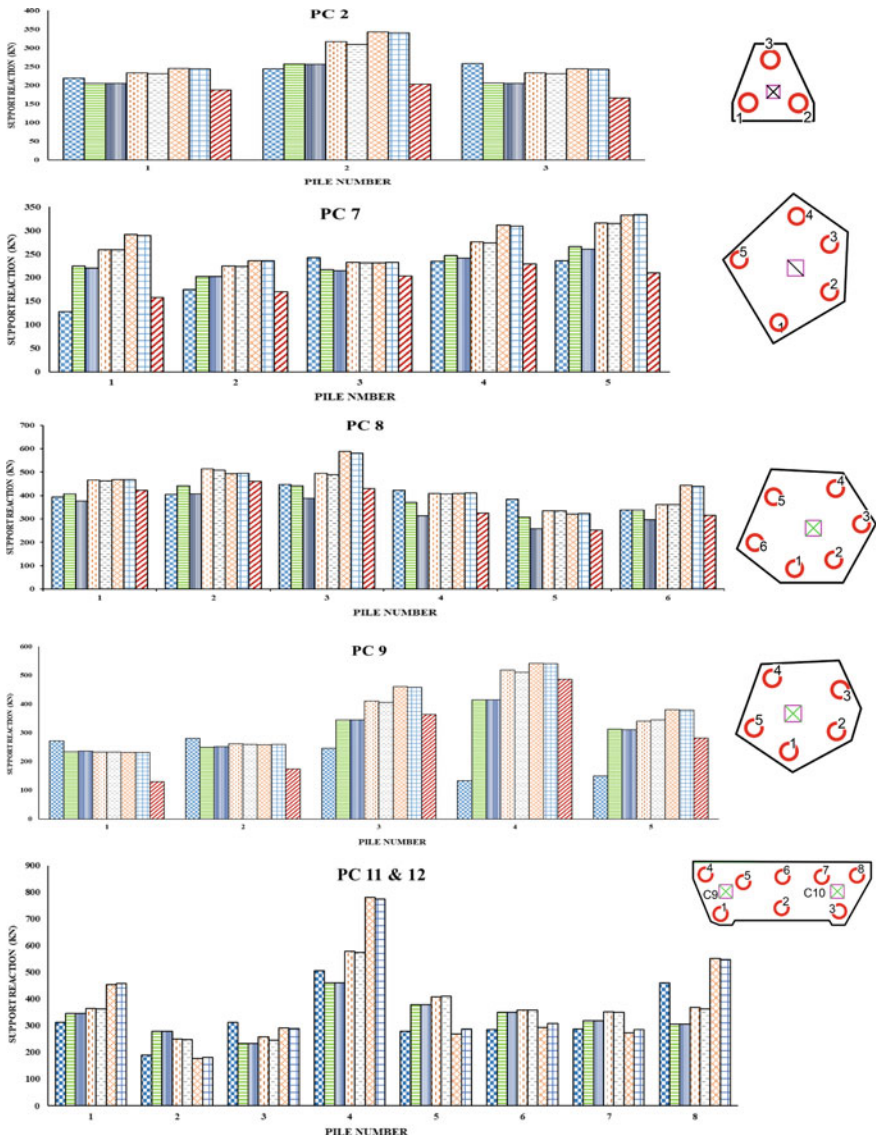

Fig. 4 Bar chart showing vertical support reaction of piles obtained with method 1 to 8 for each pile group and pile group configuration beside each bar chart
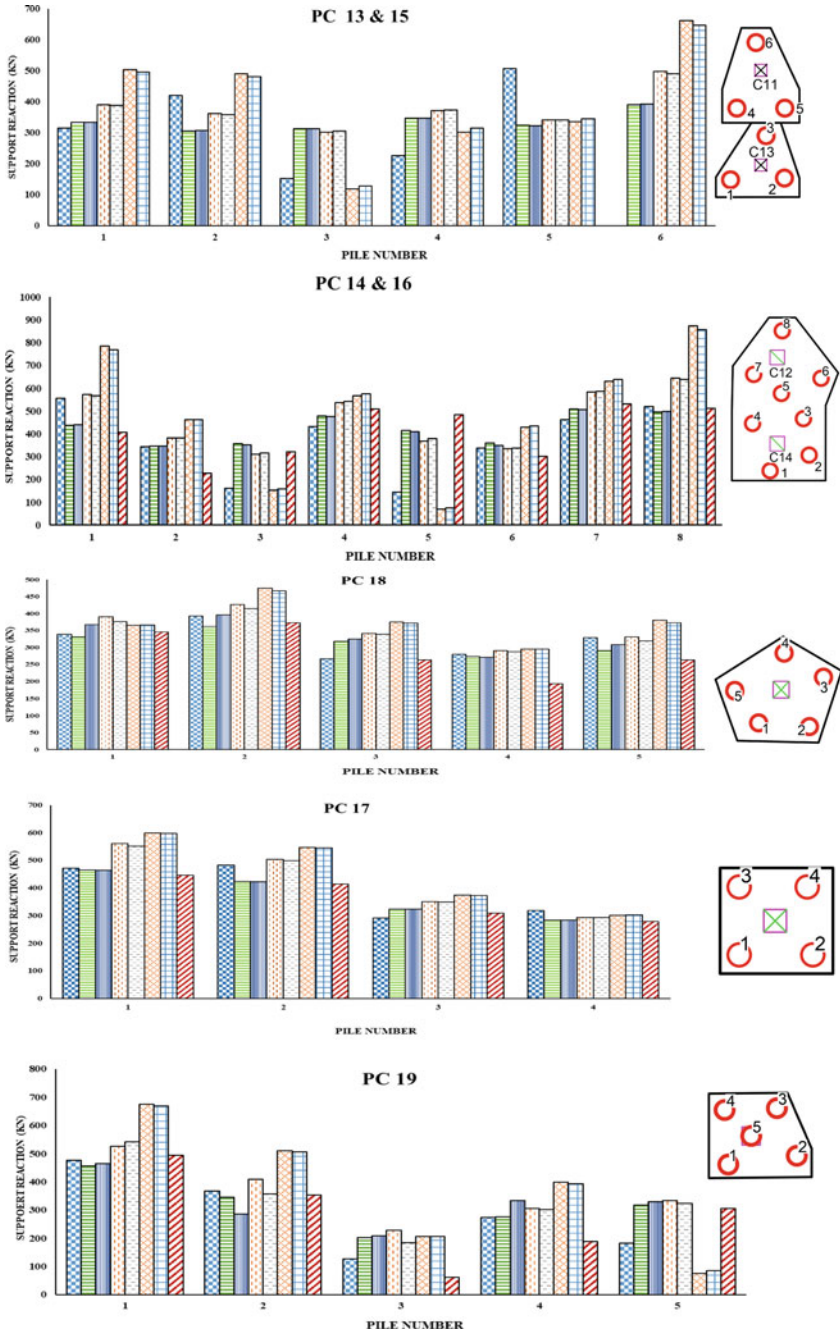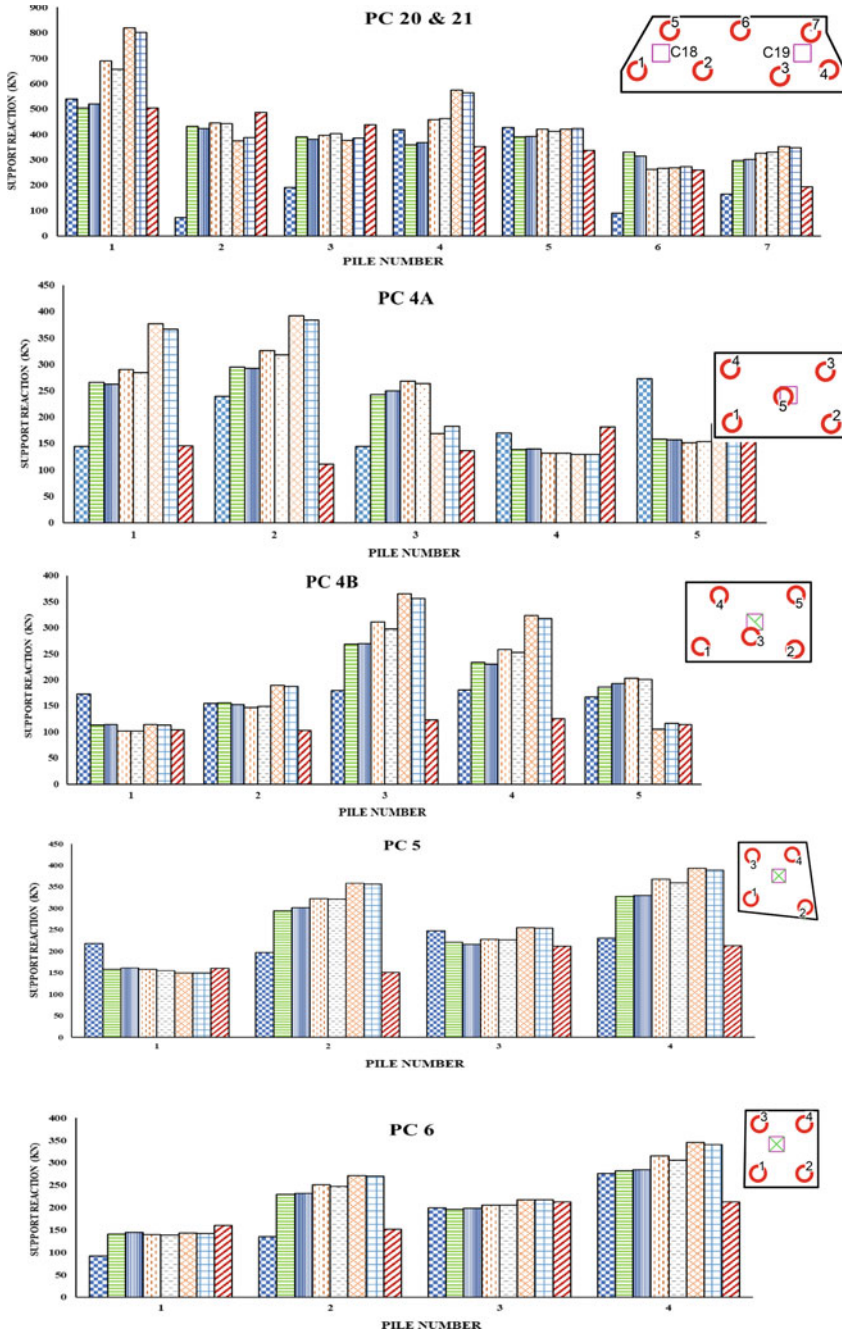
Fig. 4 (continued)

Fig. 4 (continued)

Table 3 Piled raft coefficient (bearing factor) αkpp derived with all ELPLA methods

Pile cap number	Col. No	Piled raft coefficient αkpp					
		Method 2	Method 3	Method 4	Method 5	Method 6	Method 7
PC 2	C4	79.15	78.93	92.69	91.25	98.4	98
PC7	C5	81.38	80.19	92.07	91.79	98.8	98.6
PC8	C6	83.7	81.51	93.6	92.92	98.8	98.7
PC9	C7	81.94	82.1	92.88	92.31	98.6	98.4
PC10	C8	82.7	83.28	94.24	92.8	99.5	99.4
PC 11 & 12	C9,10	85.59	85.24	94.09	93.13	99	100
PC 13 & 15	C11,13	82.7	82.76	93.06	92.61	99.1	99
PC 14 & 16	C12	84.55	83.96	92.95	93.35	98.8	98.7
PC 17	C15	81.74	81.53	93.24	92.45	99.5	99.4
PC 18	C16	82.81	87.62	93.61	92.8	99.5	98.6
PC 19	C17	84.69	85.85	92.46	90.4	98.7	98.5
PC 20 & 21	C18,19	83.91	83.81	93	92.42	98.9	98.8
PC 4A	C21	85.02	85.09	90.22	88.97	96.9	96.3
PC 4B	C28	84.34	84.43	89.86	88.13	96.7	95.9
PC 5	C14	84.04	84.57	90.21	89.07	97	96.4
PC 6	C7	84.31	85.49	90.65	89.07	97.1	96.4

for all piles. This means linear analysis and nonlinear analysis with hyperbolic stress–strain function for compressible piled raft give similar results for given problem.

(4) When vertical support reaction obtained with method 6 is compared with method 7, there is marginally 7% variation b/w these two methods for all piles. From this, it can be concluded that irrespective of size of raft, numbers of piles in piled raft and spacing between piles, method 6 can be used in alternate of method 7, i.e., ELPLA piled rigid raft can be analyzed with linear method or using nonlinear hyperbolic stress–strain function.

(5) The maximum and minimum percentage variation in vertical support reactions obtained with method 8 is compared with method 1 for PC2, PC7, PC8, PC9, PC10, PC 14 &16, PC17, PC 18, PC19, PC 20&21, PC 4A, PC4B, PC5 and PC 6 and is 35%, −24 to 2%, −13 to 35%, −226 to 53%, −11 to 21%, −237 to 35%, −6 to 14%, −2 to 32%, −67 to 51%, −565 to 22%, −7 to 54%, 40%, 27%, −75 to 23%, respectively. Here percentage value with negative sign indicates amount of support reaction obtained with method 8 is more than that obtained with method 1. The positive value indicates the amount of vertical reaction obtain with method 8 is less than that obtained with method 1.

(6) The maximum and minimum percentage variation in vertical support reactions obtained with method 2 is compared with method 1 for PC2, PC7, PC8, PC9, PC10, PC11 &12, PC13&15, PC 14 &16, PC17, PC 18, PC19, PC 20&21, PC 4A, PC4B, PC5 and PC 6 and is −6 to 20%, −75 to 11%, −9 to 20%, −212 to 14%, −26 to 2%, −48 to 34%, −107 to 37%, −189 to 22%, −11 to 13%, −20 to 12%, −74 to 6%, −489 to 15%, −85 to 19%,−50 to 35%, −50 to 28%, −70 to 2%, respectively. Here percentage value with negative sign indicates amount of support reaction obtained with method 2 is more than that obtained with method 1. The positive value indicates the amount of vertical reaction obtained with method 2 is less than that obtained with method 1. Here the positive variation for all piles ranges near to 20–35 percentage. As percentage variation between method 2 and method 3 has marginal variation of 5%, and the variation in axial reaction between method 1 and method 3 will about ±5% with that of method 1 and method 2.

(7) The maximum and minimum percentage variation in vertical support reactions obtained with method 6 is compared with method 1 for Utility Building Structures PC2, PC7, PC8, PC9, PC10, PC11 &12, PC13&15, PC 14 &16, PC17, PC 18, PC19, PC 20&21, PC 4A, PC4B, PC5 and PC 6 and is −41 to 6%, −127 to 5%, −27 to 13%, −290 to 15%, −32 to −21%, −46 to 7%, −101 to 33%, −70 to 52%, −29 to 6%, −41 to −6%, −64 to 59%, −411 to 2%, −161 to 32%, −103 to 38%, −82 to 32%, −101 to −9%, respectively. Here percentage value with negative sign indicates amount of support reaction obtained with method 6 is more than that obtained with method 1. The positive value indicates the amount of vertical reaction obtain with method 2 is less than that obtained with method 1. As percentage variation between method 6 and method 7 has marginal variation of 7%, the variation in axial reaction between method 1 and method 7 will be about ±7% with that of method 1 and method 6.

(8) The piled raft coefficient obtained with method 2 and method 3 ranges between 0.8 and 0.85; same with methods 4, 5, 6 and 7 is between 0.9 and 1 for all structures in utility area.

References

1. El Gendy, M., El Gendy, A.: Analysis of Piled Rafts by the Program ELPLA, GEOTEC Software Inc., Canada T3E 7Y7
2. Reese, L.C., Wang, S.-T., Vasquez, L.: A Program for the Analysis of a Group of Piles Subjected to Vertical and Lateral Loading (Technical Manual), for ENSOFT, INC 3003 W. Howard Lane Austin, Texas (2016)
3. Plaxis3D (2013) Plaxis 3D User Manuals. Plaxis BV, Delft, the Netherlands
4. Hemsley, J.A.: Design Application of Raft Foundations. Published by Thomas Telford Ltd, 1 Heron Quay, London E14 4JD (2000)
5. Katzenbach, R., Choudhury, D.: ISSMGE combined pile–raft foundation guideline. In: International Society for Soil Mechanics and Geotechnical Engineering (ISSMGE), Darmstadt, Germany, pp. 1–28 (2013)

6. Zeevaert, L.: Compensated friction-pile foundation to reduce the settlement of buildings on highly compressible volcanic clay of Mexico City. Proc. 4th Int. Conf. Soil Mech. Found. Engng. London 2 (1957)
7. Davis, E.H., Poulos, H.G.: The analysis of piled raft systems. Aust. Geomech. J. **2**, 21–27 (1972)
8. Hooper, J.A.: Review of behaviour of piled raft foundations. Report No. 83. London, CIRIA (1974)
9. Burland, J.B.: Piles as settlement reducers. 18th Italian Cong. Soil Mech. Pavia, (1995)
10. Sommer, H., Tamaro, G., DeBenedittis, C. Messe Turm, foundations for the tallest building in Europe. Proc. 4th DFI Conf. Stresa. 139–145 (1991)
11. Price, G. & Wardle, I. F. Queen Elizabeth II Conference Centre: monitoring of load sharing between piles and raft. Proc. Inst. Civ. Engnrs. **80**(1), 1505–1518 (1986)
12. Franke, E.: Measurements beneath piled rafts. ENPC Conference, Paris, pp. 1–28 (1991)
13. IS 2911 (PART 4): 1985 Code of Practice for Design and Construction of Pile Foundations
14. El Gendy, M.: An iteration method for design of slab on elastic foundation. In: Proceeding of the first International Conference on Civil Engineering Helewan University, Cairo, Egypt ((1998))
15. Mindlin, R.D.: Force at a Point in the Interior of a Semi-Infinite Solid Physic **8**, 195 (1936)

Seismic Stability of Unsupported Conical Excavation in Clayey Ground

Dhiraj Raj [iD] **, M. Bharathi** [iD] **, and Sanjay K. Shukla** [iD]

Abstract Conical excavations without support are often made in some field projects, such as foundations for piers, oil and water tanks. The seismic stability of these excavations has been given least importance in the research field. The instability of these unsupported excavations might increase during a seismic event. Hence, a realistic estimation of the seismic stability of unsupported excavations is a prominent issue, especially for the perpetual purpose. In the present study, seismic stability number for unsupported excavations has been proposed using the finite element (FE) analyses. Due to symmetry in the geometry about the vertical axis, axisymmetric FE models have been developed using OptumG2 software based on the finite element limit analysis approach. The soil (clay, with isotropic and constant undrained shear strength property) has been modelled as a perfectly plastic Tresca material following an associated flow rule. Boundary conditions were considered as per the field conditions, and seismic loads were considered as pseudo-static force applied in terms of horizontal seismic coefficient, α_h. Adaptive meshing technique was adopted to predict the results reasonably closer to exact solutions. The seismic stability of these conical excavations is reported in terms of stability number. Moreover, the effects of depth of excavation, inclination angle, intensity of seismic loading, etc. on the seismic stability number are explored in detail. For deeper insights and influence of various affecting parameters, non-dimensional design charts are presented. Further, it has been observed that the considered parameters have significant effects on the seismic stability of conical excavations.

Keywords Seismic stability · Conical excavation · Clay · Axisymmetric · Finite element limit analyses

D. Raj (✉) · M. Bharathi
IIT Roorkee, Roorkee 247667, India
e-mail: dhirajraj.iitr@gmail.com

S. K. Shukla
Fiji National University, Suva, Fiji

1   Introduction

Generally, unsupported excavations are found as primary stage in many projects related to construction of footings, piers, columns, underground water tanks, etc. (as shown in Fig. 1). For cohesive soils, unsupported open vertical or inclined cut can be achieved by excavating from the ground surface to the final depth of these structures and is still one of the most practical and economical methods for temporary excavations to construct the foundations of the structures. To minimize the ground movement, a temporary retaining wall, such as a braced or cantilever sheet pile wall, is usually employed for the open excavation of such constructions, but this requires the additional expense of installing a retaining wall. In the recent years, unsupported excavation problems have gained attention of most of the geotechnical projects due to its practical importance. A series of detailed investigations has been carried out on assessing the stability of these unsupported excavations. Evaluating the stability of unsupported excavation is one of the most important aspects to ensure safety in both short and long span.

Initially, remarkable contributions have been made by researchers to estimate the stability of unsupported vertical circular excavations in both cohesive and cohesive frictional soils. The most notable contributions, associated with the stability of vertical circular excavations, have been made by [1–7]. Based on the limit equilibrium

Fig. 1   Unsupported excavation adjacent to an existing building

method, the stability of cylindrical excavations formed in cohesive frictional soils was examined [2, 3]. However, these solutions were approximate in nature because of an inherent assumption associated with the geometry of the failure mechanism. With the help of an upper bound rigid block mechanism, the stability of cylindrical excavations in clays whose shear strength increases linearly with depth was evaluated [6, 8]. These analyses also require an assumption with reference to the geometry of the collapse mechanism. By using an elastoplastic finite element analysis, the stability numbers for a cylindrical excavation formed in cohesive frictional soil was computed [9]. By using an axisymmetric lower bound limit analysis and three-dimensional limit analysis, in conjunction with finite elements and linear/nonlinear programming, a series of studies are available in the literature to determine the stability numbers for an unsupported vertical cylindrical excavation [1, 5, 10–12]. Among these computational studies on cylindrical excavations, few were performed in homogeneous cohesive soils [5, 10, 11]. On the other hand, an unsupported cylindrical excavation made in cohesive frictional soils was also explored [1, 12]. By using the three-dimensional finite element limit analysis and nonlinear programming provided an upper bound solution for this excavation stability problem [1]. On account of the inherent difficulties involved in carrying out a three-dimensional analysis [1, 13], it remains, however, always a difficult task to obtain the corresponding three-dimensional solution. Based on an axisymmetric lower bound formulation, the stability numbers for an unsupported vertical cylindrical excavation in clays whose undrained shear strength increases linearly with the depth were obtained [11]. Stability of unsupported axisymmetric excavation has been explored in the past for homogenous clays using lower bound (LB) and upper bound (UB) analyses by [6] and [10]. Later on, the stability of unsupported vertical excavation was obtained using LB and UB finite element limit analysis (FELA) considering linearly increasing cohesion of soil with depth [11, 14] and cohesive frictional soils [12, 14]. Recently, detailed parametric study using FELA has been carried out to estimate the stability of unsupported conical excavation in homogeneous and nonhomogeneous clays [15] and cohesive frictional soils [16]. From existing literature, it has been found that stability of unsupported conical excavations in clay subjected to seismic loading is mostly lacking and needs to be studied in detail.

The main objective of the present study is to estimate the seismic stability number, N_c, of unsupported conical excavations in homogenous clay subjected to seismic loading (in terms of horizontal seismic coefficient, α_h) through FELA using 2D axisymmetric finite element models developed in OptumG2. The parametric study has been performed by varying dimensions of conical excavation, shear strength parameter and seismic loading. Based on this study, the design charts are developed to estimate the seismic stability number, N_c, of unsupported conical excavations.

2 Finite Element Modelling

In geotechnical engineering, limit analysis and FELA have been extensively used in the past to study various complex stability problems [17, 18]. FELA, combination of limit analysis with finite element discretization, is widely used to bracket the exact limit load by upper bound (UB) and lower bound (LB) solutions of limit analysis (assuming a rigid-perfectly plastic material with an associated flow rule) for handling complex problems in geotechnical engineering with irregular geometries, varying soil properties, loadings and boundary conditions [19, 20]. Under plane strain and axisymmetric condition, both LB and UB problems (in OptumG2) are formulated using second-order cone programming (SOCP) [21, 22] to solve geotechnical stability issues. The details of the numerical formulation of FELA in OptumG2 have been elaborated [23].

The procedure adopted for obtaining the seismic stability number, N_c, of unsupported conical excavations in homogenous clay through FELA using OptumG2 is summarized below. Taking advantage of axisymmetry, 2D axisymmetric finite element models of the conical excavations for seismic condition have been modelled with its geometric parameters (excavation height, H, radius of excavation bottom, b, and slope inclination, β), as represented in Fig. 2. The extents for FE model have been chosen based on sensitivity study so that the failure shear zone does not intersect the right and bottom boundaries and have insignificant effect on the computed results. Based on sensitivity study, the optimal sizes of the FE model along horizontal and vertical directions have been limited to 8H and 3H, respectively.

The soil mass as homogeneous clay (with undrained shear strength, S_u, and unit weight, γ) has been modelled as the rigid-perfectly plastic Tresca material with the associated flow rule. The soil mass has been discretize with six-noded triangular elements in UB analysis, where each element (with its own unique nodes) has continuous normal and shear stresses at nodes and stresses jump are allowed across shared edges of adjacent elements. However, unknown velocity components (with
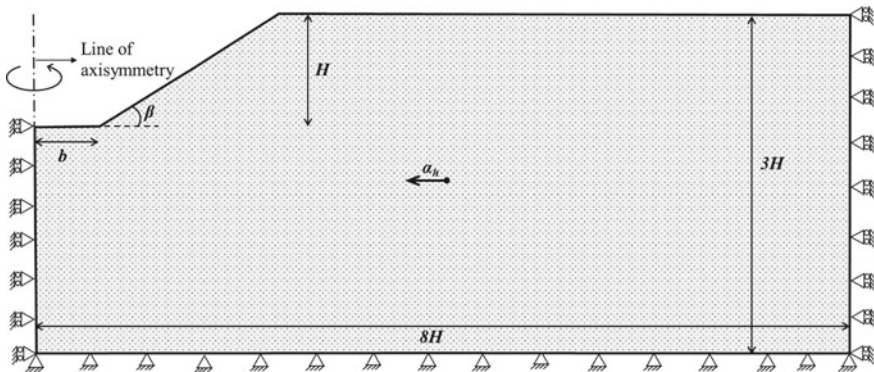

Fig. 2 Axisymmetric numerical model of unsupported conical excavation

a quadratic function within the element) are continuous across adjacent elements. In OptumG2, UB problem is formulated as SOCP, which satisfies the kinematically admissible velocity constraints, generated from velocity boundary conditions and compatibility equations with associated flow rule on average for six-noded triangular elements. For the conical excavation problem, the objective function of UB SOCP corresponds to the minimization of the soil unit weight.

In case of LB analysis, the soil mass has been discretized into three-noded triangular elements. In OptumG2, the LB problem is formulated into SOCP satisfying the statically admissible stress constraints, generated from equilibrium equations at centroid of each triangular element and along the stress discontinuities, stress boundary conditions with no violation of the yield criterion for all nodes. For the conical excavation problem, the objective function of LB SOCP corresponds to maximization of soil unit weight.

As this conical excavation problem is formulated in axisymmetry plane and seismic load (as shown in Fig. 2), applied on the entire soil mass as pseudo-static forces in terms of horizontal seismic coefficient, α_h, is non-axisymmetric. To simulate the seismic effect, non-axisymmetric load needs to be converted to axisymmetric. Generally, loading applied to a solid or shell of revolution can be described as the sum of its series components [24]. Let $\alpha_{h, 3D}$ represent seismic load in general, such as normal pressure, line load, or temperature in thermal stress analysis. A Fourier series representation of $\alpha_{h, 3D}$ is presented in Eq. 1 where, $\alpha_h{}^c$ and $\alpha_h{}^S$ are load amplitudes that depend on n (but not on θ). Here n is an integer that represents the harmonic number. Loads described by $\alpha_{h, 3D}$ can be radial, axial, or circumferential.

$$\alpha_{h,3D} = \sum_{n=0}^{\infty} \alpha_h^c \cos n\theta + \sum_{n=0}^{\infty} \alpha_h^s \sin n\theta \tag{1}$$

By locating the $\theta = 0$ plane appropriately, it often happens that only one of the two series is needed. Typical problems are solved accurately enough by using only the first few terms of the load series. When a radial load $\alpha_{h, 3D}$, partly outward and partly inward but otherwise uniform, is represented by the sine series. Cosine terms of Eq. 1 are not needed (although the loading could be described by cosine terms alone if the $\theta = 0$ plane were placed 90° to the position shown). A uniformly distributed radial load, partially inward and partially outward, can be represented by a Fourier series (Eq. 2). Thus, by computing the value of α_h in radial, axial or circumferential model, the appropriate value of α_h in 3D can be obtained by using Eq. 2:

$$\alpha_{h,3D} = \frac{4\alpha_h}{\pi} \sin \theta \tag{2}$$

Automatic mesh adaptivity was also employed for both lower and upper bound analyses to determine close upper and lower bound solutions. Adaptive meshing with five iterations was used for all the analyses where the number of elements was increased from 7,000 to 10,000 to obtain results closer to exact solutions. Using
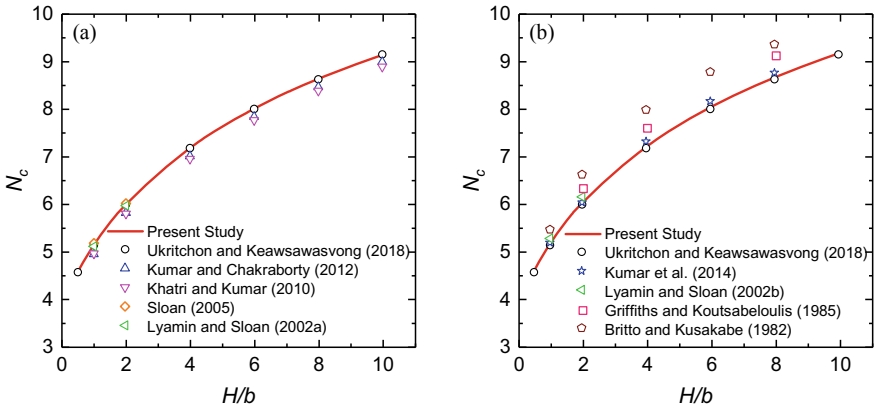
Fig. 3 Validation of the developed model using **a** LB and **b** UB solutions

adaptive mesh technique gives the advantage of predicting the failure surface exactly which is evident through the small element size adjacent to the rupture area and large elements elsewhere. The seismic stability number, N_c estimated using Eq. 3, is dependent on excavation height, H/b; slope angle, β; and seismic coefficient, α_h.

$$N_c = \frac{\gamma H}{S_u} = f\left(\frac{H}{b}, \beta, \alpha_h\right) \tag{3}$$

3 Model Validation and Comparison with Past Studies

The developed model is validated for vertical excavation ($\beta = 90°$) subjected to static loading ($\alpha_h = 0$ g) with both lower [7, 11, 12, 16, 25] and upper [1, 6, 9, 14, 16] bound solutions as shown in Fig. 3a, b, respectively. The developed FE model predicts the results closer to the results reported in literature while employing lower bound solutions, whereas when employing upper bound solution, the predicted results are quite far away especially with the results reported based on rigid block mechanism [6] and elastoplastic FE analysis [9]. Further, in this study the average of both the upper and lower bound solutions has been used for interpretation in the following sections.

4 Results and Discussion

An extensive numerical study has been performed to obtain the seismic stability number, N_c for unsupported conical excavations. The results have been presented

for $\beta = 45 - 90°$, $H/b = 0.5 - 10$ and $\alpha_h = 0 - 0.2$ g. The variation of N_c with H/b subjected to increasing loading ($\alpha_h = 0$, 0.05, 0.10, 0.15 and 0.20 g) for four different excavation angles ($\beta = 90°$, 75°, 60° and 45°) have been presented in Fig. 4. It is interesting to note that N_c decreases with increase in α_h at all excavation angles, but the decrease is more prominent at lower β values. In all considered cases, N_c increases with increase in H/b.

The variation of failure surface for vertical ($\beta = 90°$) and conical ($\beta = 75°$, 60° and 45°) excavations with $H/b = 1$, 2 and 4 subjected to $\alpha_h = 0.10$ g has been presented in Fig. 5. With the increase in H/b, the soil mass contributing to failure decreases at a particular value of β. However, this decrease is significant at lower β
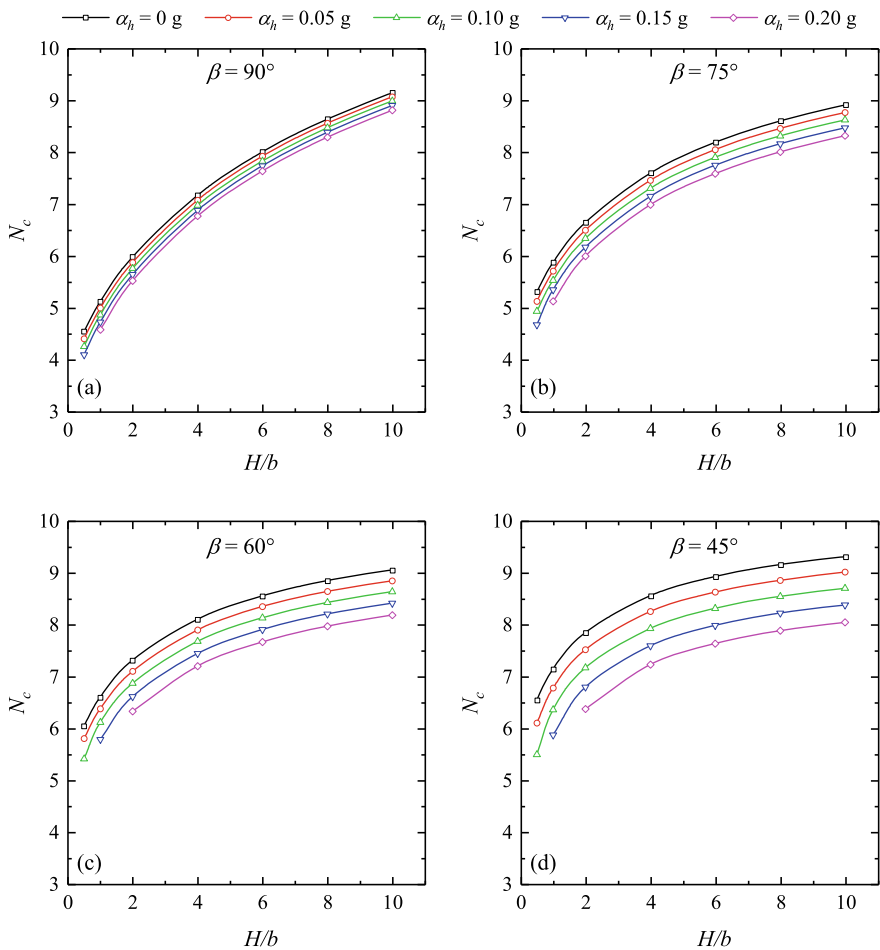

Fig. 4 Variation of N_c with H/b for different α_h and **a** $\beta = 90°$, **b** $\beta = 75°$, **c** $\beta = 60°$ and **d** $\beta = 45°$

H/b = 1   H/b = 2   H/b = 4

(a)   (b)   (c)

(d)   (e)   (f)

(g)   (h)   (i)
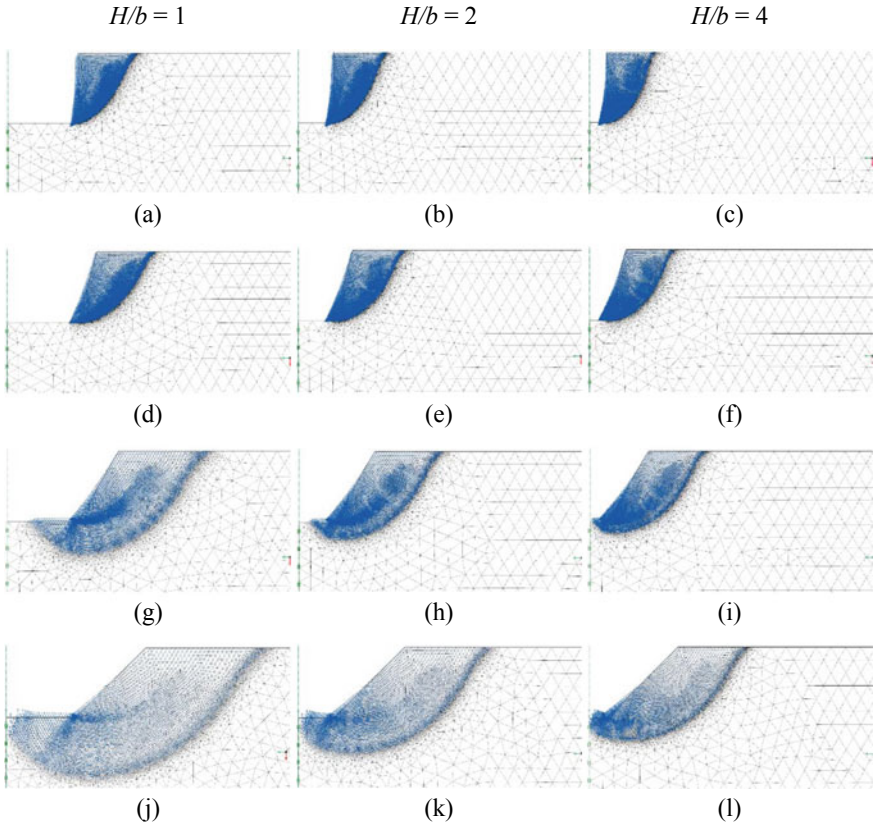
(j)   (k)   (l)

Fig. 5 Variation of failure pattern with H/b subjected to $\alpha_h = 0.10$ g for (**a–c**) $\beta = 90°$, (**d–f**) $\beta = 75°$, (**g–i**) $\beta = 60°$ and (**j–l**) $\beta = 45°$

values (i.e. $\beta = 60°$ and $45°$). For a considered H/b value, with the decrease in β the failure surface widens leading to increase in the soil mass participation.

The variation of N_c with varying α_h and H/b (0.5, 1, 2, 4, 6, 8 and 10) for four different excavation angles ($\beta = 90°$, $75°$, $60°$ and $45°$) has been presented in Fig. 6. It can be observed that at a particular β, N_c decreases with the increase in α_h. This decrease in N_c is more rapid at lower excavation angle, β. In all the considered cases, it has been observed that with the increase in H/b, N_c also increases. However, this increase is insignificant towards higher H/b for lower excavation angle, β (i.e. $60°$ and $45°$).

The variation of failure surface for vertical ($\beta = 90°$) and conical ($\beta = 75°$, $60°$ and $45°$) excavations with $H/b = 2$ and subjected to $\alpha_h = 0, 0.10$ and 0.20 g has been presented in Fig. 7. It can be observed that for a β value, with the increase in seismic load intensity the soil mass contributing to failure also increases. For a particular α_h value, with the decrease in β the failure surface widens leading to increase in the soil mass participation.
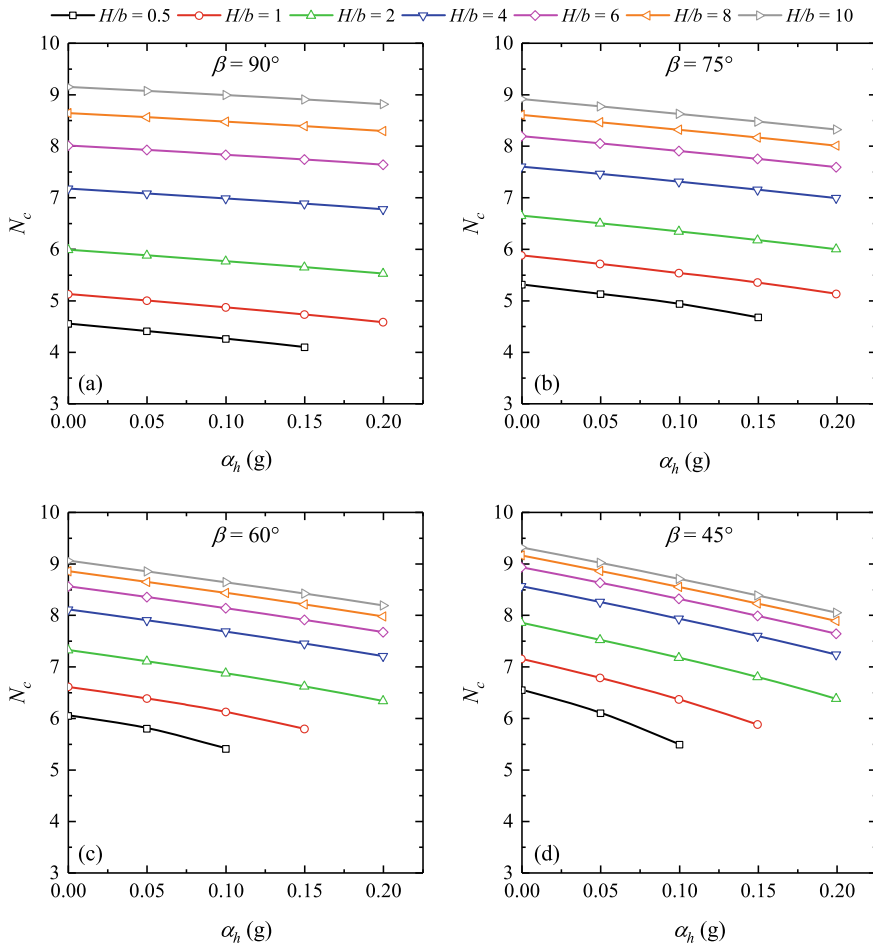
Fig. 6 Variation of N_c for α_h for **a** $\beta = 90°$, **b** $\beta = 75°$, **c** $\beta = 60°$ and **d** $\beta = 45°$

In all cases, it is interesting to note that (in Figs. 5 and 7) the failure surface mostly passes through either toe (for $\beta = 75°$ and $90°$) or base ($\beta = 45°$ and $60°$) of the conical excavation.

5 Conclusions

A numerical study has been performed to estimate seismic stability number of undrained conical excavation subjected to seismic action by employing UB and LB solutions of FELA. It has been observed that for a particular β, the soil mass contributing to failure also increases with the increase in seismic load intensity. For a
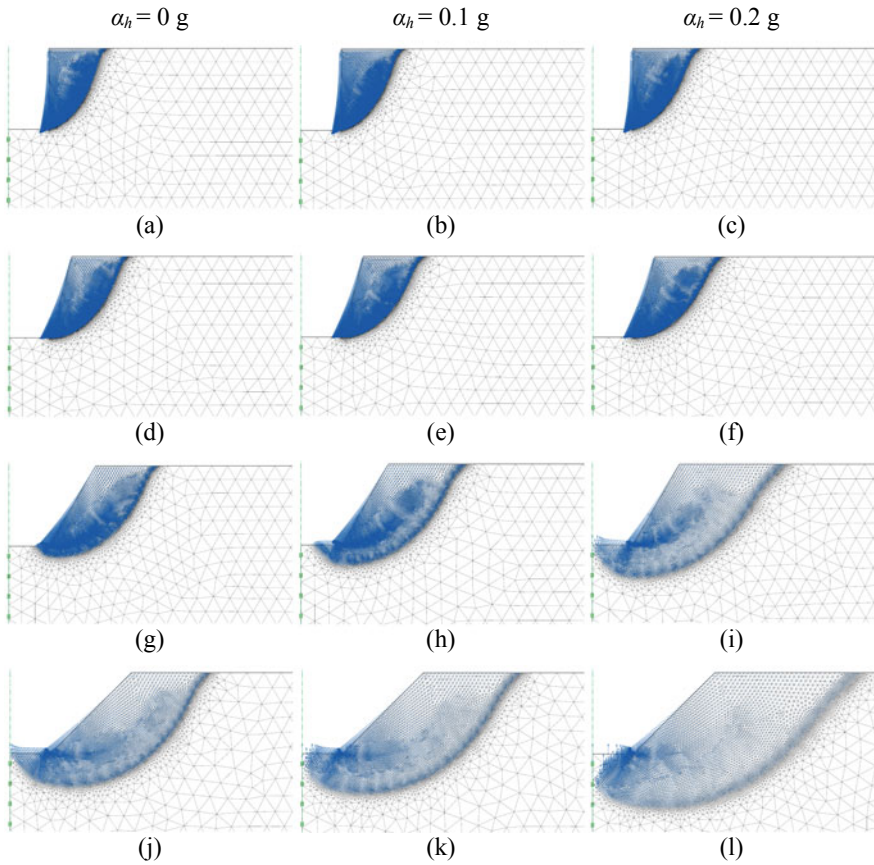
Fig. 7 Variation of failure pattern for $H/b = 2$ with α_h (**a–c**) $\beta = 90°$, (**d–f**) $\beta = 75°$, (**g–i**) $\beta = 60°$ and (**j–l**) $\beta = 45°$

particular α_h value, the failure surface widens leading to increase in soil mass participation with decrease in β. It has also been found that the failure surface for steep cut ($\beta = 75°$ and $90°$) passes through toe of conical excavation. However, in case of less steep cut ($\beta = 45°$ and $60°$) failure surface always passes through base of conical excavation.

It has been observed that N_c decreases with increase in α_h at all β, but the decrease is more prominent at lower β values. In all considered cases, it has been observed that with the increase in H/b, N_c also increases. However, this increase is insignificant towards higher H/b for lower excavation angle, β (i.e. $60°$ and $45°$).

References

1. Lyamin, A.V., Sloan, S.W.: Upper bound limit analysis using linear finite elements and non-linear programming. Int. J. Numer. Anal. Meth. Geomech. **26**(2), 181–216 (2002). https://doi.org/10.1002/nag.198

2. Bjerrum, L., Eide, O.: Stability of strutted excavations in clay. Géotechnique **6**(1), 32–47 (1956). https://doi.org/10.1680/geot.1956.6.1.32

3. Prater, E.G.: An examination of some theories of earth pressure on shaft linings. Can. Geotech. J. **14**(1), 91–106 (1977). https://doi.org/10.1139/t77-007

4. Pastor, J., Turgeman, S.: Formulation linéaire des méthodes de l'analys limite en symétrie axiale. In: 4th Congrès Francais de Mécanique. Nancy (France) (1979)

5. Pastor, J.: Analyse limite et stabilite des fouilles. In: Proceedings of the 10th International Conference on Soil Mechanics and Foundation Engineering, pp. 505–508 (1981)

6. Britto, A., Kusakabe, O.: Stability of unsupported axisymmetric excavations in soft clay. Géotechnique **32**(3), 261–270 (1982)

7. Sloan, S.: Finite element limit analysis in geomechanics. In: Proc. 9th Int. Conf. of IACMAG, Torino (Italia), pp. 141–160 (2005)

8. Britto, A.M., Kusakabe, O.: Stability of axisymmetric excavations in clays. J. Geotech. Eng. **109**(5), 666–681 (1983). https://doi.org/10.1061/(ASCE)0733-9410(1983)109:5(666)

9. Griffiths, D.V., Koutsabeloulis, N.: Finite element analysis of vertical excavations. Comput. Geotech. **1**(3), 221–235 (1985). https://doi.org/10.1016/0266-352X(85)90025-4

10. Pastor, J., Turgeman, S.: Limit analysis in axisymmetrical problems: numerical determination of complete statical solutions. Int. J. Mech. Sci. **24**(2), 95–117 (1982). https://doi.org/10.1016/0020-7403(82)90041-8

11. Khatri, V.N., Kumar, J.: Stability of an unsupported vertical circular excavation in clays under undrained condition. Comput. Geotech. **37**(3), 419–424 (2010). https://doi.org/10.1016/j.compgeo.2009.11.001

12. Kumar, J., Chakraborty, D.: Stability numbers for an unsupported vertical circular excavation in c−ϕ soil. Comput. Geotech. **39**, 79–84 (2012). https://doi.org/10.1016/j.compgeo.2011.08.002

13. Pastor, F., Kondo, D., Pastor, J.: 3D-FEM formulations of limit analysis methods for porous pressure-sensitive materials. Int. J. Numer. Meth. Eng. **95**(10), 847–870 (2013). https://doi.org/10.1002/nme.4527

14. Kumar, J., Chakraborty, M., Sahoo, J.P.: Stability of unsupported vertical circular excavations. J. Geotech. Geoenviron. Eng. **140**(7), 04014028 (2014). https://doi.org/10.1061/(ASCE)GT.1943-5606.0001118

15. Keawsawasvong, S., Ukritchon, B.: Stability of unsupported conical excavations in non-homogeneous clays. Comput. Geotech. **81**, 125–136 (2017). https://doi.org/10.1016/j.compgeo.2016.08.007

16. Ukritchon, B., Keawsawasvong, S.: A new design equation for drained stability of conical slopes in cohesive-frictional soils. J. Rock Mech. Geotech. Eng. **10**(2), 358–366 (2018). https://doi.org/10.1016/j.jrmge.2017.10.004

17. Chen, W.-F., Liu, X.: Limit Analysis in Soil Mechanics, vol. 52. Elsevier (2012)

18. Sloan, S.: Geotechnical stability analysis. Géotechnique **63**(7), 531 (2013)

19. Raj, D., Singh, Y., Kaynia, A.M.: Behavior of slopes under multiple adjacent footings and buildings. Int. J. Geomech. **18**(7), 04018062 (2018). https://doi.org/10.1061/(ASCE)GM.1943-5622.0001142

20. Raj, D., Singh, Y., Shukla, S.K.: Seismic bearing capacity of strip foundation embedded in c−ϕ soil slope. Int. J. Geomech. **18**(7), 04018076 (2018). https://doi.org/10.1061/(ASCE)GM.1943-5622.0001194

21. Makrodimopoulos, A., Martin, C.M.: Lower bound limit analysis of cohesive-frictional materials using second-order cone programming. Int. J. Numer. Meth. Eng. **66**(4), 604–634 (2006). https://doi.org/10.1002/nme.1567

22. Makrodimopoulos, A., Martin, C.M.: Upper bound limit analysis using simplex strain elements and second-order cone programming. Int. J. Numer. Anal. Meth. Geomech. **31**(6), 835–865 (2007). https://doi.org/10.1002/nag.567
23. Krabbenhoft, K., Lyamin, A., Krabbenhoft, J.: Optum computational engineering (OptumG2). Available on: www.optumce.com (2015)
24. Cook, R.D., Malkus, D.S., Plesha, M.E., Witt, R.J.: Concepts and Applications of Finite Element Analysis, 4th edn. John Wiley & Sons (2001)
25. Lyamin, A.V., Sloan, S.W.: Lower bound limit analysis using non-linear programming. Int. J. Numer. Meth. Eng. **55**(5), 573–611 (2002). https://doi.org/10.1002/nme.511

Analysis of Settlement Induced by Dissipation of Excess Pore Water Pressure Due to Piling in Soft Clay at Haldia

Akanksha Kesharwani, Abhijeet Gupta, and Ashok Kumar Khan

Abstract Consolidation settlement induced by dissipation of the excess pore water pressure due to pilling in soft clay and negative skin friction caused by it were analysed. Piling or the pile driving process usually induces excess pore water pressure in the surrounding soil. When this excess water pressure dissipates later on after the pile driving process is complete, settlement of the surrounding soil takes place and a negative skin resistance along the pile surface develops, which is undesirable (Hosseini & Rayhani in Int J Geo-Eng 2017) [5]. In this paper, PLAXIS 2D is used to take into account the nonlinear consolidation behaviour of the soil. The pile driving process was defined and analysed in terms of the expansion in a cylindrical cavity. In general, the results based on the FEM method were consistent with the actual field measurements on site. However in response to the problem, the permanent solutions are worked on.

Keywords Settlement · Consolidation · PLAXIS 2D

1 Introduction

During geophysical investigation, soil is found soft and weak up to a great depth, shallow foundation is not suitable for the intended structure, and then it is required to consider economical option between (i) soil stabilization and provide shallow foundation and (ii) deep foundation.

This study is focused on the later choice, i.e. deep foundation. Pile foundation transfers super structure load to deeper soil strata, to withstand lateral, vertical, uplift

A. Kesharwani (✉) · A. Gupta · A. K. Khan
National Institute of Technology, Jamshedpur 831014, India
e-mail: akanksha102@gmail.com

A. Gupta
e-mail: abhijeetgupta911@gmail.com

A. K. Khan
e-mail: akk.nitjsr@gmail.com

load and to minimize the settlement [3]. A structure can be founded on piles if the soil immediately beneath its base does not have sufficient bearing capacity to withstand the imposed structural loads. If it is represented in the results of site investigation that the soil at shallow depth is not stable or if the calculated settlement is beyond acceptable limits, a pile foundation will be required [1].

In this analysis, soft soil model theory and Mohr–Coulomb theory has been utilized for study purpose. The soft soil model is suitable for materials that exhibit high degrees of compressibility such as normally consolidated clays, clayey silts and peat [2]. Based on this dominant feature that should be considered in constitutive modelling of these materials is the volumetric hardening. Of course, a shear strength criterion also needed for these geomaterials, and a Mohr–Coulomb yield surface is considered for this purpose. The volumetric mechanism that captures the compressibility of the material is simulated by an elliptical cap that is very similar to the modified cam clay model. While field settlements were taken by noting rail level at centre of each oven by using total station at certain time interval.

An attempt has been made to study the foundation and allied structures supported on pile at Coke Oven Plant located near River Haldia, West Bengal. The plant was constructed over low-lying area filled up with fly ash and dredged sand. Now it is facing excessive settlement due to consolidation and release of excess pore water pressure with time. It is having four rows of heat recovery-type coke oven batteries. Each row is having 88 ovens, having 480-m-long rail track on either side for pusher car and quencher car. During operation of the plant, settlement/undulations of rail track problem are faced in positioning of pusher car and quencher car at oven centre during pushing operation due to rolling of the car.

In the paper, no use of cavity expansion theory has been done to model the pile driving process.

1.1 Problem Statement

To ensure the smooth run of the coke oven plant unit, there is a need of proper working of different machinery and structures as well. However, it was observed that oven rail track is facing problem of abrupt differential settlement. As preventive temporary method grouting of pedestal with Sika Microcrete was done, also cracked concrete was dismantled and replaced with steel girders. Therefore, this study was initiated to work out the permanent solution.

1.2 Need of the Present Study

1. Due to settlement/undulation of rail track problem is faced in positioning of pusher and quenching car at oven centre during pushing operation due to rolling of car.

2. Damage of power collector and failure of pusher and quenching car drive components.
3. Bending of thrust plates below the rail due to cracking of underlying concrete.
4. Breakage of foundation bolts.
5. Undulations in the rail track increase the impact that in turn results in progressive settlement.

1.3 Geology of the Site

The site is situated near the bank of River Haldia (Branch of Hooghly River) and surrounded by back water channels made by the river. Top few metres are made up of very recent filled up and fallowed by the sediment made by the marine and the river deposits which evaluated from the bore holes. Top 10 to 12 (average) is made up to the marine sedimentary clay (mixed with silt and sand in the bottom of the strata), and after this layer, we may get silty sand with clay and silty sand due to past alluvium activity by the marine and river (Table 1).

Table 1 Properties of soil strata

Soil strata	Depth (m)	Soil type	Properties
1	8.64e-6	Silty sand (SM)	$C' = 0$, $\varphi' = 27°$, $N = 5$, $E_s = 766 \times 5 = 3830$ kN/m^3, $\nu = 0.3$, $\gamma = 18.8$ kN/m^3
2	1.403	Soft clayey silt (CI-OI)	$C' = 19.6$ kPa, $\varphi' = 24°$, $e_o = 1.403$, $C_c = 0.4659$, $C_r = 0.097$, $P_c = 83.4$ kPa, $\nu = 0.45$, $\gamma = 17$KN/m^3, $E = 200$ to 500 $C_u = 250 \times 8$ to $500 \times 8 = 2000$ to 4000 kPa; use $E = 3600$ kPa
3	13–20	Silty sand (SM)	$C' = 0$, $\varphi' = 34°$, $N = 26$, $E_s = 766 \times 26 \approx 20,000$ kN/m^3, $\nu = 0.3$, $\gamma = 20$ kN/m^3
4	20–31	Silty clay (CH-OH)	$C' = 2$ kPa, $\varphi' = 28°$, $e_o = 1.458$, $C_c = 0.4543$, $C_r = 0.03556$, $P_c = 216$ kPa, $\nu = 0.45$, $\gamma = 17$ kN/m^3, $E = 450C_u = 450 \times 20.6 = 9270$ kPa
5	>31	Silty sand (SM)	$C' = 0$, $\varphi' = 34°$, $N = 25$, $E_s = 766 \times 26 \approx 20,000$ kN/m^3, $\nu = 0.3$, $\gamma = 20$ kN/m^3

Table 2 Parameters for soft soil model

Soft soil	CI-OI	CH-OH
Type	Undrained	Undrained
g_{unsat}	15.00	15.00
g_{sat}	17.00	17.00
k_x	8.64e-5	8.64e-5
k_y		8.64e-6
e_{init}		1.458
l^*	0.084	0.080
k^*	0.035	0.01258
C	19.60	2.00
J	24.00	28.00
Y	0.00	0.00
n_{ur}	0.200	0.200
K_0^{nc}	0.59	0.54
R_{inter}	0.67	0.67

2 Numerical Analysis

Finite element analysis is a powerful mathematical tool that makes it possible to solve complex engineering problems. The finite element method is a well-established numerical analysis technique used widely in many civil engineering applications, both for research and the solution of real engineering problems [6].

In my study, **soft soil model** and **Mohr–Coulomb model** has been used to model the soil. The elastic–plastic Mohr–Coulomb model involves five input parameters, i.e. elastic modulus (E) and Poisson's ratio (μ) for soil elasticity; angle of internal friction (ϕ) and cohesion (c) for soil plasticity, and (ψ) as an angle of dilatancy. This Mohr–Coulomb model represents a 'first-order' approximation of soil or rock behaviour [4]. Parameters for soft soil model and Mohr–Coulomb model are shown below. Also properties of concrete pedestal and pile are illustrated alongside (Tables 2, 3 and 4).

3 Result and Discussion

3.1 Results from Field Observation

Settlement has gained different values throughout the rail track, and also differential settlement has been encountered between rails at same section. Given below Fig. 1 demonstrates the graphical comparison of settlement of oven, outer track and inner track of Row 2 batteries, and Fig. 2 represents the graphical comparison of settlement of inner and outer tracks of Row 3. Both the graphs show increase in settlement as

Table 3 Parameters for Mohr–Coulomb model

Mohr–Coulomb	1 SM	2 SM	3 SM
Type	Drained	Drained	Drained
g_{unsat}	16.00	18.00	18.00
g_{sat}	18.00	20.00	20.00
k_x	0.900	0.900	0.900
k_y	0.090	0.090	0.090
e_{init}	0.500	0.500	0.500
E_{ref}	3830.0	20,000.0	20,000.0
N	0.300	0.300	0.300
G_{ref}	1473.077	7692.31	7692.31
c_{ref}	0.10	0.10	0.10
J	27.00	34.00	34.00
Y	0.00	4.00	4.00
R_{inter}	0.67	0.67	0.67

Table 4 Properties of concrete of pedestal and pile

Linear Elastic	1 Concrete pedestal tie beam	2 Pile properties
Type	Non-porous	Non-porous
g_{unsat}	25.00	25.00
g_{sat}	25.00	25.00
k_x	0.000	0.000
k_y	0.000	0.000
e_{init}	0.500	0.500
E_{ref}	24,500,000	24,500,000
N	0.150	0.150
G_{ref}	10,652,173.91	10,652,173.91
R_{inter}	0.670	0.670
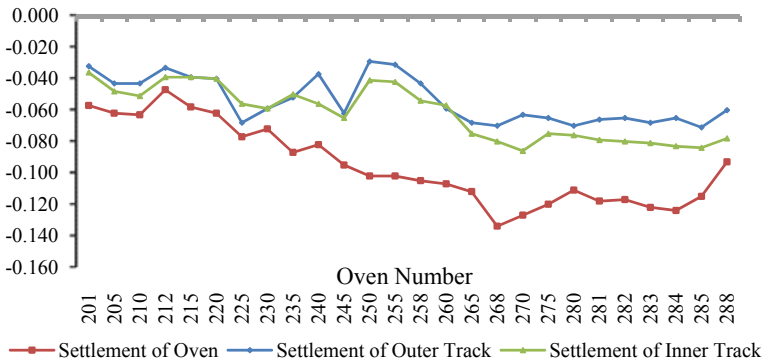
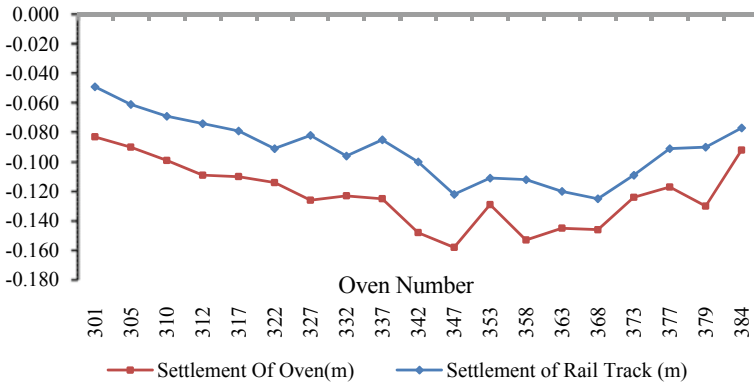**Fig. 1** Settlement of the battery and P-track (inner and outer) of Row 2

Settlement of the P-track and battery of Row 3

we proceed towards centre of the track, i.e. settlement is least in the corners while attaining its maximum value near to the centre. The maximum value taking place at the centre is due to presence of coal tower at the centre of the track, which is acting as point load and is also responsible for vibrations due to charging of coal.

3.2 Results from Numerical Analysis

Pusher Side

Figure 3 gives the plot of time versus settlement for the right and left pedestal at the load of 700 kN and 550 kN on them, respectively. Moreover, Table 5 gives the logged data from the graph of the settlement of both the pedestal. It is observed that there is differential settlement of almost 10 mm between both the pedestal, that in turn imparts twist to the outer pedestal and thereby settlement progresses. From the table, it is observed that 5–6 mm settlement is about to take place in future coming years of plant life.

Figure 4 gives the graphical representation of time vs. excess pore pressure, and for the first 30 days, incremental loading was done for generation of excess pore pressure; after that record for release of it was done. Table 6 shows the discrete values of excess pore pressure at different time interval. Table identifies that the excess PWP release is almost done to the acceptable limits.

Quencher Side

Figure 5 and Table 7 show the graphical and tabular values of the settlement of pedestal at quencher side. It can be noted that there is significant amount of settlement left to take place in future. The huge settlement predicted in future is because of the floating piles at the quencher side as the embedment length is 16 m only. Here, the piles do not rest on hard stratum instead ends at soft clay layer.
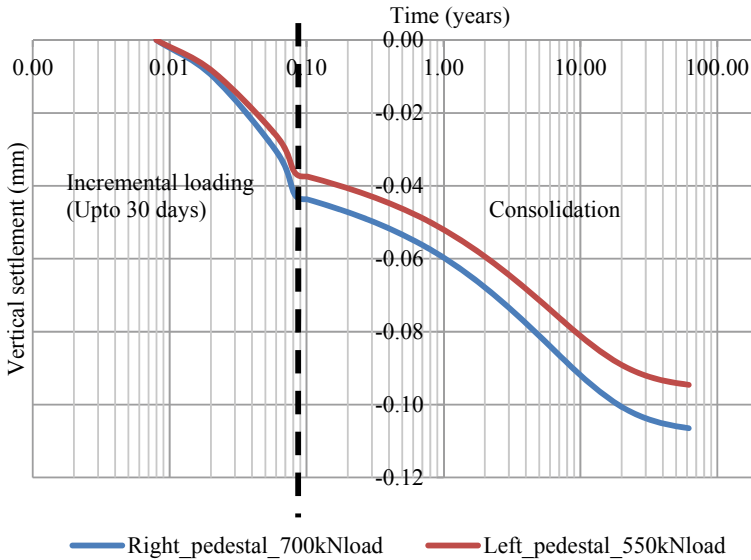
Fig. 3 Plot of time versus settlement

Table 5 Settlement of left and right pedestal with time

Time (years)	Left pedestal (mm)	Right pedestal (mm)
5.16 (~5.00)	71.80	81.70
11.70	83.20	94.30
14.40(~14.00)	85.70	96.90
24.90 (~25.00)	90.90	102.00

Given below, Fig. 6 and Table 8 provide continuous and discrete values of excess PWP with respect to time. It is observed that no significant decrease in excess PWP has taken place, and it represents that there is ample amount of PWP release to happen.

Battery Raft and Pile

It is observed from Fig. 7 and Table 9 that the settlement of battery that took place with time is less in comparison to the pusher and quencher track. The less value corresponds to the fact that piles below the battery are provided beneath the raft that minimizes the settlement by distributing the load over large area.

Figure 8 gives the plot of release of excess pore water pressure with time. It is observed that the PWP left for the release is comparatively very less as the consolidation beneath the pile–raft has almost taken place.
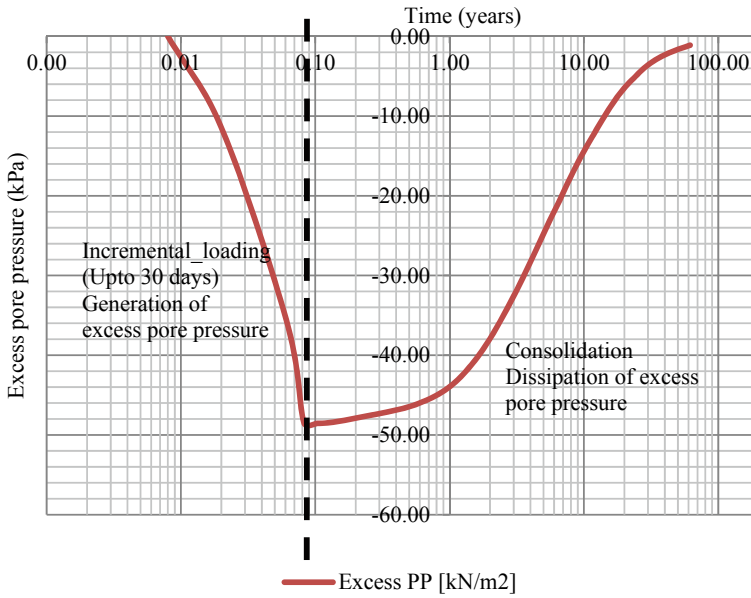
Fig. 4 Plot of time versus excess PWP

Table 6 Excess pore water pressure at time intervals

Time (years)	Excess pore pressure (kPa)
5.06(~5.00)	−24.30
11.70	−12.40
14.40(~14.00)	−9.89
24.90(~25.00)	−4.82
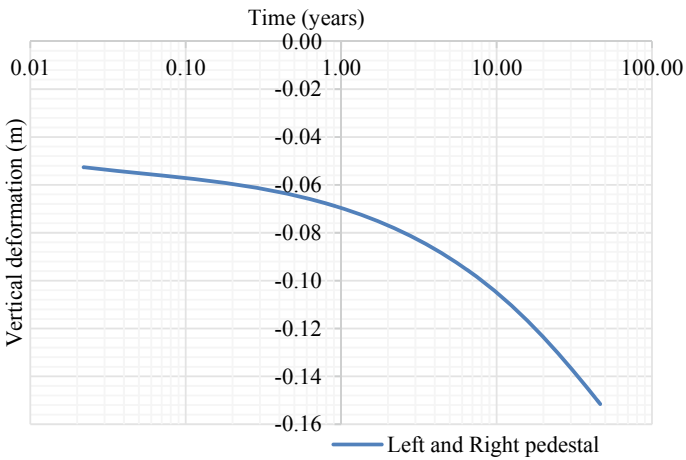
Fig. 5 Plot of time versus settlement

Table 7 Settlement of pedestal with time	Time (years)	Settlement (mm)
	5.49	92.40
	15.40	116
	23.81	129
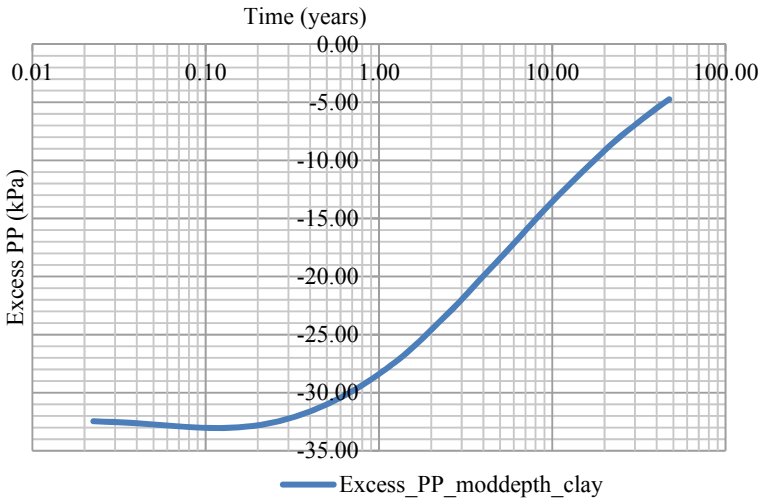
Fig. 6 Plot of time versus excess PWP

Table 8 Excess PWP at time intervals	Time (years)	Excess pore pressure (kPa)
	6	−17
	15.5	−11
	24	−7

3.3 Comparison of Actual and Predicted Settlement

Table 10 shows the comparison between the actual settlement on the site and settlement at present according to the numerical analysis. Also the settlement in the coming years is predicted. It is observed that the settlement in the field is less than the settlement noted from the numerical analysis. It was seen in the field that coal stamping tower imparts dynamic load, as dampers are provided dynamic loads were not included in the investigation. This may be the implied reason behind the variation of the settlement in the field and the settlement predicted from the numerical analysis.
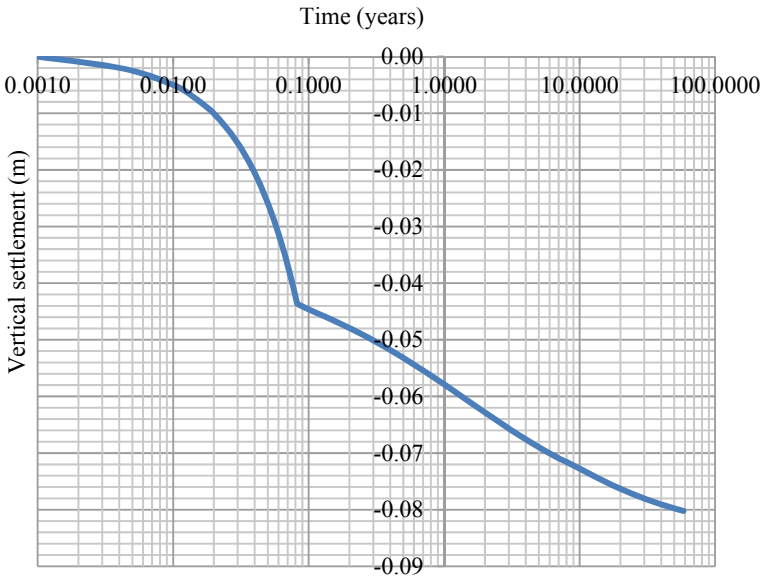
Fig. 7 Plot of time versus settlement of battery raft

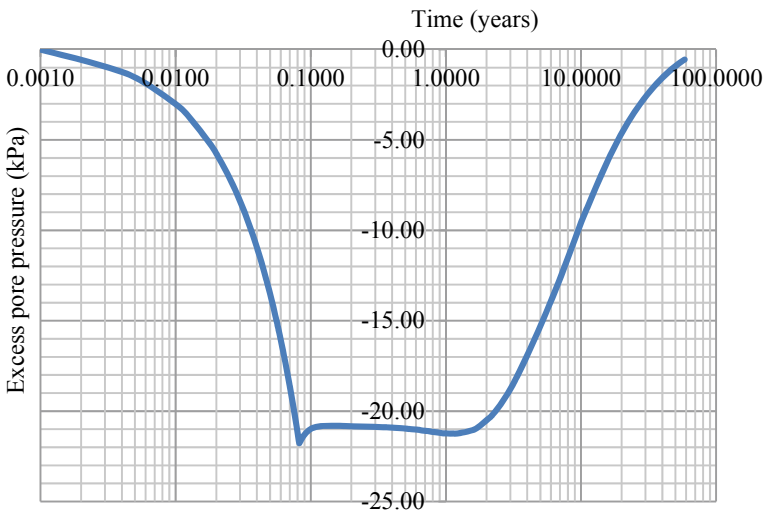| **Table 9** Settlement of raft with time	Time (years)	Settlement (mm)
	4.49	68.3
	13.70	74.4
	24.20	77.2

Fig. 8 Plot of time versus excess PWP

Table 10 Comparison of settlement based on study

	Pusher track	Quencher track	Battery
Max. avg. settlement observed	113[a]	113[b]	181[a]
Min. avg. settlement observed	21	42	73
Max. settlement predicted (14–15 years)	97	116	74.4
Max. settlement predicted after 25 years	102	129	77.2

[a]Settlement at oven number 45 at row 3
[b]Settlement at stamping post

4 Conclusions

The study is based on the data and drawings provided on the pile settlement case at Haldia. The study is based on the 2D FEM analysis of the soil strata, loading pattern and settlement. The important conclusions obtained from the results are summarized as follows:

1. It was evident from the study that the settlement at P-track has attained almost its maximum value, and it may settle 5/6 mm more in the next 10 years. The consolidation of the soil underneath the foundation has also been almost complete.
2. From the study on the Q-track, it was found that since the length of pile below Q-track is only 18 M long, the piles are floating on the underneath soft clay layer which has the maximum potential of settlement in future. As per the study, this is the most critical area where the length of piles seems inadequate to meet the settlement criteria of design.
3. The study on the coke oven battery area shows that the theoretical settlement calculated based on the design data is much smaller than the settlement observed in the field. This needs to be re-checked again after proper load calculation.
4. From the survey report to capture the settlement, it was observed that the settlement at the middle of the oven area was more than that of both ends. During the site visit, it was observed that due to huge loading coming from the coal tower which is situated at the middle of the railway track, it may be contributing towards the settlement of the railway track. The detail study needs to be done on this.
5. Going further on the settlement part, the P-track and oven area do not possess any major settlement further (as per numerical results), whereas Q-track requires major attention to tackle the future settlement potential.
6. The settlement at Q-track can be arrested to a certain limit by a long-term or a short-term solution. The long-term solution comprises of driving additional steel/FRP pipes along the existing piles of Q-track and filling them with concrete and integrating the additional pile with the existing pile cap/raft.
7. For short-term solution, it is suggested that the concrete pedestal at the P-track or Q-track is to be replaced by steel girder.

5 Future Scopes

The present study has considered the static load application for the analysis of settlement in the foundation. Due to time constraints and availability of the data from the organization, study has been done without the application of dynamic load, as data were unavailable. Numerical modelling has been done to validate the field results. Due to more settlement in the site as calculated numerically, this study needs to be extended further, in following aspects:

1. Study the settlement for the dynamic loads.
2. Extend the study for the foundation structural health.
3. Investigate the reason and solution behind the maximum settlement at the centre of the rail near coal tower.
4. Study for the design of most promising steel girder and concrete grade to overcome elastic settlement of girder during loading.
5. To study for the design of pile for pile integration on the quencher side.

References

1. Gandhi, S.R.: Observations on pile design and construction practices in India. Indian Geotech. J. **46**(1), 1–15 (2016)
2. Help manuals, Plaxis 2015
3. Henderson, G.L.: Design and Construction of Driven Pile Foundations—Lessons Learned on the Central Artery/Tunnel Project (2006)
4. Hongyuan, F.U., Xiaoyu, L.: Analysis of Settlement Induced by Dissipation of Excess Pore Water Pressure due to Piling in Soft Clay (2011)
5. Hosseini, M.A., Rayhani, M.: Evolution of pile shaft capacity over time in marine soils. Int. J. Geo-Eng. (2017)
6. Kishanrao, W.M., Prasad, A.: Numerical Modeling of Single Pile in a Two-Layered, vol. 6, pp. 105–107 (2016)

Performance Evaluation of Piles for Slope Reinforcement

Dinesh Kumar Malviya, Ganesh Kumar, and Madan Chandra Maurya

Abstract Landslides are defined as the mass movement of materials down the slope under the force of gravity. The landslides can be initiated by various causes such as rainfall, earthquake, change in ground water level and increase or decrease in shear strength of slope materials. Occurrence of landslides always causes problems to the safety and security of people and infrastructure facilities. To mitigate landslides, various slope stabilization techniques such as provision of slope drainage, soil nailing, construction of piles and retaining walls, installation of slope anchor system and biotechnical slope stabilization were employed. In this paper, studies involving pile as a reinforcing member in unstable slopes were performed experimentally using large direct shear box (LDSB) apparatus. For experimental studies, two layers of clay soil having undrained shear strength 30 kPa representing unstable soil at top and 60 kPa representing stable firm soil at bottom were prepared. Experiments were then performed with and without pile reinforcement in soil. The unstable soil slope model was reinforced with single-, two- and three-pile group system with 2D and 3D spacing to evaluate the effect of reinforcement and improvement in shear strength of unstable soil. From experimental results, it was understood that when piles installed as a reinforcing member in soil slope, the installation improves the shear strength of unstable soil, minimizes slope movement and increases the factor of safety of the slope, thus improving the safety of slope against landslide hazards.

Keywords Slope reinforcement · Pile · LDSB · Landslide

D. K. Malviya (✉) · G. Kumar
CSIR—Central Building Research Institute, Roorkee, UK 247667, India
e-mail: dineshmalviya2010@gmail.com

G. Kumar
e-mail: ganeshkumar@cbri.res.in

D. K. Malviya · M. C. Maurya
Madan Mohan Malaviya University of Technology, Gorakhpur, UP 273001, India
e-mail: mcmce@mmmut.ac.in

1   Introduction

Piles improve the stability of slope by resisting the lateral loads due to movement of unstable soil mass. Various studies in the past were performed to provide design guidelines and assessment of lateral loads on single- and multi-rowed stabilizing piles in failure soil slope [10, 11, 20–22, 26]. The lateral displacement of pile and corresponding soil element is related to the pile bending stiffness, horizontal pile–soil interaction stresses and soil modulus or stiffness, horizontal soil movement, respectively [5]. A large number of numerical studies [1, 6, 13, 23–25], centrifuge studies [3, 28, 35, 37–39] showed that effect of lateral soil movement on pile behavior varies and no standard design guidelines for slope stabilizing piles were available. Location of piles at critical slope also varied, and studies were carried out by the researchers. Hajiazizi et al. [9] suggested that pile installed at middle portion of the slope shows reasonable improvement in slope reinforcement in case of saturated sandy slope. Poulos [30] suggested that installation of stabilizing piles in row at the center of critical failure wedge improves the factor of safety of the slope. Further, through numerical modeling Cai and Ugai [4] also confirmed that maximum factor of safety for the slope increases when stabilizing piles were located in the middle portion. Rathod et al. [31], Sawant and Shukla [32] studied the effect of slope angles and embedment length of pile for a sloping ground and found that, for the increase in slope angle, the bending moment for the piles increases even for the same amount of applied lateral load. Lee et al. [27], Hassiotis et al. [11], Jeong et al. [13] and Li et al. [29] suggested that installation of piles near the crest of slope resulted in improving factor of safety. Although some case studies on successful application of stabilizing piles for slope stability improvement were reported in Australia [30], Greece [2] and Korea [33], there are some structural damages to the piles when used as slope reinforcement also mentioned in the literatures [7, 8]. In this paper, an attempt has been made to study the experimental behavior of piles for slope reinforcement through large direct shear test apparatus. Single and pile groups were installed inside the large direct shear apparatus with unstable soil at top and stable soil at bottom. The improvement in shear strength of the soil with and without pile was studied and presented.

2   Mechanism of Stabilization

Generally, piles embedded in a failure soil slope are categorized as passive piles, as in this case they are loaded by the lateral movement of surrounding soil. However in case of active piles, piles are subjected to a horizontal load at the head and transmit this load to the soil along its length (Fig. 1).

Sliding plane divides the soil profile into sliding soil and stable soil. Sliding soil is weaker (softer) than the stationary soil. Reinforcement of stabilizing piles improves the resistance to the soil movement above the sliding plane resulting in the stability

Fig. 1 Pile used to stabilize potentially unstable slope
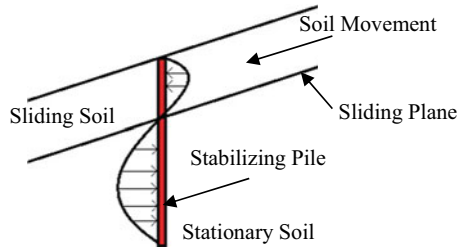
improvement. Pile design for slope reinforcement involves three main steps: (1) evaluating the shear force needed to increase the desired value of factor of safety; (2) evaluation of maximum shear force that the pile can provide to resist sliding of the potentially unstable portion of the slope; and (3) selection of the type and number of piles and the most suitable location of these piles within the piles [30, 34].When designing the stabilizing pile, estimation of lateral forces acting over will result in improvement in shear strength of unstable soil and increase in factor of safety of the slope. Ito and Matsui [20] developed a theoretical method for estimating lateral forces acting on the stabilizing piles, considering the plastic deformation of surrounding ground of pile when subjected to lateral loading.

3 Material Used

3.1 Soil

Soil sample collected from Uttarakhand was used for the laboratory investigation. The soil properties were determined as per IS 2720 (4) [16], IS 2720 (5) [17], IS 2720 (7) [18], IS 1498 [15], IS 2386 (3) [14] and presented in Table 1.

Table 1 Properties of soil

Liquid limit	42%
Plastic limit	31%
Specific gravity	2.7
Optimum moisture content	21%
Soil classification	CI-MI

3.2 Test Pile

Scaled down aluminum piles were used for the study [36]. The selected piles also verified for the boundary effects. For experimental testing, piles having 12 mm diameter with 1 mm wall thickness and 205 mm of length were selected. To simulate end bearing conditions, aluminum plate having 18 mm thickness with dimensions 298 mm × 298 mm (equivalent to grid plate dimensions) was fabricated with special threading arrangement for installing model piles. The surface of the plate also made rough to model grid plate interfacial behavior.

4 Experimental Setup

4.1 Test Setup for Static Test

All the experimental model testing was performed on large direct shear box (LDSB) apparatus at CSIR-CBRI, Roorkee. The box is 230 mm deep with a cross section of 300 mm × 300 mm. To simulate soil slope failure conditions, two layers of clayey soil having undrained shear strength 30 kPa representing unstable soil at top and 60 kPa representing stable firm soil at bottom were chosen. To compare pile reinforcement effects, initial test was carried out on the prepared layered clay profile without any reinforcement. Then, experiments were conducted with single-pile, two-pile and three-pile group with 3D spacing inside the clay bed to compare the effectiveness of the pile–slope system (Fig. 2).
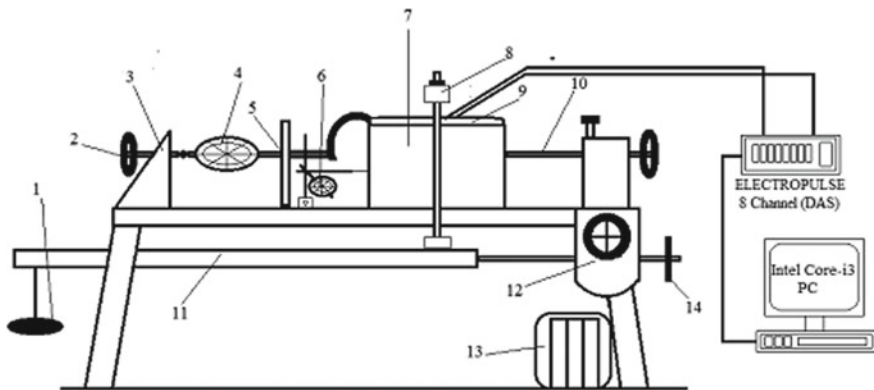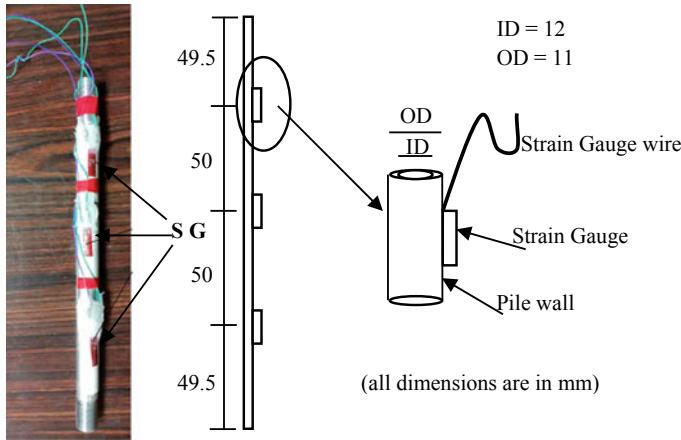

Fig. 2 Experimental setup

Fig. 3 Instrumented pile

4.2 Instrumentation and Data Acquisition System

For the single-pile experiments, the pile was instrumented with strain gauges (SG) at three locations, i.e., along the outer surface of the pile at 49.5 mm, 99.5 mm and 149.5 mm (Fig. 3), respectively, from pile top.

After mounting the strain gauges over the pile surface, gauge connections were made which are connected with DAS. To minimize surface damages, protective coating of anabond was applied over strain gauges. Then, the instrumented pile was placed in the shear box before soil filling, and the connections are checked and verified.

5 Experimental Program

Two layers of clayey soil having undrained shear strength of 30 kPa representing unstable soil at top and 60 kPa representing stable firm soil at bottom were selected for the study. The water content required to achieve the selected undrained shear strength was further verified by conducting UCC test. For experimental testing, the soil was filled inside shear box in three layers and suitably compacted to achieve desired density and required shear strength. Special care has been taken while tamping, when pile was installed for slope reinforcement test series. Tamping rod was used for compacting soil around instrumented pile, to avoid damage to the wires connecting DAQ system. The procedure is repeated for two-pile and three-pile system so that required compressive strength can be achieved. All the piles were installed with the bottom base plate placed inside the shear box simulating end bearing conditions. Unreinforced and soil with single-, two- and three-pile system is shown in Fig. 4a–d.

a) unreinforced soil   b) single pile reinforcement

c) two piles reinforcement   d) three pile reinforcement

Fig. 4 Experimental setup

Totally, four tests were performed; one test without pile reinforcement and three tests were performed using pile as reinforcement, i.e., (1) with singe pile, (2) two pile in a row with 3D spacing and (3) three-pile group with 3D spacing (group effect). Normal stress of 2.17 kPa (simulating surcharge condition) was applied using weight of 196 N (20 kg). This was selected in such a way such that it will not exceed the ultimate pile capacity. Rate of deformation of 0.125 mm/min as per IS 2720 (13) [19] guidelines suggests that the test should be conducted with minimum rate of deformation to minimize generation of pore water pressure in saturated conditions.

The entire test was performed with same normal stress with same rate of deformation. Dial gauge readings and corresponding proving ring reading were taken to compute shear strength. Strain gauge readings were also observed for the single instrumented pile using the DAS described above.

6   Results and Discussion

Resisting forces in vertically embedded stabilizing piles come mainly from the response of piles in terms of their shear and bending resistances [12]. In this study,
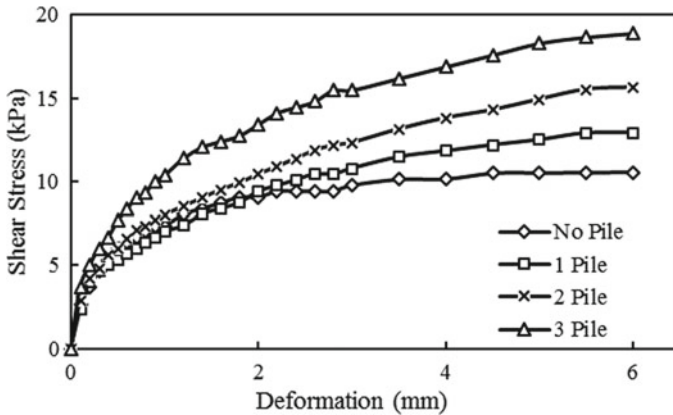
Fig. 5 Large direct shear box apparatus results

pile response to loading condition was determined by the stress–strain relationship under shear deformation using LDSB apparatus.

Shear deformation of failure soil slope with (single and group piles) and without pile reinforcement is shown in Fig. 5. Comparatively, slope reinforced with pile performs better than unreinforced soil and strength of soil increases with the increase in number of piles. This is clearly evident from Fig. 5. Installation of end bearing pile creates resistance against slope movement, creates passive pressure on its surface and minimizes slope deformation. This increases as number of pile increases. Based on experimental studies in Fig. 5, three-pile groups provided the highest resistance of 20 kPa, because the piles are installed with triangular pattern which form passive wedge slope and increases the resistance inside the soil against deformation.

Poulos [30] summarized pile behavior in three modes based on the location of sliding planes with respect to pile length: (1) flow mode (sliding plane at uppermost pile length); (2) intermediate mode (sliding plane at middle pile length); (3) short pile mode (sliding plane at bottom pile length) and suggested that the greatest resistance is provided by the stabilizing piles during intermediated mode of soil failure. He observed that for the intermediate mode, larger moments were developed at below and above the slide zone and highest in top zone (Figs. 6 and 7).

The observed experimental test results also follows intermediate mode of failure. The results obtained from the instrumented piles shows that developed larger moments at top and bottom portion of the sliding zone, which is in agreement with the Poulos [30] results.
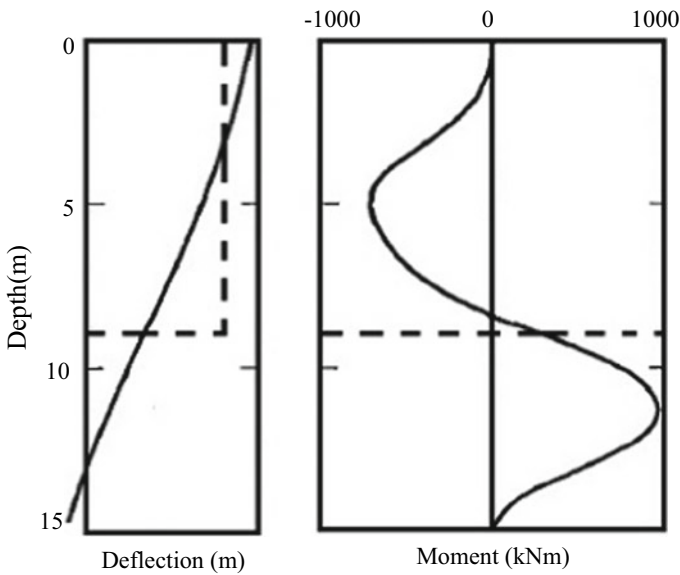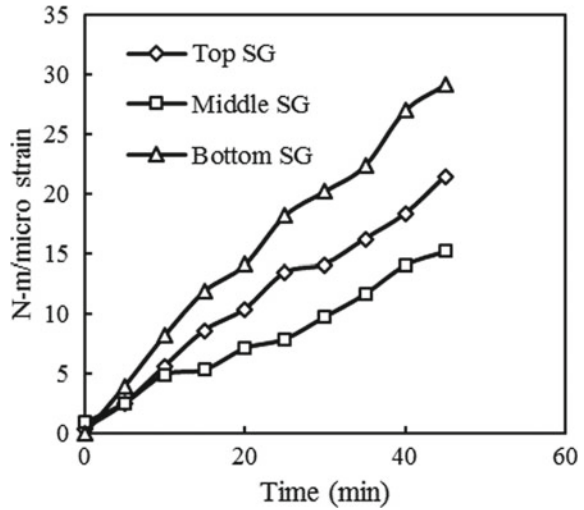
Fig. 6 Instrumented pile results

Fig. 7 Intermediate mode [30]

7 Conclusion

An experimental approach was adopted for analyzing piles for stabilization of failure soil slope. Here, pile response to loading condition was determined by the stress–strain relationship under applied shear deformation. The performance of piles used for

the stabilization of failure soil slope was examined though the large direct shear box apparatus, and pile–soil interaction was observed by performing an experiment with the single instrumented pile. It was found that increasing number of pile improved the strength of soil. However, a detailed study regarding performance assessment of pile in slope is required for improving slope stability.

References

1. Al-abboodi, I., Sabbagh, T.T.: Numerical modelling of passively loaded pile groups. Geotech. Geol. Eng. 1–15 (2018)
2. Anagnostopoulos, C., Georgiadis, K.: Stabilization of a highway with piles in a landslide area. In: 9th International Symposium on Landslides, Rio de Janerio, Brazil, pp. 1697–1700 (2004)
3. Askarinejad, A., Springman, S.M.: Centrifuge modelling of the effects of vegetation on the response of a silty sand slope subjected to rainfall. In: Computer Methods and Recent Advances in Geomechanics, pp. 1339–1344 (2015)
4. Cai, F., Ugai, K.: Numerical analysis of the stability of a slope reinforced with piles. Soils Foundation **40**(1), 73–84 (2000)
5. Chen, L.T., Poulos, H.G.: Piles subjected to lateral soil movements. J. Geotech. Geoenviron. Eng. **123**(9), 802–811 (1997)
6. Ellis, E.A., Durrani, I.K., Reddish, D.J.: Numerical modelling of discrete pile rows for slope stability and generic guidance for design. Geotechnique **60**(3), 185–195 (2010)
7. Finno, R.J., Lawrence, S.A., Allawh, N.F., Harahap, I.S.: Analysis of performance of pile groups adjacent to deep excavation. J. Geotech. Eng. ASCE **117**(6), 934–955 (1991)
8. Hagerty, D.J., Peck, R.B.: Heave and lateral movements due to pile driving. J. Soil Mech. Foundation Division, ASCE **11**, 1513–1532 (1971)
9. Hajiazizi, M., Bavali, M., Fakhimi, A.: Numerical and experimental study of the optimal location of concrete piles in a saturated sandy slope. Int. J. Civil Eng. 1–9 (2017)
10. Hassiotis, S., Chameau, J.L.: Stabilization of slopes using piles. Joint Highway Research Project JHRP 84-8, Purdue University (1984)
11. Hassiotis, S., Chameau, J.L., Gunaratne, M.: Design methods for stabilization of slopes with piles. J. Geotech. Geoenviron. Eng. **123**(4), 314–323 (1997)
12. Hazarika, H., Mujah, D., Watanabe, N., Ahmad, F., Yasufuku, N., Omine, K.: Fundamental study on Earth reinforcing effect using small diameter model steel pile. In: 13th International Summer Symposium, Japan, pp. 207–210 (2011)
13. Ho, I.: Numerical study of slope stabilization piles in undrained clayey slopes with a weak thin layer. Int. J. Geomech. **15**(5), 1–12 (2012). Jeong, S., Kim, B., Won, J., Lee, J.: Uncoupled analysis of stabilizing piles in weathered slopes. Comput. Geotech. **30**, 671–682 (2003)
14. IS: 2386 Part 3.: Indian Standards Code of Practice for Methods of tests for aggregates for concrete. Specific gravity, Density, Voids, Absorption and Bulking. BIS, New Delhi (1963)
15. IS 1498.: Indian Standards Code of Practice for Classification and identification of soils for general engineering purposes. BIS, New Delhi (1970)
16. IS 2720 Part 4.: Indian Standards Code of Practice for Methods of test for soils. Grain size analysis. BIS New Delhi (1985)
17. IS 2720 Part 5.: Indian Standards Code of Practice for Methods of test for soils. Determination of liquid and plastic limit. BIS, New Delhi (1985)
18. IS 2720 Part 7.: Indian Standards Code of Practice for Methods of test for soils. Determination of water content-dry density relation using light compaction. BIS, New Delhi (1985)
19. IS 2720 Part 13.: Indian Standards Code of Practice for Methods of test for soils. Direct shear test. BIS, New Delhi (1985)

20. Ito, T., Matsui, T.: Methods to estimate lateral force acting on stabilizing piles. Soils Foundation **15**(4), 43–59 (1975)
21. Ito, T., Matsui, T., Hing, W.P.: Design methods for stabilizing piles against landslide-one row of piles. Soils Foundation **21**, 21–37 (1981)
22. Ito, T., Matsui, T., Hing, W.P.: Extended design methods for multi-row stabilizing piles against landslide. Soils Foundation **22**, 1–13 (1982)
23. Kahyaoglu, M.R., Imancli, G., Onal, O., Kayalar, A.S.: Numerical analyses of piles subjected to lateral soil movement. KSCE J. Civil Eng. **16**(4), 562–570 (2012)
24. Kanagasabai, G., Smethrust, J.A., Powrie, W.: Three-dimensional numerical modelling of discrete piles used to stabilize landslides. Can. Geotech. J. **48**, 1393–1444 (2011)
25. Kim, Y., Jeong, S.: Analysis of soil resistance on laterally loaded piles based on 3D soil pile interaction. Comput. Geotech. **38**, 248–257 (2011)
26. Laora, R.D., Maiorano, R.M.S., Avesra, S.: Ultimate lateral load of slope-stabilizing piles. Geotech. Lett. **7**, 237–244 (2017)
27. Lee, C.Y., Hull, T.S., Poulos, H.G.: Simplified pile-slope stability analysis. Comput. Geotech. **17**, 1–16 (1995)
28. Lei, G., Wu, W.: Centrifuge modelling of slope stabilized by piles. In: 19th International Conference on Soil Mechanics and Geotechnical Engineering, Seoul, pp. 3505–3508 (2017)
29. Li, X., Pei, X., Gutierrez, M.: Optimal location of piles in slope stabilization by limit analysis. Acta Geotech. **7**, 253–259 (2012)
30. Poulos, H.G.: Design of reinforcing piles to increase slope stability. Can. Geotech. J. **32**, 808–818 (1995)
31. Rathod, D., Muthukkumaran, K., Sitharam, T.G.: Development of non-dimensional p-y curves for laterally loaded piles in sloping ground. Indian Geotech. J. **47**(1), 47–56 (2016)
32. Sawant, V.A., Shukla, S.K.: Three-dimensional finite element analysis of laterally loaded piles in sloping ground. Indian Geotech. J. **42**(4), 278–286 (2012)
33. Song, Y.S., Hong, W.P., Woo, K.S.: Behaviour and analysis of stabilizing piles installed in a cut slope during heavy rainfall. Eng. Geol. **129**, 56–67 (2012)
34. Viggiani, C.: Ultimate lateral load on piles used to stabilize landslide. In: 10th International Conference on Soil Mechanics and Foundation Engineering, Stockholm, vol. 3, pp. 555–560 (1981)
35. Viswanadham, B.V.S., Mahajan, R.R.: Centrifuge model tests on geotextile-reinforced slopes. Geosynthetics Int. **14**(6), 365–379 (2007)
36. Wood, D.M.: Geotechnical Modelling, 1st edn. Spon Press Taylor & Francis, New York (2004)
37. Yoon, B.S.: Centrifuge modelling of discrete pile rows to stabilize slopes. Ph. D. Thesis, University of Nottingham (2008)
38. Yoon, B.S., Ellis, E.A.: Centrifuge modelling of slope stabilization using a discrete pile row. Geomech. Geoeng. **4**(2), 103–108 (2009)
39. Yu-zhen, Y., Li-jun, D., Xun, S., He, L.: Centrifuge modeling of dynamic behavior of pile-reinforced slopes during earthquakes. J. Central South Univ. Technol. **17**(5), 1070–1078 (2010)

Stability Analysis of Soil Slopes Subjected to Foundation Loads During Earthquakes

Sukanta Das and B. K. Maheshwari

Abstract The stability of slopes subjected to foundations loads near the top of the slope has been investigated in the present study. The *c-φ* soil slope with different width and embedment depth of foundation has been considered here. In the present study, the building load is considered as a surcharge load on the slopes. Strength reduction method has been adopted to investigate the variation of factor of safety (FOS) of slope against the different parameters of the imposed load and slope angle. The earthquake force has been considered as fixed body force within the soil mass. From this study, the FS decreases with the increase of building or foundation loads, and at a certain distance from the edge of the slope, the FOS remained constant. The improvement of FOS has been observed with the increase of embedment depth of footing for all surcharge loads. The rapid reduction of FOS has been noted when foundation load is increased on slopes in both static and seismic case.

Keywords Slope Stability · Foundation loads · Strength reduction method · Setback distance · Earthquakes

1 Introduction

The design of shallow foundations in hill slopes is a challenging task for geotechnical engineers since ancient days. Recently, due to lack of land or increase in population, the construction of building in hilly areas is increasing. Several researchers have reported that the bearing capacity decreases with the increase of slope angle for both static and seismic conditions. The slopes get more unstable which are marginally stable before earthquake and the existing or newly constructed building loads may create a vulnerable situation. Last few earthquakes, for example, 2005 Kashmir earthquake and 2011 Sikkim earthquake, have shown the vulnerability of commercial buildings in slopes and hilly areas. Therefore, stability of the existing slopes should be checked before designing any structure on slopes.

It is expected that when a footing placed at the crest of the slope, the stability of the slope should be reduced. However, it depends on edge distance of footing, embedment depth and imposed loads on footing. Meyerhof [1] proposed an analytical formula for estimation of bearing capacity of footing on the face and near the top of the slope. Several researchers performed experimental and theoretical investigation to determine bearing capacity of footing on slopes [2–8]. In most of the study, it has been observed that the bearing capacity decreases with the increase in the slope angle. However, with the increase of edge distance (3–5 times of footing width) of footing from crest of the slope, the bearing capacity is not dependent on slope angle. Keskin and Laman [8] performed small-scale experimental test and numerical analysis to determine the bearing capacity of footing on slopes. They also checked stability of that slope after applying ultimate load on the footing. Numerical model study has been also carried by many researchers for the evolution of bearing capacity factors of footing on slopes [9–13]. Archaryya and Dey [13] studied bearing capacity of footing near the top of the soil using finite element method and compared with past experimental results. Raj et al. [14, 15] investigated the stability of the slope under the building loads. They reported that stability of slopes increases with the increase of footing width and its distance from the slope. However, they considered footing on the face of the slope. Baah-Frempong and Shukla [16] studied the stability of cohesionless soil slope supporting an embedded strip footing. This study is limited on static and sandy type of soil.

In the present study, the stability of the c-ϕ soil slope subjected to strip footing loads has been studied for both static and seismic conditions. Different influence factor on stability of slopes has been studied such as loading factor [$q/\gamma H$, where q = load intensity (kN/m^2), γ = unit weight (kN/m^3) and H = height of slope (m)], embedment depth ratio [D_f/B, where D_f = depth of footing from ground level, B = footing width] and setback distance [D_e/B, where D_e = distance of footing edge from crest of slope, B = footing width]. Duncan [17] reported the shear strength of soil must be divided by factor of safety (FOS) to bring the slopes on the verge of failure point which is commonly known as strength reduction method (SRM). A finite element limit analysis (FELA) uses optimization techniques to directly compute the upper or lower bound plastic collapse load (or limit load) for a mechanical system rather than time stepping to a collapse load, as might be undertaken with conventional nonlinear finite element techniques [18].

2 Numerical Modeling

In the present study, two homogeneous soil slopes (slope angle, β 20° and 30°) under the foundations loads have been studied. The soil properties have been taken from Panigrahi et al. [19] where the site is located at hilly terrain within the Mizoram state as shown in Table 1. The strip footing width (B = 1, 3 and 5 m) at an edge distance (D_e = 0, 3, 6, 9, 12, 15, 18 and 21 m) from the crest of the slope has been considered. The footing embedment depth (D_f = 0.5, 1 and 2 m) effect on stability of slopes is

Table 1 Basic soil properties (after Panigrahi et al. [20])

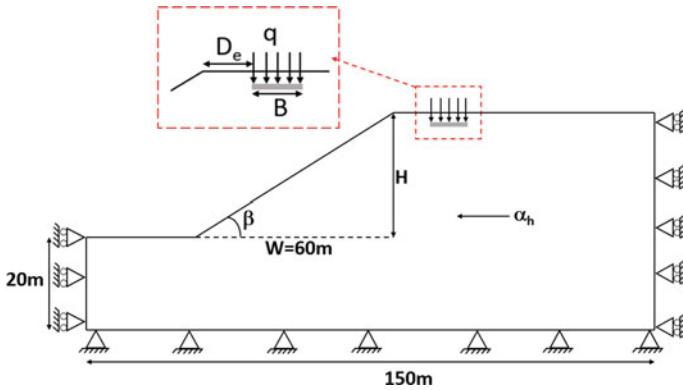| Descriptions	Values
Unit weight, γ (kN/m^3)	20
Poisson's ratio, μ	0.3
Cohesions, c (kPa)	15
Angle of internal friction, ϕ (°)	30
Young's modulus, E (MPa)	250

Fig. 1 Schematic diagram of slope subjected to footing loads

also studied. A schematic diagram of slope subjected to footing loads is presented in Fig. 1.

The 2D finite element limit analysis (FELA) based on strength reduction method (SRM) has been adopted to check the stability of slopes under the footing loads. In SRM methods, the soil strength reduced by a factor and at verge of failure factors are represented by strength reduction factor or factor of safety of the slope [20–22]. An elastoplastic constitutive model based on Mohr–Coulomb failure criterion and following associated flow rule has been used for soil modeling in FELA. The strip footing modeled as a steel plate with Young's modulus (E) compared to soil. A uniformly distributed load (UDL) has been applied to represent the super structure loads. The boundary conditions are considered in such a way that the bottom is fixed against both (horizontal and vertical) directions. While vertical edge is fixed laterally (horizontal) and free to move vertically. The model dimensions have been chosen by several trial, where the effect of boundary condition is insignificant. The sensitivity analysis has been performed for optimum (number of element at which FOS are not changing much) meshing, and approximately 8000 elements are sufficient for the present study. The 15-noded triangular plane strain elements have been considered. Loukidis and Salgado [23, 24] reported that the 15-node elements have the fastest convergence with adaptive free meshing where it yields particular location of failure slip surface in Optum G2. In this, meshing additivity system needs lesser number

of elements to produce accurate results. A fixed body force within the soil mass has been considered in the present study.

3   Results and Discussions

In the present study, using FELA method the stability of slopes in terms of factor of safety (FOS) with different condition of footing has been studied. Keskin and Laman [8] performed experimental test for bearing capacity of footing on slopes and checked FOS by limit equilibrium method. For the FELA and keeping same parameters, a comparison has been shown in Table 2. It can be observed that there is a good agreement between the test results and the present study. The maximum value of q considered in the analysis is 800 kPa.

A strip footing located at the top of the slope (20° and 30°) for different footing width and load factor has been analyzed. It is clear from Fig. 2a, b that with the increase of footing load, factor of safety (FOS) of the slope reduced for both static and seismic cases. At 30° slope, the load carrying capacity quite less compared to 20° slope. It can be observed that for small surcharge, i.e., up to load factor 0.12 there is not much effect of footing width on FOS. This phenomenon is known as global (overall stability of slope) and local failure (bearing capacity of footing) problem as explained by Paul and Kumar [25]. In local failure problem, when footing width increases the bearing FOS increase. Therefore, the FOS of the slope also increases with the footing width. A total displacement of slopes for loading factor 1 for 20° slopes has been presented in Fig. 3 (*i–iii*). In Fig. 3 (*iii*) for footing width 5 m, the deformation is more. As footing width increases, the contact pressure also increases and deformation increases as loading intensity is fixed (q in kN/m^2).

With the increase of setback distance, the effect of slope angle on bearing capacity of footing and FOS of slopes gets decreases. At a certain setback distance of the bearing capacity of footing is constant or not influenced by slope angle, and this distance is called as critical setback distance. For bearing capacity problem, the critical setback distance is 2–5 times of footing width for static case and 3–9 times of footing width for seismic case [13, 26]. The same trend has been found in this study but different critical setback distance.

Table 2 Comparison of bearing capacity, q_u (kPa) and FOS

D_f/B	Qu (kPa)		FOS at 60 kPa load	
	(K&L)	Present study	K&L	Present study
0	31.50	33.61	1	1.03
1	56.70	57.33	1.86	1.84

Note Results of footing located at different locations from the slope crest ($\beta = 30°$, $D_r = 65\%$, $B = 70$ mm), K&L means Keskin and Laman [8]
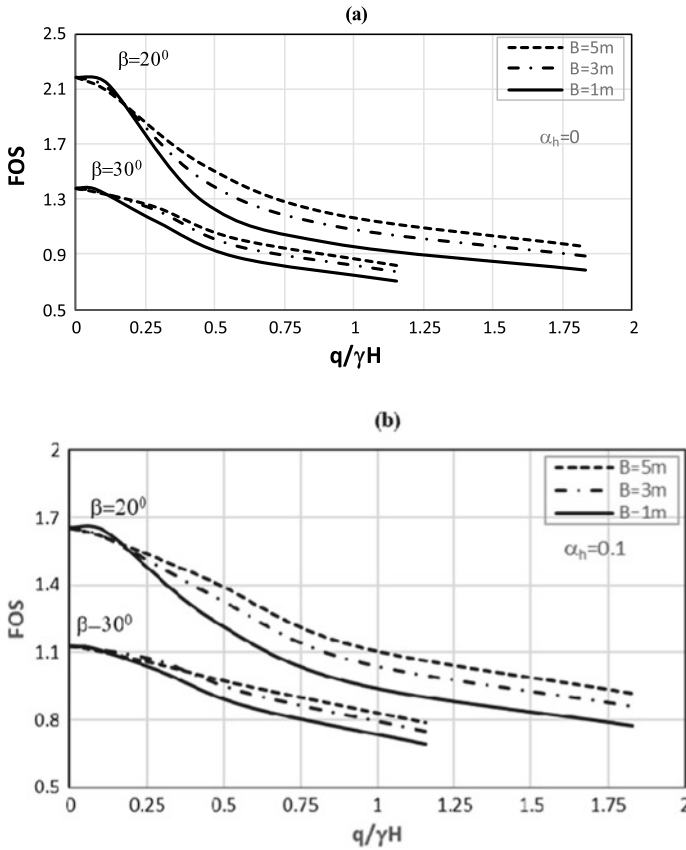
Fig. 2 Variation of FOS versus loading factor for different slope angle for $D_e = 3$ m, $D_f = 0.5$ m: **a** static case and **b** seismic case

From Fig. 4a, b, the critical setback distance is found two times of footing width for static case and 2.5 times of footing width for seismic case for 20° slopes. For 30° slopes, 5 and 5.5 times of the footing width, respectively. An overall critical setback distance can be identified from this study and past research based on bearing capacity problems. For seismic cases, the critical distance may vary for different seismic coefficient. Therefore, at 20° slope after setback distance 2–2.5 times of footing width goes into a local failure problem. Similarly, 30° slope after 5–5.5 times of the footings width the failure get transfer from global failure to local failure (Table 3).

The effect embedment depth (D_f) on stability of slopes has been presented in Fig. 5a, b. The FOS or stability of the slope increases with the increase of embedment ratio for all cases as shown in Fig. 5. The shear zones increase with the increase of embedment ratio, and the failure shape gets modified as presented in Fig. 6.
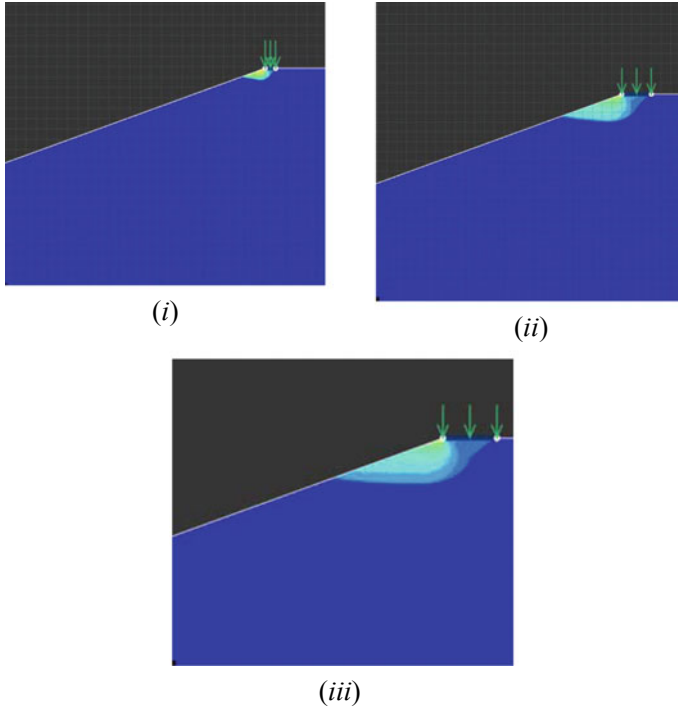
(i)

(ii)

(iii)

Fig. 3 Slope failure pattern for different footing with for $\beta = 20°$, $q = 300$ kPa, $\alpha_h = 0$ and $D_f = 0$ m: (i) $B = 1$ m (ii) $B = 3$ m and (iii) $B = 5$ m

4   Conclusions

A series of numerical analyses has been performed to check the stability of the slope subjected to foundation loading for static and seismic condition. The primary focus of the present study is to identify global and local failure problem when footing placed near the top of slope and influence of other effects that are footing loads, embedment ratio, footing width. From the above study, the following conclusions can be drawn:

1. For a given slope angle, after a certain footing load the FOS gets reduced drastically. This threshold load indicates the change of global to local failure problem. However, with the increase of slope angle the threshold load decreases.
2. Within the local failure problem, the FOS increases with the increase in footing width but within global failure problem, the effect of footing width on FOS is insignificant.
3. At a particular embedment and slope angle, the FOS of the slope is remained constant after certain setback distance. Moreover, at 20° slope, the FOS of the slope is remained constant after setback distance 2 and 2.5 times of footing width in static and seismic cases. Similarly, for 30° slope after 5 and 6 times of
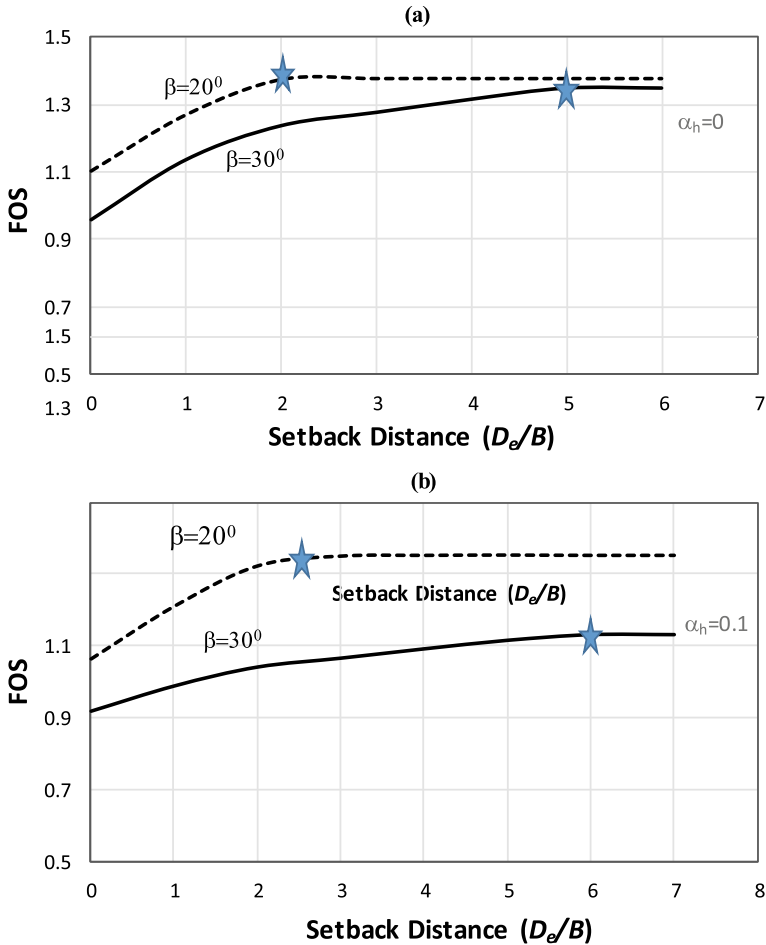
Fig. 4 Variation of FOS versus setback distance (D_e/B) for different slope angle for $q = 300$ kPa, $D_f = 0$ m and $B = 3$ m: **a** static case and **b** seismic case

Table 3 Critical setback distance (m)

	Slope angle 20°	Slope angle 30°
Static	2	5
Seismic	2.5	6

the footings width, the FOS of the slope remains constant in static and seismic cases.

4. The FOS increases with the increase in embedment depth of footing, but initially the rate of increase of FOS is higher for a constant slope angle, footing width
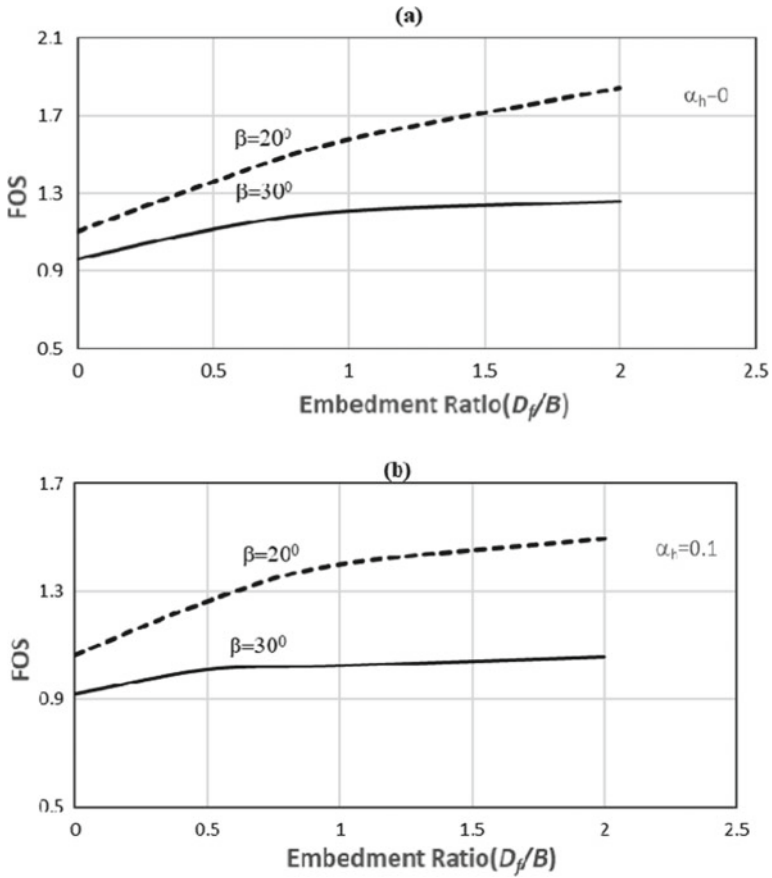
Fig. 5 Variation of FOS versus embedment ratio (D_f/B) for different slope angle for $q = 300$ kPa, $D_e = 0$ m and $B = 3$ m: **a** static case and **b** seismic case

and load. In both static and seismic cases, with the increases of slope angle the FOS decreases and the trend remained same.

5. The influence zone increased with the increases of footing width as well as embedment depth in conditions. Therefore, irrespective of slope angle and seismic conditions, the FOS is directly proportional to the footing width and embedment depth of footing.
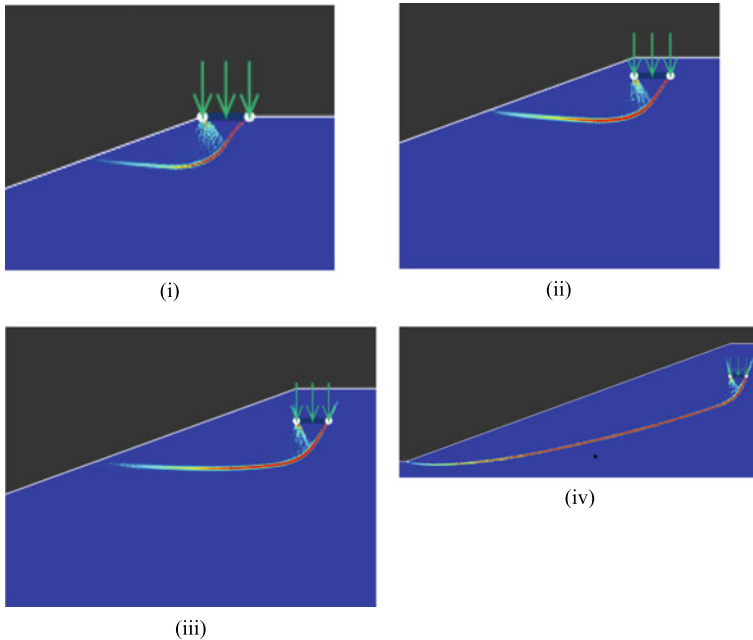
Fig. 6 Failure pattern with different embedment ratio for $\beta = 20°$, $q = 300$ kPa, $\alpha_h = 0$ and $B = 3$ m, (i) $D_f = 0$ m, (ii) $D_f = 0.5$ m, (iii) $D_f = 1$ m and (iv) $D_f = 2$ m

References

1. Meyerhof, G.G.: The ultimate bearing capacity of foundations on slopes. Proc. IV Int. Conf. Soil Mech. Found. Eng. England **1**(1), 384–387 (1957)
2. Buhan, P.D., Garnier, D.: Three dimensional bearing capacity analysis of a foundation near a slope. Soils Found. **38**(3), 153–163 (1998)
3. Castelli, F., Motta, E.: Bearing capacity of strip footings near slopes. Geotech. Geol. Eng. **28**(2), 187–198 (2010)
4. Graham, J., Andrews, M., Shields, D.H.: Stress characteristics for shallow footings in cohesionless slopes. Can. Geotech. J. **25**(2), 238–249 (1988)
5. Narita, K., Yamaguchi, H.: Bearing capacity analysis of foundations on slopes by use of log-spiral sliding surfaces. Soils Found. **30**(3), 144–152 (1990)
6. Saran, S., Sud, V.K., Handa, S.C.: Bearing capacity of footings adjacent to slopes. J. Geotech. Eng. **115**(4), 553–573 (1989)
7. Shields, D.H., Scott, J.D., Bauer, G.E., Deschemes, J.H., Barsvary, A.K.: Bearing capacity of foundations near slopes. In: Proceedings of the 9th International Conference on Soil Mechanics and Foundation Engineering, Tokyo, pp. 715–20 (1977)
8. Keskin, M.S., Laman, M.: Model studies of bearing capacity of strip footing on sand slope. KSCE J. Civil Eng. **17**(4), 699–711 (2012)
9. Georgiadis, K.: Undrained bearing capacity of strip footings on slopes. J. Geotech. Eng. **136**(5), 677–685 (2010)
10. Zhou, H., Zheng, G., Yin, X., Jia, R., Yang, X.: The bearing capacity and failure mechanism of a vertically loaded strip footing placed on the top of slopes. Comput. Geotech. **94**, 12–21 (2018)

11. Raj, D., Singh, Y., Shukla, S. K.: Seismic bearing capacity of strip foundation embedded in c-φ soil slope. Int. J. Geomech. **18**(7) (2018)
12. Gill, K.S., Shukla, S.K., Jha, J.N., Choudhary, A.K.: Experimental and numerical studies of loaded strip footing resting on reinforced fly ash slope. Geosynth. Int. **20**(1), 13–25 (2013)
13. Acharyya, R., Dey, A.: Finite element investigation of the bearing capacity of square footings resting on sloping ground. INAE Lett. **2**(3), 97–105 (2017)
14. Raj, D., Singh, Y.: Effect of building loads on stability of hill slopes. In: Geo-Chicago: Sustainability, Energy, and the Geoenvironment, ASCE GSP-271, Chicago, Illinois (2016)
15. Raj, D., Singh, Y., Kaynia, A.: Behavior of slopes under multiple adjacent footings and buildings. Int. J. Geomech. **18**(7), 101–113 (2018)
16. Baah-Frempong, E., Shukla, S.K.: Stability analysis and design charts for a sandy soil slope supporting an embedded strip footing. Int. J. Geo-Engineering **9**(13) (2018)
17. Duncan, J.M.: State of the art: limit equilibrium and finite-element analysis of slopes. J. Geotech. Geoenviron. Eng., ASCE **122**(7), 577–96 (1996)
18. Krabbenhoft, K., Lymain, A.V., Krabbenhoft, J.: OptumG2: theory. In: Optum Computational Engineering (2016)
19. Panigrahi, R.K., Guruvittal, U.K., Prasad, P.S., Mathur, S., Gupta, P.: Investigation and design for restoration of hill slope in Mizoram. Indian Geotech. J. **41**(4), 215–225 (2011)
20. Matsui, T., San, K.C.: Finite element slope stability analysis by shear strength reduction technique. Soils Found. **32**(1), 59–70 (1992)
21. Griffiths, D.V., Lane, P.A.: Slope stability analysis by finite elements. Geotechnique **49**(3), 387–403 (1999)
22. Zheng, H., Tham, L. G., Liu. D.: On two definitions of the factor of safety commonly used in the finite element slope stability analysis. Comput. Geotech. **33**(3), 188–195 (2006)
23. Loukidis, D., Salgado, R.: Bearing capacity of strip and circular footings in sand using finite elements. Comput. Geotech. **36**(5), 871–879 (2009)
24. OptumG2: Comprehensive finite element program for geotechnical stability and 435 deformation analysis, version v2.2017.03.30 (2017)
25. . Paul, D.K., Kumar, S.: Stability analysis of slope with building loads. Soil Dyn. Earthquake Eng. **16**(6), 395–405 (1997)
26. Shukla, R.P., Jakka, R.S.: Critical setback distance for a footing resting on slopes under seismic loading. Geomech. Eng. **15**(6) (2018)

Probabilistic and Deterministic Analysis of Lungchok Landslide, South Sikkim, India

Neharika Rao Ganta and Neelima Satyam

Abstract The northern part of INDIA is most vulnerable in failure of slopes due to hill region with complex geology, high-intensity rainfall and frequently occurrence of earthquakes. The stability of slopes has traditionally analyzed using deterministic methods. But uncertainty plays major role in geotechnical engineering. the probabilistic characterization of uncertainties in input variables for the assessment of slope stability is very helpful. In this paper, the safety of slope using deterministic and probabilistic methods under static and pseudo-static loads is carried for Lungchok landslide which is in south district of Sikkim state, India. The Factor of safety calculated by deterministic cannot represent the stability of slope exactly as it is limited to the single value of parameters. The stability of slope is independent of single soil parameter but dependent on random process with distribution of soil parameters. Rather than the conventional factor of safety against the sliding failure the probability of sliding failure is most useful. The stability of slope is analyzed using two approaches deterministic and probabilistic analysis under the effects of static and pseudo static forces. The deterministic approach with Morgenstern Price limit equilibrium method and the probabilistic approach with Monte Carlo simulation have been performed for the stability analysis of Lungchok landslide using Geo-Studio Software. The dependence and efficiency of the probabilistic strategies in the investigation of slope stability was highlighted in this paper.

Keywords Slope stability · Pseudo static analysis · Monte Carlo simulation

N. R. Ganta (✉)
International Institute of Information Technology, Hyderabad 500032, India
e-mail: shinyneharika65@gmail.com

N. Satyam
Indian Institute of Technology, Indore 452020, India

1   Introduction

Stability of slopes should be safe by from failure either by collapsing or sliding. The frequency of failures is increasing day by day due to many human inventions especially in hilly areas. The northern part of INDIA is more vulnerable in slope failures due to hill region with frequently occurrence of earthquakes and rainfall. The instability of slope can be occurred due too many reasons which may damage the slope either slowly or rapidly. The better understanding of behavior of the slope helps in proper stabilization.

In general, the stability of slopes is adopted with strong assumptions analyzed using deterministic and probabilistic approaches. In deterministic three approaches were involved analytical approach, limit equilibrium methods and continuum method of slices applied with finite element methods [1] with single-value input parameters. The probabilistic analysis differs with deterministic methods mainly due to input random variables of each parameter depend on many input variables. In probabilistic approach, three approaches were used First-order second moment, point estimates and Monte Carlo simulation. The Monte Carlo simulation is applied among other probabilistic analyses because of accurate probabilistic method with simple analysis like limit equilibrium analysis that can carry thousands of deterministic analyses depending upon the number of variables in the model in relatively short period of time [2]. The output from probability analysis helps to assess the probability of failure and establish the design process perfectly.

This paper compares the deterministic and probabilistic stability analysis of landslide under static and pseudo-static forces. The landslide selected for the analysis is failed during 2011 Sikkim–Nepal earthquake trigged with moment magnitude of 6.9, located near Lungchok village south district of Sikkim state, India. The Sikkim is affected with frequent landslides every year due to the two main primary effects rainfall and earthquake. In the monsoon season due to heavy rains, the pore pressures increase gradually and reduce the effective normal stresses, and these failures are intensified more during earthquakes [3]. The landslide is investigated for fully saturated and dry conditions representing arid and monsoon seasons for static and pseudo-static effect. The factor of safety of the slope from deterministic approach is employed using Morgenstern price method, and probabilistic approach is studied using Monte Carlo simulation. The current study deals with influence of single and variability of soil parameters of the Lungchok landslide determined using both approaches under static and seismic loads.

2   Study Area

The slope considered for the analysis is in south district of Sikkim state situated in between the Lungchok and Singtam villages along the roadside. The direction of slope is toward south and located at latitude and longitude of 27° 08′ 01.88″

North-88° 23′ 41.46″ East with elevation of 1686 m (Fig. 1). Determination of basic geometry of the slope for the analysis is done using Google Earth Pro [4]. The slope geometry with boundary conditions considered for the analysis (see Fig. 2). The boundary conditions applied in *X*-direction is fixed in *x* and *y* and along *Y*-direction *x* is fixed. The slope is newly activated slope observed during September 18, 2011, Sikkim earthquake. The frequency of earthquakes observed was high in the Sikkim state due to the distribution of faults, lineaments, main central thrust and main boundary thrust with seismic zone IV as per IS (1893–2016). The Lungchok landslide is 4.02 km from main central thrust and 73 kms from epicenter of 2011 Sikkim earthquake.

The frequent landslides in south district were observed due to the association of Daling group [5]. The thin phyllites and slaty half-schistose rocks are observed only in the south district when compared with other districts of the Sikkim state [6]. The south district is accumulated with fractured and weathered rocks [7].

Fig. 1 Aerial photograph of the study area (after 2011 Sikkim earthquake)
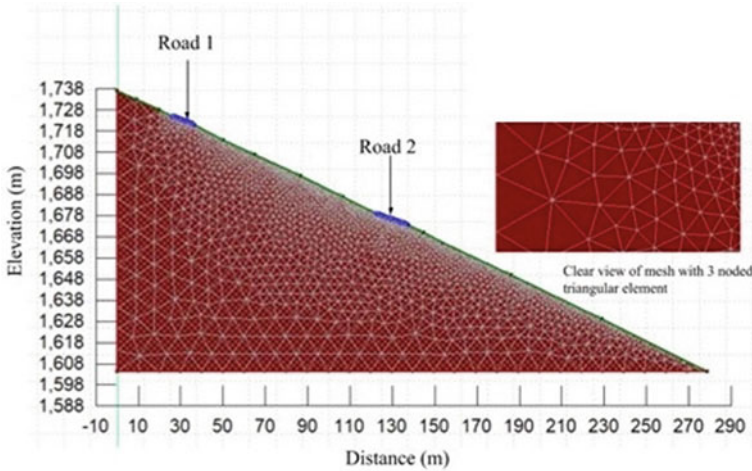
Fig. 2 Finite element model of the slope

3 Methodology

The main purpose of the study is to understand the future earthquakes and to assess the nature. The study is analyzed using probabilistic and deterministic analysis with combination of finite element method using SLOPE W software. The hundred years of earthquake data (1997–2017) is involved in the analysis using appropriate ground motion prediction equation. The three-node triangular plane strain elements are used in the entire model. The stability of the slope was examined for dry and saturated slope for static and pseudo-static conditions. The horizontal coefficient K_h 0.156 and vertical coefficient K_v 0.201 of the September 18, 2011, Sikkim earthquake was used for the pseudo-static analysis.

3.1 Deterministic Approach

In deterministic approach to analyze the slope stability, the single-valued parameters are used and the output from the analysis yields single value of factor of safety. The variables adopted are summarized in Table 1. There are many methods which are

Table 1 Geotechnical properties used in the deterministic analysis

Variable	Value
Cohesion (kN/m^2)	0.1
Friction angle (°)	23
Unit weight (kN/m^3)	17.65

Table 2 Geotechnical properties used in the probabilistic analysis

Variable	Mean value	Standard deviation	Distribution adopted
Cohesion (kN/m^2)	0.1	2	Normal
Friction angle (°)	23	2	Normal
Unit weight (kN/m^3)	17.65	2	Normal

used to calculate the slope stability depending upon their assumptions. In the present study, the Morgenstern method [8] is used as it is commonly employed method in stability analysis. The entry and exit method is used to find the critical slip surface.

Probabilistic approach. The uncertainties in the soil parameters are taken into consideration in probabilistic analysis. The probabilistic slope stability analysis is performed using Monte Carlo simulation. The least slip circle which produce minimum FoS evaluated under deterministic method is then utilized for probabilistic analysis by recomputing using Monte Carlo trials. This trial value "*N*" is dependent on the number of variables considered with respect to standard deviation and on their confidence level. The unit weight, cohesion and friction angle with different random input variables are selected based on mean value and adopted normal probabilistic distribution in the analyses is summarized in Table 2. The random value for each parameter is assigned according to the considered probability distribution function. If the input random variables are normally distributed, the probability density function of the safety factors tends to be normally distributed [9].

4 Results

The factors of safety for the four different cases are calculated with the help of deterministic method, namely Morgenstern method summarized in Table 3.

From the results, the slope is safe in saturated and dry condition but critically unstable when the pseudo-static forces are applied. The factors of safety of slope under four different conditions using probabilistic analysis were presented in Table 4. The slope with reliability index less 3 is unstable and requires stabilization [10]. In the present probabilistic analysis, the slope at dry condition was perfectly safe and the reliability index was decreased from 5.08 to 1.192 during saturated condition. The slope under pseudo-static condition was not reliable and more vulnerable to failure.

Table 3 Factor of safety's calculated in different cases (deterministic)

Cases considered	Factor of safety
Dry	1.582
Dry + Pseudo-static	0.781
Saturated	1.012
Saturated + Pseudo-static	0.588

Table 4 Factor of safety's calculated in different cases (probabilistic)

Variable	Mean factor of safety	Maximum factor of safety	Minimum factor of safety	Reliability Index	Standard deviation
Dry	1.633	2.027	1.368	5.085	0.124
Dry + Pseudo-static	0.821	0.836	0.783	−17.83	0.010
Saturated	1.112	1.412	0.925	1.192	0.925
Saturated + Pseudo-static	0.688	0.703	0.671	−51.92	0.006

From the results, the maximum factor of safety value of the slope at dry and saturated conditions is stable, but the minimum factor of safety of saturated slope indicates the slope is unstable. Thus observed that the slope is safe in dry condition and the failure was initiated during rainy season. The increase in pore pressures dragged the soil downward and created the failure plane channel and thus failed during 2011 Sikkim earthquake event. When compared to deterministic, the probabilistic analysis is more realistic corresponding to factor of safety.

5   Conclusion

The slope profile selected for the present analysis is located in south district of Sikkim state. The stability analysis of the slope was determined using deterministic and probabilistic approaches. The results from the two approaches are compared for the better efficiency of slope stability. The slope under dry and saturated condition for with and without pseudo-static forces was examined using SLOPEW software. The stability of slope under deterministic approach was analyzed using Morgenstern price method and probabilistic approach using Monte Carlo simulation. In deterministic approach, single-valued input parameters are assigned which provided the single-valued factor of safety. In probabilistic approach, the random input variables based on normal probabilistic distribution were assigned used to establish the probability of failure with mean, maximum and minimum factor of safety with risk criterion. From the deterministic approach, the slope is safe in dry and saturated conditions but is unstable in both conditions when the pseudo-static forces are applied. The slope is stable in two cases and unstable in two cases. But in the probabilistic approach, the slope is unstable in three cases with reliability index less than 3. From the whole analysis, the slope failure is initiated during rainy season and disrupted and failed during earthquake with 100% probability of failure.

References

1. Mbarka, S., Baroth, J., Ltifi, M., Hassis, H., Darve, F.: Reliability analyses of slope stability: Homogeneous slope with circular failure. Eur. J. Environ. Civ. Eng. **14**(10), 1227–1257 (2010)
2. Gibson, W.: Probabilistic methods for slope analysis and design. Aust. Geomech. **46** (2011)
3. Gupta, V., Mahajan, A.K., Thakur, V.C.: A study on landslides triggered during Sikkim earthquake of September 18, 2011. Himalayan Geol. **36**, 81–90 (2015).
4. Google: Google Earth User Guide Version 6 (2013).
5. Sikkim State Disaster Management Authority: Land Revenue and Disaster Management Department, Inventory & GIS Mapping of Landslides in North-East, West & South Sikkim and its Mitigation. Sikkim State Disaster Management Authority (2012)
6. Sikkim state Disaster Management Plan Report 2010–2011: https://www.sikkimlrdm.gov.in/downloads/publications/sdmp.pdf
7. Mehrotra, G.S., Sarkar, S., Kanungo, D.P., Mahadevaiah, K.: Terrain analysis and spatial assessment of landslide hazards in parts of Sikkim Himalaya. J. Geol. Soc. India **47**, 491–498 (1996).
8. Morgenstern, N.R., Price, V.E.: The analysis of the stability of general slip surfaces. Geotechnique **15**(1), 79–93 (1965)
9. Shen, H., Klapperich, H., Abbas, S.M., Ibrahim, A.: Slope stability analysis based on the integration of GIS and numerical simulation. Autom. Constr. **26**, 46–53 (2012).
10. Army Corps of Engineers, U.S.: Reliability Analysis and Risk Assessment for Seepage and Slope Stability Failure Modes for Embankment Dams. Engineering Technical Letter (1110-2-561). U.S. Army Corps of Engineers, Washington, DC (2006).

Experimental Study of Ugat Canal Soil for Slope Stability

Yati R. Tank, Ashika S. Patel, Pratima A. Patel, and Akhilesh R. Tank

Abstract Slope stability is one of the major aspects of geotechnical engineering and plays significance on large-scale infrastructure projects such as highways, railways or canals. Slope failure is the major problem in earthen canal due to seepage problem. Due to excess imposed loads, discharge forces, erosion and gravity forces, drainage and irrigation canals may suffer from a full or restricted slope failure. Side slope failures of irrigation at Ugat canal located near Jahangir Pura, Surat, will possibly suffer from heavy catastrophes with destructive damages to public lives and belongings. The reason of canal slope failure is due to piping in salt influenced or distributive soil, discharge forces in soft clayey or sandy soil, deficient standard of the soil mass mound same as in black cotton soil, i.e., soft clay or loose sand and accordingly dissolution due to immoderate use of irrigation water or utilizing surface irrigation method at places near to the bank. There is no generalized method of restoration for slope failures because of the distinctiveness of the attributes and situations of each site. Hence, based on characteristics of sites, each site needs to be studied individually. To prevent the failure, the side slope of the embankment is strengthened by coconut husk which reduces slope failure in earthen canal. There is significant increment in load carrying capacity of soil by adding coconut husk at various contents such as 0.5, 1.0 and 1.5% replacement by soil. At 0.5, 1.0 and 1.50% replacement, the strength increment is 1.52, 1.70 and 2.11 times of normal soil.

Y. R. Tank (✉)
Applied Mechanics Department, SVNIT, Surat, Gujarat 395007, India
e-mail: yatitank93@gmail.com

A. S. Patel
Department of Civil Engineering, CGPIT, UTU, Surat, Gujarat 394350, India
e-mail: ashika8044@gmail.com

P. A. Patel
Faculty of Civil Engineering, SCET, Surat, Gujarat 395007, India
e-mail: pratima.patel@scet.ac.in

A. R. Tank
Infinite Civil Solutions Pvt. Ltd., Ahmadabad, Gujarat 380060, India
e-mail: akhilesh_tank@yahoo.co.in

1 Introduction

1.1 Context

Slope failure is the major problem in earthen canal due to seepage. Many slope failures are observed in different canals. This slope failure is due to the liquefaction of very shallow subsurface sediments. The liquefied layer disassociated the overlying hard deposits from the fundamental sediments that permitted the upper non-liquefied matter to temporarily move back and forth in the form of ground failure called lateral spreading [1]. Ancient earthen irrigation channels in pervious soils deposits may release a plenty amount of water due to seepage. Massive amount of losses from the sides and bed of channel may result in low transport productivity, i.e., the proportion of water coming to cultivation lands turnouts to that emancipated at the water supply source, i.e., river or any stream line.

Therefore, Ugat canal is a minor canal, i.e., not lined. But, due to development of Surat city, this canal is the part of city which requires special attention. As polymer fibers have capacity to reduce seepage, even at the same loss rate per unit area, there will be a saving in water and increase in bearing capacity and shear strength of canal slope. Many scientists and geotechnical engineers related to such background stated that the hydraulic conductivity of fiber-reinforced soil can be improved by increase in fiber content [2, 3].

To prevent canal slope failure, the side slope of the embankment is strengthened by coconut husk, i.e., polymer fibers as a partial replacement of soil which reduces slope failure in earthen canal. This study focuses on the reinforced earth slope stability of canal using coconut husk. The experimental study of canal slope strengthening is selected to study the different characteristics of soil mass. The canal is situated on the Ugat Road, near Jahangir Pura, Surat (Fig. 1).

1.2 Types of Slope Failure

A slope failure is an incident in which a slope collapses quickly due to disabled self-holding ability of the earth under the effect of a rainfall or an earthquake. There are generally four types of slope failures described here.

Rotational Failure

A gliding-type landslip is a downslope motion of material that happens along a unique surface. The slide is said to be rotational if the slip surface is curved. The

Fig. 1 Canal slope failure

slip surface of a rotational landslide leads to be deep. Blocks of failed material may rotate as they fail and can at times be seen to move in reverse toward the slope [4].

Translational Failure

A slide-type landslip is a downslope movement of material that occurs along a particular surface of fragility such as a fault, joint or bedding plane. It is termed translational or planar failure if the slip surface is straight [4].

Compound Failure

A failure composing the aspects of both rotational and translational failure is known as compound failure.

Wedge Failure

A failure along an inclined plane is known as wedge failure. It is also called plane failure or block failure. It occurs when particular blocks and wedges of the soil mass become isolated.

1.3 What is Polymer Fiber Reinforcement in Soil?

An idea of soil mass reinforcement by adding a kind of fiber was performed by our ancient culture which used soil combined with accessible fiber [5]. It was helpful to increase strength and durability and of the dried brick used as construction materials. It was originated that fiber-reinforced soil proves better than natural soil [6].

1.4 Objective of Study

- To increase stability of slope that occurs in failure zone of canal system.
- To provide a cost-effective work and increase bearing capacity and shear strength of soil by adding coconut husk, i.e., polymer fiber as a partial replacement of soil at 0.5, 1.0 and 1.5% replacement to increase the stability of the adjoining road.
- To reduce soil volume, change due to temperature or moisture effect by soil stabilization.

2 Research Material and Methodology Adopted

In the experimental study, two materials were used: polymer fiber, i.e., coconut husk and soil sample, i.e., available at site. A description of coconut husk is provided as follows.

Coconut fibers are the natural fibers taken out from the coconut husk. It is widely utilized in products like doormats, floor mats, sweeping brushes and mattresses. Coir is the stiff coarse fiber from the outer husk of a coconut. It is the knotty kind of material seen between the interior shell and the outer coat of a coconut. Brown coir is made up of ripe coconut. They are further used in covering, crafting and cultivation. White coir is gathered from unripe coconuts, utilized for preparing sweepers, strings, strands and fishing mesh (Fig. 2).

Fibers are light in weight, strong and elastic. Based on experimental work performed in M-Test Laboratory, Udhana, Surat, various parameters were studied of coconut husk. The properties of coconut husk are derived from tests performed by the authors, and the results are mentioned here (Table 1).

Fig. 2 Coconut husk

Table 1 Physical characteristics of coconut husk

Characteristics	Description
Tensile strength	13.8 kN/m
Absorption	None
Elongation	30%
Diameter	10–20 µm (0.0004–0.0008 in.)
Length	10–30 cm (4–12 in.)
Density	0.67–10.0 g/cm³
Thermal conductivity	Low

3 Experimental Study

See Fig. 3.

In present experimental study, diverse soil samples have been studied, i.e., normal soil sample, i.e., 0% replacement, 0.5% replacement, 1.0% replacement and 1.5% replacement of coconut husk by weight of soil. The testing of mechanical property, i.e., shear strength was conducted by triaxial shear test.

3.1 Parameter Studied

During the research work, three parameters were studied, i.e., optimum moisture content, maximum dry density and shear strength by proctor compaction test and triaxial shear test.

Fig. 3 Proctor compaction test setup

Fig. 4 Proctor compaction equipment

3.2 Proctor Compaction Test

Proctor compaction test is the most common test to evaluate the optimum moisture content at which a tested soil sample becomes most dense and attains the relevant maximum dry density.

See Fig. 4.

3.3 Triaxial Shear Test

See Fig. 5.

Triaxial shear strength test is the most common test, i.e., widely recommended and suitable for all kinds of soils [7]. It used to assess the mechanical properties of the soil sample. In this test, soil sample is subjected to stress, in such a manner that the stress generated in one direction will be different in orthogonal direction. The material properties of the soil, i.e., shear resistance (angle of internal friction) and cohesion, and the dilatancy stress is evaluated from triaxial shear strength test. And from that, shear strength is evaluated.

4 Results and Discussions

A research work on canal slope stability was performed to assess the shear strength of treated and untreated soil sample to enhance stability at Ugat canal soil. The results of MDD and OMC of untreated soil sample are 1.67 gm/cc and 19.30%,

Fig. 5 Triaxial shear test setup

respectively, as indicated in Fig. 6. Now, from Figs. 7, 8 and 9, MDD and OMC of treated soil samples are 1.774 gm/cc and 15.50% (for 0.5% coconut husk), 1.80 gm/cc and 17.75% (for 1.0% coconut husk) and 1.648 gm/cc and 13.00% (for 1.5% coconut husk), respectively (Figs. 10, 11, 12 and 13).

The results of triaxial shear test show that there is significant increment in strength or bearing capacity of soil by adding coconut husk at various contents, i.e., 0.5, 1.0 and 1.5% replacement by soil. At 0.5% replacement, the strength increment is 1.52 times of the normal soil, at 1.0% replacement the strength increment is 1.70 times of

Fig. 6 Proctor test results of untreated soil sample
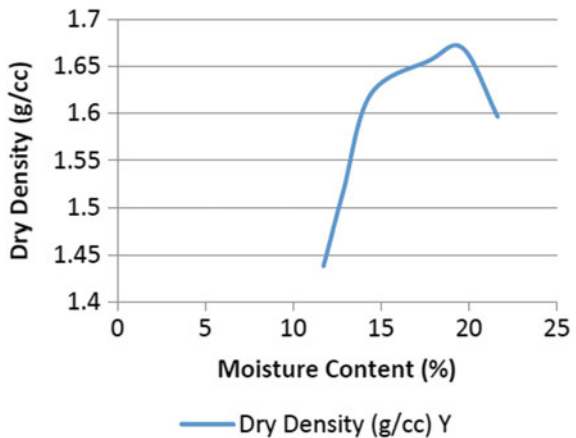
Fig. 7 Proctor test results of soil sample with 0.5% coconut husk
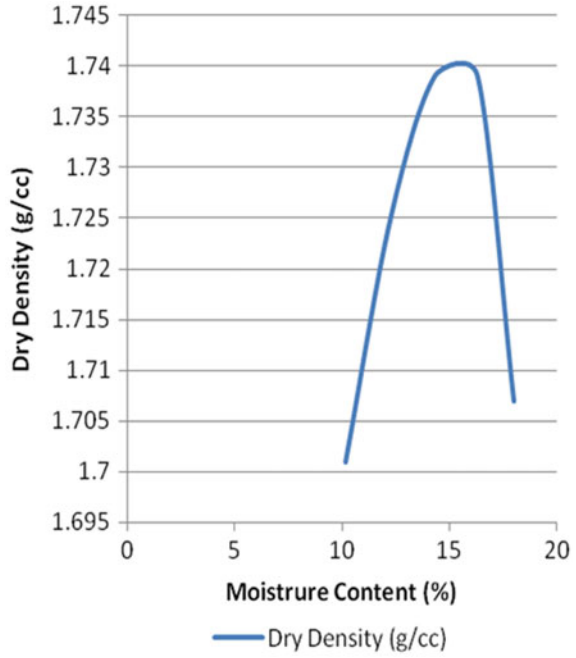
Fig. 8 Proctor test results of soil sample with 1.0% coconut husk
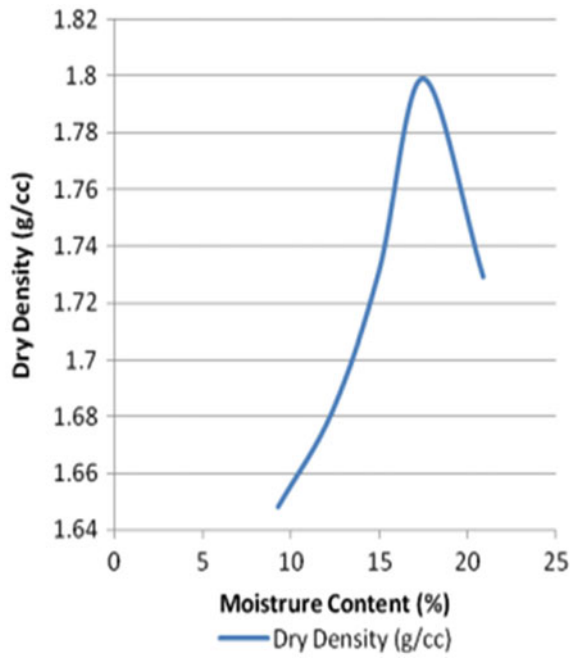
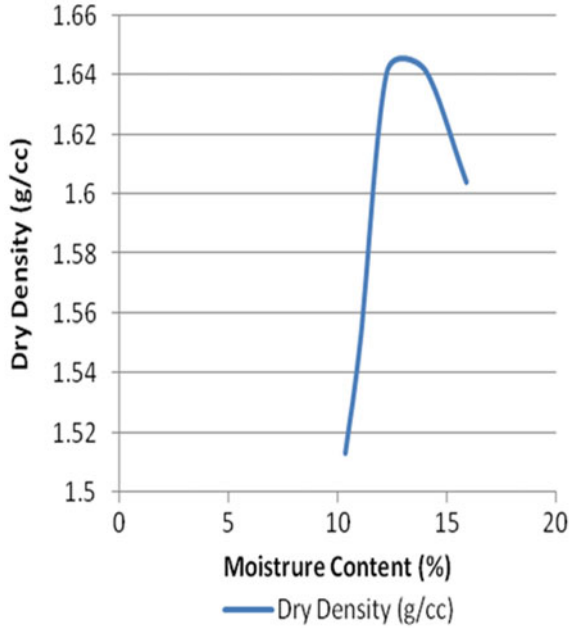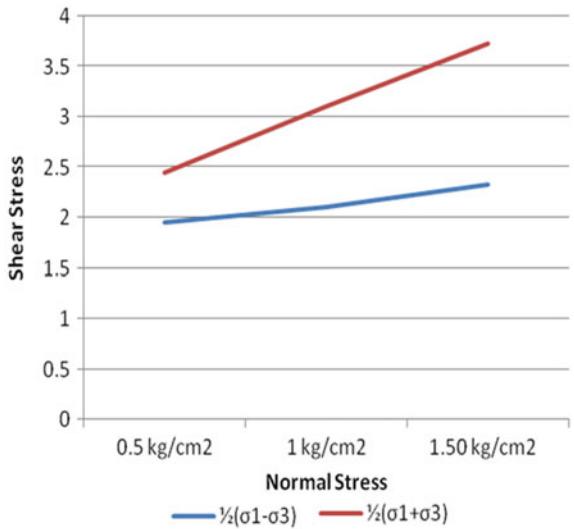**Fig. 9** Proctor test results of soil sample with 1.5% coconut husk

Fig. 10 Untreated soil C–Ø (simple soil) $C = 1.9$ kg/cm^2 $Ø = 15°$

normal soil, and at 1.5% replacement the strength increment is 2.11 times of normal soil.

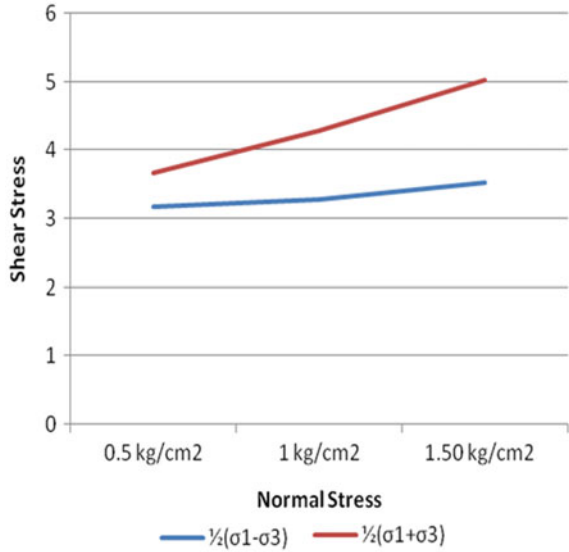**Fig. 11** Treated soil C–Ø (0.5% coconut husk) $C = 3.1$ kg/cm^2 Ø = 10°

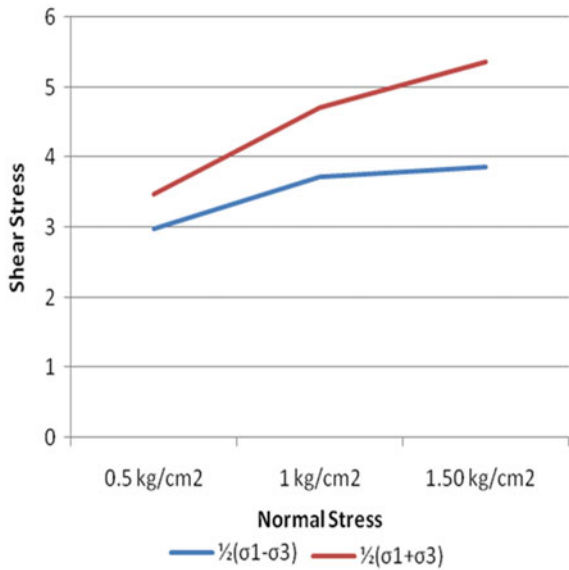**Fig. 12** Treated soil C-Ø (1.0% coconut husk) $C = 3.0$ kg/cm^2 Ø = 20°

5 Concluding Remarks

Detailed conclusions as results of the study have been discussed. The variations of the results are shown in terms of percentage. Also, these variations are related to only studied cases. Hence, these percentage changes could be varying from case to case.

Fig. 13 Treated soil C–Ø
(1.5% coconut husk) $C =$
3.5 kg/cm^2 Ø $= 16°$
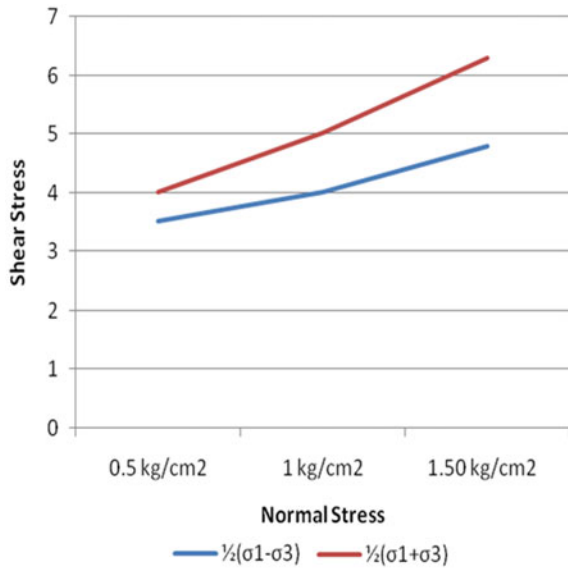
- From the various literature studies, it has been seen that the canal slope failure and bearing capacity can be prevented using alternative mineral admixtures by replacement of soil at various percentages.
- Coconut husk as a partial replacement of soil proves to be most economical, suitable solution to increase mechanical properties of soil.
- There is significant increment in shear strength or bearing capacity of soil by adding coconut husk at various contents, i.e., 0.5, 1.0 and 1.5% replacement by weight of soil. At 0.5% replacement the strength increment is 1.52 times of the normal soil, at 1.0% replacement the strength increment is 1.70 times of normal soil, and at 1.5% replacement the strength increment is 2.11 times of normal soil. Also, as the fiber content, i.e., coconut husk increased, cohesion value is also increased.
- The relative cheapness of material and potential for producing and laying the matting with local labor recommends the use of coconut waste not only as soil reinforcement but also as concrete reinforcement as a very suitable option for sustainable development scenario.
- The experimental results are restricted to Ugat canal soil embankment, and for other site the results may vary.

References

1. T. Leslie Youd, D.K. Keefer, Liquefaction during the 1977 San Juan Province, Argentina earthquake (Ms = 7.4). Eng. Geol. (1994).
2. M.R. Abdi, A. Parsapajouh, M.A. Arjomand, Effects of random fiber inclusion on consolidation, hydraulic conductivity, swelling, shrinkage limit and desiccation cracking of clays. Int. J. Civ. Eng. **6**(4) 284–292 (2008).
3. T. Thyagaraj, D. Soujanya. Polypropylene fiber reinforced bentonite for waste containment barriers. Appl. Clay Sci. (2017).
4. L.M. Highland, P. Bobrowsky, The Landslide Handbook—A Guide to Understanding Landslides. United States Geological Survey and Geological Survey of Canada, Nov 29, 2016.
5. S.A. Naeini, S.M. Sadjadi, Effect of waste polymer materials on shear strength of unsaturated clays. EJGE J. **13** (2008).
6. C.J. Miller, S. Rifai, Fiber reinforcement for waste containment soil liners. (ASCE) J. Environ. Eng. (2004).
7. B. Kalantari, B.B.K. Huat, A. Prasad, Effect of polypropylene Fibers on the California bearing ratio of air cured stabilized tropical peat soil. Am. J. Eng. Appl. Sci. (2010).

Pseudo-static Stability Analysis of Multilayered Slopes Using Sarma's Method of Non-vertical Slices

Somenath Mukherjee, Subhadeep Metya, and Gautam Bhattacharya

Abstract Stability analysis of multi-layered slopes with complex geometry and pore pressure conditions has always been a topic of immense interest to both the researchers and the practitioners in the field of geotechnical engineering. Over the decades, within the framework of limit equilibrium methods of slices, a number of rigorous methods have been proposed which are valid for general non-circular slip surfaces, satisfy all conditions of equilibrium, and take full account of the interslice forces. Among these, the Sarma method is the only method in which the slices are not necessarily vertical, and the critical inclinations of the slices are found as part of the solution and use the internal strength of material for the solution of the problem. Because of the number of iterations involved in finding the critical set of slice inclinations, Sarma method is not suitable for finding the critical slip surface. In order to compare the results obtained by using the other rigorous methods with those using Sarma's method, the latter can be used to re-analyze the critical slip surfaces determined for the other methods. In this study involving three complex slope stability problems, the critical slip surfaces determined using the Morgenstern and Price method and the Spencer method are re-evaluated using the Sarma method. The GEO5 software is utilized for the purpose. The comparison of results has brought out that compared to the Sarma method, both the Morgenstern and Price and the Spencer method consistently yields conservative values of factor of safety for each of the three example problems.

Keywords Slope stability analysis · Limit equilibrium method · Factor of safety · Critical slip surface · Sarma method · Pseudo-static approach of analysis

S. Mukherjee
C.E. Testing Company Pvt. Ltd., Kolkata, West Bengal 700092, India

S. Metya (✉)
NIT Jamshedpur, Jharkhand 831014, India
e-mail: smetya.ce@nitjsr.ac.in

G. Bhattacharya
IIEST, Shibpur, Howrah, West Bengal 711103, India

1   Introduction

Slope stability analysis has over the decades remained a topic of overwhelming importance not only to the geotechnical practitioners but also to the researchers. It is widely known that failures of slopes are caused by ground movements such as falls, topples, slides, spreads, and flows. In engineered slopes, in particular, the slide type of ground movement is predominant and such a mechanism is more amenable to theoretical analysis as compared to the other types of ground movements [1].

Various approaches to solving slope stability problems include the limit equilibrium approach, the limit analysis approach, and the finite element approach. Among these, it is the limit equilibrium approach which has all along received the researchers' attention and earned almost exclusive preference of the practicing engineers.

The widely used rigorous methods of slices valid for slip surfaces of general non-circular or arbitrary shapes include the Morgenstern and Price method [2], the Spencer method [3], the Janbu's method [4], and the Sarma method [5]. The Sarma method, however, is a class of its own. In this method, perhaps for the first time in the history of development of the limit equilibrium method of slices, the slices are not necessarily vertical and the critical inclinations of the interslice boundaries are found out as part of the solution. According to Sarma [5], the reason for using inclined slices is that vertical slice interfaces are sometimes not suitable for an evaluation of internal stresses which is the real purpose of a sophisticated limit equilibrium analysis. Furthermore, this is the only method that uses the internal strength of material for the solution of the problem.

As commented by Sarma [5], because of the large number of iterations involved in finding the critical set of inclinations of the interslice boundaries, the Sarma method is not really suitable for the analysis of sections where large numbers of probable slip surfaces have to be analyzed to determine the critical slip surface.

2   Critical Slip Surface Using Optimization

The slope stability analysis within the framework of limit equilibrium approach is essentially a problem of optimization, namely finding the critical slip surface having the minimum factor of safety. A number of softwares are currently available for efficiently carrying out this optimization. In this study, all slope stability computations are carried out using the geotechnical software GEO5 [6]. In this software, the optimization-based search for the critical slip surface proceeds through sequential changing of locations of discrete points on a slip surface and noting the change which results in the largest reduction in factor of safety. The two end points of the slip surface are moved along the slope surface while the remaining points are moved in the vertical and the horizontal directions. The initial step size is selected as one-tenth of the smallest distance between adjacent discrete points on the slip surface. In each of the subsequent cycles of search, the step size is reduced by one half. The

locations of the discrete points from left to right are considered to be the optimum when there is negligible displacement of any of the points during the last cycle. For further details, the manual of the GEO5 software may be referred.

3 Illustrative Examples

In order to draw a comparison of results of slope stability analysis of multilayered slopes based on some of the most widely used rigorous limit equilibrium methods of slices valid for general slip surfaces, three benchmark slope examples have been selected from the literature. These are described in the subsequent sections followed by their analyses and results as obtained by using the GEO5 software.

4 Example 1: Case Study of the Congress Street Cut

4.1 Description

This example concerns a failed slope reported in the literature pertaining to the case study of the 1952 historic Congress Street open cut in Chicago. As reported by Ireland [7], in 1952 in Chicago, during the open cut construction of the Congress Street 'superhighway', in which deep benched cutting was undertaken in saturated glacial clay, a large rotational slope failure occurred on the south side of the cut for a length of about 60 m when the excavation reached a depth of nearly 14.3 m [8]. An approximate cross section of the cut at the time of failure, together with an approximate position of the observed failure surface was originally presented by Ireland [7]. Recently, Ji and Low [9] have reported the dimensions of the cut at failure as shown in Fig. 1.

According to Ji and Low [9], the soil profile at the excavation site comprised a 3.35–m-thick layer of sand and miscellaneous fill (layer 1) underlain by a 13.42–m-thick layer of gritty blue clay. The failure occurred in this layer is subdivided into three sublayers: a 4.27–m-thick upper layer of stiff gritty blue clay (layer 2: Clay 1), a 6.1–m-thick middle layer of medium gritty blue clay (layer 3: Clay 2), and a 3.05 m lower layer of medium gritty blue clay (layer 4: Clay 3). The layer of gritty blue clay is underlain by a layer of stiff to very stiff gritty blue clay (hard stratum). The water table was located at a depth of nearly 2.2 m from the slope top.
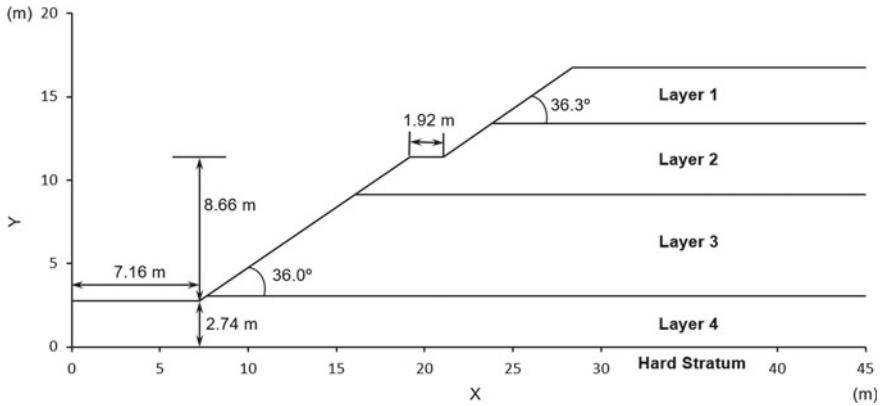
Fig. 1 Slope section for example 1: Cross section of the Congress Street open cut (after Ji and Low [9])

4.2 Present Study

As stated before, the purpose of the present study is to draw a comparison among the results of deterministic slope stability analyses carried out on the basis of three of the widely used limit equilibrium methods of slices valid for general slip surfaces. These three methods are as follows: (1) the Morgenstern and Price method [2]; (2) the Spencer method [3]; and (3) the Sarma method [5]. To this end, the following analyses have been carried out.

(i)   Determination of the critical slip surface and the associated minimum factor of safety using the Morgenstern and Price method;

(ii)   For the specific slip surface obtained in (i) above, determination of the factor of safety using the Sarma method;

(iii)   Determination of the critical slip surface and the associated minimum factor of safety using the Spencer method;

(iv)   For the specific slip surface obtained in (iii) above, determination of the factor of safety using the Sarma method.

Soil Properties: Table 1 presents the soil properties considered in the present study. These are taken from Ji and Low [9]. The values of unit weight are, however, taken from Liang et al. [10].

Analysis I: Critical Slip Surface by Morgenstern and Price Method
Based on the Morgenstern and Price [2] method, the critical slip surfaces and the associated minimum factors of safety (F_{min}) have been determined for the seismic coefficient K_h ranging from 0.0 to 0.2. The total number of slices considered in the analysis is 10. The values of F_{min} are presented in Table 2. A typical critical slip surface for the seismic coefficients $K_h = 0.10$ is shown in Fig. 2.

Table 1 Soil properties for example 1

Layer	Material	Parameter	Unit	Value
1	3.35 m sand and miscellaneous fill	c_1	kN/m^2	0.00
		ϕ_1	degree	30.00
		γ_1	kN/m^2	17.28
2	4.27 m stiff gritty blue clay (Clay 1)	c_2	kN/m^2	55.00
		ϕ_2	degree	0.00
		γ_2	kN/m^2	20.75
3	6.10 m medium gritty blue clay (Clay 2)	c_3	kN/m^2	43.00
		ϕ_3	degree	0.00
		γ_3	kN/m^2	20.11
4	3.05 m medium gritty blue clay (Clay 3)	c_4	kN/m^2	56.00
		ϕ_4	degree	0.00
		γ_4	kN/m^2	20.11

Ji and Low [9], Liang et al. [10]

Table 2 Summary of results for example 1

K_h	Values of F_{min} by the Morgenstern and Price method (1)	Values of F by the Sarma method corresponding to column (1) (2)	Values of F_{min} by the Spencer method (3)	Values of F by the Sarma method corresponding to column (3) (4)
0.00	1.04	1.24	1.06	1.22
0.05	0.96	1.14	0.99	1.11
0.10	0.92	1.02	0.92	1.02
0.15	0.80	0.94	0.85	0.94
0.20	0.74	0.87	0.78	0.85

Analysis II: Critical Slip Surface by Spencer Method

Based on the Spencer [3] method, the critical slip surfaces and the associated minimum factors of safety (F_{min}) have been determined for the seismic coefficient K_h ranging from 0.0 to 0.2. The values of F_{min} are presented in Table 2 (column 3). A typical critical slip surface, for the seismic coefficients $K_h = 0.10$, is shown in Fig. 3.

Analysis III: Evaluation of both the Critical Slip Surfaces by Sarma Method

Based on the Sarma method, the critical slip surfaces obtained based on the Morgenstern and Price method and the Spencer method have been re-evaluated, using the software GEO5. The results are summarized in Table 2 and discussed in Sect. 7.
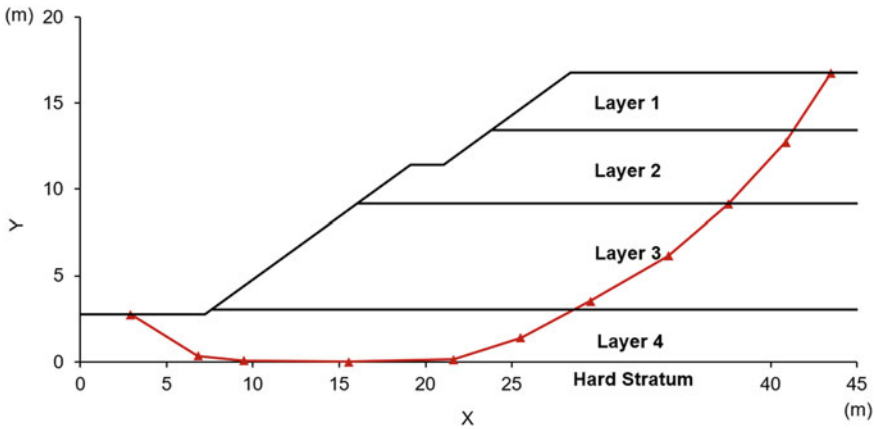
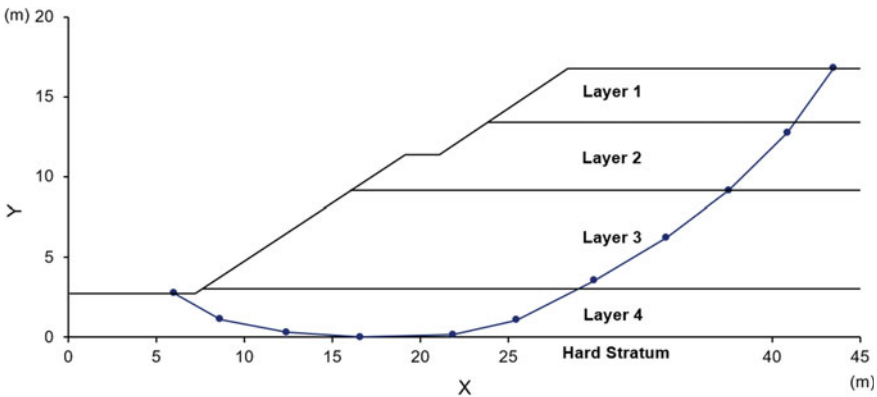**Fig. 2** Critical slip surface by Morgenstern and Price method for example 1 ($K_h = 0.10$)

Fig. 3 Critical slip surface by Spencer method for example 1 ($K_h = 0.10$)

5 Example 2: A Multilayered Slope [11]

5.1 Description

Example 2 concerns another multilayered slope comprising four layers. The slope section is shown in Fig. 4 which is similar to that considered by Zhu and Lee [11] for purposes of illustrating the application of a new limit equilibrium method of analysis proposed by the authors. The soil properties are as given in Table 3.

Analysis I: Critical Slip Surface by Morgenstern and Price Method
Based on the Morgenstern and Price [2] method, the critical slip surfaces and the associated minimum factors of safety (F_{min}) have been determined for the seismic
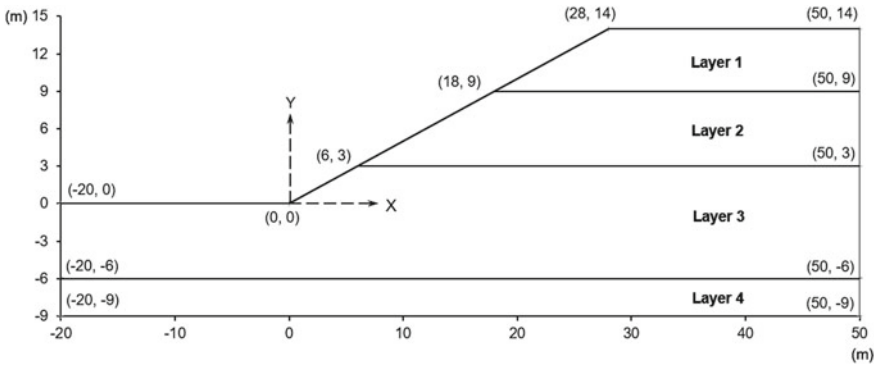
Fig. 4 Slope section in example 2 (similar to the slope section in Zhu and Lee [11])

Table 3 Soil properties for example 2

Layer	Parameter	Unit	Value	Layer	Parameter	Unit	Value
1	c_1	kN/m^2	20.00	3	c_3	kN/m^2	25.00
	ϕ_1	degree	18.00		ϕ_3	degree	26.00
	γ_1	kN/m^2	18.80		γ_3	kN/m^2	18.4
2	c_2	kN/m^2	40.00	4	c_4	kN/m^2	10.00
	ϕ_2	degree	22.00		ϕ_4	degree	12.00
	γ_2	kN/m^2	18.50		γ_4	kN/m^2	18.00

Zhu and Lee [11]

coefficient K_h ranging from 0.0 to 0.2 using the software GEO5. The total number of slices considered in the analysis is 10. The values of F_{min} are presented in Table 4. A typical critical slip surface, for the seismic coefficients $K_h = 0.2$, is shown in Fig. 5.

Table 4 Summary of results for example 2

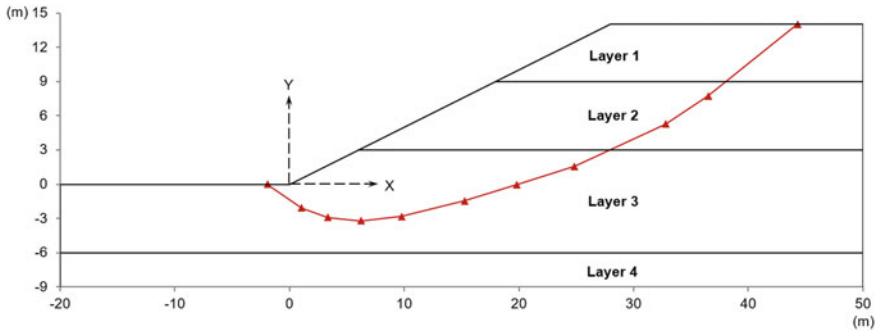| K_h	Values of F_{min} by the Morgenstern and Price method (1)	Values of F by the Sarma method corresponding to column (1) (2)	Values of F_{min} by the Spencer method (3)	Values of F by the Sarma method corresponding to column (3) (4)
0.00	1.80	1.98	2.10	2.15
0.05	1.79	1.88	1.90	1.94
0.10	1.66	1.78	1.74	1.77
0.15	1.53	1.62	1.64	1.64
0.20	1.41	1.48	1.48	1.48

Fig. 5 Critical slip surface by Morgenstern and Price method for example 2 ($K_h = 0.20$)

Analysis II: Critical Slip Surface by Spencer Method

Based on the Spencer [3] method, the critical slip surfaces and the associated minimum factors of safety (F_{min}) have been determined for the seismic coefficient K_h ranging from 0.0 to 0.2. The values of F_{min} are presented in Table 4 (column 3). A typical critical slip surface, for the seismic coefficients $K_h = 0.20$, is shown in Fig. 6.

Analysis III: Evaluation of both the Critical Slip Surfaces by Sarma Method

Based on the Sarma method, the critical slip surfaces obtained based on the Morgenstern and Price method and the Spencer method have been re-evaluated, using the software GEO5. The results are summarized in Table 4 and discussed in Sect. 7. Figure 7a, b shows the slice configurations corresponding to the re-analysis by Sarma method of the critical slip surfaces for the Spencer method and the Morgenstern method, respectively.
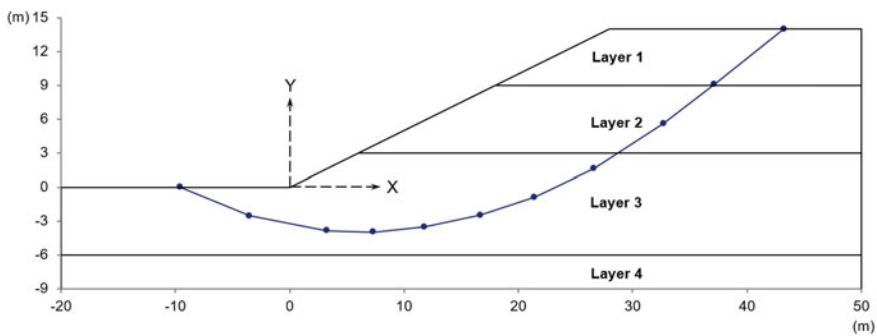

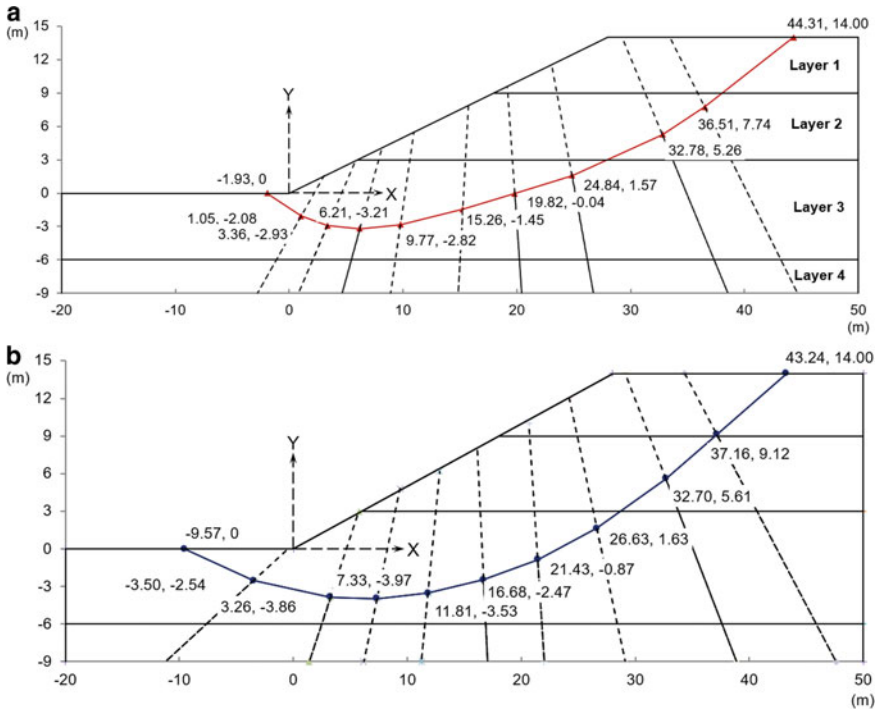**Fig. 6** Critical slip surface by Spencer method for example 2 ($K_h = 0.20$)

Fig. 7 **a** Slice configuration in Sarma method of analysis of the critical slip surface based on Morgenstern and Price method, **b** slice configuration in Sarma method of analysis of the critical slip surface based on Spencer method

6 Example 3: An Embankment on Soft Clay [12]

6.1 Description

Low [12] presented a semi-analytical procedure to calculate the factor of safety of embankments founded on soft clay using the stability numbers defined for the embankment and its foundation. Application of the proposed method was illustrated with the help of a couple of examples. The slope section in example 3, shown in Fig. 8, is similar to one of those considered by Low [12]. In this example, there are three horizontal clay layers, having 5, 4, and 5 m thickness. Values of the undrained shear strength c_u for the upper, middle, and lower strata are 30, 20, and 150 kPa, respectively. The soil unit weight is 18 kN/m^3. As shown in Fig. 8, a cut is excavated with side slope of 1 V:3H to a depth of 6 m.

Analysis I: Critical Slip Surface by Morgenstern and Price Method
Based on the Morgenstern and Price [2] method, the critical slip surfaces and the associated minimum factors of safety (F_{min}) have been determined for the seismic
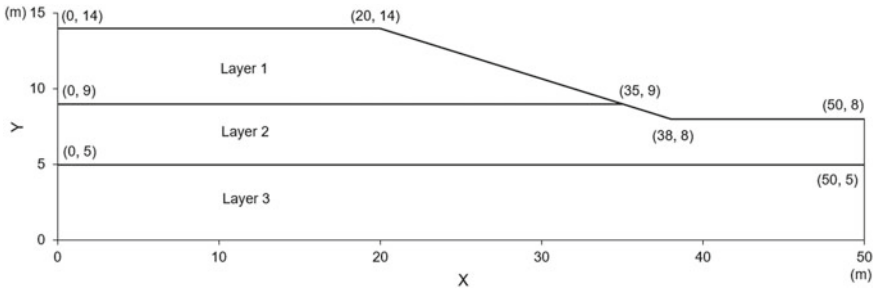
Fig. 8 Slope section in example 3 (similar to one of the slope sections in Low [12])

coefficient K_h ranging from 0.0 to 0.15 using the software GEO5. The total number of slices considered in the analysis is 10. The values of F_{min} are presented in Table 5. A typical critical slip surface, for the seismic coefficients $K_h = 0.1$, is shown in Fig. 9.

Analysis II: Critical Slip Surface by Spencer Method
Based on the Spencer [3] method, the critical slip surfaces and the associated minimum factors of safety (F_{min}) have been determined for the seismic coefficient

Table 5 Summary of results for example 3

K_h	Values of F_{min} by the Morgenstern and Price method (1)	Values of F by the Sarma method corresponding to column (1) (2)	Values of F_{min} by the Spencer method (3)	Values of F by the Sarma method corresponding to column (3) (4)
0.00	1.41	1.76	1.42	1.75
0.05	1.22	1.49	1.24	1.49
0.10	1.05	1.26	1.07	1.27
0.15	0.91	1.09	0.92	1.10

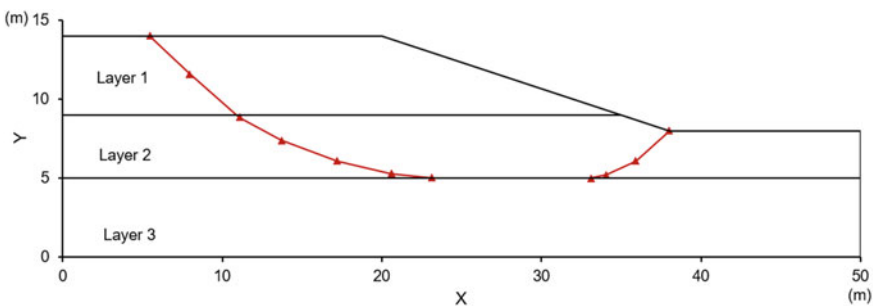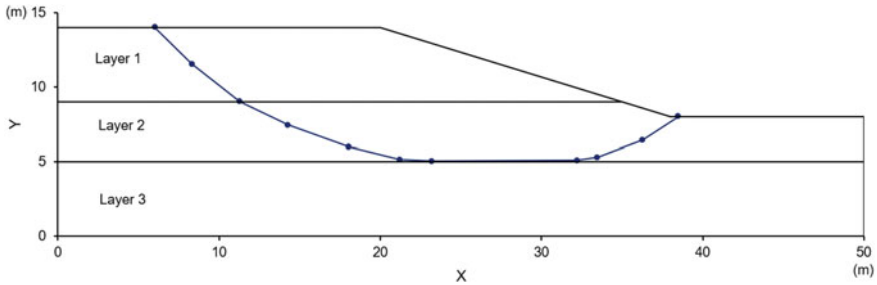**Fig. 9** Critical slip surface by Morgenstern and Price method for example 3 ($K_h = 0.10$)

Fig. 10 Critical slip surface by Spencer method for example 3 ($K_h = 0.10$)

K_h ranging from 0.0 to 0.15. The values of F_{min} are presented in Table 5 (column 3). A typical critical slip surface, for the seismic coefficients $K_h = 0.1$, is shown in Fig. 10.

Analysis III: Evaluation of both the Critical Slip Surfaces by Sarma Method
Based on the Sarma method, the critical slip surfaces obtained based on the Morgenstern and Price method and the Spencer method have been re-evaluated, using the software GEO5. The results are summarized in Table 5 and discussed in Sect. 7.

7 Concluding Remarks

Stability assessment of multilayered slopes of complex geometry based on rigorous limit equilibrium methods of slices such as the Morgenstern and Price method [2] and the Spencer method [3] valid for general slip surfaces involves lot of computational effort which is further enhanced when such slopes are analyzed under seismic condition by introducing pseudo-static earthquake forces. On the other hand, the Sarma method [5] of non-vertical slices has always attracted the attention of both researchers and practitioners in geotechnical engineering, yet its application in complex layered slopes has been limited because of the requirement of additional computing effort in the iterations involved in finding the critical inclinations of the slices. In recent times, however, making use of commercially available sophisticated slope analysis softwares, it has been practicable to attempt solving complex slope problems based on the Sarma method as well. Keeping the above in view, in the present study, such an attempt has been made to use GEO5—a slope analysis software to solve three complex slope examples selected from the literature based on all the three rigorous methods of slices mentioned above and tries to draw a comparison of the values of factors of safety so obtained. In view of the additional computations required in the Sarma method, no effort has been made to determine the critical slip surface based on this method. For purposes of comparison, the critical slip surfaces determined based on the other two methods have been re-analyzed based on the Sarma method.

Within the limited scope of the present study based on the analysis of three slope examples, a comparison of the values of factor of safety based on the three rigorous methods of slices has revealed the following:

1. Compared to both the Morgenstern and Price method [2] and the Spencer method [3], the Sarma method [5] yields, for characteristic slip surfaces, values of pseudo-static factor of safety which are on the higher side. The magnitude of the difference, of course, varies widely with the method of analysis and the value of seismic coefficient, K_h.

2. For instance, considering the specific slip surface as the critical slip surface based on the Morgenstern and Price method, the difference in the values of factor of safety obtained by the Sarma method and the Morgenstern and Price method ranges from 10 to 25% for the static case ($K_h = 0.0$) and from 5 to 22% for the seismic cases (K_h varying from 0.05 to 0.20 for examples 1 and 2 and from 0.05 to 0.15 for example 3).

3. Again, considering the specific slip surface as the critical slip surface based on the Spencer method, the difference in the values of factor of safety obtained by the Sarma method and the Spencer method ranges from 2 to 23% for the static case ($K_h = 0.0$) and from 0 to 20% for the seismic cases (K_h varying from 0.05 to 0.20 for examples 1 and 2 and from 0.05 to 0.15 for example 3).

4. The above observations are based on a total of three examples and ten slices used in each analysis. Thus, it gives a crude estimate of the difference in the values of factor of safety. For purposes of a rigorous comparison, however, analyses of more numbers of examples should be carried out, and, also, the effect of increasing the number of slices should be examined [13, 14].

5. For a more meaningful comparison of the solutions obtained from the rigorous methods of slices, attempts may be made to determine the critical slip surfaces based on the Sarma method, though it is known to be an extremely tedious job.

References

1. Huang, Y.H.: Stability Analysis of Earth Slopes. Van Nostrand Reinhold Company Inc., New York (1983)
2. Morgenstern, N.R., Price, V.E.: The analysis of the stability of general slip surfaces. Geotechnique **15**(1), 79–93 (1965)
3. Spencer, E.: The thrust line criterion in embankment stability analysis. Geotechnique **23**(1), 85–100 (1973)
4. N. Janbu, Slope stability computation. *Embankment Dam Engineering*, Casagrande Volume, ed. by R.C. Hirschfeld, S.J. Poulos (Wiley, New York, 1973), p 47–86
5. Sarma, S.K.: Stability analysis of embankments and slopes. J. Geotech. Eng. Div., ASCE **105**(12), 1511–1524 (1979)
6. GEO5 [http://schnellinformatics.com/GEO5_geotechnical_software.html]
7. Ireland, H.O.: Stability analysis of the congress street open cut in Chicago. Geotechnique **4**, 163–168 (1954)

8. S. Metya, *Reliability analysis of soil slopes using the first order reliability method*, Ph.D. dissertation, Indian Institute of Engineering Science and Technology (IIEST), Shibpur, India (2017)
9. Ji, J., Low, B.: Stratified response surfaces for system probabilistic evaluation of slopes. J. Geotech. Geoenviron. Eng., ASCE **138**(11), 1398–1406 (2012)
10. Liang, R.Y., Nusier, O.K., Malkawi, A.H.: A reliability based approach for evaluating the slope stability of embankment dams. Eng. Geol. **54**(3–4), 271–285 (1999)
11. Zhu, D.Y., Lee, C.F.: Explicit limit equilibrium solution for slope stability. Int. J. Numer. Anal. Methods Geomech. **26**, 1573–1590 (2002)
12. Low, B.K.: Stability analysis of embankments on soft ground. J. Geotech. Eng. Div., ASCE **115**(2), 211–227 (1989)
13. Metya, S., Bhattacharya, G.: Probabilistic stability analysis of the Bois Brule Levee considering the effect of spatial variability of soil properties based on a new discretization model. Indian Geotech. J. **46**(2), 152–163 (2016)
14. Metya, S., Bhattacharya, G.: Reliability analysis of earth slopes considering spatial variability. Geotech. Geolog. Eng. **34**(1), 103–123 (2016)

A Study on the Erodibility of Lateritic Soil Due to Flooding

Zoheb Faisal, P. Muhammed Shibil, P. K. Jayasree, and J. Jayamohan

Abstract Soil erosion is a process of detachment and transportation of soil materials from its original place by the action of various erosive forces. Erodibility of soils is referred to as the vulnerability of the soils to get eroded. Laterite soil is one of the major types of soil found in Kerala, which is rich in iron and aluminium content. So, the present study aims at identifying the key parameters affecting the erodibility of lateritic soils during floods as well as studying its effects on lateritic slopes. Also, the study focuses on the measurement of quantum of erosion by developing a suitable test set-up. The flood parameters are considered as the key parameters for the erodibility study. The test set-up consists of a tank with a lateritic slope inside, an inlet tank (storage tank) and a sediment collecting tank. Water is allowed to flow from the inlet tank towards the lateritic slope, and the water along with eroded soil is collected in the sedimentation tank after passing through a strainer. Tests are carried out under various flood parameters such as the velocity of flood water, the height of flood water and duration of water flow at a slope of 2.5:1 maintaining a bulk density of 18 kN/m^3. The quantum of erosion is measured in terms of the total weight of the eroded material. The variations in the erosion rate under varying flood parameters are studied**.**

Keywords Erodibility · Lateritic soil · Flood parameters · Geometric parameter

Z. Faisal (✉) · P. Muhammed Shibil · P. K. Jayasree
College of Engineering Trivandrum, Trivandrum, Kerala 695016, India
e-mail: faisal.zooman@gmail.com

P. Muhammed Shibil
e-mail: shibilpunathil774@gmail.com

P. K. Jayasree
e-mail: jayasreepk@cet.ac.in

J. Jayamohan
Lal Bahadur Shastri Institute of Technology for Women, Thiruvananthapuram, Kerala 695012, India
e-mail: jayamohan7@gmail.com

1 Introduction

Soil erosion is a process of detachment and transportation of soil materials from its original place by the action of various erosive forces. Erodibility of soils is referred to as the vulnerability of the soils to get eroded. Erosion of soil is due to the movement of various water bodies, winds, deforestation, etc. Soil erosion affects agriculture, damages infrastructure, desertifies arid and semiarid areas, etc. Laterite soil is one of the major types of soil found in Kerala, which is rich in iron and aluminium content. Lateritic soils are abundant in Kerala, and during the 2018 floods in Kerala, lateritic slopes were subjected to drastic failure. Kerala was affected by severe floods from 8 August 2018 due to unusually high rainfall during the monsoon season. The flood resulted in over 483 deaths and 14 missing. The floods also had adverse impacts on properties and structures.

2 Literature Review

Shaikh et al. [1] created empirical equations to gauge the disintegration rate of compacted unsaturated montmorillonite clay. These empirical equations are a function of the sodium adsorption ratio and tractive stress. Wan and Fell [2] introduced an empirical equation to measure the erosion by presenting the term erosion rate index, which estimates the rate of erosion, with the assistance of tests like slot erosion test and hole erosion tests, developed by the authors. It was also shown that the rate of erosion is dependent on the soil fines and clay-sized content, plasticity and dispersivity, compaction water content, density, degree of saturation, clay mineralogy and possibly the presence of cementing materials such as iron oxides. Indraratna et al. [3] conducted erosion tests by utilizing a "Process Simulation Apparatus for Internal Crack Erosion" (PSAICE). To ceaselessly gauge the erosion rate, an in-line process turbidity metre with an overall range of 0–3500 NTU was fixed near the downstream side of the soil example to constantly screen the effluent turbidity at the time of erosion test. The turbidity values were then used with the relationship between the concentration of solids (kg/m^3) and turbidity (NTU) to calculate the erosion rate. The effluent was weighed with an electronic balance for continuous flow rate measurement. An empirical equation was then established to evaluate the erosion rate of chemically stabilized soils. As indicated by Indraratna et al. [4], the expression for the rate of erosion of silty sand is based on the principle of conservation of energy. The authors inferred that the rate of erosion can be found out if the packing arrangements of soil particles in compacted samples, shear characteristics, mean flow velocity, mean particle size and the specific gravity of the soil are known.

3 Methodology

The proposed methodology for the present study is shown in Fig. 1.

3.1 Test Soil

Laterite soil is one of the major types of soil found in Kerala, and most of the slopes and embankments consist of this soil. Moreover, lateritic slopes and embankments were severely affected during the 2018 Kerala floods. So, the type of soil considered for the erodibility study is the laterite soil, and it is collected from Balaramapuram in Trivandrum district, Kerala. Laterite soil is rich in aluminium and iron content. Due to the presence of high iron oxide content, almost all the laterites are red in colour. Table 1 shows the properties of the laterite soil collected for the study. It is observed that the soil has no gravel-sized particles, and the plasticity of the soil is low. The optimum moisture content and maximum dry density were found to be 18% and 16.75 kN/m^3, respectively.
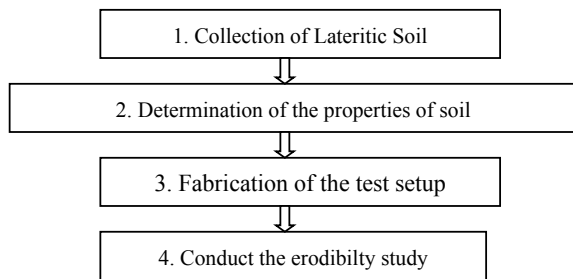
Fig. 1 Proposed methodology

1. Collection of Lateritic Soil

⇩

2. Determination of the properties of soil

⇩

3. Fabrication of the test setup

⇩

4. Conduct the erodibilty study

Table 1 Properties of test soil

Specific Gravity	2.41
Percentage of gravel (%)	0
Percentage of sand (%)	59
Percentage of silt (%)	22
Percentage of clay (%)	19
Liquid limit (%)	34
Plastic limit (%)	26
Plasticity index (%)	8
O. M. C. (%)	18
Maximum dry density (kN/m^3)	16.75

3.2 Test Set-Up

A test set-up is fabricated for conducting the erodibility study of lateritic soils. The test set-up consists of three primary parts, 1.An inlet tank to store water at a head, 2. A test tank where erosion of the lateritic slope takes place and 3. A collecting tank with a sieve to collect the eroded soil. The primary parts of the test set-up are shown in Figs. 2, 3 and 4.

A 0.3 m³ PVC water tank is used as the inlet tank to store the water required for conducting the test. This tank is placed on a movable scaffolding, which enables to conduct the test at different velocities by varying the head difference between water levels in the inlet tank and test tank. A plastic hose connected to tap is used for filling water in the inlet tank. A test tank is made using acrylic glass of dimensions 0.8 m × 0.5 m × 0.6 m. The test tank has three inlet PVC pipes of 25.4 mm diameter and an outlet PVC pipe of 50.8 mm diameter. The test tank and the inlet tank are connected using 25.4 mm diameter PVC pipes.
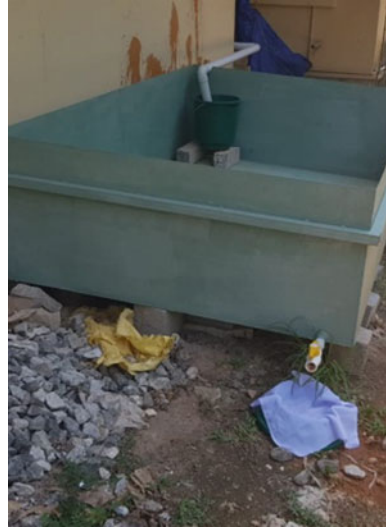
The collecting tank has a dimension of 2.44 m × 1.55 m × 0.62 m. It was made of MS steel sheet and was welded together. The collecting tank has a 25.4 mm valve

Fig. 2 Inlet tank

Fig. 3 Test tank

Fig. 4 Collecting tank

at its one bottom corner. There are two sieves, one inside and the other outside the collecting tank. The sieve inside the tank is placed inside a plastic bucket. On top of the sieve, a polyester cloth is placed, and this is to collect the soil but allows the water to pass. If the eroded soil does not get collected by the sieve inside the tank due to the overflowing of the bucket, it will get collected in the sieve placed outside the tank.

3.3 Test Procedure

The properties of the test soil were determined including the specific gravity, particle size distribution, consistency limits, optimum moisture content, etc. The test soil was filled in the test tank with a slope 2.5:1 maintaining a bulk density of 18 kN/m^3. After filling and compacting the soil in the test tank, experiments were conducted to study the effects of the flood parameters on the quantity of erosion. The flood parameters considered are the duration of the flood, the height of flood and velocity of the flood. Tests are conducted by keeping two parameters as constant while the third parameter is varied. After each experiment, the total weight of eroded soil was measured. Using this, the rate of erosion was computed.

4   Results and Discussion

The various heights of the flood, duration of flood and velocity of flood considered for the study are shown in Table 2.

Each experiment is repeated three times, and the mean of the three rate of erosion was calculated.

4.1   *Height of Flood*

Here, the duration and the velocity of the flood were kept constant, and the height of flood is varied. The duration of the flood was 5 min, and the velocity of the flood was 0.42 m/s. Tests are conducted at three different heights, $h/3$ (0.08 m), 2 $h/3$ (0.16 m) and h (0.24 m). The variation in the rate of erosion with the height of flood is shown in Fig. 5.

The trend shows a nonlinear decrease. This is because the toe failure is predominant at low heights of flood.

Table 2 Flood parameters

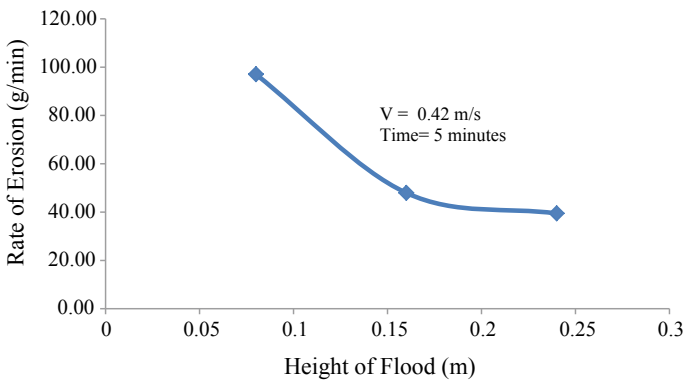| Height of flood (m)	$h/3 = 0.08$	$2\,h/3 = 0.16$	$h = 0.24$
Duration of flood (minutes)	5	10	15
Velocity of flood (m/s)	0.42	0.45	0.47

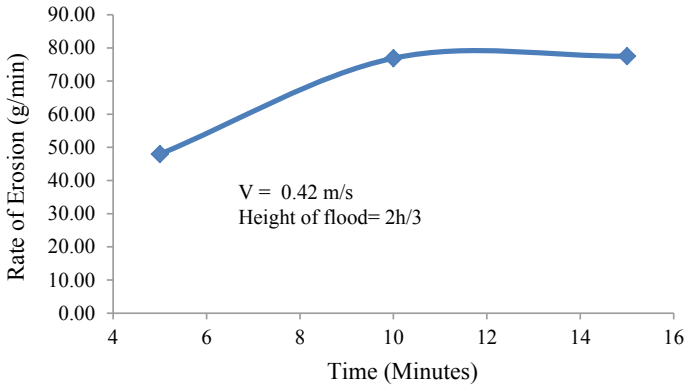**Fig. 5** Variation in the rate of erosion with height of flood

Fig. 6 Variation in the rate of erosion with duration of flood

4.2 Duration of Flood

Here, the velocity and height of the flood were kept constant, and the duration of flood is varied. The flood velocity was 0.42 m/s, and the height of flood was $2h/3 = 0.16$ m. The tests are conducted at three different durations, 5, 10 and 15 min. The variation in the rate of erosion with the duration of flood is shown in Fig. 6.

The trend shows a nonlinear increase. This is because as the duration of flood increases, the amount of eroded soil increases hence the rate of erosion increases.

4.3 Velocity of Flood

Here, the duration and height of the flood were kept constant, and the velocity of the flood is varied. The duration of the flood was 5 min, and the height of flood was $2h/3 = 0.16$ m. The tests are conducted at different velocities, 0.42 m/s, 0.45 m/s and 0.47 m/s. The variation in the rate of erosion with velocity of flood is shown in Fig. 7.

The rate of erosion first increases and then decreases with increase in velocity.

5 Conclusion

Laterite soil is one of the major types of soil found in Kerala, and most of the slopes and embankments consist of this soil. Moreover, lateritic slopes and embankments were severely affected during the 2018 Kerala floods. So, the type of soil considered for the erodibility study is the laterite soil, and it is collected from Balaramapuram
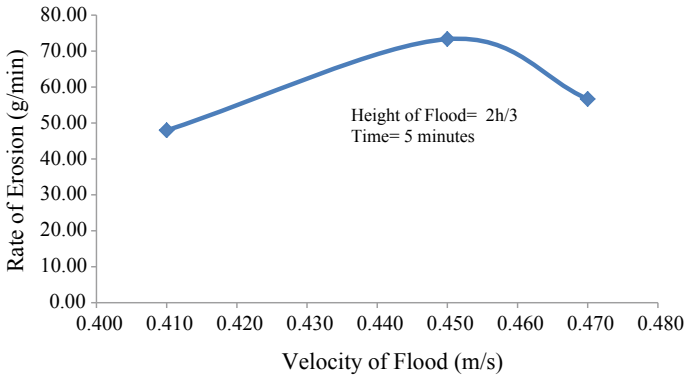
Fig. 7 Variation in the rate of erosion with velocity of flood

in Trivandrum district, Kerala. Experiments were conducted to study the effects of the flood parameters on the quantity of erosion. The flood parameters considered for the experiments are the duration of flood (5, 10 and 15 min), height of flood ($h/3 = 0.08$ m, $2\,h/3 = 0.16$ m and $h = 0.24$ m) and velocity of flood (0.42 m/s, 0.45 m/s and 0.47 m/s). Two parameters are kept constant while the third parameter is varied. After each experiment, the total weight of eroded soil was taken after each experiment. Then the rate of erosion was computed.

The following conclusions were inferred:

1. The flood parameters affecting erodibility of lateritic slopes during floods were identified, namely height of flood, duration of flood and velocity of flood.
2. Rate of erosion decreased by 59.34% when height of flood increased from 0.08 to 0.24 m.
3. Rate of erosion increased by 61.62% when duration of flood increased from 300 to 900 s.
4. Rate of erosion increased by 52.93% when velocity of flood increased from 0.42 to 0.45 m/s.
5. Rate of erosion decreased by 22.73% when velocity of flood increased from 0.45 to 0.47 m/s.

References

1. Shaikh, A., Ruff, J.F., Charlie, W.A., Abt, S.R.: Erosion rate of dispersive and nondispersive clays. Journal of Geotechnical Engineering **114**(5), 589–600 (1988)
2. Wan, C.F., Fell, R.: Investigation of rate of erosion of soils in embankment dams. Journal of Geotechnical and Geoenvironmental Engineering **130**(4), 373–380 (2004)

3. Indraratna, B., Muttuvel, T., Khabbaz, H., Armstrong, R.: Predicting the erosion rate of chemically treated soil using a process simulation apparatus for internal crack erosion. Journal of Geotechnical and Geoenvironmental Engineering **134**(6), 837–844 (2008)
4. Indraratna, B., Muttuvel, T., Khabbaz, H.: Modelling the erosion rate of chemically stabilized soil incorporating tensile force–deformation characteristics. Can. Geotech. J. **46**(1), 57–68 (2009)

Experimental Investigations on Rainfall-Induced Landslides

Ganesh Kumar, Shantanu Sarkar, Mayank Gupta, and Priyanka Devi

Abstract In recent times, the occurrence of natural hazards in India and around the world is increasing day by day. Landslides are one of the most destructive natural phenomena which not only cause extensive damages to the structures but also result in loss of lives. Among various factors, rainfall is one of the most important triggering factors for inducing landslides. In most of the time during rainfall, due to infiltration of water into the soil, the pore water pressure increases which destabilizes the slope resulting in landslide. This paper presents detailed laboratory experimental studies on the behaviour of rainfall-induced landslides. For experimental testing, indigenous test system has been developed at CSIR-CBRI for investigating rainfall-induced landslide. The system comprises a tilted channel and artificial rainfall simulator system. The arrangement of rainfall simulator can able to reproduce landslide triggering under varying intensities of rainfall with uniform rain distribution. For the present study, a model slope was created with the landslide debris soil material brought from the Lesser Himalayan region of Uttarakhand State. After soil characterization, rainfall experiments were conducted on the equivalent slope model using artificial rainfall simulator system. The rainfall experiments were performed with rainfall intensity equivalent to some reported high rainfall intensity experienced in the past in the Himalayan region. During rainfall experiments, the increase in soil moisture and soil movement was monitored continuously. The time at which slope failure initiated was observed and corresponding soil moisture and slope movement pattern was evaluated. Finally, the mechanism of slope failure was analysed and possible slope protection measures were suggested.

Keywords Rainfall-induced landslide · Artificial rainfall simulator · And slope stability

G. Kumar (✉) · S. Sarkar · M. Gupta · P. Devi
Geotechnical Engineering Division, CSIR-Central Building Research Institute, Roorkee 247667, India
e-mail: ganeshkumar@cbri.res.in

1 Introduction

Rainfall-induced landslides pose major problems in steep hilly terrain regions. The reduction in soil strength due to water infiltration destabilizes the slope and creates huge problems to population in the region every year. Although there are number of reasons responsible for creating instability in slopes, many failures occur mainly due to rainfall infiltrating stable slope. The ingress of rainwater infiltrates into the voids creating cracks which propagate further creating failure with continuous rainfall. To validate and examine slope stability, there are softwares available through which the existing slope model has been generated and analysed for estimating factor of safety of the slope. To examine rainfall-induced slope stability analyses, change in groundwater level has to be incorporated in the numerical analyses and factor of safety of the slope was estimated. When the given groundwater configuration simulating actual conditions for the existing slope, the analyses provide accurate prediction. However in most of the cases, the actual groundwater conditions were not considered which results in improper estimation of factor of safety of the slope. Thus, only experimental study provides possible triggering mechanism associated with rainfall-induced landslides.

To simulate rainfall-induced landslide mechanism experimentally, various researchers worked in different landslide conditions and concluded that rainfall-induced landslides occur due to different mechanisms. Johnson and Sitar [1] and Fannin and Jaakkola [2] studied pore water pressure generation in slope under saturated conditions with intense rainfall conditions and modelled groundwater seepage affecting the stability of the slope. Also, several researchers during their experimental study observed slope failure due to rainfall infiltration and without formation of pore water pressure in soil and found slope failure mainly due to loss in unsaturated shear strength [3, 4]. From these studies, researchers found that rainfall-induced landslides are a complex problem involving analysis seepage forces, soil infiltration characteristics under saturated and unsaturated conditions, and shear strength of soil under saturated and unsaturated conditions. Additionally, the researchers found that for simulating rainfall-induced landslides better, the experimental facility requires effective artificial rainfall simulator system [5, 6]. Also, the rainfall simulator system should simulate rainfall conditions equal to natural rainfall in terms of drop size, intensity, and uniformity and should not erodes the soil mass from slope.

The present study involves developing an artificial rainfall simulator system can able to generate varying intensity of rainfall from 30 to 130 mm/h. Then using artificial simulator facility, model slope was prepared with the debris materials collected from Lesser Himalayan region, and the slope was tested for rainfall-induced landslide testing conditions. Using soil moisture sensors, the rise in volumetric water content was monitored continuously and the time of initiation and occurrence of slope failure was identified. Finally, possible slope protection measures for improving stability of slope under rainfall conditions were discussed and presented.
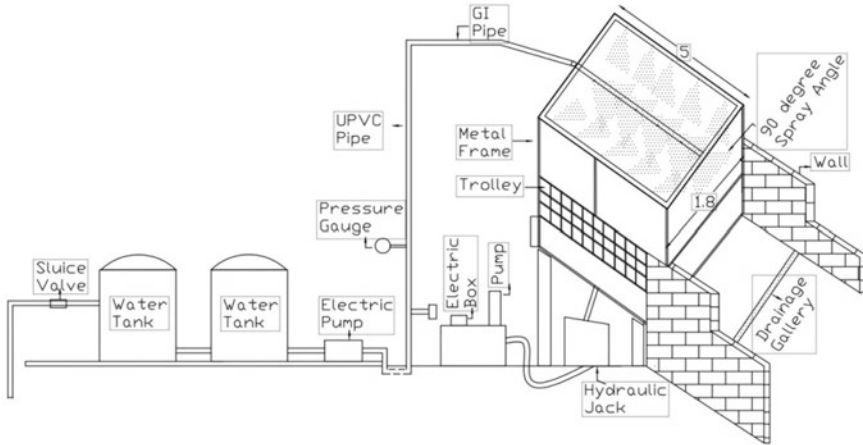
Fig. 1 Artificial rainfall simulator system

2 Development of Rainfall Simulator System

For the development of rainfall simulator system, a pressurized multi-nozzle arrangement has been designed. The nozzle system was designed such that improving infiltration characteristics rather than creating soil erosion. Accordingly, the pattern and location of nozzles has been selected. For the present study, it was planned to develop rainfall intensity of 30–130 mm/h. To achieve this selected intensity, nozzles were placed in square pattern having centre to centre distance of 0.5 m at 1.4 m height above the laboratory test fume. The nozzles were positioned above test fume and calibrated for the selected intensity of rainfall. Using pressure regulator, the water flow into the nozzles was controlled, and accordingly, intensity of rainfall was maintained. To improve maximum uniformity in rainfall distribution, the arrangement of nozzle system was made in three rows with 10 nozzles in each row. Schematic view of entire set-up was shown in Fig. 1.

3 Experimental Studies on Rainfall-Induced Landslide Testing Conditions

Heavy rainfall in slopes increases pore water pressure inside the soil causing reduction in strength and makes the slope unstable. To evaluate the effect of rainfall in slope stability, slope was prepared and tested under artificially simulated rainfall conditions. Tests were conducted on large-scale model fume having dimensions 5 m × 1.5 m × 1.0 m. To reduce sidewall friction effects, the sidewalls of the tank were made with thick perspex material. For experimental study, debris material collected

Table 1 Properties of the debris soil

1	Specific gravity, G	2.7
2	Grain size analysis	Gravel—4% Sand—48% Silt—35% Clay—13%
3	IS classification	SM
4	MDD	19.2 kN/m^3
5	OMC	15%
6	Cohesion, C	9 kPa
7	Angle of internal friction, φ	36°

from Lesser Himalayan region was selected and soil characterization was performed. The properties for the collected debris material were given in Table 1. After soil characterization, soil slope was prepared. For testing, slope having 2 m × 1.5 m × 1 m dimensions was constructed. The crest and toe length was kept as 0.5 m and 0.4 m, respectively, with slope angle 37°. To minimize scaling effects, mass density and geometric size were taken as control variables. The slope was prepared with 19.2 kN/m^3 mass density and with corresponding 13% water content. For slope preparation, the required quantity of soil was calculated and slope was prepared in three layers to achieve maximum uniformity. The slope was then subjected to a rainfall intensity of 100 mm/h. To measure variation in volumetric water content during rainfall, three soil moisture sensors were installed at crest, slope face, and toe position of the slope. The slope was then subjected to a continuous rainfall for 150 min. The slope was monitored continuously to observe variation in volumetric water content during rainfall. The slope and rainfall system also verified to ensure that the generation of raindrop should be sufficient to infiltrate into the prepared soil mass and does not initiate any soil erosion characteristics.

4 Results and Discussions

The observed variation in volumetric water content (VWC) with time was given in Fig. 2. When the slope was subjected to continuous rainfall, slowly the slope gets saturated with the increase in time. The same can be verified from incremental part of volumetric water content in the graph. As expected, the increase in volumetric water content was found to be maximum at crest and toe. Comparatively lesser variation was observed in slope since limited infiltration is possible slope position. After continuous rainfall, due to infiltration the slope gets saturated completely which initiates rise in pore water pressure inside the slope. When there is an increment in pore water pressure, small displacement was observed from crest of the slope. The displacement propagates further which creates instability of the slope. The same was observed after 90 min. After 90 min, cracks get wider at crest of the slope and
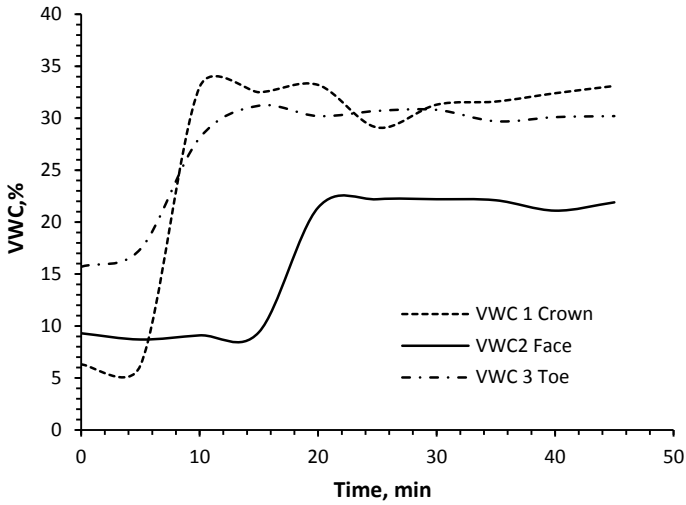
Fig. 2 Variation in volumetric water content with time

travel further to slope region causing shallow type failure. After 140 min, the slope experiences shallow-type slope failure. The failure pattern of the slope mass was shown in Fig. 3. The ingress of water inside the slope suggesting that infiltration plays a major role in affecting stability of the slope. Due to infiltration, the water penetrated into the slope causing water table fluctuation and increases pore water pressure. When

Fig. 3 Slope at failure

pore water pressure increases, the shear strength of the slope is reduced causing slope failures. This was evident from the experimental study. Hence to mitigate rainfall-induced landslide, the slope was protected from rainfall infiltration, i.e., providing geosynthetic reinforcement system. The selected geosynthetic materials should have alternate permeable and impermeable layer such that it prevents water infiltration during rainfall and also relieves generated pore water pressure inside the slope due to variation in groundwater table conditions.

5 Conclusions

Rainfall-induced landslides always pose problems in hilly regions. Hence before implementing stabilization measures, it is important to understand the geologic origin and geotechnical characteristics of the slope. Also, the mechanism of rainfall-induced landslides varies for different regions. Considering the above, an attempt has been made to study the characteristics of rainfall-induced landslides using debris material from Lesser Himalayan region. To simulate rainfall conditions, artificial rainfall simulator has been designed and slope was tested under rainfall conditions. It was observed that infiltration plays a major role affecting shear strength of the soil resulted in destabilizing the slope. Due to water infiltration, the slope gets saturated with continuous rainfall and after saturation, the pore water pressure increases causing instability to the soil due to reduction in soil shear strength. To mitigate this rainfall-induced landslide, the slope should be protected from infiltration especially in crest part. To minimize these infiltrations, providing geosynthetic confinement over the slope covering crest was suggested. Also, the geosynthetic system should consist of both permeable and impermeable membranes such that it protects the slope from infiltration and also minimizes the generation of pore water pressure thus improving the stability of the slope.

References

1. Johnson, K.A., Sitar, N.: Hydrologic conditions leading to debris-flow initiation. Can. Geotech. J. **27**, 789–880 (1990)
2. Fannin, R.J., Jaakkola, J.: Hydrological response of hill slope soils above a debris-slide headscarp. Can. Geotech. J. **36**(6), 1111–1122 (1999)
3. de Campos, L.E.P., Menezes, M.S.S.: A proposed procedure for slope stability analysis in tropical soils. In: Proceedings of 6th International Symposium on Landslides, vol. 2, Christchurch, New Zealand, Balkema, Rotterdam, The Netherlands, pp. 1351–1355 (1991).

4. Rahardjo, H., Fredlund, D.G.: Procedures for slope stability analyses involving unsaturated soils. In: Developments in Deep Foundations and Ground Improvement Schemes, Balkema, Rotterdam, The Netherlands, pp. 33–56 (1995).
5. Fredlund, D.G.: Second Canadian geotechnical colloquium: appropriate concepts and technology for unsaturated soils. Can. Geotech. J. **16**, 121–139 (1979)
6. Rahardjo, H., Lim, T.T., Chang, M.F., Fredlund, D.G.: Shear strength characteristics of a residual soil. Can. Geotech. J. **32**, 60–77 (1995)

Study on Stability Analysis of South Bank of River Brahmaputra and Its Tributaries in the Reaches of Upper Assam

Khagana Buragohain and P. K. Khaund

Abstract This work presents the results of an investigation aimed at evaluating the stability of riverbanks along the Brahmaputra River and some of its Southern tributaries—Burhidihing, Disang, Jhanji, Bhogdoi and Kakodonga. Continuous erosion and failure of the alluvial riverbanks have led to serious loss of land, life and property, and an attempt has been made to address the same. Soil samples were collected from the seven riverbank sites and the geotechnical characteristics of the samples were determined. Stability analysis was carried out based on a Culman-type analysis of steep, cohesive riverbanks proposed by Osman and Thorne (J Hydraul Eng, ASCE 114(2):134–150, [1]). The riverbank stability is checked for bank angles ranging from 60° to 85°. Critical bank angles are determined and the factor of safety (FOS) is computed. Attempts have been made in this work to address the stability of the riverbanks of the proposed sites and thereby help to adopt necessary measures to mitigate such failures.

Keywords Culman-type analysis · Bank material property · Bank stability · Critical bank angles · FOS

1 Introduction

The River Brahmaputra has been the lifeline of North-Eastern India since time immemorial. This mighty river runs through China, India and Bangladesh for 2880 kms. During its course from Kobo to Dhubri, it is joined by about twenty important tributaries on its North bank and fifteen on its South bank. The banks of the river Brahmaputra and its tributaries for the most part are extremely unstable. Several factors contribute toward destabilization of riverbanks, in particular erosion,

K. Buragohain (✉) · P. K. Khaund
Jorhat Engineering College, Jorhat, India
e-mail: khagana.buragohain@gmail.com

P. K. Khaund
e-mail: prasannakhaund@yahoo.co.in

which has been recognized to have a significant contribution toward the instability [2–6]. During its recent history of observations, the Assam valley portion of the Brahmaputra River has lost approximately 7.4% of its land area due to unstable riverbanks. It has caused more major human and economic disasters than the annual flooding prevalent.

In this work, an attempt has been made to identify the unstable riverbanks at the proposed sites of the Brahmaputra River and some of its Southern tributaries by computing the factor of safety (FOS) for the riverbanks. A Culman-type stability analysis of steep, cohesive riverbanks proposed by Osman and Thorne [1] is adopted for the purpose. The analysis has been done with an aim that remedial measures will be provided to mitigate the unstable river banks identified.

2 Materials and Methodology

2.1 Materials Used

The bank soil samples used for the present study were collected from seven locations, i.e., from near the riverbanks of river Brahmaputra (Bogibeel and Nimatighat), river Burhidihing, river Disang, river Jhanji, river Bhogdoi and river Kakodonga for the study of their geotechnical properties.

2.2 Methodology

Grain size analysis of the bank soil samples was performed as per IS: 2720 (Part 4)-1985. Sieve analysis was conducted for gradation of the respective soil samples. Figure 1 shows the gradation curves for different soil samples.

The liquid limit, plastic limit and plasticity index were determined following established standard procedure (IS: 2720, Part V, 1965). Table 1 shows LL, PL and PI of respective riverbank soil samples.

From the gradation curves (% finer vs grain size) and the plasticity chart, the types of soil were determined. The soil samples under study were grouped as silty sand (SM), silt with low compressibility (ML), silt with medium compressibility (MI) and clay with medium compressibility (CI) types.

The different engineering properties viz. water content, bulk unit weight, dry unit weight, shear strength (cohesion and angle of internal friction) and co-efficient of permeability of the soil samples collected from the field were determined in the laboratory to study the stability of the river banks. Experiments performed for the study were standard proctor test, direct shear test and falling head permeability test. All tests performed were as per the respective IS standards. Figure 2 shows the compaction curves of the bank material of sample locations. Figure 3 shows the
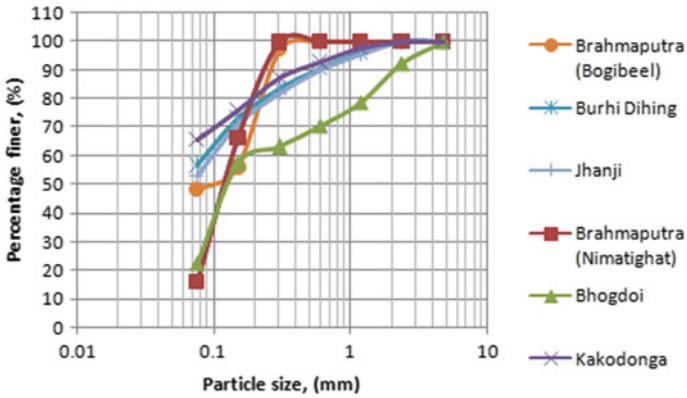
Fig. 1 Gradation curve for different soil samples

Table 1 LL, PL and PI of respective riverbank soil samples

Riverbank	Liquid limit (LL) (%)	Plastic limit (PL) (%)	Plasticity index (PI)
Brahmaputra (Bogibeel)	30.45	25.9	4.55
Burhidihing	32	24	8
Disang	36.9	25	13.18
Jhanji	34	25	9
Brahmaputra (Nimatighat)	31	26.2	4.8
Bhogdoi	23.17	18	5.17
Kakodonga	43	20.5	22.5
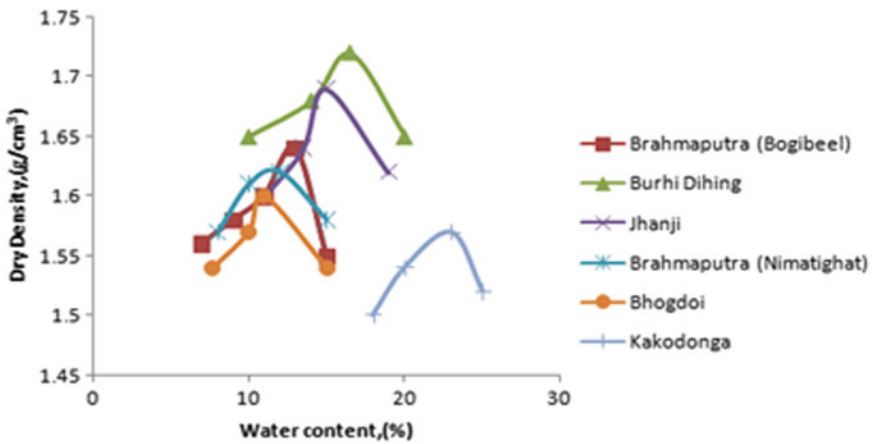
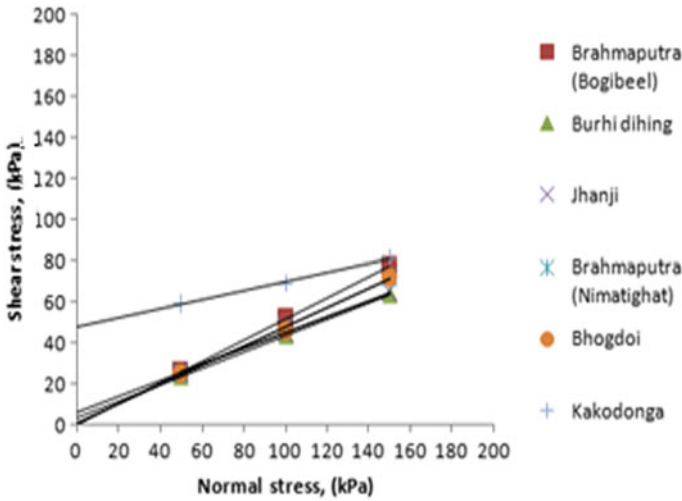**Fig. 2** Compaction curves of the bank material of sample locations

Fig. 3 Shear strength parameters (C and φ) of the bank material of sample locations

shear strength parameters (C and φ) of the bank material of sample locations. The engineering properties of the bank material of sample locations are tabulated in Table 2.

For the bank stability analysis, a Culman-type stability analysis of steep, cohesive riverbanks [1, 7, 8] is adopted. Instability of cohesive riverbanks due to bed degradation and lateral erosion is analyzed herein. These are the two processes that most commonly cause bank instability. The stability of the bank depends on the soil properties and bank geometry. The stability relations developed here on the basis of these

Table 2 Engineering properties of the bank material of sample locations

Riverbank	Water content (w) (%)	Maximum dry density, γ_d (g/cc)	Optimum moisture content, Omc (%)	Bulk unit weight, γ_t (g/cc)	Permeability K, cm/s
Burhidihing	34	1.72	16.5	1.84	6.93×10^{-5}
Disang	38	1.68	17	1.85	1.78×10^{-7}
Jhanji	36.54	1.69	15	1.84	4.28×10^{-6}
Kakodonga	45.54	1.575	23	1.83	2.56×10^{-8}
Brahmaputra (Bogibeel)	32.99	1.64	13	1.744	1.23×10^{-4}
Brahmaputra (Nimatighat)	33.54	1.62	12	1.73	2.4×10^{-4}
Bhogdoi	25.71	1.60	11	1.71	1.60×10^{-3}

parameters can be used to predict the stability of the banks due to bed degradation, lateral erosion or a combination of both these processes.

Figure 4a shows the geometry of a steep riverbank. Figure 4b shows the geometry after erosion. ΔZ is the degradation depth, H_0 is the initial bank height above the bed, and $H^{/}$ is the bank height above point B in Fig. 4b. The term i is the initial bank angle, β is the angle that the failure plane makes with the horizontal, y is the depth of tension cracking and H is the bank height above the riverbed. The terms $C^{/}$, γ and $\varphi^{/}$ are the effective cohesion, specific weight and the effective angle of friction, respectively.

In this analysis to achieve acceptable results, a few conditions have been considered and assumed for the present study. The soil mass is considered relatively homogeneous and isotropic in nature, so that average soil properties can be applied. The failure surface passes through the toe of the bank. Other types of failure are not
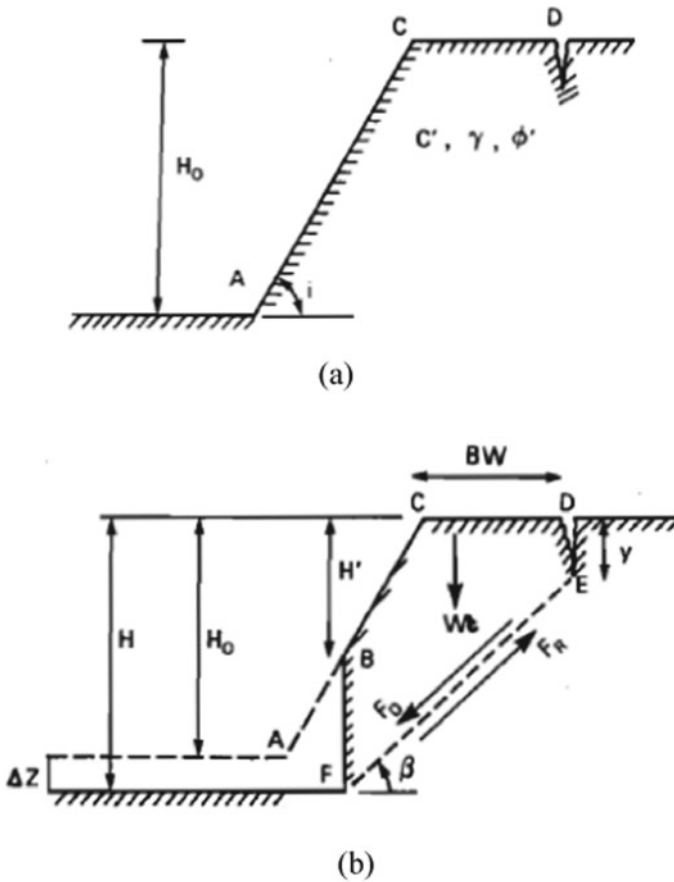

(a)

(b)

Fig. 4 a Riverbank before erosion; **b** riverbank after erosion. (Osman and Thorne [1])

considered in the analysis since toe failures are most commonly observed. Factors such as vegetation density and type, water table, surface runoff and seepage need not be considered directly in the analysis, although these factors may be important at particular locations and might be accounted for by modifying the analysis. Stability relations are developed herein only for steep banks and has been checked for bank angles ranging from 60° to 85°. The soil samples are collected under submerged condition thereby C and φ are taken as effective cohesion and effective angle of internal friction, respectively. The degradation depth, i.e., ΔZ is taken based on field measurements and data collected from Water Resource Department, Govt. of Assam. For the depth of tension cracking, $y = K \times H$, K is taken based on the angle of internal friction obtained for the different bank soil samples. The factor of safety (FOS) is defined as

$$\mathbf{FOS} = \frac{\text{Resisting force}}{\text{Driving force}} = \frac{F_{\mathrm{R}}}{F_{\mathrm{D}}} \tag{1}$$

The resisting force (F_{R}) is proportional to the effective cohesion $C^{/}$ and angle of friction, $\varphi^{/}$, and is defined as:

$$F_{\mathrm{R}} = C^{/}\mathbf{FE} + \mathbf{N}\tan\phi^{/} \tag{2}$$

where N = component of the weight, W_{t}, normal to the failure surface = $W_{\mathrm{t}}\cos\beta$; and FE = length of the failure surface = $(H - y)/\sin\beta$.

Hence,

$$F_{\mathrm{R}} = \frac{(H - y)C^{/}}{\sin\beta} + W_{\mathrm{t}}\cos\beta\tan\emptyset^{/} \tag{3}$$

The driving force, F_{D}, is given by

$$F_{\mathrm{D}} = W_{\mathrm{t}}\sin\beta \tag{4}$$

where W_{t} = weight of the failure block, given by

$$W_{\mathrm{t}} = \frac{\gamma}{2}\left(\frac{H^2 - y^2}{\tan\beta} - \frac{H^{/2}}{\tan i}\right) \tag{5}$$

Hence,

$$F_{\mathrm{D}} = \frac{\gamma}{2}\left(\frac{H^2 - y^2}{\tan\beta} - \frac{H^{/2}}{\tan i}\right)\sin\beta \tag{6}$$

Failure plane angle,

Table 3 Parameters considered for checking the stability of riverbank

Riverbank	Degradation depth, ΔZ, (m)	Tension crack depth, y (m)	Cohesion, C (kN/m²)	Angle of internal friction, φ
Brahmaputra (Bogibeel) (SM)	0.35	1.35	7.5	32°
Kakodonga (CI)	0.15	1.29	48	20°
Brahmaputra (Nimatighat) (SM)	0.3	1.29	6.5	32.23°
Bhogdoi (SM)	0.15	0.85	7.8	31°
Burhidihing (ML)	0.25	1.16	10	24.23°
Jhanji (ML)	0.15	1.14	9.9	23°
Disang (MI)	0.20	1.22	10.5	22°

$$\beta = \frac{1}{2}\left\{ tan^{-1}\left[\left(\frac{H}{H^{/}}\right)^{2}\left(1 - K^{2}\right)\tan i \right] + \varphi \right\} \tag{7}$$

If FOS computed is less than 1, the bank slope is considered to be unstable, and if greater than 1, the bank slope is considered to be stable. If FOS = 1, then the bank slope is considered to be critical. Table 3 shows the parameters considered for checking the riverbank stability. Table 4 shows the computation of FOS for different bank angles of respective riverbanks.

3 Results and Discussion

The bank stability analysis has been done by determining the driving force and resisting force based on the bank material properties of the riverbank soil samples and bank geometry. Stability has been checked for bank angles ranging from 60° to 85°. It is seen from the analysis carried out that an increase in bank height, degradation depth and tension crack depth causes an increase in the driving force. Failure plane angles have been determined for each bank angle for the analysis and it is seen that it increases as the bank becomes steeper. Critical bank angles have also been determined for different riverbanks based on the FOS obtained. It is seen from Figs. 5 and 6. that FOS decreases as bank becomes steeper. The Brahmaputra (Nimatighat) riverbank (SM) is found to be the least stable (Fig. 5) with Kakodonga riverbank (CI) being the most stable (Fig. 6). The SM riverbank is found to be stable for a critical bank angle (FOS = 1) of 72° beyond which the bank becomes unstable. The CI riverbank is found to remain stable even at an angle of 90°. This can be attributed to the fact that clayey soils have cohesion in them, thus enabling them to even stand laterally unsupported to a particular depth. The Brahmaputra (Bogibeel) and Bhogdoi

Table 4 Computation of FOS for different bank angles of respective riverbanks

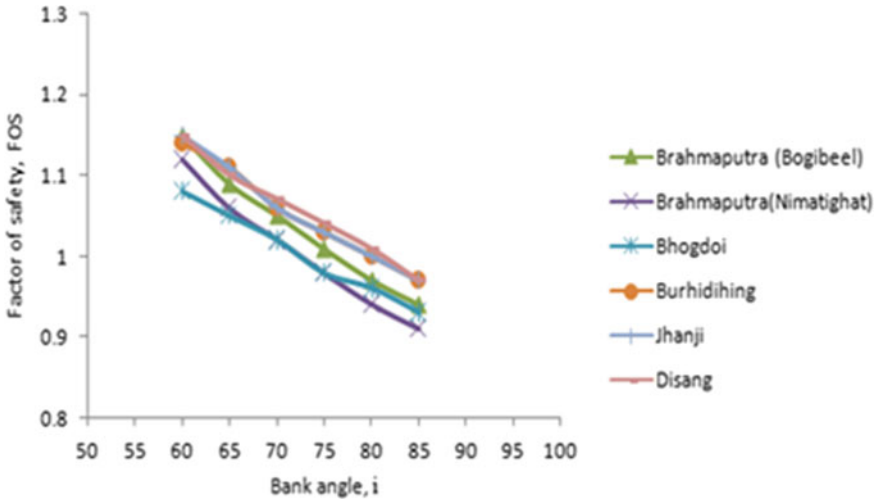| Riverbank	Bank angle, i	Bank height, H_0, (m)	Critical bank angle, i_{cr}	Failure plane angle, β	FOS
Brahmaputra (Bogibeel) (SM)	60°	4	76.12°	54.44°	1.15
	65°			55.30°	1.09
	70°			56.11°	1.05
	75°			56.87°	1.01
	80°			57.89°	0.97
	85°			58.30°	0.94
Kakodonga (CI)	60°	2.5	–	49.62°	3.84
	65°			50.64°	3.70
	70°			51.58°	3.57
	75°			52.48°	3.45
	80°			53.34°	3.34
	85°			54.18°	3.24
Brahmaputra (Nimatighat) (SM)	60°	4	72°	54.99°	1.12
	65°			55.85°	1.06
	70°			56.64°	1.02
	75°			57.39°	0.98
	80°			58.11	0.94
	85°			58.81	0.91
Bhogdoi (SM)	60°	2.5	73.44°	55.93°	1.08
	65°			56.80	1.05
	70°			57.61°	1.02
	75°			58.37	0.98
	80°			59.09	0.96
	85°			59.80	0.93
Burhidihing (ML)	60°	2.5	80°	52.14°	1.14
	65°			53.09°	1.11
	70°			53.96°	1.06
	75°			54.79°	1.03
	80°			55.58°	1.00
	85°			56.35°	0.97
Jhanji (ML)	60°	2.5	80°	51.44°	1.15
	65°			52.39°	1.11
	70°			53.29°	1.06
	75°			54.13°	1.03
	80°			54.94°	1.00
	85°			55.72°	0.97
Disang (MI)	60°	2.5	81°	50.87°	1.15
	65°			51.84°	1.10
	70°			52.75°	1.07
	75°			53.59°	1.04
	80°			54.42°	1.01
	85°			55.21°	0.97

Fig. 5 Stability graph of respective riverbanks
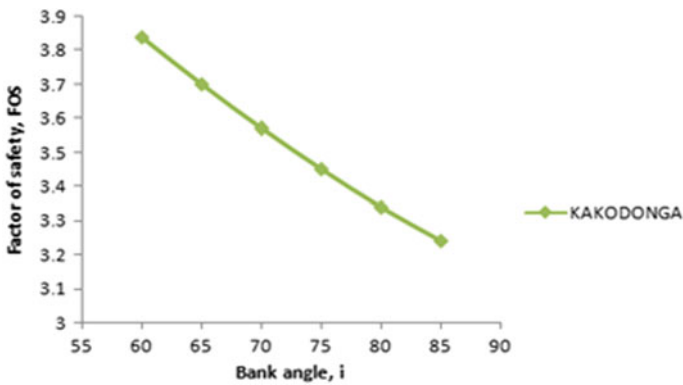

Fig. 6 Stability graph of Kakodonga riverbank

riverbank composed of SM soil is found to be stable for a critical bank angle of 76.12° and 73.44°. Similarly, the Burhidihing and Jhanji riverbank composed of ML soil is found to be stable for a critical bank angle of 80°. The Disang riverbank composed of MI soil is found to be stable for a critical bank angle of 81°.

4 Conclusion

The geotechnical properties of the bank soil samples and bank stability analysis along the Brahmaputra River and its tributaries have provided valuable information

in relation to instability of riverbanks. Almost all the riverbanks under this study were found to be constituted of SM, ML and MI soils having low plasticity index (PI) and low cohesion value making it erodible except the sample of Kakodonga riverbank (CI) which was found to be more cohesive having a plasticity index (PI) >15. The permeability of the bank soil samples was also found to be very low. The bank stability analysis carried out based on Culman's method showed that the Brahmaputra (Nimatighat) riverbank composed of SM soil was the least stable with Kakodonga riverbank (CI) the most stable. The riverbank (SM) was found to be stable for a critical bank angle (FOS = 1) of 72° beyond which the bank became unstable. The riverbank (CI) was found to remain stable even at an angle of 90°. This could be attributed to the fact that clayey soils have cohesion in them thus enabling them to even stand laterally unsupported to a particular depth. A much more promising and accurate result can be obtained by adopting the FEM methods. In FEM methods, the FOS for critical bank angle is automatically obtained, i.e., trial-and-error calculations are not required to find out the critical bank angle because the failure occurs through the zone of weakest material properties, and automatically, the critical bank angle is determined. Also, displacements, stress and strains at various nodes in the slope domain are obtainable from FEM method. The technique also makes it possible to visualize the development of failure mechanisms. Due to their being limited publications of adopting FEM methods in terms of dealing with stability analysis of riverbanks, they have not received widespread acceptance among Geotechnical Engineers. The stability of riverbanks is a multifaceted issue, and thereby, it is expected that this type of integrated study along with other geomorphic studies will help to allocate necessary base line information relating to instability of riverbanks. Also, the problem of unstable riverbank slopes can be mitigated by (1) strengthening the bank: Riverbank riprap and retaining walls, bioengineering and vegetation, (2) reducing hydrodynamic force: Flow control structure. Such mitigation measures to check and control the unhindered loss of land, life and property due to riverbank erosion can be undertaken.

References

1. Osman, A.M., Thorne, C.R.: Riverbank stability analysis. 1: theory. J. Hydraul. Eng., ASCE, **114**(2), 134–150 (1988)
2. Darby, S.E., Thorne, C.R.: Numerical simulation of widening and bed deformation of straight sand-bed rivers. II: model evaluation. J. Hydraul. Eng. **122**(4), 194–202 (1996)
3. Goodson, J.M., Gurnell, A.M., Angold, P.G., Morrissey, I.P.: Riparian seed banks along the lowerRiver Dove UK—their structure and ecological implications. Geomorphology **47**, 45–60 (2002)
4. Hooke, J.M.: Magnitude and distribution of rates of river bank erosion. Earth Surf. Process. Landf. **5**, 143–157 (1980)
5. Millar, R.G.: Influence of bank vegetation on alluvial channel patterns. Water Resour. Res. **36**(4), 1109–1118 (2000)
6. Millar, R.G., Quick, M.C.: Effect of bank stability on geometry of gravel rivers. J. Hydraul. Eng., ASCE **119**(12), 1343–1363 (1993)

7. Ponce, V.M.: Generalized stability analysis of channel banks. J. Irrig. Drainage Div., ASCE, **104**(4), 343–350 (1978)
8. Thorne, C.R., Murphey, J.B., Little, W.C.: Bank Stability and Bank Material Properties in the Bluffline Streams of Northwest Mississippi. Appendix D. Report to the U.S. Army Corps of Engineers, Vicksburg District Office, on Stream Channel Stability, 258 pp (1981)

Analysis of Rainfall-Induced Shallow Slope Failure

Tehseena Ali, Himanshu Rana, and G. L. Sivakumar Babu

Abstract Rainfall-induced shallow slope failure has proved to be disastrous in many parts of the world. Majority of slope failures pose a significant risk to infrastructure and public-safety largely due to rainfall-induced slope failures. The stability analysis of slope generally seeks to understand the cause of the slope failure. The penetrating water reduces matric suction within the soil thereby reducing the shear strength of the soil slopes. In this direction, this paper attempted to analyze the slope behavior under different rainfall intensities and at slope angles. A series of numerical analysis was conducted under a fully coupled flow deformation in PLAXIS finite element modeling code. The numerical trials to check the stability of slope were performed under two dissimilar states, (1) rainfall of certain intensity was applied to the slope for a period of 24 h, and (2) the slope stability was analyzed using soil nailing technique. Different rainfall intensities were applied to evaluate the maximum deformation and variation of pore-water pressure of the shallow slope. Results showed that with increasing rainfall duration, slope deformation increased thereby making the slope unstable. In addition, it is observed that the horizontal deformation in case of the reinforced slope gets reduced, hence increasing slope stability.

Keywords Rainfall-induced slope failure · PLAXIS · Coupled flow · Soil nailing · Grouted nails

1 Introduction

Kashmir often experiences precipitation-triggered landslides on national highway NH-44, which is the lifeline of Kashmir valley as well as Leh-Ladakh area. These landslides result in the closure of the highway for the most part of the year, thus considerably affecting the normal life of people. At soil-atmosphere interface, the flux boundary conditions (i.e., infiltration and evaporation) directly affect the characteristics of major parameters of slope stability like matric suction, the flow of water,

T. Ali (✉) · H. Rana · G. L. S. Babu
IISc Bangalore, Bengaluru 560012, India
e-mail: tehseena.ali0578@gmail.com

and strength of the soil. The rise of water pressure and groundwater level and reduction in matric suction during rainy seasons results in more frequent slope failures. Cai and Ugai [1] concluded that hydraulic characteristics of soil, initial volumetric moisture content, the intensity of rainfall, and duration of rainfall significantly affect the water pressure in slopes which in turn results in instability of slope during rainfall. It was deduced from the analysis done by Zhang et al. [2] that rainfall intensity was the main parameter influencing the matric suction under steady-state conditions, whereas in case of transient flow conditions, water storage function and saturated permeability along with rainfall infiltration affect the profile of matric suction. An analytical formulation was used by Collins et al. [3] which verified that positive pore-water pressure gets developed during high infiltration rates in coarse-grained soils and therefore seepage forces lead to the failure in the slope. Whereas, in the case of fine-grained soils with low infiltration rates, loss of suction occurs which leads to a reduction in shear strength and thus the failure of slope.

Understanding the precipitation-initiated slope failure problem requires mechanical modeling and flow simulation, particularly in an unsaturated groundwater flow condition. A common theory related to groundwater flow and mechanical deformation was previously embraced for different numerical examinations. In such theories, as presented by Rahimi et al. [4], the flow field of groundwater was decoupled from the field of mechanical deformation. However, the interaction between the hydraulic field and mechanical field is the basic reason of rainfall-induced slope failures, and thus, a strong tool is required to coordinate a progression of numerical trials for the study of such problems. These problems can be more precisely simulated by coupling the hydrological-mechanical behavior as done by Chinkulkijniwat et al. [5]. A series of parametric studies were performed by Yubonchit et al. [6], and the results demonstrated that slope failure may occur during infiltration stage or rising water table stage and depends on the infiltration capacity at saturated state. At saturated state, if infiltration capacity is higher than rainfall intensity, the slope is steady due to residual matric suction throughout the infiltration stage and may fail during rising water table stage. Whereas, if rainfall intensity exceeds the infiltration capacity at the saturated state, matric suction completely vanishes throughout the infiltration stage, and consequently more chances of the slope failure during the infiltration stage.

Among several slope stabilization techniques, soil nailing is an economical and straightforward remedial measure. The soil slopes that are unstable in nature are being treated by soil nailing; existing slopes are particularly being reinforced using this technique. The essential idea of soil nailing includes raising shear strength of the in situ soil and restricting its deformation by placing reinforcing components which are moderately slender and are spaced close to each other, thereby creating a rational gravity structure. Limit equilibrium method (LEM) and several working stress design methods are among the different soil nailing design methods. The tensile forces that are resisting in nature get developed in the inclusions and are passed on through friction mobilized at the soil/nail interfaces into the soil thereby, restricting the deformation of soil and limiting failure during excavation as discussed by Luo et al. [7]. Yuan et al. and Babu and Singh [8, 9] draw a conclusion that soil and nail parameters are vulnerable in nature as a result of which there are still the chances of

failure, therefore, in order to assess the stability a helpful probability method should be proposed and applied.

The main objective of the current study is to examine the slope behavior under different rainfall intensities and to check the response of soil nails in case of the reinforced slope. The analysis was conducted with shallow slope (unreinforced and reinforced) under finite element conditions. A few numerical examinations were performed to analyze the maximum deformation, variation of pore-water pressure, and development of axial forces in soil nails. In case of the nailed slope, axial force plays the main part in stabilizing the slope than bending and shear force therefore; only axial force is considered in the analysis.

2 Methodology

A finite element modeling code PLAXIS [10], with fully coupled flow-deformation, was used here for the analysis. In association with the unsaturated conditions, shear strength of soil was stated using the Mohr–Coulomb failure criterion and bishop's effective stress concept as expressed in Eq. 1. In order to simulate transient flow through unsaturated soil, Richard's Equation [11] was used as the hydrological process.

$$\tau = c' + (\sigma_n - u_a)\tan\phi' + \mathcal{X}(u_a - u_w)\tan\phi' \tag{1}$$

where τ = shear strength of unsaturated soil; σ_n = total normal stress; u_a and u_w are pore air pressure and pore-water pressure, respectively; $(\sigma_n - u_a)$ = net normal stress; $(u_a - u_w)$ = matric suction; c' = effective cohesion; ϕ' = internal soil friction angle; and $\mathcal{X}$ = scalar multiplier.

In the case of unsaturated zones, the permeability is depicted by the soil water characteristics curve (SWCCs). The relation between pressure head and moisture content is termed as SWC. Van Genuchten model and van Genuchten-Mualem model explain SWC, and the permeability function, respectively. Equations (2) and (3) present the van Genuchten model and van Genuchten-Mualem model, respectively:

$$\theta_e = \frac{\theta_w - \theta_{res}}{\theta_{sat} - \theta_{res}} = \left[\frac{1}{1 + \{\alpha(u_a - u_w)\}^n}\right]^{1-1/n} \tag{2}$$

$$k(h) = k_{sat} \frac{\left[1 - \{\alpha(u_a - u_w)\}^{n-1}\left[1 + \{\alpha(u_a - u_w)\}^n\right]^{1/n-1}\right]^2}{\left[1 + \{\alpha(u_a - u_w)\}^n\right]^{1/2-n/2}}. \tag{3}$$

where θ_w, θ_{res}, and θ_{sat} denote volumetric moisture content, residual volumetric moisture content, and saturated volumetric moisture content, respectively. Saturated permeability of soil is represented by k_{sat}, and α and n are the fitting parameters. The parameters required in PLAXIS to carry out an analysis for slopes exposed to rainfall

infiltration include strength parameters (c', φ) and hydraulic-related parameters (a, n, k_{sat}).

In PLAXIS, a plane-strain condition was used to model the soil nails. In order to sulate soil nails, plate structural elements can be used as they account for the bending stress [12]. To simulate the plate elements, flexural rigidity (bending stiffness) EI and the axial stiffness EA are main input parameters. For the proper simulation of circular soil nails as rectangular plates, equivalent axial and bending stiffness's are used. To consider, the role of elastic stiffness's of grout envelope and reinforcement bar, equivalent modulus of elasticity E_{eq} was used and was determined as:

$$E_{eq} = E_n \left(\frac{A_n}{A} \right) + E_g \left(\frac{A_g}{A} \right) \tag{4}$$

where E_g, E_n, and E_{eq} are elasticity modulus of grout material, elasticity modulus of a nail, and equivalent elasticity modulus of grouted soil nail, respectively, A_n is the total cross-sectional area and A is the area of grout cover. Knowing horizontal spacing S_h, drill hole diameter D_{DH}, and the equivalent modulus of elasticity (Eq. 4), axial and bending stiffnesses were determined from Eqs. (5) and (6), respectively.

$$\text{Axial stiffness EA[kN/m]} = \frac{E_{eq}}{S_h} \left(\frac{\pi D_{DH}^2}{4} \right) \tag{5}$$

$$\text{Bending stiffness EI[kN/m]} = \frac{E_{eq}}{S_h} \left(\frac{\pi D_{DH}^4}{64} \right) \tag{6}$$

3 Materials and Methods

Sl properties adopted in this study were gathered from the relevant literature on slope failure together with Yubonchit et al. [9]. An elastoplastic model was used for soil with yield criterion of Mohr–Coulomb, and the hydraulic behavior was modeled as a van Ganuchten model. The soil parameters for Mohr–Coulomb comprising strength, hydraulic, and deformation parameters are tabulated in Table 1.

Soil nails in reinforced slope were modeled as plate elements available in PLAXIS. Six rows of soil nails were assigned as shown in Fig. 2 and the length of each nail was 4 m. The vertical spacing for the bottom 4 rows was 2 m and for the top two rows was 3 m. Table 2 gives the parameters adopted for the simulation of soil nails.

As plotted from Eq. 4, with the magnitudes from Table 1, Fig. 1 shows the soil-water characteristic curve (SWC). The parameters like c', φ', α, and η were kept constant with the value of 7 kPa, 36°, 0.16 kPa^{-1}, and 1.56, respectively. A saturated permeability of 1×10^{-5} m/s was used in the examination.

The study was carried out on two different types of slopes: (a) slope without any reinforcement and (b) slope reinforced with soil nails. Three different rainfall

Table 1 Soil parameters adopted for Mohr–Coulomb model

Material property	Parameter	Symbol	Value	Unit
Mechanical	Mechanical model	_	Mohr–Coulomb	
	Material type	_	Undrained A	
	Cohesion	c	7	kPa
	Friction angle	φ	36	Degrees
	Modulus of elasticity	E	30,000	kPa
	Poisson's ratio	υ	0.3	_
Hydraulic	Hydraulic model	_	Van Genuchten	_
	Saturated permeability	k_{sat}		m/s
	H	η	1.56	_
	A	α	0.16	kPa^{-1}
General	Dry unit weight	γ_{unsat}	17	kN/m^3
	Total unit weight	γ_{sat}	17	kN/m^3

Table 2 Parameters adopted for numerical simulations of soil nails

Parameter	Symbol	Value	Unit
Material model	_	Elastic	_
Nailing type	_	Grouted	_
Yield strength of reinforcement	f_y	415	MPa
Nail diameter	D	0.02	m
Drill hole diameter	D_{DH}	0.1	m
Length of nail	L	4	m
Declination w.r.t horizontal	I	15	Degree
Modulus of elasticity of nail	E_n	200	GPa
Modulus of elasticity of grout	E_g	22	GPa
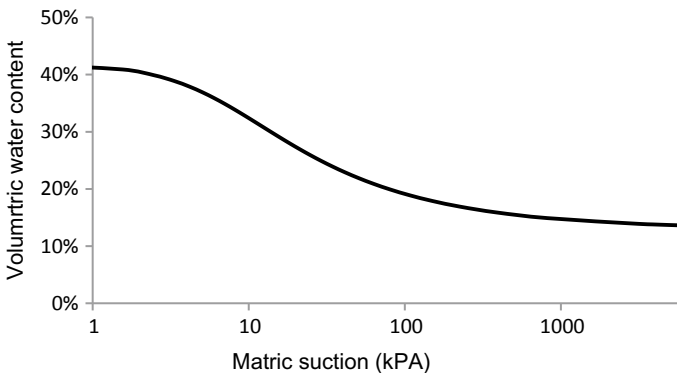
Fig. 1 SWC curve

intensities viz., 24.8, 20, and 13.75 mm/h were applied on the slopes to check the stability and deformation of the slope. The rainfall intensities were derived from the intensity-duration-frequency (IDF) relationship of Srinagar area of Jammu and Kashmir (J&K) with a return period of 1, 10, and 50 years [13]. The simulation consists of 12 cases of a simulation run, six cases for a slope with 60° and 70° each. A rainfall period of 24 h was used in all 12 cases. Out of 12 cases, six cases were conducted on the unreinforced slope and other six on the reinforced slope and for each slope, aforementioned rainfall intensities were assigned.

4   Analysis Setup

A finite element model with two-dimensional plane-strain was arranged to represent a 15 m high slope with an inclination of 60° and 70° to the horizontal. Fifteen noded triangular finite element meshes are used. Slope geometry, fixity, and boundary conditions allotted for the study are shown in Fig. 2. A steady-state flow calculation was performed before assigning desired rainfall intensity. Initially, the pore-water pressure was supposed to vary from −100 to 0 kPa from top of the slope to the bottom of slope, which represents the conditions of ground before the application of rainfall. At the bottom boundary, no lateral and vertical movements were allowed, whereas the only vertical movement was allowed along the right and left boundaries. The preferred intensity of rainfall was applied along the inclined surface CD as boundary flux. Boundaries AB, GH, and AH were defined as impervious boundaries, while, along the side boundaries BC and EF, boundaries were no flux was assigned.
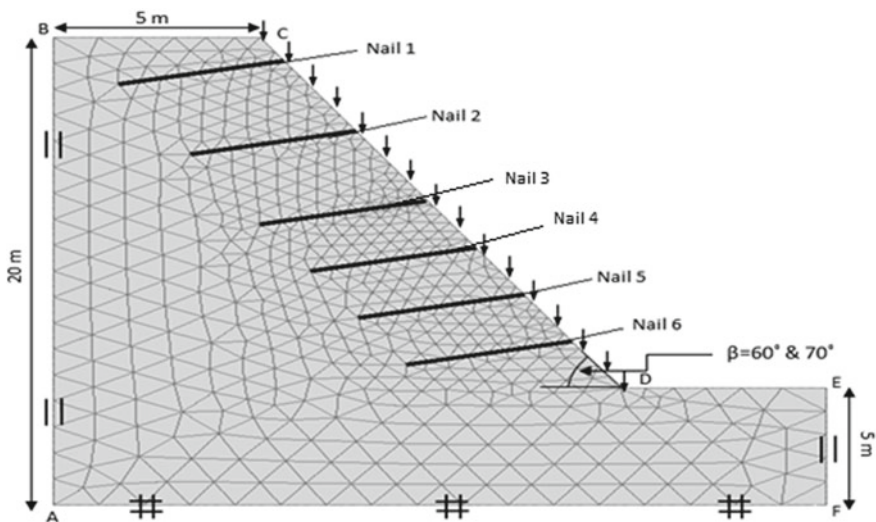
Fig. 2 Slope geometry and boundary conditions

After 2–3 days of drainage of surplus water, there is insignificant free drainage and the remaining water content held in the soil is termed as the water content at field capacity (θ_{fc}). For any soil type which has pore-water pressure of -34 kPa corresponds to θ_{fc} [14]. If no extra water is added for 2–3 days after precipitation, the moisture content may further diminish due to consumption by plant roots and evaporation. Therefore, the value of θ_i is possibly between θ_{fc} and θ_{res}. The pore-water pressure allotted to the model ranging from -100 to 0 kPa presents the range of water content from 19% to 0 as per SWC of the model in Fig. 1.

5 Results and Discussion

Numerical investigation results are displayed and discussed as three perspectives: (1) maximum deformation attribute of slope exposed to specific precipitation, (2) the probable failure mechanism identified with the response of pore-water pressure, and (3) variation of maximum axial forces of different nails with varying rainfall intensity.

5.1 Maximum Deformation Attribute of Slope Exposed to a Specific Precipitation

The comparison of the maximum displacement of the slope with and without soil nail reinforcement against the simulated rainfall duration is demonstrated in Fig. 3. The figure presents the comparison for slopes with two different slope angles ($\beta = 60°$ and $70°$) and for three rainfall intensities (25.83, 20, and 13.75 mm/h). The unreinforced slope with a slope angle of $60°$ and rainfall intensities of 25.83, 20, and 13.75 mm/h failed after 0.2, 0.3, and 0.4 days of rainfall infiltration. While the soil nailed slope with same inclination (i.e., $60°$) and rainfall intensities of 25.83, 20, and 13.75 mm/h had maximum displacements of 10.89, 7.97, and 6.31 mm, respectively, after rainfall duration of 24 h.

In case of the slope with $70°$ slope angle, the failure was observed only after 0.1 days of rainfall duration for all three rainfall intensities. Whereas the maximum displacements of the soil nailed slope with a slope angle of $70°$ were 36.1, 34.9, and 11.8 mm for rainfall intensities of 25.83, 20, and 13.75 mm/h, respectively, and rainfall duration of 24 h. The examination result demonstrated that the deformation of the slope was reduced significantly by the impact of soil nails. The displacement of the slope after the end of the rainfall was restricted as well.
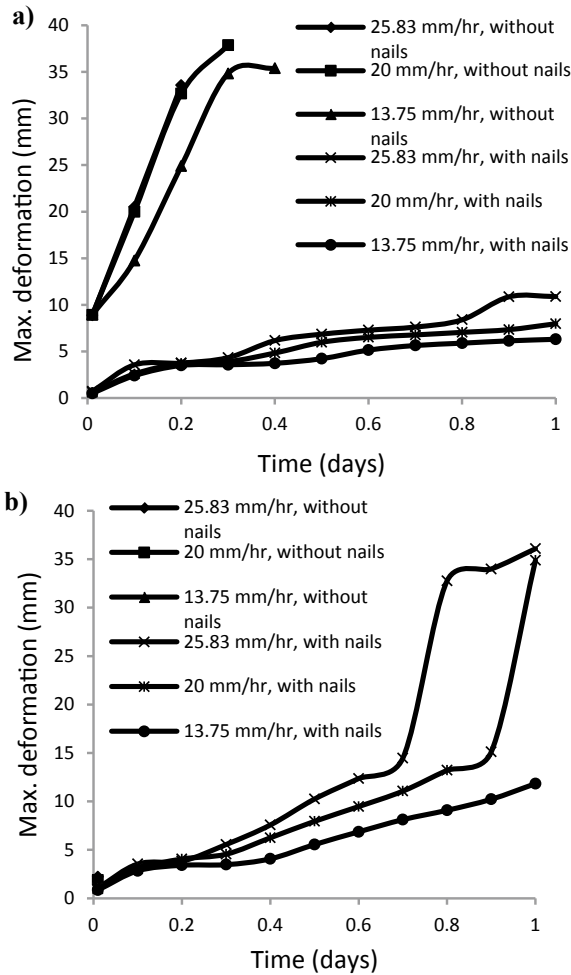
Fig. 3 Deformation attribute of slope (with and without soil nails) exposed to a constant rainfall intensity **a** slope angle 60° and **b** slope angle 70°

5.2 The Possible Failure Mechanism Identified with the Response of Pore-Water Pressure

To study the response of pore-water pressure in the shallow layer, vertical sections of depth 3 meters were selected at the maximum deformation zone for analysis. The pore-water pressure profiles for slopes with slope angle 60° and 70° are shown in Figs. 4 and 5. Two stages can describe the pore-water pressure: a stage of rainfall infiltration and a stage of water table rising. Throughout the infiltration stage, the magnitude of the negative pore-water pressure keeps decreasing from the initial value
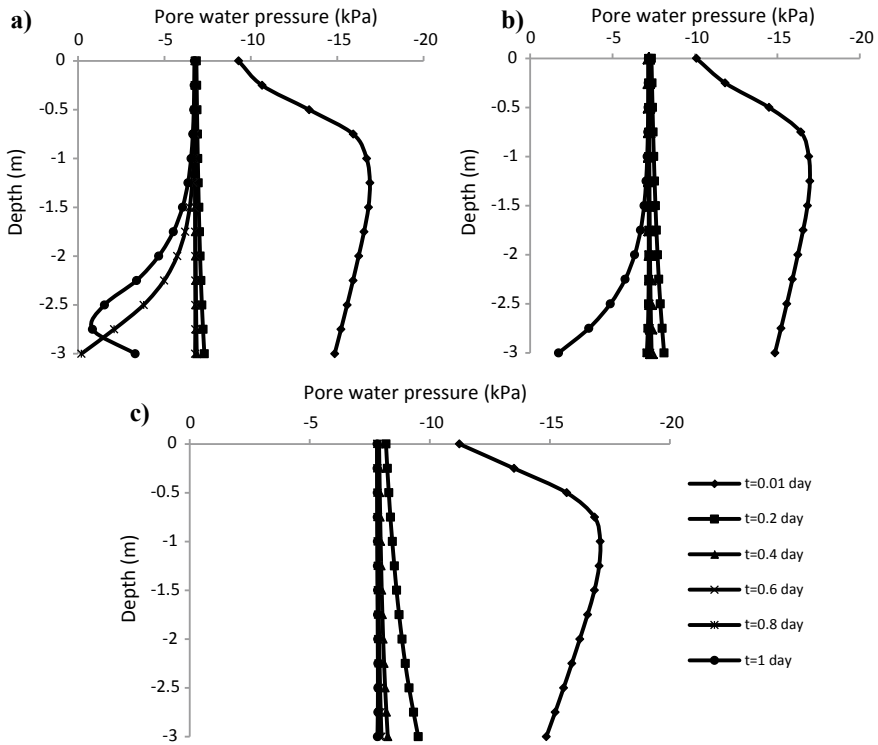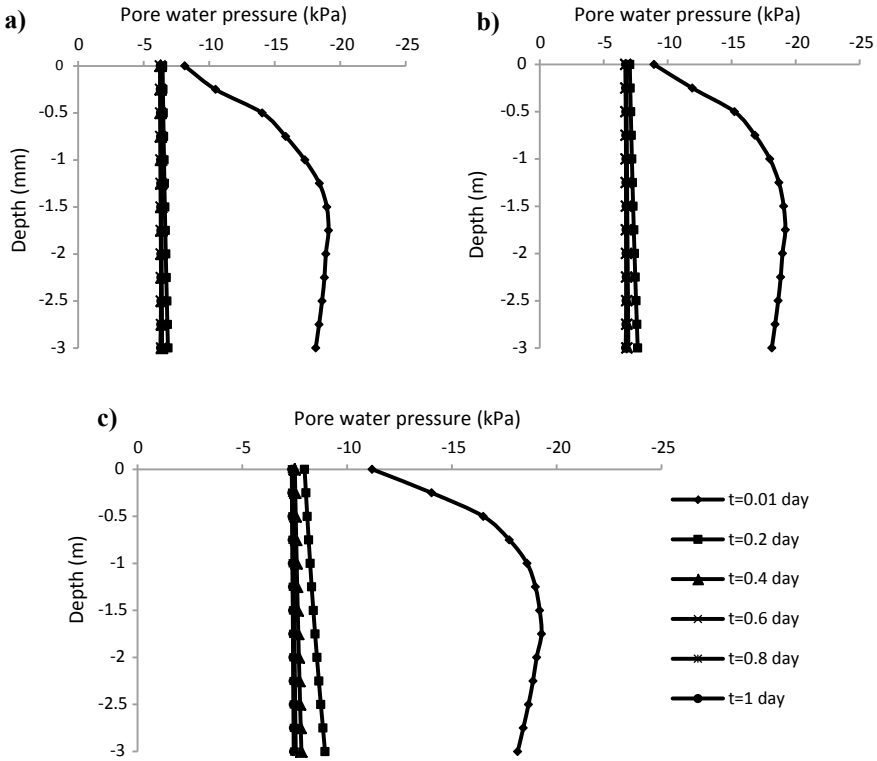
Fig. 4 Development of pore-water pressure profile for the reinforced slope with $\beta = 60°$ for different rainfall intensities **a** $i = 25.83$ mm/h, **b** $i = 20$ mm/h, and **c** $i = 13.75$ mm/h

and achieves a single highest magnitude. Therefore, at any depth, the value of pore-water pressure is this single highest value. Hydraulic properties and flux boundary of the soil effects this constant value of pore-water pressure [6]. At shallow depths, negative pore-water pressure starts to dissipate immediately after the initiation of rainfall.

Figure 4 shows the pore-water pressure profile of reinforced slope with slope angle 60° and rainfall intensities 25.83, 20, 13.75 mm/h. For the rainfall intensity of 25.83 mm/h pore-water pressure ranges from −6.7 kPa to −0.84 kPa, for rainfall intensity of 20 mm/h, it ranges from −7.1 kPa to −1.8 kPa, and for rainfall intensity of 18.75 mm/h, it reaches to a value of −7.8 kPa with depth. Similarly, Fig. 5 presents the change in pore-water pressure for the reinforced slope with slope angle 70°. It is seen that for the rainfall intensity of 25.83 mm/h ranges from −6.3 kPa, for rainfall intensity of 20 mm/h, it ranges from −6.7 kPa, and for rainfall intensity of 18.75 mm/h, it reaches to a value of −7.4 kPa with depth.

Fig. 5 Development of pore-water pressure profile for the reinforced slope with $\beta = 70°$ for different rainfall intensities **a** $i = 25.83$ mm/h, **b** $i = 20$ mm/h and **c** $i = 13.75$ mm/h

5.3   The Variation of Maximum Axial Force of Different Nails with Varying Rainfall Intensity

The development of axial forces in soil nails in case of the reinforced slope was analyzed for all nails at different positions were selected. Nail 1 and 2 were from the upper portion of the slope, Nail 3 and 4 were from the middle portion of the slope, whereas Nail 3 and 4 were from the lower portion of the slope. Figures 6 and 7 show the distribution of maximum axial force in nails for the duration of 24-h rainfall. The positive stress represents the tensile force and the negative stress represents compressive force. As shown in the figures, the maximum axial forces in the Nail 1 were approximate 0 for the slope with $\beta = 60°$ (Fig. 6) and became tensile for higher rainfall intensity for the slope with $\beta = 70°$ (Fig. 7). The maximum axial force in the remaining nails was tensile in nature for both the cases (i.e., $\beta = 60°$ and $70°$) for all rainfall intensities. Axial force for Nail 6 was the largest for all the cases. In the case of the slope with $\beta = 60°$, as depicted in Fig. 6 the axial forces are increasing
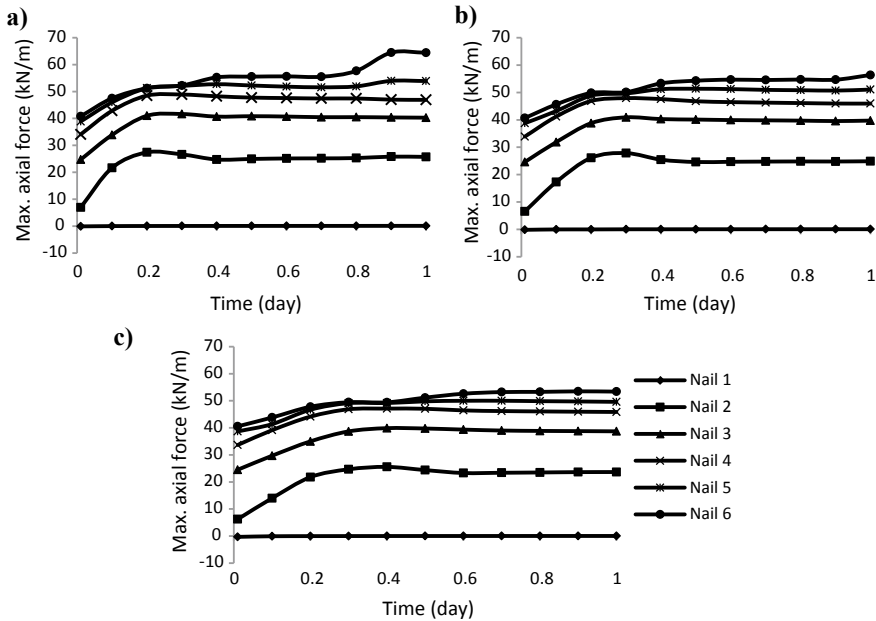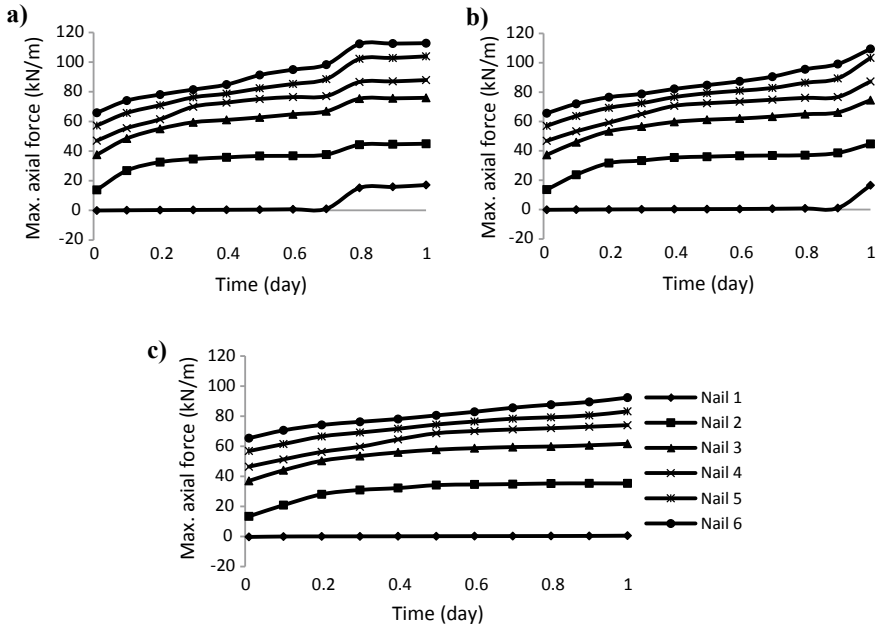
Fig. 6 Variation of axial forces for different nails at different time intervals for slope with $\beta = 60°$ **a** $i = 25.83$ mm/h, **b** $i = 20$ mm/h, and **c** $i = 13.75$ mm/h

at a very low rate and the highest value of Nail 1 after 24 h of rainfall reaches 64.5, 56.4, and 53.4 kN/m for rainfall intensities of 25.83, 20, and 18.75 mm/h.

On the contrary, in case of the slope with $\beta = 70°$ (Fig. 7), the axial forces are increasing at a higher rate compared to former case and the highest values reached for Nail 1 for rainfall intensities 25.83, 20, and 18.75 mm/h are 112.8, 109.4, and 92.4 kN/m, respectively.

The relation between the factor of safety against tensile strength failure (FS_T) and nail number embedded at different depths is shown in Fig. 8. It is depicted from the figure that the factor of safety against tensile strength failure (FS_T) decreases with an increase in the depth of nail embedment from the top of the slope. FS_T being very high for Nail 1, it is excluded from the figure. For $i = 25.83$ mm/h, FS_T for bottom most nail in case of slope with $\beta = 70°$ is 1.15 and with $\beta = 60°$ is 2.02. Therefore, nails at lower portion experience much higher forces compared to the top nails.

6 Conclusions

A series of numerical analysis was conducted under a fully coupled flow-deformation in PLAXIS finite element modeling code. The numerical experiments to check the

Fig. 7 Variation of axial forces for different nails at different time intervals for the slope with $\beta = 70°$ **a** $i = 25.83$ mm/h, **b** $i = 20$ mm/h, and **c** $i = 13.75$ mm/h
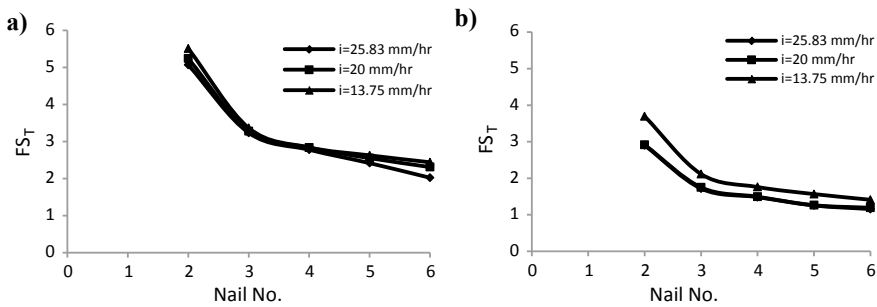
Fig. 8 Factor of safety against nail tensile strength failure (FS$_T$), **a** $\beta = 60°$ and **b** $\beta = 70°$

stability of slope were performed under two states and the conclusions that were drawn from the analysis are as follows:

- The examination results demonstrated that the deformation of the slope was large in case of steeper slope and was significantly reduced by the impact of soil nails. Consequently, a continuous slip surface was developed in case of the unreinforced slope, which may cause a shallow failure.

- After the initiation of rainfall, negative pore-water pressure starts to dissipate at the shallower depths which results in a decrease in stability. Although there was not much change in pore-water pressure profile due to the introduction of soil nails, the continuous slip surface development was prevented in the slope.
- The maximum axial forces for nails were mainly tensile in nature, and for the nails selected in this study, the value was minimum for the nail in the upper portion of slope and highest for the nail in the lower portion. Also, for the steeper slope with higher rainfall intensity, the rate of increase of axial force is high compared to the other case.

References

1. Cai, F., Ugai, K.: Numerical analysis of rainfall effects on slope stability. Int. J. Geomech. **4**, 69–78 (2004). https://doi.org/10.1061/(ASCE)1532-3641(2004)4:2(69)
2. Zhang, L.L., Fredlund, D.G., Zhang, L.M., Tang, W.H.: Numerical study of soil conditions under which matric suction can be maintained. Can. Geotech. J. **41**, 569–582 (2004). https://doi.org/10.1139/t04-006
3. Collins, B.D., Znidarcic, D.: Stability analyses of rainfall induced landslides. J. Geotech. Geoenviron. Eng. **130**, 362–372 (2004). https://doi.org/10.1061/(ASCE)1090-0241(2004)130:4(362)
4. Rahimi, A., Rahardjo, H., Leong, E.-C.: Effect of hydraulic properties of soil on rainfall-induced slope failure. Eng. Geol. **114**, 135–143 (2010). https://doi.org/10.1016/J.ENGGEO.2010.04.010
5. Chinkulkijniwat, A., Horpibulsuk, S., Semprich, S.: Modeling of coupled mechanical-hydrological processes in compressed-air-assisted tunneling in unconsolidated sediments. Transp. Porous Media **108**, 105–129 (2015). https://doi.org/10.1007/s11242-014-0295-6
6. Yubonchit, S., Chinkulkijniwat, A., Horpibulsuk, S., Jothityangkoon, C., Arulrajah, A., Suddeepong, A.: Influence factors involving rainfall-induced shallow slope failure: numerical study. Int. J. Geomech. **17**, 04016158 (2017). https://doi.org/10.1061/(ASCE)GM.1943-5622.0000865
7. Luo, S.Q., Tan, S.A., Yong, K.Y.: Pull-out resistance mechanism of a soil nail reinforcement in dilative soils. Soils Found. **40**, 47–56 (2000). https://doi.org/10.3208/sandf.40.47
8. Yuan, J.-X., Yang, Y., Tham, L.G., Lee, P.K.K., Tsui, Y.: New approach to limit equilibrium and reliability analysis of soil nailed walls. Int. J. Geomech. **3**, 145–151 (2003). https://doi.org/10.1061/(ASCE)1532-3641(2003)3:2(145)
9. Babu, G.L.S., Singh, V.P.: Reliability analysis of soil nail walls. Georisk Assess. Manag. Risk Eng. Syst. Geohazards. **3**, 44–54 (2009). https://doi.org/10.1080/17499510802541425
10. Brinkgreve, R.B.J., Swolf, W.M., Engine, E.: PLAXIS: Users Manual (2010)
11. Richards, L.A.: Capillary conduction of liquids through porous mediums. Physics **1**, 318–333 (1931). https://doi.org/10.1063/1.1745010
12. Babu, G.L.S., Singh, V.P.: Plaxis practice—Stabilization of vertical cut using soil nailing. Plaxis Bull. October, N, 6–9 (2007)
13. Dar, A.Q., Maqbool, H.: Rainfall Intensity-Duration-Frequency Relationship for different regions of Kashmir Valley (J&K) India. In: 3rd International Conference on Science and Management, pp. 651–662, India International Centre, New Delhi (2016)
14. Dingman, S.L.: Physical Hydrology. Prentice Hall, Upper Saddle River, NJ (2002)

Slope Stability Analysis of an Earthen Dam Using GEOSTUDIO 2007 Software

Saurav Shekhar Kar and **L. B. Roy**

Abstract Analysis of an earthen dam, especially its slopes, is very important these days as its failure may cause huge loss of lives and properties. These days numerical models are used to check the stability of an earthen dam. Numerical models simulate all the parameters, which affect the safety of an earthen dam. The most important parameters are properties of the soils used for the construction of an earthen dam. For the numerical modeling in this study, a finite element analysis software is used, i.e. GEOSTUDIO 2007 (SEEP/W and SLOPE/W). The parameters considered in this analysis are the site and its foundation conditions, soil material characteristics and hazard potential associated with the particular site. To find the factor of safety, a numerical model of SLOPE/W and SEEP/W program of GEOSTUDIO software is tested for steady-state condition and sudden drawdown. The Morgenstern-Price method, based on limit equilibrium, which is incorporated in SLOPE/W to analyse the model for four cases, namely earth dam without berm and without a toe drain, earth dam with berm without a toe drain, earth dam without berm with a toe drain and earth dam with berm with a toe drain. The results showed that out of four cases, the best case to improve the factor of safety of the slope is the fourth case, i.e. earth dam with berm with a toe drain.

Keywords Slope stability analysis · Steady-state seepage · Sudden drawdown · Berm · Drained blanket

1 Introduction

The construction of earthen dams has become more common as compared to other type of dams (i.e. concrete dam) in recent days, since earth dams are generally made up of locally available raw soil in their natural state with minimum of processing. The main purpose for this common usage is the construction method, which is based on easy techniques with utilization of cheap raw earth and subsurface materials. The

S. S. Kar (✉) · L. B. Roy
National Institute of Technology Patna, Patna, India
e-mail: kar.sauravshekhar2008@gmail.com

advantages for the construction of earthen dams are that rigorous conditions are not required for the dam foundation, soil is easily available in most parts of the world close to possible dam sites, and easy handling of soil and lesser cost of construction.

In olden days, designing of slopes was based on the experience of geotechnical engineers and design approach was based on prevailing site conditions. This approach of designing slopes has resulted in extensive property damage and occasionally resulted in the huge loss of lives and properties. Nowadays, there is an increased demand for engineering cut and fill slopes in construction projects. The construction of finite height sloped embankments is a common practice in dams, highways and railway projects. The finite element analysis of stability failures and seepage analysis demands increased in order to handle complex problems in the construction field. Embankments of earthen dams must be designed to construct stable slopes against any type of force conditions which develops in the life of the structure. Mostly loading conditions are critical like sudden drawdown and steady seepage which can cause piping through the foundation or within the embankment.

To derive factor of safety, slope stability analysis of the embankment has been carried out for the 14 m height of the homogeneous dam. The analysis has been performed using Mohr-Coulomb failure envelop. There are many methods of analysis such as Method of Slices, Bishop's method, Janbu's method and Morgenstern Method etc. using any of the methods one can determine the stability analysis.

GEOSLOPE is developed by GEO-SLOPE International, Canada, based on the principle of limit equilibrium which incorporates the finite element method, which is developed specially for determining the stability of an embankment. It includes modelling of stability with SLOPE/W, modelling of seepage with SEEP/W, modelling of stress and deformation with SIGMA/W, modelling of dynamic with QUAKE/W, modelling of thermal with TEMP/W, modelling of containment with CTRAN/W and modelling of vadose zone with VADOSE/W. SLOPE/W and SEEP/W have been used with "Morgenstern method" to do the stability analysis. SLOPE/W uses the theory of limit equilibrium of forces and moments to compute the factor of safety against failure. SLOPE/W solves two factor of safety equations; one equation satisfies force equilibrium and the other satisfies moment equilibrium. All the commonly used methods of slices can be visualized as special cases of the General Limit Equilibrium (GLE) solution.

One of the major factors for the failure of earthen dams is the seepage from their body and foundation. In order to prevent the failure of an earthen dam, it is necessary to control the seepage in dams. Therefore, seepage analysis for earthen dam is the main step and one of the major issues that has been considered in the present study and by many researchers. There are many commercially available softwares [1, 2] which provide the facilities of both seepage and stability analyses of an earthen dam. Zomorodian et al. [3] studied the effect of horizontal drains on upstream side of earthen dams during rapid drawdown condition using finite element method and limit equilibrium methods. They determined the quantity of water seepage through the dam using the Seep/w program and factor of safety for the slope stability analysis by using the Slope/w program. Mula and Zhang [4] studied the effect of earthquake vibration on slope stability analysis using Geo-studio and

Plaxis 2D software. The critical slip surface and factor of safety are calculated by using finite element method, limit equilibrium method and Morgenston – Price. They also studied the effect of dam height and its geometry on stability and liquefaction due to earthquake. Kamanbedast and Delvari [5] studied the behaviour of maroon soil dam with various parameters, which is situated at 19 km from North of Bahaman on maroon river. The stability analysis of maroon soil dam has been done using Ansys software and the results were compared with the result obtained from Geo studio Software. Karimi et al. [6] studied the seepage analysis in Ilam earth fill dam using seep/w software. The four mesh sizes, i.e. fine, medium, coarse and unstructured mesh were considered during the study. The results shows that average flow rate of seepage under the different mesh size for Ilam dam equal to 0.836 l/s for the whole length of the dam. Slope/w software is used with different methods such as Bishop, Janbu, ordinary method of slides and Morgenstern method for slope stability analysis. The minimum factor of safety obtained from each of the above method is considered as a factor of safety of the slope. Dodagoudar et al. [7] studied the seepage and stability analyses of an earth dam using finite element method. The seepage analysis is divided into two categories, i.e. steady-state analysis and transient analysis. The study showed that with the increase in the value of young's modulus of core and shell, the maximum crest displacement decreases. Goswami and Borah [8] studied a case of a hydro-electric dam in the north-eastern region of India. The dam is an earth dam and section of the dam has been assumed as per the criteria and analysed using GEOSTUDIO software for the static case. Seepage analysis was conducted using seep/w software for the steady state and transient state. To determine the factor of safety of the upstream and downstream slopes, the slope stability analysis was performed using slope/w software. The slopes of the dam are considered to be reinforced with layers of geotextile. Devi and Anbalagan [9] studied the slope stability analysis of an earthen dams using GEOSTUDIO software. To derive factor of safety, a numerical model of SLOPE/W and SEEP/W program of GEOSTUDIO software was tested for steady state and sudden drawdown. Morgenstern and Price [10] reconstructed the method of slice, for circular and non-circular failure surface, by considering the inter-slice forces satisfying both moment and force equilibrium. Lowe [11] introduced a method satisfying only force equilibrium by considering both inter-slice normal as well inter-slice shear force with a difference in assumption for the inter-slice force function. Himanshu and Burman [12] studied the seepage and slope stability analyses of the earthen embankment dam of Durgawati reservoir project in the region of Kaimur–Bihar using geotechnical software GEOSTUDIO 2007.

2 Materials

For dam embankment, clay is used and for drain and sand is used. The properties like unit weight, cohesion and angle of internal friction for clay and sand are listed in Tables 1 and 2.

Table 1 Embankment properties

Type of soil	Symbol	Prpperty	Assumed value
Clay	γ	Unit weight of soil (kN/m^3)	16
	c	Cohesion of soil (kN/m^2)	45
	ϕ	Angle of internal friction (°)	5
	k	Permeability (m/s)	8.149×10^{-7}

Table 2 Drain properties

Type of Soil	Symbol	Property	Assumed value
Sand	γ	Unit weight of soil (kN/m^3)	18
	c	Cohesion of soil (kN/m^2)	0
	ϕ	Angle of internal friction (°)	38
	k	Permeability (m/s)	9.65×10^{-6}

3   Methodology

The stability of slope is characterized by the term factor of safety (FOS), defined as the ratio of the summation of shear resistance and shear mobilized for individual slices:

$$\text{FOS} = \frac{\sum \text{shear resistance}}{\sum \text{shear mobilized}} \tag{1}$$

For steady-state seepage analysis, the mathematical formula associated with it is expressed as:

$$\frac{\partial}{\partial x}\left(k_x \frac{\partial H}{\partial x}\right) + \frac{\partial}{\partial y}\left(k_y \frac{\partial H}{\partial y}\right) + Q = 0 \tag{2}$$

where H = total available hydraulic head difference, k_x = the hydraulic conductivity in the horizontal x-direction, t = time, Q = applied boundary flux, i.e. discharge and k_y = the hydraulic conductivity in the vertical y-direction.

The earthen dam height is assumed to be 14 m with a free board of 2 m. The water level is maintained at 12 m on upstream side. The embankment section is having upstream slope of 2.5 H: 1 V and downstream slope of 2 H: 1 V. The top width of dam is taken as 6 m. A berm of 4 m is provided on the downstream side at the height of 7 m and toe drain having 2 m depth and 4 m in length. In this study, two loading conditions, i.e. steady-state analysis and sudden drawdown analysis are used. SEEP/W has been applied together with SLOPE/W. "Entry-exit" type of slip surface is used. The Morgenstern-Price Method is based on limit equilibrium, which is incorporated in SLOPE/W to analyse the model with all the four cases to find out

the factor of safety on downstream sides of the earthen dam. The four cases, namely earthen dam without berm and without a toe drain, earthen dam with berm without a toe drain, earthen dam without berm with a toe drain and earthen dam with berm with a toe drain are illustrated in Figs. 1, 2, 3 and 4.
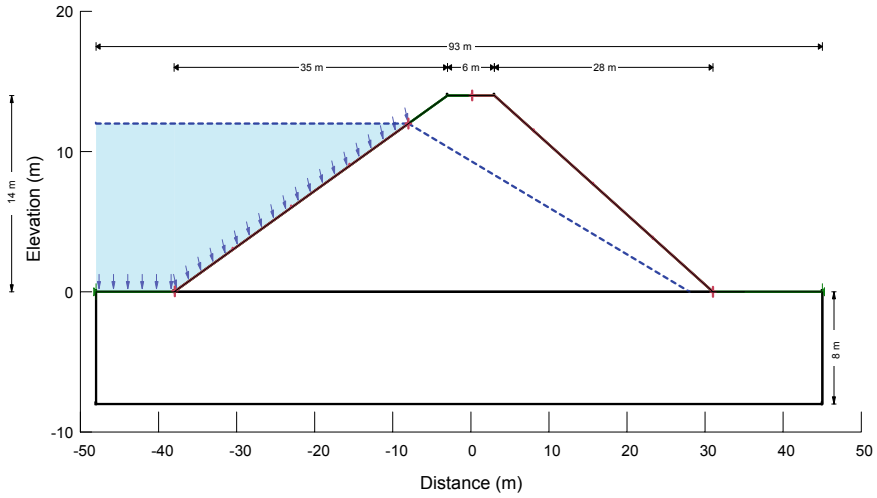

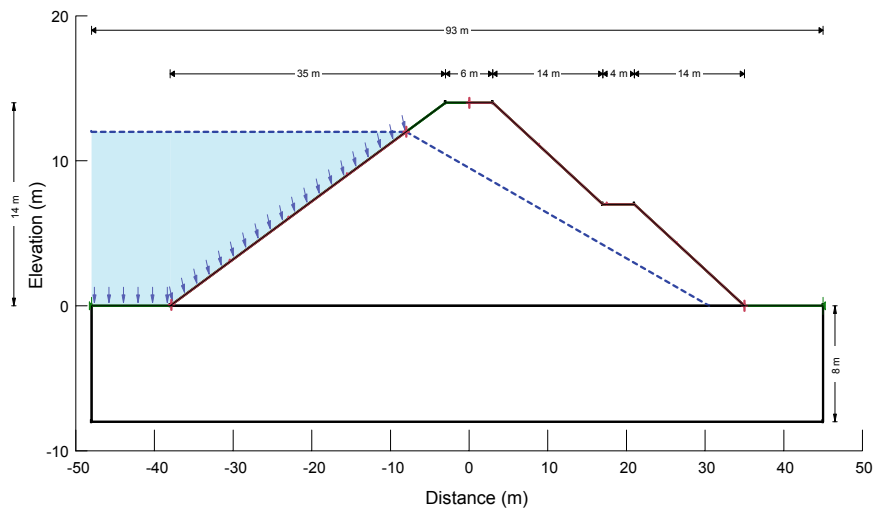**Fig. 1** Earthen dam model without berm and without drain

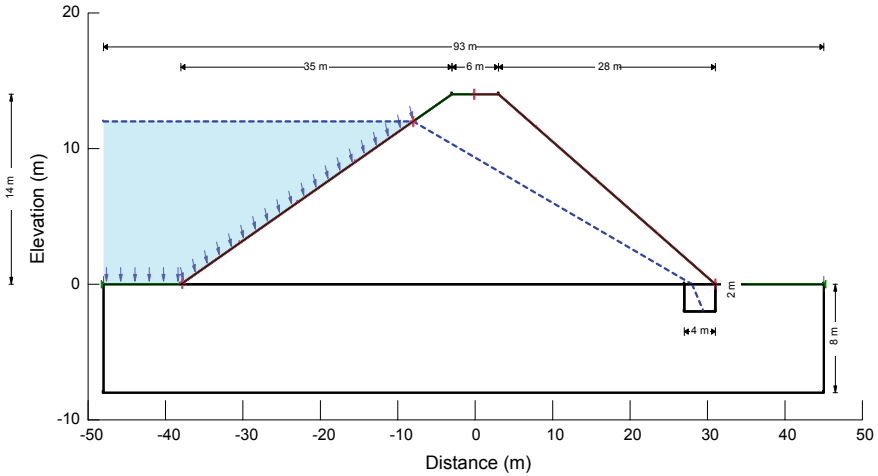**Fig. 2** Earthen dam model with berm and without drain
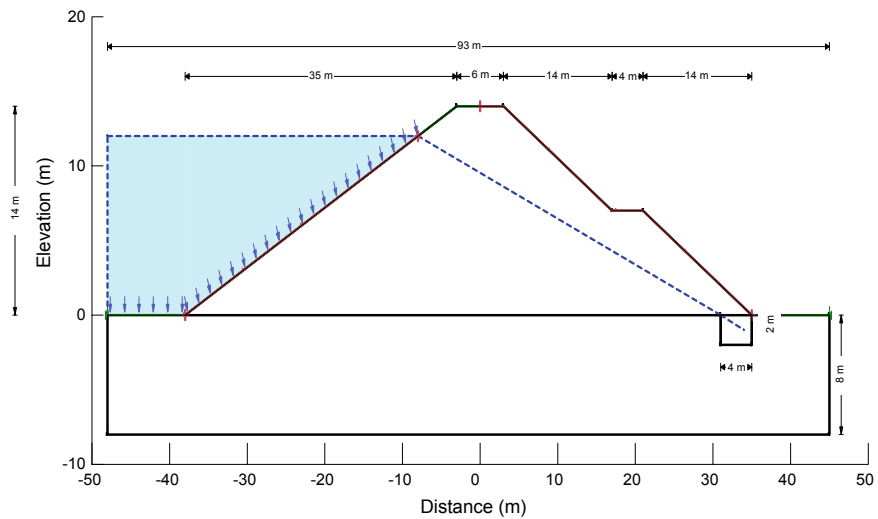
Fig. 3 Earthen dam model without berm and with a drain

Fig. 4 Earthen dam model with berm and with a drain

4 Results and Discussion

The results were obtained for the four different cases, i.e. the factor of safety for the earthen dam model without berm and without drain is found out to be **1.908** and **2.229** (for downstream side and upstream side, respectively) as shown in Figs. 5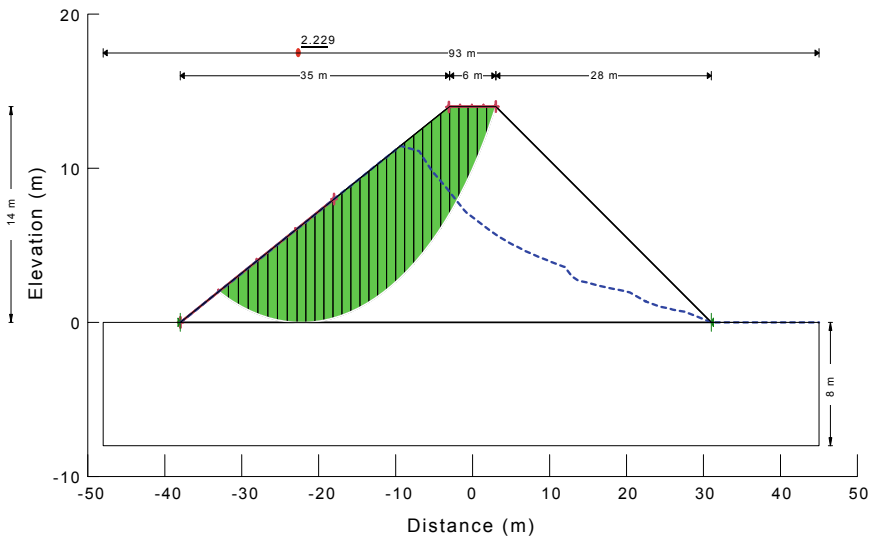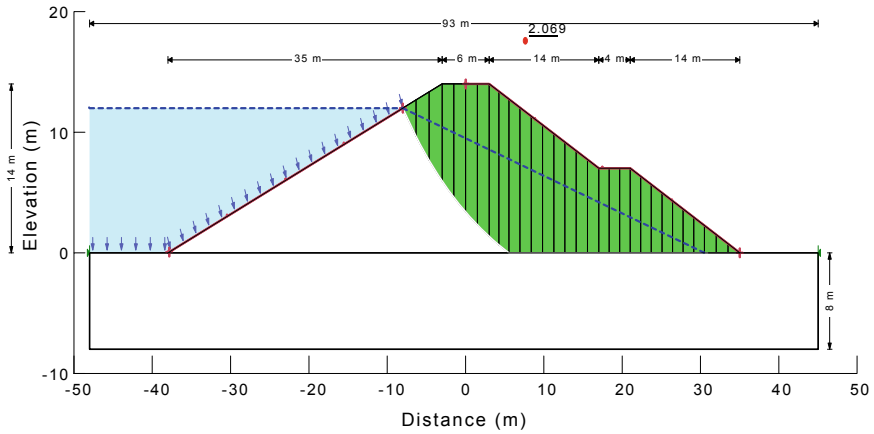 and 6, for the earthen dam model with berm and without drain is found out to be **2.069** and **2.220** (for downstream side and upstream side, respectively) as shown in Figs. 7
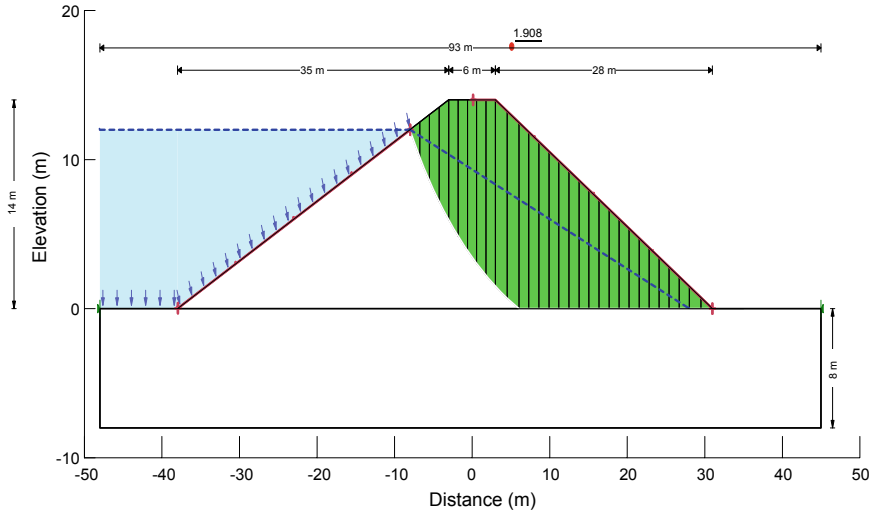
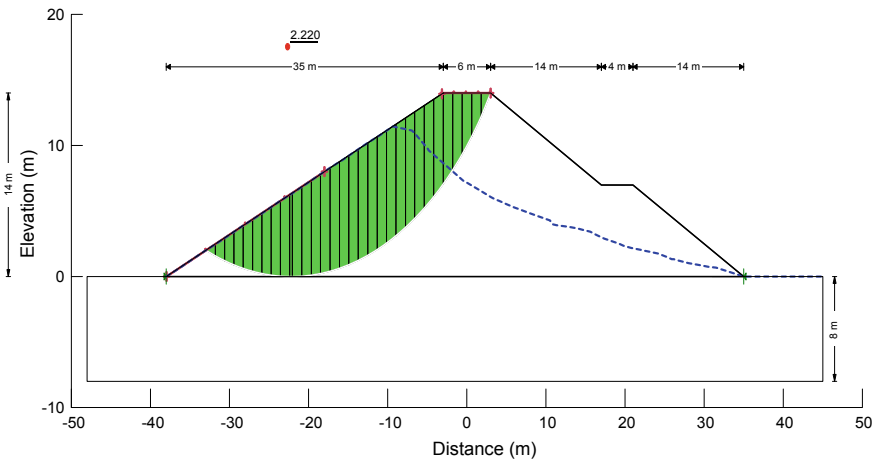**Fig. 5** Result obtained for earthen dam model without berm and without drain for D/S

Fig. 6 Result obtained for earthen dam model without berm and without drain for U/S

and 8, for the earthen dam model without berm and with drain is found out to be **2.189** and **2.243** (for downstream side and upstream side, respectively) as shown in Figs. 9 and 10 and for the earthen dam model with berm and with drain is found out to be **2.390** and **2.205** (for downstream side and upstream side, respectively) as shown in Figs. 11 and 12.

Fig. 7 Result obtained for earthen dam model with berm and without drain for D/S

Fig. 8 Result obtained for earthen dam model with berm and without drain for U/S

4.1 Stability of D/S Slope During Steady Seepage Condition

The berm is provided on the downstream side and also drainage filter is provided at the bottom of the toe on the downstream side to improve the shear strength of the soil in the failure zone. After providing berm and drain on the downstream side, the factor of safety is improved (Fig. 11) as compared to above three cases (Figs. 5, 7, 9). The failure slip circle was generated by specifying the entry of the slip circle at the toe and exit at the top of the embankment. The critical slip circle locates the corresponding factor of safety (Figs. 5, 7, 9, and 11).
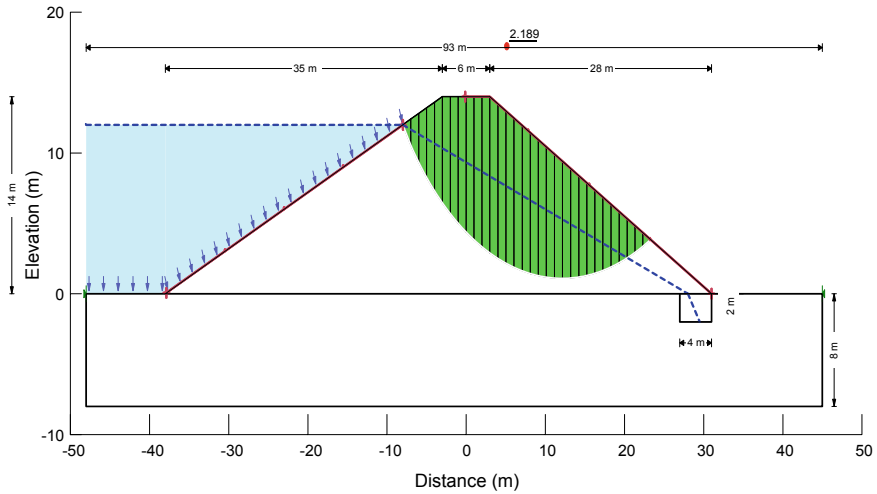
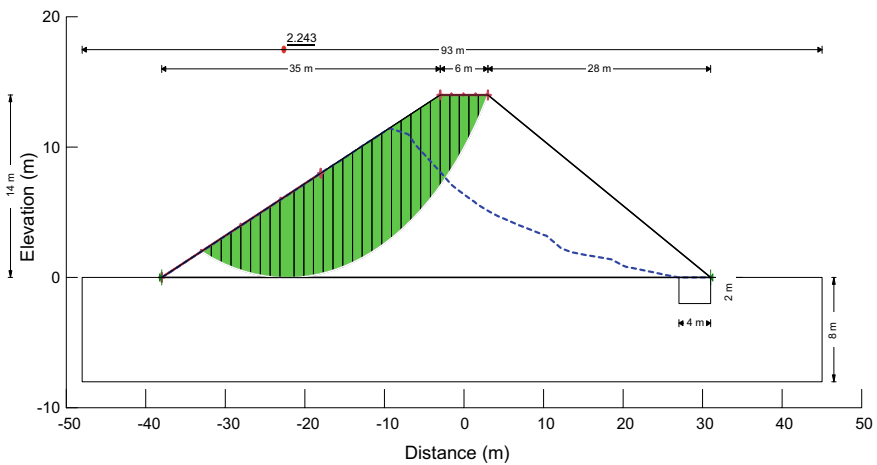**Fig. 9** Result obtained for earthen dam model without berm and with drain for D/S

Fig. 10 Result obtained for earthen dam model without berm and with drain for U/S

4.2 Stability of U/S Slope During Sudden Drawdown Condition

Berm is neglected on the downstream side and drainage filter is provided at the bottom of the toe on the downstream slope to improve the shear strength of the soil and applied the drawdown condition on the upstream slope to find the critical slip surface (Fig. 10). The critical slip surface for other three cases is also found out (Figs. 6, 8, and 12). The failure slip surface is generated by specifying the entry of
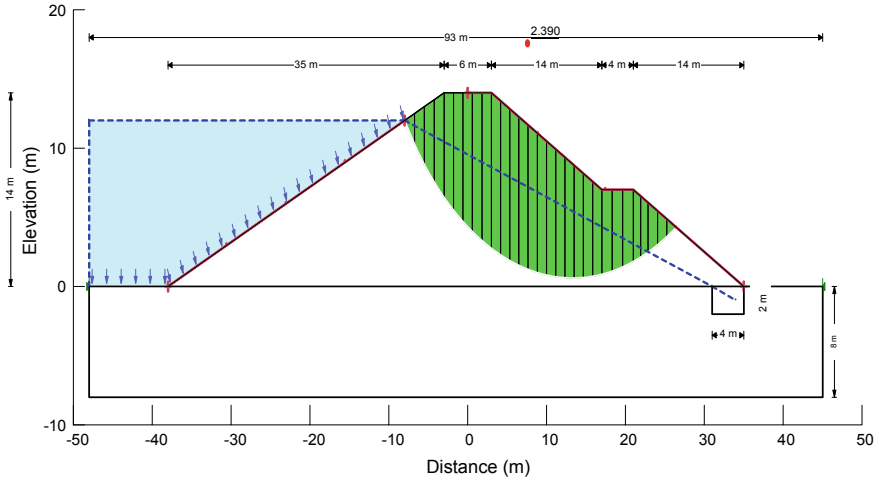
Fig. 11 Result obtained for earthen dam model with berm and with drain for D/S
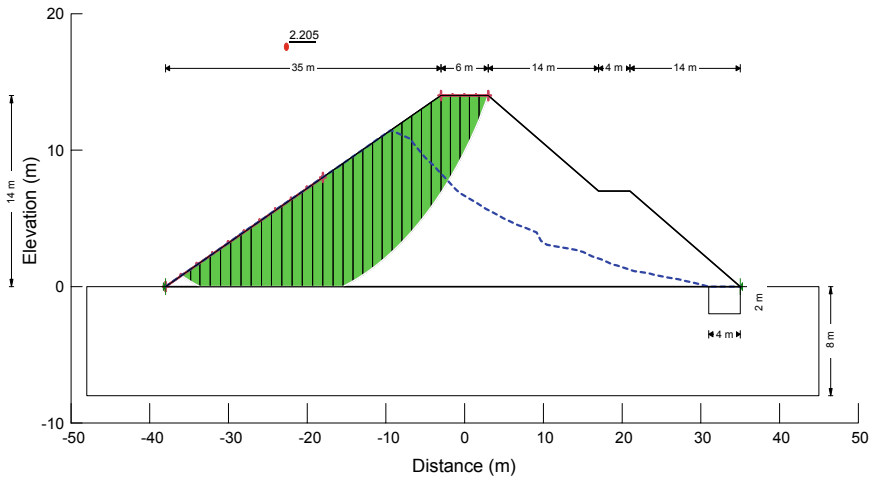

Fig. 12 Result obtained for earthen dam model with berm and with drain for U/S

the slip circle at the toe, and exit at the top bank of the embankment on the upstream side. The critical slip circle locates the corresponding factor of safety (Figs. 6, 8, 10, and 12). Finally, all the factor of safety values for different cases are shown in Table 3.

Table 3 Factor of safety for different cases

Cases	Factor of safety	
	Steady state	Sudden drawdown
I. Without berm without drain	**1.908**	**2.229**
II. With berm without drain	**2.069**	**2.220**
III. Without berm with drain	**2.189**	**2.243**
IV. With berm with drain	**2.390**	**2.205**

5   Conclusions

Based on the above results, the following conclusions are made

1. The factor of safety is increased on downstream section after providing the berm on the d/s side.
2. The factor of safety is increased on downstream section after providing the toe drain.
3. Out of four cases, the best case to improve the factor of safety of the slope is the fourth case, i.e. earthen dam with berm and with a toe drain.

References

1. SLOPE/W: Stability Analysis, Users Guide Version 5, GeoSlope Office, Canada, (2002). http://www.geoslope.com. Last accessed 2019/08/27
2. GeoStudio Tutorial Manual: GEO-SLOPE International Ltd. http://www.geo-slope.com. Last accessed 2019/08/27
3. Zomorodian, S., Abodollahzadeh, M.: Effect of horizontal drains on upstream slope stability during rapid drawdown condition. Int. J. Geol. **42**(66), 29–34 (2010)
4. Zhang, L., Maula, B.H.: Assessment of embankment factor safety using two commercially available programs in slope stability analysis. In: The Twelfth East Asia-Pacific Conference on Structural Engineering and Construction, vol. 14, pp. 559–566. Elsevier (2011)
5. Delvari, A., Kamanbedast. A.: Analysis of Earth Dam: seepage and stability using Ansys and Geo-Studio Software. World Appl. Sci. J. **17**(9), 1087–1094 (2012)
6. Hasani, H., Mamizadeh, J., Karimi, H.: Stability of slope and Seepage analysis in Earth fills dams using numerical models (Case Study: IIam DAM-Iran). World Appl. Sci. J. **21**(9), 1398–1402 (2013)
7. Athani, S.S., Shivamanth, Solanki, C.H., Dodagoudar, G.R.: Seepage and stability analyses of Earth Dam using finite element method. ICWRCOE 2015, vol. 4, pp. 876–883. Elsevier (2015)
8. Goswami, D., Borah, U.: Analysis and design of Earth and Rockfill Dams. In: Indian Geotechnical Conference IGC 2016
9. Anbalagan, R., Devi, D.: Study on slopes of earthen dam by using GEOSTUDIO Software. IJARIIT **3**(6), 408–414 (2017)
10. Morgenstern, N.R., Price, V.E.: The analysis of the stability of general slip surfaces. Geotechnique **15**(1), 77–93 (1965)

11. Lowe, J.: Stability analysis of embankments. J. Soil Mech. Found. Div. ASCE **93**(4), 1–33 (1967)
12. Himanshu, N., Burman, A.: Seepage and stability analysis of Durgawati earthen dam: a case study. Indian Geotech. J. **49**(1), 70–89 (2019)

Static and Dynamic Analysis of Nailed Slope

Chappidi Srinivas and M. Padmavathi

Abstract In the present study, slope stability analysis is carried out for a nailed slope with 50° slope angle and 20 m height. Analysis is carried out by both 2D limit equilibrium and finite element methods using a geotechnical modeling software GeoStudio. Sections of slope without and with nails are analysed for stability with respect to static, pseudo-static and dynamic conditions. Dynamic response of nailed slope is analysed against an earthquake with PGA of 0.15 g by finite element method. The acceleration–time history is used as an input to simulate the earthquake in the numerical model. A parametric study is carried out to analyse the effect of nail inclination, nail spacing and nail length on the stability of nailed slope. The variation of factors of safety, shear stresses and displacements during earthquake is also analysed by finite element method using Geo-slope. From the analysis, it is found that the slope is unstable without nails with factor of safety 1.116 in static condition. And the factor of safety increases to about 1.628 by soil nailing. The slope with optimum nail inclination and spacing is analysed for dynamic response. The nailed slope is critical at 7th second of earthquake with factor of safety of 1.35 for an average acceleration 0.124 m/s^2. Horizontal displacement of 60 mm is obtained at the top of the nailed slope due to earthquake. The displacements decrease from top to the bottom of the slope.

Keywords Soil nailing · GeoStudio · Dynamic analysis

C. Srinivas (✉) · M. Padmavathi
Jawaharlal Nehru Technological University, Hyderabad 500085, India
e-mail: chsrinivas954@gmail.com

M. Padmavathi
e-mail: mpadmace@gmail.com

1   Introduction

Soil nailing is a technique of in situ ground reinforcement which is widely used in the natural slopes, excavations and retaining structures. The unstable slopes can be improved and made stable by the insertion of nails into the slope. Soil nailing system has many special advantages like high flexibility, light structure, simple construction process, fast construction speed, economic benefits and little effect on the environment.

   Soil nailing system is effective to reinforce the slope. Therefore, many scholars have studied on it. They have developed the limit equilibrium methods to analyse the stability of nailed slopes [1–3]. The stability of nailed slope mainly depends on nail pull-out strength and nail tensile strength. The laboratory model tests and field tests are proposed to determine the pull-out strength and stability of the nailed slope [4–6]. Numerical modeling, limit equilibrium methods and finite element methods (FEM) are used to analyse the stability of nailed slope, failure zone, soil nonlinearity and the staged construction effect to predict the actual site conditions [7–10]. Numerical modeling of reinforced slope by finite element methods has proved very useful in prediction of slope deformations, stresses. The effect of nail length, nail spacing, nail inclination on stability of the nailed slope is also analysed by the numerical models. Mohamed proposed design charts for nailed walls with different nail lengths, nail spacing's and nail inclinations for different soils [11]. However, the slopes are more prone to failure when they are subjected to earthquake loading. So the researchers proposed new methods to analyse the stability of slopes against dynamic loading. The conventional seismic stability of slopes is based on Pseudo-static method [12]. Though it is very simple approach but its applicability in seismic condition is very limited. It considers only the earthquake forces and neglects amplification of waves into soil stratum. Pseudo-dynamic (Steedman and Zeng 1990) method is the concept which imports amplification of vibrations into the analysis [13]. Numerical methods are used to study the nailed slope failure pattern, deformations and stresses during earthquake by dynamic analysis [14].

2   Methodology

For the purpose of illustration and better understanding, a slope with 50° slope angle and 20 m height is considered for the study. The stability analysis is carried out for static, pseudo-static and dynamic conditions. Pseudo-static and dynamic conditions refer to seismic condition in limit equilibrium and finite element analysis, respectively. The analysis is carried out by both 2D limit equilibrium and finite element methods using a geotechnical modeling software, GeoStudio. In limit equilibrium analysis, Bishop's simplified method of slices is used to find the stability of nailed slope by SLOPE/w module of GeoStudio. QUAKE/w module of GeoStudio is used to carry out the analysis by finite element method.

3 Numerical Modeling

3.1 SLOPE/W Modeling for Static Analysis

SLOPE/W is one of the modules of software tool, GeoStudio. In the present study, stability analysis for a slope with 20 m height and 50° slope angle is carried with and without nails. SLOPE/W module enables to construct the soil slope by drawing the slope regions. The dimensions of soil slope are scaled down to incorporate into the SLOPE/W to create the numerical model. The slope is modeled at different slope angles by coordinate system present in the SLOPE/W. Materials of slope are defined and assigned to regions, once the slope regions have been determined. The soil properties used in the analysis are summarized in Table 1 [15]. The numerical model of the slope is presented in Fig. 1.

SLOPE/W module provides the option to input reinforcement in the form of anchors, nails, piles and geosynthetics. Nail element option is used to model reinforcement in the nailed slope. The nail properties used in the analysis are summarized in Table 2. The slip surface is simulated by providing the range of the slip surface along the ground surface. In the present study, entry–exit option is used to simulate the range of slip surface. SLOPE/W provides different limit equilibrium methods

Table 1 Soil properties used in the analysis

Property	Symbol	Value
Unit weight (kN/m^3)	γ	18 kN/m^3
Cohesion (kn/m^2)	c	20 kN/m^2
Friction angle (°)	ϕ	28°
Coefficient of permeability (m/s)	k	1.16×10^{-8} m/s
Poisson's ratio	μ	0.35
Young's modulus	E	37,000 kPa
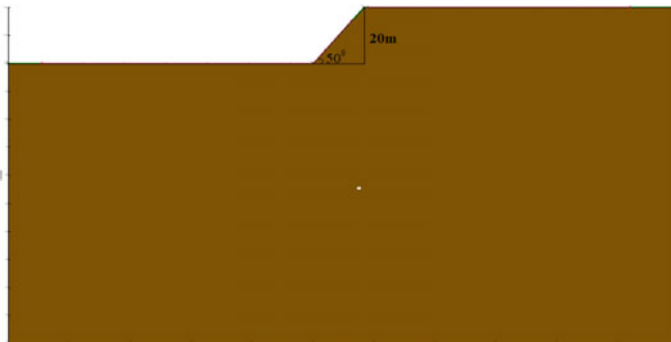
Fig. 1 Slope without nails

Table 2 Optimum nails details used in the analysis

Nail property	Symbol	Value
Yield strength	f_y	415 MPa
Nail diameter	d	25 mm
Nail length	l	0.6 H (12 m)
Nail inclination	λ	15°
Horizontal spacing Vertical spacing	S_h S_v	1 m 1 m

to analyse the problem. Bishop's simplified method is considered in the present analysis.

3.2 SLOPE/W Modeling for Pseudo-static Analysis

The slope is further analysed to find the stability against an earthquake of given PGA. Pseudo-static analysis considers seismic loading in terms of horizontal and vertical seismic coefficients of earthquake. The slope modeling and assigning materials in pseudo-static analysis are similar to static analysis. The magnitudes of both horizontal and vertical seismic coefficients of earthquake are given as input once the modeling of slope is done. In the present study, seismic coefficients of $k_h = 0.15$ and $k_v = 0.075$ are considered for the analysis. The failure slip circle and factor of safety (FOS) are the major results from the pseudo-static analysis.

3.3 QUAKE/W Modeling for Dynamic Analysis

The dynamic analysis is carried out to analyse the stability of the slope during the period of earthquake. The acceleration–time history of the earthquake is taken into consideration to analyse the behaviour of the slope during earthquake. In the present study, the optimum nailed slope obtained in static and pseudo-static analysis is considered for dynamic analysis.

In the present study, the dynamic analysis is carried out in four phases. The first and second phases are carried out in QUAKE/W and third and fourth phases are carried out in SLOPE/W to find the FOS by considering the first two phases as parent analysis. In first stage, initial static stresses are calculated in QUAKE/W. The construction of slope regions by coordinate system and assigning materials to the regions is similar to the process in SLOPE/W. QUAKE/W provides an option to input slope boundaries to the model. History nodes have been selected where the results are required to retrieve after the analysis.

The static stresses obtained in first phase are considered as input in second stage. The dynamic analysis is carried out by equivalent dynamic method in the present

Fig. 2 Earthquake
acceleration–time history
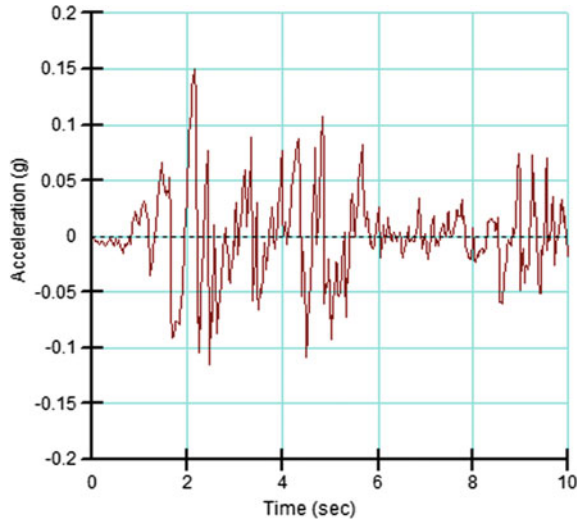
study. The acceleration–time history of the earthquake is given as an input in the second phase. An earthquake of 0.15 g PGA is considered for the dynamic analysis. Figure 2 shows the acceleration–time history used in the analysis. The complete slope model is divided into elements to generate the finite element mesh. Slope deformation and stresses distribution during the earthquake are the primary results in the dynamic analysis.

The variation of stresses and displacements during the earthquake is stored from the above two phases. These stresses are incorporated into SLOPE/W to find FOS. In third phase, initial static stresses are considered as parent analysis. The range of slip surface is once again specified in this phase like in static condition. The factor of safety before earthquake is obtained in this phase as an output. In final phase, equivalent linear dynamic analysis is considered as parent analysis. This analysis is performed to find factor of safety during the earthquake by Newmark's deformation method in SLOPE/W. The nailed slope with history nodes is presented in Fig. 3.

4 Results and Discussion

4.1 Results of Static Analysis

The factor of safety of slope without nails in static condition is found to be 1.116 which is far below the safe value of FOS of 1.5 as shown in Fig. 4 [2].

Soil nailing technique is employed to stabilize the slope. The nailed slope design is optimized with the optimum values of nail length, nail spacing and nail inclinations. To find the optimum design, the numerical model of nailed slope is analysed for
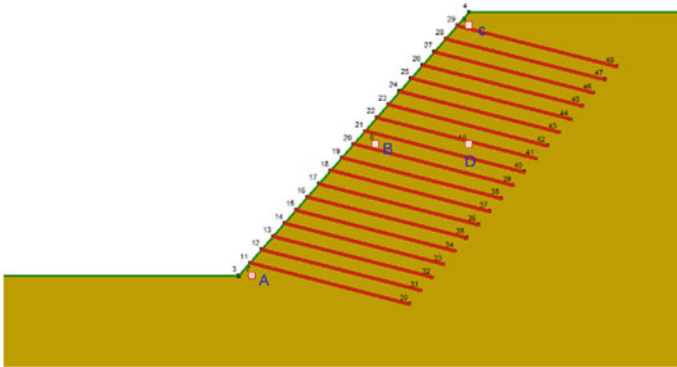
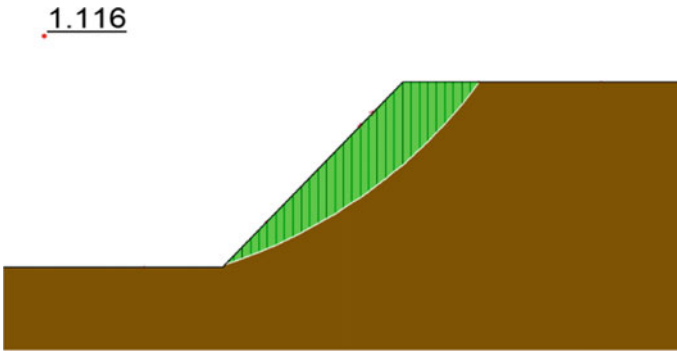**Fig. 3** Nailed slope with history nodes *A*, *B*, *C* and *D*

Fig. 4 Critical slip surface of slope without nails in static condition ($H = 20$ m, $\theta = 50°$)

different combinations of nail lengths from 0.5 to 0.75 H, nail inclinations from 10°
to 25° and nail spacing from 1 to 2 m in both directions.

Effect of Nail Inclination
Initially, the nailed slope is analysed for stability at different nail inclinations of 10°,
15°, 20° and 25°. The length and spacing of nails are kept constant with 0.7 H and
1.5 m, respectively, to find the optimum nail inclination. Figure 5 depicts the variation
of FOS with nail inclination.

From Fig. 5, it is observed that the nailed slope with 15° nail inclination attains
maximum FOS of 1.577 which is more than minimum value of FOS of 1.5 [2]. Hence
nail inclination of 15° is considered as optimum nail inclination for the study.

Effect of Nail Length
The nailed slope is further analysed for stability at different nail lengths of 0.5, 0.55,
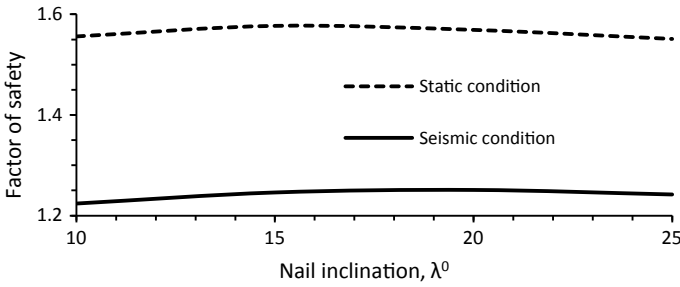0.6, 0.65, 0.7, 0.75 and 0.8 H. The nail inclination and spacing are kept constant at

Fig. 5 Influence of nail inclination on factor of safety ($H = 20$ m, $\theta = 50°$, $l = 0.7\,H = 14$ m, $S_h = S_v = 1.5$ m)
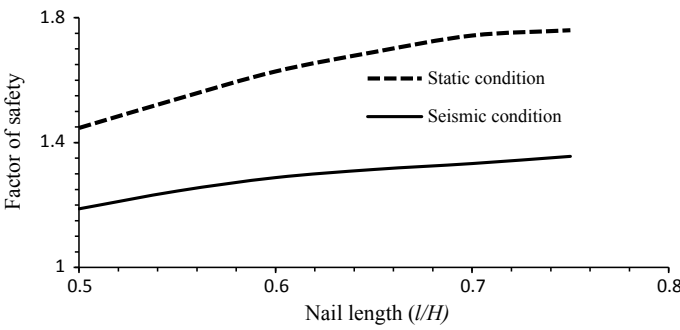

Fig. 6 Influence of nail length on factor of safety ($H = 20$ m, $\theta = 50°$, $\lambda = 15°$, $S_h = S_v = 1$ m)

15° and 1 m to study the effect of nail length on stability. The results are presented in Fig. 6.

The factor of safety increases with increase in nail length from up to about 0.7 H and then shows an asymptotic variation. Based on the results presented in Figs. 5 and 6, the nailed slope with 12 m (0.6 H) length nails at 15° inclination and 1 m spacing in both directions is considered as optimum with FOS of 1.628 which is more than minimum recommended value of FOS of 1.5. The critical slip circle of nailed slope with optimum parameters is given in Fig. 7.

4.2 Results of Pseudo-static Analysis

The stability of the nailed slope against an earthquake of 0.15 g PGA is analysed with the help of numerical model in SLOPE/W module. The horizontal seismic coefficient, $k_h = 0.15$ and vertical seismic coefficient, $k_v = 0.5\,k_h = 0.075$ are used to import the seismic loading into the analysis. The FOS obtained from numerical analysis by Geoslope is verified analytically by Bishop's simplified method of slices
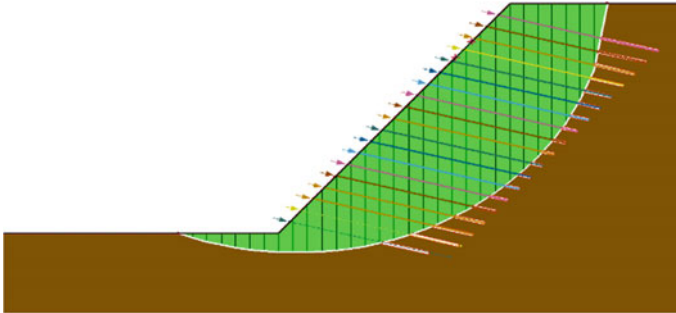
1.628

Fig. 7 Nailed slope with critical slip surface ($l = 0.6$ H, $S_h = S_v = 1$ m, $\lambda = 15°$)

Table 3 Results of static and pseudo-static analysis

Slope	Minimum recommended FOS [2]		Obtained FOS			
	Static condition	Seismic condition	Static analysis		Pseudo-static analysis	
			Geoslope	Analytical method	Geoslope	Analytical method
Without nails	1.5	1.1	1.116	1.081	0.881	0.87
Nailed slope	1.5	1.1	1.628	1.601	1.288	1.268

[1]. The results from both methods are almost same. The results that are presented in Table 3 belong to slope before and after nailing with 12 m length nails at 15° nail inclination with 1 m spacing in both directions.

4.3 Results of Dynamic Analysis

The dynamic analysis helps to analyse the behaviour of slope during earthquake. The variation of FOS, stresses distribution and displacements at history nodes during the earthquake of 0.15 g PGA is studied in the dynamic analysis.

Shear stress variation
Variation of the maximum shear stresses developed at history nodes during the earthquake of PGA 0.15 g in the slope without and with nails is presented in Figs. 8 and 9, respectively.
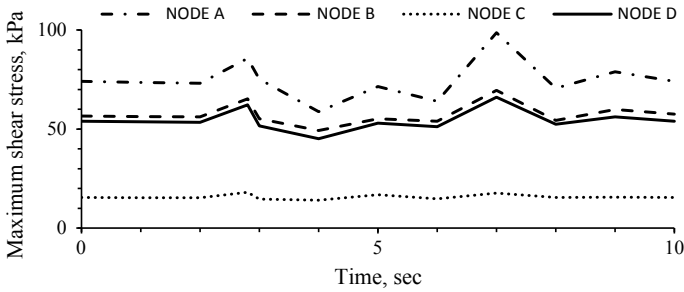
Fig. 8 Variation of shear stresses at history nodes in the slope without nails
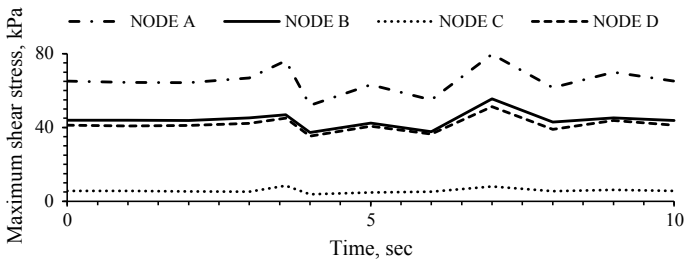

Fig. 9 Variation of shear stresses at history nodes in nailed slope

The maximum shear stress is found at NODE A which is located at bottom of the slope for both the cases of slope with and without nails. It deceases from 98.69 to 79 kPa by the inclusion of nails into the slope. The minimum shear stress is found at the top of the slope at NODE C with a value of about 10kN in the nailed slope.

Nail Axial Force

The distribution of nail axial force along the length in both bottom and top nail row is depicted in Fig. 10. The maximum nail axial force is developed in bottom nail row.

Maximum nail axial forces in top and bottom nail rows are 24.44 kN and 50.38 kN, respectively. Nail axial force increases along nail length. It attains maximum in between the lengths of 0.6 L (7.2 m) to 0.9 L (10.8 m) from nail head and then decreases towards nail tip. Location of maximum nail force is presented in Fig. 11.

Horizontal Displacements

The variation of horizontal displacements of nailed slope at history nodes during the earthquake of 0.15 g PGA is presented in Fig. 12.
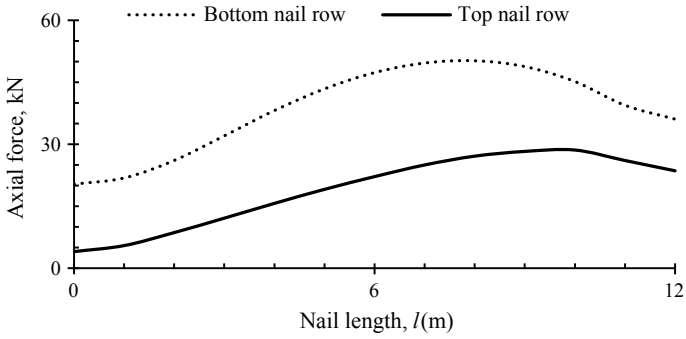
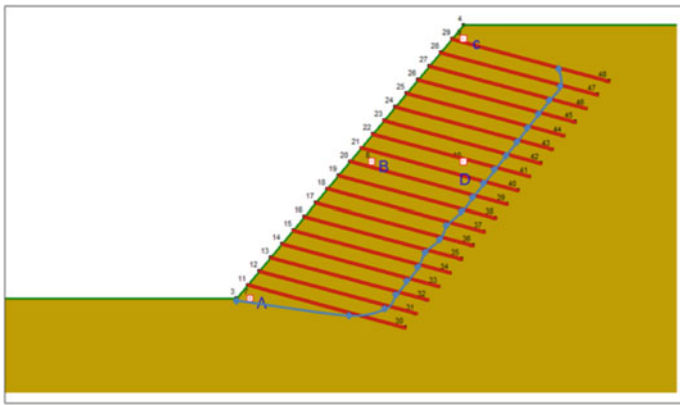**Fig. 10** Variation of nail axial force along the length
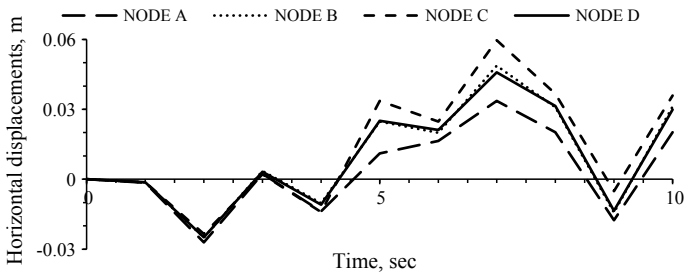

Fig. 11 Location of maximum nail axial force

Fig. 12 Variation of horizontal displacements in nailed slope ($H = 20$ m, $\theta = 50°$, $l = 0.6$ H = 12 m, $\lambda = 15°$, $S_h = S_v = 1$ m)

Nailed slope experiences maximum horizontal displacement of 60 mm at NODE C which is at the top of the slope. It experiences minimum horizontal displacement of 28 mm at the bottom of the slope at NODE A.

Results of Newmark's Deformation Analysis

The variation of FOS during the total period of the earthquake (PGA of 0.15 g) is presented in Fig. 13. The nailed slope attains minimum FOS of 1.352 at 7th second of ground motion which is more than the safe FOS of 1.1 [2]. Hence the slope with nails of length, 12 m inserted at 15° inclination and 1 m spacing is stable even during earthquake of PGA 0.15 g.

Influence of Nail Spacing on Stability of Slope

The analysis is carried out in SLOPE/W for different nail spacing's like 1, 1.25, 1.5, 1.75 and 2 m in both static and pseudo-static condition. The remaining all parameters are kept constant and the results are presented in Fig. 14. Square nail pattern ($S_h = S_v$) is used to analyse the effect of nail spacing on slope stability.

The factor of safety decreases with increase in nail spacing due to decreasing the resisting force developed by nails at failure surface. The slope with 1.25 m spaced nails also attains factor of safety of 1.538 (FS > 1.5) but leads to facing failure. Hence nails pattern with 1 m spacing is preferred for design.

Influence of Earthquake PGA on Stability of Slope

The analysis is carried out to find the effect of earthquake on slope stability by considering different PGA. A graph is drawn and presented as Fig. 15 between PGA and FOS to show the variation of FOS against different earthquake PGA.

The factor of safety decreases with increase in PGA due to increase in driving force at critical failure surface.

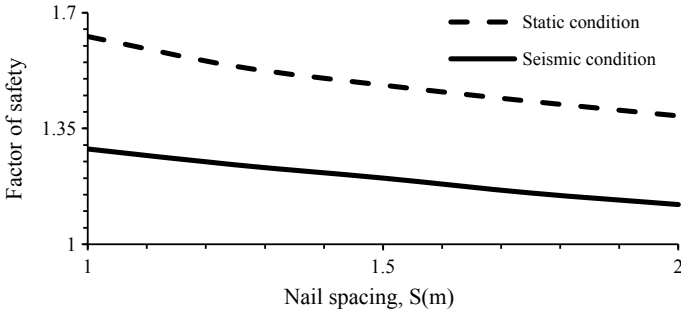**Fig. 13** Variation of FOS with time in nailed slope
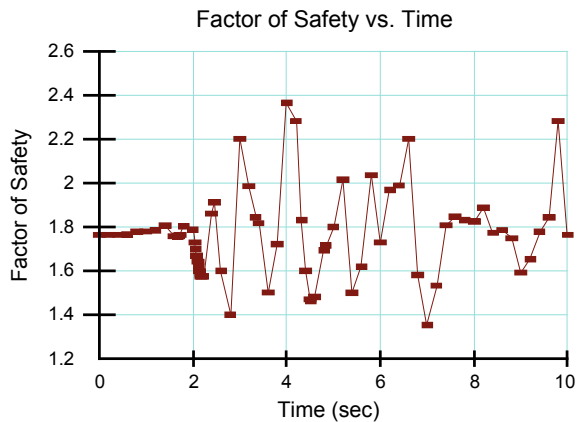
Fig. 14 Influence of nail spacing on factor of safety ($H = 20$ m, $\theta = 50°$, $l = 0.6$ H $= 12$ m, $\lambda = 15°$)
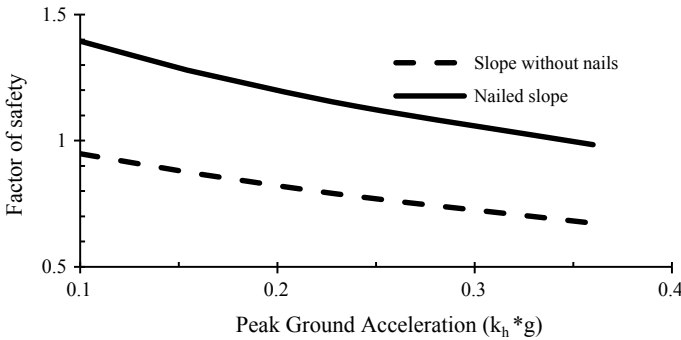
Fig. 15 Influence of PGA on factor of safety

5   Conclusions

Following conclusions are made based on the results obtained from the study.

1. The slope is stabilized by the inclusion of nails of length 12 m at 15° inclination and 1 m spacing in both directions. The FOS increases from 1.116 to 1.628 after nailing.

2. From dynamic analysis, the horizontal displacements of nailed slope decrease from top to the bottom of the slope. The slope experiences displacement of 60 mm in horizontal direction at the top of the slope. The inclusion of 12 m nails with 15° inclinations at 1 m spacing into the slope leads to 20% reduction in shear stress.

3. The soil slope considered in the analysis is safe with the inclusion of 12 m length nails at 15° slope angle and 1 m spacing in both directions for seismic conditions up to a PGA of 0.3 with a factor of safety of 1.1.

References

1. Prasanth, A., Mukherjee, M.: Soil Nailing for Stabilization Steep Slopes Near Railway Tracks. Research Gate, 1-203 (2015)
2. Federal Highway Administration, FHWA: Reference manual, 7th edn, USA FHWA-NHI-14-007 (2015)
3. Basudhar, P.K., Anubhav, Lakshminarayana, M.R.: Three-dimensional limit-equilibrium stability analyses of slopes and effect of inclusion of soil nails. Int. J. Geo-mech. **17**(9), 1–11 (2017)
4. Wong, I.H., Low, B.K., Pang, P.Y., Raju, G.V.R.: Field performance of nailed soil wall in residual soils. J. Perform. Constr. Facil. **11**(3), 105–112 (1997)
5. Chu, L.M., Yin, J.-H.: Comparison of interface shear strength of soil nails by both direct shear box tests and pull-out tests. J. Geotech. Geo Environ. Eng. **131**(9), 1097–1107 (2005)
6. Seo, H.J., Lee, Loizos, P.: Net load–displacement estimation in soil-nail pullout tests. Geotech. Eng. **170**, 534–547 (2017)
7. Fan, C.C., Luo, J.H.: Numerical study on the optimum layout of soil nailed slopes. Comput. Geotech. **35**, 585–599 (2008)
8. Sivakumar Babu, G.L., Singh, V.P.: 2D numerical simulations of soil nail walls. Geotech. Geol. Eng. **28**, 299–309 (2009)
9. Sahoo, S., Manna, B., Sharma, K.G.: Stability analysis of un-reinforced and reinforced soil slopes. Geo-China **257**, 74–81 (2016)
10. Rawat, S., Gupta, A.K.: Analysis of a nailed soil slope using limit equilibrium and finite element methods. Int. J. Geo-Synthetics Gr. Eng. **2**(34), 1–23 (2016)
11. Mohamed, A.: Design Charts for Soil Nailing. Research Gate, 1-221 (2010)
12. Jonathan, D., Thaleia, T.: Pseudo static slope stability procedure. In: 5th International Conference of Earthquake Geotechnical Engineering, pp. 10–13, Santiago, Chile (2011)
13. Kramer, S.L.: Geotechnical Earthquake Engineering. Pearson Education, Singapore (2018)
14. Rawath, P., Chatterjee, K.: Seismic stability analysis of soil slopes using soil nails. Geotech. Earthq. Eng. Soil Dyn. **293**, 79–87 (2018)
15. Shrestha, S., Ravichandran, N., Raveendra, M., Attenhofer, J.A.: Design and analysis of retaining wall backfilled with shredded tire and subjected to earthquake shaking. Soil Dyn. Earthq. Eng. **90**, 227–239 (2016)

Design and Analysis of Earth Slopes Using Geosynthetics

N. Vijay Kumar [iD]**, S. S. Asadi, D. Satish Chandra, A. Shivamanth** [iD]**, and G. Pradeep Kumar**

Abstract In the aspect of geotechnical engineering problems, slope stability is a condition of inclined soil, waste heaps to withstand or undergo movement. Slope is an unprotected ground surface that can be necessitated at an angle of horizontal. Slopes are necessitated in the construction of railway embankments and highways, levees, bridges, earth dams, reservoirs and canals etc., and are generally less expensive. Failures of natural and man-made slopes have demise and demolition. Analysis and stability slopes consist of determining and comparing the shear stress developed along the potential rupture surface with the shear strength of the soil. The awareness of the surface drainage is very important factor. Slope stability can be evaluating the ground water, shear strength of the soil. For a secure slope, factor of safety should not be less than 1. In recent times, electronic computers made it feasible to more easily repetitious mechanism and the use of OASYS GE software has simplified the analysis to a great extent. In this present study, OASYS GE Slope software has been to analyze the homogeneous earth slopes for different cohesive strengths, and also we study the improvement of stability of slopes using geomembrane and we also consider the effect of ground water table on stability of slopes.

Keywords OASYS GE · Slope · Slip surface · Ground water table · Geomembrane · Black cotton soil

N. V. Kumar (✉) · D. S. Chandra
Department of Civil Engineering, Koneru Lakshmaiah Education Foundation Deemed to be University, Vaddeswaram, Andhra Pradesh 5225022, India
e-mail: nasarivijay156@gmail.com

S. S. Asadi
Department of Civil Engineering, Vignan's Foundation for Science Technology and Research, University, Guntur, India

A. Shivamanth · G. P. Kumar
Department of Civil Engineering, St. Martins Engineering College, Secunderabad 500100, India

1   Introduction

A slope is an unsupported, inclined surface of a like soil mass. Slopes can be natural or man-made. These may be above ground level as embankments or below ground level as cuttings. Earth slopes are formed for railway embankments, earth dams, canal banks, levees at many locations. Instability-related problems in engineered as well as natural slopes are common challenges to both research scholars and professional. Instability results may be due to sudden rain, sudden increasing water table and also sudden change in stress conditions. The natural slopes are very strong but due to geometry and external forces, there is sudden fall and loss of shear strength. In addition, the long-term stability is associated with the weathering and chemical influences that may decrease the shear strength. In such circumstances, the evaluation of slope stability conditions becomes a primary concern everywhere. When a mass of soil has an inclined surface, the potential of slope to slide from higher level to lower level always exist. The sliding will occur if shear stress developed in the soil exceeds corresponding shear strength of soil. However, certain practical considerations make precise stability analyses of slope difficult in practices. The engineering solutions to slope instability problems require good understanding of analytical methods, investigative tools and stabilization measures. Bishop [1] says, "The primary aim of slope stability analyses is to contribute to the safe and economic design of excavation, embankment and earth slopes".

Objectives of the study:

- By using Oasys slope 19.0 Software, to determine the minimum factor of safety values of the slopes.
- Determining the critical failure of slope's surface and application of engineering judgment in determining, whether the slopes will be stable or not stable as recommended by BS8006:1995.
- Design and implementation of solutions for detection, control, remediation and prevention of subsurface contamination.

2   Literature Review

Abramson et al. [2] have worked on the slice models for evaluating slopes. It has been realized that new slice model predicts the minimum factor of safety. They have said that cutting into existing ground disturbs the mechanics of the surrounding area, which can result in slope failure. This particular information gives the comprehensive data about slope stability analysis. It includes detailed discussions of methods used in slope stability analysis, including the ordinary method of slices such as simplified Bishop's method, Janbu's method, Spencer's method and limit equilibrium method and use of computer programs to solve problems. Swedish (1950) developed the Swedish method and he neglected all the internal forces acting on the slices. Iteration analysis is not necessary during the calculation of factor of safety. When comparing

to other strict methods, the processing of computer calculations is very easy and simple. The assumptions of boundary conditions make Classical Swedish Methods results more conservative. Using this method, a factor of safety can be estimated quicker than other methods of design in practice. Bishop [1] Bishop's method of slope stability analysis is the most common methods. It is the most talk able method in all kinds of geotechnology book and throughout the world. Circular failure surface slope stability will be analyzed using this method. In case of undrained condition, Swedish method and Bishop's method are more identical to each other. Janbu (1957) simplified method will completely satisfy the equilibrium of force even though the moment equilibrium was not satisfied. This method is also used worldwide. The Janbu method is used for non-circular critical surface that appears in sand. After a rigorous change in formula, moment equilibrium is also taken into an account. The value of factor of safety using the simplified method comes very close to the rigorous method results. Bacicn (2014) "Slope stability analysis" in that paper, they conclude a methodology of slope stability analysis and provide an insight into the basic of landslides and their general terms. Natural process of constant is affected by change in relationship for shearing stress and resistance.

3 Study Area, Materials Preparation and Methodology

3.1 Study Area

Slope is taken at Dundigal area in Hyderabad. The soil sample is also taken at Dundigal village dump area, and it is located at a distance of nearly 15 km kompally. A trench is made at embankment at a depth of 1 m to fix the HDPE sheet. To the below mentioned leachate pond reinforced material, i.e. geomembrane is placed to avoid soil pollution and ground water pollution because when a solid waste is dumped into a landfill, that land fill produces liquid, i.e. leachate and that leachate is discharged in a pond with the help of a HDPE sheet, it does not allow on the surface. HDPE sheet is known as protection of leachate not to flow on the surface or ground. Geomembrane which gives tensile nature to the ground surface. Leachate which is coming from landfill is collected as shown in Fig. 1 (Table 1).

Physical properties: Thickness-500 μm, density-0.94 g/cm^3, mass per unit area 6.4 kg/m^2, UV radiation 2%, compressive strength-2200 Mpa, type-HDPE virgin, color-black.

Chemical properties: HDPE-35%, LLDPE-25%, PVC-25%, Flexible polypropylene-10%, chlorosulfonated polyethylene-2%, ethylenepropylenedine + polymer-3%.

Fig. 1 Preparation of slope for leachate pond and placing of geomembrane at slope

Table 1 Tensile properties of geomembrane ASTM D6693

Property	GM2.0
Thickness	2.00 mm
Density	0.940 g/cc
Strength at break KN/m	26
Strength at yield KN/m	40
Elongation at break (%)	11
Elongation at yield (%)	600

3.2 Materials Preparation

The black cotton (BC) soil has a high percentage of clay, which is predominantly montmorillonite in structure and black color. An essentially impermeable geosynthetic composed of one or more synthetic sheets is known as geomembrane. Geomembranes are giant impermeable membranes made of unreinforced polymeric materials and used to stabilize earth and to secure landfills ensuring containment of hazardous or municipal wastes and their leachates. The sample preparation and the laboratory testing have been done as shown in Fig. 2. Understand the soil properties of the existing site have been taken into account. Testing of soil sample, mainly we consider the angle of internal friction and cohesion values. These values will be used in the Oasys slope software, and then finally we get the output as factor of safety regarding the slope.

These samples were collected to determine the shear parameters cohesion, c and φ using direct shear test. Table 2 shows the water content, bulk density, cohesion, and angle of internal friction.

Figure 3 shows a typical effective stress failure envelope of soil sample for calculation of shear parameters.

3.3 Analysis

1. Limit Equilibrium Methods

Fig. 2 Laboratory tests

Table 2 Geotechnical properties of soil sample at Dundigal Village

Soil sample	Water content (%)	Bulk density (KN/m³)	Cohesion c (KN/m²)	Angle of internal friction (φ°)
1	14.30	19.60	2.5	8.2
2	8.90	18.30	4.6	26.7
3	6.70	17.066	5.2	24.50
4	11.0	16.90	6.5	22.6
1	5.72	16.50	4.9	25.70

The various limit equilibrium methods are (1) Swedish circle method, (2) Friction circle method, and (3) Bishop's method.

2. Bishop's Method

The analysis has been performed using Bishop's method of slices. In this method, the failure section is divided into a series of vertical slices. The slice width is sufficiently small that the actual shape can be replaced with a rectangular. It is assumed that the slice weight W acts through the midpoint of the area.
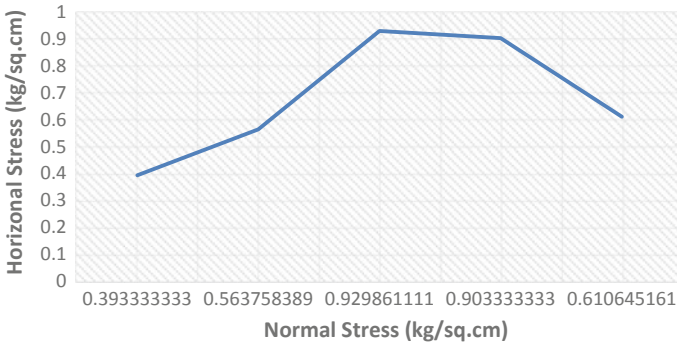
Fig. 3 Direct shear test

$$FS = \frac{1}{\sum_{i=1}^{i=\infty} W \sin\theta} \sum_{i=1}^{i=\infty} \frac{c'b + W(1 - ru)\tan\emptyset'}{m\theta}$$

where, F = Factor of safety

w = weight of slice

c = cohesion

b = width of slice

Φ = angle of internal friction

U = pore pressure at each slice

An iterative analysis is necessary to obtain the factor of safety. Since this is trial and error method, this section deals with the method of slope stability analysis using Oasys slope Software tool. Slope is a system which is utilized for investigating the stability of slopes. The system is additionally pertinent to earth weight and bearing limit issues. The systems are relevant likewise to shake slopes and waste stacks. There are three strategies of analysis may be performed using slope software tool, they are circular and non-circular slip surfaces. Circular surfaces are characterized by a rectangular matrix of centers and either various diverse radii, a regular point through which all rounds pass or a digression surface which the loop practically touches. Non-circular slip surfaces are characterized separately. The segment to be examined is spoken to by an arrangement of soil or rock strata with limits characterized via Cartesian co-ordinates. The pore water weight appropriation could be changed in every stratum.

Table 3 Reinforcement results

Description	Possible capacity KN/m	Actual capacity KN/m	Governing criterion	Applied pre-stress KN/m	Additional capacity KN/m
Geomembrane reinforcement	15.00	50.00	50.00	Tensile	50.00

4 Slope Stability Analysis Using OASYS Software

4.1 Data Input in Oasys Slope 19.1

Oasys software was established in 1976; Oasys is now recognized as a leading commercial developer for structural and geotechnical, crowd analysis, and pedestrian modeling solutions. Oasys slope is the ideal choice for 2D slope stability analyses, and for a wide variety of slope stability analysis, simple and easy to use. Reinforcing components like rock bolts, soil nails, earth field anchors, and geotextiles are analyzed. Innovative solutions from Oasys slope stability software are characterized attractive, self-generated interfaces, and fast and powerful with which users can trial opinion rapidly and worthwhile. Authorize designer to precisely specify and calculate the most analyzable of plan issues, with full assurance in agreement with global standardized characteristic with different major combination. The following data can be entered into the software with different soil strata and in the presence of the groundwater Table 3. The data can be entered in both tabular and graphical forms. The methods are fully interchangeable and will update automatically. Before the analysis, the input and after the analysis, output data has been shown in Figs. 3 and 4.

4.2 Graphical Output

See Fig. 5.

5 Result and Analysis

The factor of safety (FS) against pullout is required because of uncertainty in the maximum mobilized shear strength. Selection of the safety factor, therefore, depends on the designer's confidence in the value of this strength and how critical the slope is with respect to a potential failure. The soil-geosynthetics friction is influenced by both the soil with geosynthetics and without geosynthetics. The Bishop's method is experimented use of in the evaluation of factor of safety. The factor of safety
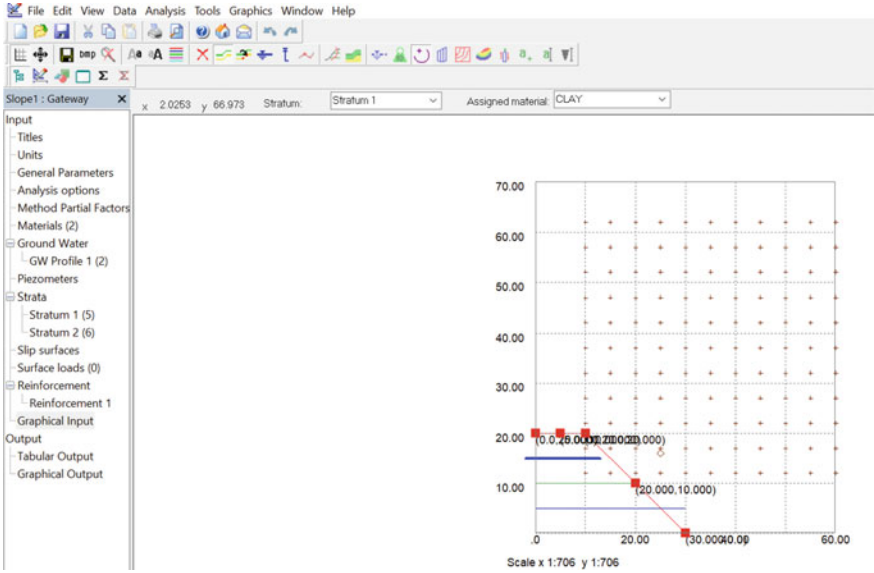
Fig. 4 Graphically represented input data in Oasys software (data entry screens)
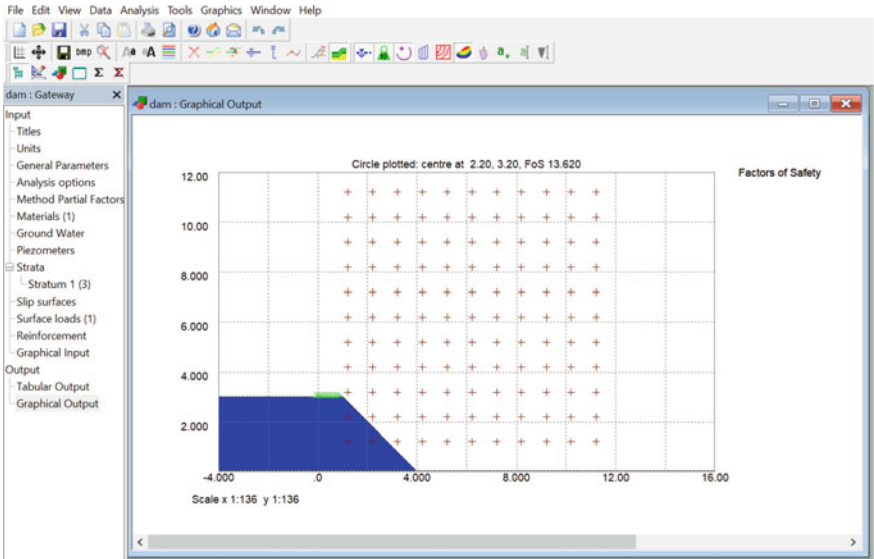

Fig. 5 Graphically represented output data in Oasys software (data entry screens)

obtained was 1.32 without geosynthetics as shown in Fig. 5. In the case of with geosynthetics, the factor of safety obtained is 1.36, which is giving around 4% more than as compared to FS obtained as shown in Figs. 6 and 7.

Note: The applied pre-stress force is the lesser of the specified pre-stress and the actual capacity for this slip surface. The additional capacity is the actual capacity minus the applied pre-stress force. If the angle of reinforcement is greater than the angle from the circle center to the point of intersection with the slip surface, only the applied pre-stress force is taken into account.
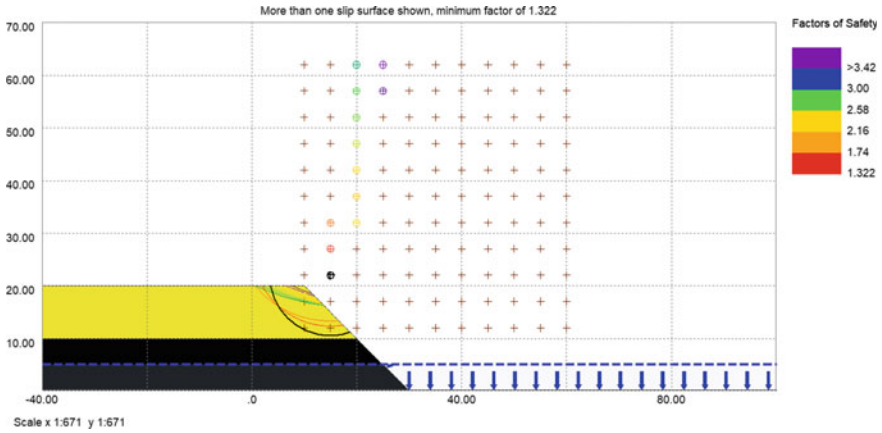

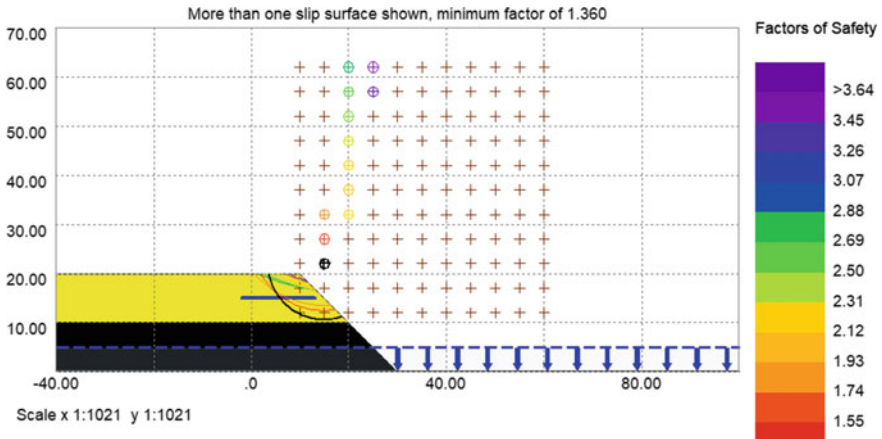**Fig. 6** Graphical output without geosynthetics section I

Fig. 7 Graphical output with geosynthetics section II

6 Conclusions

1. Factor of safety obtained for the section I without geosynthetic material yields values less than 1.5, which indicates that the slope is unsafe against failure, which is from the slip that have occurred during monsoons.
2. Factor of safety obtained for the section II with geosynthetics material yield stress greater than 1.5 which indicate slope is safe conditions.
3. Results of software analysis are within 0–4% for both sections without geomembrane and with geomembrane. Hence, the Bishop's method can effectively be used to determine the factor of safety of the slope.
4. The 0–4% difference in FOS can be attributed to capability of Oasys software to optimize the number of slices in Bishop's method and selection of ideal trial slip circle.
5. Factor of safety values less than 1.5 indicate the susceptibility of slope to failure. At present, the sites show signs of erosion and slips and if ignored, they may develop into major landslides in the near future due to excessive rainfalls.
6. From this study, it concluded that the factor safety values increase when we are introducing the geomembrane as a liner material which is given better values and slope also safe.

This project aims study of limit equilibrium method in various slope stability analyses based on significant works with regards to stability of slopes. Various parameters and factor of safety equations are described. In this project, we study the comparisons made between strength reduction technique and the effect of search techniques on the results obtained from limit equilibrium method using commercially available programs. A numerical investigation is carried out to compute the present condition of Hyderabad city protection slope under seismic load to protect soil from hazardous waste.

References

1. Bishop, A.W.: The use of the slip circle in the stability analysis of Earth slopes. Géotechniques **5**(1), 7–17 (1955). https://doi.org/10.1680/geot.1955.5.1.7
2. Abramson, L.W., Lee, T.S.: Slope Stability and Stabilization Methods. Wiley, New York (1996). ISBN: 0471106224
3. Tanaka, Y., Baker, R.: A convenient alternative representation of Taylor's stability chart. In: Proceedings of International Symposium on Slope Stability Engineering, pp. 253–257 (1999). https://doi.org/10.1061/(asce!1090-0241)(2002)128:4(351)

4. Bottero, A., Negre, R., Pastor, J., Turgeman, S.: Finite element method and limit analysis theory for soil mechanics problems. Comput. Methods Appl. Mech. Eng. **22**(1980), 131–149 (1980). https://doi.org/10.1016/0045-7825(80)90055-9
5. Chakraborty, S., Bhattacharya, G., Jana, D., Ojha, S.: Direct search for minimum reliability index of earth slopes. Comput. Geotech. **30**(6), 455–462 (2003). https://doi.org/10.1016/S0266-352X(03)00059-4
6. Chen, J., Yin, J.-H., Lee, C.F.: Slope Stability Analysis Using Rigid Element. The Hong Kong poly Technical University (2004). https://doi.org/10.1139/t03-032
7. Lee, C.F., Jian, Chen, Yin, J.H.: Upper bound limit analysis of slope stability using rigid finite elements and nonlinear programming. Can. Geotech. J. **40**(2003), 742–752 (2003). https://doi.org/10.1139/T03-032
8. Chen, R.H.: Three-dimensional slope stability analysis. Joint Highway Research Project, Eng. Experiment station, Purdue University, Report JHRP-81-17. Project No.: C-36-36 N File No.: C-14-14 (1981)
9. Janbu: Application of composite slip surfaces for Stability Analysis. In: Proceedings of Europen conference on the stability of earth slops, vol. 3, pp. 43–49. Stockholm (1957)
10. Swedish: Soil sampler with metal foils swedish geo technical institute. In: Proceedings no. 1, 75p (1957)
11. Bacicn, B.: Slope stability analysis. Géotechniques 5(1), 7–17 (2014)

Stability Analysis of Slope in Kuranjeri During Kerala Flood 2018 Using PLAXIS-3D

Lakshmi Manohar and A. K. Vasudevan

Abstract Landslide or landslip is defined as a type of mass movement in which a mass of rock, debris or earth down a slope under the direct influence of gravity. In this study, Kuranjeri of Thrissur district has been selected where landslides occurred during 2018 Kerala floods. In this case, landslide was triggered by incessant heavy rainfall followed by mass movement of debris. An investigation was carried out to discern index properties and soil parameters on the collected soil samples. Limit equilibrium method (LEM) is the most common approach for analysing slope stability by investigating the equilibrium of a soil mass tending to slide down under the influence of gravity. As a powerful alternative advanced numerical method, Finite element method (FEM) quantifies factor of safety against slope instability by strength reduction method of stability analysis using PLAXIS-3D. A comparison is then made between the results of LEM and FEM by in cooperating properties of in situ soil on slope failures. The analysis result unveils that the infiltration of water into the slope resulted in the failure of the slope on account of reduction of shear strength parameter of the soil.

Keywords Landslide · Kerala flood 2018 · Rainfall · Slope stability analysis · PLAXIS-3D

L. Manohar (✉) · A. K. Vasudevan
Thejus Engineering College Vellarakkad, Thrissur, Kerala 680584, India
e-mail: lakshmimanohar454@gmail.com

A. K. Vasudevan
e-mail: vasudevanarikkath@gmail.com

1   Introduction

1.1   *Landslide*

Landslides, described as mass movement of soil or rock, differ from other types of soil or rock movement (falls, topples or flows) by its shear displacement along one or several rupture surfaces, which are either visible or maybe reasonably inferred [5, 7]. Landslip or landslide is a dynamic phenomenon in the hilly terrains around the world and is a part of ongoing evolution of the landscapes that constitute a major threat to both lives and property worldwide causing long term impact on society as well as nation. The tropical climate, unstable land forms, deforestation and unplanned developmental activities make the hilly areas of India prone to landslides as an annual and recurring event.

The groundwater table for most of the high slopes is located deep below the ground surface. And the pore-water pressure of the soil above ground water table is negative. This negative porewater pressure known as matric suction, when referenced to pore-air pressure, contributes to the stability of unsaturated soil slopes. Hence the effect of rainfall infiltration on slope could result in changing soil suction and positive pore pressure, or main water table as well as raising soil unit weight, reducing shear strength of rock and soil [2, 4]. Generally, unsaturated soil slope failures happen most frequently during rain periods. The infiltration of rainfall will increase the groundwater level as well as the corresponding water pressure, which in turn decrease the matric suction of unsaturated soils.

1.2   *Slope Stability*

The slope stability analysis is usually carried out to assess the safe and economic design of natural or man-made slopes. Slope stability can be defined as the resistance of an inclined surface to failure by either sliding or collapsing [9]. The possible failure mechanism as well as the site conditions can be considered as two major factors governing the analysis technique. The basic concept of slope stability is to determine the minimum factor of safety.

Different methods used in the slope stability analysis are limit equilibrium method, limit analysis theorem, numerical modelling, etc. Limit equilibrium method satisfies force and/or moment equilibrium of a soil mass above the potential failure wedges. Limit analysis is used due to its physical significance and strict solving range [8]. Numerical modelling has been emerged as a tool based on the application of finite element and upper bound analysis of plasticity limit analysis.

The advantages of adopting numerical techniques (Finite Element) in slope stability problems are [3],

- failure occurs naturally through the zones within the soil mass in which soil shear strength is unable to withstand the applied shear stresses.
- No assumption needs to be made in advance about the shape or location of the failure surface. There is no concept of slices and hence no assumptions are required for inter-slice side forces.
- The solutions from numerical methods provide information about deformations at working stress levels.
- Progressive monitoring of failure is possible.

1.3 Kerala Flood

Kerala has witnessed one of the worst floods of the century after the great flood of 99 that happened in 1924. In the month of August alone, Kerala had recorded excess rainfall of 41% that led to opening of 34 out of 39 dams which resulted in loss of 483 lives and a damage of Rs. 40,000 crore. Thrissur district alone received an increase in rainfall around 16%. Thrissur District Administration has informed a loss of Rs. 1300 crore. Within the district, 42 villages in and around the Cole fields and on the banks of Conolly canal and Herbert canal were inundated with the Karuvannur river changing its direction. 98 roads in Thrissur were submerged in flood water. 14 landslides were recorded within the district.

1.4 Study Area

In this study, Kuranjeri of Thrissur district has been selected where landslides occurred for the first time in its history during Kerala flood in August 2018. Kuranjeri is a forest area situated in Thekkumkara/Minaloor Panchayath of Thalapilly Taluk, Thrissur district, Kerala. The study area witnessed one of the largest landslides of the district. The site is located at a latitude of N 10° 37′ 41.2″ and longitude of E 76° 13′ 48.1″. The failure area comprised toe of width 65 m with an elevation of 63 m. At an elevation of 128 m subsidence occurred. During the landslide, the soil got displaced to an extent of 500 m and resulted in loss of 19 lives. In addition, four houses were washed away with severe damage to roads, crops, other material property. Figure 1 shows the landslide that occurred in Kuranjeri.

Topography. The area consists of dry deciduous vegetation, teak being the major among them. The hill has a slope of 34° with a height of 152 m from the MSL. Laterite has orange to red colour and clay of white colour. Soils exhibited medium to fine grained texture. A channel was present at the bottom of the failure surface where sand and boulder sized particles were observed.

Geomorphology. The lithology of the terrain includes forest tree underlaid by forest soil followed by 4 m thick laterite with fragments of weathered crystalline rock below

Fig. 1 Shows landslide at Kuranjeri on 16/08/18

which weathered bed rock was present as shown in Fig. 2. Some clay patches were observed in the site. A newly formed under developed cracks were present just a few meters below the crest.

Rainfall. During the occurrence of landslide, Thrissur district marked rainfall as shown in Table 1 collected from Kerala Agricultural University, Vellanikara.

Fig. 2 Lithology at the site of failure at Kuranjeri

Table 1 Rainfall data

Dates	15/08/18	16/08/18	17/08/18
Rainfall (mm)	140.6	253.6	148.4

2 Materials and Methods

For this study, a reconnaissance survey was conducted and all the necessary details were collected from the site as well as from the locals from the area. The samples were collected from four locations at 1 m depth from ground surface that comprises two from the slide mass portion and two from the unaffected areas at a distance of 15 m apart marked as S1A, S1B, S1C and S1D as shown in Fig. 3. Both disturbed as well as undisturbed soil samples were collected from four locations. The undisturbed soil samples were taken with help of sampling tube and were tightly sealed to preserve the natural properties of the soil while transporting. The field density of the soil samples was determined from the site itself. Detailed experimental investigation was conducted to determine the geotechnical properties of the collected soil samples in the laboratory using the standard procedures put forward by Indian Standard codes.

2.1 Experimental Investigation

The collected samples were tested in laboratory to classify the soil as well as for determining the shear strength characteristics of the soil. The studies were carried out using the procedures outlined by IS 2720. The soil samples of all four locations had high percentage of sand sized particles of range 52%, 87%, 86% and 67% with fines in it. The fines have intermediate plasticity for the first three locations and low

Fig. 3 Location of sample collected

plasticity for S1D. The soils were classified as per the Indian Standard Classification System and they are clayey sand (SC), clayey sand (SC), silty sand (SM), and clayey sand (SC), respectively. The index properties of the soil samples of the four locations are given in Table 2.

The shear strength parameters of the soil sample were determined by triaxial unconsolidated undrained test, i.e. drainage from the soil specimen is not permitted during the application of chamber pressure. The test specimen is sheared to failure by the application of deviator stress. Modulus of elasticity required for numerical analysis in PLAXIS-3D using Mohr Coulomb model was determined by taking the slope of initial tangent drawn to the stress versus strain curve with respect to total stress. Theoretical method for the determination of pore water pressure, suggested by Skempton was used to determine the effective strength parameters. The engineering properties of the four soil samples are tabulated as shown in Table 3.

Figure 4 and 5 depict the modified failure envelope obtained in terms of total stress and effective stress for the four samples. The failure envelopes were drawn for the ultimate stress.

Table 2 Index properties of soil samples

Properties		S1A	S1B	S1C	S1D
Natural water content (%)		3	5	5	5
Field density (kN/m^3)		17	17	18	17
Saturated density (kN/m^3)		23	23	25	24
Specific gravity		2.5	2.5	2.7	2.6
Atterberg limit	Liquid limit (%)	37	44	38	34
	Plastic limit (%)	24	25	25	24
	Plasticity index (%)	14	19	13	11
	Shrinkage limit (%)	17	19	20	22
Particle size distribution	Gravel-sized particles (%)	3	1	1	5
	Sand-sized particles (%)	52	87	86	67
	Fine-sized particles (%)	45	12	13	28

Table 3 Engineering properties of the soil samples

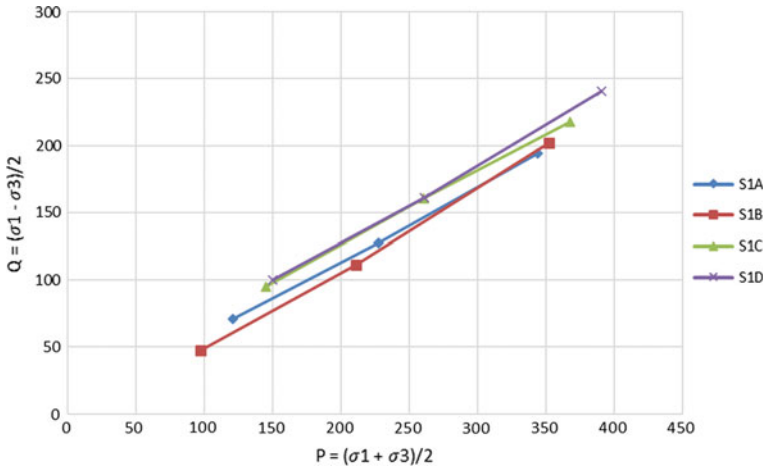| Properties		S1A	S1B	S1C	S1D
Compaction characteristics	OMC (%)	21	18	12	20
	MDD (kN/m^3)	18	17	18	18
Triaxial	c (kN/m^2)	6	5	14	10
	ϕ (°)	33	29	33	36
	E (kN/m^2)	10,000	17,500	25,000	18,000
	c' (kN/m^2)	4	2	13	9
	ϕ' (°)	26	21	27	30

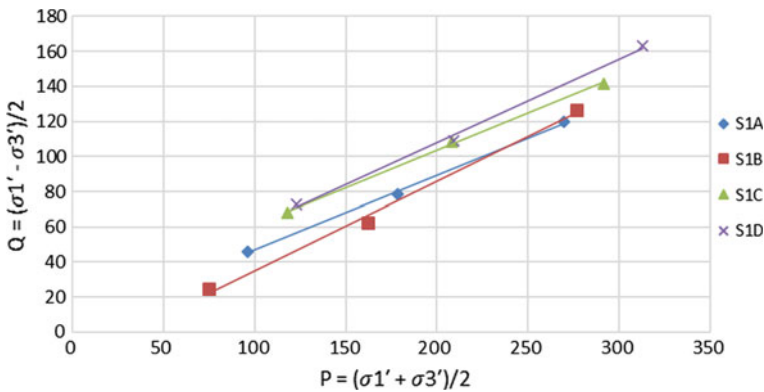**Fig. 4** Modified failure envelope under total stress

Fig. 5 Modified failure envelope under effective stress

2.2 Limit Equilibrium Method

Limit equilibrium methods investigate the equilibrium of a soil mass tending to slide down under the influence of gravity. These methods include conventional limit equilibrium method (LEM) like the method of slices, Bishop's modified method, force equilibrium methods, etc. Transitional or rotational movement is considered on an assumed or known potential slip surface below the soil or rock mass. All these methods are based on the comparison of forces, moments, or stresses resisting movement of the mass with those that can cause unstable motion. The output of the analysis is a factor of safety, defined as the ratio of the shear strength (or, alternatively, an equivalent measure of shear resistance or capacity) to the shear stress (or other

equivalent measure) required for equilibrium. If the value of factor of safety is less than 1.5, the slope is unstable.

Analysis of Finite Slope. If the slope is of limited extent that connects land at one elevation to land that is not far away but is at different elevation, it is called a finite slope. They may exist in nature and man-made. The examples of finite slopes are the inclined faces of earth dam, embankments, cuts, etc. Failure of finite slopes occurs along a surface which is a curve. In stability computations, the curve representing the real surface of sliding is usually replaced by an arc of a circle or logarithmic spiral. The stability of a finite slope can be investigated by a number of methods. Some of them being the Culmann's method of planar failure surface, the Swedish circle method (slip circle method), the friction circle method and the Bishop's method [6].

The method developed by Swedish engineers is based on the assumption that the rotational angle of sliding during failure is circular [1]. This method requires summing of the moments of all forces acting on the slope, including the gravitational force on the soil mass and the shear stress along the failure surface. If the moments are unbalanced in favour of movement, the slope fails else it will remain stable. The factor of safety can be calculated in this case as the ratio of the moments resisting failure to those causing failure. The analyses were carried out in different trials for different slip circles centred at different points of the Fellinius line drawn. The minimum factor of safety was selected from these trials. The slip circle with minimum factor of safety is called the critical surface. The slip circle is generally divided into 6–12 slices. Normal and tangential components of weight of each slice were found. The factor of safety against sliding is given by equations below.

1. For total stress

$$\text{F.S.} = \frac{cLa + \tan\varphi \sum N}{\sum T} \tag{1}$$

2. For effective stress

$$\text{F.S.} = \frac{c'La + \tan\varphi' \sum N'}{\sum T'} \tag{2}$$

2.3 PLAXIS

PLAXIS 3D is a finite element package intended for three-dimensional analysis of deformation and stability in geotechnical engineering with a full 3D pre-processor that allows CAD objects to be imported and further processed within a geotechnical context. The program is supplied as an extended package, including static elastoplastic deformation, advanced soil models, stability analysis, consolidation and safety analysis.

PLAXIS is intended to provide a practical analysis tool for use by geotechnical engineers who are not necessarily numerical specialists. Quite often practicing engineers consider nonlinear finite element computations cumbersome and time consuming. The PLAXIS research and development team has addressed this issue by designing robust and theoretically sound computational procedures, which are encapsulated in a logical and easy-to-use shell. As a result, many geotechnical engineers world-wide have adopted the product and are using it for engineering purposes.

The safety analysis in PLAXIS is determined by Phi-c reduction which is executed by successively reducing the strength parameters of the soil until the collapse of the soil occurs. The reduction of these parameters is controlled by total multiplier ΣMsf which is equal to the ratio of the available strength over strength at failure.

2.4 Stability Analysis of Slope

For both the analyses, the slopes were considered to be finite as well as homogenous for all the four samples. The LEM analyses were carried out in different trials for different slip circles centered at different points of the Fellinius line drawn graphically. The critical failure surface was converted into circular form and analysis was carried out. For FEM analysis, the geometry of slope and the necessary soil parameters were entered required to analyse the slope. The soil was modelled as Mohr-Coulomb model and the meshing was carried out by using fine option in order to attain greater accuracy. Many numbers of trials were carried out using different depth of wetting.

3 Results and Discussions

Both the analytical and numerical analyses were carried out for all the four samples considering the height of the hill slope to be 89 m inclined at an angle of 34°. The analysis was carried out in terms of both total stress as well as in effective stress condition. For the analysis, the water table was not taken into consideration. Tables 4 and 5 tabulate the factor of safety obtained for LEM and FEM in terms total stress and effective stresses, respectively.

Table 4 Factor of safety obtained in terms of total stress

Type of analysis		Factor of safety			
		S1A	S1B	S1C	S1D
LEM	Swedish method	1.069	0.822	1.144	1.277
FEM	PLAXIS-3D	1.097	0.9356	1.177	1.266

Table 5 Factor of safety obtained in terms of effective stress

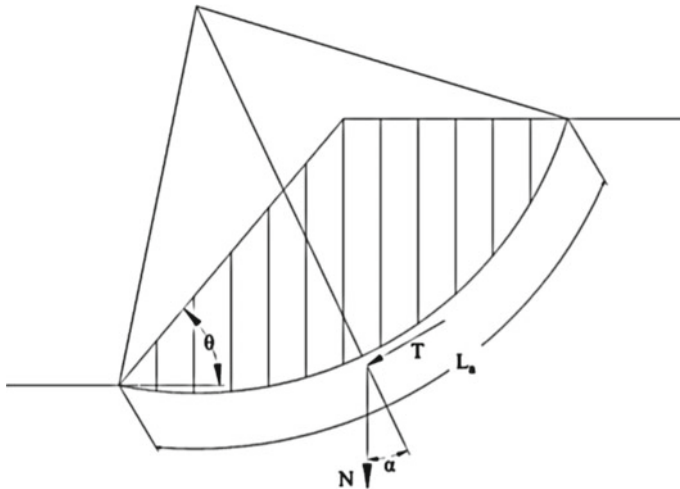| Type of analysis		Factor of safety			
		S1A	S1B	S1C	S1D
LEM	Swedish method	0.798	0.592	0.903	0.991
FEM	PLAXIS-3D	0.813	0.6026	0.949	1.024

Fig. 6 Swedish circle method of analysis

Figure 6 represents slip surface divided into 12 slices for Swedish circle method of analysis.

Figure 7 is the resulting plot of the incremental displacement of S1B obtained from PLAXIS-3D that shows a good impression of the failure mechanism.

It is known that for higher intensity of rainfall for a longer duration leads to higher wetting depth. In the month of August, the study area had received incessant rainfall continuously. Table 6 tabulates the factor of safety obtained without wetting as well as wetting depth at 1 m, 2 m, 3 m, 4 m, 5 m and 6 m

The decrease in factor of safety is comparatively more prominent from a depth of 4 m to 5 m. Figures 8, 9 and 10 represent the results of strength reduction analysis carried out in PLAXIS-3D without wetting depth and at depth of wetting 4 and 5 m, respectively, for S1D.

4   Conclusions

For the first time in the history of Kuranjeri landslide occurred in the month of August during Kerala flood of 2018. The study area had received comparatively
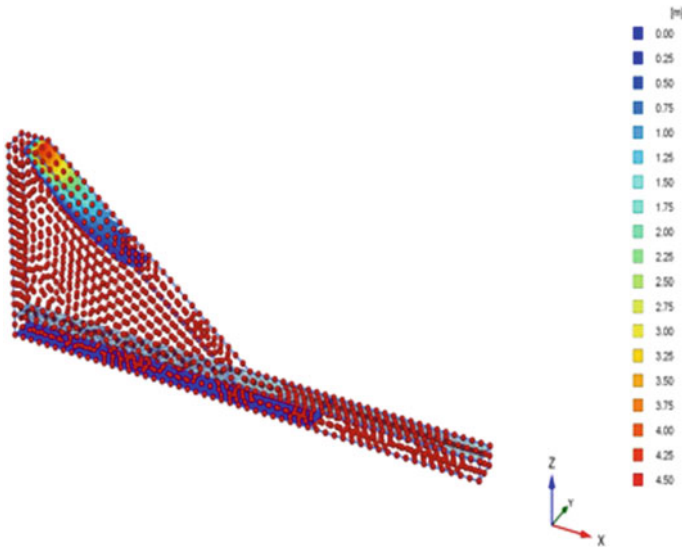
Fig. 7 Shadings of total incremental displacement indicating the most applicable failure mechanism obtained for S1B using PLAXIS-3D

Table 6 Slope stability analysis results of PLAXIS-3D for different depths of wetting

Wetting depth (m)	Factor of safety			
	S1A	S1B	S1C	S1D
0	0.8340	0.6040	1.086	1.111
1	0.8125	0.5998	0.9237	1.006
2	0.8114	0.6000	0.9225	1.004
3	0.8114	0.6009	0.9228	1.004
4	0.8115	0.6008	0.9221	1.005
5	0.8082	0.5990	0.9197	1.000
6	0.8056	0.5979	0.9176	0.9978

excess rainfall with longer duration nearly 16% for the month of August compared to the previous years. Hence, the effect of rainfall infiltration on slope resulted in changing positive pore pressure as well as raising soil unit weight thereby reducing shear strength of soil.

The results obtained from both the LEM and FEM analysis of slope stability were found to be in close agreement. The factor of safety obtained from the LEM and FEM analysis shows that the four slopes were having low factor of safety. The decrease in the factor of safety can be attributed to the fact that the shear strength parameters get reduced with infiltration due to introduction of pore pressure which results in the
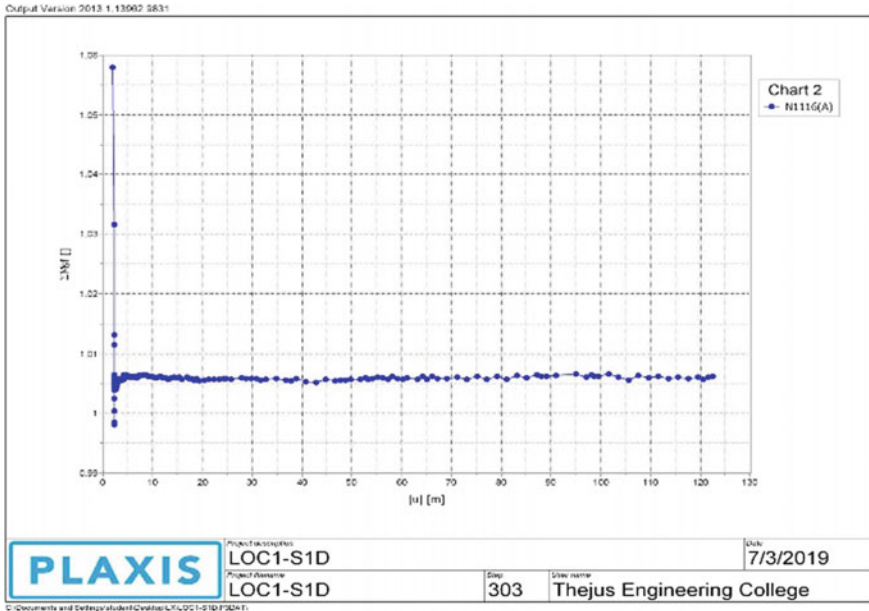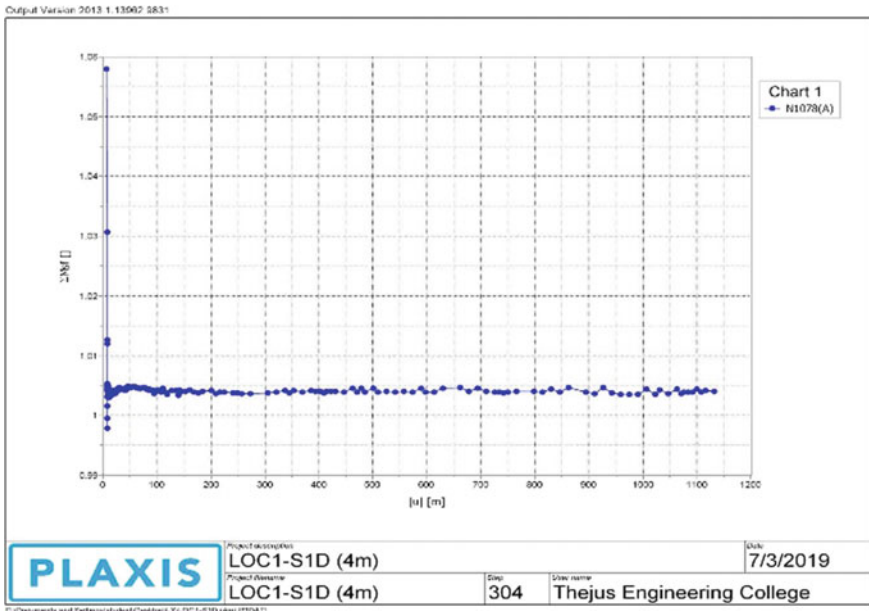
Fig. 8 Analysis without wetting for S1D using PLAXIS-3D

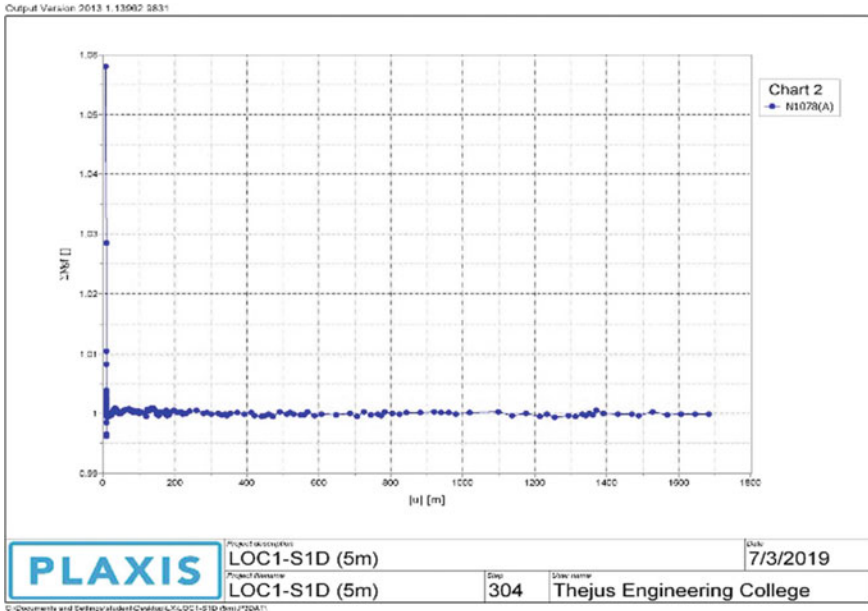**Fig. 9** Analysis with 4 m wetting for S1D using PLAXIS-3D

Fig. 10 Analysis with 5 m wetting for S1D using PLAXIS-3D

reduction of the strength parameters. The wetting depth of the study area was found to be between 4 and 5 m.

By providing suitable conventional or bio engineering methods that couples with proper drainage for the diversion or collecting arrangement of the rainwater may help to reduce the future slope failures.

References

1. Arora, K.R.: Soil Mechanics and Foundation Engineering, 7th edn. Standard Publishers Delhi (2008)
2. Ering, P., Kulkarni, R., Kolekar, Y., Dasaka, S.M., Sivakumar Babu, G.L.: Forensic analysis of Malin landslide in India. IOP Conf. Ser.: Earth Environ. Sci. 1–12. ISGG (2015)
3. Griffiths, D.V., Lane, P.A.: Slope stability analysis by finite elements. Geotechnique **49**(3), 387–403 (1999)
4. LNCS Homepage, https://link.springer.com/article/10.1007/s11069-016-2241-0
5. Praveen, K., Premalatha, K.: Stability analysis of slopes during monsoon in Nilgiris, Indian Geotechnical Conference Bengaluru (2018)
6. Punmia, B.C., Ashok, K.J., Arun, K.J.: Soil Mechanics and Foundation, 17th edn. Laxmi Publication, Delhi (2017)
7. Steven, L.K.: Geotechnical Earthquake Engineering. Prentice Hall, New Jersey (1996)

8. Suman, H., Sima, G., Richi, P.S.: A comparative study of soil slope stability under seismic loading condition. In: Madhavi, P., Raghuveer, R. (eds.) Geohazards Proceedings of IGC 2018, pp. 11–22. Springer (2018)
9. Wrachien, D.D.: Monitoring, Simulation, Prevention and Remediation of Dense and Debris Flows III. WIT Press (2010)

Generalized Three-Dimensional Slope Stability Analysis of Soil Using Plaxis 3D

P. M. Shafna and T. R. Anjana

Abstract Slope stability analysis requires sound geotechnical knowledge as well as sophisticated computer code for the design. The set of simplified design charts for analyzing the stability of soil slopes is developed by conducting a number of three-dimensional slope stability analysis using finite element code Plaxis 3D. Three-dimensional slope stability analysis was done for homogeneous clay under varying cohesion in different slope height. Also, the variations factors of safety for dry and partially saturated condition were compared. It is observed that the factor of safety increases when cohesion increases and decreases with increase in slope height.

Keywords Slope stability · Finite element analysis · PLAXIS 3D

1 Introduction

Slope stability analysis is found to gain more importance due to the huge constructions which are taking place on slopes. A slope stability problem essentially a 3-D problem and its analysis require sound geotechnical knowledge as well as an effective use of a sophisticated computing code for the design. Three-dimensional analysis methods consider the 3-D shapes of the slip surface [1]. In complex geometric structures, the three-dimensional analysis becomes more important. The geometry of the slope and slip surface varies significantly in the lateral direction. The material properties are highly homogeneous or anisotropic, and the slope is locally surcharged. The slope with a complicated shear strength and/or pore-water pressure requires combining the effect of slope geometry and shear strength to determine the direction of movement. It leads to a minimum factor of safety or to back calculate the shear strength of the failed slope. In these situations, a 3D analysis may be necessary [5].

P. M. Shafna (✉) · T. R. Anjana
Thejus Engineering College Vellarakad, Thrissur, Kerala 680584, India
e-mail: sachumohammed123@gmail.com

T. R. Anjana
e-mail: anjanatr@gmail.com

Parameters	Subsoil	Soil slope
Height (m)	10	6 and 8
Young's modulus (kN/m^2)	15×10^4	50×10^3
Unit weight (kN/m^3)	16	18
Saturated unit weight (kN/m^3)	19	20
Cohesion (kN/m^2)	28	12–25
Friction angle (deg)	30	0

The 3D slope stability analysis is found to give more reliable results than 2-D slope stability.

The factor of safety against slope instability is determined by gradually reducing the strength of the soil. As this is done, deformations occur, and at some value of the strength reduction factor, the deformation becomes very large, and the numerical process will no longer converge [4]. This numerical instability is interpreted as physical instability, and the value of the strength reduction factor when this happens is the factor of safety—the factor by which the strength must be reduced to bring the slope to a rate of barely stable equilibrium [3].

2 Geometry of Model for Homogeneous Soil

Firstly, a homogeneous soil with top width of 12 m, slope angle = 30° and slope height = 6 m and 8 m, respectively, as presented in the below figure, was investigated in this study. Here, the analysis was done for both dry and partially saturated condition. The fill and entire soil material were modeled as Mohr–Coulomb [2]. Table 1 states the summarized soil properties used in this Plaxis 3D model.

3 Method of Analysis

The stability analysis of soil slope has been done by finite element method using Plaxis 3D. The Mohr–Coulomb model was used as the analysis of the problem considered. Here, different slope height and cohesion and the combination of both considered and both analyses were done in dry and mid-depth saturated condition where we get the displacement and factor of safety and the relation between these two important factors for all variable data set.

4 Soil Slope Stability Analysis—Without Surcharge Condition

Slope stability analysis for without surcharge condition was done in dry and mid-depth saturated condition. The construction of soil model and generation of mesh are shown in Figs. 1 and 2, respectively.

4.1 Without Surcharge: At Dry Condition

The analysis was conducted in both 6 m and 8 m, respectively, under varying cohesion in homogeneous clay. The results obtained from the analysis are shown in Table 2 where the obtained factor of safety and incremental displacement were listed.

The variation of obtained factor of safety under cohesion is shown in Fig. 3. From the analysis, it was clear that when factor of safety increases cohesion increases and decreases when slope height increases.

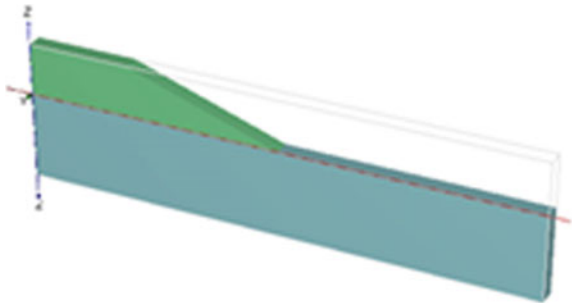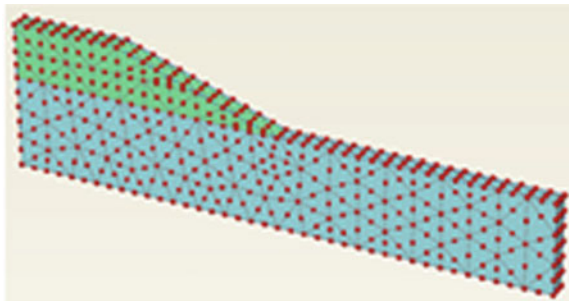**Fig. 1** Soil slope constructed above the subsoil

Fig. 2 Mesh generation

Table 2 Slope stability analysis of cohesive soil under dry condition

Height (m)	Cohesion (kN/m^2)	Incremental displacement (m)	Factor of safety
6	13	0.022	1.52
	15	0.016	1.80
	17	0.015	2.05
	19	0.014	2.29
	21	0.013	2.53
8	13	0.034	1.29
	15	0.031	1.49
	17	0.027	1.69
	19	0.025	1.88
	21	0.022	2.08

Fig. 3 Factor of safety versus cohesion in dry condition
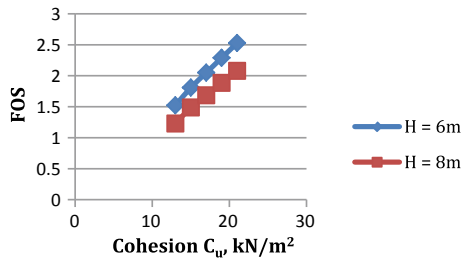
4.2   *Without Surcharge: At Mid-Depth Saturated Condition*

In mid-depth saturated condition, the obtained factor of safety value was lesser than in dry condition. Factor of safety obtained under varying cohesion of two different slope heights is shown in Table 3, and here, the incremental displacement was also listed.

Factor of safety versus cohesion was plotted in Fig. 4 which shows the variation of increasing factor of safety under cohesion.

5   Soil Slope Stability Analysis—With Surcharge Condition

Here, the soil slope is designed as embankment for the construction of road. From IRC: 58-2002, the tire pressure for the commercial highway vehicles was obtained as 800 kN/m^2. For the road of commercial vehicle, the load safety factor may be taken as 1.1. So, the stress acting on the embankment was obtained as 880 kN/m^2 (Fig. 5).

Table 3 Slope stability analysis of cohesive soil under mid-depth saturated condition

Height (m)	Cohesion (kN/m^2)	Incremental displacement (m)	Factor of safety
6	13	0.035	1.44
	15	0.033	1.66
	17	0.031	1.88
	19	0.028	2.06
	21	0.026	2.32
8	13	0.040	1.11
	15	0.037	1.28
	17	0.035	1.46
	19	0.033	1.63
	21	0.030	1.80

Fig. 4 Factor of safety versus cohesion in mid-depth saturated condition
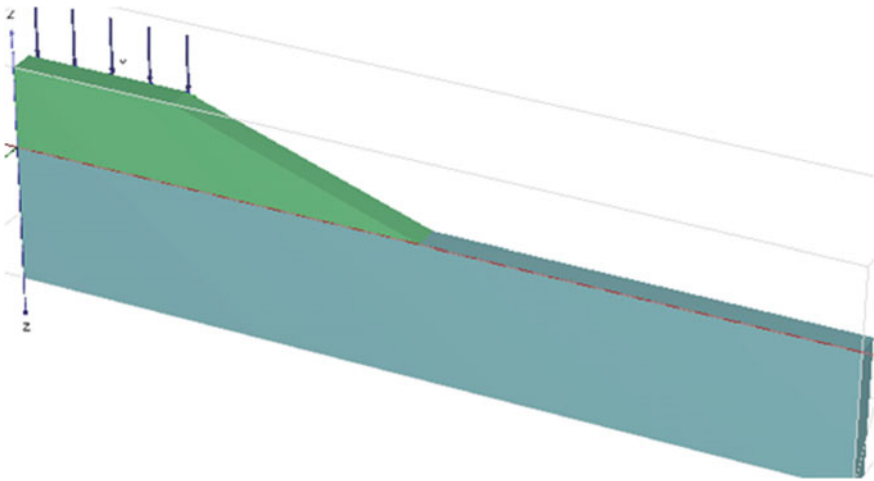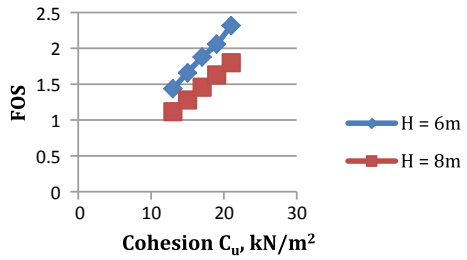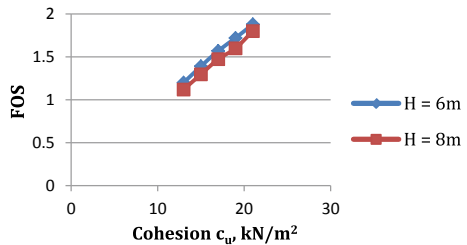

Fig. 5 Structure by loading condition

Table 4 Slope stability analysis of cohesive soil under dry condition

Height (m)	Cohesion (kN/m²)	Incremental displacement (m)	Factor of safety
6	13	0.042	1.20
	15	0.034	1.39
	17	0.030	1.57
	19	0.026	1.72
	21	0.023	1.88
8	13	0.095	1.12
	15	0.076	1.30
	17	0.070	1.47
	19	0.047	1.63
	21	0.043	1.81

Fig. 6 Factor of safety versus cohesion in dry condition

5.1 With Surcharge: At Dry Condition

The factor of safety obtained in the analysis under varying cohesion was shown in Table 4.

Figure 6 shows the variation of safety values under cohesion. And the analysis shows that factor of safety decreases when slope height increases.

5.2 With Surcharge: At Mid-Depth Saturated Condition

The lowest safety value was obtained in this analysis. Here, the slope became unstable with a height of 8 m under cohesion of 13 kN/m². The obtained factor of safety and incremental displacement from the analysis were shown in Table 5.

The variation of factor of safety was shown in Fig. 7. Here, graph was plotted between safety value and cohesion. And the lowest safety value was obtained in slope height of 8 m.

Table 5 Slope stability analysis of cohesive soil under mid-depth saturated condition

Height (m)	Cohesion (kN/m^2)	Incremental displacement (m)	Factor of safety
6	13	0.013	1.18
	15	0.129	1.32
	17	0.126	1.50
	19	0.119	1.69
	21	0.115	1.83
8	13	0.163	0.96
	15	0.158	1.05
	17	0.154	1.13
	19	0.152	1.34
	21	0.149	1.52
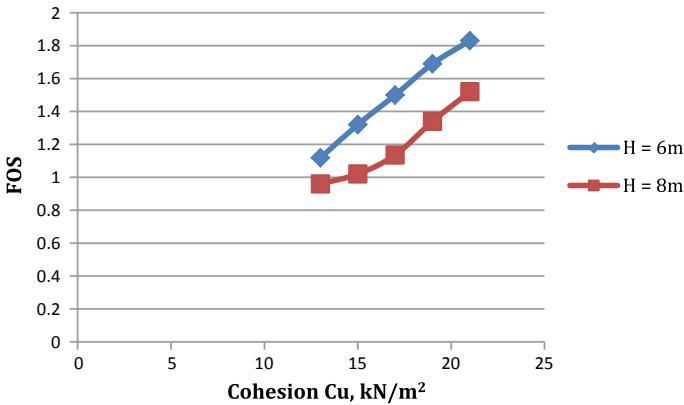
Fig. 7 Factor of safety versus cohesion in mid-depth saturated condition

6 Discussion

Stability of soil slopes depends on type of soil and soil height. And the soil became more stable in dry condition than saturated condition. From the analysis, it was found that the lowest factor of safety was obtained as 0.96 in 8 m slope height for the cohesion of 13 kN/m^2 under mid-depth saturated condition in loading case. And the higher safety value obtained in 6 m slope height is 2.53 of cohesion 21 kN/m^2 under dry condition without loading case.

7 Conclusions

This study proposes a method of analysis for soft soil embankment. The use of Plaxis software makes the analysis easier and practical. Factor of safety mainly depends on slope height, cohesion and soil condition. When slope height increases, factor of safety decreases, and it increases with increase in cohesion. The factor of safety varying from 1.2 to 1.88 and 1.18 to 1.83 for dry and saturated condition, respectively, under varying cohesion from 13 kN/m² to 21 kN/m² in 6 m slope height. And the slope is safer in dry condition than saturated condition. Least factor of safety was obtained as 0.96 for saturated condition of 6 m slope height.

References

1. Ali, F., Elias, F.: Slope stability analysis using numerical modelling. ASCE **2**, 60–67 (2014)
2. Binod, T., Ryan, D.: Application of GIS tools for three-dimensional slope stability analysis of preexisting landslides. ASCE **17**, 479–488 (2012)
3. David, A.: Importance of three-dimensional slope stability analysis in practice. ASCE **138**, 18–32 (2013)
4. Dov, L., Ching-Chuan, H.: Generalized three-dimensional slope stability analysis. ASCE **131**, 1748–1764 (2014)
5. Gilson, G., Maracos, A.: Three-dimensional slope stability model using finite element stress analysis. ASCE **131**, 191–198 (2016)
6. Li, H., Shao, L.: Three-dimensional finite element limit equilibrium method for slope stability analysis based on the unique sliding direction. ASCE 48–55 (2011)

Stability Assessment of a Soil Slope in Meghalaya, North-Eastern India

Antareep Kumar Sarma, **Ashesh Choudhury**, **Koustavjit Sarma**, and **Anangsha Alammyan**

Abstract Landslides are a common occurrence in hill slopes in the seismically active north eastern part of India. The soil slopes are highly vulnerable to failure due to heavy earth cuttings, rainfall and blasting activities during road construction. When landslides occur in transportation corridors running along hill slopes, there is the risk of huge loss to lives and property. In addition, the communication through these networks could be brought to a standstill during such catastrophes, resulting in considerable amount of time and resources expended in restoration of traffic and causing huge inconvenience to commuters. In this scenario, the need arises for a proper investigation on failure mechanisms of hill cut soil slopes and to envisage on appropriate mitigation measures. In the present study, stability analysis is carried out of in situ soil slopes newly exposed during a road widening along National Highway-40, a strategic road corridor in Meghalaya. The analysis consists of a limit equilibrium approach wherein the slope has been modelled using in situ soil conditions. The factors of safety of the slope against sliding failure have been calculated and the critical slip surface has been found by limit equilibrium analysis. The results of numerical modelling using the commercially available software SLOPE/W indicate unstable slopes potentially vulnerable to failure under adverse conditions. Necessary mitigation measures that need to be taken have been suggested based on the vulnerability condition of the slope.

Keywords Slope stability · Landslides · Limit equilibrium analysis · Factor of safety · Meghalaya

A. K. Sarma · A. Choudhury · K. Sarma · A. Alammyan (✉)
National Institute of Technology, Silchar, Silchar, AS 788010, India
e-mail: anangsha.nits@gmail.com

A. K. Sarma
e-mail: antreep247sarma@gmail.com

A. Choudhury
e-mail: contact.ashesh@gmail.com

K. Sarma
e-mail: koustabhjit@gmail.com

1 Introduction

Landslide is a geological phenomenon where a mass of earth slides or moves due to the loss in its stability in instances characterised by steep or gentle slope gradients. The main cause of landslides which affect the stability of slope is the gravity force. But generally, landslides occur due to the triggering by some other event such as incessant rainfall, earthquake, etc. Nowadays, landslides have become common along the highways and rail lines where natural hill slopes are cut and disturbed during the road and railway track construction. In the north-eastern part of India, landslides in this scenario are triggered by heavy rainfalls during the monsoon due to which the main national and state highways and the railway lines are blocked.

Two of the major landslides seen in this region in the recent years that disrupted the road and rail connectivity are mentioned herewith:

(1) Landslide incidence along Lumding–Badarpur Railway Line, Dima Hasao district, Assam (14 June 2018)—Incessant rainfall from 12 to 14th June 2018 triggered landslides blocking the Lumding–Badarpur railway service in Dima Hasao district of Assam. A high 382 mm of rainfall was recorded on 14.06.2018 which triggered four landslides between 2:00 P.M. and 3:00 P.M. along the Lumding–Badarpur Railway Line. The Bandarkhal landslide, located between Bridge No. 305 and Tunnel No. 19 led to the suspension of railway service in the Lumding–Badarpur line for three consecutive days [1].

(2) Landslide incidence at Sonapur, East Jaintia Hills District, Meghalaya—On 7th May 2018 (01:00 hrs), heavy rainfall triggered few landslides along NH-6 connecting Shillong with Barak Valley of Assam, Mizoram and Tripura which blocked 10 m stretch of the important road corridor for more than 12 h [2].

Due to such severity of the landslides, it is necessary to conduct a detailed slope stability analysis of the area both before and after the construction of roadways and railways so that the best method of prevention, control and stabilisation can be suggested and implemented.

1.1 Background of the Study

Analysing the stability of earth structures is the oldest type of numerical analysis in geotechnical engineering. The idea of splitting a potential sliding mass into slices was introduced early in the twentieth century and has gained significance in slope stability analysis problems around the world. The stability analysis of the Stigberg Quay in Gothenberg, Sweden, was studied where the slip surface was taken to be circular and the sliding mass was divided into slices [3]. In the next few decades, the scope of the method was expanded, and the Ordinary or Swedish method of slices was introduced. Further advancement in terms of application of circular slip surfaces and use of composite slip circles, etc., were developed in this method in the

mid-1950s [4, 5]. In 1965, a new technique was developed based on mathematically more rigorous formulations [6]. The reason for the limit equilibrium method being adopted so readily is that solutions could be obtained by hand-calculations. Simplifying assumption had to be adopted to obtain solutions, but the concept of numerically dividing a larger body into smaller pieces for analysis purpose was rather novel at the time.

The method of slices was initially believed to be true for slices where the normal stress along the sliding surface is primarily influenced by gravity. However, including reinforcement in the analysis makes its use far beyond intended intentions. While modern software is making it possible to analyse ever increasingly complex problems, the same tool is also making it possible to better understand the limit equilibrium method itself. Computer-assisted graphical viewing of data used in calculations makes it possible to look beyond the factor of safety. Salient features of limit equilibrium method are: (1) It satisfies force and moment equilibrium due to resisting and driving force on each slide. (2) For stable slope, the factor of safety is greater than 1. (3) Solution techniques differ on how equilibrium conditions are satisfied between interslice shear and interslice normal forces. (4) Solution technique differs in handling interslice shear forces for example Spencer method: constant function, Morgenstern-Price method: half sine, clipped sine, trapezoidal or user defined etc. (5) the slip surface shape is either arc, polygonal or composite [7–11]. A brief summary of the LEM analysis methods is provided in Table 1.

Finite Difference Method

The finite difference method is an approximate method which is used for solving partial differential equations. It is used for solving a wide array of problems including linear and nonlinear, time dependent and independent problems and their analysis. It also applies to problems with different boundary shapes, boundary conditions and for

Table 1 LEM analysis methods [4–7]

Method	Strength	Weakness
Bishop (1955)	Short analysis time	Inaccurate results when horizontal force is acting
	Applicable to arc/polygonal	
Janbu (1954)	Short analysis time	More conservative results
	Suitable for shallow slopes	
Spencer (1967)	Applicable to arc/polygonal	Longer analysis time
	More accurate safety factor	More sensitive convergence
Morgenstern and Price (1965)	Predictable internal normal force	Longer analysis time
	More accurate safety factor	More sensitive convergence
Sarma (1973)	Suitable for rock slope analysis	Longer analysis time and more sensitive convergence
	More accurate safety factor	Assumptions for cohesion and friction angle

a region containing a large number of different materials. With the development of high-speed computers having large-scale storage capability, many numerical solution techniques appeared for solving partial differential equation. However, due to the ease of application of the finite difference method, it is still a valuable means of determining the factor of safety and slope stability. The FLAC/Slope is a software which is based on finite difference method. Salient features of finite difference method are as follows: (1) Precise analysis method. (2) Iterative analysis. (3) The slope to be analysed is divided into several zones and each zone is analysed separately. (4) Simulates actual slope failure mechanism. (5) Both stress and strain conditions are satisfied [13].

Contrast Between Finite Difference Method and Limit Equilibrium Method

The difference between finite difference method (numerical method) and limit equilibrium method is that, in finite difference analysis, the slope to be analysed is divided into a finite number of zones or elements and characteristics of solution are representative of the natural evolution of the physical failure plane in the slope because they satisfy both of stress and strain (kinematics) but limit equilibrium methods satisfies only stress. A comparison between the characteristics of finite difference and limit equilibrium methods in solving for the factor of safety of slopes was done and was concluded that continuum mechanics based numerical methods have the following advantages: (1) No pre-defined slip surface is needed. (2) The slip surface can be of any shape. (3) Multiple failure surfaces are possible. (4) No statistical assumptions are needed. (4) Kinematics (stress and strain) is satisfied [14].

1.2 Description of the Site

An observational study was carried out along a stretch of highway along the NH-6 (previously named as NH-40) [15]. The cut-slope was analysed using the finite difference method and was found to be vulnerable. This paper analyses the stability of the slope using limit equilibrium method. The key characteristics of the site of study have been pointed out below.

Study Area

The study was carried out along a stretch of the along a stretch of highway along the NH-6 (previously named as NH-40) extending from Barapani and Jyntru village, Meghalaya. The area has a tough hilly terrain where the inclination of the slopes extends from being less than 10° to about 56°.

Geological composition

The slopes which were modelled had rocks of the Shillong Group and were basically meta-sediments, gneiss and granite.

Table 2 Geotechnical properties of soil used in the modelling (after [15])

Parent rock	Maximum wet density (g/cm³)	Cohesion (kPa)	Angle of internal friction (°)
Meta-sediments	1.95	17.85	24
Gneiss	2.00	19.22	26
Granite	2.073	20.8	27

Soil Properties

Based on the experiments conducted, the various important findings were as follows

(a) Significant amount (> 65%) of silt and clay particles was present.
(b) Soil was highly plastic.
(c) Natural moisture content (NMC) > optimum moisture content (OMC).

The various geotechnical properties used in this paper for modelling in SLOPE/W software are mentioned in Table 1.

The maximum wet density was used in the model as it was seen that in the site of the study, rainfall is predominant almost throughout the year, experiencing high to very high rainfall from the months of April to October [15]. During this time, landslides are seen to occur the most as the slopes remain very wet throughout the day. To get the most critical result, thus, the authors have used the maximum wet density.

Geometry of slopes

Four varying slopes are identified and modelled using LEM. The physical dimensions and geometry of the slopes are mentioned in Table 2.

The present study aims to assess the vulnerability to sliding of a newly exposed in situ soil slope along National Highway-40 in Meghalaya using the limit equilibrium analysis. The properties of the soil and the slope have been listed above, and the methodology applied is discussed herewith.

2   Methodology

The modelling of the concerned hill slopes was done in the software SLOPE/W of Geostudio-2019 [12] student edition. SLOPE/W software analyses the slope stability by satisfying the equations of statics and thus the limit equilibrium formulations. The general limit equilibrium formulation comprises of two factors of safety, one of which is derived by equating moments and the other by equating internal shear forces between the slices. Out of the several methods for computing factor of safety, Morgenstern-Price method was chosen as it computes the factor of safety by satisfying both moment and force equilibrium.

The general factor of safety equation with respect to moment equilibrium is:

$$F_m = \frac{\sum \left(c'\beta R + (N - \mu\beta) R \tan \tan \emptyset' \right)}{\sum Wx - \sum Nf \pm \sum Dd} \tag{1}$$

The factor of safety equation with respect to horizontal force equilibrium is:

$$F_f = \frac{\sum \left(c'\beta \cos \cos \alpha + (N - \mu\beta) \tan \tan \emptyset' \cos \cos \alpha \right)}{\sum N \sin \sin \alpha - \sum D \cos \cos \omega} \tag{2}$$

where,

c' is the effective cohesion, $\emptyset'$ is effective angle of friction, μ is the pore-water pressure, N is the slice base normal force, W is the slice weight, D is the concentrated point load, β, R, x, f, d and ω are geometric parameters and α is the inclination of slice base.

An equation was proposed to relate the interslice shear forces to the normal forces [6], which is-

$$X = E\lambda f(x)$$

where:

$f(x)$ interslice shear function,
λ the percentage (in decimal form) of the function used,
E the interslice normal force and
X the interslice shear force.

The choice of the interslice shear function is one of the major differences between the methods of computing factor of safety. Among these, only the Morgenstern-Price method (M-P method) gives the users the freedom of selecting interslice shear function. This present study considers half sine function for the M-P method in this study as the half sine function tends to concentrate the interslice shear forces towards the middle of the sliding mass and diminishes the interslice shear in the crest and toe areas. M-P method computes the required factor of safety for the slopes by satisfying both Eqs. 1 and 2 through several iterations.

2.1   Numerical Modelling

Four hill slopes were modelled in the SLOPE/W software by maintaining the geometrical parameters of the hill slopes given in Table 2. General procedure and guidelines of the software were followed during modelling. Some assumptions were taken in the modelling are: (1) The width of the four-lane highway (NH-6, previously called as NH-40) passing by the slopes was taken to be 23.5 m which is in accordance with the guidelines of Indian Road Congress, (2) The maximum wet density was used in the model as it was seen that in the site of the study, rainfall is predominant

almost throughout the year, experiencing high to very high rainfall from the months of April to October. During this time, landslides are seen to occur the most as the slopes remain very wet throughout the day. To get the most critical result, thus, this study considers the maximum wet density, (3) The pore water pressure conditions were chosen to be given by the piezometric line. But, the slopes to be modelled were hill slopes and hence the water table lies at a great depth.

3 Results and Discussions

The present study deals with the stability investigation of road cut hill slopes along NH-40 in Meghalaya, India. These exposed soil slopes were analysed by Morgenstern-Price method based on LEM. The four soil slope profiles with landslide events were analysed for stability using the strength properties of soil determined at its optimum moisture content. The factor of safety (FoS) values for the slopes have been found out to be in the range of 0.821–1.147. First two soil slopes from meta-sediments rock type of Shillong Group (Figs. 1 and 2) gives FoS values of 0.821 and 0.86, respectively, which indicates complete instability at maximum wet density of the existing soil. Maximum shear resistance of the critical slip surfaces of these two slopes are found out to be 62.85 kPa and 59.82 kPa, respectively. The soil mass of both slopes was oversaturated because of heavy and prolonged rainfall during the period which results in the loss of shear strength of the soil mass. The third slope near Karbalu village consisting of gneiss as parent rock gives FoS value of 0.903 indicating complete instability. The maximum shear resistance of circular failure
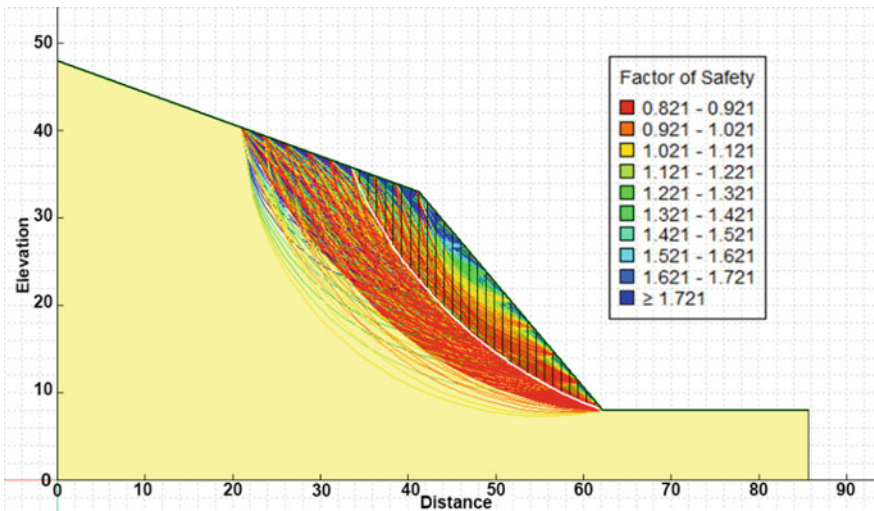

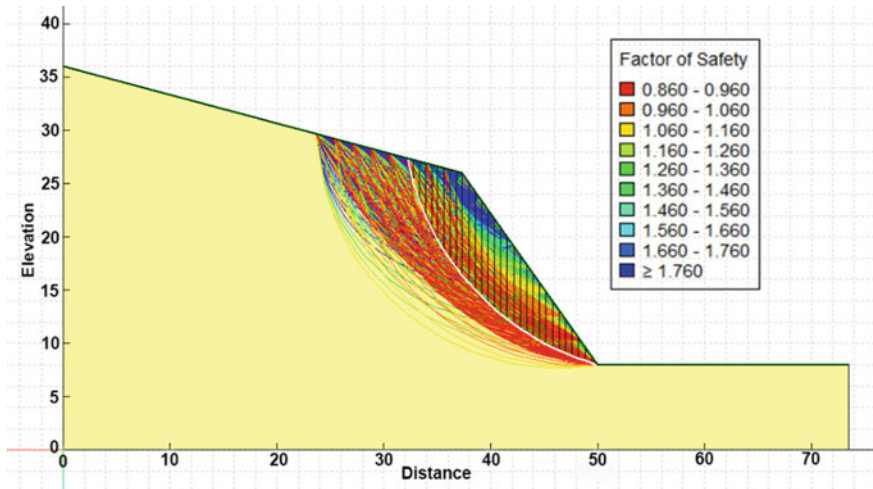**Fig. 1** Slip surfaces of slope 1 (metasediments)

Fig. 2 Slip surfaces of slope 2 (metasediments)

surface is 64.73 kPa. The Jyntru village slope comprised of granite-based rock has a FoS of 1.147, which indicates that the shear resistance is greater than the maximum shear stress on the critical slip surface. The value of maximum shear resistance of the critical failure surface of the slope is around 61 kPa. The main reason behind the increased FoS of the fourth slope is seemed to be the lesser inclination of the natural slope above the cut slope, which implies lesser impact of gravity force in the direction of the slip surface. Although the FoS value of the fourth slope is greater than 1, but it is still not acceptable as per the standard guidelines of slope stability which suggests minimum FoS value of 1.25 [16]. The impending failure mode of all the four slopes is found out to be toe failure with circular failure surface. Table 3 sums up the results found out from the present analysis (Tables 4 and 5).

Note: The white line in Figs. 1, 2, 3 and 4 signifies the critical slip surface.

Table 3 Geometry of soil slopes (after [15])

Parent rock	Slope height (m) and slope angle (°)	
	Cut slope	Natural slope
Meta-sediments	25 m, 50°	15 m, 20°
	18 m, 55°	10 m, 15°
Gneiss	15 m, 60°	5 m, 25°
Granite	15 m, 50°	2 m, 5°

Table 4 Results of the stability check of the concerned hill slopes from this study

Parent rock of slope	Factor of safety (FoS)	Maximum shear resistance of slip surface (kPa)	Impending failure mode	Stability
Metasediments 1	0.821	62.85	Toe	Unstable
Metasediments 2	0.86	59.82	Toe	Unstable
Gneiss	0.903	64.73	Toe	Unstable
Granite	1.147	61.00	Toe	Stable

Table 5 Results of the stability check of the concerned hill slopes (after [15])

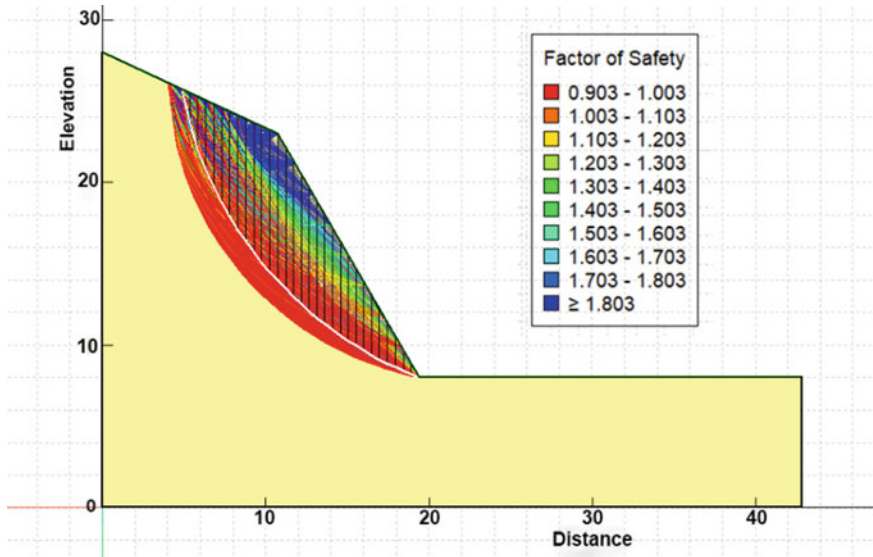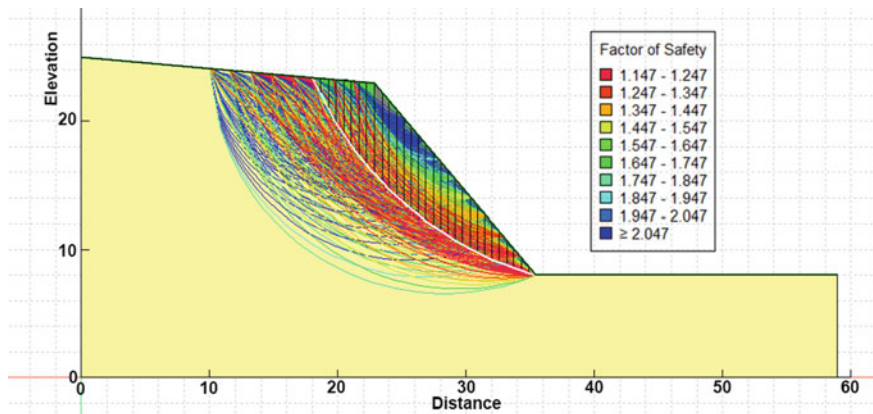| Parent rock of slope	Factor of safety (FoS)	Maximum shear strain rate	Stability
Metasediments 1	0.39	4.5×10^{-8}	Unstable
Metasediments 2	0.22	4.5×10^{-4}	Unstable
Gneiss	0.26	8.0×10^{-4}	Unstable
Granite	0.47	4.25×10^{-6}	Unstable

Fig. 3 Slip surfaces of slope 3 (gneiss)

Fig. 4 Slip surfaces of slope 4 (granite)

4 Conclusion

The main objective of this study was to compare the results obtained from the investigation of the hill cut slopes along NH-6 (previously called as NH-40) in India, where Finite difference method (FDM) was used for the analysis [15] with the results obtained using limit equilibrium method (LEM). It is necessary to validate the results LEM because it is a widely known method—the concept of which is properly known even to students who have just started learning geotechnical engineering. Moreover, the results in LEM satisfy only the stress characteristics but FDM, which is a numerical method satisfies both stress and strain characteristics. So, it becomes necessary to compare both the results. The FoS, maximum shear resistance and the impending failure mode were found out using the SLOPE/W software. The results obtained from this study are almost following the same trend of slope instability as obtained by FDM method with fourth slope being an exception as the FoS for that slope has come out to be greater than one. The results obtained are signifying a dangerous scenario of impending slope failure of the concerned hill cut slopes which necessities the importance of a detailed slope stability analysis before expanding or constructing any roads through hilly terrain. In order to resist the slope failure, several stabilisation measures such as implementation of surface and subsurface drainage system, soil grouting as well as buttressing the toe of the slopes w can be effective to certain extent. Since the results are indicating the mode of failure to be toe failure, proper attention should be given at the base of the slopes to prevent the landslides. Being in one of the north eastern states, the slopes are severely affected by the continuous high intensity rainfall in the monsoon season. Hence, keeping in view of this scenario, properly maintained drainage system should be ensured before exposing these hill-cut slopes. Apart from that, re-excavation of the slopes to make them flatter and encouraging vegetation growth can be the last option to get over the disaster.

References

1. Tep, Y., Kikon, A.: Note on preliminary investigation of landslides along the hill section of Lumding-Badarpur Railway Line, Northeast Frontier Railway
2. Singh, G., Kumar, S., Jamir, I.: Geological Survey of India, NER-Shillong. Report of the Sonapur 4 km milestone landslide, East Jaintia Hills District, Meghalaya
3. Brand, E.W., Brenner, R.P.: Soft Clay Engineering. Elsevier Scientific Publishing Company (1981)
4. Janbu, N.: Application of composite slip circles for stability analysis. In: Proceedings of the Fourth European Conference on Stability of Earth Slopes, vol. 3, pp. 43–49 (1954)
5. Bishop, A.W.: The use of slip circles in the stability analysis of earth slopes. Geotechnique **5**(1), 7–17 (1955)
6. Morgenstern, N.R., Price, V.E.: The analysis of the stability of general slip surfaces. Geotechnique **15**, 79–93 (1965)
7. Bishop, A.W., Morgenstern, N.: Stability coefficient for earth slopes. Geotechnique **10**(4), 164–169 (1960)
8. Lu, K., Zhu, D., Yang, Y., Gan, W., Zhou, Y.: A rigorous limit equilibrium method for the slope stability analysis. Disaster Adv. **6**, 135–141 (2013)
9. Zhi Huang, C., Hua Cao, Y., He Sun, W.: Generalized limit equilibrium method for slope stability analysis. Appl. Mech. Mater. **170–173**, 557–568 (2012). https://doi.org/10.4028/www.scientific.net/AMM.170-173.557
10. Yang, H., Wang, J., Liu, Y.: A new approach for the slope stability analysis. Mech. Res. Commun. **28**, 653–669 (2001). https://doi.org/10.1016/S0093-6413(02)00217-3
11. Dongping, D., Zhao, L.-H., Li, L.: Limit equilibrium method for slope stability based on assumed stress on slip surface. J. Central South Univ. **23**, 2972–2983 (2016). https://doi.org/10.1007/s11771-016-3361-0
12. Geo Slope: SLOPE/W Manual. GEO-SLOPE International Ltd. (2015)
13. Slope, F.: Flac Slope Manual. Itasca Consulting Group Inc., Minneapolis (2002)
14. Kanjanakul, C., Chubuppakarn, T.: Comparison between numerical and limit equilibrium methods for slope stability analysis. Published in 18th National Convention on Civil Engineering (2013)
15. Umrao, R.K., Singh, R., Sharma, L.K., Singh, T.N.: Soil slope stability along a strategic road corridor in Meghalaya north-eastern India. Published in Saudi Society for Geosciences 2017
16. WSDOT: Geotechnical Design Manual. M46-03.08 (2013)

Assessment of an Open Cast Coal Mine Slope Stability at Mohanpur Block, Raniganj Coalfield, West Bengal, India

Agami Pramanik, Avishek Adhikary, and Supriya Pal

Abstract A large open cast coal mine always needs a stable side slope to prevent collapse due to excessive overburden pressure. The present study was undertaken to assess the stability of slope of an open cast coal mine located in Mohanpur block in the Raniganj coalfield area in West Bengal, India. The pseudo-static approach of stability analysis was performed using Plaxis 3D software package under strength reduction technique. A Mohr–Coulomb constitutive model was considered for the simulation of geological materials under drained and undrained conditions. The average overall depth of the mine slope was considered as 144 m. The slope was designed following the coal mine regulations of mechanized open cast mining (CMR 2017) [1], Ministry of Labor and Employment, Govt. of India. The maximum vertical deformation and safety factor were examined to ascertain the optimized slope angle of the Mohanpur open cast pit. Three trial slopes were considered using three different slope angles. The slope angle of 40° was selected as the design slope as the safety factor as well as vertical deformation was found to satisfy the permissible limits under seismic accelearations considered in the present study.

Keywords Slope stability analysis · Open cast coal mine · Optimized slope angle · Pseudo-static approach · Plaxis 3D

A. Pramanik (✉) · A. Adhikary · S. Pal
Department of Civil Engineering, National Institute of Technology Durgapur, Durgapur 713209, West Bengal, India
e-mail: pramanikagami44@gmail.com

A. Adhikary
e-mail: avishek.adhikary31@gmail.com

S. Pal
e-mail: supriya070478@gmail.com

1 Introduction

Optimum design of the open cast mine pit slope is important from both stability and economic point of view. Hence, the aim of the design of an open cast mine is to provide the best possible outline of excavation with respect to safety, ore recovery and financial return [2]. The most crucial part of the design is to find the optimum slope angle which depends upon the strength parameters of the overburden soil/rock materials involved. Also, it is known that the sloping walls of the large mines are generally steeped in nature with alternate flat and sloping portions known as step/bench and batter, respectively. These act as an extra safeguard toward sliding/slipping of loose sloping mass soils/ rocks. Generally, the height of each batter varies in between 10 and 15 m, and the width of the bench is 20–40 m. The scientific studies of open cast mine pits force the use of sound geotechnical practice in their design for the sake of cost-effective and safe mining.

For many decades, limit equilibrium methods were used in solving geotechnical engineering and particularly slope stability problems. In this method, the safety factor (SF) is calculated as the ratio of the existing shear strength to the shear stress at equilibrium [3]. However, the design of mine slopes is quite complex in nature. Therefore, the simple limit equilibrium method is no longer considered by the scientists/researchers for precise design of mine slopes. In this case, the application of finite element method (FEM) has proven better analysis tool for the stability analysis of the open cast pit slopes and safe design of mines. FEM is more refined and powerful because no assumption needs to be made about the location, direction and shape of slip surfaces. Failure naturally occurs through sections on which soil's shear strength is not capable of sustaining the applied shear stresses [4, 5]. Also, the stress, displacements in different planes throughout the cross section can be found out easily. But in the framework of large-scale mining slopes, obtaining realistic input information and interpreting the results are the trickiest aspects of numerical modeling [6].

The primary objective of the paper is to analyze the open cast mining slope of Mohanpur block under seismic accelerations with the help of Plaxis 3D software and to find out how the design parameters of the mine are responsible in the stability of the slope. The geometric modeling of the slope was performed using the Plaxis software package, and thereafter, seismic excitation was considered in the structure globally. The safety analysis of the slope was then carried out to obtain the safety factor. In this paper, different trial slopes with varying angle of inclinations were considered to evaluate the optimum slope angle considering a benchmark factor of safety (FOS) of 1.5.

2 Problem Statement and Numerical Model

Open cast mining involves the extraction of ore from seams relatively near the surface by means of an open pit. Construction of an open pit mine requires the information of the ore underground. Drilling of boreholes in the ground is required followed by plotting each hole location on the map. The data collected through the holes provide an idea of the extent of the ore's body under the Earth surface. In this study, a typical cross section of an open cast mine at Mohanpur block in Raniganj coalfield is taken into account. The geometric features are indicated in Fig. 1.

- Maximum height of each lift at OB portions = 12 m (top soil of 3 m).
- Maximum height of each lift at coal seam portions = 6 m,
- Minimum exposed width of each berm = 30 m,
- Angle of slope of one stage with above configuration = 70°, 50° and 40°.
- First working bench of 50 m exposed width at 22 m height from the pit bottom.
- Second working bench of 50 m exposed width at 44 m height from the pit bottom.
- Third working bench of 50 m exposed width at 76 m height from the pit bottom.
- Forth working bench of 50 m exposed width at 108 m height from the pit bottom.

The overall depth of the mine is 144 m. The coal layers are indicated in hatch lines. The top soil was observed up to a depth of 6 m below ground surface, and rest of the overburden in the slope comprises sandstone and shale.

2.1 Assumptions of Models

The primary assumption is that the major cause of slope failure occurred due to the development of excessive shear stress in the structure. The mine slope is analyzed here numerically based on the self-weight/overburden pressure and varying earthquake load for different earthquake excitations. The boundary condition in X and Y direction is set as "Normally fixed" and free in the negative Z direction (here, upward direction is taken as positive Z) in the numerical model of the slope stability analysis. The linear-elastic perfectly-plastic Mohr–Coulomb model is considered in the geo-material modeling in the analysis. The geo-material properties such as Young's modulus (E), the cohesion (c), the friction angle (φ), Poisson's ratio (ν) and unit weight of soil (γ), used in the model as input parameters, were evaluated through experiments performed at the Soil Mechanics and Foundation Engineering laboratory, Department of civil engineering, National Institute of Technology Durgapur, West Bengal, India. In this case, dilatancy angle was taken as zero, since it is close to zero for clay and for sands with a friction angle less than 38°. The slope is analyzed for both drained and undrained conditions. At the undrained condition, instant pore water pressure is generated even above the groundwater table. It is done to find the SF in a worst case scenario when all the soil pores are blocked and water cannot drain out through them.

Fig. 1 Sectional layout of open cast coal mine at Mohanpur block (all dimensions are in m)

2.2 Material Properties

Table 1 provides the properties of pit slope materials.

3 The Shear Strength Reduction (SSR) Technique

Computation of safety factor in Plaxis was performed considering phi-c reduction technique at each stage of slope modeling. In this calculation, the load advancement number of step procedure is followed. The incremental multiplier M_{sf} is used to specify the increment of the strength reduction of the first calculation step. The strength parameters are reduced sequentially at each step until all the steps have been performed. The final step results in a fully developed failure mechanism. Otherwise, the calculation is repeated with a higher number of additional steps. Once the failure mechanism is obtained, the factor of safety is estimated based on following expression:

$$ \text{SF} = \frac{\text{Available shear strength}}{\text{Shear strength at failure}} = \Sigma M_{sf}(\text{value of } Msf \text{ at failure}) \qquad (1) $$

The SSR technique is widely applied in stability studies of open pit slopes. This is so because it contains all the benefits of limit equilibrium analyses, and at the same time, it allows the user to assess the displacement of the slope that are often critical in the evaluation of open pit stability [7].

Table 1 Geotechnical properties of pit slope materials

	Sandstone and shale materials	Coal samples	Top Soil
γ (kN/m^3)	24.71–26.53	15.83–16.65	19.11–20.37
c (kN/m^2)	94–132	62–76	17–22
Φ (°)	33–35	18–20	28–32
E (MN/m^2)	457–546	79–101	165–176
μ	0.30–0.31	0.39–0.40	0.32–0.34

where
$\gamma = $ Unit weight of the material
$\Phi = $ Angle of friction
$c = $ Cohesion
$\mu = $ Possion's ratio
$E = $ Modulus of elasticity

4 Results and Discussions

In the present work, the angle of the slope was optimized by trial and error method. Three trials were made with three different slope angles, viz. (i) 70°, (ii) 50° (iii) 40°. In Plaxis 3D, dynamic loading can be considered in a pseudo-static way [9] by specifying global acceleration which is taken into account for different earthquake zones as given in Table 2. The results are given below:

4.1 70° Slope Angle

Initially, the slope angle was chosen 70°. Pseudo-static stability analysis of the slope was done using Plaxis 3D software in three stages. The drainage conditions of the materials were set to "undrained". The horizontal seismic coefficient for Zone III was included in the numerical analysis. The safety factor (SF) was found out to be 1.12 following SSR technique in Plaxis 3D model (Fig. 2).

Table 2 Horizontal Seismic Coefficient for Different Earthquake Zones [8]

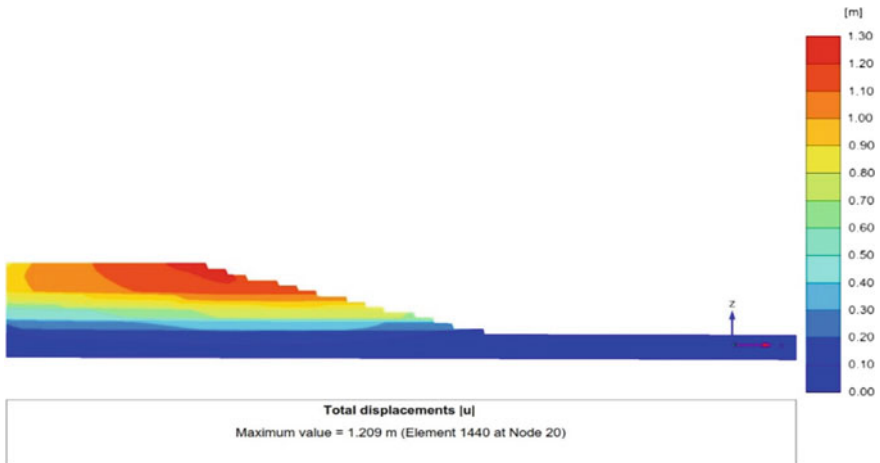| Earthquake zones	Zone II	Zone III	Zone IV	Zone V
Horizontal acceleration coefficient	0.02	0.04	0.05	0.08

Fig. 2 Total vertical displacement of mine slope (angle of inclination of 70°) at Mohanpur block using Plaxis 3D software

Total displacements |u|
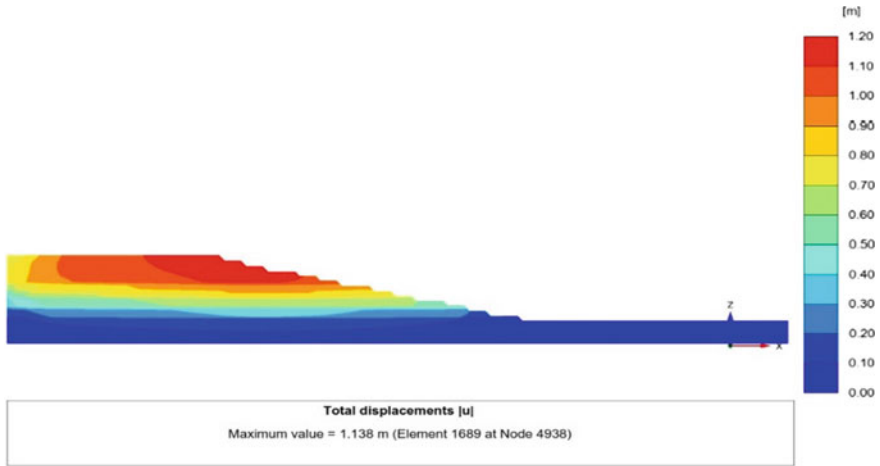Maximum value = 1.138 m (Element 1689 at Node 4938)

Fig. 3 Total displacement along X-axis of mine slope (50°) at Mohanpur block in Plaxis

Table 3 Results for open pit slope at Mohanpur block (70° and 50° slope)

Zone 3 (undrained condition)		
Slope	70° slope	50° slope
Safety Factor	1.12	1.21

4.2   50° Slope Angle

As the SF is less than 1.5 for 70° slope, next trial was made with the reduced slope angle of 50°. Pseudo-static stability analysis of the slope was carried out in Plaxis 3D in the same manner as stated above keeping all the parameters same as previous analysis. In this case, the safety factor (SF) was obtained as 1.21 (Fig. 3 and Table 3).

4.3   40° Slope Angle

From the above results, it is clearly seen that the safety factor was less than 1.5 for both 70° and 50° angle. This clearly states that such steep slope angles are not appropriate for this mine pit. Therefore, the slope angle is further reduced to 40°, and the slope stability analysis is done. Results are given in Table 4 as depicted.

Therefore, it is clearly seen that with the reduction of slope angle to 40°, the design of slope satisfies the required critical factor of safety as well as nominal vertical displacement of the slope is observed. Thus, this slope can be applied in the field to get a safe working condition without the risk of collapse of the slopes due to excessive overburden pressure (Figs. 4 and 5).

Table 4 Results for open pit slope stability analysis at Mohanpur block (40° slope)

Eartquake zones	Factor of safety and horizontal displacement							
	Zone 2		Zone 3		Zone 4		Zone 5	
Horizontal acceleration coefficient	0.02		0.04		0.05		0.08	
Drainage	Drained	Undrained	Drained	Undrained	Drained	Undrained	Drained	Undrained
SF	2.187	1.889	1.991	1.74	1.903	1.682	1.679	1.489
Horizontal displacement (m)	0.196	0.17	0.23	0.198	0.25	0.218	0.324	0.283
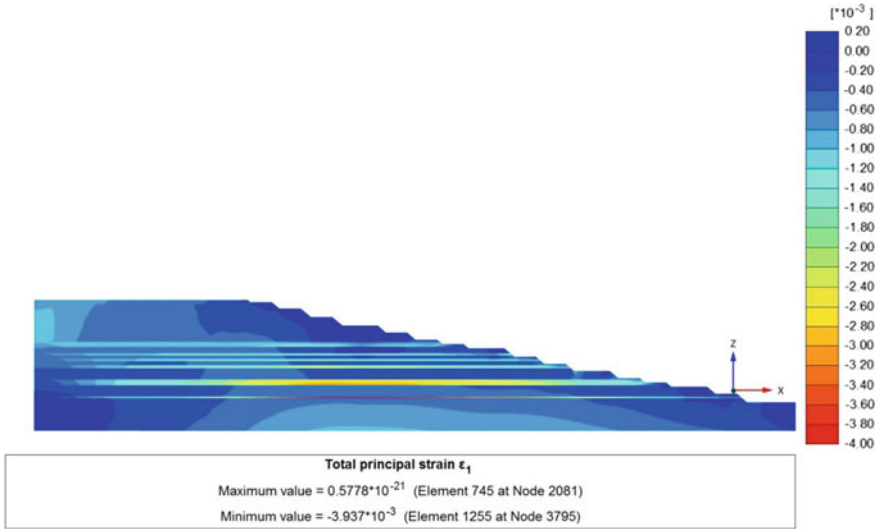
Fig. 4 Total principle strain of mine slope (40°) at Mohanpur block in Plaxis
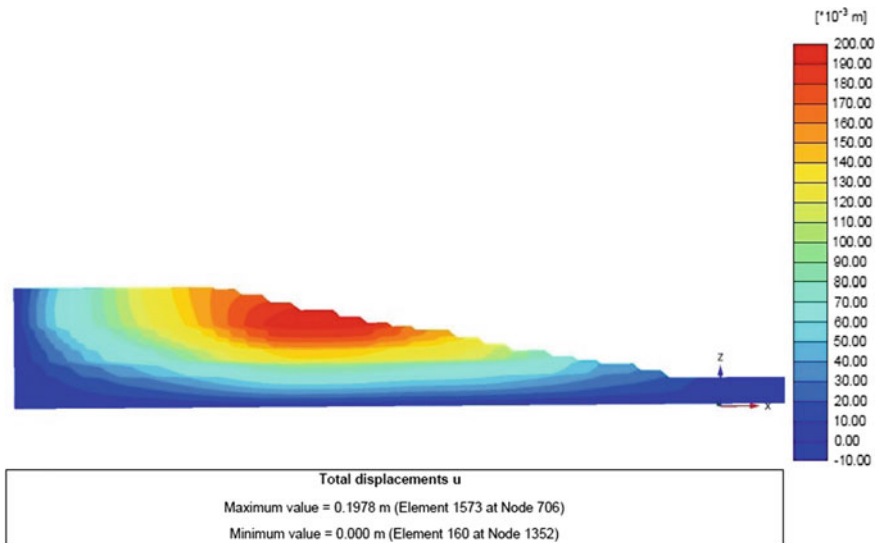

Fig. 5 Total vertical displacement of mine slope (angle of inclination of 40°) at Mohanpur block using Plaxis 3D software

5 Conclusions

In the present study, a number of trials were performed with varying slope angles of the open cast mine in order to design the side slopes which can withstand the overburden pressure without showing signs of collapse. It was observed that keeping all other parameter same, the factor of safety decreases with increase in seismic acceleration coefficient.

The safety factor is less for undrained condition in comparison with drained condition of the slope mass. Assuming that all the drainage paths are blocked, in undrained condition, instant pore water pressure is generated within the soil/rock even above the water table making it a worst case scenario. Therefore, the factor of safety was found decreased in undrained condition.

There is no well-defined failure surface was observed in the mine slopes. As the mine is not homogeneous, coal seams are much weaker than the surrounding sandstone and shale. Therefore, strain is higher in the coal seams. And there is no continuity within the parting.

Displacement is higher in drained condition than undrained condition of the sloping mass. In drained condition, the pore water pressure in the soil/rock mass is completely dissipiated, and therefore, settlement is more. However, in the undrained condition, instant pore water pressure is generated, and therefore, it takes long time to settle. So, the displacement is higher in drained condition than undrained condition of the soil.

References

1. Coal Mine Regulation [Part II, Sec 3 (i)], Ministry of Labour and Employment, Govt. of India (2017)
2. Read, J., Stacey, P.: Guidelines for Open Pit Slope Design. CSIRO Publishing, Australia (2009)
3. Duncan, J.M., Wright, S.G.: Soil Strength and Slope Stability. Wiley (2005)
4. Duncan, J.M.: State of the art: limit equilibrium and finite-element analysis of slopes. J. Geotech. Eng. **122**(7), 577–596 (1996)
5. Griffiths, D., Lane, P.: Slope Stability analysis by finite elements. Géotechnique **49**(3), 387–403 (1999)
6. Hustrulid, W., McCarter, M., Van Zyl, D.: Slope Stability in Surface Mining, Society for Mining, Metallurgy & Exploration (SME) (2001)
7. Hoek, E.: Fundamentals of Slope Design, Keynote address, Slope Stability 2009, Santiago, Chile, 9–11 (2009)
8. Earthquake Resistant Design of Structures IS 1893:2016 [Part I]
9. PLAXIS 3D Reference manual

A Numerical Study on Geotextile-Reinforced Slopes

Hardik V. Gajjar and Veerabhadra M. Rotte

Abstract In recent times, use of geosynthetics has gained widespread acceptance and has been used as reinforcing component in numerous geotechnical engineering structures. During construction of geotextile-reinforced slope, it become essential to maintain certain value of factor of safety for each stages of construction. In this paper, a numerical study on slopes reinforced with and without geotextiles is presented. To capture the trend of development of axial forces in the geotextile layers under plastic analysis, four different slope inclinations (β) (i.e., $\beta = 45°, 60°, 75°$ and $90°$) with slope height of 7 m were selected. Reinforced slopes were provided with equal number of geotextile layers along with uniform length (L_g) of 6.4 m. The uniform vertical spacing (S_v) of 1.0 m between any two geotextile layers was chosen. To simulate staged construction method which is adopted at site, finite element tool PLAXIS 2D was used for stability analysis. The construction of slopes was simulated in seven stages of equal height for all the slope inclinations. The results showed that minimum axial forces were developed at the top most geotextile layer for all the four slope inclinations ($\beta = 45°, 60°, 75°,$ and $90°$). Maximum axial forces were observed to develop in all geotextile layers for the slope having $\beta = 90°$ when it compared to other slope inclinations. With an increase in axial stiffness (EA) of geotextile layers by 100%, it was noticed that only 16% increase in axial force at the bottommost geotextile layer for the slope with 75° inclination.

Keywords Axial force · Slope inclinations · Reinforcement stiffness · Geotextile-reinforced slopes

H. V. Gajjar · V. M. Rotte (✉)
Department of Civil Engineering, Institute of Infrastructure Technology Research and Management, Ahmedabad 380026, India
e-mail: vmrotte@iitram.ac.in

1   Introduction

Geotextile-reinforced slopes (GRS) are mainly compacted embankments which are incorporated with geotextile layers as a reinforcement element. In geotextile-reinforced slopes, firstly, failure plane is assumed and the length of geotextile beyond the failure plane is considered for resisting moment. Resisting moment depends upon the tensile capacity, interface friction developed between geotextile and soil and placing pattern of reinforcements. Koerner [7] was one of the few early researcher who provided analysis method of geotextile reinforced slope (GRS) based on limit equilibrium concept. Taking forward the concept, Mandal and Labhane [8] carried out parametric studies (i.e. in terms of slope inclination and length of reinforcement layer) on GRS. For ease of calculation, few researcher [5, 6] provided the design charts for overall stability and local stability of GRS.Over the period of time finite element method was widely and many researchers [2, 3] set few of the benchmark example by validating with LE method. Influence of reinforcement parameter (i.e. tensile capacity, vertical spacing, placement pattern etc.) was studied using computational study [1, 4, 9, 11]. For solving the complex geometry problem in geotechnical engineering, one cannot deny the fact that centrifuge modeling has proven to be one of the robust modeling technique in understanding deformation and failure mechanism [10, 12, 13].

2   Problem Description

Available literature shows diverse opinions regarding the development of maximum axial force along slope height. Few literatures show that researchers have assumed maximum axial force at the toe of the slope. Other researchers found maximum axial force at mid height of the slope. In the present work, a parametric study has been carried out on geotextile-reinforced slope using finite element-based software PLAXIS 2D to identify the location of maximum axial force along geotextile layers for various slope inclinations (β).

3   Modeling GRS in PLAXIS 2D

The finite element method (FEM) has become essential tool in modeling and simulation of advanced engineering projects. In building complex engineering projects, engineer and designer go through a complicated process of modeling, simulation, visualization, analysis, design, prototyping and testing. In all this phases, FEM become a standard tool. The behavior of physical phenomenon in a system depends upon the geometry, property of the material or medium, boundary conditions, initial and final loading conditions. In nature, most of the problem exists in sophisticated

geometry and difficult boundary conditions. Creating the geometry model is the first step toward preparation of finite element model. Geometry is nothing but the representation of problem statement. Geometry is prepared using points and lines. Once the required geometry is prepared, multiple soil strata can be assigned in it along with structural objects. Once the geometry is made, it is discretized into smaller pieces known as elements or cells, and this process is usually referred as meshing. As the numbers of elements increases, it increases the computational time of the simulation. Meshes should be selected according nature of the problem. For 2D Problem, the meshing is carried out usually in triangular (15 Nodes) or quadrilateral shape. Majority of slope stability geometry does not have any curved boundaries but if one encounter any curved surface, higher order element can be used. When there is more than one material, nodes should be provided at the interface. Nodes should also be provided at discontinuity points. Three types of fixities are available which can be assign in the geometry that is horizontal fixities (Displacement in X direction $= 0$), Vertical fixities (Displacement in Y direction $= 0$) and total fixities (Displacement in X & Y direction $= 0$).

$$[K_E]\{\Delta d_e\} = \{\Delta R_E\} \tag{1}$$

$$\{\Delta d\} = \left\{ \begin{array}{c} \Delta u \\ \Delta v \end{array} \right\} = [N] \left\{ \begin{array}{c} \Delta u \\ \Delta v \end{array} \right\}_n = [N]\{\Delta d\}_n \tag{2}$$

$$\Delta \varepsilon_x = \frac{\partial (\Delta u)}{\partial x} \tag{3}$$

$$\Delta \varepsilon_y = \frac{\partial (\Delta v)}{\partial y} \tag{4}$$

where $[K_E]$ is the element stiffness matrix, $\{\Delta d_E\}$ is the vector of incremental element nodal displacements and $\{\Delta R_E\}$ is the vector of incremental element nodal forces. In an Eqs. 3 and 4, $\Delta \varepsilon_x$ and $\Delta \varepsilon_y$ are the strain corresponding to the displacements. In an Eq. 2 'N' is the shape function. In PLAXIS 2D, the analysis is done in three stages (i) Gravity loading: stress due to gravity is calculated (ii) Plastic analysis: show the actual deformation of slope (iii) Safety analysis. In design of an embankment it is necessary to check the stability during each stage of construction along with over all stability. Phi–c reduction method (Shear strength reduction) has been used in current studies for reinforced slopes. Several earlier research works show successful usage of this method [3]. Phi-c reduction calculation type was used, which reduces the values of cohesion (c) and angle of internal friction (ϕ) in steps until the soil body fails, the following equation is used

$$\frac{C}{C_r} = \frac{\tan \varphi}{\tan \varphi_r} = \sum M_{\text{Sf}}$$

c_r and ϕ_r are the reduced strength parameter that are just large enough to maintain equilibrium. The safety factor is then defined as the value of $\sum M_{sf}$ at the failure, provided that at failure a more or less constant value is obtained for number of successive load steps. For most reinforced slope stability / safety analyses, $\sum M_{sf} = 0.1$ is an adequate first step to start up the process. During the calculation process, the development of the total multiplier for the strength reduction $\sum M_{sf}$ is automatically controlled by load advancement procedure. Figure 1 shows sketch of modeled GRS geometry used for the finite element analysis. Soil parameter as well as reinforcement parameters are tabulated in Table 1.
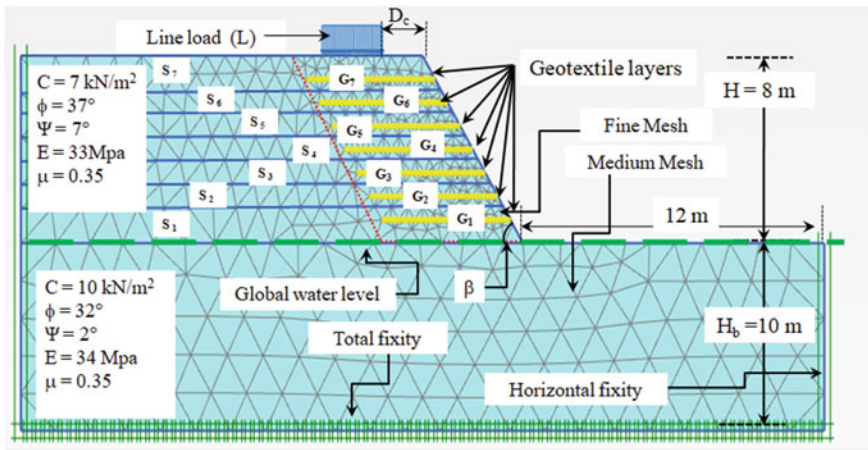
c = cohesion , D_c = Distance of line load from crest of slope, E = Modulus of elasticity, G_i= Geogrid layer, H= Height of embankment , H_b = Base layer height, L= Line load, S_i = Stage of construction , ϕ = Angle of internal friction Ψ = Dilatancy angle , μ = Poisson's ratio, β = slope inclination,

Fig. 1 Modeled geotextile-reinforced slope adopted for finite element analysis

Table 1 Summary of the soil properties and reinforcement parameters used in FEA

Soil/reinforcement	Ψ (°)	c (kN/m²)	ϕ (°)	μ	E (MPa)	EA (kN/m²)	L_g (m)	S_v (m)
Embankment	7	7	37	0.35	33	NA		
Base layer	2	10	32	0.35	34			
Geotextile	NA					4500–13,500	6.4	1.0

c = cohesion, E = Modulus of elasticity, EA = Reinforcement stiffness, L_g = Length of geotextile, N.A = Not applicable, S_v = Vertical spacing of geotextile layers, ϕ = Angle of internal friction, Ψ = Dilatancy angle, μ = Poisson's ratio

4 Model Validations

Model validation was carried out in two phase, i.e., (i) validating values of factor of safety for different values of c_e/c_f (c_e = cohesion for foundation soil and i_f = cohesion of embankment) (ii) validation of factor of safety under reinforced condition. To validate the methodology adopted for the analysis of unreinforced slope under various shear strength value, embankment having weak foundation layer has been taken from the literature (Example 4 Griffith and Lane [3]). Here, $c_e/\gamma H = 0.25$ was kept constant in all the cases generated to validate the model. Figure 3 shows the geometry adopted for the model validation. The slope inclination was kept as 26.56°. The height of the embankment (H) was kept same as the height of foundation layer as mentioned in the literature. The shear strength of the homogenous embankment was kept constant, while shear strength of the foundation layer was varied. The validation model shows a good agreement with the literature for all the values of c_e/c_f. The results obtained from the analysis were compared in the form of factor of safety. Figure 2 shows the validation of computed factor of safety under various values of c_e/c_f. To validate the methodology adopted for the analysis of geotextile-reinforced slope, slope having inclination of 45° and four geotextile layer of equal length were adopted [4]. Moreover, the vertical spacing was kept constant for any two geotextile layer. Tensile stiffness of the geotextile was kept as 1000 kN/m. Geometry for the validation of geotextile-reinforced slope is shown in Fig. 4. Soil properties used in the validation work are summarized in Table 2. The factor of safety (FOS) value obtained was 1.51 through strength reduction method for reinforced conditions. Corresponding FOS for reinforced slope obtained by finite difference program, FLAC was 1.55 reported by Han et al. [4].
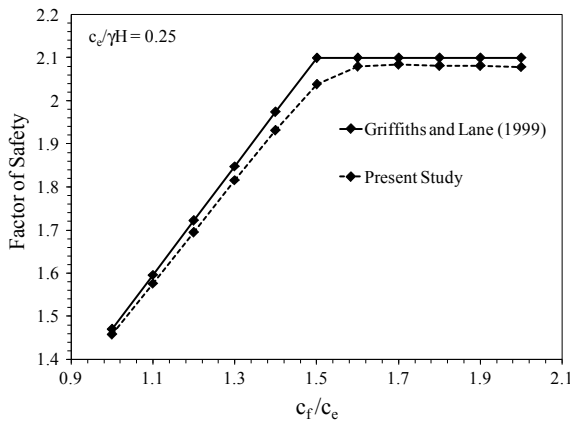

Fig. 2 Validation of computed factor of safety under various values of c_e/c_f
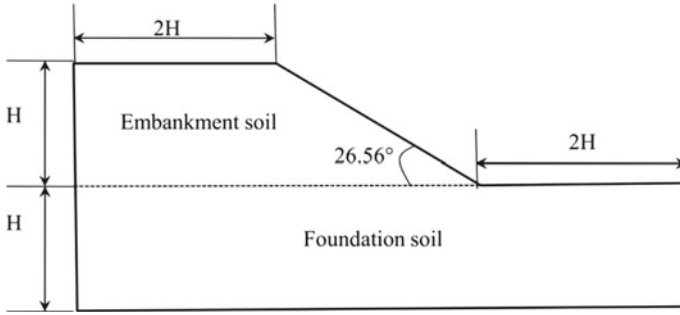
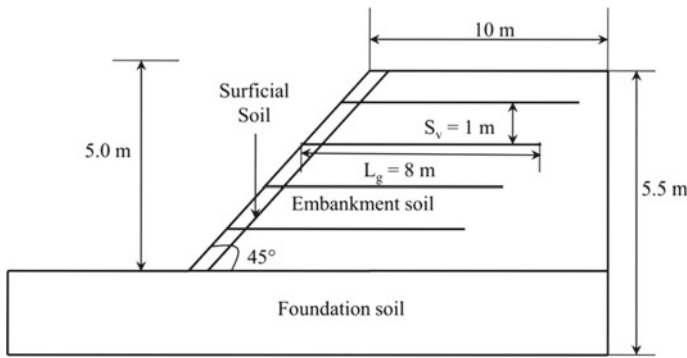**Fig. 3** Geometry for the validation of FOS of slope under unreinforced slope [3]

Fig. 4 Geometry for the validation of FOS of slope under unreinforced slope [4]

Table 2 Summary of soil properties used for validation of reinforced slope

Soil	γ (kN/m^2)	c (kPa)	ϕ (°)	μ	E (MPa)
Embankment	18	2	30	0.3	20
Foundation	18	100	24	0.3	1000
Surficial	18	20	30	0.3	20

c = Cohesion, E = Modulus of elasticity, ϕ = Angle of internal friction, γ = Unit weight, μ = Poisson's ration of soil

5 Results and Discussions

5.1 Effect of Slope Inclination

To capture the trend of development of axial force in the geotextile layers under plastic analysis, various slope inclinations were modeled having same number of geotextile layers and length of each geotextile were kept same. Required length for

the geotextile layer under selected soil inclinations and soil parameters was selected as per Jewell's charts. The selected length for all the geotextile layer was 6.4 m. The uniform vertical spacing of 1.0 m between any two geotextile layers was chosen. Sequential construction method was adopted during analysis process in which whole soil strata was divided into seven stages. During analysis of stage 1, only bottom most geotextile layer, i.e., G1 was kept active, and while for stage 2, bottom two layers were kept active (i.e., G1 and G2). Likewise, similar fashion was adopted for remaining all stages. The trend capture for development of axial force for the slope inclination (β) $\geq 45°$ was almost same. As the slope inclination increase, the maximum horizontal displacement was observed on the upper most portions of the slopes rather than at toe of the slope. While for $\beta \leq 45°$, maximum horizontal displacement was observed at bottom as well as middle portion of slope. Figures 6, 7, and 8 show the development of the axial force along the stage construction for $\beta = 75°$, $\beta = 60°$, and $\beta = 45°$, respectively. For any project it is essential to check factor of safety at each stage. Figure 9 shows the reduction in factor of safety along with stage construction for various slope inclinations. For slope inclination of 75°, the variation in the safety factor is least compare to other slope inclination. The intensity of horizontal displacement was higher compare to vertical displacement irrespective to slope inclination (Fig. 5).

Contradicting current design assumptions, the distribution of axial force with height does not show a triangular pattern with a maximum value at the toe. Instead, the results show that during plastic analysis for $\beta < 45°$ maximum axial force is located approximately at mid-height of the slope. With increase in the slope inclination, the location of the maximum axial force is shifting toward the bottom reinforcement layers. With the slope inclination >60° or 65°, location of maximum overburden shifts downwards at the toe of the slope. The magnitude of maximum axial force almost increases to 7 times when the slope inclination is increase from 45° to 75° (Figure 9).

Fig. 5 Influence of reinforcement stiffness on development of axial force
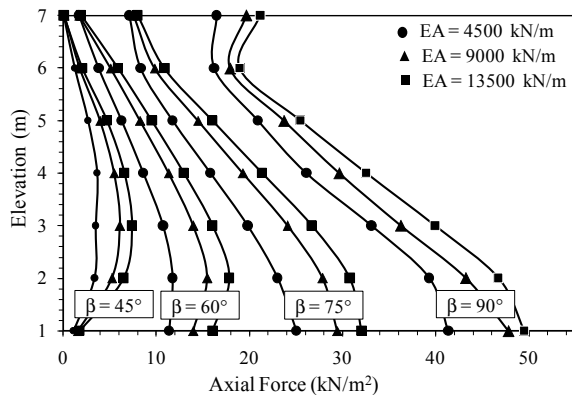
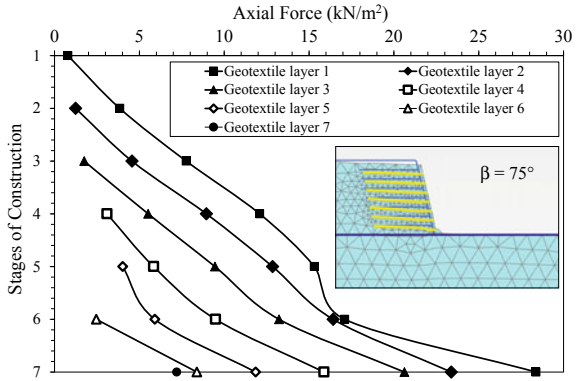**Fig. 6** Development of axial force for geotextile layers for various stages of construction with $\beta = 75°$

Fig. 7 Development of axial force for geotextile layers for various stages of construction with $\beta = 60°$
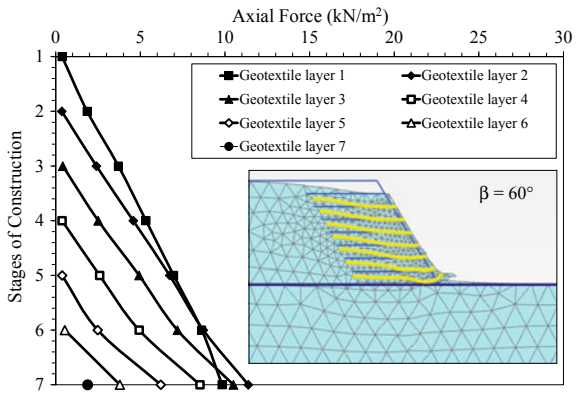

Fig. 8 Development of axial force for geotextile layers for various stages of construction with $\beta = 45°$
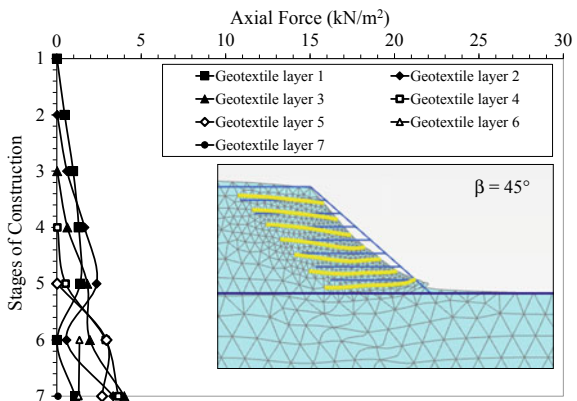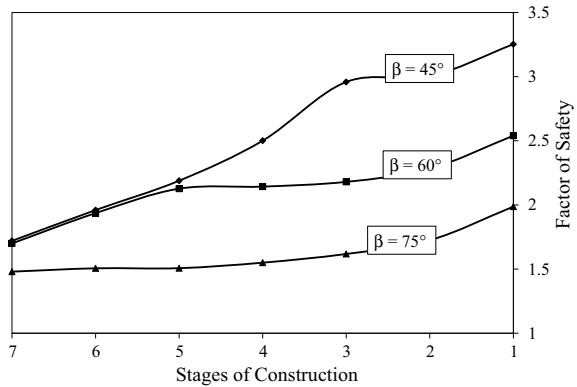
Fig. 9 Variations in factor of safety during stage construction

5.2 Effect of Reinforcement Stiffness

To decide the initial value of stiffness (EA), trial and error method was adopted. The minimum value at which slope with $\beta = 90°$ remains stable was selected. For $\beta = 90°$ with increase in stiffness by 100% from the initial value percentage increase in axial force in bottom most layer of geotextile (i.e., G1) was nearly 14.63%. Moreover, with increase in stiffness value by 200% from the initial value, the percentage increase in axial force was observed to be 19.51% which is also reflected in Fig. 5.

6 Conclusions

A numerical parametric analysis has been performed in order to understand the axial force distribution across geotextile layers for various slope elevations. The following conclusions can be drawn from this study.

- Development of maximum axial force in the reinforcement layers gets influence by slope inclinations. The location of maximum axial force tends to shifts downward with increase in slope inclinations.
- Stresses developed in bottom most geotextile layer in all steep slopes increase with increase in stages of construction. Hence, due to this, axial force tends to be increasing. For slope having lower inclination angle, maximum axial force is obtained at second or third stage of construction.
- Location of maximum axial force is not influenced by the stiffness of the geotextile layers.
- Maximum axial forces were observed to develop in all geotextile layers for the slope having $\beta = 90°$ when it compared to other slope inclinations. With an increase in axial stiffness (EA) of geotextile layers by 100%, it was noticed that only 16% increase in axial force at the bottommost geotextile layer for the slope with 75° inclination.

References

1. Bergado, D.T., Long, P.V., Murthy, B.R.S.: A case study of geotextile reinforced embankment on soft ground. Geotext. Geomembr. **20**, 343–365 (2002)
2. Duncan, J.M.: State of the art: limit equilibrium and finite element analysis of slopes. J. Geotech. Eng. ASCE **122**(7), 577–596 (1996)
3. Griffith, D.V., Lane, P.: Slope stability analysis by finite elements. Geotechnique **49**(3), 387–403 (1999)
4. Han, J., Leshchinsky, D., Shao, Y.: Influence of tensile stiffness of geosynthetic reinforcement on performance of reinforced slopes. In: Proceedings in Geosynthetics-7 ICG-Delmas, pp. 197–200 (2002)
5. Holtz, R.D., Barry, R.C., Berg, R.R.: Geosynthetic design and construction guidelines (1998)
6. Jewell, R.A., Paine, N., Wood, R.I.: Design methods for steep reinforced embankments. In: Proceedings of the Polymer Grid Reinforcement Conference London, pp. 70–81 (1984)
7. Koerner, R.M.: Designing with Geosynthetics, 5th edn. Pearson Prentice Hall, New Jersey (2005)
8. Mandal, J.N., Labhane, L.: A procedure for the design and analysis of geosynthetics reinforced soil slope. Geotech. Geol. Eng. **10**, 291–319 (1992)
9. Rotte, V.M., Gajjar, H.V.: Influence of reinforcement pattern on the performance of geotextile-reinforced slopes. In: Advances in Computer Methods and Geomechanics. Lecture Notes in Civil Engineering, vol. 56, pp. 397–408. Springer (2020)
10. Sommers, A.N., Vishwanadham, B.V.S.: Centrifugal model test on the behavior of strip footing on geotextile reinforced slopes. Geotext. Geomembr. **27**, 497–505 (2009)
11. Tiwari, G., Samadhiya N.K.: Factors influencing the distribution of peak tension in geosynthetic reinforced soil slopes. Indian Geotech J **46**(1), 34–44 (2016)
12. Vishwanadham, B.V.S., König, D.: Centrifuge modeling of geotextile reinforced slopes subjected to differential settlement. Geotext. Geomembr. **27**, 77–88 (2009)
13. Zornberg, J.G., Arriaga, F.: Strain distribution within geosynthetic reinforced slope. J. Geotech. Geoenviron. Eng. **123**(1), 32–45 (2003)